buzas.krisztina_52_23

MTA DOKTORI ÉRTEKEZÉS

DAGANATOK KOMMUNIKÁCIÓS STRATÉGIÁI AZ IMMUNRENDSZER VÁLASZAINAK TÜKRÉBEN

DR. BUZÁS KRISZTINA

SZEGEDI TUDOMÁNYEGYETEM
SZENT-GYÖRGYI ALBERT ORVOSTUDOMÁNYI KAR -
TERMÉSZETTUDOMÁNYI ÉS INFORMATIKAI KAR
IMMUNOLÓGIAI TANSZÉK

EÖTVÖS LORÁND KUTATÁSI HÁLÓZAT
SZEGEDI BIOLÓGIAI KUTATÓKÖZPONT
BIOKÉMIAI INTÉZET

SZEGED
2023

buzas.krisztina_52_23

„A természet nem ért tréfát: mindig igaz,
mindig komoly, mindig szigorú, mindig igaza van;
a hibák és tévedések mindig az emberéi.”
Johann Wolfgang von Goethe

buzas.krisztina_52_23

TARTALOMJEGYZÉK

FONTOSABB RÖVIDÍTÉSEK JEGYZÉKE

	Angol	**Magyar**
AFM	atomic force microscopy	atomerő mikroszkópia
Alix	ALG-2 interacting protein X	ALG-2 interaktív X fehérje
ANOVA	analysis of variance	varianciaanlaízis
AUC	area under the curve	görbe alatti terület
BBB	blood-brain barrier	vér-agy gát
BMDCs	bone marrow-derived cells	csontvelő eredetű sejtek
BOLD	bleomycin, oncovin, lomustine, dacarbazine	bleomicin, onkovin, lomusztin, dakarbazin
C. pn.	*Chlamydophila pneumoniae*	*Chlamydophila pneumoniae*
C. pneumoniae	*Chlamydophila pneumoniae*	*Chlamydophila pneumoniae*
CA	classification accuracy	osztályozási pontosság
CAF	cancer associated fibroblast	tumor asszociált fibroblaszt
CCR	chemokine receptor	kemokin receptor
CT	computed tomography	komputertomográfia
CNS	central nervous system	központi idegrendszer
CXCL	C-X-C motif ligand	kemokin C-X-C motívum ligand
CXCR	C-X-C chemokine receptor	kemokin C-X-C motívum receptor
CSF	cerebrospinal fluid	cerebrospinális folyadék
CSF	colony stimulating factor	kolónia-stimuláló faktor
DAMP	danger-associated molecular pattern	veszély asszociált molekuláris mintázat
DAPI	4′,6-diamidino-2-phenylindole	4′,6-diamidino-2-fenilindol
DC	dendritic cell	dendritikus sejt
DMEM	Dulbecco's Modified Eagle Medium	Dulbecco-féle módosított Eagle médium
DPBS	Dulbecco's phosphate-buffered saline	Dulbecco-féle foszfát-pufferelt sóoldat
EBV	Epstein-Barr virus	Epstein-Barr vírus
ECM	extracellular matrix	extracelluláris mátrix
ELISA	enzyme-linked immunosorbent assay	enzimhez kötött immunoszorbens vizsgálat
EMT	epithelial-mesenchymal transition	epitéliális-mezenchimális átmenet
ER	endoplasmatic reticulum	endoplazmatikus retikulum
EV	extracellular vesicle	extracelluláris vezikula
FACS	fluorescence-activated cell sorting	áramlási citometria
FBS	fetal bovine serum	magzati szarvasmarha szérum
FDR	false discovery rate	hamis felfedezési arány
G1 phase	gap1 phase	gap1 fázis
G2 phase	gap2 phase	gap2 fázis
HBSS	Hanks' Balanced Salt solution	Hank-féle pufferelt sóoldat
HNSCC	head and neck squamous cell carcinoma	fej-nyaki laphámsejtes karcinóma
HRP	horseradish peroxidase	tormaperoxidáz
HSP70	70 kDa heat shock protein	70 kDa-os hősokkfehérje
IFN	interferon	interferon
IL	interleukin	interleukin

	Angol	**Magyar**
IL-24	interleukin-24	interleukin-24
IPA	Ingenuity Pathway Analysis	Ingenuity Pathway Analysis
ITG	integrin	integrin
LC-MS/MS	liquid chromatography-tandem mass spectrometry	folyadékkromatográfiával kapcsolt tömegspektrometria
LRR	leucine-rich repeats	leucinban gazdag ismétlődések
LPS	lipopolysaccharide	lipopoliszacharid
M phase	mitosis phase	mitózis fázis
MAPK	mitogen-activated protein kinase	mitogén-aktivált protein kináz
MDA-7	melanoma differentiation-associated gene-7	melanóma differenciálódással asszociált gén-7
MEF	mouse embryonic fibroblast	egér embrionális fibroblaszt
MISEV2018	Minimal information for studies of extracellular vesicles 2018	Alapvető információk az extracelluláris vezikulák tanulmányozásához 2018
MLANA	melan-A	melan-A
MMP-(n)	matrix metalloproteinase	mátrix metalloproteináz
MMP-9	matrix metalloproteinase 9	mátrix metalloproteináz 9
MRI	magnetic resonance imaging	mágneses rezonancia képalkotás
mRNS	messenger RNA	hírvivő RNS
MSC	mesenchymal stem cell	mezenchimális őssejtek
MSC^{PD-1+}	melanoma-like PD-1+ MSC	melanómaszerű PD-1+ MSC
MVB	multivesicular body	multivezikuláris test
MyD88	myeloid differentiation primary-response protein 88	mieloid differenciációs primer válasz fehérje 88
ncRNS	non-coding RNA	nem kódoló RNS
NK	natural killer cell	természetes ölősejt
NO	nitric oxide	nitrogén-monoxid
NPC	nasopharyngeal carcinoma	nazofaringeális karcinóma
NTA	nanoparticle tracking analysis	nanorészecske-követő analízis
PAMP	pathogen-associated molecular pattern	patogén asszociált molekuláris mintázat
PCA	principal component analysis	főkomponens analízis
PCR	polymerase chain reaction	polimeráz láncreakció
PD-1	programmed cell death protein-1	programozott sejthalál protein 1
PD-1L	programmed cell death protein ligand-1	programozott sejthalál protein 1 liganduma
PET	positron emission tomography	pozitronemissziós tomográfia
PMN	pre-metastatic niche	pre-metasztatikus niche
Q-PCR	quantitative polymerase chain reaction	kvantitatív polimeráz láncreakció
ROC	receiver operating characteristic	vevő működési karakterisztika
ROI	reactive oxygen intermediates;	reaktív oxigén intermedierek
RT	room temperature	szobahőmérséklet
sEV	small extracellular vesicle	kisméretű extracelluláris vezikula
S phase	synthesis phase	szintézis fázis
SD	standard deviation	szórás
SEM	standard error of the mean	szóráshiba
SEM	scanning electron microscopy	pásztázó elektronmikroszkópia
sEV	small extracellular vesicles	kisméretű extracelluláris vezikula

	Angol	**Magyar**
SNV	standard normal variate	standard normál változó
SOLiD	sequencing by oligonucleotide ligation and detection	szekvenálás oligonukleotid ligálással és detektálással
SVM	support vector machine	tartó vektor mechanizmus
TAM	tumor associated macrophages	tumor asszociált makrofágok
TEM	transmission electron microscopy	transzmissziós elektron mikroszkópia
TIR	toll-interleukin-1 receptor	toll-interleukin-1 receptor
TLR	toll-like receptors	toll-like recetorok
TME	tumor microenvironment	tumor mikrokörnyezet
TNF	tumor necrosis factor	tumor nekrózis faktor
Tsg101	tumor susceptibility gene 101	tumorérzékenységi gén 101

A dolgozatban mindössze néhány alkalommal előforduló rövidítések magyarázata a szövegben található.

BEVEZETÉS

A dolgozatban ismertetett kísérletes munkák a daganatsejtek környezetükkel való kommunikációjának módjaira és azok következményeinek feltárására irányultak.

Megmutattuk, hogy kísérletes modellekben a melanóma sejtek és a tumor asszociált makrofágok szolubilis faktorokkal történő kommunikációja TLR ligandummal befolyásolható, ezáltal a daganatot infiltráló, tumortámogató tulajdonságú immunsejtek antitumorális polaritásúvá tehetők. A szolubilis kommunikációs elemek közül mélyebben vizsgáltuk az antitumorális hatásáról ismert interleukin-24-et, amelyről kimutattuk, hogy a TLR ligandok hatására is termelődő interleukin, G protein kapcsolt jelátviteli mechanizmusokon keresztül *in vitro* és *in vivo* is segíti a mieloid sejtek migrációját.

A daganatsejtek intercellulárisan megvalósuló vezikuláris kommunikációja kapcsán *in vitro* kísérletes rendszerben bebizonyítottuk, hogy a melanóma exoszómák képesek a daganatszövet mátrixának őssejtes elemeiben onkogén genetikai programot, többek közt PD-1 expressziót indítani. *In vivo* modellekben ezen folyamatok a daganatos megbetegedés progressziójához vezettek.

Az extracelluláris vezikulák tanulmányozása során arra a következtetésre jutottunk, hogy a vezikulák információtartalma függ a kibocsájtó sejt típusától, valamint molekuláris mintázatuk stresszorok hatására is megváltozik. Ezen vátozások a vezikulákat felvevő sejtek biológiai működését is befolyásolják, többek között a sejtciklust, a migrációs vagy aggregációs kapacitást, osztódási, illetve apoptotikus hajlamot.

Klinikai vizsgálatainkban arra a következtetésre jutottunk, hogy a központi idegrenszer tumoraiból származó szérum vezikulák a megbetegedésre jellemző molekuláris mintázatot hordoznak, amely a vezikulák Raman spektrumában is megnyilvánul. A fehérjemintázatok és Raman spektrumok mélytanuló módszerekkel történő analízise invazív beavatkozások nélkül alkalmassá tehető a betegcsoportok egyértelmű elkülönítésére.

1. SZAKIRODALMI ÁTTEKINTÉS

1.1 TLR ligandumok hatása a daganatos mikrokörnyezetben

A toll-like receptor (TLR) család a mintázatfelismerő receptorok egy olyan csoportját képezi, amelyek ugyan nem indukálják az immunsejtek fagocitikus aktivitását, de a sejtek működését drámaian megváltoztató jelátviteli mechanizmusokat indíthatnak be. Mivel a veleszületett immunitás elemeinek, a makrofágoknak, illetve a dendritikus sejteknek a felszínén is megtalálhatóak, gyorsan reagáló, hatékony eszközeit képesek mozgósítani a védekezőrendszerünknek, amennyiben megfelelő aktivációs jelet kapnak. Bár felfedezésük Jules Hoffmann, Bruce Beutler, és Ralph Steinman nevéhez kötődik, amit 2011-ben Nobel díjjal ismertek el, a veleszületett immunitás antitumorális komponenseinek aktiválása már több mint egy évszázada is felmerült, Coley korai munkáiban (McCarthy, 2006).

A TLR-ek felismerik mind a szervezetet támadó exogén kórokozókat a speciális patogén asszociált molekuláris mintázataiknál (PAMP) fogva, mind pedig a nem-kórokozókból származó, de a testünk biológiai identitását kockáztató, endogén eredetű, veszély asszociált molekuláris mintázatokat (DAMP), amelyek daganatos elváltozásokkal is társíthatók lehetnek (Matzinger, 1994, 2002). Speciális eloszlásuk és működésük kapcsán szerepet játszanak a veleszületett és a szerzett immunitás összekapcsolásában. A ligandumok TLR-ekhez való kapcsolódása specifikus intracelluláris jelátviteli kaszkádokat aktiválnak, amelyek elindítják a gazdaszervezet védekezési reakcióit. Az ilyen kötődések és következményeik természetesen ligandum- és sejttípus-függőek, de többnyire a gyulladásgátló, Th1-es citokinek és I. típusú interferon (IFN) termeléséhez vezetnek (El-Zayat et al., 2019). A TLR-ek daganatos folyamatok elleni védekezésben való részvétele egyértelműnek látszik a DAMP-okra adott potenciális válaszreakciók miatt, azonban jelen dolgozat első szakasza a közvetett, PAMP-ok által indukált immunológiai folyamatok antitumorális hatásait vizsgálja.

1.1.1 A TLR2 és a TLR4 felépítése és jelátviteli mechanizmusai

A TLR-ek hírvivő RNS-ének (mRNS) expressziója nem korlátozódik az immunszövetekre, mint például a lép, a csecsemőmirigy, a mandulák, a nyirokerek és a nyirokcsomók, hanem eloszlik az összes szövetben, beleértve ebbe a perifériás vér leukocitáit vagy a szívet, a májat, a hasnyálmirigyet, a vastagbelet, a vékonybelet, a tüdőt, vesét, petefészeket, placentát, herét, prosztatát, vázizmot de még a központi idegrendszert is (Zarember & Godowski, 2002; Qi et al., 2011). Kifejeződnek az összes veleszületett immunsejten, beleértve a makrofágokat, a természetes ölősejteket (NK), a dendritikus sejteket (DC) és a keringő leukocitákat, például a

monocitákat és a neutrofil granulocitákat, valamint kifejeződnek az adaptív immunsejteken, például a T- és B-limfocitákon, de nem-immunsejteken, például az epitheliális és endoteliális sejteken, valamint a fibroblasztokon is (Delneste et al., 2007). Így elmondható, hogy a TLR-ek eloszlása arra predesztinálja ezt a receptor családot, hogy a lehető legszélesebb körben képesek legyenek antigén ingerek érzékelésére és válaszreakciók elindítására.

A TLR-ek I. típusú transzmembrán fehérjék, amelyek extracellulárisan 20-27, leucinban gazdag ismétlődésekkel (LRR), transzmembrán doménekkel és intracelluláris toll/interleukin-1 (IL-1) receptor (TIR) régiókkal rendelkeznek, amelyek szükségesek egyrészt a PAMP/DAMP szignálok felismeréséhez, megkötéséhez, másrészt a downstream jelátviteli utak aktiválásához. A TLR-eket megkülönböztető legfontosabb jellemzők a ligandum specifitása, az aktiválható jelátviteli utak és a szubcelluláris lokalizáció különbözőségei (Singh et al., 2014).

A TLR-ek funkcionálisan csoportosíthatóak, mégpedig a sejtmembránhoz kötött, illetve az intracelluláris receptorok családjaira:

- A sejtmembránon megjelenő TLR-ek, mint a TLR2-TLR1 heterodimerek, a TLR6, a TLR4, TLR5, és a TLR10.
- Intracelluláris TLR-ek a nukleinsav szenzorok, mint a TLR3, TLR7, TLR8, és TLR9. Ezek értelemszerűen az endoplazmatikus retikulum (ER), az endoszómák, és a lizoszómák területére lokalizálódnak (Sellge & Kufer, 2015).

Bár endogén és exogén ligandumokat is képesek a TLR-ek érzékelni és azokra válaszreakciókat kialakítani, a dolgozat szempontjából az exogén ligandumok feldolgozása a hangsúlyosabb. Exogén ligandumok közé sorolhatóak azok a PAMP struktúrák, amelyek például bakteriális komponensekből származnak, mint a Gram negatív baktériumok sejtfalából származó lipopoliszacharid (LPS) vagy a Gram pozitívak lipoteikol sav (LTA) komponense (El-Zayat et al., 2019).

Emlősökben a TLR ligandumok megkötése során aktiválódó szignál mechanizmusok lefutását öt különböző adaptor molekula segíti:

- Mieloid differenciációs primer válasz fehérje 88 (MyD88).
- TIR domén-t tartalmazó adaptor protein (TIRAP or MAL).
- TIR domén-t tartalmazó adaptor protein indukálta IFN-β (TRIF).
- TRIF-kapcsolt adaptor molekula (TRAM).
- Steril α- és armadillo-motívumot tratalmazó protein (SARM) (Akira et al., 2006).

Így, bár pontos és minden részletében tisztázott magyarázat egyelőre nem létezik a TLR ligandumok antitumorális immunitásban betöltött szerepére, feltehetően két, egymással szorosan összefüggő mechanizmusnak lehet kulcsfontosságú szerepe a daganatellenes válaszokban, nevezetesen a TLR-ek által indukált Th1 tengelynek és az ezzel együttműködő makrofágpolarizációnak.

Az MyD88 szignálútvonal elengedhetetlen a TLR2, 4, 5, 7, 8, és 9 aktiválódása során bekövetkező sejtbiológiai folyamatok lefutásához (Burns et al., 2003), illetve a TIRAP aktivációja is MyD88-függő és asszociált a TLR2 és 4 indukciójával (Mansell et al., 2004; Bernard & O'Neill, 2013).

Mindezek a molekuláris mechanizmusok vezetnek el azon folyamatok megértéséhez, amelyek a TLR-ek működését antitumorális mechanizmusokkal kapcsolják össze.

1891-ben William B. Coley ortopéd sebész arra a megfigyelésre alapozva, hogy „amelyik daganat elfertőződik, az meggyógyul", inoperábilis, szarkómában szenvedő betegeibe streptococcus kivonatot fecskendezett, elindítva ezzel az immunterápiák alkalmazását a daganatos megbetegedések esetében. Bár a beavatkozás meglehetősen veszélyes volt és páciensei közül többen belehaltak a bakteriális fertőzésbe, az alkalmazott baktériumszuszpenzió a daganatok méretének csökkenését, esetenként teljes gyógyulást hozott az egyébként menthetetlen betegek számára (McCarthy, 2006). A kezdeti terápiás próbálkozások tapasztalatai alapján *Streptococcus pyogenes* és *Serratia marcenscens* inaktivált szuszpenziójával vizsgálatokat indítottak a daganatos betegek kezelésére (Hobohm, 2001; Coley, 1891, 1991). 2003-ban az European Organization for Research and Treatment of Cancer által végzett nagy klinikai tanulmány váratlan bizonyítékot szolgáltatott a mikrobiális indukció rákos megbetegedésekre gyakorolt pozitív hatására. Krone B. és mtsai. kimutatták (Krone et al., 2005), hogy a lázzal járó fertőzések, valamint a gyermekek olyan intracelluláris kórokozókkal történő vakcinálása, mint a Bacillus Calmette-Guerin vagy a vaccinia vírus, jelentősen csökkenti a melanóma előfordulását (Bickels et al., 2002; Hall, 1997). Ennek ellenére, mivel ezen izgalmas adatok reprodukálhatósága alacsony, még mindig hiányoznak a részletes és meggyőző magyarázatok, illetve a TLR ligandumok immunterápiás szerként való használatára vonatkozó terápiás protokollok.

Bár általánosan elfogadott, hogy a daganatellenes immun effektor mechanizmusok átfedésben vannak a baktériumok elleni immunválaszokkal (JAMA, 1894; McCarthy, 1995; Hoption Cann et al., 2003; COLEY, 1934), a mikrobák által kiváltott pontos tumorellenes mechanizmus még nem ismert minden részletében. A daganatellenes folyamatokat tekintve

azonban az is elfogadott tény, hogy az immunrendszer polarizációs mintázatának megváltozása határozza meg a rosszindulatú betegségek kimenetelét (Codman, 1935; Johnston & Novales, 1962). Ez utóbbi esetben az immunválasz egyik kulcsszereplői azok a makrofágok, amelyek M1 típusú polarizációja közvetíti az immunrendszer tumorellenes hatását (Nauts & McLaren, 1990; Chang & Shu, 1996; Chamberlain & Kaufman, 2000).

1.1.2 Polarizált makrofágok

Amint az közismert, a daganatszövet nem egy homogén sejtcsomó, számos sejttípus alkotja. A sokszor genetikailag és morfológiailag is heterogén tumorsejt populációkon kívül fibroblasztok, endotélsejtek, szöveti őssejtek, immunsejtek közössége tartja életben és működteti a tumort. Az immunsejtek a daganat által termelt szolubilis elemeknek, növekedési faktoroknak, citokineknek, kemokineknek megfelelően polarizált funkciókkal rendelkezhetnek. Amíg az I. típusú polarizálódás – legyen az makrofág, neutrofil granulocita, citotoxikus T sejt vagy plazmocitoid dendritikus sejt – a daganatok regresszióját eredményezi, addig a II. típusú polarizáció egy immunszuppresszív állapotot idéz elő és a daganatok túlélésének, progressziójának irányába mutat. Így a tumorok túlélése erősen függ az I. és a II. típusú immunsejtek arányától. Egyben ezen állapotokból az is egyenesen következik, hogy a polaritás I. irányba való eltolódása akadályozhatja a daganatok progresszióját (Hinshaw & Shevde, 2019; Vitale et al., 2019).

A makrofágok szerepe az antitumorális immunitásban nem ismert minden vonatkozásában. Még azt sem tudjuk, hogy egészen pontosan milyen tényezők aktiválják a tumor asszociált makorfágok (TAM) antitumorális irányba fordulását. Feltételezhetően a DAMP-ok, illetve a gyulladásos citokinek (IFN-γ, TNF- α, IL-1ß) segítik a makorfág aktivációt illetve makrofág polarizációt, melynek a végkimenetele többnyire a nitrogén-monoxid (NO) termelés révén történő sejtpusztítás kell legyen (Martinez & Gordon, 2014; Curren Smith, 2015; Dehne et al., 2017).

A tumor asszociált makrofágok az alternatív makrofágpolarizáció során az IL-13 és IL-4 hatására kollagénszintézisre és fibrotikus folyamatok elindítására képesek, amely szöges ellentétben áll az IFN-γ által kiváltott, elsőként leírt antimikrobiális és antitumorális makrofág válaszokkal. Ezen alternatívan aktiválódó, II. típusú makorfágok a kollagénszintézis folyamatain kívül leállítják a gyulladásos folyamatokat és érképződést generálnak, amely a daganat túlélésének irányába hat. Jól látható tehát, hogy a kényes M1 és M2 egyensúly kruciális kérdés a daganatok életciklusában. Azonban az M1 és M2 polaritási állapotok nem tekinthetőek diszkrét értékeknek, sokkal inkább egy kontinuum tagjainak, ahol a kontinuum

számos, kevert típusú makrofág alpopuláció elegyét jelentheti. Mindazonáltal az I. és II. típusú makrofágok jellegzetes citokin-kemokin profillal és cluster determináns molekulákkal rendelkeznek (Mantovani et al., 1992). Ezen profilok egyensúlya meghatározza az adott pillanatban fennálló polaritási viszonyokat (Mantovani et al., 2002; Dehne et al., 2017; Boutilier & Elsawa, 2021). Vizsgálataink időpontjában Mantovani munkáit tekintettük mérvadónak a polaritási típusok meghatározásához (**1. ábra**).

A fentebb említett kontinuum bemutatását szolgálja az **1. ábra**. Az M1 sejtek alapvetően azokat a tulajdonságokat hordozzák, amelyeket a klasszikus LPS illetve IFN-γ indukció képes kiváltani (zöld). Az M2 sejtek esetében az IL-4-re és az IL-13-ra adott válaszreakciók (sárga), az IL-10 hatások (piros) illetve az IL-4, IL-13 és IL-10 eredőjéből (kék) kialakuló változások a mérvadóak. Azon makrofágok, amelyek a klasszikus aktivációs szignáloknak, az IFN-γ-nak illetve az LPS-nek kitettek, opszonizáló receptorokat expresszálnak (pl. FcγRIII/CD16), míg a II. típusú makrofágok nem-opszonizáló receptorokkal karakterizálhatóak (pl. mannóz receptor – MR). Az M1 sejtekben magasabb a redukált glutation arány, amely szintén az IFN-γ és az IL-4 ellentétes reduktív státuszának köszönhető (Dobashi et al., 2001). Az IL-1 jelátviteli utak különbözőképpen szabályozottak a polarizált makrofág populációkban. Az IL-4, az IL-13 és a glükokortikoid hormonok a II. típusú decoy receptorok expresszióját fokozzák, míg az IFN-γ és az LPS gátolják azt. Az IFN-γ és az LPS upregulálja az I. típusú receptort, és az IL-1R járulékos proteint (IL-1RacP) (Mantovani et al., 2001). Az IL-4 és az IL-13 indukálja az IL-1ra produkciót és gátolja az IL-1-et. Tehát az IL-1 tengely pro- és anti-inflammatórikus komponensei összehangoltan szabályozottak olyan szignálok által, amelyek az I. illetve a II. típusú makrofág polarizációt is meghatározzák. Az IL-10 upregulálja a CCR1, CCR2 és CCR5 kemokin receptorokat, míg a CXCR2 és a CXCR4 csak részlegesen downregulálódik ugyanezen kondíciók mellett. Az IL-4 és az IL-13 nem módosítja a CC kemokin receptorok expresszióját, azonban a monocitákon indukálja a CXCL8 (IL-8) receptorok kifejeződését. Ezzel ellentétben az LPS és az IFN-γ monocitákon downregulálja a CCR1, a CCR2 és a CCR5 megjelenését (Sozzani et al., 1998).

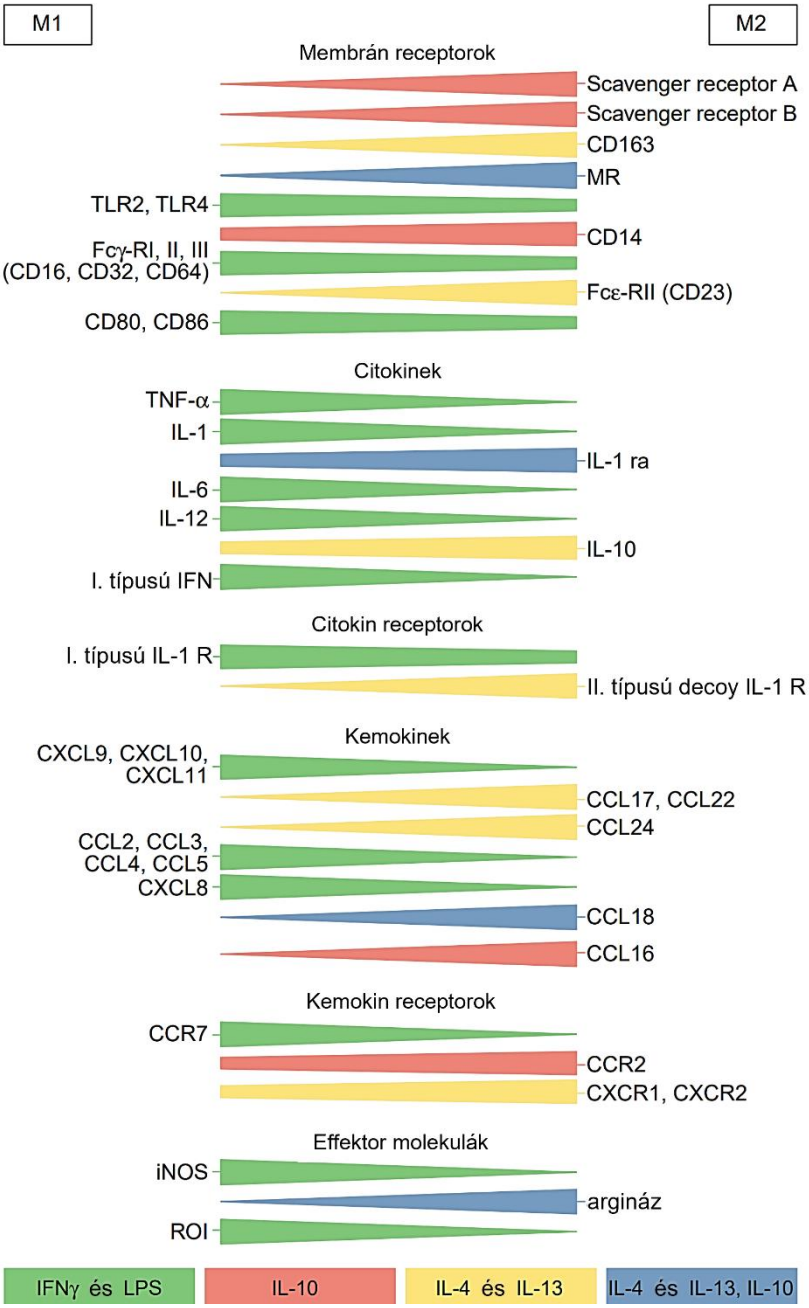

1. ábra. M1 és M2 makrofágok, a kontinuum szélső pontjai.

A polarizált makrofágok expresszálta receptorok, effektor molekulák, citokinek és kemokinek (Mantovani et al., 2002).

1.1.3 TLR ligandumok által befolyásolt makrofág válaszok

Az antigénbemutató sejtek, közöttük a monociták, illetve makrofágok – amelyek fontos szerepet játszanak az elsővonalbeli riasztások őrszemeiként vagy közvetítőiként – az adekvát adaptív immunválasz kialakulásához szükségesek. Mikrobiális antigének hatására a makrofágok többnyire mikrobicid hatáskörre tesznek szert, vagyis ez általában hatékony immunválaszok kialakulásához vezet (Hoebe et al., 2004; Benoit et al., 2008).

A makrofágok bakteriális fertőzésekre adott közös válasza elsősorban az M1 polarizációban részt vevő gének felszabályozását foglalja magában. A hivatásos antigénprezentáló sejtek TLR-jeinek, illetve PAMP-jainak bakteriális ligandumokkal való aktiválása után a génexpressziós mintázat vizsgálata túlnyomórészt M1 polarizációra utal.

Ide tartoznak olyan citokineket kódoló gének, mint például a TNF, IL-6, IL-12, IL-1β, a citokin receptorok, például az IL-7R és az IL-15RA, egyes kemokinek, például a CCL2, CCL5 és CXCL8, valamint a CCR7 kemokin receptor. Más, M1-hez kapcsolódó, szabályozott gének kódolják az indolamin-pirrol 2,3 dioxigenáz és NO szintetáz 2 (NOS2) enzimeket, amelyek részt vesznek a makrofág mikrobicid aktivitásban, valamint a kostimuláló molekulákat, mint például a CD80 és CD86. Úgy tűnik, hogy az IL-1ra az egyetlen gén, amely az M2 polarizációjához kapcsolódik, és amelyet bakteriális fertőzés után fejeznek ki. Valószínű, hogy ez a robusztus M1-hangsúlyos aktiváció megfelel a makrofágokban indukált baktériumok elleni közös riasztási szignálnak, mivel ezeknek a géneknek a többsége a baktériumfajtól függetlenül indukálódik (Benoit et al., 2008).

Szakirodalmi adatok számos, bakteriális fertőzés kapcsán kialakuló M1 polarizációt mutatnak be. Ilyen például az a kutatás, amely M1 makrofágok protektív szerepét írja le olyan egerekben, amelyekben sérült az IL-12 útvonal lefutása (Jouanguy et al., 1999). De például a *Mycobacterium tuberculosisra* adott egér makrofág-válaszok kezdeti transzkriptomikai elemzése is a mycobacteriumok és az IFN-γ által modulált gének átfedését írja le, ami szintén megfeleltehető egy M1 programnak (Ehrt et al., 2001). Aktív tuberkulózisban szenvedő betegektől gyűjtött klinikai adatok alapján az *M. tuberculosis* fertőzés korai szakaszában a makrofágok az M1 profil irányába polarizálódnak (Chacón-Salinas et al., 2005). Más mycobacterium betegségeket, például a Buruli betegséget (*Mycobacterium ulcerans*) és az opportunista fertőzéseket (*Mycobacterium avium*) szintén a makrofágok M1 polarizációja jellemzi és szabályozza (Kiszewski et al., 2006; Murphy et al., 2006). Immunhiányos betegekben és terhes nőkben akár fatális kimenetelű fertőzéseket is okozó *Listeria monocytogenes* M1 programot indukál, ezzel megakadályozza a bakteriális fagoszóma escape-et, és stimulálja a baktériumok intracelluláris *in vitro* és *in vivo* elpusztítását (Shaughnessy & Swanson, 2007). Azok az egerek, amelyekből hiányzik az IFN-γ és a TNF, az M1 polarizáció két kanonikus markere, elpusztulnak a *L. monocytogenes* fertőzés következtében (Pfeffer et al., 1993). A *Salmonella typhi*, a tífuszos láz és a *Salmonella typhimurium*, a gasztroenteritisz kórokozója indukálja az emberi és egér makrofágok M1 polarizációját, és ez az indukció összefüggésben áll a fertőzés kordában tartásával.

Hasonlóképpen, a chlamydia fertőzések akut fázisát IFN- γ vezérelte M1 polarizáció jellemzi (Rottenberg et al., 2002). A sor még hosszasan folytatható lenne például *a Coxiella burnetii, Yersinia enterocolica, Salmonella dublin, Brucella suis* kórokozók által kiváltott immunválaszok illetve makrofágpolarizáció bemutatásával.

A fentebb bemutatott példák a molekuláris biológia eszközeivel már olyan bizonyítékokkal szolgálnak, amelyek tényszerűen alátámasztják azokat a korai, klinikai tapasztalatokon alapuló megfigyeléseket, amelyek a bakteriális antigének antitumorális immunválasz kifejlődését elősegítő hatásairól szóltak. Ezen bakteriális antigénekre adott immunválaszok egyaránt magukba foglalják a makrofágok, illetve egyéb immunsejtek I. típusú polarizációját, kostimulációs molekulák overexpresszióját, a Th1-es tengelyhez sorolható kemokinek és citokinek termelődését vagy a reaktív oxigén gyökök képzésére való képesség kifejeződését. Az ilyen TLR, illetve PAMP ligandumok hatására kialakuló antibakteriális immunválaszok egyrészt közvetlenül elősegíthetik a daganatos sejtek pusztulását, másrészt a közvetett hatásuk révén az adaptív immunválasz beindítása segítségével bizonyíthatóan antitumorális hatással bírnak (Fan et al., 2022).

1.2 Az IL-24 jellemzői

1.2.1 Az IL-24 szerkezete és helye a citokinek családjában

Az interleukin-24 (IL-24) a melanóma differenciálódással asszociált gén-7 (MDA-7) terméke, amely az IL-10 géncsaládról átíródó, szekretálódó citokinek csoportjának a tagja. Felfedezése során a HO-1 melanóma sejteket az áttétképző képesség csökkentése céljából, a terminális differenciáció érdekében IFN-β és mezerein kezelésben részesítettek. A terminális differenciációt megelőző, majd azt követő cDNS könyvtárak elkészítésekor találták meg az MDA-7 gént, mint az egyik legnagyobb expressziós különbséget mutató régiót (Menezes et al., 2018). Az emberben az 1q32–33 kromoszómán található MDA-7 gén hét exont és hat intront tartalmaz. Az MDA-7 cDNS-e 1718 bázispárból áll, a róla képződő fehérje pedig 206 aminosavat kódol (E. Y. Huang et al., 2001). Szekretált citokin lévén az IL-24 egy 49 aminosavból álló N-terminális hidrofób szignálpeptidet tartalmaz és három feltételezett N-glikozilációs helyet a 85., 99. és 126. aminosav pozíciókban (Sauane, Gopalkrishnan, Sarkar, et al., 2003). Ezenkívül a 101–121. aminosavak közötti régióban azonosítottak egy IL-10 signature motívumot; három protein kináz C konszenzus foszforilációs helyet (a 88., 133. és 161. aminosavaknál) és három kazein-kináz II konszenzus foszforilációs helyet (a 101., 111. és 161. aminosavaknál) (Sauane, Gopalkrishnan, Sarkar, et al., 2003). Az IL-24 prediktálható harmadlagos szerkezete egy kompakt globuláris molekula, amely négy spirális

régióból áll (Sauane, Gopalkrishnan, Lebedeva, et al., 2003). Az IL-24 intermolekuláris diszulfid kötéseken keresztül N-kapcsolt glikozilált dimereket is képezhet, amelyek funkcionálisan is aktívak lehetnek.

Ahogyan az IL-10 citokin család tagjai, úgy az IL-24 is receptordimereken keresztül kommunikál, amelyek hosszú citoplazmatikus doménnel rendelkező R1 típusú és rövid citoplazmatikus doménnel bíró R2 típusú alegységekből állnak. Az IL-10 citokin receptor család három R1 és két R2 alegységet tartalmaz. Az R1 alegységek az IL-10R1, IL-20R1 és IL-22R1, az R2 alegységek pedig az IL-10R2 és IL-20R2. Az IL-24 két heterodimer receptort, az IL-22R1/IL-20R2-t és az IL20-R1/IL-20R2-t használja a downstream jelátvitel aktiválására (M. Wang et al., 2002).

Az IL-24-et kísérletes modellekben termelhetik immunsejtek (mieloid sejtek és limfoid sejtek egyaránt) lipopoliszachariddal, concanavalin A-val vagy specifikus citokinekkel végzett kezelés hatására (Caudell et al., 2002; Buzas et al., 2011). Fiziológiás szintje indukálódik naiv CD4+ T-sejtekben, főleg anti-CD3 monoklonális antitesttel történő aktiváció során (Schaefer et al., 2001; Sahoo et al., 2011). B-sejt receptor jelátvitelének aktivációja szintén kiváltja az IL-24 expresszióját a B-limfocitákban (Maarof et al., 2010). Számos *in vitro* és *in vivo* tanulmány kimutatta, hogy a citokinekkel stimulált hámsejtek is IL-24-et szekretálhatnak (Buzas et al., 2011; Whitaker et al., 2012; Persaud et al., 2016). Ezenkívül az IL-1 is serkentheti az IL-24 expresszióját keratinocitákban és humán vastagbélsejtekben is (Andoh et al., 2009). Az IL-24 alapszintű expressziója fiziológiásan megfigyelhető a melanocitákban, azonban ez fokozatosan csökken, ahogy a melanociták elkezdenek melanóma irányba transzformálódni (H. Jiang et al., 1995; Ekmekcioglu et al., 2001; Ellerhorst et al., 2002).

Bár az IL-24-et több évtizeddel ezelőtt fedezték fel, a citokin normál fiziológiás működésekben, valamint számos, humán patológiai folyamatban betöltött szerepére vonatkozóan még mindig vannak új kutatási eredmények. Megerősítést nyert, hogy az IL-24 nemcsak a normál immunműködésben és a sebgyógyulásban vesz részt, hanem számos más jótékony hatása is van különböző kórképekben. Az IL-24 figyelmet kapott, mint daganatellenes fehérje többek között melanómában (Lebedeva et al., 2002; D. Sarkar et al., 2008), prosztatarákban (Lebedeva, Sarkar, et al., 2003; Lebedeva, Su, et al., 2003; Greco et al., 2010), az emlőtumorok bizonyos csoportjában (D. Sarkar et al., 2005; Bhutia et al., 2013; Menezes et al., 2015; Pradhan et al., 2017), oszteoszarkómában (Zhuo et al., 2017), neuroblasztómában (Bhoopathi et al., 2016), hasnyálmirigyrákban (S. Sarkar et al., 2015) és vesekarcinómában (Park et al., 2009), leukémiában (Rahmani et al., 2010), tüdőrákban (Lv et

al., 2016; Shapiro et al., 2016), nyelőcső laphámsejtes karcinómában (Q. Ma et al., 2016), és hepatocelluláris karcinómában is (X. Wang et al., 2007). Az IL-24 védelmet nyújthat az autoimmun betegségek és bizonyos bakteriális fertőzések ellen (Leng et al., 2011; Y. Ma et al., 2009). Az IL-24-nek szerepet tulajdonítanak a rheumatoid arthritis (RA) (Kragstrup et al., 2008) és a szív- és érrendszeri betegségek (Vargas-Alarcón et al., 2014) esetén is.

1.2.2 Az IL-24 daganatos folyamatokban betöltött szerepe

A daganatok heterogén sejtpopulációkból állnak, amelyek eltérő biológiai tulajdonságokkal rendelkeznek. A tumorőssejtek a heterogén daganatszövet olyan sejtjei, amelyek önmegújító tulajdonságot mutatnak, osztódhatnak és differenciálódhatnak, így heterogén sejtpopulációt hoznak létre, amelyben a sejtek egy része távoli daganatokat képezhet (Talukdar et al., 2016). A tumorőssejtek az elsődleges daganatról leválva vándorolnak, és távolabbi helyeken megtapadva ott daganatokat generálhatnak, áttéteket képezhetnek. Ezek az újonnan képződő sejtcsoportok viszont a hagyományos terápiákkal szemben is ellenállóak lehetnek, és megnövekedett osztódási potenciállal rendelkezhetnek (Morrison et al., 2013). Különböző adenovírus rendszerekben – ahol vektorokkal biztosították az IL-24 túltermelését – azt tapasztalták, hogy gátolta az emlőtumor-őssejtek növekedését, a tumorsejtekben apoptózist, illetve az endoplazmatikus retikulum károsodását idézte elő. Az IL-24 a β-catenin és PI3K működését befolyásoló útvonalakon keresztül gátolta a tumorőssejtek adhézióját, illetve a szferoid képzést, amelyek a daganatsejtek túlélését befolyásolták. Az IL-24 rekombináns adenovírus konstrukció (Ad-24) szelektív apoptózist indukál a tumoros sejtekben, de nem a normál szomatikus sejtekben, bár a szelektív tumorsejthalál pontos mechanizmusai nem teljesen ismertek (Kotenko & Langer, 2004; M. Wang & Liang, 2005; Gupta et al., 2006; Fisher et al., 2007; D. Sarkar et al., 2007).

A tumorsejtek pusztulását előidéző mechanizmusok megértéséhez hozzájárulhat, hogy az Ad-24 számos sejtes jelátviteli molekula aktiválását eredményezi, beleértve a kaszpáz kaszkádot, beavatkozva a PKR, a p38, a STAT3, illetve a PI3K, GSK-3, ILK-1, BAX, BAK, Fas, DR4, TRAIL, iNOS, IRF-1 és IRF-2 (Kotenko, 2002; D. Sarkar et al., 2002; Yacoub et al., 2004; Qian et al., 2008) érintett jelátviteli mechanizmusokba, és a sejtciklus G2/M fázisában is zavart okoz (C.-J. Wang et al., 2006). Fontos, hogy ezeket a jelátviteli molekulákat nem egyenletes mennyiségben fejezik ki a daganatos és normál sejtek, ami arra utal, hogy az IL-24 szelektív apoptotikus aktivitása nem a jelszintnek köszönhető, hanem a jel meglétének vagy hiányának (Lebedeva et al., 2007).

Ugyanezen citokin család tagjairól korábban kimutatták, hogy a sejtek migrációját indukálják. Így például az IL-10 fokozza a Langerhans-sejtek migrációját. De közvetett hatásokon keresztül is hat a sejtek motilitására, mivel fokozza a CCL2 (MCP-1) expresszióját humán monocitákon (Musso et al., 2005), a CCR6 expresszióját Langerhans sejteken (Dieu-Nosjean et al., 2001), illetve a B-sejtek CXCL12 (SDF-1) kezelését követő citoszkeletális átszerveződését (Balabanian et al., 2002). A család másik tagja, az IL-20, az IL-20R1-en és IL-20R2-n keresztül indukálja az endotélsejteken a MAP kináz család tagjainak foszforilációját, ami korrelál a HUVEC migrációjával és a kapillárisképződéssel (Hsieh et al., 2006).

Az IL-24, az IL-22 stimulálásán keresztül gátolja az endotéliális sejtek differenciálódását és migrációját (Ramesh et al., 2003). Továbbá az IL-24 gátolja a TGF-α által kiváltott keratinocita proliferációt is. Az IL-24 stimulálja az immunrendszert, hogy olyan citokineket állítson elő – mint például a TNF-α és IL-1 –, amelyek daganatellenes immunválaszt váltanak ki (Caudell et al., 2002; Buzas et al., 2011).

Az IL-24 a gazdaszervezet védekezésében is kiemelkedő szerepet játszik azáltal, hogy veleszületett immunválaszt indukál a hámszövetben fertőzés és gyulladás során kemokinek indukálásával és a leukociták toborzásával, illetve aktiválásával (Tamai et al., 2012; Jin et al., 2014; Persaud et al., 2016). Az IL-24 expresszió kiváltható olyan TLR-ek vagy PAMP-ok jelátvitelével, amelyeket különböző kórokozók, mint például Staphylococcus speciesek indukálhatnak LPS vagy lipoteikolsav alkotóelemeik segítségével (Buzas & Megyeri, 2006). Mivel ezen inducerek a normál baktériumflóra tagjaiban is megtalálhatóak, az IL-24 Th1-es citokineket indukáló hatása és az immunsejtekre gyakorolt kemotaktikus aktivitása mind az antitumorális válaszok része lehet, de mindenképpen a daganatos mikrokörnyezet egyik érdekes szolubilis eleme. Mindezen tulajdonságai alapján, kiemelve a TLR ligandumok, bakteriális antigének álatali indukálhatóságát, érdemesnek találtuk az IL-24 szerepét megvizsgálni azokban a helyzetekben, amikor az immunsejtekre gyakorolt hatása, az immunsejtek migrációjának elősegítése a tumoros folyamatokba való hatékony beavatkozást jelenthet.

1.3 A vezikuláris információtranszfer szerepe tumoros folyamatokban

1.3.1 A sejtek között megvalósuló információtranszfer formái, a vezikuláris jelátvitel

Két sejt között különböző jelátviteli mechanizmusok segítségével történhet meg az információcsere. A szolubilis elemekkel, receptor-ligand kölcsönhatásokkal megvalósuló kommunikáció lehetőségeiből az előző fejezetben mutattam be példákat. A testfolyadékainkban azonban nem csupán oldott formában keringő molekulák, de partikuláris elemek is közvetíthetnek jeleket. Ezen formák közül kiemelkedő jelentőséggel bírnak az extracelluláris vezikulák (EV-k).

Az EV-ket először vérlemezkékből származó részecskékként figyelték meg a normál plazmában. Eredetileg Chargaff és West (Waters & Bassler, 2005) számolt be 1946-ban az EV-kről, Wolf 1967-ben „vérlemezke dust”-ként emlegette (Wolf, 1967). A korai megfigyelések közé tartoznak a mátrix hólyagok is, amelyeket Anderson 1969-ben a csont meszesedése során azonosított (Anderson, 1969). Az 1970-es és 1980-as években EV-ket figyeltek meg a végbél adenóma mikrobolyhos sejtjeiből felszabaduló membránhólyagok formájában (De Broe et al., 1975) is. Körülbelül ugyanebben az időben történtek az első észlelések a tumor eredetű membránfragmensekről (Taylor et al., 1980), és kimutatták prokoaguláns tulajdonságukat is (Dvorak et al., 1981). 1983-ban azonban már részletes ultrastrukturális vizsgálatok igazolták, hogy az éretlen vörösvértestek differenciálódása során a sejtmembránnal összeolvadó multivezikuláris testekből (MVB) szabadulnak fel membránhólyagok (Harding et al., 1983; Pan & Johnstone, 1983). A felfedezések kezdetén a sejtek hulladékának, a felesleges anyagok egyik eltávolítási módjának tartották az extracelluláris vezikulák képződését. A sejt- és molekuláris biológia vizsgálómódszereinek fejlődésével azonban nagyon hamar bebizonyosodott, hogy a „sejtszemét” eltávolításánál jóval összetettebb feladatokat látnak el a foszfolipid kettősréteggel határolt vezikulák. Ezen kezdeti megfigyelések után EV-ket izoláltak a legtöbb sejttípusból és testfolyadékból, például nyálból, vizeletből, magzatvízből, anyatejből, plazmából, szérumból és ondófolyadékból is (Pisitkun et al., 2004; Caby et al., 2005; Poliakov et al., 2009; Keller et al., 2011; Lässer et al., 2012).

Az extracelluláris vezikulák nevezéktana még mindig tartalmaz bizonytalansági tényezőket. Mivel a keletkezés útvonala, a különböző molekuláris markerek megléte vagy hiánya az esetek jelentős részében nem határozható meg nagy bizonyossággal, a "Minimal Information for Studies of Extracellular Vesicles 2018", röviden MISEV2018 (Théry et al., 2018) ajánlás alapján leginkább az izolálás alapjául szolgáló sajátságok, például a méret szerinti besorolás

a kézenfekvő. Ezen nomenklatura szerint jelen dolgozat a kisméretű, 200 nm-nél kisebb átmérőjű EV-kel, az úgynevezett small extracellular vesicle-kel (sEV) foglalkozik. Annak, hogy sok esetben előfordul az „exoszóma" kifejezés, két oka van. Egyrészt az értekezésben szereplő eredmények egy része még a 2018-as MISEV állásfoglalás előtt született. Másrészt a nevezett sEV-k meglehetősen rigorózus karakterizáláson estek keresztül, így az exoszómákra jellemző méret és alak mellett olyan molekuláris markerek is azonosításra kerültek, mint a CD9, CD63 vagy a CD81.

Az EV-k funkciója, csakúgy, mint az összetételük, rendkívül változatos és sokrétű. Pleiotróp szerepet játszanak a sejt-sejt kommunikációban, és számos biológiai folyamatot befolyásolnak. Mivel biológiailag aktív EV-k szabadulnak fel a felnőtt szervezet minden sejtjéből, beleértve a normál és rosszindulatú sejteket is (Pan & Johnstone, 1983; Pisitkun et al., 2004; Keller et al., 2011; Lässer et al., 2012), egyensúlyi állapotban jelen vannak a testfolyadékokban, többek közt a vérplazmában, intercelluláris folyadékban, cerebrospinális folyadékban, vizeletben, spermában, epében, ízületi folyadékban, nyálban és anyatejben is (Yáñez-Mó et al., 2015). Patológiás helyzetekben a testfolyadékokban megnövekszik az EV-k száma, igaz ez a daganatos megbetegedésekre is (Pisitkun et al., 2004; Keller et al., 2011; Lässer et al., 2012). Ezen patológiás folyamatok következtében keletkező EV-k molekuláris összetételükben is különböznek. A célsejteken az EV-mediált információtranszfernek többféle mechanizmusa lehetséges. A célsejt plazmamembránján receptor-ligand kölcsönhatások révén intracelluláris jelátviteli folyamatokat aktiválhatnak, endocitotikus folyamatok (fagocitózis, mikropinocitózis, receptor-mediált endocitózis) révén internalizálódhatnak, vagy közvetlenül a plazmamembránnal is fúzionálhatnak (Maia et al., 2018). Ezáltal a célsejtekbe juttatott vezikuláris moleluláris tartalom – amely leginkább mRNS-ből, miRNS-ből, fehérjékből, bioaktív lipidekből és jelátviteli molekulákból vagy hormon-szerű anyagokból áll – megváltoztathatja a célsejt fenotípusát és módosíthatja biológiai funkcióit.

Az EV-k biológiai jelentősége többek között azon alapul, hogy

- jelátviteli platformként funkcionálhatnak: a sejteket a külső lipidrétegükbe ágyazott ligandumokkal stimulálhatják,
- a sejtek fenotípusát módosíthatják sejtmembrán-receptorok, egyéb felületi struktúrák sejtek közötti átvitelével,
- információcsomagokként működhetnek mRNS, miRNS, fehérjék, lipidek és néhány kis sejtorganellum sejtek közötti cseréjével,

- a membránburkuk stabilitása révén a beltartalmuk védve van az enzimatikus hasításoktól, hordozónak tervezve, gyógyszerek, bioaktív vegyületek átvitelére, vagy akár genetikai anyag célbajuttatására is képesek (M. Z. Ratajczak & Ratajczak, 2020).

Ezen kívül további bizonyítékok utalnak arra, hogy az EV-k szerepet játszanak bizonyos kórokozók, pl. vírusok és prionok terjedésében (Rozmyslowicz et al., 2003; J. Ratajczak et al., 2006; Mattei et al., 2009). Jelenleg vizsgálják annak lehetőségét, hogy az EV-k molekuláris ujjlenyomata az úgynevezett folyadék-biopsziák részeként hogyan hasznosítható a diagnosztikában (Kucharzewska & Belting, 2013; Veziroglu & Mias, 2020).

1.3.2 A tumoros mikrokörnyezet kialakulása, intercelluláris kommunikációs mechanizmusai

Régóta közismert tény, hogy a tumoros sejtek nem elszigetelten, hanem egy összetett környezetben, úgynevezett tumor mikrokörnyezetben léteznek. Ez a bonyolult niche több sejttípusból áll, amelyek extracelluláris mátrixba (ECM) vannak ágyazva, és alapvető szerepet játszanak a tumor progressziójában. A daganatfejlődés során a neoplasztikus sejtek aktívan toborozzák környezetükbe az egészséges sejteket, amelyek többféle módon támogatják a rosszindulatú daganatok progresszióját. Ebben az összefüggésben az endoteliális sejtek és periciták nagy jelentőséggel bírnak, mivel felelősek a tumor érellátásának kialakulásáért és működéséért (Weis & Cheresh, 2011); de ugyanígy a fibroblasztok, amelyek az ECM előállításában vesznek részt. Azonban a daganatsejtek mátrixbontó enzimeket és oldható növekedési faktorokat is szekretálnak (Kalluri & Zeisberg, 2006). Kemokinek termelése révén a daganatok helyére vonzott, majd ott tumortámogatóvá átprogramozott immunrendszer sejtjei, amelyek immunszuppresszív és növekedést serkentő elemként szolgálhatnak (de Visser et al., 2006), szintén a tumorok növekedését segítik. A tumortömeg háromdimenziós szerveződését és felépítését a tumoros ECM biztosítja, amely a normál mátrixszal ellentétben jellemzően számos fehérjében, például I. típusú kollagénben és erősen glikozilált glikoproteinekben, azaz proteoglikánokban gazdag. Ezenkívül a tumor sztróma szabályozza a sejtes jelátvitelt, és a növekedési faktorok rezervoárjaként is működik (Lu et al., 2012). A rosszindulatú daganatok sikeres növekedéséhez és terjedéséhez aktív együttműködésre van szükség a rosszindulatú- és a sztrómasejtek között. Ennek megfelelően a rosszindulatú sejtek és a sztrómasejtek közvetlen sejt-sejt kapcsolatok, valamint jelzőmolekulák, például oldható növekedési faktorok, ECM-fehérjék (Lorger, 2012) és az EV-k (Camussi et al., 2011) felszabadulásával kommunikálnak (**2. ábra**).

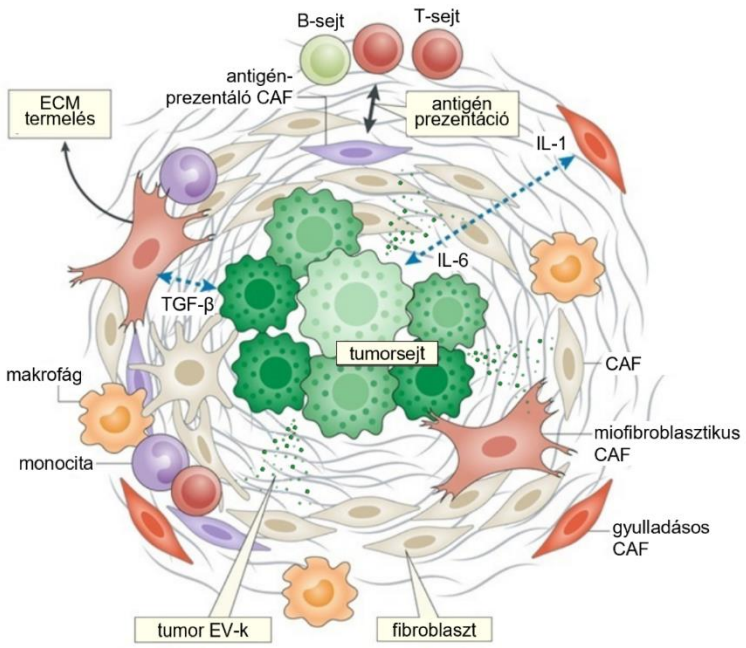

2. ábra. Kommunikációs mechanizmusok a tumoros mikrokörnyezetben.
Az intercelluláris kommunikációban sejt-sejt kapcsolatok, szolubilis faktorok és EV-k is részt vesznek. BioRender.com használatával módosított ábra (Ho et al., 2020) alapján.

A tumor mikrokörnyezeti evolúciójának mozgatórugói a transzformálódott sejtek genetikai instabilitása és a környezeti szelekciós nyomások, amelyek magukban foglalják az endogén, tehát a daganatnövekedés által kiváltott stresszingereket, mint például a hipoxiát, acidózist, éhezést, oxidatív stresszt, biomechanikai stresszt és immunszerkesztést, valamint az exogén stresszeket is. Ide tartoznak például különböző terápiás beavatkozások (Kucharzewska & Belting, 2013; Gillies et al., 2012).

1.3.3 Az sEV-k molekuláris tartalma és jelentősége daganatos folyamatokban, vezikuláris onkogén átprogramozás

Az exoszómák és az EV-k más osztályai a sejt-sejt kommunikáció fontos közvetítői, és alapvető szerepet játszanak a tumorbiológiában. Régóta köztudott, hogy a daganatos sejtek nagyobb mennyiségű EV-t választanak ki, mint az egészséges sejtek. Az EV-ket nagyobb számban mutatták ki tumoros betegek plazmájában az egészségesekéhez képest, valamint tumorsejttenyészetekben, mint primer kultúrákban (Cappello et al., 2017; Johnsen et al., 2019).

Az exoszómák jelentősen hozzájárulnak a tumor progressziójához, inváziójához és metasztázisok képzéséhez azáltal, hogy horizontális transzfer során képesek továbbítani a különböző felszíni molekulákat, onkogén fehérjéket és egyéb szignálmolekulákat a célsejtekhez, amelyek ezáltal megváltoztatják viselkedésüket (Parayath et al., 2020; Yang et al., 2020). Például lokálisan, a tumor mikrokörnyezetben (TME) a daganatból származó EV-k

gyógyszerrezisztenciát közvetíthetnek a szomszédos daganatsejtek között. Ezek az EV-k a fibroblasztokat és a mezenchimális őssejteket is átnevelhetik, vagy aktiválhatják az endoteliális sejteket, ezáltal angiogenezist indukálhatnak. Szisztémás szempontból az EV-k döntő szerepet játszanak az immunmodulációban és a metasztatikus niche kialakításában (**3. ábra**) (Gulei et al., 2018; Nogués et al., 2018; Tao & Guo, 2020). A kommunikáció azonban nem egyirányú a daganatokban. Éppen ellenkezőleg, a daganatfejlődéssel párhuzamosan komplex, szisztémás kommunikációs hálózat alakul ki (Maia et al., 2018; Harmati et al., 2021).

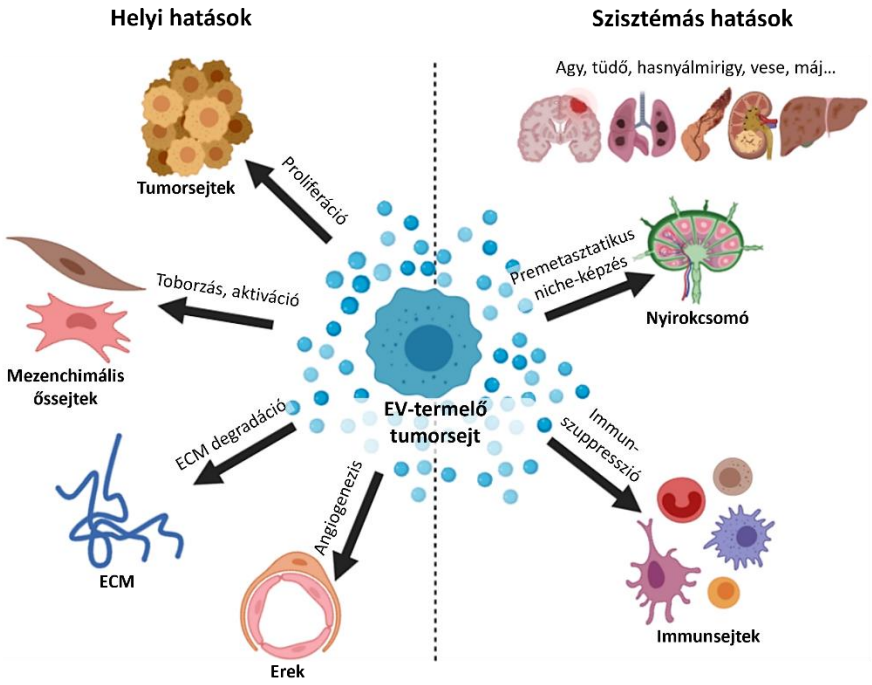

3. ábra. A daganatsejtekből származó EV-k helyi és szisztémás hatásai.

Az EV-k megváltoztathatják a TME-t, modulálhatják az immunválaszokat és előkészíthetik a távoli szöveti helyeket a metasztázisokhoz. Az ábrán néhány példát láthatunk a tumor eredetű EV-k mikro- és makrokörnyezeti hatásaira (Harmati et al., 2021).

A metasztázisok képződése jelentősen növeli a daganatos megbetegedések rosszabbodását. Ahogyan már Paget „seed and soil" hipotézise is megfogalmazta, az áttétes daganatsejtek kolonizációjához specifikus mikrokörnyezetre van szükség a célszervben (Paget, 1889), amelyre napjainkban pre-metasztatikus niche-ként (PMN) hivatkozunk (Kaplan et al., 2005). Számos tanulmány kimutatta, hogy a tumoros sEV-k részt vesznek a PMN kialakulásában azáltal, hogy indukálják az érpermeabilitást és az angiogenezist, aktiválják a fibroblasztokat és elősegítik a gyulladást (Costa-Silva et al., 2015; Zeng et al., 2018; Kong et al., 2019; Zhao et al., 2019). A tumorsejtek által kibocsájtott sEV-k az intercelluláris kommunikáció révén alapvető szerepet játszanak az epiteliális-mezenchimális átmenetben (EMT) (J. Jiang et al.,

2022). Az EMT folyamata során a sejtmorfológia átalakul az epiteliális állapotból a mezenchimális állapotba. Ez egy kulcsfontosságú folyamat, mely során az E-cadherin expressziója csökken a tumorsejtekben, ami csökkent adhéziót, illetve az apikális polaritás elvesztését és a bazális horgonyzást eredményezi, ami lehetővé teszi a tumorsejtek számára, hogy könnyen elhagyják az elsődleges léziót és más szervekbe vándoroljanak (Pastushenko & Blanpain, 2019). Az sEV-k olyan metabolitokat és jelzőmolekulákat hordoznak a donor sejtekből indulva, amelyeket a célszerv sejtjei endocitózissal felvesznek, majd aktiválják az EMT-vel kapcsolatos jelátviteli útvonalakat, és elősegítik az EMT kialakulását (Hu et al., 2019; L. Wang et al., 2019; Lin et al., 2020; H. Wang et al., 2020).

1.3.4 Az sEV-k molekuláris tartalmának változásai környezeti nyomások hatására

Az sEV-k jellegzetes molekuláris ujjlenyomata erősen függ a szülő/donor sejt állapotától. Többek közt, a daganatos sejtek metabolikus állapota befolyásolja az exoszómák szekrécióját és tartalmát. A hipoxia, az éhezés és az acidózis azok a tipikus metabolikus állapotok, amelyeken a tumorsejtek átesnek, és nemcsak az exoszóma szekréció sebességét, hanem az exoszómák molekuláris összetételét is befolyásolják (Kucharzewska & Belting, 2013; Harmati et al., 2017, 2019). Az, hogy foszfolipid kettősréteg veszi körül a nem véletlenszerűen becsomagolódott jelátvivő molekulák összességét, kivételesen hatékony jelátvitelt biztosít, hiszen megóvja a beltartalmat az enzimatikus hasításoktól vagy a mechanikai hatásoktól. Így az sEV-k kiemelkedő jelentőséggel bírnak a daganatos mikrokörnyezet formálásában.

1.3.5 Mezenchimális őssejtek szerepe a daganatos mikrokörnyezetben

A heterogén tumorszövet sokféle, egymással keveredő, együttműködő sejtből áll. Térbeli és időbeli együttélésük elősegíti a közvetlen kommunikációt és rendkívül sikeres sejtközösséggé teszi a daganatokat. A tumoros sejtek nemcsak oldott anyagokkal és receptor-ligandum kölcsönhatásokkal (Li et al., 2007), hanem vezikulák felszabadításával is hozzájárulnak a tumor niche kialakulásához (Nogués et al., 2018), amelyek molekuláris tartalma összetett információs csomagot eredményez. Ezen tumoros mikrokörnyezet elemei és a felszabaduló sEV-k targetjei a mezenchimális őssejtek (MSC), amelyeket először a csontvelő sztrómasejtjeiként írtak le, multipotens differenciálódási képességgel és jellegzetes immunmoduláló hatással (P.-M. Chen et al., 2011). Az MSC-k szerepéről a tumor progressziójában immunológiai és differenciálódási tulajdonságaikkal kapcsolatban máig vita folyik (Ridge et al., 2017). Valójában a sejtek sorsa függhet a daganat típusától és az érintett MSC-k állapotától is. Az aktivált MSC-k szolubilis pro-angiogén faktorokat szekretálhatnak,

és képesek differenciálódni akár tumor asszociált fibroblasztokká is (CAF) (Mishra et al., 2009). Baglio és munkatársai kimutatták, hogy a tumor által kiválasztott EV-k elősegítik az oszteoszarkóma progresszióját, mégpedig a TGF-β által kiváltott IL-6 termelésen keresztül (Baglio et al., 2017). Peinado és munkatársai azt találták, hogy az erősen metasztatikus melanómákból származó exoszómák növelik az elsődleges daganatok áttétképző képességét azáltal, hogy a MET receptor tirozin kinázon keresztül tartósan nyomás alá helyezik a csontvelő progenitorokat (Peinado et al., 2012).

1.3.6 A daganatos mikrokörnyezet speciális tulajdonságai melanómában

A fentiekben felsorolt példákon kívül érdemes megfigyelni az sEV-k szerepét melanómában is, hiszen a melanóma egy erősen invazív, nagy metasztatikus potenciállal rendelkező tumor típus rossz prognózissal és túlélési aránnyal (Ugurel et al., 2017). Mivel a melanómát régóta erősen immunogén daganatként tartják számon, a terápiás megközelítések különböző immunológiai mechanizmusokat céloznak meg az agresszív bőrrákban szenvedő betegek kezelésére. Az elmúlt évtizedben az IL-2 és CTLA-4 terápiák mellett a PD-1:PD-L1 blokád hatékony kezelésnek bizonyult áttétes melanóma esetén (Callahan & Wolchok, 2013; Ott et al., 2013; Kee & McArthur, 2017; Willsmore et al., 2021). A programozott sejthalál protein 1 (PD-1), amelyet főként immunsejtek, például aktivált T-sejtek, dendritikus sejtek és makrofágok expresszálnak, egy sejtfelszíni receptor, amely központi szerepet játszik a T-sejtes válaszok modulálásában. A PD-1 ligandumához (PD-1L) való kötődése apoptózist és az immunsejtek anergiáját eredményezheti. Tehát a PD-1 expresszió nem alapértelmezett funkcionális tulajdonsága a melanóma sejteknek, sokkal inkább a tumorszövetet infiltráló immunsejteknek. Mindezek fényében igen érdekes az a megfigyelés, hogy a PD-1-et túlzottan expresszáló melanóma sejt alpopulációk különösen agresszívek, és hogy a melanóma PD-1:PD-L1 kölcsönhatásai modulálják az mTOR jelátvitelt, ezáltal megzavarják a programozott sejthalált (Kleffel et al., 2015). Bár ezek a megfigyelések rendkívül hasznosak a PD-1 túlzott expressziójának és a PD-1 funkciók kísérleti gátlásának következményei tekintetében, de nem határozzák meg azokat a tényezőket, amelyek a PD-1-et túlzottan expresszáló melanóma sejt alpopulációk kialakulásához vezetnek (Gyukity-Sebestyén et al., 2019). Ez a kérdés különösen érdekes, ha figyelembe vesszük, hogy a ma elérhető egyik leghatékonyabb immunterápia a fent említett PD-1:PD-1L interakció blokádján alapul (Bersanelli & Buti, 2017; Y. Jiang et al., 2019; A. C. Huang & Zappasodi, 2022).

1.4 Központi idegrendszeri tumorok molekuláris ujjlenyomatai, a keringő extracelluláris vezikulák diagnosztikai jelentősége

1.4.1 Az extracelluláris vezikulák diagnosztikai és prognosztikai értéke

Az extracelluláris vezikulák olyan ígéretes biomarkerek, amelyek folyadékbiopsziákból elérhetők, mivel stabilan megtalálhatók minden típusú testfolyadékban. Az EV-k a donorsejt citoszoljának mintázatát tartalmazzák, beleértve egyaránt nukleinsav jellegű hírvivőket, mint a DNS, mRNS, miRNS, fehérjéket és más jellemző anyagokat, miközben külső membránjuk illetve felszíni molekuláik is hasonlítanak a sejtre, amelyből származnak (Sheridan, 2016).

A közelmúltban az EV-k a daganatok diagnosztizálásában és terápiájában is szerepet kaptak (Basu & Ghosh, 2019; Kosaka et al., 2019; Scavo et al., 2020), mint biomarker komplexek, amelyek nagy szenzitivitással és specifitással azonosíthatók különböző primer tumorokban (Möhrmann et al., 2018; Dobra et al., 2020). Például hasnyálmirigyrák tekintetében Melo és munkatársai azt találták, hogy a keringő exoszómák kifejezetten gazdagok egy sejtfelszíni proteoglikánban, a glipikán-1-ben (GPC1). A GPC1-et alkalmasnak találták a korai és késői stádiumú hasnyálmirigyrák és a jóindulatú hasnyálmirigy-betegségek 100%-os pontosságú megkülönböztetésére (Melo et al., 2015).

Nukleinsav markerekre érdekes példa a cirkuláris RNS (circRNS), az exoszómákban található nukleinsavmolekulák egy típusa, kovalens kötéssel kötött zárt hurkot képez 5′ sapka vagy 3′ poli(A)-farok nélkül. Szerkezetileg stabil, széles körben elterjedt és szövetspecifikus. A circRNS-ek az mRNS-ek alternatív splicingjával kialakuló, általában fehérjét nem kódoló RNS-molekulák (ncRNS-ek). Mindamellett, hogy számos daganatos betegségek progressziójának irányába mutató folyamatban részt vesznek, egyes circRNS-ek emelkedett szintjét figyelték meg a nyelőcső lapjhámsejtes karcinómájában, annak nyirokcsomó áttéteiben, gyomorrákban vagy kissejtes tüdőrák esetében is (Ye et al., 2022).

Számos közlemény foglalkozik az EV-k szerepével és diagnosztikai, illetve prognosztikai értékével I. típusú diabéteszben és annak szövődményeiben. A teljesség igénye nélkül, kiemelve néhány példát: számos miRNS folyamatosan felülszabályozott az I. típusú diabéteszben, köztük a miR-21-5p, miR-100-5p, miR-150-5p, miR-181a-5p, miR-210-5p és miR-375, amelyek közül sok megtalálható az EV-kben (Z. Wang et al., 2017; Negi et al., 2019). A fiatal, újonnan diagnosztizált diabéteszes betegek mintáinak tanulmányozása során az EV miRNS-ek eltérő módosulásait azonosították az egészséges kontrollokhoz képest, a miR-195 és miR-455 szintje csökkent, míg a miR-185 szintje emelkedést mutatott (Tesovnik et al., 2020).

1.4.2 Az extracelluláris vezikulák diagnosztikai jelentősége CNS tumorokban

Számtalan példa hozható az EV-k diagnosztikai vagy prognosztikai értékére, de szerepük különösen felértékelődik a központi idegrendszer (CNS) megbetegedéseiben (Azam et al., 2019; Osti et al., 2019; H. Wang et al., 2019; Dobra et al., 2020; Bukva et al., 2021; Monteiro-Reis et al., 2021). Amennyiben szövettani mintát szükséges venni a pontos diagnózis felállításához és a terápia meghatározásához, megkezdéséhez, az igen komoly nehézséget jelent mind a páciens, mind az egészségügy számára. Egyrészt az ilyen beavatkozások nagy terhet rónak az egészségügyi ellátórendszerre, hiszen a betegek hospitalizációja, az ápoló- és technikai személyzet munkája mellett egy teljes idegsebészeti munkacsoport felállítása és a műtőkapacitás kihasználása mind a szakmai, mind az anyagi erőforrásokat erősen igénybe veszi. Másrészről a diagnózis felállítása sok esetben nem jár elegendő haszonnal a sokszor igen rossz általános állapotú beteg számára, a műtéti terhelés, a szövődmények kockázata mind mérlegelendő tényező. Jelenleg azonban nem létezik olyan alternatíva, amely egyaránt megnyugtató a betegek, a hozzátartozóik és a gyógyítók nézőpontjából.

Ezért is kivételes lehetőségeket hordoz magában az a tény, hogy az sEV-k átjutnak a vér-agy gáton (Choy & Jandial, 2016; Matsumoto et al., 2018; Morad et al., 2019) és a keringésben megjelenve lehetőséget adhatnak a központi idegrendszeri elváltozások megállapítására.

A központi idegrendszeri barriereknek többféle típusa létezik (Ramirez et al., 2018). Talán a legszélesebb körben ismert a vér-agy gát (BBB), amely a parenchimális mikroerek szintjén helyezkedik el, és speciális endotélsejtek rétegéből áll, amelyet a nagy ellenállású tight junction struktúrák jellemeznek, és amelyet a glia limitans fed le. A vér-cerebrospinális gát (BCSFB) az érhártya plexus epiteliális sejtjeiből áll (az agykamrákban lokalizálva), amelyek elválasztják a vér által szállított elemeket a cerebrospinális folyadéktól (CSF) (Ueno et al., 2016). Egy harmadik típusú központi idegrendszeri gát, a vér-leptomeningeális gát (BLMB) a mikroerek endotélsejtjeinek rétegéből jön létre, amely a pia materen és a fedő szubarachnoidális téren (SAS) keresztül halad, és a BCSFB egy másik típusának tekinthető (Engelhardt & Ransohoff, 2012). Magáról az epithelioid pia materről azt feltételezik, hogy további központi idegrendszeri gátként működik, szabályozva az oldott anyag és a sejt forgalmat a SAS-ban lévő CSF és a subpialis parenchyma között (Filippidis et al., 2012; Engelhardt et al., 2016). Bár technikailag a központi idegrendszeren kívül található, létezik egy vér-retina gát (BRB), amely retina pigment epiteliális sejtekből és retina kapilláris endoteliális sejtekből áll, amelyeket szorosan összekapcsolnak a BBB-ben találhatókhoz hasonló speciális junkciós komplexek (Lightman et al., 1987). Mindezek a komplex és jól

szervezett struktúrák első hallásra úgy tűnhetnek, hogy lehetetlenné teszik a nanométeres partikulák perifériás vérbe kerülését. Azonban a patológiás állapotokban ezek a barrierek mégsem zárnak ennyire szorosan. Erre egyik jellemző példa a glioblastoma multiforme. A glioblasztóma egy rendkívül agresszív, erősen vaszkularizált agydaganat, amelyet nagyon rossz prognózis jellemez. Nagy mennyiségű ödéma is társul a daganat által kiváltott vaszkuláris 'leakage', érszivárgás miatt (Abbruzzese et al., 2017). Ez a vaszkuláris szivárgás, legalábbis részben, a glioblasztómán belül termelődő Semaphorin3A (Sema3A) pro-permeabilitási faktorból ered, amely leggyakrabban a neuropilin 1 (NRP1) receptorának bekapcsolásával váltja ki az endotél barrier permeabilitását (Roth et al., 2016). A közelmúltban kimutatták, hogy a betegektől származó glioblasztómasejtek által kibocsájtott, felszínükön Sem3A-t hordozó EV-k *in vivo* és *in vitro* NRP1-függő módon megzavarhatják az agy endotél gát funkcióját (Treps et al., 2016). Így sokkal könnyebben elképzelhető, hogy a daganatsejtek által kibocsájtott EV-knek szerepe lehet akár a BBB és a parenchimális sejtek közötti kommunikációban, de megjelenhetnek a perifériás vérben is.

2. CÉLKITŰZÉSEK

1. Munkánk során arra kerestük a választ, hogyan befolyásolhatják TLR ligandumok a daganatos mikrokörnyezet immunológiai elemeit. Ennek során megvizsgáltuk a tumort infiltráló makrofágok polaritását befolyásolásoló bakteriális eredetű antigének hatását.
2. Célul tűztük ki, hogy megvizsgáljuk a bakteriális antigénekkel is indukálható, antitumorális hatásáról is ismert interleukin-24 immunsejtekre gyakorolt kemotaktikus hatását.
3. Kísérleteink során arra kerestük a választ, megváltoznak-e a tumoros mikrokörnyezet bizonyos elemei daganatsejtek által termelt vezikulák hatására. Célul tűztük ki a melanóma exoszómák PD-1 expresszióra gyakorolt hatásának leírását. Megvizsgáltuk, történik-e a daganatok környezetében található sejteken extracelluláris vezikulák által vezérelt onkogén átprogramozás.
4. Célunk volt leírni a mikrokörnyezeti stresszoroknak a vezikulák molekuláris mintázatára gyakorolt hatását.
5. Megvizsgáltuk a mikrokörnyezeti stresszorok nyomása alatt termelődő extracelluláris vezikulákra adott sejtbiológiai válaszokat.
6. Tanulmányoztuk a központi idegrendszeri tumorok molekuláris ujjlenyomatának megjelenését a perifériás vérben, különös tekintettel az MMP-9-re.
7. Célul tűztük ki a központi idegrendszeri tumorok extracelluláris vezikula alapú diagnosztikájának fejlesztését.

3. EREDMÉNYEK ÉS DISZKUSSZIÓJUK

3.1 Az antibakteriális és daganatellenes immunválaszok hasonlóságai

Bár általánosan elfogadott, hogy a daganatellenes immunmechanizmusok számos eleme átfed az antibakteriális immunválaszokkal (K. Chen et al., 2007; García-Rodríguez, 2007; Adams, 2009; Sakuishi et al., 2011), a mikrobák által kiváltott pontos daganatellenes mechanizmusok a mai napig nem ismertek részleteikben.

Ami a daganatellenes mechanizmusokat illeti, köztudott, hogy a teljes immunrendszer polarizációs mintázatában bekövetkezett változások meghatározzák a rosszindulatú betegségek kimenetelét (Mantovani et al., 2002; Guiducci et al., 2005; Solinas et al., 2009), és ebben az antitumorális immunválaszban kulcsszereplők a makrofágok, amelyek M1 típusú polarizációja közvetíti az immunrendszer daganatellenes hatását (Mantovani, et al., 2005; Sinha et al., 2005; Sica et al., 2008).

3.1.1 A bakteriális antigének hatása a daganatos mikrokörnyezet makrofágjainak polaritására

Az alább részletezett vizsgálatot egy olyan klinikai megfigyelés indította el, amely fókuszában egy 37 éves, IV. stádiumú, bőr metasztatikus melanómában szenvedő beteg állt. A betegnek a terápia során váratlan, teljes tumorregressziója következett be. A BOLD (bleomicin, onkovin, lomusztin, dakarbazin) kemoterápia során multifaktoriális szepszis szindrómában szenvedett, bakteriális antigének által kiváltott immunreakciók zajlottak a beteg szervezetében. A betegség idővonala az **1. táblázatban** található.

A szepszis célzott antibiotikumos kezelése és a kombinált szövődménymentes kemoterápia után nemcsak a fizikai állapota javult a betegnek, hanem az áttétek is eltűntek, a páciens azóta is teljesen tünet- és áttétmentes, amit PET-CT is igazol.

1. táblázat: A klinikai esetjelentés idővonala

nap	
-360	A beteg önmagán egy vérző, anyajegyszerű elváltozást észlelt a hátán, valamint egy megnagyobbodott axilláris nyirokcsomót is talált; cselekvés nem történt.
-120	Kórházlátogatás. A röntgen, mammográfia és hasi ultrahang vizsgálatok negatívnak bizonyultak, axilláris nyirokcsomó biopsziát javasoltak. A beteg nyomonkövetése átmenetileg megszűnt.
0	**Kórházlátogatás hasi fájdalom miatt, gyomorhurutot diagnosztizáltak, és eltávolítottak egy gyomorpolipot. Daganatot találtak a retroperitoneális nyirokcsomókban (15-20 mm), a lépben (67 mm) és a hólyagban (40x68 mm). Továbbá, CT vizsgálattal egy agyi tumort is kimutattak (40 mm).**
4	Az intrakraniális tumort műtéti úton eltávolították, és amelanotikus melanóma-metasztázisként diagnosztizálták.
24	A koponya sugárkezelése megkezdődött.
30	A beteg leukocitózis és láz miatt Amoxicillin + klavulánsav kezelésben részesült.
32	A sugárkezelés befejeződött.
35	BOLD (bleomicin, onkovin, lomusztin és dakarbazin) kemoterápia megkezdődött.
37	A kemoterápia 3. napján hányás és láz miatt felfüggesztették azt. A gyomornedvben *Escherichia coli* és *Candida albicans* volt. *Clostridium difficile* toxint is kimutattak. Fluconazol és ceftriaxon (később metronidazol) kezelést kezdtek.
52	A CVC-t eltávolították feltételezett *Pseudomonas aeruginosa* fertőzés miatt. Ezt később vérvizsgálattal igazolták.
59	A primer tumort eltávolították és megvizsgálták (Melanoma malignum, Br. 1,52 mm, Cl. III., pT2b).
77	BOLD, 2. kezelési ciklus. Az axilláris és abdominális metasztázisok zsugorodását észlelték.
120	BOLD, 3. ciklus. Az axilláris és intraabdominális metasztázisok további javulását mutatták ki. Intraabdominális nyirokcsomó-megnagyobbodás nem volt, egyetlen májmetasztázist és egy zsugorodó lépmetasztázist találtak.
162	BOLD, 4. ciklus. Az axilláris és abdominális metasztázisok teljes remisszióját figyelték meg.
210	BOLD, 5. ciklus. Az axilláris és abdominális metasztázisok teljes remisszióját figyelték meg.
255	BOLD, 6. ciklus. A beteg tünetmentes és PET-CT-vel igazoltan áttétmentes.
>1500	A beteg tünetmentes és PET-CT-vel igazoltan áttétmentes.

Rövidítések: CT – komputertomográfia, BOLD – bleomicin, onkovin, lomusztin és dakarbazin, CVC – centrális vénás katéter, Br – Breslow vastagság, Cl. – Clark skála, pT2b – patológiai stádiumbeosztás 2b (tumorvastagság 0,01-2mm, van ulceráció), PET-CT – pozitronemissziós tomográfia-komputertomográfia.

A IV. stádiumú melanóma általános túlélése még mindig nagyon rossz. Mivel az immunreakciók a melanóma kimenetelében is döntő tényezőként szerepelnek (Shimanovsky et al., 2013; Ridnour et al., 2013), feltételeztük, hogy a bakteriális szepszis a polarizált, „együttes” antibakteriális és tumorellenes immunválaszok kiváltásával tumorregressziót indukált. A hipotézis tesztelése érdekében a következő kérdéseket vizsgáltuk meg:

- Lehetséges, hogy a bakteriális szepszis a BOLD kemoterápia első kezelési ciklusa során jelentősen hozzájárulhatott a megfigyelt teljes regresszióhoz?
- Ha igen, mik lehettek a mögöttes mechanizmusok?
- Reprodukálható-e a jelenség és a mögöttes eseménylánc egy *in vivo* kísérleti modellben?

Munkánk során egereken végzett *in vivo* kísérletben bebizonyítottuk, hogy a melanóma tüdőáttétek kezelése intracelluláris kórokozóval, a *Chlamidophila pneumoniae*-val (*C. pneumoniae*, C. pn.) (amelyet betegünk szepszisből való felépülése után sikeresen azonosítottak az elsődleges melanómában; **4. ábra**) jelentős tumorregressziót indukál.

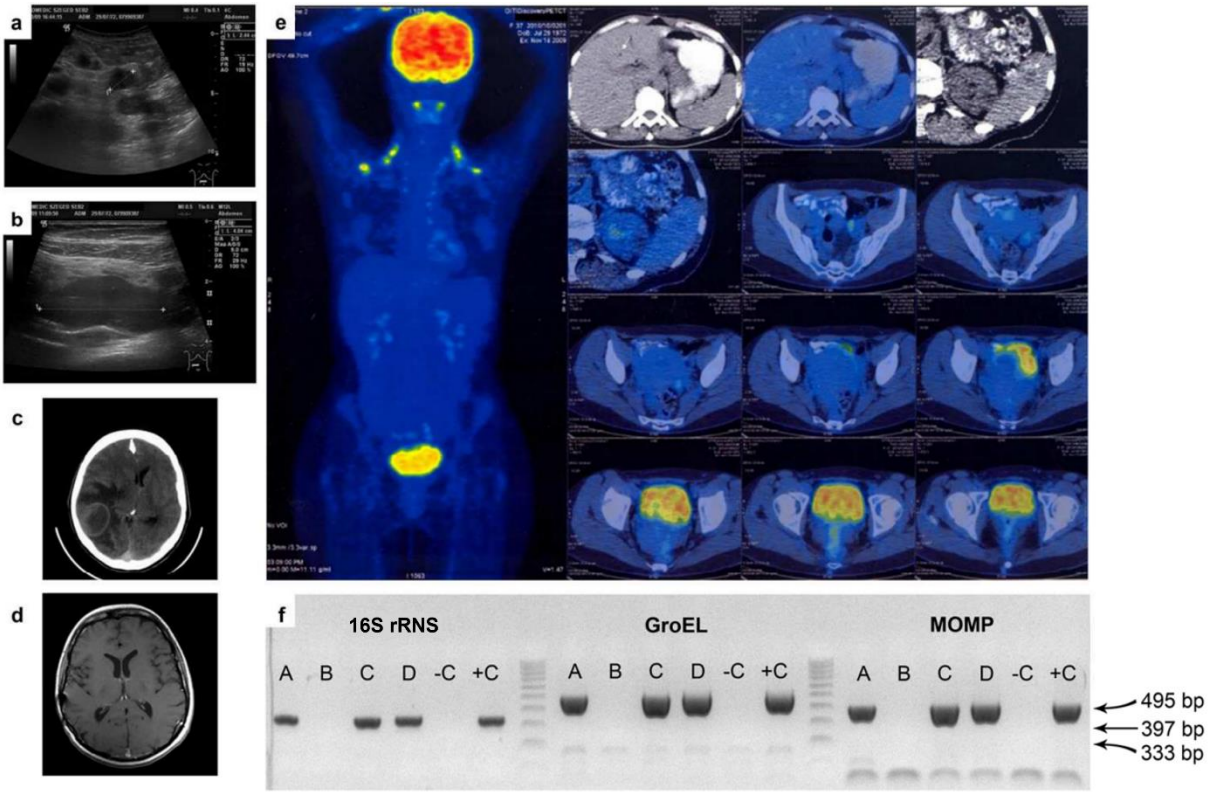

4. ábra. PET-CT-vel igazolt teljes melanóma metasztázis regresszió és retrospektív PCR elemzésen alapuló C. pneumoniae kimutatása.

(a, b) Ultrahang; nagy daganatterhelés a hasüregben. (c, d) CT és MRI vizsgálatok; a műtét előtti agyi metasztázis a temporo-occipitalis lebenyben és a műtét utáni tumormentes agyi állapot. (e) PET-CT-vizsgálatok; teljes daganatregresszió a szervezetben röviddel a szeptikus esemény és a BOLD-kezelés után. (f) C. pneumoniae-specifikus gének retrospektív kimutatása qPCR-ral. Rövidítések: 16S rRNS: a C. pn. housekeeping génje. GroEL: A C. pn. hősokkfehérje 60, az elemi testek felszínén expresszálódó I. csoportba tartozó chaperonin. MOMP: A C. pn. fő külső membránfehérje génje. A-D: FFPE minták az elsődleges melanóma különböző szakaszaiból; -C: PCR negatív kontroll (nem fertőzött Hep2 sejtek); +C: PCR pozitív kontroll (C. pneumoniae TW183 törzzsel fertőzött Hep2 sejtek).

3.1.2 A *C. pneumoniae* kezelés a melanóma metasztázisok regresszióját eredményezi, és növeli az állatok túlélését, valamint a tumorszövetek CD11b+ és CD80+ immunsejt-infiltrációját

Az adaptív immunrendszer szerepének tisztázása érdekében a *C. pneumoniae* által kiváltott daganatellenes immunmechanizmusokban tüdőáttéteket generáltunk immunkompetens C57BL/6 egerekben vagy immunhiányos NSG egerekben. Az állatokat ezután *C. pneumoniae*-val kezeltük, megfelelő negatív kontrollok mellett.

Modellünk speciális tulajdonságai között meg kell említeni, hogy (i) a melanóma sejtek intravénás injektálásával a sejtek beadása után 7 napon belül látható tüdődaganatok alakulnak ki a melanóma sejtekből anélkül, hogy jelentős mértékben átterjednének más szervekbe, így a tüdődaganatok nagy biztonsággal vizsgálhatóak; és (ii) a *C. pneumoniae* egy tüdőspecifikus intracelluláris kórokozó, amely jelentős inváziós rátával még a tüdőmetasztázisokba is behatol.

Megfigyeltük, hogy immunkompetens állatokban a tüdőmetasztázisok száma (**5a ábra**) szignifikánsan csökkent (p = 0,003), míg a túlélés (**5b ábra**) szignifikánsan nőtt (p = 0,04) a *C. pneumoniae*-vel kezelt csoportban a kontroll csoporthoz képest. Nagyon fontos, hogy ilyen jelenségek nem figyelhetőek meg immunhiányos egerekben. A kezelt állatok nem voltak lázasak (33,2 ºC±1,0 kontroll vs. 34,8 ºC±0,5 kezelt) és nem tapasztaltunk magas plazma TNF-α szintet, ami ellentmond a bakteriális antigéneknek tulajdonított „lázhipotézisnek” a daganatok remissziós folyamataiban (Wiemann & Starnes, 1994; Hobohm, 2001).

A szövettani vizsgálatok során megfigyeltük, hogy a kontroll, melanómát hordozó, immunkompetens egerek tüdejének metszete nagyszámú áttétet mutatott, gyakori daganaton belüli nekrózissal, ami nagy daganatterhelést és a normál tüdőszövetet felváltó daganattömeget jelzett (**5c ábra**). Ezzel szemben a *C. pneumoniae*-val kezelt, immunkompetens állatokban a regresszív metasztázisok kevesebb és kisebb gócait figyeltük meg (**5d ábra**). Ezen túlmenően, ebben a csoportban a regresszív metasztázisokban nagyszámú, tumort infiltráló mononukleáris hisztiocitát és limfoid sejtet azonosítottunk összehasonlítva a kontroll mintákkal. Figyelemre méltó, hogy mind a kontroll, mind a *C. pneumoniae*-val kezelt immunhiányos NSG egerekben a metasztázisok nem mutattak szignifikáns intratumorális immunreakciókat (**5e, f ábra**). A *C. pneumoniae*-val kezelt melanómát hordozó C57BL/6 egerek tüdejében tapasztalható jelentősen megnövekedett reaktivitást a CD11b és CD80 sejtfelszíni aktivációs markerek immunfestésével is igazoltuk (**5h, j ábra**). Az immunsejtek inváziója nem volt kimutatható a kontroll csoportban, ahol az

immunsejtek főként a daganatok marginális zónáiban koncentrálódtak (**5g, i ábra**). A *C. pneumoniae*-val kezelt állatok daganatos sztrómájának a belsejében azonban drámaian megnövekedett számú, tumort infiltráló, aktivált limfocitát mutattunk ki (**5h, j ábra**); a különbségek szignifikánsak voltak (**5k, l ábra**) (p = 0,0001).

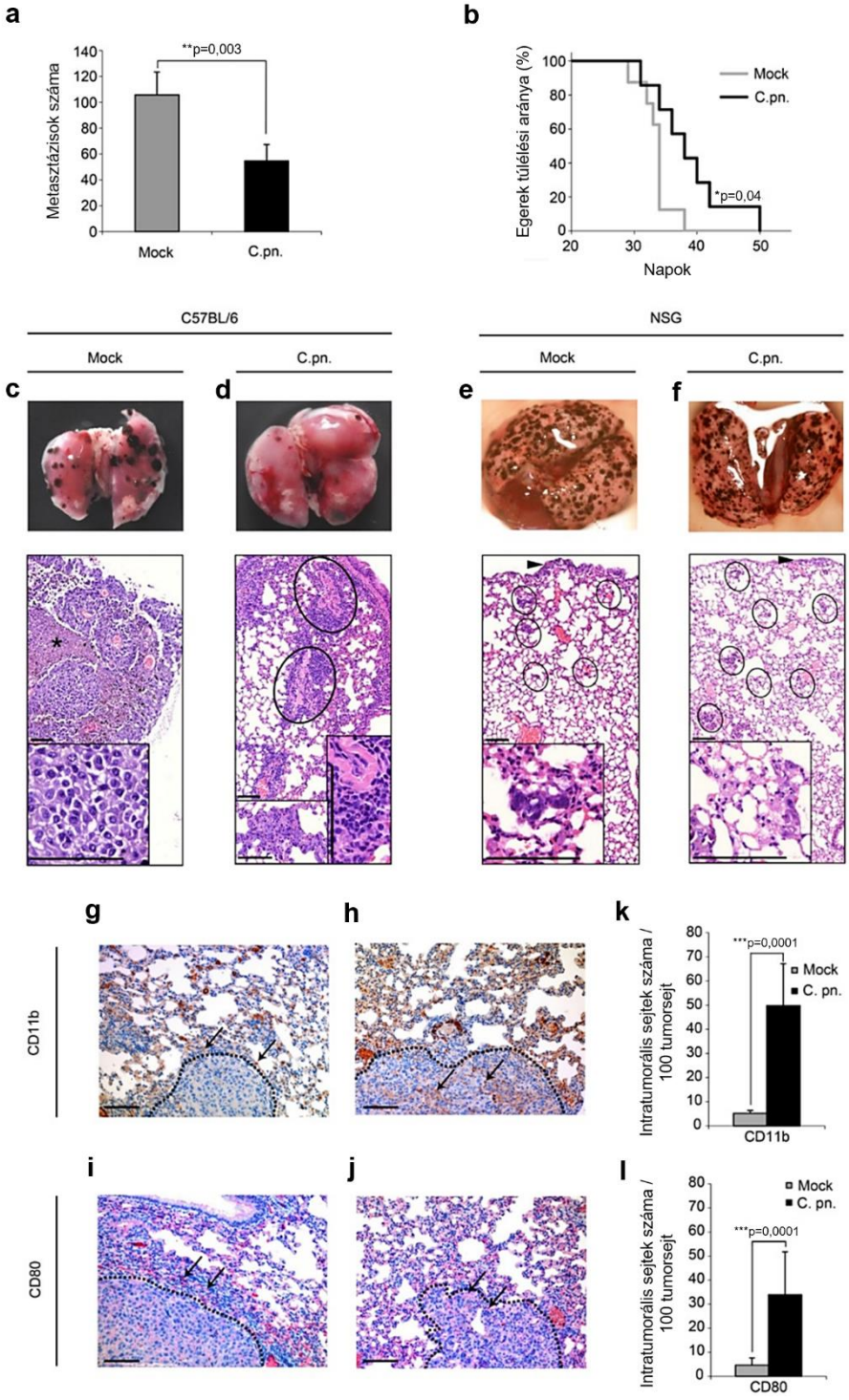

5. ábra. A C. pneumoniae kezelés a melanóma metasztázisok regresszióját eredményezi, és növeli az állatok túlélését, valamint a tumorszövetek CD11b+ és CD80+ immunsejt-infiltrációját.

A tüdőmetasztázisok száma (a) és a túlélési arány (b) kontroll (Mock)- vagy C. pneumoniae (C. pn.) -kezelt immunkompetens C57BL/6 egerek esetében. Reprezentatív fotók és hematoxilin-eozin (H&E) festett szövettani metszetek kontroll (c) és C. pneumoniae-val kezelt (d) immunkompetens egerek, valamint kontroll (e) és C. pneumoniae-val kezelt (f) immunhiányos (NSG) állatok tüdejéről. Méretarány-jelző sáv: 100 µm. (c) Csillaggal jelölt trofikus nekrózisok, amelyek nagy daganatterhelést jeleznek. Nagyított képrészletek: atipikus daganatsejtek és nekrotikus régiók. (d) Körök és jobb oldali nagyított képrészletek, regresszív metasztázisok gócai, bal oldali nagyított képrészlet: C. pneumoniae kezelés utáni reziduális tüdőgyulladás területei. (e, f) Mind a Mock, mind a C. pneumoniae-val kezelt NSG egerekben áttétek alakultak ki szubpleurálisan (nyílhegyek) és intraparenchymálisan (körök) jelentős gyulladásos reakciók nélkül (nagyított képrészletek: intraparenchymalis metasztázisok). A CD11b (g, h, diaminobenzidin, barna) és a CD80 (i, j, fast red, piros) immunhisztokémiája Mock (g, i) vagy C. pneumoniae (h, j) kezelt C57BL/6-os egerek tüdején. A szaggatott vonalak jelzik a tumor határát. (g-j) A nyilak a beszűrődő immunsejteket jelzik. A CD11b+ (k) és CD80+ (l) sejtek intratumorális számát 100 tumorsejt arányában határoztuk meg. (a, k, l) Az adatokat átlag + SD-ben fejezzük ki.

3.1.3 A *C. pneumoniae* kezelés M1 típusú makrofág polarizációt vált ki

Megvizsgáltuk, hogy a *C. pneumoniae* kezelés indukálta-e a makrofágok polarizációját. A makrofágok polarizációjának felmérésére M1 (tumorellenes) vagy M2 (pro-tumorális vagy tumortámogató) makrofág-specifikus citokin és kemokin transzkriptom profilalkotást végeztünk (Mantovani et al., 2004). A makrofág markereket qPCR-ral detektáltuk poolozott tüdőmintákból 2, 4 és 12 órával a Mock vagy *C. pneumoniae* kezelés után. Négy órával a *C. pneumoniae* alkalmazása után a CCL2, CCL3, IL6, CXCL10, CCL7, CD80, CXCL11, CXCL9, IL23 és TNF-α M1-specifikus mRNS transzkriptumainak jelentősen megnövekedett szintjét mutattuk ki. Ezekkel az adatokkal összhangban a CD163, CCL1, TGF-β és IL10 (M2 típusú) mRNS-ek expressziója csökkent a kezelés hatására; a fontos M2 markerek (CXCL13, IL1Ra) szintje azonban megemelkedett (**6a ábra**). A daganatellenes folyamatok szempontjából nagy jelentőségű, hogy *C. pneumoniae* alkalmazása után 4 óra elteltével az M1 típusú citokinek és kemokinek mRNS mennyisége szignifikánsan megnőtt (p = 0,014) az M2 típusú makrofág markerekhez képest (**6b ábra**).

A COX-1 (M2 marker) és COX-2 (M1 marker) expressziós mintázatának megváltozása a makrofág polarizáció egyik kulcsfontosságú markere (Martinez et al., 2006; Mantovani et al., 2013). A Western blot analízis kimutatta, hogy 12 órával a *C. pneumoniae* kezelés után a COX-1 fehérje expressziója, amelyet valószínűleg a tumort támogató M2 típusú makrofágok termelnek, felére csökkent, míg az antitumorális M1 típusú makrofágok által szintetizált COX-2 több mint kétszeres emelkedést mutatott (**6c, d ábra**).

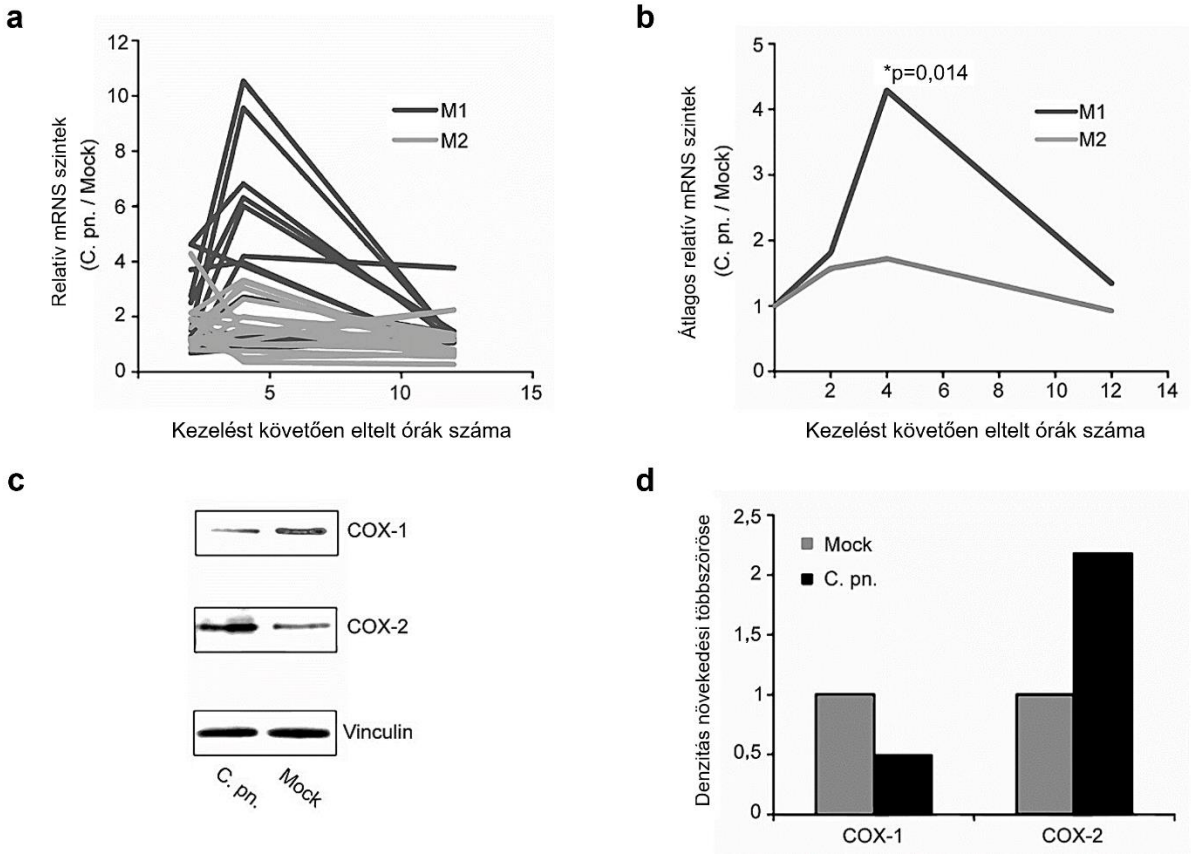

6. ábra. A C. pneumoniae kezelés M1 típusú makrofág polarizációt vált ki.

(a) Az egyedi M1 típusú és M2 típusú citokin/kemokin specifikus mRNS-transzkriptumok szintjének relatív változásai C. pneumoniae (C. pn.) vs. Mock kezelt C57/BL6 egerek tüdőmintáiban, real time qPCR segítségével meghatározva. (b) A relatív M1 és M2 citokin és kemokin mRNS expresszió átlagértékei a kezelés után 4 órával szignifikánsan különböztek egymástól (kétmintás t-próba). (c) Reprezentatív Western-blot. A COX-1 és COX-2 (és a belső kontroll vinculin) expresszióját tüdőmintákban határoztuk meg 12 órával a melanómát hordozó C57BL/6 egerek C. pneumoniae vagy Mock kezelését követően (d) Denzitometriás analízis. Meghatároztuk a COX-1 és COX-2 immunreaktív sávjainak intenzitását, majd vinculinra normalizáltuk. Az adatok a Mock csoport (egynek tekintett) értékéhez viszonyítva többszörös növekedést mutattak. Az ismétlések száma minden esetben legalább három.

3.1.4 A *C. pneumoniae in vivo* és *in vitro* is kiköti a CXCL1-et

A citokinek és kemokinek detektálása alapján 2 órával a *C. pneumoniae* kezelés hatására a CXCL1, a melanóma növekedését és inváziójét elősegítő fehérje (Dhawan & Richmond, 2002) immunreaktivitása teljesen eltűnt a tüdőszövetekből (**7a, b ábra**). Annak megállapítására, hogy ez az *in vivo* jelenség a baktériumok és a CXCL1 közötti közvetlen kölcsönhatás következménye-e, állandó mennyiségű rekombináns CXCL1-et inkubáltunk (proteázgátlók jelenlétében) növekvő mennyiségű *C. pneumoniae* mellett *in vitro*, majd meghatároztuk a CXCL1-szinteket Western-blot segítségével (**7c ábra**). Amint a **7d ábrán** látható, a *C. pneumoniae* dózisfüggő módon kititrálta a CXCL1-et a mintákból, ami arra utal, hogy a baktériumok erősen és közvetlenül kötődnek a CXCL1-hez. Így tehát mindamellett, hogy a bakteriális eredetű antigének polarizációs mechanizmusai az antitumorális válaszokat erősítik, közvetlenül, egy, a melanóma növekedését és inváziójét elősegítő fehérje kititrálása révén is a daganat növekedésének ellenében hat a hőinaktivált baktérium szuszpenzió.

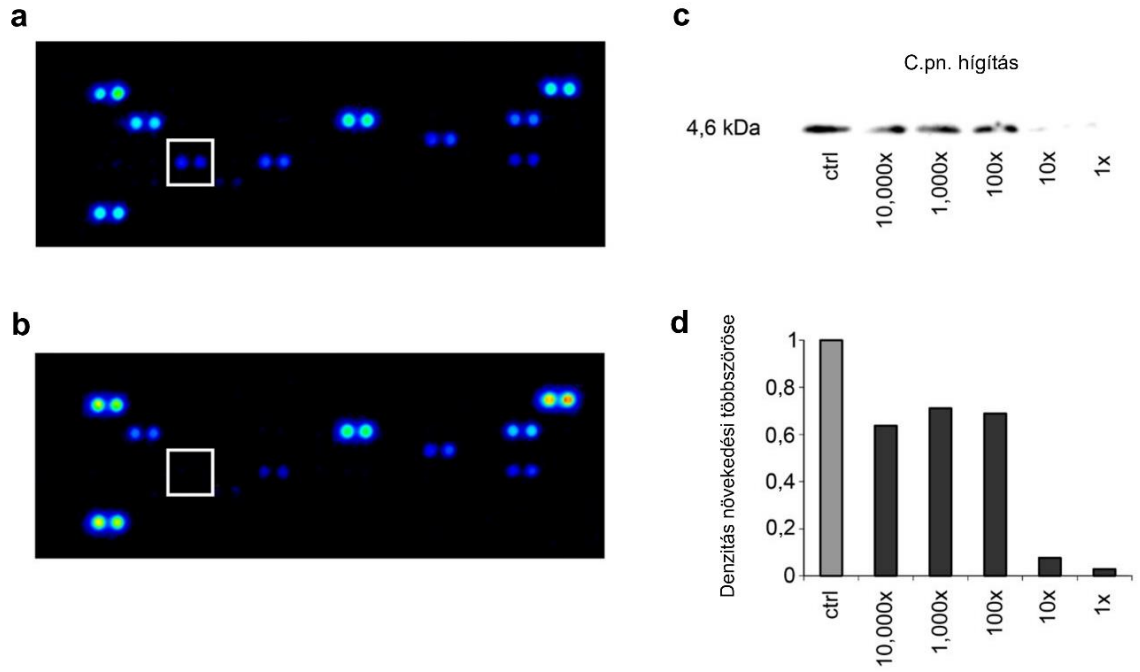

7. ábra. A C. pneumoniae in vivo és in vitro is kiköti a CXCL1-et.

A citokinek és kemokinek szintjének detektálása Proteome profiler kit (R&D Systems) segítségével a melanómát hordozó C57BL/6 egerek tüdejében 2 órával a Mock (a) vagy a C. pneumoniae (C. pn.) (b) kezelés után. A négyzetek a CXCL1-et jelzik, amely a C. pneumoniae kezelés után 2 órával eltűnt (c) Reprezentatív Western blot. Rekombináns egér CXCL1 fehérjét (0,5 µg) in vitro inkubáltunk 500 IFU (inklúzió formáló egység)/µl (1x) C. pneumoniae, vagy annak 10x, 100x, 1000x és 10 000x hígításaival, majd Western blot-ot végeztünk. (d) A c) panelen látható immunreaktív sávok denzitometriás elemzése. A kontroll (ctrl, vivőanyaggal kezelt) csoport értékeit 1-nek tekintettük.

3.2 Az interleukin-24 immunsejtekre gyakorolt kemotaktikus hatása

Az IL-24 receptorain keresztül képes a daganatsejtek szelektív apoptózisát kiváltani, ahogyan az a bevezetőben ismertetésre került. Ugyanezen citokin azonban a bőrön gyakran előforduló *S. aureus* törzsek által is indukálódhat, így a bőr mikrobiótája TLR ligandumai révén hozzájárulhat az antitumorális mikrokörnyezet kialakításához (Buzas & Megyeri, 2006; Stange et al., 2022). Mivel a daganatos mikrokörnyezet alakításában a szövetet infiltráló immunsejteknek komoly szerepe van, így érdemesnek találtuk megvizsgálni, vajon az indukálható IL-24 rendelkezik-e kemotaktikus hatással a mieloid sejtekre.

3.2.1 Az IL-24 *in vitro* humán monocita és neutrofil sejtek migrációját eredményezi

Rekombináns humán IL-24 segítségével *in vitro* sejtmigrációs vizsgálatokat végeztünk. A citokin logaritmikus hígításait használva; 0,125-0,0125 ng/ml tartományban figyeltünk meg maximális migrációt. (**8. ábra**). Az irányított migráció vagy kemotaxis és a fokozott véletlenszerű mozgás vagy kemokinézis közötti különbség kimutatásának egyik módszere, hogy a migrációs vizsgálat elvégzése előtt IL-24-et adunk a sejtekhez. Ha a migráció irányított, akkor amikor a sejteket a migráció maximális koncentrációnak (0,125 ng/ml) megfelelő vagy annál alacsonyabb koncentrációnak tesszük ki, a sejteknek a médiumkontrollhoz képest szignifikáns változások nélkül kell migrálniuk. Továbbá, ha a vándorlás irányított, akkor a sejteket a vándorlási maximum koncentrációnál magasabb IL-24 koncentrációval keverve a sejtek nem vándorolhatnak az alacsonyabb IL-24 koncentrációk felé.

A **2. táblázat**ban látható, hogy az IL-24 által indukált monocita migráció nem kizárólag irányított, hanem kemotaktikus és kemokinetikus migrációt is eredményez. Ezt jelzi a migráció növekedése, amelyet akkor figyelhettünk meg, amikor a sejteket 0,001 ng/ml IL-24-gyel előkezeltük, majd 0,12 ng/ml IL-24 migrációs hatásának tettük ki, valamint az a tény is ezt támasztja alá, hogy az 1,2 ng/ml-es előkezelés nem blokkolta teljesen a migrációt, bár a spontán migráció csökkent. Eredményeink bizonyítják, hogy az IL-24 képes *in vitro* a human monociták és neutrofilek migrációját indukálni.

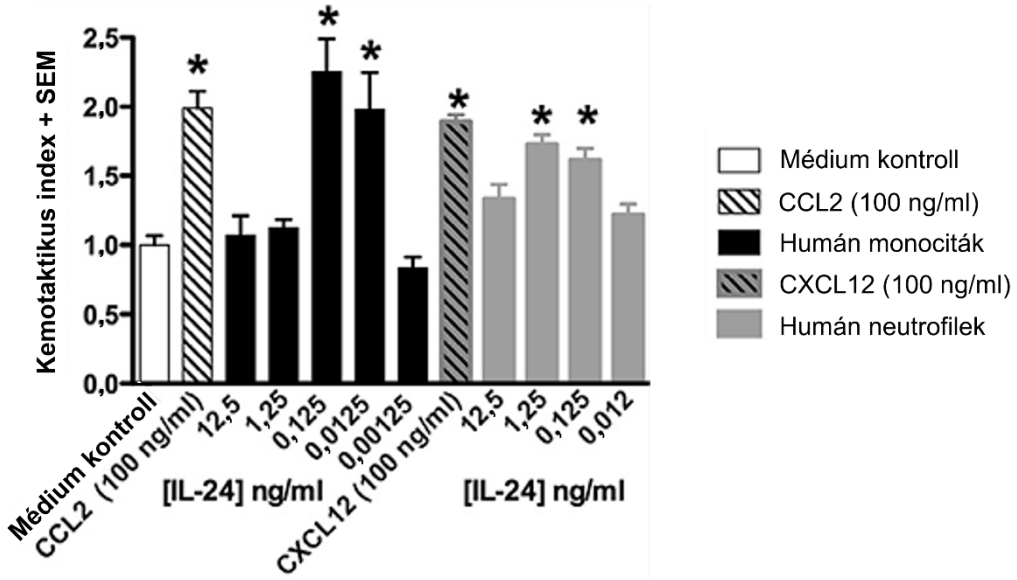

8. ábra. Az IL-24 által indukált humán monocita és neutrofil migráció - in vitro.

*A humán monociták kemotaktikus aktivitását mikro-Boyden kamra segítségével vizsgáltuk. A rekombináns humán IL-24-et az R&D Systems-től szereztük be, és kemotaxis médiumban hígítottuk. A kemotaktikus index az y-tengelyen látható, és a spontán migrációhoz viszonyítva, átlag + SEM szerepel. A humán monociták migrációját sraffozott és fekete sávok, míg a humán neutrofilek migrációját sraffozott és szürke sávok mutatják. A spontán migrációhoz viszonyított * p-érték < 0,001, párosítatlan t-próbával meghatározva; n > 6.*

2. táblázat Az IL-24 által indukált monocita migráció elemzése

Előkezelés a felső lyukakban/ alsó lyukak	**1,2 ng/ml**	**0,12 ng/ml**	**0,001 ng/ml**	**0 ng/ml**
0 ng/ml	$5,9 \pm 1,0^{\#}$	$7,0 \pm 1,0$	$10,18 \pm 1,5$	$8,8 \pm 1,1$
0,001 ng/ml	$7,7 \pm 1,0$	$15,4 \pm 1,6^{**}$	$7,3 \pm 0,7$	$6,7 \pm 1,2$
0,12 ng/ml	$12,6 \pm 1,8^{*}$	$18,4 \pm 2,6^{**}$	$20,9 \pm 3,9^{**}$	$18,4 \pm 3,0^{**}$
1,2 ng/ml	$10,4 \pm 1,9$	$10,4 \pm 2,2$	NA	$12,4 \pm 2,1$

*A humán monocitákat 30 percig alapmédiummal (0 ng/ml), 1,2 ng/ml, 0,12 ng/ml vagy 0,001 ng/ml IL-24-gyel kezeltük elő a mikro-Boyden kemotaxis vizsgálat előtt. A táblázat felső sorában az előkezelési körülmények, a táblázat első oszlopában pedig az alsó kamrákban alkalmazott kemoattraktáns (IL-24) koncentrációk láthatók. Ebben a táblázatban a migrált monociták átlagos sejtszáma szerepel képmezőnként 400 × nagyítás mellett (átlag ± SEM, n = 3). Rövidítések: NA = nincs adat minden donor esetén, # p = 0,01 – az esetszám csökkent, * p = 0,05 – az esetszám emelkedett, ** p ≤ 0,006 – az esetszám emelkedett.*

3.2.2 Az IL-24 *in vivo* indukálja a leukociták migrációját

Ezután azt vizsgáltuk, hogy az IL-24 *in vivo* vajon toboroz-e sejteket. Korábbi tanulmányok alapján, amelyek szerint *in vivo* 10-szer több kemoattraktánsra van szükség, mint amennyi a maximális *in vitro* aktivitáshoz szükséges (Sironi et al., 1999), az IL-24-nek egerenként 0,1 és 10 ng/ml közötti tartományát vizsgáltuk. Amint a **9. ábra** mutatja, a 0,1 ng/ml-es IL-24 dózis 2-szeres növekedést idézett elő az egér légzsák modellben visszanyert összsejtszámban, míg a CCL2 1000 ng/ml-es dózisa 1,5-szeres növekedést idézett elő. Mindkét növekedés statisztikailag szignifikáns. Ezek az eredmények azt jelzik, hogy az IL-24 *in vivo* és *in vitro* is képes sejtmigrációt indukálni.

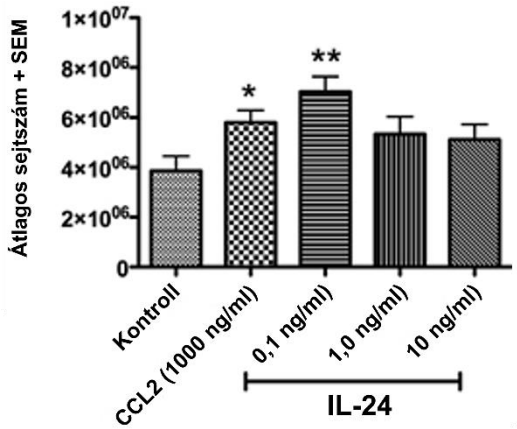

9. ábra. Az IL-24 által indukált leukocita migráció - in vivo.

*A HBSS-ben hígított rekombináns IL-24-et C57BL/6 egerek hátán kialakított légzsákokba fecskendeztük. 24 órával később a sejteket a légzsákokból kinyertük és megszámoltuk. A sejtek átlagos számát milliós + SEM értékben ábrázoltuk az egyes kezelési körülményekre vonatkozóan, a kontroll kemoattraktáns-mentes HBSS volt. Ábrajelölés: kétmintás t-próba kontrollhoz viszonytva *p = 0,01 és **p = 0,003; n > 4.*

3.2.3 Az IL-24 a leukociták egyes alcsoportjait különböző mértékben toborozza

Az IL-24 által az egér légzsákba toborzott leukociták alcsoportjainak értékelésére áramlási citometriai (FACS) analízist végeztünk. Arányosan kevesebb CD3+ CD45+ leukocitát vonzott az IL-24, mint a CCL2 (**10a, b ábra**). Míg a CCL2, vagy az IL-24 által toborzott sejtek többsége CD11b+ mieloid sejt, az IL-24 statisztikailag több CD11b+ F4/80+ rezidens makrofágot toboroz (**10c, d ábra**). Mind az IL-24, mind a CCL2 hasonló arányban toborzott CD11b+, Ly6G-et magasan reprezentáló neutrofileket (ezen adatok nem kerültek bemutatásra).

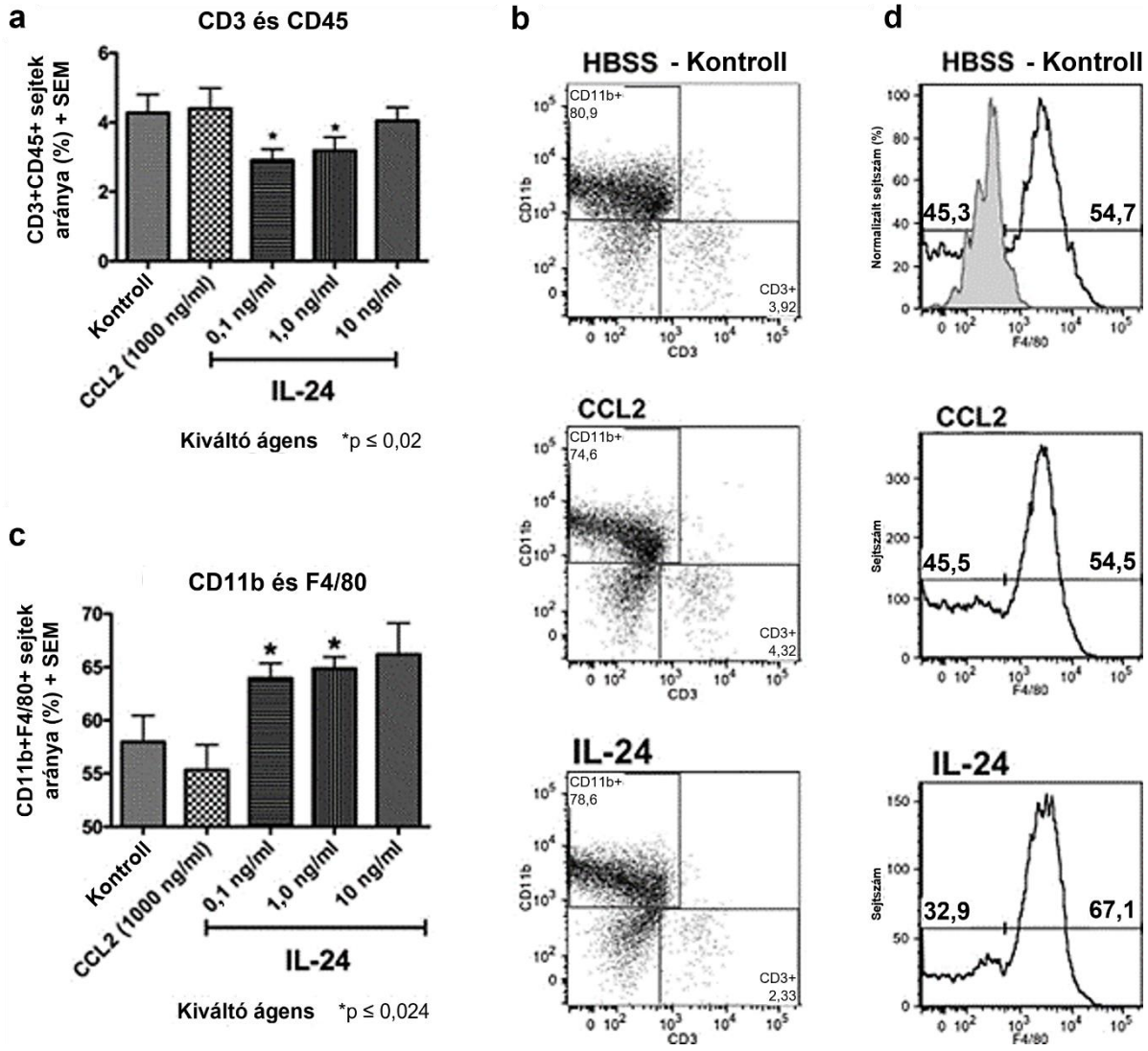

10. ábra. Az in vivo rekrutált leukociták FACS analízise.

*(a) Az összes rekrutált leukocita átlagos százalékos aránya (+ SEM), amely mind a CD45-re, mind a CD3-ra pozitívan festődik, összehasonlítva a légzsákba injektált különböző kiváltó ágensekkel (n > 4). (b) Reprezentatív pontdiagram a rekrutált CD45+ kapuzott sejtekről, amelyek az x-tengelyen CD3-ra, illetve az y-tengelyen CD11b-re festődtek. A CD3 vagy CD11b szempontjából pozitívan festődő CD45+ kapuzott sejtek százalékos aránya a bekeretezett részekben láthatók. (c) Az F4/80-ra is pozitívan festődő, rekrutált CD11b+ sejtek átlagos százalékos aránya (+ SEM), összehasonlítva a légzsákba injektált különböző koncentrációjú IL-24 által rekrutált sejtekkel (n > 4). (d) A CD11b+ sejtek F4/80-pozitív festődése. A pozitív (jobbra) vagy negatív (balra) százalékos arányt a mellékelt számok mutatják. Az árnyékolt hisztogram az F4/80 izotípusos kontrollját mutatja. *p ≤ 0,024 a légzsákba injektált HBSS kontrollhoz képest.*

3.2.4 Az IL-24 migrációs receptorok osztályai a leukocitákon

Az IL-24 által a leukocitákon használt receptorok osztályainak kategorizálása érdekében monocitákat kezeltünk szignálkaszkád-gátlókkal. Mivel a kemoattraktáns receptorok többsége G-proteinhez kötött receptor, amelyek érzékenyek a pertussis toxin gátlására, megvizsgáltuk a pertussis toxin hatását az IL-24 által kiváltott migrációra. Amint a **11a ábrán** látható, az IL-24 által indukált migráció érzékeny volt a pertussis toxin kezelésre, így a Giα alcsaládba tartozó G fehérjéhez kapcsolt receptor szerepet játszik az IL-24 által indukált sejtmigrációban.

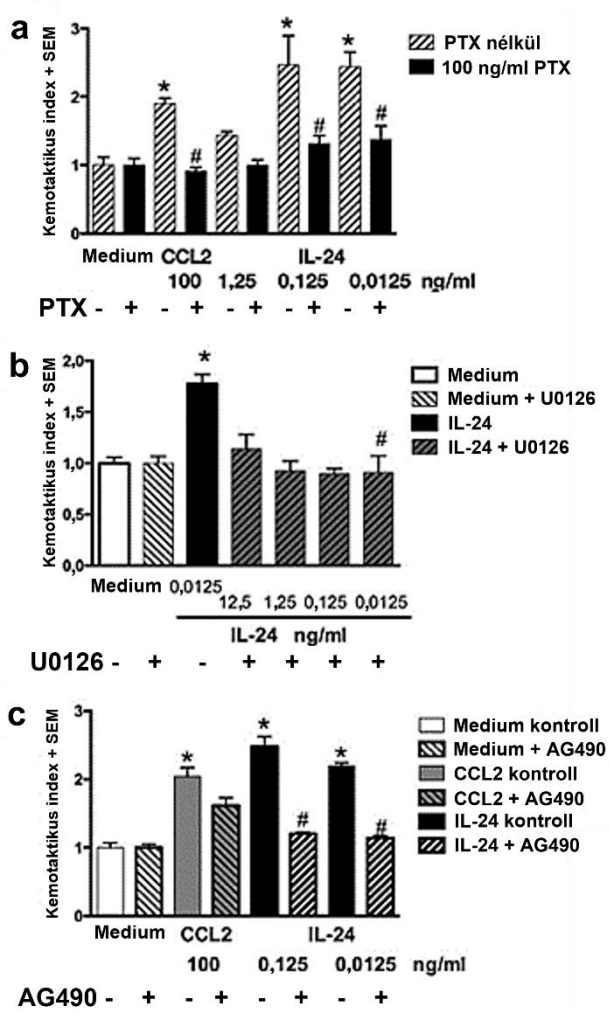

11. ábra. Az IL-24 által indukált humán monocita migráció gátolható.

*(a) A pertussis toxin (PTX) előkezelés gátolja az IL-24 indukálta monocita kemotaxist. A médiumra, CCL2-re vagy IL-24-re történő kemotaxist a sraffozott sávok mutatják. A 100 ng/ml pertussis toxinnal 30 percig előkezelt monociták kemotaxisát a tömör fekete sávok mutatják. *a migráció növekedését jelzi, p-érték < 0,001 a médiumkontrollhoz képest, # a migráció csökkenését jelzi, p-érték < 0,01 a pertussis toxin nélküli kemoattraktáns azonos koncentrációjához képest. (b) A monociták U0126-kezelése gátolja az IL-24 által kiváltott monocita kemotaxist. Humán monocitákat 30 percig 50 μM U0126-tal (MEK-inhibitor) előkezeltük, mielőtt a sejteket mikro-Boyden kamrába helyeztük. A fehér sávok a kontroll*

*médiumot mutatják. Az IL-24 fekete sávokkal ábrázolva látható. Az U0126-kezelést a sraffozott sávok jelzik. *a migráció növekedését jelzi p < 0,001 értékkel a médiumkontrollhoz képest, # a migráció csökkenését jelzi p < 0,001 értékkel az U0126-kezelés nélküli esetekhez képest. (c) A monociták AG490-nel történő előkezelése gátolja az IL-24 által kiváltott monocita kemotaxist. Humán monocitákat 50 μM AG490-nel (JAK-inhibitor) inkubáltuk 30 percen keresztül, mielőtt a kemotaxiskamrába helyeztük a sejteket. A médiumot fehér, a CCL2-t (100 ng/ml) szürke, az IL-24-et fekete oszlopokkal ábrázoltuk. Az AG490-nel kezelt sejteket sraffozott oszlopok mutatják. * a migráció növekedését jelzi p < 0,001 értékkel a médiumkontrollhoz képest, # a migráció csökkenését jelzi p < 0,001 értékkel az AG490 kezelés nélküli esetekhez képest; n > 6.*

Számos olyan növekedési faktor receptorról ismert, amely másodlagos migrációs hatással rendelkezik, hogy a MAPK család tagjait aktiválja (Tian et al., 2007). Az IL-24 endotélsejtek által expresszált receptorairól, az IL-20R2/IL-20R1-ről és az IL-20R2/IL-22R-ről ismert, hogy a JAK/STAT útvonal aktiválásán keresztül szignalizálnak (Kotenko & Langer, 2004; M. Wang & Liang, 2005). Ezért teszteltük ezen útvonalak gátlóit, és azt találtuk, hogy a MEK gátlók, (sraffozott oszlopok az egyszínű oszlopokhoz képest, **11b ábra**) és a JAK gátlók (sraffozott oszlopok az egyszínű oszlopokhoz képest, **11c ábra**) szignifikánsan csökkentik az IL-24 által kiváltott monocita migrációt.

3.3 Tumoros mikrokörnyezet elemeinek változása daganatsejtek által termelt vezikulák jelenlétében, a melanóma exoszómák PD-1 expresszióra gyakorolt hatása

A mezenchimális őssejteknek a daganatok progressziójában betöltött szerepéről akár immunológiai, akár differenciálódási tulajdonságaikkal kapcsolatban különböző vélemények születnek. Feltételezhető, hogy a daganatmasszában és annak közvetlen környezetében megtalálhatóak olyan plasztikus, kevéssé differenciálódott sejtek (MSC-k), amelyek különböző külső hatásokra képesek daganatsejt vagy daganatőssejt-szerű fenotípust mutatni.

Az eredmény a tumor típusától és az érintett MSC-k állapotától is függ. Az aktivált MSC-k pro-angiogén oldható faktorokat választanak ki, képesek differenciálódni tumor asszociált fibroblasztokká (CAF). Baglio és munkatársai 2017-ben publikálták, hogy a tumor eredetű exoszómák által befolyásolt mezenchimális őssejtek elősegítik az oszteoszarkóma progresszióját. Ezek az adatok az exoszóma-MSC kommunikáció tumorevolúcióban betöltött központi szerepére utalnak (Baglio et al., 2017).

Az MSC-k melanóma exoszómák hatására bekövetkező fenotípusos változásai közül kiemelkedő jelentőségűnek találtuk a PD-1 megjelenését a kérdéses sejtpopulációban. Ez a

kérdés azért különösen érdekes, mert a ma elérhető egyik leghatékonyabb immunterápia a PD-1:PD-1L interakció blokádján alapul (Bersanelli & Buti, 2017).

Az elmúlt évtizedben az IL-2 és CTLA-4 terápiák mellett a PD-1:PD-L1 blokád hatékony kezelésnek bizonyult áttétes melanóma esetén (Kee & McArthur, 2017). A programozott sejthalál protein 1 (PD-1), amelyet főként immunsejtek, például aktivált T-sejtek, dendritikus sejtek és makrofágok expresszálnak, egy sejtfelszíni receptor, amely központi szerepet játszik a T-sejtes válaszok modulálásában. A PD-1 ligandumához, a PD-1L-hez való kötődése apoptózist és az immunsejtek anergiáját eredményezheti.

Azonban a PD-1 expresszió nem a melanóma sejtek alapértelmezett tulajdonsága és különös jelentőséggel bír Kleffel et al. munkája, melyben kimutatták, hogy a PD-1-et túlzottan expresszáló melanóma sejt alpopulációk különösen agresszívek, illetve hogy a melanóma PD-1:PD-1L kölcsönhatásai modulálják az mTOR jelátvitelt, ezáltal megzavarják a programozott sejthalál folyamatának lefutását (Kleffel et al., 2015). Bár ez a munka rendkívül hasznos a PD-1 túlzott expressziójának és a PD-1 funkciók kísérleti gátlásának (Pdcd1-shRNS vagy anti-PD-1 antitest) következményei tekintetében, nem nevezi meg azokat a tényezőket, amelyek aktiválása a PD-1 túlzottan expresszáló alpopulációk kialakulásához vezetnek.

A fentiek alapján a következő kérdések megválaszolására törekedtünk:

- Egyértelműen meghatározhatóak-e az MSC tenyészetek melanóma eredetű exoszóma-indukált, intercelluláris kommunikáció által közvetített malignus transzformációjának sejtes és molekuláris jelei?
- Kimutatható-e a melanóma eredetű, exoszóma által kiváltott tumor progresszió *in vivo?*
- Milyen változás mutatható ki a PD-1, a melanóma progresszió markerének és terápiás célpontjának expressziójában, melanóma eredetű exoszómák hatására?

Az extracelluláris vezikulák kutatásának már egészen kezdeti stádiumában kiderült, hogy a vezikulák immunológiai szempontból nem inertek. Korai közleményünkben bemutattuk, hogy a melanóma exoszómák – bár az immunolóiai aktivitásuk polaritásáról nem sikerült egyértelmű információkat nyernünk – egészen biztosan aktiválják az immunológiai mechanizmusok egyik karmesterét, az nF-κB-t (Marton et al., 2012). Ezért joggal feltételeztük, hogy a melanóma exoszómák a tumorsztómában található MSC-kre is hatással lehetnek.

Az alábbiakban részletesen bemutatom azokat az eredményeket, melyek alapján kijelenthetjük, hogy a melanóma exoszómák komplex onkogén molekuláris átprogramozás közvetítésével PD-1-et túltermelő, melanóma-szerű MSC$^{PD\text{-}1+}$ (MSC$^{PD\text{-}1+}$) sejtpopuláció kialakulását indukálják naiv MSC-kből. Ezek az MSC$^{PD\text{-}1+}$ sejtek egy új entitást képviselnek, melanóma-szerű génexpressziós profillal és fenotípusos tulajdonságokkal. Ezenkívül az exoszómák és az exoszómákkal aktivált MSC$^{PD\text{-}1+}$ sejtek gyors tumorprogressziót indukálnak *in vivo*, köszönhetően az onkogén dominanciát mutató faktorok emelkedett expressziójának és a programozott sejthalálra való csökkent érzékenységüknek.

3.3.1 Az izolált vezikulák exoszómális tulajdonságokat mutatnak

Először extracelluláris vezikulákat izoláltunk a B16F1 egér melanóma sejtek felülúszóiból. Amint azt a pásztázó elektronmikroszkópia (SEM) és az atomerő mikroszkópia (AFM) kimutatta (**12a, b ábra**), az izolált frakció valóban feldúsulva tartalmazott exoszómákat, a részecskék jellegzetes alakúak voltak, és méretük a 40-120 nm tartományba esett. Ezután az exoszómákra (Yáñez-Mó et al., 2015; Théry et al., 2018) jellemző molekulák (CD9, CD63, CD81 és HSP70) jelenlétét Western blottal mutattuk ki (**12c ábra**).

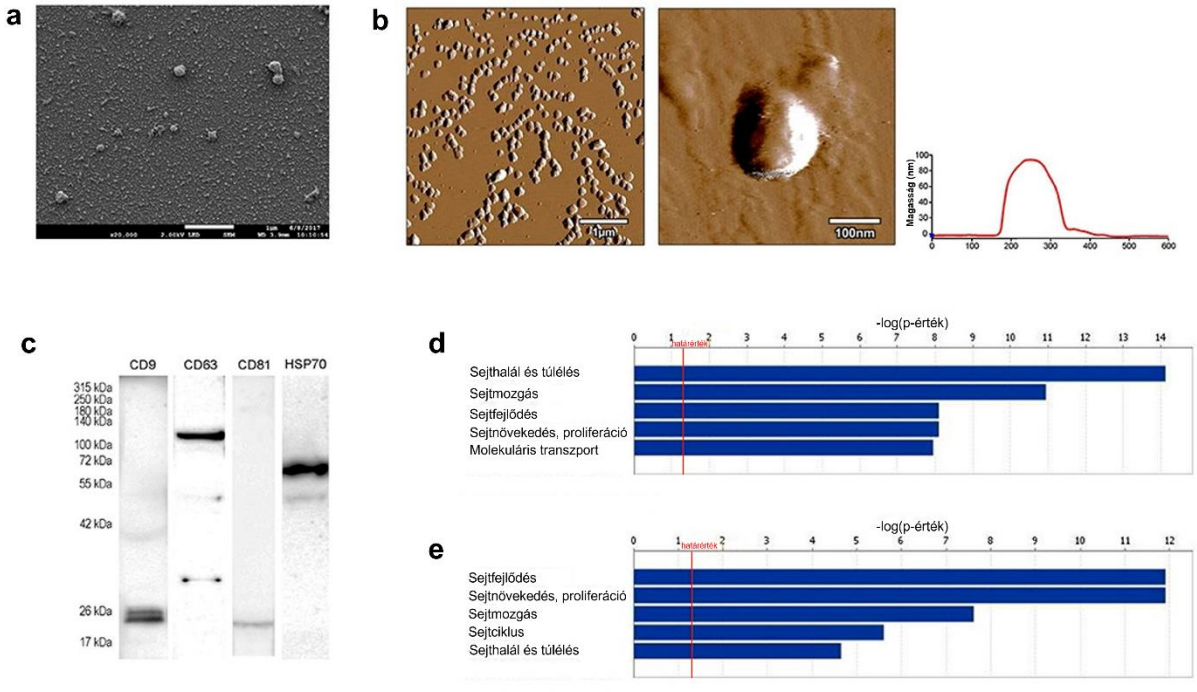

12. ábra. B16F1 melanóma sejttenyészetből származó exoszómák jellemzése.
(a) Melanóma exoszómák pásztázó elektronmikroszkópos felvétele. (b) Az exoszómák atomerő mikroszkópos felvételei. A bal és a középső kép a vezikulák alakját és felszíni topográfiáját, a jobboldali grafikon a magassági profilt ábrázolja. (c) Az exoszóma markerek (CD9, CD63, CD81 és HSP70) Western blot analízise. (d, e) Az exoszómális fehérjék és miRNS-ek Ingenuity Pathway Analízisével azonosított 5 legfontosabb molekuláris és sejtfunkció.

Az exoszómákat ezután tömegspektrometriai elemzésnek és miRNS szekvenálásnak vetettük alá, hogy meghatározzuk fehérje- és miRNS-profiljukat. A teljes proteomanalízishez folyadékkromatográfia-tömegspektrometriát (LC-MS/MS) használtunk és bioinformatikai eszközök segítségével az exoszóma proteomikai spektrumának elemeit az UniProt adatbázisban azonosítottuk, valamint az eredmények összehasonlítására az ExoCarta adatbázist vettük igénybe. Ezen eljárások segítségével 95 különböző fehérjét azonosítottunk melanóma exoszómákban, melyek 86,3%-os átfedést mutattak az ExoCartában jellegzetes exoszómális fehérjemolekulákkal (**3. táblázat**).

3. táblázat: Az LC-MS/MS analízis során azonosított exoszómális fehérjék listája.

Azonosító	Szimbólum	Entrez gén elnevezése
P97857	ADAMTS1	ADAM metallopeptidase with thrombospondin type 1 motif 1
Q3TNX8	ADAMTS4	ADAM metallopeptidase with thrombospondin type 1 motif 4
Q640N1	AEBP1	AE binding protein 1
P05064	ALDOA	aldolase, fructose-bisphosphate A
P97429	ANXA4	annexin A4
P48036	ANXA5	annexin A5
P08226	APOE	apolipoprotein E
Q3TWT5	ASAH1	N-acylsphingosine amidohydrolase 1
Q3TXF9	ATP1A1	ATPase Na+/K+ transporting subunit alpha 1
P97370	ATP1B3	ATPase Na+/K+ transporting subunit beta 3
Q1XID4	ATP6AP2	ATPase H+ transporting accessory protein 2
Q9JL18	BACE2	beta-site APP-cleaving enzyme 2
O55107	BSG	basigin (Ok blood group)
Q8R2Q8	Bst2	bone marrow stromal cell antigen 2
Q9WVT6	CA14	carbonic anhydrase 14
P41731	CD63	CD63 molecule
P35762	CD81	CD81 molecule
P10605	CTSB	cathepsin B
P18242	CTSD	cathepsin D
P29812	DCT	dopachrome tautomerase
P57776	EEF1D	eukaryotic translation elongation factor 1 delta
Q3UAM9	ENG	endoglin
P17182	ENO1	enolase 1
P19096	FASN	fatty acid synthase
P30416	FKBP4	FK506 binding protein 4
P11276	FN1	fibronectin 1
P09528	FTH1	ferritin heavy chain 1
P16858	GAPDH	glyceraldehyde-3-phosphate dehydrogenase
P08752	GNAI2	G protein subunit alpha i2
Q3TAV1	GPNMB	glycoprotein nmb
P19157	GSTP1	glutathione S-transferase pi 1
P11499	HSP90AB1	heat shock protein 90 alpha family class B member 1

Azonosító	Szimbólum	Entrez gén elnevezése
B1B0C7	HSPG2	heparan sulfate proteoglycan 2
Q9CQW9	IFITM3	interferon induced transmembrane protein 3
G3UYZ1	IGSF8	immunoglobulin superfamily member 8
Q91VK4	ITM2C	integral membrane protein 2C
P02468	LAMC1	laminin subunit gamma 1
Q60961	LAPTM4A	lysosomal protein transmembrane 4 alpha
P35951	LDLR	low density lipoprotein receptor
Q07797	LGALS3BP	galectin 3 binding protein
Q3U2W5	LGALS8	galectin 8
P16056	MET	MET proto-oncogene, receptor tyrosine kinase
P21956	MFGE8	milk fat globule-EGF factor 8 protein
Q2TA50	MLANA	melan-A
Q6NVG5	MREG	melanoregulin
Q9EPX2	PAPLN	papilin, proteoglycan like sulfated glycoprotein
Q3UIP2	PCOLCE	procollagen C-endopeptidase enhancer
Q811J2	LOC72520	LOC72520 protein
Q80Y09	PDCD6IP	programmed cell death 6 interacting protein
P62962	PFN1	profilin 1
P09411	PGK1	phosphoglycerate kinase 1
P52480	PKM	pyruvate kinase, muscle
Q9CZB2	PMEL	premelanosome protein
P17742	PPIA	peptidylprolyl isomerase A
P35700	PRDX1	peroxiredoxin 1
Q61171	PRDX2	peroxiredoxin 2
Q543S0	PRELP	proline and arginine rich end leucine rich repeat protein
P53994	RAB2A	RAB2A, member RAS oncogene family
Q8CCG5	RALB	RAS like proto-oncogene B
O89086	RBM3	RNA binding motif (RNP1, RRM) protein 3
P35980	RPL18	ribosomal protein L18
Q3U5P4	SCPEP1	serine carboxypeptidase 1
O08992	SDCBP	syndecan binding protein
Q0VGP2	SEMA3B	semaphorin 3B
P32261	SERPINC1	serpin family C member 1
P10852	SLC3A2	solute carrier family 3 member 2
Q3UQM7	SLC7A5	solute carrier family 7 member 5
O09044	SNAP23	synaptosome associated protein 23
Q64337	SQSTM1	sequestosome 1
Q8CI59	STEAP3	STEAP3 metalloreductase
Q3TDG9	STX12	syntaxin 12
O70439	STX7	syntaxin 7
P40749	SYT4	synaptotagmin 4
O88968	TCN2	transcobalamin 2
Q542D9	TFRC	transferrin receptor

Azonosító	Szimbólum	Entrez gén elnevezése
P39876	TIMP3	TIMP metallopeptidase inhibitor 3
Q4FJX7	TINAGL1	tubulointerstitial nephritis antigen like 1
Q9DCS1	TMEM176A	transmembrane protein 176A
Q9R1Q6	TMEM176B	transmembrane protein 176B
Q9CZX7	TMEM55A	transmembrane protein 55A
Q9QY73	TMEM59	transmembrane protein 59
O88746	TOM1	target of myb1 membrane trafficking protein
O89023	TPP1	tripeptidyl peptidase 1
Q3UCW0	TSG101	tumor susceptibility 101
Q4FJW7	TSPAN4	tetraspanin 4
Q8BJU2	TSPAN9	tetraspanin 9
P11344	TYR	tyrosinase
P07147	TYRP1	tyrosinase related protein 1
O70404	VAMP8	vesicle associated membrane protein 8
Q8R0J7	VPS37B	VPS37B, ESCRT-I subunit
Q8R105	VPS37C	VPS37C, ESCRT-I subunit
O88384	VTI1B	vesicle transport through interaction with t-SNAREs 1B
A8DUQ1	HBBT1	beta-globin
P70356	MELA	Gag-pol poliprotein
P70355	MELA	envelope protein

Továbbá a miRNS szekvenálás (SOLiD 5500xl technológiával) 168 ismert miRNS elemet azonosított (**4. táblázat**), amelyek a proteomikai adatokhoz hasonlóan nagy (93,5%-os) átfedést mutattak az ExoCartában jellegzetes exoszómális miRNS molekulákkal.

4. táblázat. A SOLiD 5500xl technológiával azonosított exoszómális miRNS-ek listája.

Szimbólum	Magrégió	Azonosító
let-7a-3p	UAUACAA	mmu-let-7a-1-3p
		mmu-let-7b-3p
		mmu-let-7c-2-3p
		mmu-let-7f-1-3p
let-7a-5p	GAGGUAG	mmu-let-7a-5p
		mmu-let-7b-5p
		mmu-let-7c-5p
		mmu-let-7d-5p
		mmu-let-7e-5p
		mmu-let-7f-5p
		mmu-let-7g-5p
		mmu-mir-98-5p
let-7d-3p	UAUACGA	mmu-let-7d-3p
let-7i-3p	UGCGCAA	mmu-let-7i-3p

Szimbólum	Magrégió	Azonosító
miR-100-5p	ACCCGUA	mmu-mir-99a-5p
		mmu-mir-99b-5p
miR-101-3p	ACAGUAC	mmu-mir-101a-3p
miR-103-1-5p	GCUUCUU	mmu-mir-107-5p
miR-103-3p	GCAGCAU	mmu-mir-103-3p
		mmu-mir-107-3p
miR-10a-5p	ACCCUGU	mmu-mir-10a-5p
		mmu-mir-10b-5p
miR-1191a	AGUCUUA	mmu-mir-1191a
miR-1249-3p	CGCCCUU	mmu-mir-1249-3p
miR-125b-5p	CCCUGAG	mmu-mir-125a-5p
		mmu-mir-125b-5p
		mmu-mir-351-5p
miR-126a-5p	AUUAUUA	mmu-mir-126a-5p
miR-128-3p	CACAGUG	mmu-mir-128-3p
miR-129-1-3p	AGCCCUU	mmu-mir-129-1-3p
		mmu-mir-129-2-3p
miR-129b-5p	CUUUUUG	mmu-mir-129b-5p
miR-130a-3p	AGUGCAA	mmu-mir-130a-3p
		mmu-mir-130b-3p
		mmu-mir-301a-3p
		mmu-mir-301b-3p
miR-130a-5p	CUCUUUU	mmu-mir-130a-5p
miR-130b-5p	CUCUUUC	mmu-mir-130b-5p
miR-132-3p	AACAGUC	mmu-mir-132-3p
miR-132-5p	ACCGUGG	mmu-mir-132-5p
miR-135a-5p	AUGGCUU	mmu-mir-135a-5p
miR-138-5p	GCUGGUG	mmu-mir-138-5p
miR-139-5p	CUACAGU	mmu-mir-139-5p
miR-140-3p	ACCACAG	mmu-mir-140-3p
miR-140-5p	AGUGGUU	mmu-mir-140-5p
miR-142-3p	GUAGUGU	mmu-mir-142a-3p
miR-143-5p		mmu-mir-143-5p
miR-144-3p	ACAGUAU	mmu-mir-144-3p
miR-144-5p	GAUAUC	mmu-mir-144-5p
miR-145-5p	UCCAGUU	mmu-mir-145a-5p
miR-146a-5p	GAGAACU	mmu-mir-146a-5p
miR-148a-3p	CAGUGCA	mmu-mir-148b-3p
miR-151-3p	UAGACUG	mmu-mir-151-3p
miR-15a-3p	AGGCCAU	mmu-mir-15a-3p
miR-15b-3p	GAAUCAU	mmu-mir-15b-3p
miR-16-2-3p	CCAAUAU	mmu-mir-16-2-3p

Szimbólum	Magrégió	Azonosító
miR-16-5p	AGCAGCA	mmu-mir-15a-5p
		mmu-mir-15b-5p
		mmu-mir-16-5p
		mmu-mir-195a-5p
		mmu-mir-322-5p
		mmu-mir-497a-5p
miR-17-3p	CUGCAGU	mmu-mir-17-3p
miR-17-5p	AAAGUGC	mmu-mir-106b-5p
		mmu-mir-17-5p
		mmu-mir-20a-5p
		mmu-mir-93-5p
miR-181a-1-3p	CCAUCGA	mmu-mir-181a-1-3p
miR-181a-5p	ACAUUCA	mmu-mir-181a-5p
		mmu-mir-181b-5p
		mmu-mir-181c-5p
		mmu-mir-181d-5p
miR-1827	GAGGCAG	mmu-mir-709
miR-1839-3p	GACCUAC	mmu-mir-1839-3p
miR-185-5p	GGAGAGA	mmu-mir-185-5p
miR-186-5p	AAAGAAU	mmu-mir-186-5p
miR-187-3p	CGUGUCU	mmu-mir-187-3p
miR-188-3p	UCCCACA	mmu-mir-188-3p
miR-188-5p	AUCCCUU	mmu-mir-188-5p
miR-18a-5p	AAGGUGC	mmu-mir-18a-5p
miR-191-5p	AACGGAA	mmu-mir-191-5p
miR-193a-3p	ACUGGCC	mmu-mir-193a-3p
miR-1981-3p	AUCUAAC	mmu-mir-1981-3p
miR-199a-3p	CAGUAGU	mmu-mir-199a-3p
		mmu-mir-199b-3p
miR-199a-5p	CCAGUGU	mmu-mir-199a-5p
		mmu-mir-199b-5p
miR-19b-3p	GUGCAAA	mmu-mir-19a-3p
		mmu-mir-19b-3p
miR-204-5p	UCCCUUU	mmu-mir-211-5p
miR-21-5p	AGCUUAU	mmu-mir-21a-5p
miR-210-3p	UGUGCGU	mmu-mir-210-3p
miR-210-5p	GCCACUG	mmu-mir-210-5p
miR-219a-5p	GAUUGUC	mmu-mir-219a-5p
miR-22-3p	AGCUGCC	mmu-mir-22-3p
miR-22-5p	GUUCUUC	mmu-mir-22-5p
miR-221-3p	GCUACAU	mmu-mir-222-3p
miR-223-3p	GUCAGUU	mmu-mir-223-3p
miR-224-5p	AAGUCAC	mmu-mir-224-5p

Szimbólum	Magrégió	Azonosító
miR-23a-3p	UCACAUU	mmu-mir-23a-3p
		mmu-mir-23b-3p
miR-24-1-5p	UGCCUAC	mmu-mir-24-2-5p
miR-24-3p	GGCUCAG	mmu-mir-24-3p
miR-26a-5p	UCAAGUA	mmu-mir-26a-5p
miR-26a-5p	UCAAGUA	mmu-mir-26a-5p
		mmu-mir-26b-5p
miR-27a-3p	UCACAGU	mmu-mir-27a-3p
		mmu-mir-27b-3p
miR-29a-5p	CUGAUUU	mmu-mir-29a-5p
miR-29b-1-5p	CUGGUUU	mmu-mir-29b-1-5p
miR-29b-3p	AGCACCA	mmu-mir-29a-3p
		mmu-mir-29b-3p
		mmu-mir-29c-3p
miR-3065-5p	CAACAAA	mmu-mir-3065-5p
miR-30c-5p	GUAAACA	mmu-mir-30a-5p
		mmu-mir-30b-5p
		mmu-mir-30c-5p
		mmu-mir-30d-5p
		mmu-mir-30e-5p
miR-31-3p	GCUAUGC	mmu-mir-31-3p
miR-31-5p	GGCAAGA	mmu-mir-31-5p
miR-3176	CUGGCCU	mmu-mir-378d
miR-324-5p	GCAUCCC	mmu-mir-324-5p
miR-328-3p	UGGCCCU	mmu-mir-328-3p
miR-329-3p	ACACACC	mmu-mir-362-3p
miR-33-5p	UGCAUUG	mmu-mir-33-5p
miR-330-5p	CUCUGGG	mmu-mir-326-3p
miR-331-3p	CCCCUGG	mmu-mir-331-3p
miR-339-5p	CCCUGUC	mmu-mir-339-5p
miR-340-3p	CCGUCUC	mmu-mir-340-3p
miR-344a-5p	CAGGCUC	mmu-mir-484
miR-345-5p	CUGACCC	mmu-mir-345-5p
miR-3473b	GGCUGGA	mmu-mir-3473b
		mmu-mir-3473e
miR-34a-5p	GGCAGUG	mmu-mir-34a-5p
		mmu-mir-34b-5p
		mmu-mir-34c-5p
miR-34c-3p	AUCACUA	mmu-mir-34b-3p
miR-350	UCACAAA	mmu-mir-350-3p
miR-361-5p	UAUCAGA	mmu-mir-361-5p
miR-362-5p	AUCCUUG	mmu-mir-362-5p
miR-374b-5p	UAUAAUA	mmu-mir-374b-5p

Szimbólum	Magrégió	Azonosító
miR-378a-3p	CUGGACU	mmu-mir-378a-3p
		mmu-mir-378c
miR-378a-5p	UCCUGAC	mmu-mir-378a-5p
miR-3909	GUCCUCU	mmu-mir-877-3p
miR-423-3p	GCUCGGU	mmu-mir-423-3p
miR-423-5p	GAGGGGC	mmu-mir-423-5p
miR-425-5p	AUGACAC	mmu-mir-425-5p
miR-451a	AACCGUU	mmu-mir-451a
miR-501-5p	AUCCUUU	mmu-mir-501-5p
miR-503-5p	AGCAGCG	mmu-mir-503-5p
miR-532-5p	AUGCCUU	mmu-mir-532-5p
miR-542-3p	GUGACAG	mmu-mir-542-3p
miR-574-5p	GAGUGUG	mmu-mir-574-5p
miR-582-5p	UACAGUU	mmu-mir-582-5p
miR-652-3p	AUGGCGC	mmu-mir-652-3p
miR-670-5p	UCCCUGA	mmu-mir-670-5p
miR-700-5p	AAGGCUC	mmu-mir-700-5p
miR-744-3p	UGUUGCC	mmu-mir-744-3p
miR-744-5p		mmu-mir-744-5p
miR-7a-5p	GGAAGAC	mmu-mir-7a-5p
miR-872-3p	GAACUAU	mmu-mir-872-3p
miR-872-5p	AGGUUAC	mmu-mir-872-5p
miR-9-5p	CUUUGGU	mmu-mir-9-5p
miR-92a-3p	AUUGCAC	mmu-mir-25-3p
		mmu-mir-32-5p
		mmu-mir-92a-3p

A proteomikai és miRNS-szekvenálási adatok funkcionális jelentőségének feltárására az Ingenuity Pathway Analysist (IPA) alkalmaztuk. Az IPA szoftver olyan számítógépes algoritmusokra épül, melyek az ’Ingenuity Knowledge Base’-t használva értelmezik a molekulák közti funkcionális kapcsolatokat. Ezekhez az *in silico* analízisekhez ’kísérletesen bizonyított’ konfidencia intervallumot választottunk, amely lehetővé teszi a szakirodalmi adatokon alapuló analízist, de kizárja a bizonyítatlan predikciókat. Az értekezésben szereplő, aposztrófok közti kifejezések ’IPA-specifikus kifejezések’.

Az IPA elemzés kimutatta, hogy az azonosított fehérjék olyan sejt- és molekuláris folyamatokban vehetnek részt, mint a ’sejthalál és túlélés’, a ’sejtmozgás’, a ’sejtfejlődés’, a ’sejtnövekedés és proliferáció’, valamint a ’molekuláris transzport’ (szignifikanciatartomány: $p = 7{,}53 \times 10^{-15} – 9{,}32 \times 10^{-4}$) (**12d ábra**). Az azonosított miRNS-ek funkciói – a fehérjefunkciókhoz nagyon hasonlóan – a ’sejtfejlődés’, a ’sejtnövekedés és proliferáció’, a

’sejtmozgás’, a ’sejtciklus’, valamint a ’sejthalál és túlélés’ mechanizmusaihoz kapcsolódnak (szignifikanciatartomány: $p = 1{,}25 \times 10^{-12} – 4{,}88 \times 10^{-2}$) (**12e ábra**).

A fentiekben felsorolt eredmények alapján a MISEV2018 (Théry et al., 2018) ajánlásait is figyelembe véve a kísérletekben használt kisméretű extracelluláris vezikulák exoszómális tulajdonságokat mutatnak, ezért a következő eredmények bemutatásában ezt az elnevezést használjuk.

3.3.2 Az MSC-k melanóma exoszómákkal történő expozíciója *in vitro* onkogén programot indított az őssejtekben

Kísérleteinkben a tumorsztróma alkotói közül általánosan elfogadott modellként (Baglio et al., 2017), mezenchimális őssejteket (MSC) használtunk, hogy megvizsgáljuk a melanóma exoszómák sejtfiziológiai folyamatokra (pl. proliferáció, túlélés, stb.) gyakorolt hatásait. Ezekhez a kísérletekhez az MSC tenyészeteket egér hasi zsírszövetből izoláltuk (Szebeni et al., 2012), és melanóma exoszóma kezelésnek vetettük alá.

Először is felmértük, hogy az exoszómákat internalizálták-e az MSC-k. A nagy áteresztőképességű mikroszkópos vizsgálat azt mutatta, hogy az MSC-k (a DiOC18(3) lipidfestékkel zöldre jelölve) már az alkalmazás után 1-2 órával felvették az exoszómákat (amelyeket a DilC18(3) lipidfesték pirosra jelölt). 24 óra elteltével a képelemzés és a statisztikai értékelés 91%-os internalizációs hajlamot mutatott, vagyis az MSC-k túlnyomó többsége felvette az exoszómákat **(13a, b ábra)**. Ebből arra következtethetünk, hogy a későbbiekben kimutatott funkcionális változások az exoszómák által indukált sejtpopulációnak, nem pedig az egyedi sejtszintű hatásoknak tudhatók be.

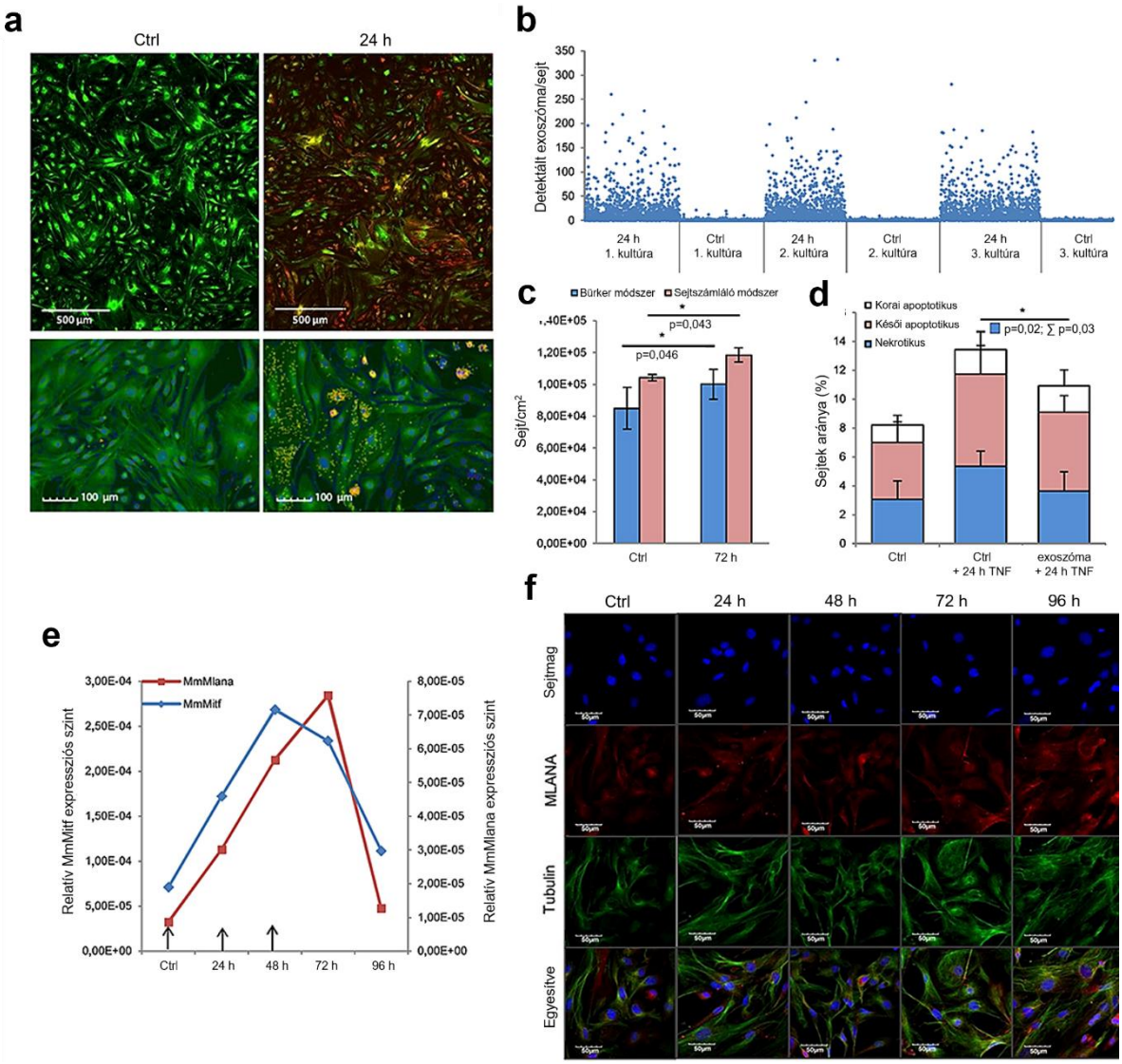

13. ábra. Az internalizált melanóma exoszómák a recipiens MSC-k rosszindulatú átalakulását indukálják.

(a) MSC-k exoszóma-felvétele fluoreszcens képeken. A zöld lipidfestékkel (DiO) jelölt sejteket 24 órán át piros lipidfestékkel (Dil) jelölt exoszómákkal kezeltük, majd 4%-os PFA oldattal fixáltuk. A kontroll sejteken az eljárást megismételtük exoszómák hozzáadása nélkül. A képek egy nagy áteresztőképességű Operetta mikroszkóppal (PerkinElmer) készültek. Az alsó két kép esetén a sejtmagokat DAPI-val festettük. Az exoszómákat egy erre a célra készült A-trous wavelet transzformációval azonosítottuk és sárga színnel emeltük ki. (b) Az exoszóma-felvétel kvantitatív analízise. A diagram a sejtenként detektált exoszómák számát mutatja (Y tengely) az összes vizsgált sejtben (X tengely) 3 exoszóma-kezelt (24 h) és 3 kontroll kultúrában (Ctrl). c) Exoszómával kezelt MSC kultúrák sejtproliferációs vizsgálata. A sejtek egy részét exoszómával kezeltük, és 72 órával a kezelést követően a sejtszám szignifikánsan megnövekedett a kezeletlen sejtkultúrákhoz képest. Az eredményeket átlag ± SD (n = 3) formájában adjuk meg. (d) Az exoszómával kezelt MSC sejtek apoptózis-elemzése áramlási citometriával. Mind a TNF-α által indukált teljes sejthalál (Σ), mind a nekrózis szignifikánsan alacsonyabb volt (p = 0,03, illetve p = 0,02) az exoszómával előkezelt sejttenyészetekben a

megfelelő kontroll sejtekhez képest. Az eredményeket átlag + SD (n = 3) formájában ábrázoltuk. (e) Mlana és Mitf qRT-PCR vizsgálata a 24 óránként exoszómákkal kezelt MSC kultúrákban, a kezeléseket a grafikonon nyilak jelezik. Mindkét mRNS expressziója növekedett exoszóma kezelés után, de eltérő kinetikával. (f) A MLANA fluoreszcens immunocitokémiája exoszómával kezelt MSC kultúrákban, Alexa Fluor 555 konjugált antitestet alkalmazva (vörös). A sejtek α-tubulin hálózatát Alexa Fluor 488 konjugált antitest (zöld) jelölte, és a sejtmagokat DAPI-val (kék) festettük.

Ezután meghatároztuk, hogy az internalizált exoszómák képesek-e kiváltani az MSC-k melanómaszerű, tumoros irányba mutató átalakulását. Két komplementer sejtszámláló módszer alkalmazásával is azt találtuk, hogy az MSC-k proliferációs rátája szignifikánsan felgyorsult 72 órával az exoszóma expozíció után (**13c ábra**). Áramlási citometriával azt is kimutattuk, hogy az exoszómával kezelt MSC-k részleges ellenállást mutattak a 100 ng/ml TNF-α sejthalált kiváltó hatásaival szemben, mivel ezekben a tenyészetekben az elhalt sejtek aránya szignifikánsan csökkent. (**13d ábra**).

Mivel az exoszómákat melanóma sejtekből izoláltuk, kíváncsiak voltunk arra, vajon a fenti változások (melyek mind az exoszóma expozíciónak kitett sejtek rosszindulatú átalakulása mellett szólnak) eredményezték-e a melanóma-specifikus jellemzők *de novo* megjelenését a transzformált MSC-kben. A kérdés megválaszolásához olyan melanóma-specifikus markerek expresszióját vizsgáltuk, mint a MLANA és a MITF. Az adott fehérjék mRNS-ére specifikus qRT-PCR elvégzése után azt találtuk, hogy mindkét marker transzkriptumainak szintje jelentősen megemelkedett az MSC-kben az exoszóma kezelés hatására (**13e ábra**), bár a két molekula emelkedési kinetikája kissé eltérő volt. Ezen túlmenően, az mRNS adatokkal összhangban, az immunfluoreszcens jelölés azt mutatta, hogy az exoszóma expozíció jelentősen növelte a MLANA expresszióját fehérje szinten is (**13f ábra**).

Ezt követően felmértük, hogy az MSC-k rosszindulatú transzformációját kiváltó exoszómák fenti hatásait kíséri-e a célsejtek molekuláris szinten lezajló, onkogén átprogramozása. A naiv MSC-ket standardizált térfogatú exoszómáknak tettük ki különböző időintervallumokban (a variancia csökkentése érdekében, több független *in vitro* kísérletből gyűjtöttünk egyesített mintákat). Ezután a mintákat qRT-PCR elemzésnek vetettük alá egy saját tervezésű, 40 onkogénből és tumorszuppresszor génből álló panel segítségével, amelyekről korábban azt feltételezték, hogy szerepet játszanak a melanóma progressziójában (**5. táblázat**).

5. táblázat. Saját tervezésű qRT-PCR panel: onkogén fehérjéket kódoló, vizsgált mRNS-ek listája

Gén	Fehérje	Funkció
Alcam	ALCAM (CD166) aktivált leukocita sejtadhéziós molekula	fontos szerepet játszik a humán malignus melanóma progressziójában, valamint a lokoregionális és távoli metasztázisok kialakulásában
Bmi1	BMI1 B-sejt specifikus murine leukémia vírus 1-es integrációs hely	invazív sajátságokat indukál melanómában, amely elősegíti az áttétképződést és a kemorezisztenciát
Cd44	CD44	a CD44s kölcsönhatása a hialuronsavval kritikus szerepet tölt be a sejtek invazivitásában
Eng	ENG endoglin (CD105)	döntő szerepet játszik az angiogenezisben, fontos a daganat növekedéséhez, túléléséhez és áttétképzéséhez
Flot2	FLOT2 flotillin-2	hozzájárul a melanóma progressziójához
Itga2	ITGA2 alfa-2 integrin	a melanóma fokozott kockázatával társul
Itga4	ITGA4 alfa-4 integrin	az α4β1 integrin fontos szerepet játszik a melanóma metasztázisában
Itga6	ITGA6 alfa-6 integrin	az α6β1 integrin laminin receptorként expressziós összefüggést mutat egy erősen metasztatikus melanóma sejtvonal invazivitási képességével
Itgb1	ITGB1 béta-1 integrin (CD29)	az α4β1 integrin fontos szerepet játszik a malignus melanóma metasztázisában
Kit	KIT (CD117) hízósejt/őssejt növekedési faktor receptor	a c-Kit jelátvitel aktiválja a MAPK és PI3K jelátviteli kaszkádokat
Muc1	MUC1 sejtfelszín-asszociált mucin-1	elősegíti a melanóma migrációját az AKT jelátviteli útvonalon keresztül
Pecam1	PECAM1 (CD31) vérlemezke - endotélsejt adhéziós molekula	szerteágazó szerepe lehet a melanóma kialakulásával, nyugalmi állapotával, migrációjával/invaziójával és angiogenezisével kapcsolatos folyamatokban
Prom1	Prominin-1 (CD133)	melanóma-őssejt marker
Thy-1	Thy-1 membrán glikoprotein (CD90)	sejtadhéziós molekula, a melanóma sejtek az endotélsejteken lévő Thy-1-et használják az áttétképzéshez
Cdc42	CDC42 sejtosztódást szabályozó fehérje, 42-es homológ	létfontosságú az endomembránokból kiinduló transzformáló Ras jelhez
Tiam1	TIAM1 T-sejt limfóma invázió és metasztázis induktor fehérje 1	döntő szerepet játszik az aktin citoszkeleton, a sejtmigráció, a sejtciklus, a géntranszkripció és a sejtadhézió szabályozásában
Bcl2	BCL-2 B-sejtes limfóma 2	kulcsszerepet játszik a migrációs és invazív fenotípushoz kapcsolódó molekulák szabályozásában; ezáltal, a hipoxiával együttműködve, hozzájárul a tumor progressziójához
Casp9	CASP9 kaszpáz-9	kapcsolódik a mitokondriális halál útvonalhoz
Casp8	CASP8 kaszpáz -8	központi szerepet játszik a sejtek apoptózisának végrehajtási fázisában
Cdk4	CDK4 ciklin-dependens kináz 4	elősegíti a sejtciklus progresszióját és gátolja mind a sejtek öregedését, mind az apoptózist

Gén	Fehérje	Funkció
Elk1	ELK1 ETS domén-tartalmú fehérje	az ETS onkogén család tagja, transzkripciós aktivátor
Ets1	ETS1 E26 transzformáció-specifikus 1	szükséges a migrációhoz az aktív RAS/ERK jelátviteli útvonallal rendelkező sejtvonalakban
Hgf	HGF hepatocita növekedési faktor	aktiválhatja a MAP-kináz útvonalat, amely a c-MET proto-onkogénen keresztül általában felülszabályozott melanómában
Jak2	JAK2 Janus kináz 2	aktivátorként működik a STAT transzkripciós útvonalban, amely központi szerepet tölt be a melanóma sejtbiológiájában
Met	MET hepatocita növekedési faktor receptor	számos biológiai válaszreakciót indukál, amelyek együttese invazív növekedési programot eredményez
Myb	MYB transzkripciós activátor Myb	transzkripciós faktor, amely többek között a Kit, Bcl2, Ets-2 és N-Ras transzkripcióját szabályozza
Nras	NRAS neuroblasztóma RAS virális onkogén homológ	számos intracelluláris jelátviteli útvonalat stimulál, többek közt a Raf/MEK/ERK mitogén aktivált protein kináz (MAPK) útvonalat, vagy a PI3K/AKT útvonalat
Stat3	STAT3 jelátalakító és transzkripció aktivátor 3	elősegíti számos olyan gén átírását, amelyek részt vesznek a melanóma metasztázisban
Kitl	KIT-ligand őssejt faktor (CD117)	c-KIT receptorhoz kötődő citokin, amely fontos szerepet játszik a melanogenezisben
Rb1	RB1 retinoblasztóma 1 fehérje	egy tumorszuppresszor fehérje, amely számos rákos megbetegedésben diszfunkcionális
Pik3ca	PI3K foszfatidil-inozitol-3-kináz	a PI3K/AKT útvonal kulcsszerepet játszik a tumor kialakulásában, növekedésében és az áttétképződésben melanóma esetén
Raf1	RAF1 protoonkogén szerin/treonin-protein kináz	az ERK MAP-kináz jelátviteli kaszkád egyik kulcsfontosságú szabályozója
Mtor	mTOR szerin/treonin protein kináz	a rapamicin mechanisztikus célpontja, egy szerin/treonin protein kináz, amely szabályozza a sejtnövekedést, a sejtproliferációt, a sejtmozgást és a sejtek túlélését
Akt1	AKT protein kináz B	kulcsszerepet játszik számos sejtes folyamatban, például a glükóz-anyagcserében, az apoptózisban, a proliferációban, a transzkripcióban és a migrációban
Map2k1	MEK1 mitogén-aktivált protein kináz kináz 1	a MAP-kináz jelátviteli útvonal kulcsfontosságú komponense, számos sejtszintű folyamatban részt vesz, például a proliferációban, a differenciálódásban, vagy a transzkripció szabályozásában
Map2k2	MEK2 mitogén-aktivált protein kináz kináz 2	kritikus szerepet játszik a mitogén növekedési faktor jelátvitelben, foszforilálja és ezáltal aktiválja a MAPK1/ERK2-t és a MAPK2/ERK3-at
Mapk3	ERK1 extracelluláris szignál-szabályozott kináz 1	a Ras-Erk1/2 kulcsfontosságú szabályozó útvonal a melanóma sejtek proliferációjában
Mapk1	ERK2 mitogén-aktivált protein kináz 1	a Ras-Erk1/2 kulcsfontosságú szabályozó útvonal a melanóma sejtek proliferációjában
Rac1	RAC1 Ras-függő C3 botulinum toxin szubsztrát 1	több jelátviteli útvonalban is szerepet játszik, ami a sejtek adhéziójához, migrációjához, proliferációjához és transzformációjához vezet

Amint az a **14a ábrán** látható, a melanóma exoszómáknak kitett MSC-k génexpressziós mintázata egyértelmű onkogén dominanciát mutatott (a kontroll, exoszómális expozíciónak ki nem tett sejtekhez képest). Ezt az összes vizsgált molekula átlagos relatív génexpressziós szintjének statisztikai elemzésével igazoltuk. Szignifikánsan magasabb értékeket kaptunk az exoszómával kezelt sejtek esetében a kontrollokhoz képest (p = 1,9 × 10^{-5}, p = 0,031 és p = 2,3 × 10^{-8} a 6 órás, 24 órás és 72 órás időpontokban).

3.3.3 A melanóma exoszómák hatására az őssejtekben PD-1 expresszó indukálódik

Ahogy fentebb említettük, Kleffel et al. kimutatta, hogy a PD-1-et túlzottan expresszáló melanóma sejt szubpopulációk meglehetősen érdekes módon, figyelemreméltóan megnövekedett invazivitással és agresszív növekedési tulajdonságokkal bírnak (Kleffel et al., 2015). A szerzők azonban nem határozták meg azokat a faktorokat, amelyek a túlzott PD-1 expressziót indukálták. Mivel a fenti megállapítás erősen arra utalt, hogy a melanóma exoszómák „MSC átnevelési" képessége daganatos habitust vált ki, a következő lépésben a PD-1 expresszióját vizsgáltuk az MSC tenyészetekben.

Ahogy az várható volt, a kontroll, nem kezelt MSC-kben csak jelentéktelen PD-1 expressziót tudtunk azonosítani (mRNS és fehérje szinten is). Ezzel szemben qPCR-rel a PD-1 expressziójának markáns, szignifikáns és időfüggő emelkedését észleltük exoszóma kezelés hatására (**14b ábra**). A PD-1 drámai felülszabályozódását Western blot-tal és immuncitokémiai elemzéssel igazoltuk (**14c és d ábra**), és szuperrezolúciós mikroszkópiával egy-molekula szinten is kimutattuk az exoszómával kezelt MSC-kben (**14e ábra**).

Fontos, hogy mivel a proteomikai elemzés nem azonosította a PD-1 jelenlétét az exoszómákban, ezek az adatok arra utalnak, hogy az exoszómának kitett MSC-k magas PD-1 fehérjetartalma *de novo* indukció eredménye, és nem exoszóma által közvetített horizontális molekula transzferé. Eredményeink tehát arra utalnak, hogy a sejtek melanóma exoszóma által közvetített „átnevelése" egy új MSC populációt eredményezett, amelyet a továbbiakban $MSC^{PD\text{-}1+}$ néven azonosítunk.

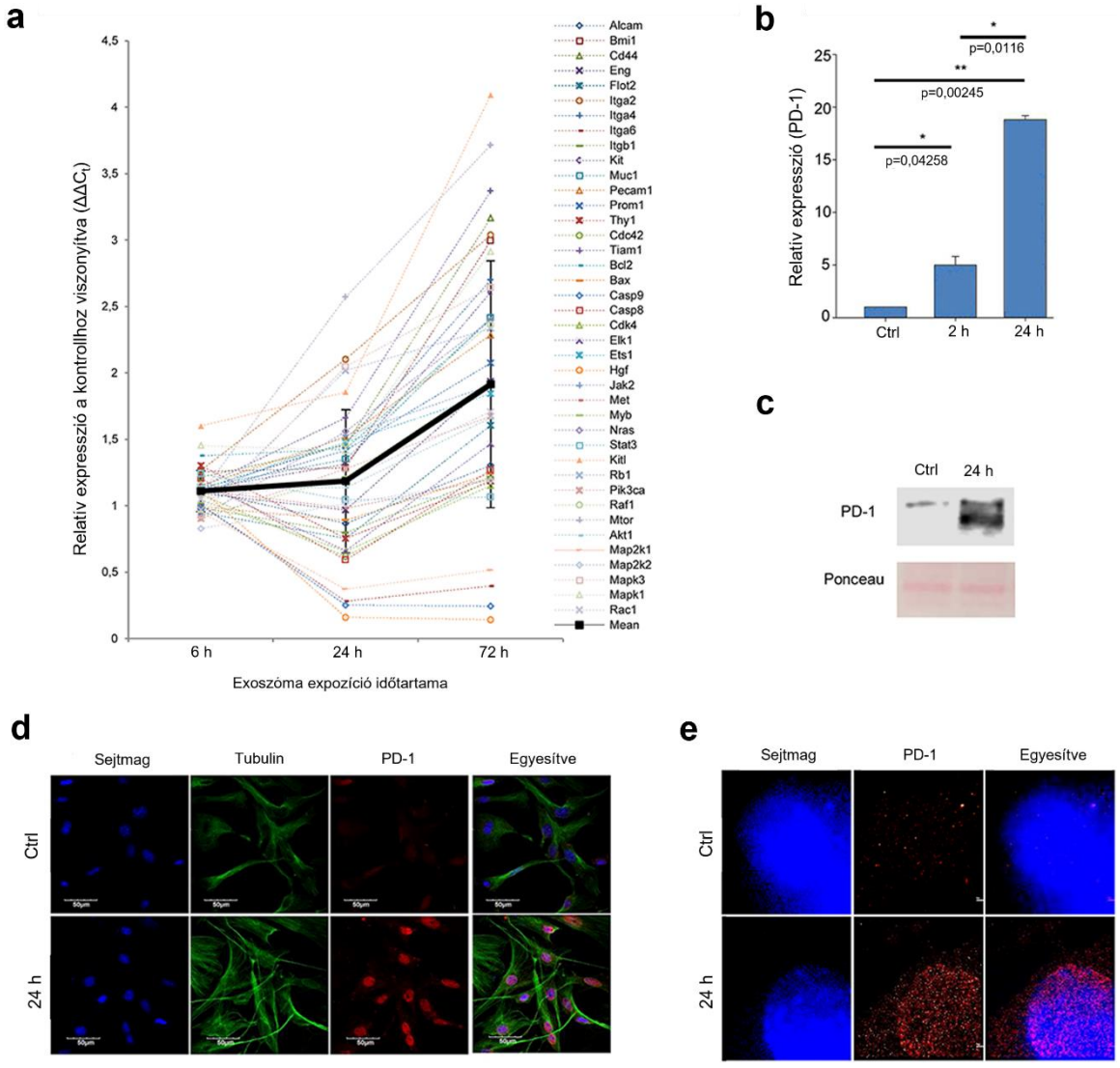

14. ábra. Az exoszómák által átnevelt MSC-k onkogén dominanciát és PD-1 expressziót mutatnak.

(a) 40-féle, daganatos transzformációval kapcsolatos gén qRT-PCR elemzése exoszómának kitett MSC-kben egy saját tervezésű panel segítségével. A grafikon az egyes gének relatív expressziós értékeit mutatja 6, 24 és 72 órás exoszóma expozíció után. A megváltozott génexpressziós mintázat trendvonala (vastag fekete vonallal jelezve) idővel növekvő tendenciát mutat (átlag ± SD). (b) A PD-1 qRT-PCR elemzése MSC-kben 2 és 24 órás exoszóma expozíció után. A grafikon az átlagot + SEM-et ábrázolja (n = 3). (c) A PD-1 fehérje expressziójának reprezentatív immunoblotja a kontroll és az exoszómának kitett MSC-kben 24 órás exoszóma kezelés után. (d, e) A PD-1 fluoreszcens immuncitokémiája 24 órás exoszómával indukált MSC tenyészetekben, PD-1 elleni primer patkány antitest és patkány IgG elleni másodlagos Alexa Fluor 647 konjugált antitest (piros) felhasználásával. A sejtmagok DAPI-val jelöltek. (d) A sejtek α-tubulin hálózatát közvetlenül egy Alexa Fluor 488 konjugált antitesttel jelöltük (zöld). A képeket konfokális mikroszkóppal készítettük. (e) A képeket STORM szuperrezolúciós mikroszkóppal készítettük. A PD-1 STORM szuperfelbontású képalkotása azt mutatta, hogy a PD-1 leginkább a sejtmag körül lokalizálódott.

3.3.4 A B16F1 exoszómák *in vivo* tumorigenezise

Miután a 3.3.2-3.3.3 pontokban bemutatott eredmények alapján bizonyítottnak láttuk az exoszómák *in vitro* tumorigén indukciós potenciálját tenyésztett MSC-ken, feltételeztük, hogy ez a jelenség *in vivo* is azonosítható. Ennek a feltevésnek a vizsgálatára a jól ismert, laboratóriumainkban rutinszerűen használt állatmodellt (Buzás et al., 2016) alkalmaztuk, amelyben egerekben, elsősorban a tüdőben kialakuló daganatokat hozunk létre egér B16F1 melanóma sejtek farokvénába történő beadásával. Kísérleteinkben a mikrometasztázisok kialakulását követően, a daganatos egerek kontrollként fiziológiás puffert, ugyanazon B16F1 melanóma sejtekből izolált exoszómákat, vagy exoszómával indukált $MSC^{PD\text{-}1+}$ sejteket kaptak. A kísérleti elrendezés az „Anyagok és módszerek" fejezetben a **34. ábrán** kerül bemutatásra.

A kísérleti állatokban tapasztaltak alapján, az exoszómával érintett csoportokban (azaz exoszóma-, vagy $MSC^{PD\text{-}1+}$-oltott állatokban) jelentősen megnövekedett a tüdőszövet daganattal borított méretének az aránya (a növekedés szignifikánsnak bizonyult az $MSC^{PD\text{-}1+}$ csoportban) (**15a ábra**). Továbbá mindkét exoszómával érintett csoportban a távoli metasztázisok száma is szignifikánsan megemelkedett a kontrollhoz képest (**15b ábra**). Amint azt korábbi vizsgálataink során is láthattuk (Buzás et al., 2016), ezek a metasztázisok többnyire a kontroll tumoros állatok petefészkeiben és veséiben (és nagyon ritkán a nyirokcsomókban) lokalizálódnak. Ezen helyek mellett azonban az exoszómák jelenléte gyakori metasztázisokat eredményezett a nyirokcsomókban és megjelentek az áttétek a májban is. Érdekes módon az $MSC^{PD\text{-}1+}$-kezelt egerekben, FISH segítségével, exoszómával transzformált MSC-ket lehetett azonosítani a paraortikus nyirokcsomókban (**15c ábra**), amely igazolja az $MSC^{PD\text{-}1+}$ sejtek sikeres *in vivo* adherenciáját.

A különböző csoportok tüdőszöveteit 14 nappal az exoszómák vagy $MSC^{PD\text{-}1+}$ sejtek injektálása után mélyreható expressziós profilozásnak vetettük alá. qRT-PCR analízist végeztünk egy saját tervezésű, 40 génből álló panel segítségével; a háztartási gének mellett vizsgáltuk:

- proto-onkogének expresszióját,
- a rosszindulatú transzformációban feltehetően részt vevő gének expresszióját,
- a melanóma kialakulásában és progressziójában szerepet játszó gének expresszióját.

A génexpressziós mintázatok hierarchikus klaszteranalízise egyértelműen robusztus proto-onkogén dominancia jelenlétét mutatta ki az exoszómával érintett csoportok

tüdőmintáiban a kontroll szövetekkel összehasonlítva. Kísérleteink eredményeként 23 és 26 gén jelentős *de novo* indukcióját azonosítottuk: Alcam1, Eng, Flot2, Itga4, Itga6, Kit, Pecam1, Prom1, Thy, Cdc42, Tiam1, Bcl2, Bax, Casp9, Casp8, Ets1, Hgf, Jak2, Met, Myb, Map2k1, Map2k2, Mapk1 mindkét csoportban és Elk1, Rb1, Itga2 az exoszóma csoportban. További hat, illetve három gént azonosítottunk legalább 10-szeres növekedéssel (Cd44, Itgb1, Muc1, Pik3ca, Akt1, Rac1 az exoszóma csoportban és Cd44, Itgb1, Rac1 az $MSC^{PD\text{-}1+}$ csoportban). Ezenkívül hat, illetve nyolc gén legalább kétszeres mRNS-szint emelkedést mutatott (Bmi1, Cdk4, Stat3, Kitl, Raf1, Mtor az exoszóma csoportban és Bmi1, Muc1, Cdk4, Stat3, Kitl, Pik3ca, Mtor, Akt1 az $MSC^{PD\text{-}1+}$ csoportban). A **15d ábra** az exoszóma expozíció által kiváltott, túlexpresszált gének indikatív adatainak hőtérképét mutatja be.

A továbbiakban kimutattuk, hogy a fenti gének mellett a PD-1 expressziója is szignifikánsan megnövekedett mindkét exoszómával érintett csoportban (**15e ábra**). Ugyanakkor bár a PD-1 mRNS-transzkriptum szintje közel kétszeres volt az $MSC^{PD\text{-}1+}$ tüdőszövetekben a csak-exoszómás csoport mintáihoz képest, a különbség nem volt szignifikáns, valószínűleg az állatok közötti variabilitás okozta nagy SD miatt.

Összeállítottunk egy Venn-diagramot (**15f ábra**), hogy bemutassuk az összes lehetséges logikai kapcsolatot a **15d ábrán** bemutatott különféle génexpressziós mintázatok között. Fontos, hogy a klaszteranalízis szerint egyetlen gént sem tudtunk azonosítani, amely hiányozna az exoszómákkal érintett csoportokból a kontroll tumoros egerekhez képest. Más szóval, míg ezek az exoszómával érintett csoportok csak rájuk jellemző génexpressziós profilokat mutattak, a kontroll csoportban ilyen egyedi profilt nem lehetett kimutatni.

Pontosítva az eredményeket, a következő génexpressziós mintákat határoztuk meg:

- három gén (Elk1, Rb1, Igta2) kizárólag az exoszómával kezelt csoportban indukálódott;
- huszonhárom gén (Prom1, Tiam1, Bcl2, Bax, Casp9, Hgf, Jak2, Met, Mapk2k2, Alcam1, Eng, Flot2, Itga4, Itga6, Kit, Pecam1, Thy, Cdc42, Casp8, Ets1, Myb, Map2k1, A Mapk1) mind az exoszómával, mind az $MSC^{PD\text{-}1+}$ sejtekkel kezelt csoportban felfelé szabályozódott;
- tizennégy gén (Bmi1, Cd44, Itgb1, Muc1, Cdk4, Nras, Sat3, Kitl, Raf1, Mtor, Akt1, Mapk3, Pik3ca, Rac1) mindhárom csoportban felülszabályozottnak bizonyult (**15f ábra**).

Végül meg kell jegyezni, hogy az exoszómákkal érintett csoportokban látható drámai génexpressziós változások kizárólag az exoszómák jelenlétének tulajdoníthatók, mivel olyan gén nincs a Venn diagramon, ami csak az „MSC$^{PD\text{-}1+}$ klaszterhez tartozna (**15f ábra**).

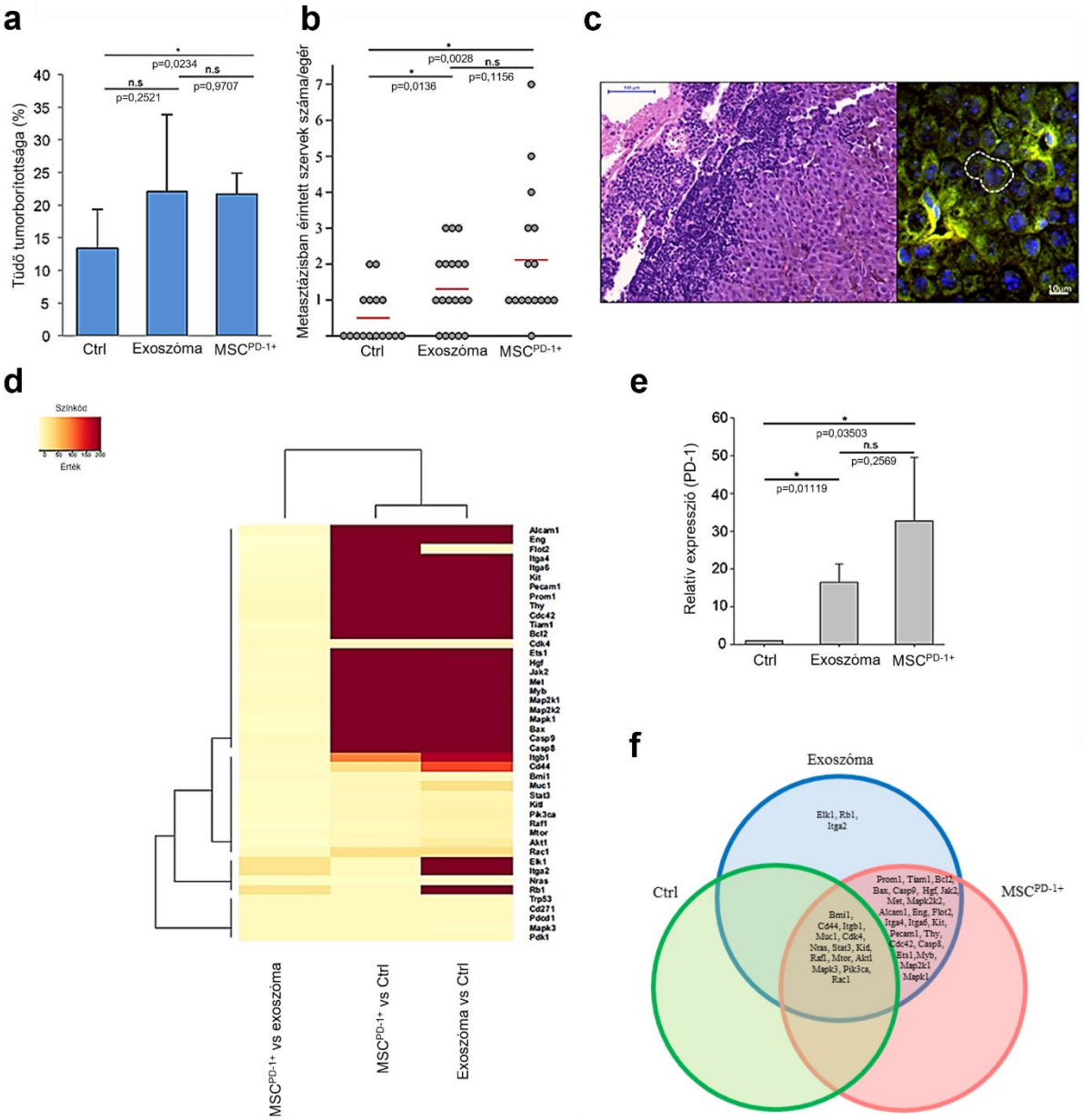

15. ábra. A melanóma exoszómák in vivo elősegítik a tumor progresszióját és a metasztázisok képződését.

(a) A tüdő daganatos lefedettsége a 15. napon a különböző állatcsoportokban. A grafikon az átlagot + SD-t ábrázolja (n = 3). (b) Távoli metasztázisok száma a 25. napon. Egy pont minden csoportban egy állatot jelöl, a piros vonalak a metasztázisok egy állatra vonatkozó átlagos számát mutatják. (c) Paraortikus nyirokcsomó-metasztázisok FISH-analízise, amely exoszómával indukált MSC jelenlétét mutatta ki. A hím egér eredetű MSC Y-kromoszómáját (piros pont) egy nőstény egér metasztázisában mutattuk ki. (d) A génexpressziós mintázat hőtérképe és klaszteranalízise (profilalkotás), amelyek protoonkogén dominanciát mutatnak exoszóma vagy MSC$^{PD\text{-}1+}$ csoportokban. A génexpressziós adatokban a kiválasztott csoportok

között bekövetkezett többszörös változáson alapuló, robusztus hierarchikus klaszterezés több felső osztályra osztja a kezelt csoportokat. Az exoszóma- vagy MSC$^{PD\text{-}1+}$- kezelt csoportokat összehasonlítottuk a kezeletlen kontrollokkal. Az exoszóma és az MSC$^{PD\text{-}1+}$ kezelések szorosan összefüggtek egymással. (e) A PD-1 qPCR elemzése a tüdőmintákban TaqMan próbákkal (n = 3). (f) A Venn-diagram a génexpressziós profilalkotás alapján a különböző állatcsoportokban mért expressziós mintázatok átfedését mutatja.

3.3.5 Melanóma exoszómák promotálják a tumorigén és a sejtek túlélését támogató szignálútvonalakat

A **16. ábra** azon szignálútvonalak potenciális kölcsönhatásait mutatja, amelyek az *in vivo* kísérletekben overexpresszált molekulák (piros szimbólumok) kifejeződésén alapulnak. Három olyan fő jelátviteli útvonal elemeinek overexpresszióját mutattuk ki, amelyek részt vesznek a tumor progressziójában és a metasztázis képződésében (Flaherty et al., 2012). Az IPA útvonaltervezőjének (’Path Designer – Grow’ funkció) segítségével interakciós térképet hoztunk létre, amely a felülexpresszált gének (piros szimbólumok) által kódolt fehérjéket (vagy kialakult komplexeiket), valamint az exoszómális miRNS-eket és fehérjéket (szürke dobozok) tartalmazza. Ezekről korábban kimutatták, hogy szabályozzák vagy befolyásolják a megjelölt jelátviteli molekulákat.

Ezen eredmények bemutatására és a lehetséges kiváltó exoszómális tényezők feltárására ismét IPA-t végeztünk. Az elemzés lehetővé tette a mögöttes molekuláris folyamatok és útvonalak további finomítását, amelyek részt vesznek ennek a génexpressziós profilnak az összesített hatásában. A korábban leírt, 40 génből álló qPCR panel a sejtmozgással és -migrációval, a sejtek túlélésével és a kötőszövet fejlődésével és működésével kapcsolatos génekben gazdagodott. További érintett folyamatok közé tartozott a tumorsejtek növekedése és proliferációja, valamint a PD-1:PD-1L kölcsönhatás (és annak következményei). A PD-1 és mTOR útvonalra összpontosítva olyan hálózat építhető ki az IPA ’Path Designer – Path Explorer’ segítségével az overexpresszált génekből és komplexeikből, amelyekről ismert, hogy kapcsolatban állnak a tumor progressziójával.

Ezután megvizsgáltuk a fehérjék és a miRNS-ek oldaláról is a tumoros exoszómák által generált folyamatokat. Létrehoztunk egy olyan könyvtárat, amely tartalmazza az LC-MS/MS által kimutatott exoszómális fehérjéket és a SOLiD szekvenálással azonosított, exoszómális miRNS-eket. Az IPA ’Path Designer – Grow’ eszköze jelentős kölcsönhatásokat tárt fel az exoszómák által kiváltott expressziós hálózat és a vezikulák molekuláris tartalma között. Az így létrejövő hálózat direkt és közvetett interakciókat is mutat, viszont kizárólag kísérletileg igazolt kapcsolatokat tartalmaz. Ez a hálózat azt bizonyítja, hogy 61 exoszómális

molekula befolyásolhatja a tumor progresszióját olyan kulcsfontosságú összetevők által szabályozott útvonalakon keresztül, mint a MET, Ras, RAF1, Mek, ERK1/2, MITF, BCL2, PI3K, Akt, mTOR, PD-1, KIT, JAK STAT3 vagy ETS1 (**16. ábra**).

Összességében ezek az eredmények azt mutatják, hogy az exoszómák és az MSC-k közötti kölcsönhatások tumorszerű fenotípust indukálnak, amely eredményeket igazolja az *in vitro* megfigyelt naiv MSC-k PD-1 overexpressziója és az *in vivo* bekövetkező gyors tumorprogresszió.

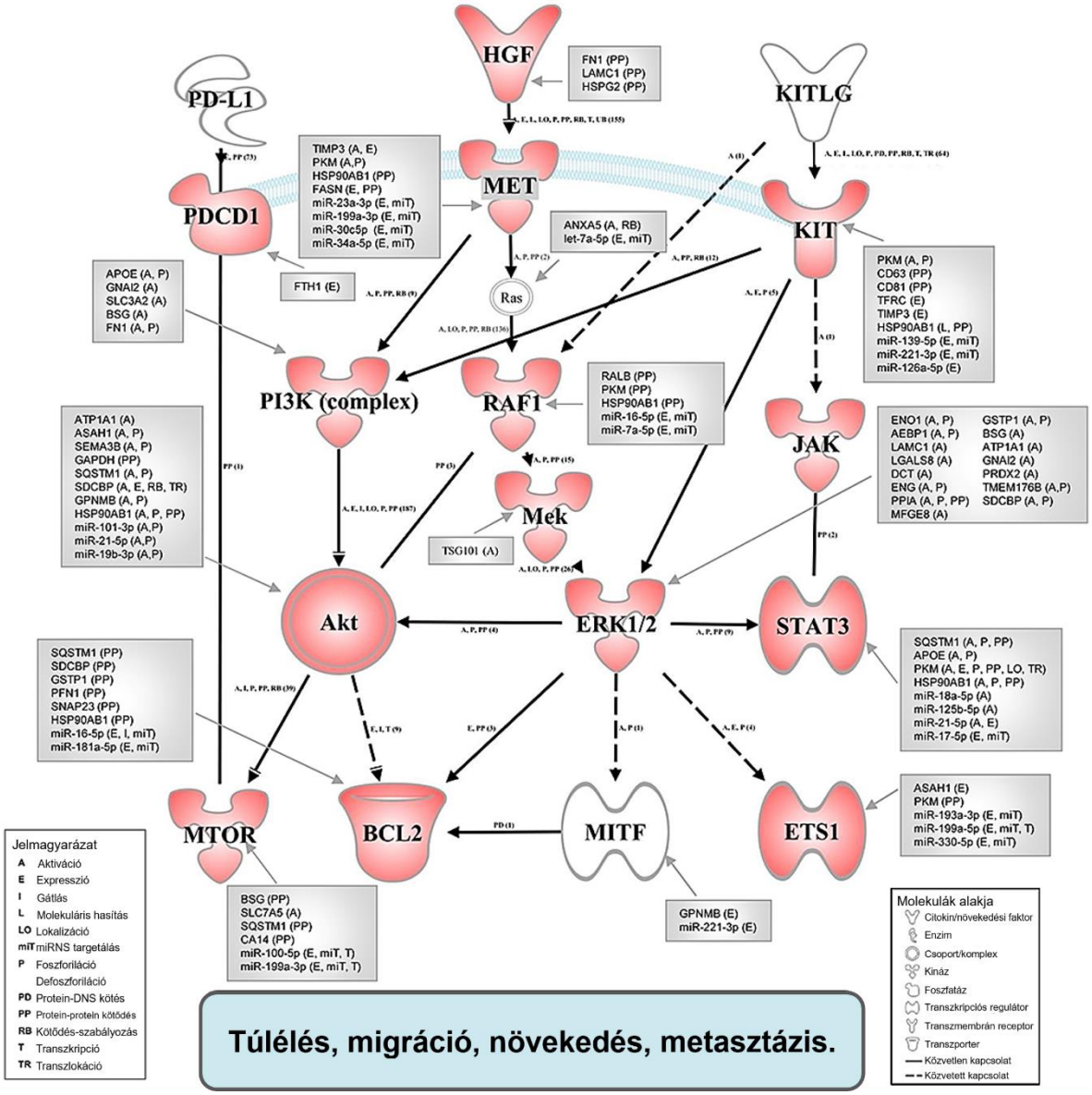

16. ábra. Az in vivo overexpresszált gének integrált asszociatív hálózata, kiegészítve a kölcsönhatásban lévő exoszómális faktorokkal.

Az overexpresszált gének (piros szimbólumok) hálózatát irodalmi adatok alapján szerkesztettük meg. A molekulák közötti kapcsolatokat az IPA adatbázis támasztotta alá. A hálózat vizualizálása az IPA 'Path Designer – Path Explorer' eszközeivel történt. Az exoszómális fehérjéket és a miRNS-eket (szürke dobozok) az IPA 'Path Designer – Grow'

funkciójának segítségével kapcsoltuk össze a hálózat elemeivel úgy, hogy az IPA adatbázisából kizárólag a kísérleti adatokkal alátámasztott folyamatokat emeltük ki, hipotetikus predikciókat nem alkalmaztunk. A kísérleti adataink alapján szerkeszett hálózat bemutatja azokat a szignálmolekulákat, amelyek a bizonyítottan jelen lévő exoszómális komponensekkel aktiválva elősegíthetik a tumorsejtek túlélését, migrációját, növekedését és metasztázisát.

A melanóma exoszómák daganatos mikrokörnyezetben tanulmányozott viselkedése a vizsgálatainknak egyik, leginkább funkcionalitáson alapuló tanulmányozását ölelte fel. Azonban ezeknek a meglehetősen stabil, komplex információs egységeknek a rendkívül hatékony információtranszfere felveti a kérdést, vajon valamilyen módon befolyásolható-e az EV-kbe csomagolt molekulák összetétele, aránya és hogy ez a megváltozott kompozíció nyomon követhető-e a recipiens sejtek működésében. Mivel az alkalmazott modellek döntő többsége tumor eredetű, így a vezikulatartalom befolyásolása különböző daganatellenes terápiák alkalmazásával valósult meg. Modelljeinkben nazofaringeális karcinóma és melanóma sejteket vettünk górcső alá. A doxorubicin, mint klasszikus kemoterápiás szer, a fényindukált Ag-TiO_2 eredetű szabadgyökök és az alkalmazott hőstressz biztosította a környezet paramétereinek megváltozását.

3.4 Nazofaringeális karcinóma (NPC) eredetű sEV-k vizsgálata

A kezeletlen 5-8F sejtvonal eredetű sEV-ket differenciálszűrés és ultracentrifugálás segítségével izoláltuk, és AFM-mel analizáltuk. Az 5-8F sejtkultúrákat 0,6 μM doxorubicin (Doxo) és 2,5 μg/ml fényindukált Ag-TiO_2 (Ag-TiO_2) kezelések segítségével, citosztatikus és oxidatív stressznek vetettük alá. Kontrollként (Ctrl) kezeletlen kultúrákat használtunk. 72 óra elteltével a stresszelt szövetkultúrák felülúszóiból szeparáltuk az sEV-ket, melyeket nanorészecske-követő analízis (NTA) segítségével kvantifikáltunk. A miRNS-készletüket SOLiD szekvenálás segítségével határoztuk meg. A kapott miRNS-adatokat *in silico* elemeztük az IPA szoftver használatával, hogy prediktáljuk az sEV-csoportok funkcionalitásbeli eltéréseit.

3.4.1 Különböző mikrokörnyezeti stresszorok mellett termelt NPC eredetű sEV-k leíró jellemzése

Miután az AFM vizsgálatok igazolták a vezikulák exoszómális alakját és méretét (**17a ábra**), az sEV-számokat a különböző csoportokban NTA analízis segítségével hasonlítottuk össze. A kontroll kultúrákhoz képest szignifikánsan megnövekedett az 5-8F sejtek sEV-termelése citosztatikus (p = 0,0146) és oxidatív stressz (p = 0,0006) hatására (**17b ábra**).

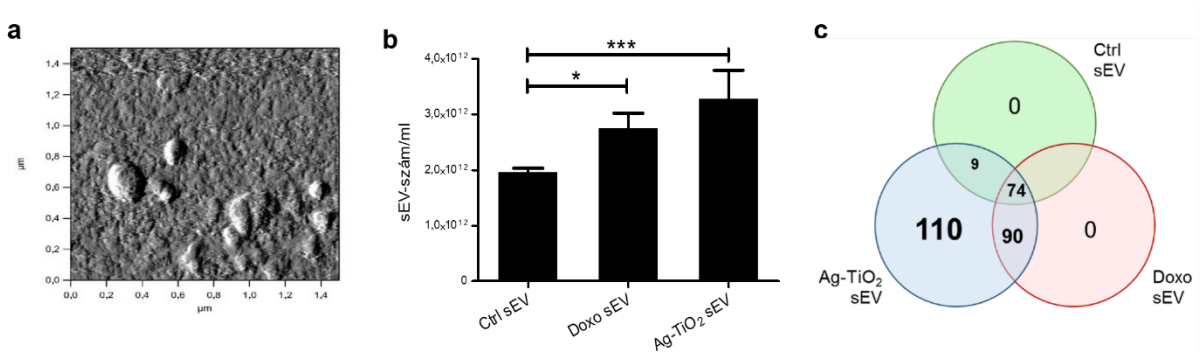

17. ábra. Az 5-8F eredetű sEV-k jellemzése.

*(a) Intakt sEV-k nagy felbontású AFM képe. (b) Az NTA módszerrel meghatározott csoportonkénti vezikulaszámok (n = 4); az oszlopok átlag + SD értékeket ábrázolnak; * p < 0,05; *** p < 0,001. (c) A három sEV-csoport miRNomjának összehasonlítása.*

A miRNS-diverzitás szintén jelentősen növekedett mindkét stressztípus esetén. Összesen 283 miRNS-t azonosítottunk, melyek 26,15%-a (283-ból 74) mindhárom sEV-csoportban előfordult, míg 31,80%-a (283-ból 90) volt detektálható mindkét stressz esetén (de a Ctrl sEV-csoportban nem), és 38,87%-a (283-ból 110) kizárólag csak az Ag-TiO_2 sEV-kben volt fellelhető (**17c ábra**). Olyan miRNS-ek, amelyek Ctrl és Doxo sEV-specifikusak lettek volna, nem találtunk. Mivel citosztatikus stressz esetén 2,22-szer, oxidatív stressz esetén pedig 3,82-szer többféle miRNS-t tudtunk azonosítani, ezért megalapozott az a kijelentésünk, mely szerint az alkalmazott környezeti nyomások hatására a miRNS diverzitás drámaian növekszik, feltehetően a hatékonyabb túlélési stratégiák kialakulása érdekében.

3.4.2 Az sEV-csoportok funkcionális különbségeinek *in silico* analízise

A molekulák széles választékát tartalmazó exoszómális jelszállítmány a recipiens sejtekben, komplex információs csomagként, számos biológiai folyamatban részt vehet. Az elkövetkezőkben bemutatott vizsgálatokban ezen biológiai folyamatok azonosításával próbálkoztunk. Azért, hogy a miRNS analízisből származó eredményeinket biológiai kontextusba helyezhessük, az IPA használatával bioinformatikai analízist végeztünk.

A ‘Comparison analysis’ során számos NPC-vel kapcsolatos ‘Biofunction’-t azonosítottuk, melyekre valamely sEV-csoport szignifikáns hatást gyakorolhat ($p \leq 0{,}00001$). Ezen analízisek szerint az sEV-k nemcsak intracelluláris és celluláris, hanem szisztémás és immunológiai folyamatokban is részt vehetnek.

Az IPA ‘Grow’ eszköze lehetővé tette egy válogatott ‘Biofunction’ lista és a vezikuláris molekulák közti kölcsönhatások azonosítását. Majd az IPA ‘MAP’ funkciójával prediktálni tudtuk, hogy a különböző sEV-csoportok összességében milyen szabályozó hatást (aktivációt,

vagy gátlást) fejthetnek ki a vizsgált ’Biofunction’-re, ahol számos különbség mutatkozott az sEV-csoportok közt. Mindez azt mutatja meg, mennyire fontosak a mikrokörnyezeti kondíciók, amelyek között az sEV-k képződnek.

Általánosságban a Ctrl sEV-k tumortámogató hatásokat mutattak: az IPA predikciók szerint aktiválhatják a tumorsejtek epiteliális-mezenchimális tranzícióját, proliferációját, életképességét és migrációját, miközben gátolhatják a tumorsejtek szeneszcenciáját és apoptózisát. Ezzel szemben a Doxo és Ag-TiO_2 sEV-k tumortámogató hatása gyengébb volt, vagy akár ellenkező előjelűvé vált a vizsgált ’Biofunction’ lista esetében. Például, az IPA az életképességre Doxo sEV-k esetén alacsonyabb konfidenciájú aktiváló hatást, Ag-TiO_2 sEV-k esetén pedig gátlást jósolt. A migráció szabályzása mindkét sEV-hatására gátlóra változott. Ez arra utal, hogy bizonyos stresszhatásokra termelt NPC sEV-k miRNomja elveszítheti tumortámogató sajátságait.

3.5 A melanóma eredetű sEV-k vizsgálata

A mikrokörnyezeti hatásokat boncolgató kutatásunk következő fejezetében stresszindukált B16F1 melanóma sejtek sEV-mediálta intercelluláris kommunikációját vizsgáltuk.

Az izolált B16F1 sEV-k exoszómális markereinek igazolását követően a vezikulák citosztatikus, hő-, és oxidatív stressz indukálta változásait vizsgáltuk. A melanóma sejteket öt különböző módon kezeltük: a kontroll (Ctrl) kultúrák pusztán tápfolydékot kaptak, a citosztatikus stresszt (Doxo) 0,6 µM doxorubicinnel váltottuk ki, a hőstresszelt kultúrákat (Hs) 3× 2 h-ra 42 °C-os inkubátorba helyeztük, az oxidatív stresszt (Ag-TiO_2) 2,5 µg/ml fényindukált Ag-TiO_2-kezeléssel idéztük elő. Utóbbi kontrolljaként megvilágított médiummal kezelt kultúrákat (Ag Ctrl) használtunk. Az öt sejtkultúra-csoport sEV-izolátumait NTA, SOLiD szekvenálás és LC-MS/MS módszerekkel tanulmányoztuk, a kibocsájtott vezikulák számának, miRNomjának ás proteomjának jellemzése céljából.

Funkcionális különbségeiket elsőként az IPA segítségével a kapott miRNS- és fehérjeadatok alapján *in silico* prediktáltuk, majd *in vitro* kísérletekben igazoltuk a recipiens sejtek tumorhoz köthető sejtfunkcióinak, úgymint Ki-67-expressziójának, sejtciklus-dinamikájának, migrációs kapacitásának és mikroszövet-képzésének vizsgálatával (**18. ábra**).

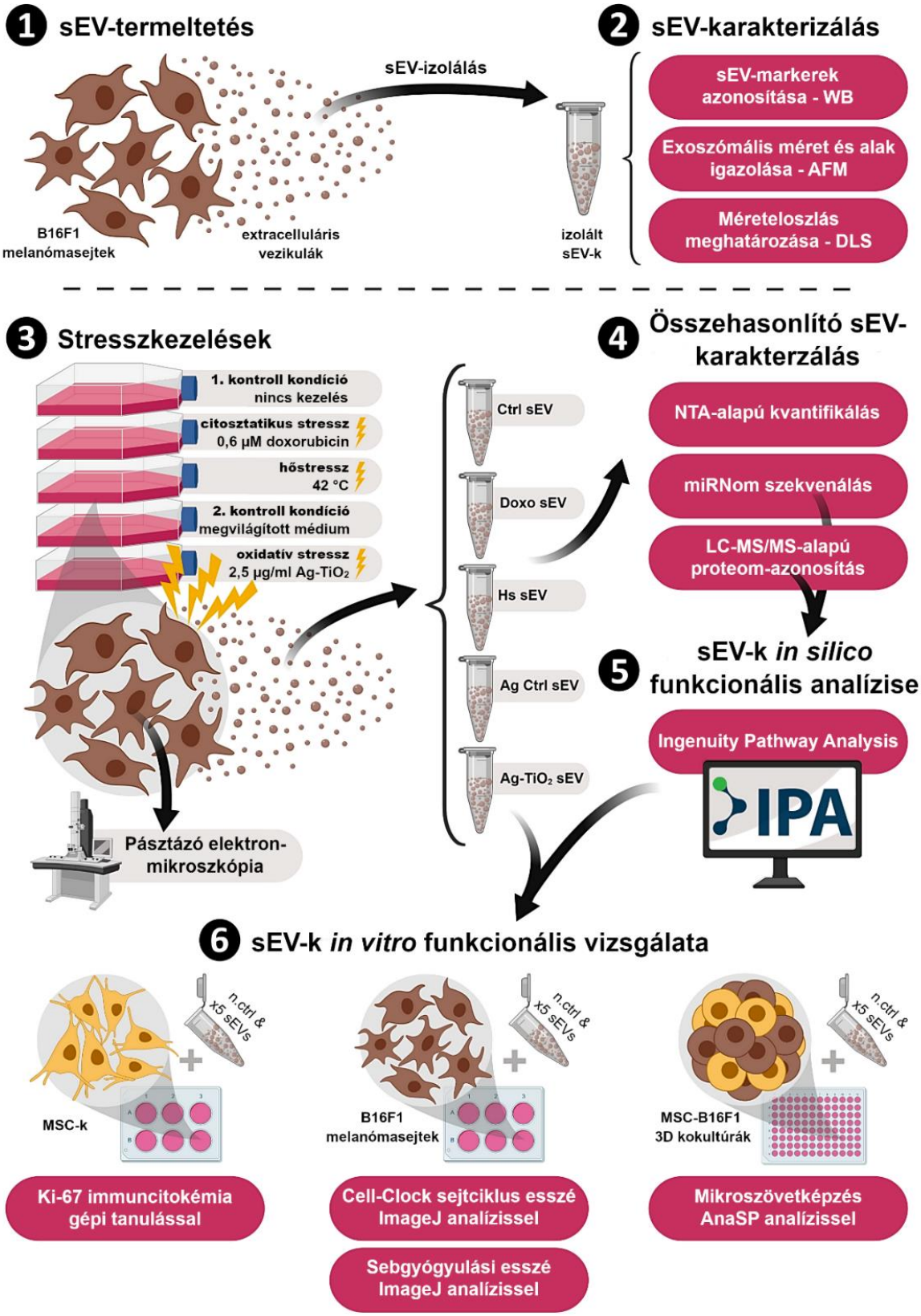

18. ábra. Melanóma sEV-k vizsgálatának kísérleti elrendezése.

Jelmagyarázat: n.ctrl: negatív kontroll, x5 sEVs: 5-féle sEV-kezelés.

3.5.1 A különböző mikrokörnyezeti stresszorok nyomása alatt kibocsájtott melanóma sEV-k leíró jellemzése

3.5.1.1 Szuboptimális körülmények mellett a melnómasejtek vezikulakibocsájtásának mértéke megnő

A B16F1 sejtek mindhárom stresszhatás (Doxo, Hs és Ag-TiO_2) esetén, 24 órával a kezeléseket követően, a SEM képek alapján látványos morfológiai változásokon mentek keresztül (**19a ábra**). 20.000×-es nagyításban a sejtfelszíni struktúrák, többek közt az exoszómális méretű vezikulák is láthatóvá váltak, melyek száma szintén magasabb volt, mint a Ctrl sejteken (p_{Doxo} = 0,00297; p_{Hs} = 0,03928; $p_{Ag\text{-}TiO2}$ = n.s.; n = 5; **19a, b ábra**).

Az izolált vezikulák számát NTA segítségével határoztuk meg. Donorsejtjeink vezikulatermelése mindhárom stresszhatásra szignifikánsan megnövekedett a Ctrl sejtekhez képest (p_{Doxo} = 0,00021; p_{Hs} = 0,03006; $p_{Ag\text{-}TiO2}$ = 0,02462; n = 3; **19c ábra**).

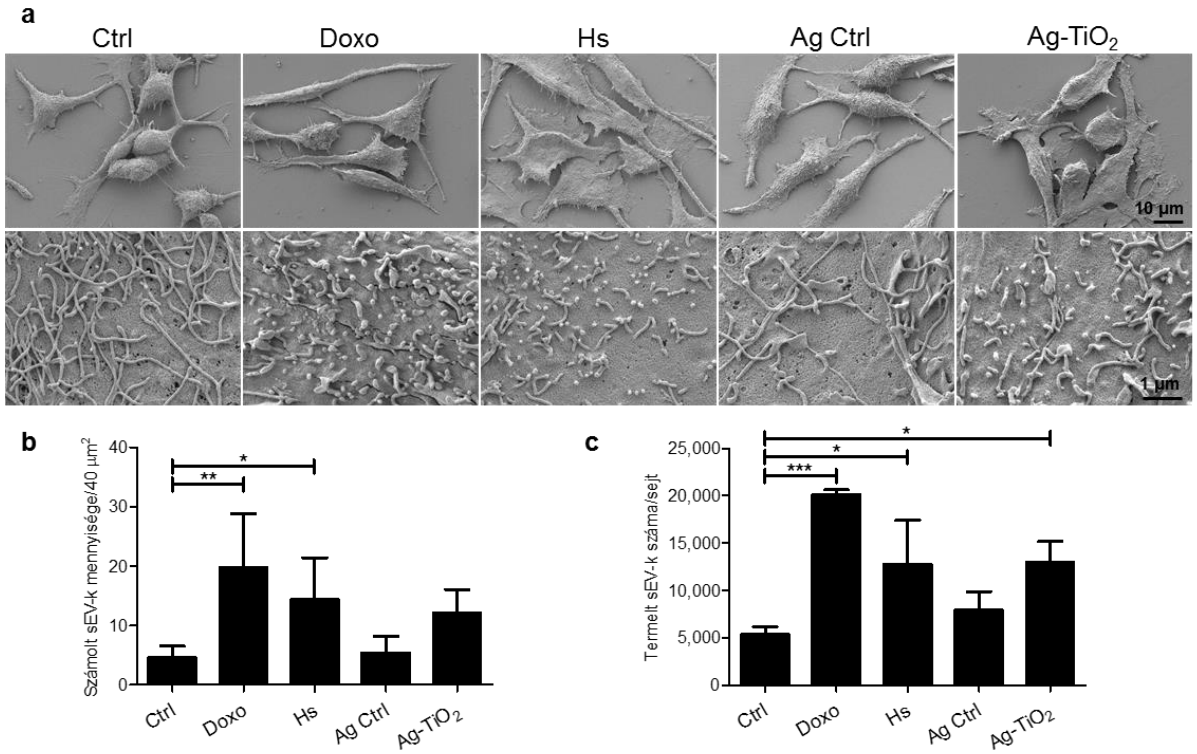

19. ábra. A mikrokörnyezeti stresszfaktorok morfológiai változásokat és megnövekedett sEV-termelést váltottak ki a melanóma sejteken.

*(a) A sejtek pásztázó elektronmikroszkópos képei. (b) A sejtfelszíni exoszómális méretű vezikulák száma az ImageJ értékelések alapján (n = 5). (c) A sejtenként termelt vezikulák száma az NTA mérések szerint (n = 3). A diagramok átlag + SD értékeket ábrázolnak; *p < 0,05; **p < 0,01; ***p < 0,001.*

A vezikulák stresszorokra vonatkozó horizontális transzfere kapcsán fluoreszcens spektroszkópiát alkalmazva megmértük a Doxo sEV-k doxorubicintartalmát. Ez alacsonyabbnak bizonyult az egér melanóma sejteken mért medián letális dózisnál (LD50 = 100 ng/ml). Így az átvitt doxorubicin hatása elhanyagolható a recipiens sejtekben.

Ugyanakkor az Ag-TiO_2 nanopartikulumok sEV-kbe történő becsomagolódásának lehetőségét dinamikus fényszórás (DLS), kemilumineszcens detekció és transzmissziós elektronmikroszkópia segítségével kizártuk.

3.5.1.2 A melanóma sEV-k molekuláris mintázata függ a donorsejtekre ható mikrokörnyezeti tényezőktől

A vezikuláris információtartalom mikrokörnyezeti stressz indukálta változásainak jellemzése érdekében az sEV-csoportok miRNS- és fehérjetartalmát SOLiD szekvenálással és LC-MS/MS-sel analizáltuk. A detektált miRNS-ek 35,04%-a (254-ből 89) és az azonosított fehérjék 59,72%-a (216-ból 129) fordult elő minden sEV-csoportban (**20. ábra**). Azonban az öt sEV-csoport molekuláris mintázata igen eltérő volt, amely az sEV-mediált kommunikációban a vezikulatermelés körülményeinek kivételes jelentőségéről árulkodik.

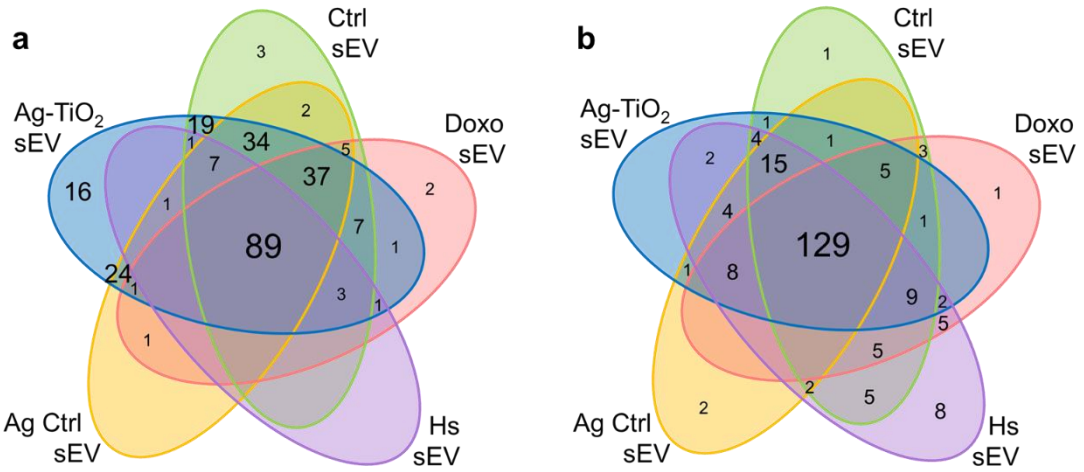

20. ábra. A melanóma sEV-k molekuláris mintázata stressztényezőnként eltérő volt.
A Venn-diagramok az öt sEV-csoport (a) miRNomját és (b) proteomját mutatják be.

3.5.1.3 Az sEV-csoportok funkcionális különbségeinek in silico analízise

A melanóma sEV-csoportok által befolyásolt biológiai folyamatok azonosítása végett, miRNS- és fehérjeadatainkat bioinformatikai analízisnek vetettük alá.

Az IPA-ban végzett ‘Comparison analysis’ alapján, hasonlóan az NPC-n végzett kísérleteinkhez, számos, melanómához köthető ‘Biofunction’-t tudtunk azonosítani, melyekre az sEV-k szignifikáns hatást gyakorolhatnak ($p \leq 0{,}00001$). Szintén találtunk intracelluláris funkciókat, mint a ‘Tumorsejtvonalak G1 fázisának megállítása’, sejtszintű folyamatokat, mint a ‘Melanóma sejtvonalak mozgása’, szisztémás folyamatokat, mint a ‘Sejtek metasztatizálása’ és immunológiai funkciókat is, mint a ‘Leukociták aktivációja’.

3.5.1.4 A tumormátrix-sejtek melanóma sEV-k indukálta válaszainak vizsgálata in silico predikciókon alapuló in vitro kísérletekkel

Az aktiváló és gátló hatások tekintetében, az IPA ‘Grow’ és ’MAP’ funkciói révén sok olyan ‘Biofunction’-t találtunk, melyeken a különböző sEV-k szabályzó hatása eltérő lehet. Ezért, az *in silico* prediktált, sEV-indukálta válaszokat *in vitro* módszerekkel elemeztük.

3.5.1.5 Az Ag-TiO_2 sEV-k fokozzák az MSC-k proliferációját

Az *in silico* analízisek a Ki-67-expresszió aktivációját prediktálták a Ctrl, Hs és Ag-TiO_2 sEV-k hatására, és az ‘Őssejtek proliferációjának’ aktivációját jelezték elő minden sEV-csoport esetén. Eszerint a vezikulák felvételét követően a recipiens őssejtekben háromféle sEV fokozhatja a Ki-67-expressziót és mind az ötféle sEV sejtosztódást válthat ki (**21. ábra**).

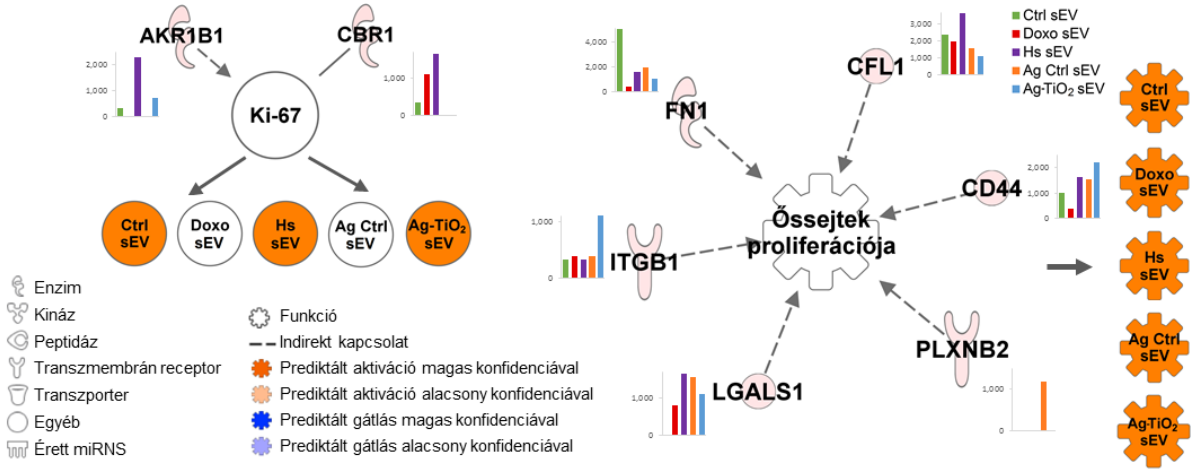

21. ábra. Az sEV molekulák Ki-67-expresszióra és ‘Őssejtek proliferációjára’ gyakorolt szabályozó hatásának IPA-predikciója.

Az ábrákon minden szabályozó fehérjét feltűntettünk. A hozzájuk tartozó oszlopdiagramok a normalizált expressziós értékeiket mutatják minden sEV-csoportban. Az sEV-csoportok neveivel ellátott színes ◌ és ✲ szimbólumok a vezikulák prediktált szabályzó hatását jelzik a vizsgált molekulán, illetve ‘Biofunction’ esetén.

Az sEV-k Ki-67-szabályzására vonatkozó predikciók teszteléséhez MSC kultúrákat 200 µg/ml sEV-, vagy negatív kontrollként (negatív Ctrl) Dulbecco-féle foszfát-pufferelt sóoldat (DPBS)-tartalmú médiummal kezeltünk. 24, illetve 72 óra elteltével a sejtek Ki-67-expresszióját immuncitokémiával vizsgáltuk. A kísérlet kvantitatív értékeléséhez egy nagy áteresztő képességű képalkotó rendszert (PerkinElmer - Operetta) és egy képanalizáló, gépi tanulással működő szoftvert (SCT Analyzer 1.0) használtunk. Az Ag-TiO_2 sEV-indukált kultúrákban, 72 órás kitettségnél szignifikáns növekedést tapasztaltunk a Ki-67-pozitív sejtek arányában (p = 0,03572; n = 4; **22a ábra**).

Az MSC-k proliferációját közvetlen sejtszámolás révén vizsgáltuk, melyhez DAPI-festést, és képalkotáson alapuló gépi tanulási módszert használtunk. A sejtek proliferációja Hs és Ag-TiO_2 sEV-kezelések esetén már 24 óra elteltével megnőtt, de minden kezelésnek eltérő hatása volt (**22b ábra**).

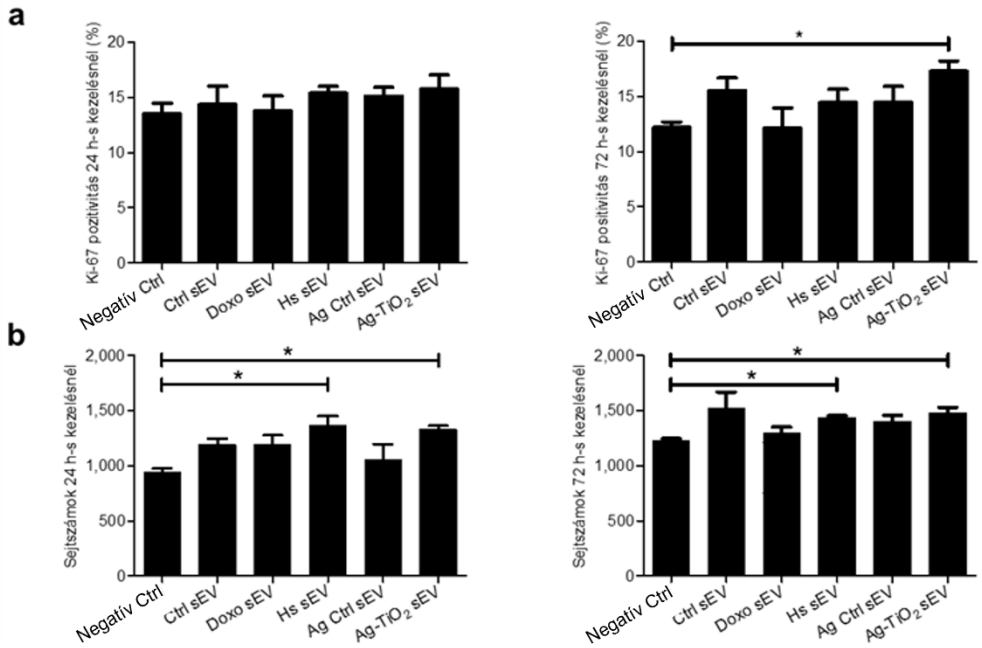

22. ábra. Az sEV-indukált MSC-k osztódási sajátságai.

*(a) Ki-67-pozitív sejtek százalékos aránya 24 óra (baloldalt) és 72 óra (jobboldalt) elteltével. (b) sEV-indukált kultúrákban kapott sejtszámok a 24 órás (baloldalt) és 72 órás (jobboldalt) inkubációs időpontokban. A diagramok átlag + SD értékeket ábrázolnak; *p < 0,05.*

In vitro eredményeink arra utalnak, hogy más-más mikrokörnyezeti tényezők befolyása alatt termelt melanóma sEV-k eltérően befolyásolják az őssejtek proliferációját, azonban az IPA által prediktált molekuláris interakciókon kívül, más molekulák és más tényezők is részt vehetnek ebben a folyamatban, mint például az sEV-k szállította doxorubicin.

3.5.1.6 A Doxo és Ctrl sEV-k befolyásolják a tumorsejtek sejtciklusának alakulását

Az IPA-analízisek a ‘Tumorsejtvonalak G1 fázisának’ és a ‘Tumorsejtvonalak G1/S fázisátmenetének’ gátlását prediktálták a Ctrl, Doxo és Hs sEV-kre (**23. ábra**). Vagyis, ezen vezikulák molekula-készlete feltartóztathatja a recipiens tumorsejteket a G1 fázisban és nem engedi a sejteket az S fázisba lépni.

Az sEV-k *in silico* prediktált, tumorsejtciklusra gyakorolt hatásainak teszteléséhez az ún. Cell-Clock esszét használtuk, ahol sEV-, vagy negatív kontrollként DPBS-kezelt B16F1 melanóma-sejteket vizsgáltunk 24 , 48 és 72 órás kezeléseket követően. A teszt működése egy redox festéken alapul, melynek színe a sejtciklus fázisaitól függően változik (G1: sárga, S/G2: zöld, M: kék).

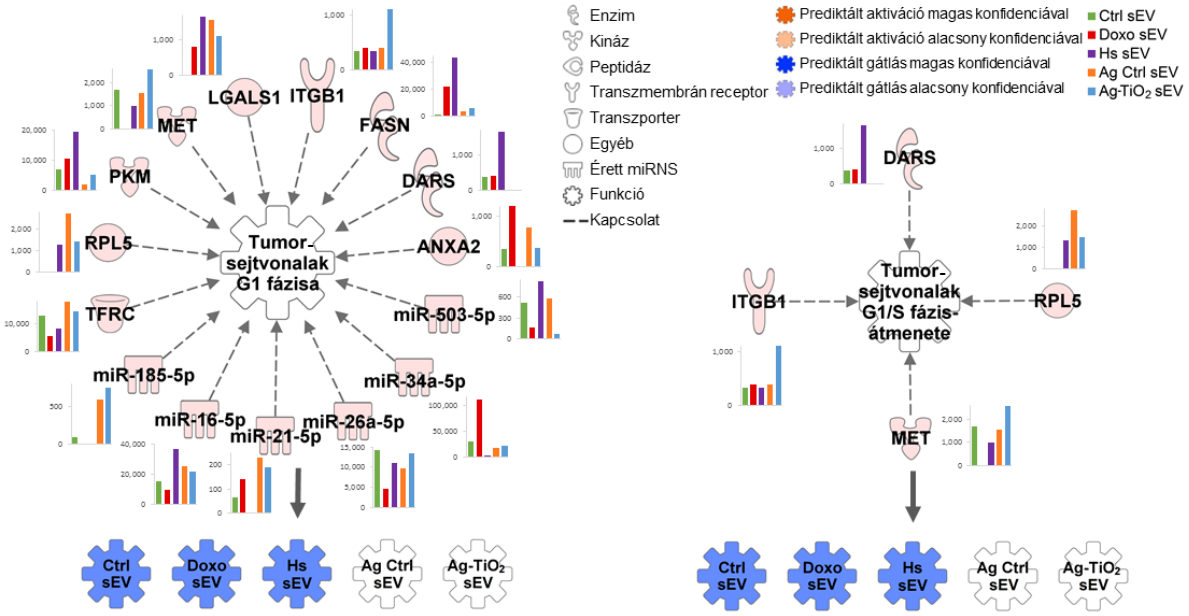

23. ábra. Az sEV molekulák ‘Tumorsejtvonalak G1 fázisára’ és ’Tumorsejtvonalak G1/S fázisátmenetére’ gyakorolt szabályzó hatásának IPA-predikciója.

Az ábrákon minden szabályozó fehérjét és miRNS-t feltűntettünk. A hozzájuk tartozó oszlopdiagramok a normalizált expressziós értékeiket mutatják minden sEV-csoportban. Az sEV-csoportok neveivel ellátott színes szimbólumok a vezikulák prediktált szabályzó hatását jelzik a vizsgált ‘Biofunction’ esetében.

A **24. ábrán** látható, hogy a Ctrl és a Doxo sEV-indukciók az idő függvényében szignifikánsan növelték a sárga, azaz a G1 fázisú sejtek arányát (p_{Ctrl} = 0,00346; $p_{Doxo} = 4{,}28 \times 10^{-6}$; n = 4), amely alátámasztotta az IPA által prediktált sejtciklusgátló hatást a Ctrl és a Doxo sEV-kre (ellenben a Hs sEV-kre nem). Eredményeink arra utalnak, hogy ezen stresszorok nyomása alatt termelődő vezikulák gátolhatják a tumorsejtek proliferációját.

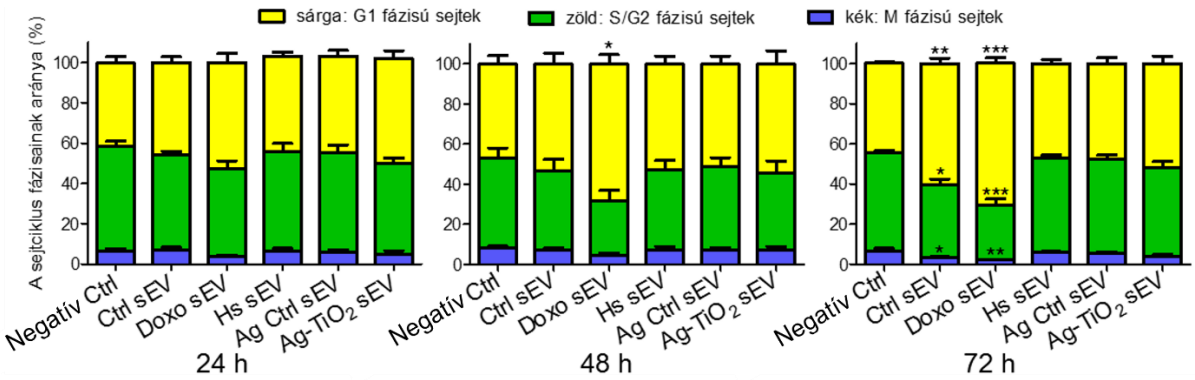

24. ábra. A G1, S/G2 és M fázisú sejtek aránya megváltozik az sEV-kezelt B16F1 kultúrákban.

*A diagramok átlag + SD értékeket ábrázolnak (n = 4); *p < 0,05; **p < 0,01; ***p < 0,001.*

3.5.1.7 Az sEV-mediált sejtmigráció nemcsak a vezikulák típusától, hanem a recipiens sejttől is függ

Az IPA-predikciók szerint az sEV-k számos sejtmozgással kapcsolatos 'Biofunction'-t befolyásolhatnak. Ezek közül a 'Melanóma-sejtvonalak migrációját' és az 'Endotélsejtek migrációját' választottuk *in vitro* tesztelésre, melyek esetében az *in silico* analízisekben igen változatos sEV-hatásokat olvashattunk. Míg predikciók alapján a Doxo és Ag-TiO_2 sEV-k elősegíthetik a melanóma sejtek migrációját, a maradék három sEV-csoport gátolhatja azt. Ezzel szemben az endotélsejtek migrációját mind az ötféle sEV-csoport serkentheti (**25. ábra**).

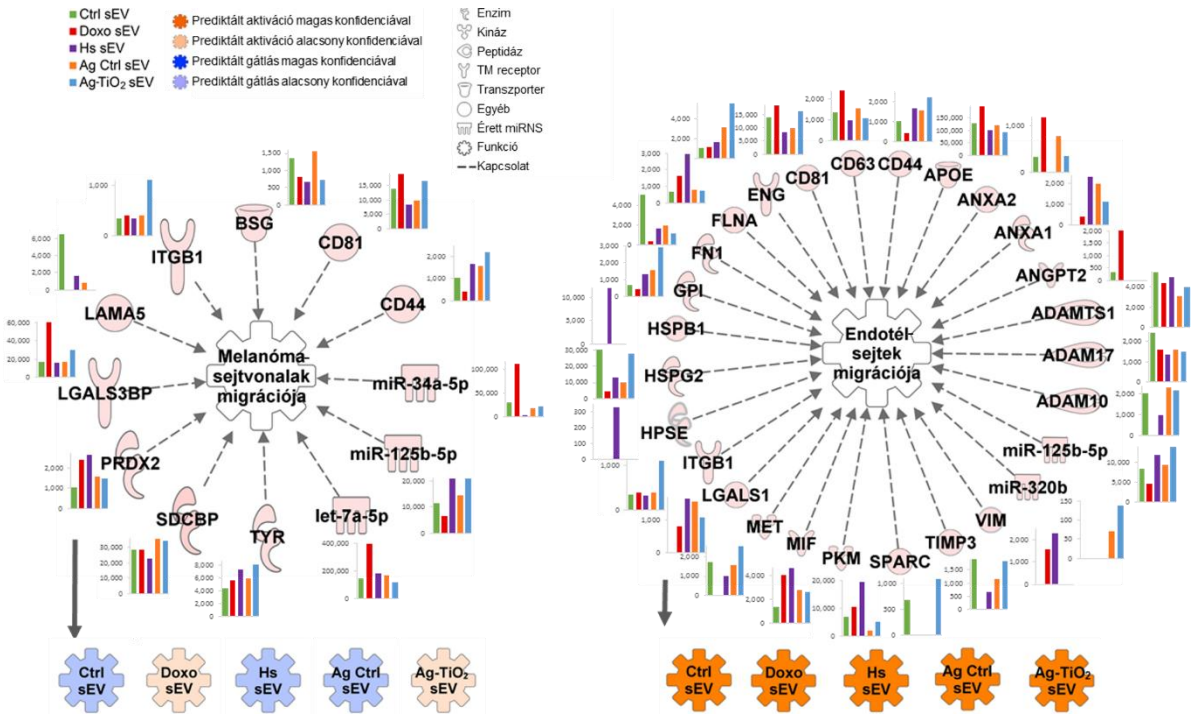

25. ábra. Az sEV molekulák 'Melanóma-sejtvonalak migrációjára' és 'Endotélsejtek migrációjára' gyakorolt szabályozó hatásának IPA-predikciója.

Az ábrákon minden szabályzó molekulát feltűntettünk. A hozzájuk tartozó oszlopdiagramok a normalizált expressziós értékeiket mutatják minden sEV-csoportban. Az sEV-csoportok neveivel ellátott színes ❁ szimbólumok a vezikulák prediktált szabályzó hatását jelzik a vizsgált 'Biofunction' esetében.

Az *in silico* prediktált sEV-hatásokat a sebgyógyulási esszékben B16F1 melanóma- és bEnd.3 endotélsejteken vizsgáltuk, ahol a predikciókhoz hasonló tendenciákat figyelhettünk meg. A melanóma sejtek migrációja a Ctrl és az Ag Ctrl sEV-k jelenlétében enyhén csökkent a negatív Ctrl sejtekhez képest. A Doxo sEV-k viszont felgyorsult sebzáródást váltottak ki (n = 8), míg a Hs és Ag-TiO_2 sEV-k nem befolyásolták a tumorsejt-migrációt (**26a ábra**). Ez azt jelenti, hogy citosztatikus stresszhatás alatt az sEV-k olyan üzeneteket közvetíthetnek a szomszédos tumorsejteknek, akár mintegy menekülésképpen, amelyek fokozzák azok migrációját.

Az endotélsejtek migrációját a Ctrl sEV-k fokozták a legnagyobb mértékben, amely arra utal, hogy a normál körülmények mellett kibocsájtott vezikulák elősegíthetik az angiogenetikus folyamatokat, de bizonyos stresszténye zők akár mérsékelhetik is ezt az sEV-hatást (**26b ábra**).

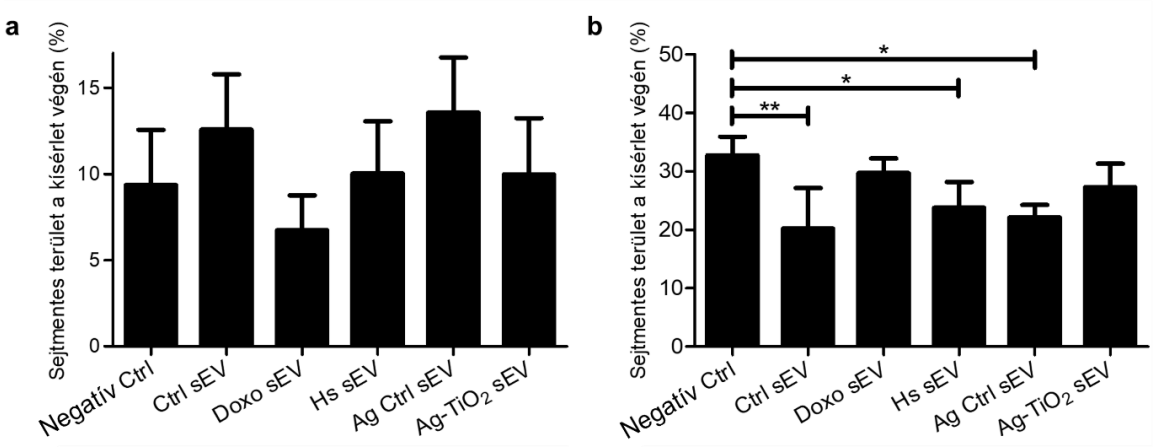

26. ábra. Az sEV-indukált (a) B16F1 és (b) bEnd.3 sejtkultúrák migrációs kapacitása eltérő tendeciákat mutat.

*A diagramok a sebgyógyulási esszé eredményeit mutatják, melyet az ImageJ sebgyógyulási kiegészítőjével értékeltünk. Az oszlopok átlag + SD értékeket ábrázolnak (n_{B16F1} = 8, $n_{bEnd.3}$ = 4); *p < 0,05; **p < 0,01.*

3.5.1.8 Az sEV-k mikroszövetképzést elősegítő hatása nem függ az sEV-típustól

Az IPA-predikciók szerint mind az öt sEV-csoport aktiváló hatást gyakorolhat olyan folyamatokra, amelyek egy 3D-s sejtinterakciós mátrix kialakulását segíthetik elő. Ilyen 'Biofunction' többek közt, a 'Sejtek aggregációja' vagy az 'ECM-képzés' (**27. ábra**).

A különböző sEV-k aktiváló hatásának intenzitása viszont eltéréseket mutat, például a ‘Sejtek aggregációjára’ prediktált aktiváció a Doxo és a Hs csoportban a legerősebb.

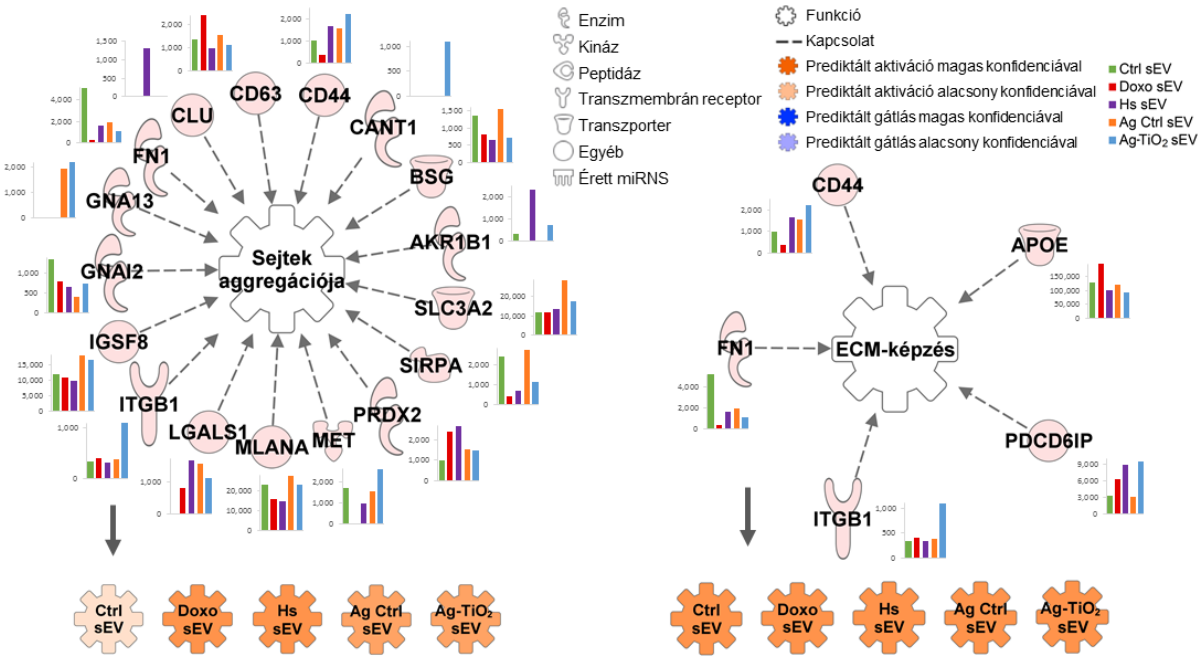

27. ábra. Az sEV-molekulák ‘Sejtek aggregációjára’ és ’ECM-képzésre’ gyakorolt szabályozó hatásának IPA-predikciója.

Az ábrákon minden szabályozó fehérjét feltűntettünk. A hozzájuk tartozó oszlopdiagramok a normalizált expressziós értékeiket mutatják minden sEV-csoportban. Az sEV-csoportok neveivel ellátott színes ✲ szimbólumok a vezikulák prediktált szabályozó hatását jelzik a vizsgált ‘Biofunction’ esetében.

Ezen *in silico* predikciókat is teszteltük *in vitro* kísérletekben. Az *in vivo* körülmények imitálása céljából létrehoztunk egy leegyszerűsített 3D-s tumormátrix modellt, ahol MSC, vagy egér embrionális fibroblaszt (MEF) sejteket és B16F1 sejteket tenyésztettünk együtt függőcsepp lemezeken. A kétféle sejttípust 1:1 arányban alkalmazva (5000 sejt/lyuk) 72 órán át követtük a mikroszövetek kialakulását sEV- és kontrollként alkalmazott DPBS-kezelések mellett. A mikroszövetekről készült képeket az AnaSP szoftver segítségével elemeztük, amelyet szferoidok automatikus képanalízisére fejlesztettek. A kísérletek során minden sEV-csoport elősegítette a mikroszövetképzést, azonban a legkisebb és legkompaktabb struktúrák a Doxo sEV-kezelés esetén jöttek létre (**28. ábra**). Ez azt jelenti, hogy a felszín-térfogat arány magasabb volt az sEV-indukált mikroszöveteknél, amely fokozhatja az oxigén, a növekedési faktorok és a tápanyagok felvételét, ráadásul kompaktabb struktúrák esetén a gyógyszerek penetrációja is mérséklődhet.

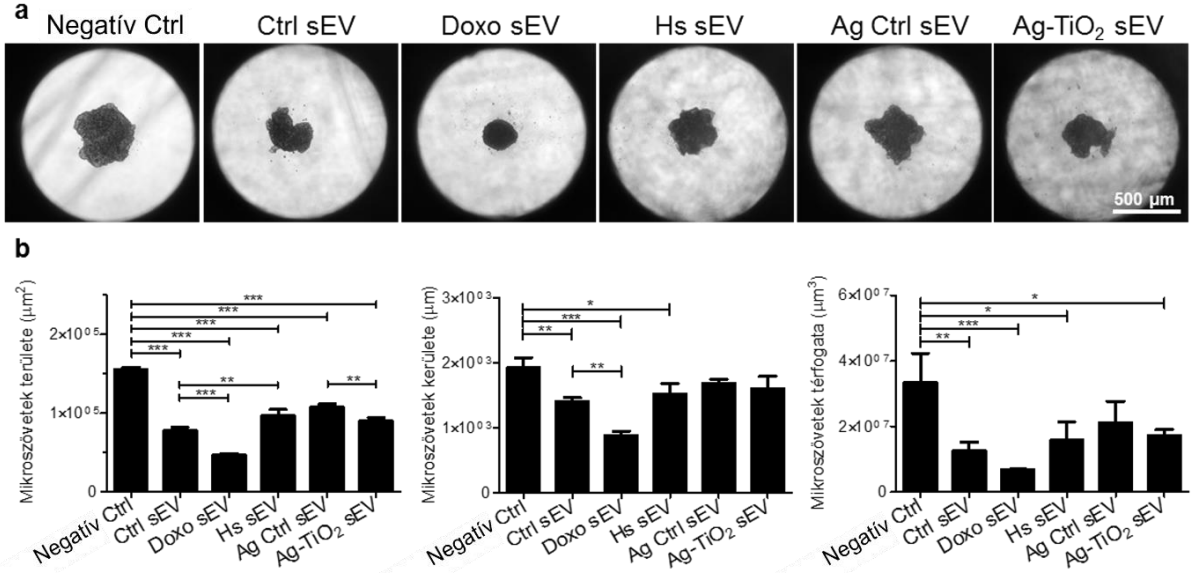

28. ábra. MSC-B16F1 ko-kultúrák mikroszövet-képzése.

*(a) A kialakult mikroszövetek reprezentatív képei 72 órás sEV-kezeléseket követően. (b) Az oszlopdiagramok a mikroszövetek területére, kerületére és térfogatára vonatkozó statisztikáit mutatják átlag + SD értékekkel (n = 3); *p < 0,05; **p < 0,01; ***p < 0,001.*

Mindezen eredmények abba az irányba mutatnak, hogy a sejt-sejt kommunikáció vizsgálatát – különösen, ha terápiás szerek hatásait tanulmányozzuk – mindenképpen érdemes kiterjeszteni az intercelluláris kommunikáció vezikuláris útvonalának a megfigyelésére is, hiszen számottevő, esetenként kritikus hatásokkal számolhatunk az sEV-k molekuláris információkat átadó kapacitását figyelembe véve.

3.6 Az sEV-k, mint jelerősítők, segítik a központi idegrendszeri tumorok perifériás vérből történő detektálását

Ahogyan azt már a bevezető fejezetekben ismertettem, a biomarkerek (pl. szérumfehérjék és extracelluláris vezikulák) vizsgálatára szolgáló, folyadékbiopszián alapuló módszerek segíthetnek az agydaganatok nyomon követésében (Alix-Panabières & Pantel, 2021; Lone et al., 2022; Preusser, 2014). A következőkben bemutatott proteomika-alapú vizsgálatban a központi idegrendszeri (CNS) daganatokhoz kapcsolódó jellegzetes fehérje-ujjlenyomat azonosítását tűztük ki célul. Összesen 96 humán szérummintát vizsgáltunk négy betegcsoportból, nevezetesen glioblastoma multiforme (GBM), nem kissejtes tüdőrák agyi metasztázisa (BM), meningeóma (M) és lumbális porckorongsérves (CTRL) betegekből. Az sEV-k izolálása, NTA-val és AFM-mel történő jellemzése után LC-MS/MS-t végeztünk két különböző mintatípuson (teljes szérum és szérum sEV-k). A betegcsoportok összehasonlítására statisztikai elemzéseket végeztünk (arányszám, Cohen-féle d hatásnagyság, vevő működési karakterisztika - ROC). A két mintatípus közötti különbségek

felismerésére páros összehasonlításokat (Welch *t*-próba) és *in silico* funkcionális analíziseket (IPA) végeztünk.

Az azonosított 311 fehérje közül 10 teljes szérum fehérje és 17 sEV fehérje mutatta a legnagyobb csoportközi különbségeket. 65 fehérje szignifikánsan feldúsult az sEV-mintákban, míg 129 fehérje szintje szignifikánsan csökkent a teljes szérumhoz képest. A főkomponens-elemzések (PCA) alapján az sEV-k alkalmasabbak a betegcsoportok megkülönböztetésére. Eredményeink alátámasztják, hogy az sEV-k nagyobb potenciállal rendelkeznek a CNS-tumorok monitorozására, mint a teljes szérum.

3.6.1 Az LC-MS/MS adatok statisztikai elemzése különbséget tárt fel a szérum és az sEV minták klasszifikációs hatékonysága között

Célunk az volt, hogy azonosítsuk a négy betegcsoport közötti különbségeket, és hogy feltárjuk a betegcsoportokat megkülönböztető fehérjeprofilokat. A > 2 vagy < 0,5 átlagintenzitás arányt és a 2-es Cohen-féle d hatásnagyságot küszöbértékként használva megvizsgáltuk, hogy mely fehérjék mutatnak megbízható különbséget, és mely fehérjék képesek legalább egy csoportot elkülöníteni a többitől a ROC-analízis alapján. Továbbá, a k-közép klaszterizálással végzett PCA-t alkalmazva össze tudtuk hasonlítani, hogy a két különböző mintatípus alkalmas-e a szóban forgó CNS-tumorok megkülönböztetésére. A **29. ábra** a statisztikai elemzések eredményeit mutatja.

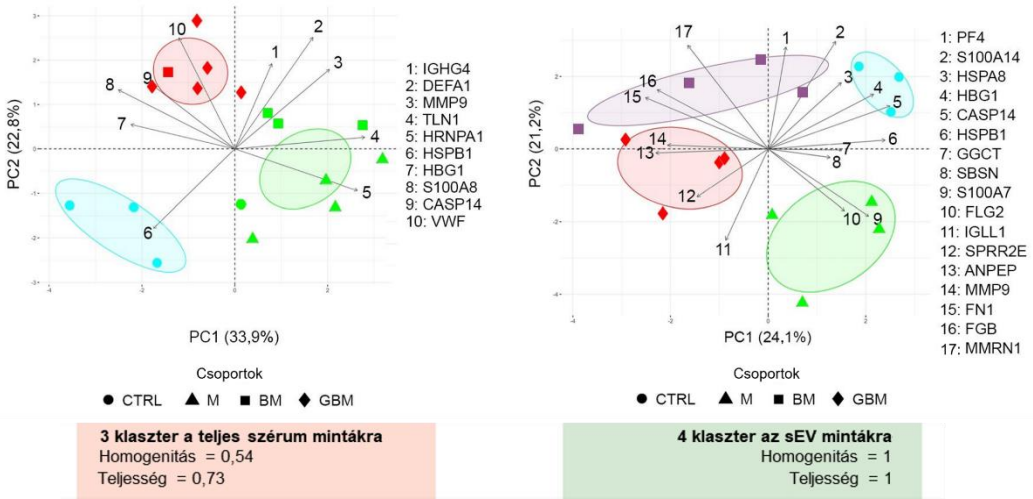

29. ábra. A diagramok a PCA és a k-közép klaszterizálás eredményeit szemléltetik.
A PCA biplotok X és Y tengelyei az 1. főkomponenst (PC1) és a 2. főkomponenst (PC2) mutatják a magyarázott varianciákkal. A PCA biploton a vektorok a fehérjéket ábrázolják az első két főkomponens mentén. A vektorok hossza és iránya jelzi, hogy az adott fehérje milyen mértékben kapcsolódik az első két főkomponenshez. A különböző alakzatok a 4 betegcsoportot jelölik. A színek a k-közép klaszterizálással kialakított klasztereket jelzik; a 95%-os konfidenciaintervallumot jelző ellipsziseket a klaszterek súlypontjai körül alakítottuk ki.

A PCA-elemzések és a k-közép klaszterizálás eredményei jelentős különbségeket mutatnak a teljes szérum és az sEV-minták között (**29. ábra**). A k-közép klaszterizálás a teljes szérum esetében 3 inhomogén vagy hiányos klasztert eredményezett. A számított klaszter-homogenitási és -teljességi pontszáma 0,56, illetve 0,73. A teljes szérummintáktól eltérően az sEV minták csoportosítása homogén és teljes klasztereket alkotott, 1-es homogenitási és teljességi pontszámmal. Megállapítottuk, hogy a különböző CNS tumorok megkülönböztetésének pontossága növelhető a szérumból izolált sEV-kből azonosított fehérjepanel használatával, a teljes szérumminták elemzéséhez képest.

3.6.2 Az LC-MS/MS adatok statisztikai értékelése a két mintatípus közötti alkalmassági különbségek hátterének feltárása érdekében.

Az sEV és a teljes szérumminták proteomjának statisztikai összehasonlítását azért végeztük el, hogy feltárjuk a különböző mintatípusok alkalmasságát befolyásoló mennyiségi különbségeket, amelyek a CNS tumorok állapotának monitorozására szolgáló biomarkerekké válhatnának. Páros statisztikai összehasonlítást (Welch *t*-próba) alkalmaztunk az sEV-mintákban a teljes szérummintákhoz képest szignifikánsan feldúsult vagy lecsökkent fehérjék azonosítására (**30. ábra**).

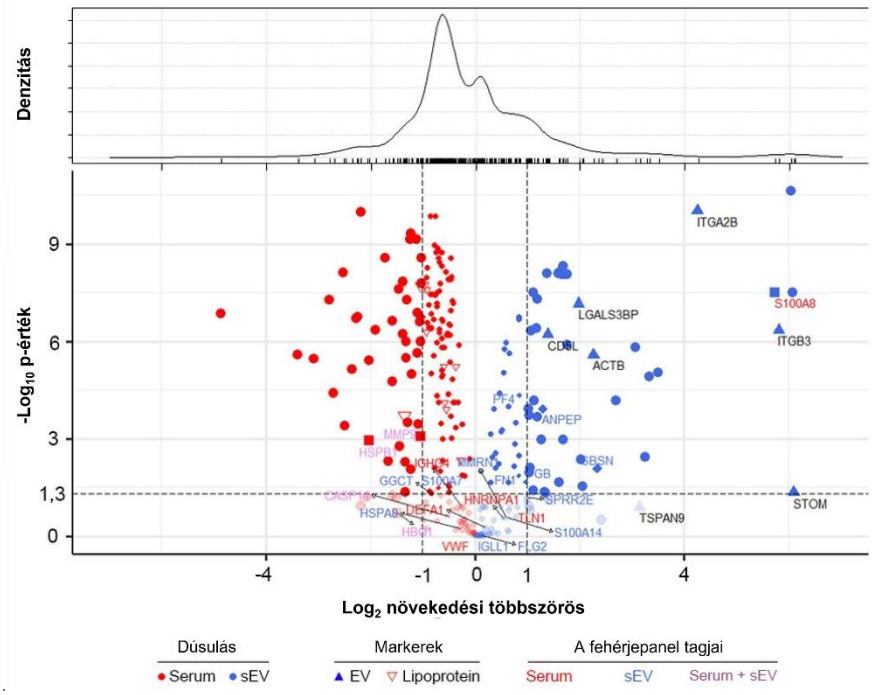

30. ábra. A sEV és a teljes szérum minták proteomjának kvantitatív összehasonlítása

A diagram az átlagos MS intenzitások megfigyelt változásait mutatja a páros sEV/szérum összehasonlításban. A fehérjedúsulást piros és kék színű szimbólumok jelzik a teljes szérumban, illetve az sEV-kben. A lipoproteinek (üres piros, fejjel lefelé fordított háromszögek), a teljes szérumfehérje panelünk elemei (piros betűk, négyzet szimbólumok), az

sEV fehérje panel (kék betűk, rombusz szimbólumok) és a két fehérje panel közös tagjai (lila betűk) kiemelve látható. A –log (p) értékeit páros Welch-tesztből kaptuk sEV/szérum összehasonlításban. A log2 értékek sűrűségbecslése látható felül.

65 fehérje szignifikánsan feldúsult az sEV-mintákban, míg 129 fehérje intenzitása szignifikánsan lecsökkent ($p < 0,05$). A Módszerek fejezetben részletezett sEV-tisztítási protokollunk alkalmazásával a partikulák mérettartománya egységesnek tekinthető, habár az sEV-proteomban a teljes szérumhoz képest bekövetkezett mennyiségi változások lipoprotein és szérumfehérje-szennyeződések lehetséges jelenlétét mutatta. Az apolipoproteinek szintje csökkent ugyan az sEV mintákban (az sEV/szérum átlagos aránya 0,66), azonban ezt a frakciót nem sikerült teljesen eltávolítani. Emellett a jól ismert, nagy mennyiségben előforduló szérumfehérjék (pl. ALB) domináltak az sEV minták fehérjetartalmában is. A nem szövetspecifikus (ITGA2B, ITGB3, LGALS3BP), hámsejt (CD5L) és vérlemezkékkel kapcsolatos (STOM, TSPAN9) EV marker fehérjék (de Menezes-Neto et al., 2015) feldúsulása azonban megerősíti az sEV feldúsulást (az sEV/szérum átlagos aránya 26,58), ugyanakkor a véralvadás során keletkező sEV-k jelenlétét is bizonyítja.

A leírt sEV marker panel 17 fehérjéje közül csak 6 fehérje intenzitása volt szignifikánsan magasabb az sEV mintákban, a specifikus szérum panel 10 fehérjéje közül 5 fehérje nagyobb mennyiségben volt jelen a teljes szérumban.

Az sEV minták esetében az újabb mintafeldolgozási lépések, név szerint az sEV izolálás nagyobb technikai varianciát eredményezhetnek a teljes szérumhoz képest, amely csökkentheti e mintatípus analitikai alkalmasságát. Ennek ellenére az elemzésünk hasonló szintű varianciát mutatott ki az egyes mintatípusokban azonosított fehérjék intenzitása esetén (a szennyeződések kivételével), mert a variációs koefficiensek betegcsoportokon belüli medián értékei az sEV-mintáknál 20,78%-23,87%, a szérummintáknál pedig 20,21%-24,45% között mozogtak.

Kutatásunk során fény derült arra, hogy a betegcsoportok tökéletes megkülönböztetéséhez nem elegendő egy-két molekula, helyette több molekulát tartalmazó fehérjepanelre (szérum esetében 10, sEV-k esetében 17 fehérjére) van szükség. Ez magyarázatot adhat arra, miért nem írtak még le korábban egy, a klinikumban jól alkalmazható szérum tumormarkert a glioblastoma multiforme azonosítására.

Eredményeink továbbá azt sugallják, hogy az sEV minták alkalmasabbak a megfelelő biomarkerek kutatására és azonosítására, mint a klinikumban jelenleg alkalmazott teljes

szérum analízise. A mi közleményünk volt az első olyan publikált összehasonlító tanulmány, amely rámutatott a teljes szérum és az sEV analízise közötti különbségekre a diagnosztikus és prognosztikus potenciáljuk tekintetében.

3.7 Szérumból izolált extracelluláris vezikulák MMP-9 tartalma, mint prognosztikus marker az agydaganatokban

A 3.6 fejezetben kifejtett tanulmányunkban megállapítottuk, hogy a teljes szérum helyett a szérumból izolált EV minták felhasználásával lehetővé válik az agydaganatokból, és az immunreakcióból származó jelek felerősítése (Dobra et al., 2020).

A statisztikai analízisek során találtunk egy olyan molekulát, amely minden alkalommal képes volt megkülönböztetni a betegcsoportokat, nevezetesen a mátrix metalloproteináz 9-et (MMP-9). A panel fehérjéi közül az MMP-9 volt a leghatékonyabb jelölt a betegcsoportok szétválasztásában markáns p és AUC értékkel (p = 0,0065, multiROC AUC = 0,86).

Az MMP-9 egy cink-függő endopeptidáz, melynek legfőbb feladata az ECM átrendezése, de számos más fiziológiás folyamatban szerepet játszik, mint például az angiogenezis, proliferáció, sejtmigráció (Mondal et al., 2020). Az ECM lebontása mellett az MMP-k többféle biológiai funkciót is ellátnak a daganat minden stádiumában, a kezdetektől a metasztázisok kialakulásáig (Chambers & Matrisian, 1997; Barillari, 2020). Rao és munkatársai azt is kimutatták, hogy erősen rosszindulatú gliómában az MMP-9 tumorszövetben mért overexpressziója korrelál a progresszióval, ami arra utal, hogy az MMP-9 szerepet játszik a megfigyelt invazivitás elősegítésében (Rao et al., 1996).

Elhatároztuk tehát, hogy minden rendelkezésünkre álló szérummintából kisméretű extracelluláris vezikulákat izolálunk, megmérjük azok MMP-9 tartalmát, amelyet a betegadatokkal összevetve elemzünk, hogy meghatározzuk a vezikuláris MMP-9 szint diagnosztikai és prognosztikai értékét. A klinikai hasznosíthatóság érdekében a tömegpspektrometriai vizsgálatot enzimhez kötött immunoszorbens vizsgálatra (ELISA) váltottuk, hiszen a klinikai gyakorlatban a tömegspektormetria kevéssé elterjedt módszer. További célunk az volt, hogy intenzitások helyett a teszt szenzitivitásának és specificitásának meghatározására alkalmas koncentrációkat kapjunk.

A vizsgálatba újabb mintákat vontunk be, 222 sEV minta MMP-9 tartalmát mértük meg egyesével. A hisztopatológia ismerete, a mintavétel ideje (preop és posztop), a kezelések vagy az elsődleges, illetve kiújult tumor megléte alapján az analízis során alcsoportok kialakítására is lehetőségünk volt, melyet az Anyagok és Módszerek fejezet **7. táblázata** mutat be.

3.7.1 Számos tényező befolyásolhatja a szérumból származó sEV-k MMP-9 szintjét

Egy klinikai vizsgálatban elengedhetetlen, hogy kiszűrjük azokat a faktorokat, amelyek a betegségeken kívül is befolyásolhatják az MMP-9 szintjét (**31. ábra**).

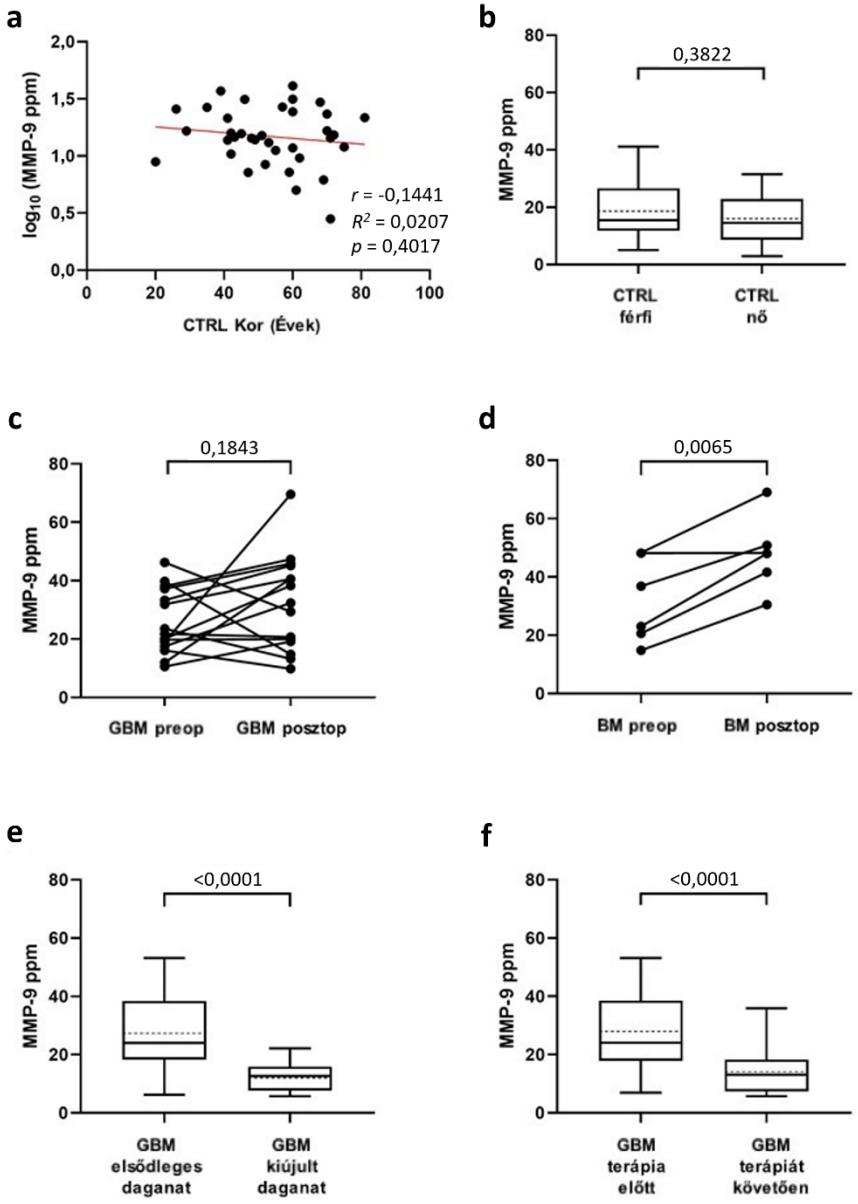

31. ábra. A szérumból származó sEV-k MMP-9 szintjét befolyásoló tényezők.

(a) Az életkor és az MMP-9 szint közötti kapcsolat a kontroll csoportban. (nCTRL = 36). (b) A két nem MMP-9 szintje a kontroll csoportban (a diagramok a mediánt mutatják interkvartilis tartománnyal, az átlagot szaggatott vonallal jelöltük, a hibasávok az 5-95 percentilis között mozognak; nCTRL férfi = 16, nCTRL nő = 20). (c, d) Változások az egyes betegek MMP-9 szintjében a műtéti reszekció előtt és után a GBM és a BM csoportban (nGBM preop-posztop = 14, nBM preop-posztop = 6). (e) A szérumból származó sEV-k MMP-9 szintjei az elsődleges daganatra és a kiújulásra vonatkozóan a műtéti reszekció előtt a GBM csoportban (nGBM elsődleges daganat = 52, nGBM kiújult daganat = 14). (f) MMP-9 szintek a GBM csoportban a terápiától függően (nGBM a terápia előtt = 52, nGBM terápiát követően = 15).

Megvizsgáltuk tehát, hogy van e különbség a férfiak és a nők MMP-9 szintje között, és hogy változik-e a vezikulaminták MMP-9 szintje a kor függvényében. Ehhez a kontroll csoportot használtuk. A tesztek alapján az MMP-9 szintje nemtől és kortól független (**31a, b ábra**).

Az irodalomban számos ellentmondásos eredménnyel találkozhatunk az operáció MMP-9 szintet befolyásoló hatásával kapcsolatosan (ezek szérum vagy plazma vizsgálati eredmények, nem szérum EV-k) (Hormigo et al., 2006; Osti et al., 2019). Vizsgálatainkban nem tapasztaltunk szignifikáns különbséget az operációt megelőzően, illetve 3-4 nappal azt követően mért vezikuláris MMP-9 szintek között glioblasztómás betegek esetén, azonban agyi metasztázisnál igen (**31c, d ábra**).

A preoperatív GBM mintákon végzett további vizsgálatokban az eredeti és a kiújult daganat között is különbséget találtunk, a kiújulás szignifikánsan alacsonyabb sEV MMP-9 szintet mutatott ($p < 0{,}0001$) (**31e ábra**). Az alkalmazott terápia hatásának meghatározásakor az sEV minták MMP-9 szintjeit összehasonlítottuk annak alapján, hogy a GBM betegek részesültek-e kezelésben a mintavétel időpontjában. Eredményünk ($p < 0{,}0001$) azt jelzi, hogy a terápia csökkentheti a keringő sEV-k MMP-9 szintjét (**31f ábra**).

A fentiek alapján megállapítható, hogy a betegségtípusokon kívül a műtéti reszekció, a recidíva és a terápia is befolyásolhatja a szérum eredetű sEV-k MMP-9 szintjét. Ezeknek a megállapításoknak köszönhetően a további elemzéseket (betegcsoportok összehasonlítása és túlélés vizsgálata) kizárólag a sebészeti reszekció és a terápia beadása előtt vett mintákon végeztük el.

3.7.2 A szérum sEV-k MMP-9 szintje különbözik a különböző központi idegrendszeri daganatokban, ami pozitívan korrelál a tumor agresszivitásával

Első lépésként a kontroll csoportot az összes daganatos beteggel hasonlítottuk össze. A kontroll csoporthoz képest a tumoros betegek szérumából izolált sEV-k MMP-9 szintje szignifikánsan magasabb ($p = 0{,}0002$), habár a 16 ppm küszöbértékhez tartozó legmagasabb specificitási és szenzitivitási értékek nem túl markánsak.

A daganat agresszivitásával összefüggésbe hozható növekvő tendenciát láthatunk abban az esetben, ha az MMP-9 szinteket betegcsoportonként ábrázoljuk, a csoportok közötti különbség a kontroll és a malignus daganatok között ($p < 0{,}0024$), illetve a malignus és benignus daganatok között mutatkozott szignifikánsnak ($p < 0{,}0102$) (**32. ábra**).

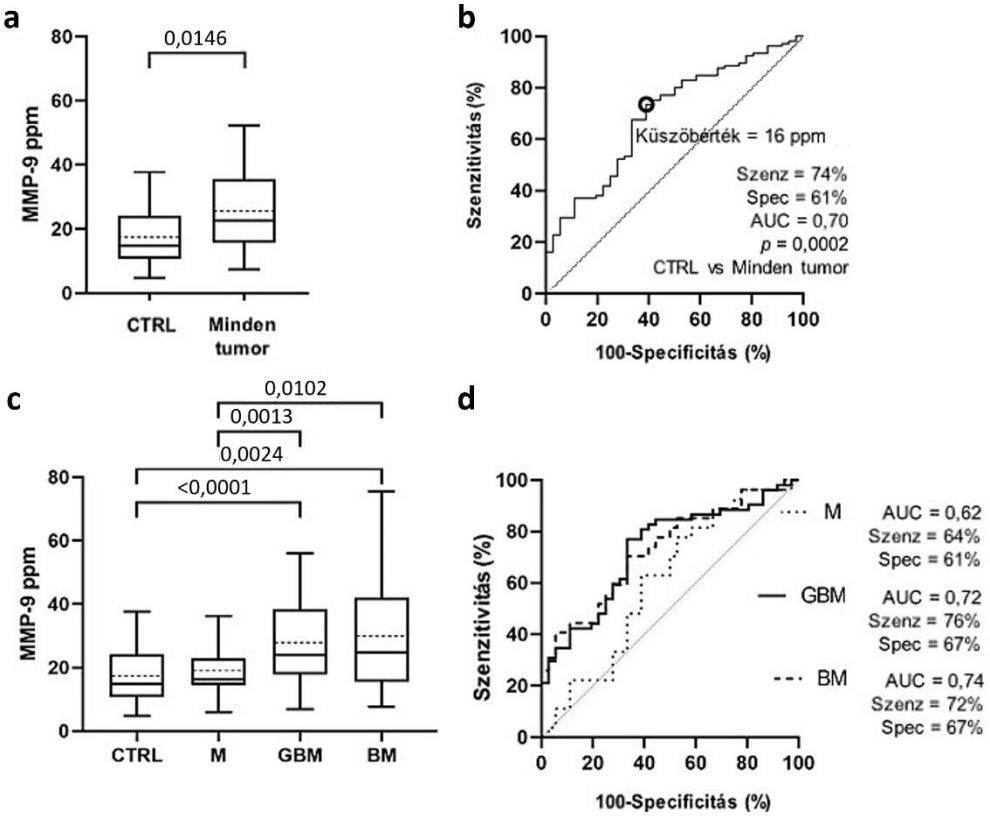

32. ábra. A szérum sEV MMP-9 szintjének összehasonlító elemzése a négy fő csoportban. *(a) A grafikon a kontroll csoport MMP-9 szintjét mutatja, összehasonlítva az összes daganatos betegével (medián interkvartilis tartománnyal, átlag szaggatott vonallal, hibasávok az 5-95 százalékos tartományban; nCTRL = 36, nMinden tumor = 105). (b) A ROC (Receiver Operating Characteristic) görbe a kontroll csoport és az összes daganatos beteg MMP-9 szintje közötti különbségeket ábrázolja (nCTRL = 36, nMinden tumor = 109). (c) A diagram a szérum sEV MMP-9 szintjét mutatja a négy betegcsoportban (nCTRL = 36, nM = 27, nGBM = 52, nBM = 27). (d) A ROC görbék a három tumorcsoport és a kontroll csoport összehasonlítását mutatják (nCTRL = 36, nM = 27, nGBM = 52, nBM = 27).*

Adataink azt igazolják, hogy a rosszindulatú agydaganatban szenvedő betegek a szérum sEV MMP-9 szintje alapján megkülönböztethetők a kontroll betegektől, és ez a szint különbözik az egyes központi idegrendszeri daganattípusok esetén, pozitív korrelációt mutatva a tumor agresszivitásával.

3.7.3 Az sEV-k MMP-9 szintje a GBM betegek túlélési esélyeinek prognosztikus markereként szolgálhat

A csoportok közötti különbség elemzése után arra kerestük a választ, hogy az MMP-9 szint korrelál-e a beteg túlélésével, közvetve a betegség progressziójával. Az analízis időpontjában 27 olyan primer GBM betegminta állt rendelkezésünkre, amely megfelelt a vizsgálati kritériumoknak (mintavétel az operáció és terápia megkezdése előtt történt, és ismeretes volt a túlélési idő) (**33. ábra**).

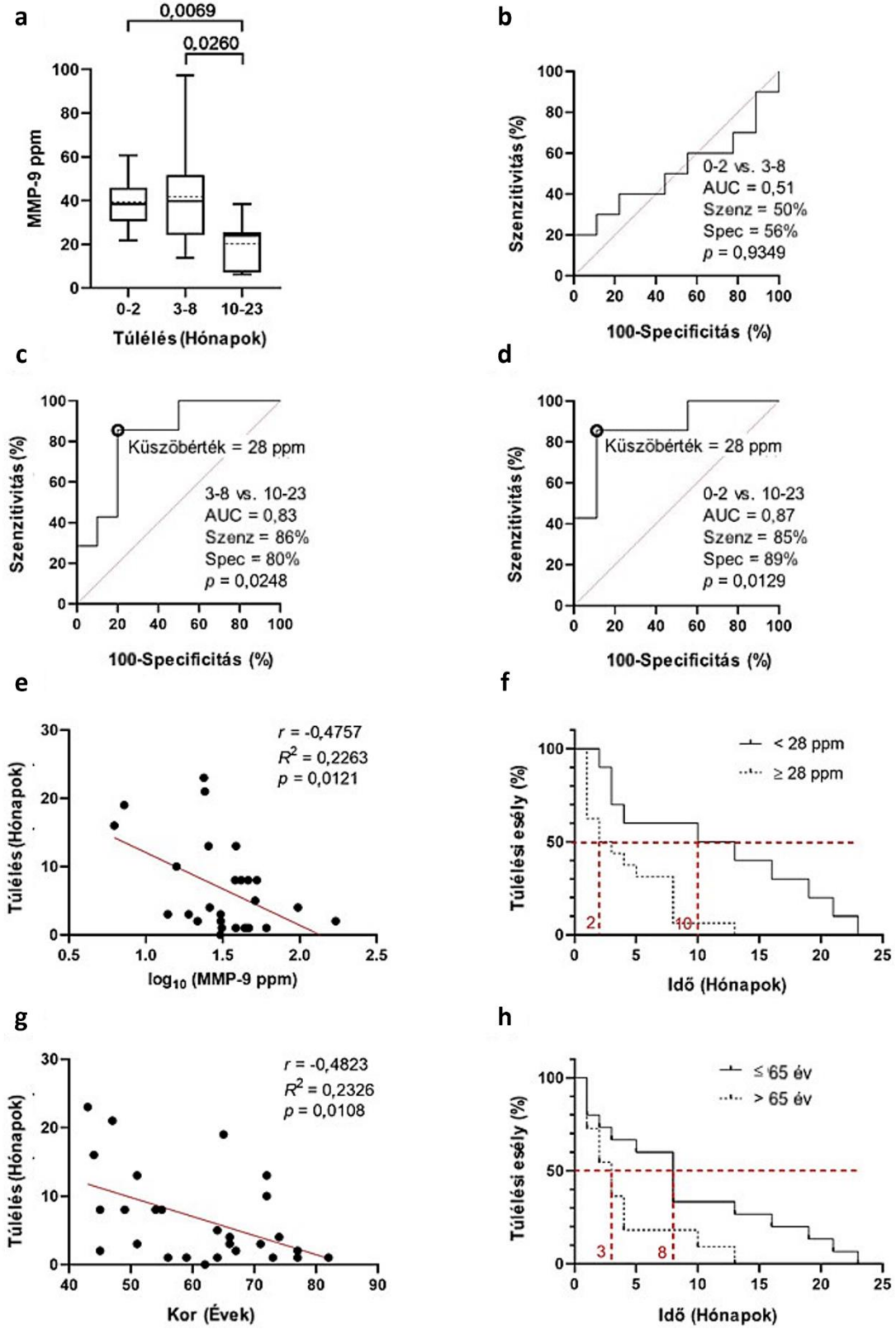

33. ábra. A túlélés vizsgálata GBM betegekben.

(a) Különbségek a rövid-, közép- és hosszútávú túlélés között a GBM betegek szérumból származó sEV-inek MMP-9-szintje alapján (medián interkvartilis tartományban, átlag szaggatott vonallal, hibasávok az 5-95 percentilis között, pontozott vonalak az átlagértékeket jelölik). (b–d) ROC görbék a rövid (0-2 hónap), a közepes (3-8 hónap) és a hosszútávú (10-23 hónap) túlélési csoportok (a csoport küszöbértékei) összehasonlítására (csoporthoz tartozás

pontszámának megfelelő küszöbértékeit fekete körök jelölik). (e) Korreláció az MMP-9 szint és a túlélés között a GBM csoportban (nGBM = 27). (f) Túlélés esélye az alacsony (n < 28 ppm = 10) és a magas (n ≥ 28 ppm = 17) MMP-9 szint szerint. (g) Az életkor és a túlélés közötti kapcsolat a GBM csoportban (nGBM = 27); (h) Túlélés esélye az életkor szerint (n ≤ 65 év = 16 és n > 65 év = 11).

Első megközelítésben a betegeket a túlélés idő alapján három csoportra osztottuk (rövid-, közép- és hosszútávú), a 10-23 hónapos túlélési idővel rendelkező betegek MMP-9 szintje szignifikánsan alacsonyabbnak mutatkozott a másik két csoporténál (**33a ábra**).

A ROC analízisekből megtudhattuk, hogy a legmagasabb szenzitivitási és specificitási értékek a 28 ppm-es küszöbérték esetén érhetőek el (**33b-d ábra**), ezért a betegeket újabb két csoportra osztottuk most már az MMP-9 szintjük alapján (**33e ábra**). A Kaplan-Meier diagram alapján, a vizsgálati csoportban a 28 ppm-nél alacsonyabb MMP-9 szinttel rendelkező betegek 8 hónappal kedvezőbb medián túlélést mutattak, mint a magas MMP-9-et képviselők (**33f ábra**).

Meg kell jegyeznünk, hogy az életkor is hasonló befolyással van a túlélésre (**33g ábra**). A vizsgált populáció alapján a fiatalabb betegek 5 hónapnyi medián túlélési előnyre tesznek szert (**33h ábra**), de mivel a kor és az MMP-9 szint nem mutat korrelációt (lásd **31. ábra**), ezért az MMP-9 szint kortól függetlenül befolyásolja a túlélést.

Összefoglalva tehát a daganatszövet által kibocsájtott vezikulák átlépve a vér-agy gátat a perifériás keringésbe jutnak, és ha a vérvétel után ezen vezikulák MMP-9 tartalmát megmérjük, akkor információt gyűjthetünk a daganat agresszivitására és a betegség kimenetelére vonatkozóan, amely segítséget nyújthat a klinikai döntéshozatalban.

Bizonyítást nyert, hogy szérumból izolált kisméretű extracelluláris vezikulák mátrix metalloproteináz 9 tartalma prognosztikus markerként alkalmazható invazív agydaganatok esetén.

3.8 A központi idegrendszeri tumorok extracelluláris vezikula alapú diagnosztikájának spektroszkópiai megközelítése

Ahogyan a korábbiakban már említettem, az sEV-k molekuláris összetételének vizsgálata tumordiagnosztikai célokra is egyre népszerűbbé válik (Melo et al., 2015; Scavo et al., 2020), különösen olyan betegségek esetében, amelyek diagnosztizálása kihívást jelent, mint például a CNS rosszindulatú daganatai (Aldape et al., 2019). Az sEV-k molekuláris tartalmának alapos vizsgálata Raman-spektroszkópiával ígéretes, de alig vizsgált megközelítés e

daganattípusok azonosításának esetében. Munkánk során megkíséreltük feltárni a szérumból származó sEV-k Raman-spektroszkópiai elemzésében rejlő lehetőségeket a CNS-tumorok diagnosztizálásában, releváns számú klinikai minta felhasználásával. Projektünkben összesen 138 szérummintát gyűjtöttünk négy betegcsoportból (GBM, BM, M, CTRL). Az sEV-k izolálása, jellemzése és Raman-spektroszkópiai értékelése után a páronkénti osztályozáshoz a Raman-spektrumokon a PCA-SVM (főkomponens analízis-tartó vektor mechanizmus) algoritmust alkalmaztuk.

3.8.1 A PCA-SVM algoritmus segítségével magas osztályozási hatékonysággal lehet megkülönböztetni a betegcsoportokat

Az izolált 138 minta Raman-spektroszkópiai elemzése során mintánként 5 spektrumot kaptunk. A 801 cm^{-1} és 3100,5 cm^{-1} közötti spektrális tartományt vizsgáltuk. Standard normál változó (SNV) normalizálás és PCA-transzformáció után a minták osztályozását SVM-algoritmussal végeztük. Az osztályozási hatékonyságot az osztályozási pontosság (CA), a szenzitivitás, a specificitás és a ROC-analízisből származó görbe alatti terület (AUC) értékével jellemeztük. A releváns spektrális különbségeket PCA segítségével mutattuk ki. A Raman-spektroszkópiai adatfeldolgozás folyamatábráját az Anyagok és Módszerek fejezet **36. ábrája** mutatja be.

Az SNV normalizálást követően a négy betegcsoport mintáinak spektrumát páronként hasonlítottuk össze (minden betegcsoportot a kontrollhoz hasonlítottunk, ezeken felül a BM-et a GBM-hez) egyrészt egy osztályozási algoritmus kifejlesztése és tesztelése, másrészt a releváns spektrális különbségek azonosítása céljából. A páros összehasonlításokra alkalmazott PCA csökkentette a többváltozós adatok dimenzióit az eredeti változók (hullámszámok) kisebb számú új változóivá, azaz főkomponensekké (PC-k) való átalakításával.

A páros összehasonlításokat a lineáris SVM algoritmus segítségével végeztük el, és minden egyes párosított csoportra osztályozási modelleket kaptunk. A tesztmintákra vonatkozó predikciókhoz meghatároztuk a csoportokhoz tartozás pontszámának minimális küszöbértékét. Az e küszöbérték feletti pontszámmal rendelkező tesztmintákat a célcsoportba soroltuk. Az optimális pontszámküszöböket automatikusan úgy állítottuk be, hogy azok megfeleljenek a legmagasabb osztályozási pontosságnak (CA, a helyesen osztályozott minták aránya az összes mintához viszonyítva).

A CA 85,6% volt a CTRL vs. GBM, 91,4% a CTRL vs. BM, 82,9% a CTRL vs. M és 92,5% a BM vs. GBM esetében. A legjobb osztályozási teljesítményt akkor értük el, ha bizonyos számú PC-t bevontunk a modellekbe: CTRL vs. GBM esetében 30 PC, CTRL vs. BM esetében 38 PC, CTRL vs. M esetében 27 PC, BM vs. GBM esetében 26 PC (**34. ábra**).

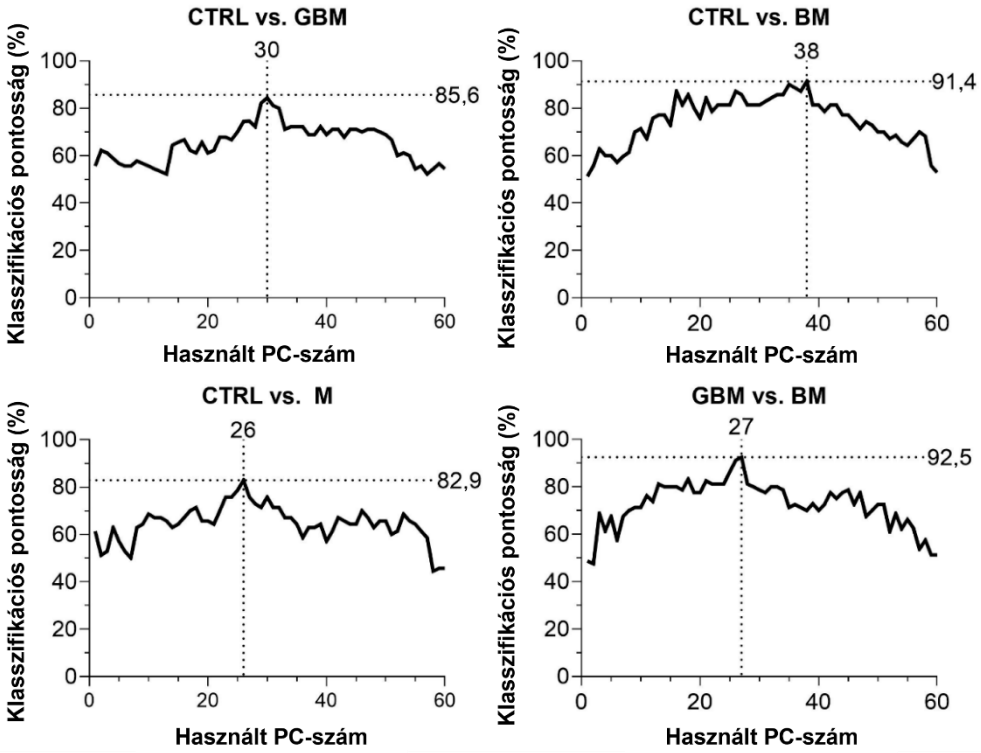

34. ábra. Az osztályozási pontosság (CA) eredményei a modellben szereplő PC-k számának függvényében (legfeljebb 60 PC).

A fekete szaggatott vonalak adott PC-számhoz tartozó legmagasabb CA-csúcsokat mutatják. (Rövidítések: PC, főkomponens).

Az osztályozási teljesítmény további mérőszámaiként értékeltük a tesztek szenzitivitását és specificitását. A páros osztályozási modellek ROC-elemzései négy grafikont eredményeztek, amelyek az automatikusan beállított optimális küszöbértékeket (a legmagasabb CA-értékkel) mutatják, a kapcsolódó szenzitivitási, specificitási és AUC, valamint a p-értékkel együtt.

Amint a **35. ábra** grafikonjain látható, az optimális küszöbértékek alkalmazásával az osztályozási modellek 90%-os és 80%-os, 93,75%-os és 90%-os, illetve 80%-os és 85%-os szenzitivitással és specificitással tudták megkülönböztetni a GBM, BM és M betegeket a CTRL betegektől. Az osztályozási modell segítségével a két rosszindulatú daganatot, a BM-et és a GBM-et 98%-os szenzitivitással és 83,3%-os specificitással lehetett megkülönböztetni egymástól. A páronkénti összehasonlítások azonos sorrendjében (GBM, BM és M betegek

vs. CTRL, illetve BM vs. GBM) az AUC értékek 0,87, 0,95, 0,82 és 0,9 voltak ($p < 0,0001$ minden esetben), amelyek kiemelkedő osztályozási teljesítményre utalnak.

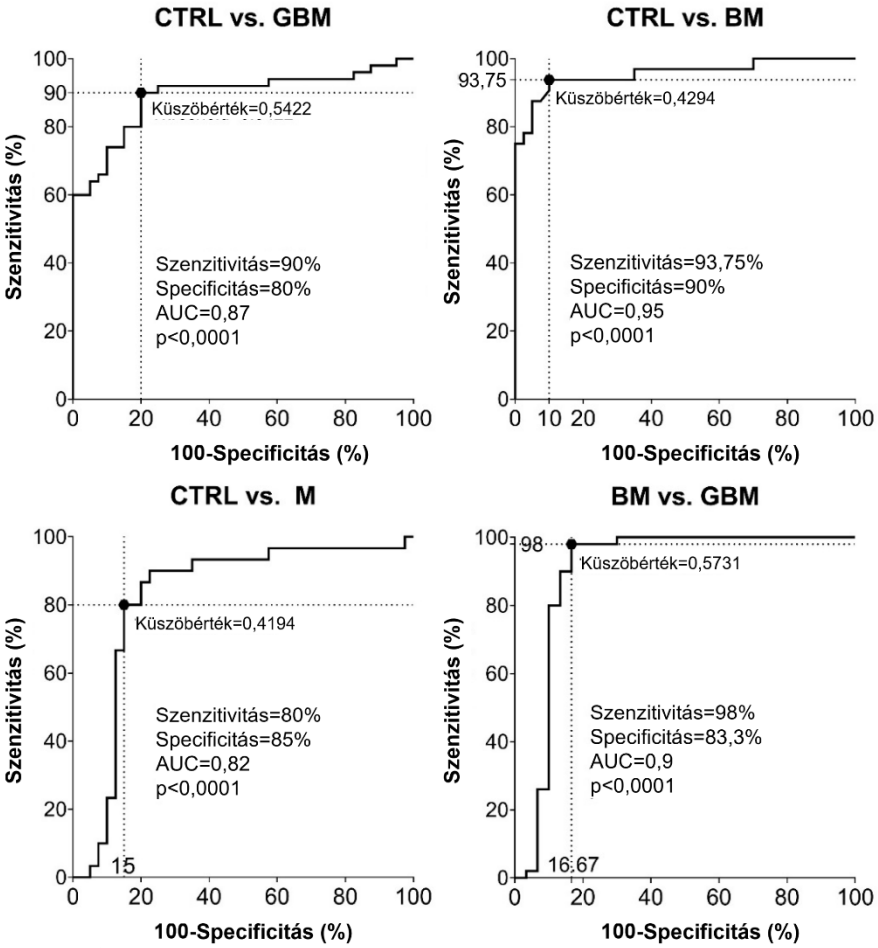

35. ábra. Az osztályozási modellek ROC görbéi.

Az egymást metsző fekete szaggatott vonalak a legoptimálisabb szenzitivitást és specificitást, valamint a csoporthoz tartozás pontszámának megfelelő küszöbértékeit mutatják, a metszéspontjaikban fekete kitöltött körökkel.

Eredményeink alátámasztják, hogy a szérumból származó sEV-vel dúsított izolátumok Raman-spektroszkópiai elemzése ígéretes módszer, amelyet tovább lehet fejleszteni annak érdekében, hogy alkalmazható legyen a CNS tumorok diagnosztikájában.

3.8.2 A PC-k elemzése képes magyarázni a diszkriminatív spektrális különbségeket

Ezután az egyes csoportok szérumból származó sEV izolátumok molekuláris tartalmának különbségeit vizsgáltuk, hogy feltárjuk az osztályozás szempontjából releváns spektrális különbségeket. Az SNV-normalizált spektrumokat és a PCA-ból kapott PC-ket a FreeViz módszerrel elemeztük a releváns spektrális különbségek feltárása és vizualizálása érdekében.

A FreeViz módszer a többváltozós adatsorok optimalizált vetületeit egy kétdimenziós szórásdiagramban jelenítette meg (**36. ábra**). A PC-vektorok hossza és iránya alapján két

PC választható ki, amelyekről kiderült, hogy a legfontosabb szerepet játszanak az egyes párosított csoportok megkülönböztetésében (a **36. ábrán** sárga háttérrel jelölve). Ezeket tovább értékeltünk a diszkriminatív spektrális jellegzetességek meghatározása érdekében.

A FreeViz módszer eredményei és a Welch t-próbából származó p-értékek alapján a PC14 és PC2, PC9 és PC13, P10 és PC19, valamint PC2 és PC3 magyarázta a legtöbb diszkriminatív különbséget a CTRL vs. GBM, CTRL vs. BM, CTRL vs. M és BM vs. GBM összehasonlításokban ($p < 0,05$ minden esetben).

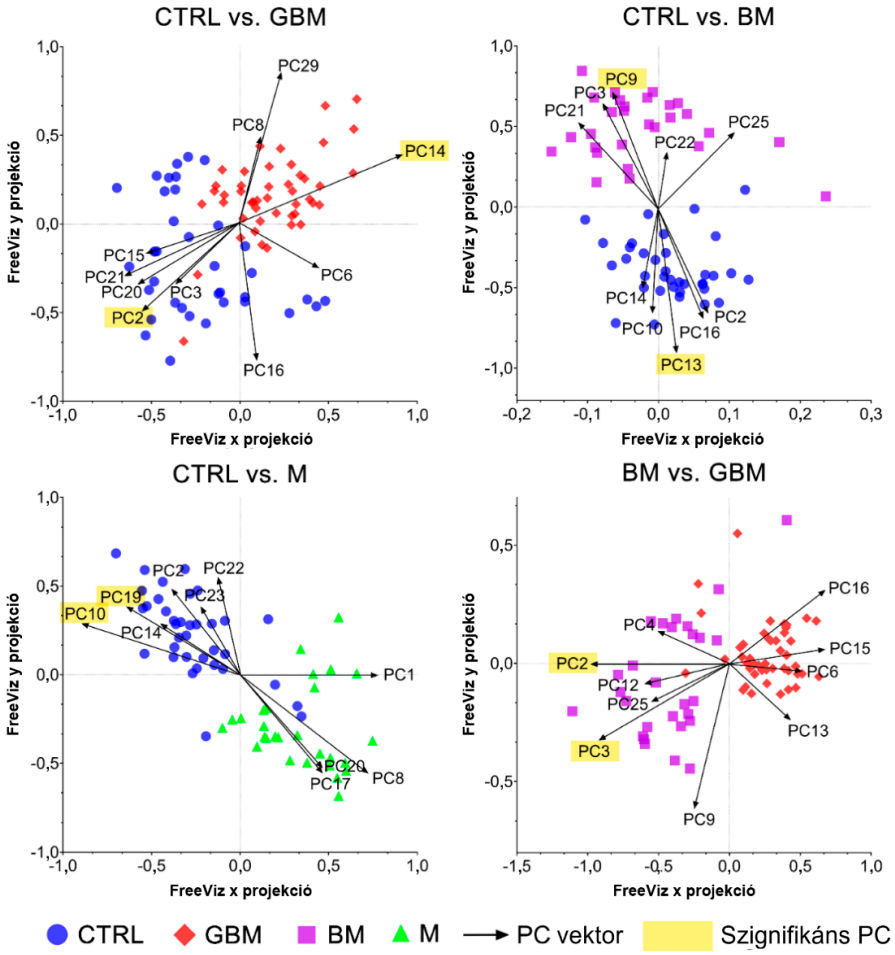

36. ábra. a páros összehasonlítások FreeViz projekciói.

A PCA-transzformált adatok FreeViz módszerrel történő elemzése négy grafikont eredményezett. A különböző pontok és színek a betegcsoportokat és az egészséges kontrollokat jelölik. A fekete vektorok a PC-ket képviselik. Mindegyik grafikonon csak a 10 legjelentősebb PC-vektort ábrázoltuk. Minden egyes összehasonlításnál a sárga háttérrel jelölt PC-k a 2 legjelentősebb PC-t jelölik.

A kiválasztott PC-ket kiértékelve megpróbáltuk megtalálni az összehasonlított csoportok megkülönböztetésében fontos szerepet játszó spektrális különbségeknek megfelelő kémiai kötéseket és funkcionális csoportokat.

A CTRL vs. GBM összehasonlítás tekintetében a legtöbb megkülönböztető spektrális különbség a szénhidrátokra jellemző volt, mint például a piranóz gyűrűhöz kapcsolódó sávok (800-975 cm^{-1}), az O-H deformációs rezgések (1030-1080 cm^{-1}) és a C-O nyújtási rezgések (1030-1290 cm^{-1}). Ezek a sávok nagymértékben átfednek a nukleinsavakra jellemző régiókkal, beleértve a foszfát-cukor váz rezgéseihez (800-1000 cm^{-1}), a szimmetrikus és aszimmetrikus foszfátcsoport nyújtási rezgéseihez (1000-1250 cm^{-1}), a glikozidos kötés rezgéseihez (1250-1550 cm^{-1}) és a bázisok síkbeli kettőskötés rezgéseihez (1530-1780 cm^{-1}) kapcsolódó sávokat (**37. ábra**).

A CTRL vs. BM összehasonlításánál a különbségtételben fontos szerepet játszó hullámszámok elsősorban a lipidekkel korreláltak (CH_3 aszimmetrikus hajlítás (1470-1490 cm^{-1}), CH_2 és CH_3 szimmetrikus és aszimmetrikus nyújtási rezgésekkel (2700-3100 cm^{-1})) és aminosavakkal (-NH_3^+ deformációs sáv (1485-1150 cm^{-1}), -NH_3^+ aszimmetrikus nyújtás (3000-3100 cm^{-1}), karboxilátion nyújtás (1560-1600 cm^{-1}) és a karboxilcsoport C=O nyújtási rezgései (1700-1755 cm^{-1})). A CTRL vs. M és BM vs. GBM összehasonlításokat tekintve a hullámszámok erősen korreláltak a lipidek acilláncaiból származó rezgésekkel, mint például a CH_3 és CH_2 szimmetrikus és aszimmetrikus nyújtási rezgésekkel (2700-3100 cm^{-1}).

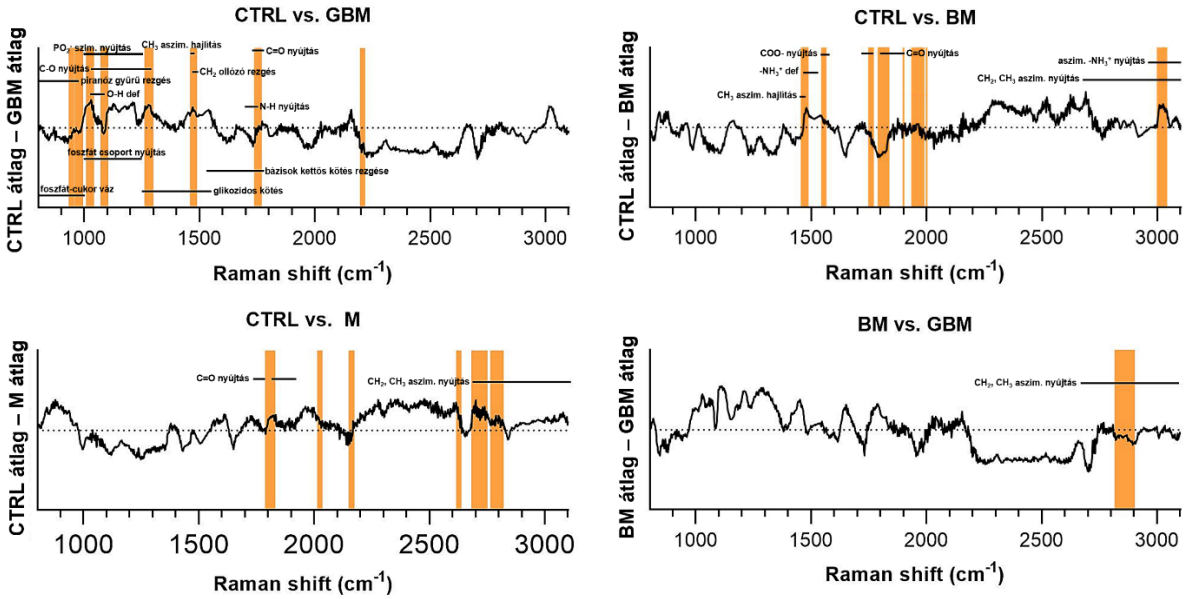

37. ábra. A páronkénti összehasonlítások maradék spektrumai.

A maradék spektrumokat az összehasonlított csoportok átlagos jelintenzitásainak kivonásával állítottuk elő. A szignifikáns PC-khez az átlagosnál nagyobb mértékben hozzájáruló spektrális régiókat narancssárga sávokkal jelöltük. Minél telítettebb egy sáv, annál jobban reprezentált az adott régió a kiválasztott PC-ken. A szaggatott vízszintes vonal nulla különbséget jelöl. Rövidítések: szim. - szimmetrikus; def - deformáció; aszim. - aszimmetrikus.

4. ANYAGOK ÉS MÓDSZEREK

Célkitűzéseink megválaszolásához alkalmazott módszerek legfontosabb munkafolyamatainak, logikájának és a kísérleteinkben felhasznált néhány speciális eljárásnak ismertetése.

4.1 A makrofág polarizáció vizsgálatának kísérletes modelljei

Munkánk során arra kerestük a választ, hogyan befolyásolhatják bakteriális eredetű antigének a tumort infiltráló makrofágok polaritását.

Etikai engedélyek: Minden állatkísérletet a nemzeti (1998. XXVIII; 40/2013) és az európai (2010/63/EU) állatetikai irányelveknek megfelelően végeztünk. A kísérleti jegyzőkönyveket az MTA Szegedi Biológiai Kutatóközpont Állatkísérleti és Etikai Bizottsága és az Országos Állatkísérleti és Etikai Bizottság hagyta jóvá (engedélyszám: XVI./03521/2011).

Egérmodell: B16F1 melanóma sejteket (ECACC) intravénásan ($1x10^5$ sejt/100 µl) adtunk 6-8 hetes nőstény, immunkompetens C57BL/6 vagy immunhiányos NOD/Scid IL2rg null (NSG) egereknek (Charles River Laboratories). Egy héttel a tumorsejtek beadása után az egereket Hep2 sejtekben (ATCC) szaporított *C. pneumoniae* CWL-029 törzzsel (ATCC) kezeltük (Mantovani és mtsai., 2004). A *C. pneumoniae*-t és a Mock kontrollt (feldolgozott Hep2 sejtek) 30 percig 90˚C-on hőinaktiváltuk. Az egereket nátrium-pentobarbitállal (7,5 mg/ml) enyhén szedáltuk, és a tumorsejtek injektálása után 7, 9, 11, 14 és 16 nappal intranazálisan 1×10^6 IFU *C. pneumoniae*-vel kezeltük. Az immunhiányos egerek esetében, mivel az NSG egerek fizikai állapota rendkívül gyorsan romlott, az állatokat a harmadik *C. pneumoniae*-kezelést követő 14. napon elaltattuk. E modell különleges előnyei a következők: (i) a melanóma sejtek farokvénába juttatásával az injekciózást követő 7 napon belül látható tüdőtumor-metasztázisok alakulnak ki, anélkül, hogy más szervekbe jelentős mértékben terjednének; és (ii) a *C. pneumoniae* tüdőspecifikus intracelluláris kórokozó, amely jelentős mértékben kolonizálja még a tüdőmetasztázisokat is. Két órával az 1. inhaláció után (7. nap), 4 órával a 2., 12 órával a 3. és 24 órával az 5. inhaláció után csoportonként 3 állatot elaltattunk, és a tüdejüket fehérje-, mRNS- és szövettani elemzéshez begyűjtöttük. A fennmaradó egerek 4. (14. nap) és 5. (16. nap) kezelést is kaptak, ebben az esetben a túlélést követtük nyomon. A végponton az állatokat elaltattuk, eltávolítottuk a tüdejüket, és 3 független személy megszámolta a felszíni metasztázisok számát.

Citokinek és kemokinek kimutatása: A citokinek és kemokinek detekcióját klasszikus immunológiai módszerekkel, specifikus antitestek használatával, illetve qPCR segítségével végeztük. A specifikus primer párok szekvenciái a kooperációs partnertől kérésre kikérhetők.

C. pneumoniae kimutatása a beteg primer tumorából PCR segítségével: A DNS-t a formalinban rögzített, paraffinba ágyazott (FFPE) mintákból a Nucleospin® FFPE DNS-kit (Macherey-Nagel) segítségével, a gyártó utasításainak megfelelően extraháltuk. A páciens szövettani mintáját érintő kísérletet a Nemzeti és Regionális Etikai Bizottság VI-R-039/01840-2/2012; 25363/2012/EKU; 448/PI/2012 számú etikai engedélyének megfelelően végeztük. A kísérleti jegyzőkönyveket a Nemzeti és Regionális Etikai Bizottság jóváhagyta (engedélyszám: MCC-INTER-001).

4.2 Az IL-24 immunaktiváló hatásának vizsgálata

Célul tűztük ki, hogy megvizsgáljuk a bakteriális antigénekkel is indukálható, antitumorális hatásáról ismert interleukin-24 immunsejtekre gyakorolt kemotaktikus hatását.

Migrációs vizsgálatok: Az *in vitro* kemotaxis vizsgálatokhoz a mikro-Boyden kamrákat a Neuro Probe szállította. A sejteket 1×10^6/ml koncentrációban újraszuszpendáltuk kemotaxis tápközegben (RPMI, amely 1% szarvasmarha-szérumalbumint (Sigma) és 25 mM HEPES-t, pH 8 (Gibco) tartalmazott). Szabványos polikarbonát track-etch (PCTE) membránokat (5 µm pórusméretű) használtunk a felső lyukakban reszuszpendált sejtek elkülönítésére a kemoattraktánsokkal hígított kemotaxis közegtől. A neutrofileket 60 percig 37 °C-on inkubáltuk a mikro-Boyden kamrákban, míg a monocitákat 90 percig. A sejtspecifikus migrációs idő letelte után a membránt eltávolítottuk a mikro-Boyden kamrából, a sejtoldalt letöröltük, hogy eltávolítsuk a membránon át nem vándorolt sejteket, és a vándorolt sejteket tartalmazó membránt H&E-vel megfestettük. A membránon átjutott, tehát a vándorló, H&E-vel festett sejtek számát mikroszkóppal határoztuk meg 400-szoros nagyításban. A kemotaktikus indexet úgy számítottuk ki, hogy az indukált migráció során megszámlált sejtek számát elosztottuk a spontán migráció során megszámlált sejtek számával. A vizsgálatokat legalább hatszor megismételtünk. A statisztikai elemzést GraphPad Prism segítségével végeztük el.

A „sakktábla” kemokinézis vizsgálathoz a monocitákat 37 °C-on előkezeltük rekombináns IL-24-gyel a jelzett koncentrációkban 30 percig, mielőtt a mikro-Boyden kamra felső lyukaiba töltöttük volna őket. A GiCPR jelátvitelének gátlására 100 ng/ml pertussis toxint (List Biological Laboratories) használtunk. 50 µM AG490-et (Calbiochem) használtunk a JAK család inhibitoraként és 50 µM U0126-ot (Sigma) a MEK1 és a MEK2 inhibitorként.

A tápfolyadékban szuszpendált sejteket a specifikus koncentrációjú inhibitorokkal 30 percig kezeltük 37 °C-on vízfürdőben.

Egér légzsák modell: Protokollunk Sironi et al. módszerén alapszik (Clish et al., 1999; Sironi et al., 1999). Az 1. napon a lokális szőrzet leborotválása után, 3 ml levegőt fecskendeztünk szubkután a tesztegerek hátbőre alá, hogy légzsákot formáljunk. A 3. napon a folyamatot 2,5 ml levegővel ismételtük a légzsák stabilizálása céljából. A 6. napon 1 ml steril HBSS (w/o Ca^{2+}/Mg^{2+})-ben oldott hatóanyagot fecskendeztünk a légzsákba. A tesztelt hatóanyagok és koncentrációk: 1000 ng/ml CCL2, valamint 0,1, 1,0 és 10 ng/ml IL-24 a HBSS kontroll mellett. 24 óra elteltével az egereket CO_2-dal elaltattuk és a légzsákokban megjelenő leukocitákat összegyűjtöttük. Minden kezelési csoport 5 állatot tartalmazott, a CCL2 esetén 5, míg az IL-24 esetén 4 kísérletet végeztünk. Az adatokat átlag + SEM értékben ábrázoltuk és kétmintás Student-féle *t*-próbával elemeztük a GraphPad Prism szoftver segítségével.

4.3 A melanóma eredetű vezikulák vizsgálata

Kísérleteink során arra kerestük a választ, megváltoznak-e a tumoros mikrokörnyezet bizonyos elemei daganatsejtek által termelt vezikulák hatására. Célul tűztük ki a melanóma exoszómák PD-1 expresszióra gyakorolt hatásának leírását. Megvizsgáltuk, történik-e a daganatok környezetében található sejteken extracelluláris vezikulák által vezérelt onkogén átprogramozás. A munkafolyamat az **38. ábrán** követhető nyomon.

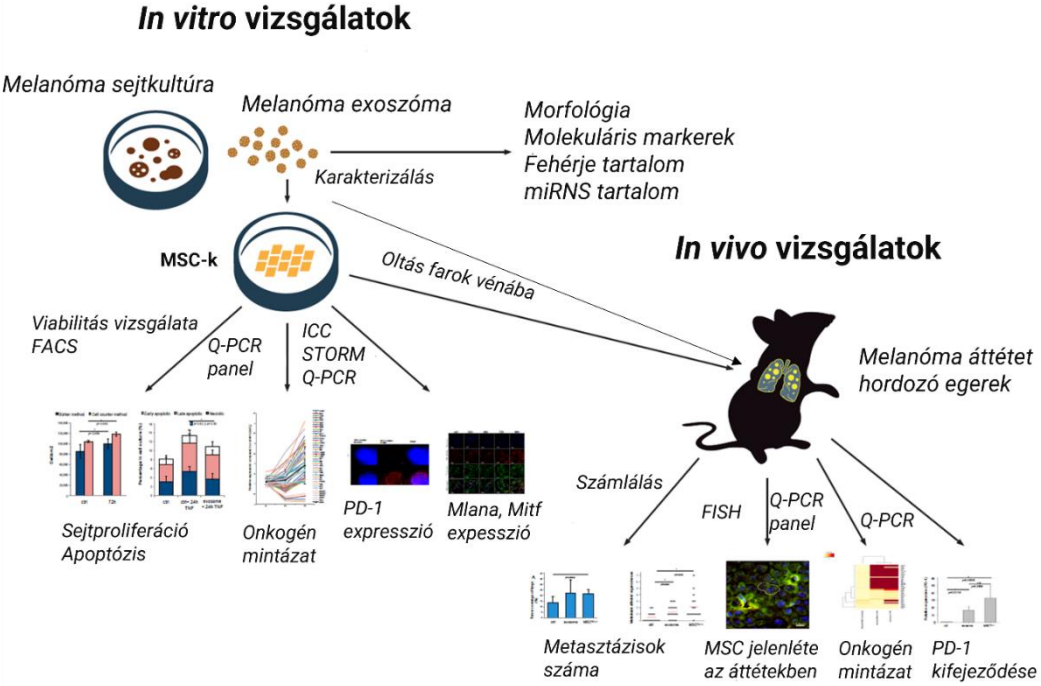

38. ábra. Kísérleti elrendezés a mezenchimális őssejtek melanóma exoszómákkal történő átprogramozásának vizsgálatára.

Etikai engedélyek: A C57BL/6N egereket a Charles River Laboratories-tól (Sulzfeld, Németország) szereztük be. Az egereket kórokozómentes körülmények között tartottuk, a kísérleteket az 1998. XXVIII.; 40/2013 és a 2010/63/EU állatetikai irányelvekkel összhangban végeztük. A kísérleti jegyzőkönyveket jóváhagyta a Szegedi Biológiai Kutatóközpont Állatkísérleti és Etikai Bizottsága és a Magyar Nemzeti Állatkísérleti és Etikai Bizottság (engedélyezési számok: CSI/01/3929-4/2017, és CSI/01/3929-4/2017).

Egérmodell az exoszómális kezeléshez: A B16F1 melanóma sejteket intravénásan (1×10^5 sejt/100 µl) oltottunk 6-8 hetes C57BL/6N nőstény egerekbe. Egy héttel később a daganatot hordozó egereket randomizáltuk és 3 csoportra osztottuk (n = 10/csoport). Az egereknek intravénásan kontroll puffert (100 µl), exoszómával kezelt MSC-ket (1×10^5 sejt/100 µl) vagy exoszómákat (40 µg/100 µl) adtunk be 7, 8, 9, 10 és 11 nappal a tumorinjekció után. Egy héttel az első exoszóma és MSC-oltás után csoportonként 3 állatot elaltattunk, a tüdejüket eltávolítottuk, lefényképeztük és -80 °C-on tároltuk a további fehérje, mRNS- és szövettani elemzéshez. A kísérletben tartott egereket további 10 napig figyeltük. A végponton az állatokat elaltattuk, és a tumor áttéteket nemcsak a tüdejükben, hanem testszerte is vizsgáltuk, majd az érintett szerveket begyűjtöttük szövettani elemzés céljából. A kísérleteket 3 alkalommal ismételtük meg.

Tumor lefedettség: A tüdő daganatos lefedettségét eltávolítás után a szervekről készített fotók elemzésével határoztuk meg az ImageJ szoftver segítségével. Megmértük a tumorok és az egészséges régiók területét, és meghatároztuk a tumorlefedettség százalékos arányát. Az SD-t és a *p*-értékeket a Microsoft Excel programban számoltuk ki.

Az áttétekkel kapcsolatos érátmérő kvantitatív meghatározása: A natív állatok tüdejéből 4 µm-es kriosztátmetszeteket készítettünk szilanizált tárgylemezekre, majd Fix&Perm A-B oldattal (Thermo Fisher Scientific) 20 percig fixáltuk. A metszeteket 30 percig hagyományos hematoxilinnal ellenfestettük, majd csapvízzel mostuk és fedőlemezre helyeztük. A metszeteket automata diaszkennerrel (3DHistech, Hu) digitalizáltuk, a 3DHISTECH Pannoramic Viewer (3DHistech, Hu) szoftver segítségével. A szigorú tumorhatárt gondosan megjelöltük, majd megmértük az erek átmérőjét.

Exoszóma izolálás és jellemzés: Az exoszómákat Peinado és munkatársai (Peinado et al., 2012) protokolljának adaptálásával izoláltuk melanóma sejtek felülúszójából. A B16F1 felülúszókat legyűjtöttük, kiegészítettük proteáz inhibitor koktéllal (Roche), és 780 × g-n 5 percig 4 °C-on centrifugáltuk az intakt sejtek és sejttörmelék eltávolítása érdekében. Ezután a felülúszókat 3900 × g-n 15 percig 4 °C-on centrifugáltuk, majd 0,2 µm-es membránon

(Millipore) szűrtük át a nagyobb sejtfragmentumok és mikrovezikulák eltávolítása érdekében. Az exoszómákat ultracentrifugálással pelletáltuk 150.000 × g-n (T-1270 rotor, 40.500 fordulat/perc) 1 órán keresztül 4 °C-on. A pelletet kétszer mostuk, majd DPBS-ben reszuszpendáltuk és -80 °C-on tároltuk. Az exoszómális fehérjék koncentrációját a Pierce BCA Protein assay kit (Thermo Fisher Scientific) és egy Benchmark Microplate Reader (Bio-Rad) segítségével határoztuk meg, a gyártó utasításai szerint, majd az EV-izolátumot AFM-mel és/vagy SEM-mel, NTA-val és Western blottal jellemeztük.

PD-1 meghatározások: A PD-1 fehérje kimutatása Western blot technikával anti-PD-1 egér monoklonális ellenanyag segítségével történt (clone: RMP1-14, 1:1000 dilution, Biolegend). qPCR-hez a specifikus primer próbák az online Roche Universal Probe Library Assay Design Center használatával lettek tervezve. A PD-1 immunfluoreszcens kimutatásához elsődleges ellenanyagként 1:200 anti-PD-1 (clone: RMO1- 14, Biolegend), másodlagos ellenanyagként 1:100 Alexa Fluor 647 konjugált anti-rat ellenanyagot (Jackson ImmunoResearch Laboratories) használtunk.

A dSTORM szuperrezolúciós kísérletet egy egyedi gyártású invertált Nikon Eclipse Ti-E vázon alapuló inverz mikroszkópon végeztük. Kondícionálás után az alkalmazott lézersugarakat a hátoldalra fókuszáltuk (mikroszkóp objektív Nikon CFI Apo 100x, NA = 1,49). A megvilágítás szögét egy, a készülékbe szerelt billenőtükörrel állítottuk be. Az összes dSTORM képeket 647 nm-es gerjesztési hullámhosszú EPI-megvilágítással készítettük el (Nikon 647 nm, 300 mW). A lézer teljesítményét, amelyet egy akuszto-optikai hangolható szűrőn (AOTF) keresztül szabályoztunk 4 kW/cm^2 -re állítottuk be a mintasíkon. Egy további lézert (Nichia, 405 nm, 60 mW) használtunk mind a reaktiváláshoz, mind a referencia-mérésekhez. A képeket egy Andor iXon3 897 BV EMCCD digitális fényképezőgéppel (512 × 512 pixel, 16 μm-es pixelmérettel) készítettük. A minta megvilágított területének mérete megfelelt a detektor méretének, amely meghatározta a látómezőt (FOV = 80 × 80 μm^2). A felvett és tárolt képhalmazokat a rainSTORM lokalizációval értékeltük, elemeztük és vizualizáltuk. A többszínű összevont képeket ImageJ szoftverrel hoztuk létre.

Célunk volt továbbá leírni a mikrokörnyezeti stresszoroknak a vezikulák molekuláris mintázatára gyakorolt hatását és megvizsgáltuk a mikrokörnyezeti stresszorok nyomása alatt termelődő extracelluláris vezikulákra adott sejtbiológiai válaszokat. A munkafolyamat a **18. ábrá**n követhető nyomon.

Stresszkörülmények: A B16F1 70%-os konfluenciájú sejtkultúráit öt különböző módon kezeltük EV-mentesített FBS-tartalmú közegben 72 órán keresztül. A kontroll csoport csak friss tápfolyadékot kapott. Citosztatikus stressz gyanánt a sejteket 0,6 μM doxorubicinnel kezeltük, a hőstresszelt sejteket 42 °C-on inkubáltuk 2 órán át minden 24 órában (összesen 3 alkalommal), az oxidatív stressznek kitett sejteket 2,5 μg/ml Ag-TiO_2-vel kezeltük, fotokatalízist kiváltó megvilágítás mellett. A fotoreaktív Ag-TiO_2 nanorészecskéket alacsony nyomású higanylámpával indukáltuk ($\lambda \geq 360$ nm, GCL303T5/4 típus, LightTech) 60 percig 3 cm távolságból, a médium térforgatának 75%-ban, hogy csökkentsük a médiumréteg fényelnyelését és fényvisszaverését, majd a megvilágítás után a médiumot a végleges térfogatra állítottuk be. Megvilágítási kontrollként pedig létrehoztunk egy második kontroll csoportot, amely ugyanilyen módon megvilágított tápfolyadékot kapott. A citosztatikus és oxidatív stressz paramétereit a korábbi optimalizálás és proliferációs vizsgálat alapján határoztuk meg. A hőstressz körülményeit az irodalmi adatok alapján alakítottuk ki. Minden csoportban 72 órás felülúszókat gyűjtöttünk, 6 párhuzamos sejttenyészetből, ezeket összevontuk és elvégeztük az sEV izolálást.

A mikroszövetek előállítása és analízise: A különböző sEV-k sejt-sejt kontaktusra és sejt-ECM kölcsönhatásokra gyakorolt hatását vizsgáltuk MSC-B16F1 és MEF-B16F1 ko-kultúrákban egy egyszerűsített 3D-s tumormátrix modell segítségével. Egyenlő számú MSC vagy MEF és B16F1 sejtet 96 lyukú GravityPLUS függőcsepp lemezekre (InSphero AG) tettünk ki sEV- vagy DPBS-tartalmú médiumban (lyukanként 5000 sejt / 40 μl). A mikroszövetek keletkezését 72 órán keresztül követtük, és 24 óránként felvételeket készítettünk egy Axiovert S100 mikroszkóp (Zeiss) és egy Nikon D5000 kamera segítségével. A mikroszövetek méret- és alakbeli különbségeinek számszerűsítése érdekében, a 72 órás felvételeket szürkeárnyalatos formátumban az AnaSP szoftverrel (Piccinini, 2015) elemeztük. A mikroszövetek mért paraméterei a következők voltak: ekvivalens átmérő, legnagyobb átmérő a centroidon át, legkisebb átmérő a centroidon át, domborúság, tömörség, gömbölyűség, terület, kerület és térfogat. A kísérleteket háromszor ismételtük meg.

4.4 A keringő vezikulák diagnosztikai potenciáljának vizsgálata

Jelen kísérletsorozatban tanulmányoztuk a központi idegrendszeri tumorok molekuláris ujjlenyomatának megjelenését a perifériás vérben és célul tűztük ki a központi idegrendszeri tumorok extracelluláris vezikula alapú diagnosztikájának fejlesztését.

Szérum minták előkészítése, sEV izolálás és jellemzés: A perifériás vér szobahőmérsékleten (RT) történő 1 órás alvadását követően az sEV izolálást a szérummintákból differenciál-

centrifugálással végeztük (20 perc 3000 × g-n, 10 °C-on; 30 perc 10.000 × g-n, 4 °C-on; 70 perc 100.000 × g-n, 4 °C-on). Az utolsó centrifugálási lépés után a pelletet DPBS-ben reszuszpendáltuk, és a további feldolgozásig -80 °C-on tároltuk.

Az sEV-k jellemzéséhez a "Minimal Information for Studies of Extracellular Vesicles 2018" (MISEV 2018) című útmutatóban foglalt főbb javaslatokat és követelményeket követtük (Théry et al., 2018).

NTA: Az sEV-ket részecskementes DPBS-ben hígítottuk, és 532 nm-es lézerrel ellátott NanoSight NS300 műszerrel (Malvern Panalytical Ltd.) elemeztük. Minden mintáról hat darab 60 s-os videót rögzítettünk állandó beállítások mellett (kameraszint: 15; küszöbérték: 4, 25 °C; 60-80 részecske/képkocka), majd ezeket elemeztük, hogy információkat kapjunk a méreteloszlásról és a részecskekoncentrációról.

Westen blot analízis: A klasszikus EV-markereket Western blot-elemzéssel vizsgáltuk NuPAGE-reagensek és egy XCell SureLock Mini-Cell System (Thermo Fisher Scientific) segítségével, a gyártó protokollja szerint. A CD81, Alix és Calnexin markerek kimutatásához nyúlban termeltetett anti-humán CD5L (1:2000) anti-humán CD81 (1:1000), anti-humán Alix (1:1000) és anti-humán Calnexin (1:10.000, (minden elsődleges ellenanyag a Sigma-Aldrich-tól) elsődleges antitestet és HRP konjugált anti-nyúl IgG (1:1000, R&D Systems) másodlagos antitestet használtunk. A THP-1 sejtvonal (ATCC) lizátumát használtuk a Calnexin pozitív kontrolljaként.

Transzmissziós elektron mikroszkópia: Az sEV morfológiájának vizsgálatához TEM-analízist végeztünk egy Tecnai G2 20 X-Twin típusú műszerrel (FEI, Hillsboro), 200 kV-os gyorsítófeszültségen. A TEM-mérésekhez a mintákat rácsra (200 mesh-es rézrácsokkal ellátott karbon filmre (CF200-Cu, Electron Microscopy Sciences) vittük fel, és festés vagy más fixáló eljárás nélkül szárítottuk.

Betegek: A Debreceni Egyetem Idegsebészeti Klinikáján 2015 márciusa és 2018 januárja között kezelt 96 beteg vérmintáit elemeztük. A mintákat primer glioblastoma multiforme (GBM), meningeóma (M) és nem kissejtes tüdőrákból (BM) származó agyi metasztázisban szenvedő betegektől nyertük. A kontroll mintákat (CTRL) olyan betegektől gyűjtötték, akiknél a gerinc porckorong sérv műtétre érkeztek és nem volt egyéb, daganatos megbetegedésre utaló jel. Ez a nem daganatos betegcsoport szolgált kontroll csoportként a különböző intrakraniális tumorral rendelkező betegekkel összehasonlítva, hogy megkülönböztessük a tumoros folyamatok hatását a CNS érintettségétől a keringő sEV-kre

vonatkozóan. Mindegyik csoport 24 vegyes életkorú és nemű egyént tartalmazott (**6. táblázat**). Az egyénekből hat mintacsoportot hoztunk létre, így csoportonként négy párhuzamos mintát tudtunk vizsgálni. A vérmintákat egy nappal az idegsebészeti beavatkozás előtt vettük minden egyes tumoros esetben. Egyik beteg sem kapott sugár- vagy kemoterápiát a tumor reszekciója előtt. A vérmintákat a debreceni Neurosebészeti Agydaganat- és Szövetbank tárolta a Nemzeti Kutatási Etikai Bizottság kritériumainak megfelelően. A beleegyező nyilatkozatot minden beteg aláírta; a vizsgálatot a Helsinki Nyilatkozatnak megfelelően végeztük. A vizsgálatot két etikai jóváhagyás alapján hajtottuk végre, nevezetesen: 51450-2/2015/EKU (0411/15), Orvosi Kutatási Tanács, Tudományos és Kutatási Etikai Bizottság, Budapest, 2015. október 30. és 121/2019-SZTE, Szegedi Tudományegyetem, Humán Vizsgálatok Felügyelő Bizottsága, Szent-Györgyi Albert Klinikai Központ, Szeged, 2019. július 19.

6. táblázat: Az LC-MS/MS analízisek betegcsoportjainak jellemzése

♦ Glioblastoma Multiforme	**GBM**	**GBM1**	**GBM2**	**GBM3**	**GBM4**
Betegek száma	***n = 24***	*n = 6*	*n = 6*	*n = 6*	*n = 6*
Életkor: Medián (tartomány) Átlag	**67 (33–82)** **64,9**	64,5 (38–82) 62,7	69,5 (33–76) 63,8	67,5 (49–74) 64,7	66,5 (63–77) 68,5
Nem (%): Férfi Nő	**13 (54,2)** **11 (45,8)**	3 (50) 3 (50)	3 (50) 3 (50)	5 (83,3) 1 (16,7)	2 (33,3) 4 (66,7)
■ Brain Metastasis	**BM**	**BM1**	**BM2**	**BM3**	**BM4**
Betegek száma	***n = 24***	*n = 6*	*n = 6*	*n = 6*	*n = 6*
Életkor: Medián (tartomány) Átlag	**64 (42–82)** **64**	66,5 (51–82) 67,7	68 (62–71) 67,5	63,5 (42–81) 59,7	59,5 (53–64) 59,5
Nem (%): Férfi Nő	**13 (54,2)** **11 (45,8)**	2 (33,3) 4 (66,7)	3 (50) 3 (50)	4 (66,7) 2 (33,3)	4 (66,7) 2 (33,3)
▲ Meningioma	**M**	**M1**	**M2**	**M3**	**M4**
Betegek száma	***n = 24***	*n = 6*	*n = 6*	*n = 6*	*n = 6*
Életkor: Medián (tartomány) Átlag	**60 (30–79)** **58,0**	54,5 (39–69) 53,5	62 (30–66) 53	61,5 (44–75) 59,3	66,5 (52–79) 66
Nem (%): Férfi Nő	**4 (16,7)** **20 (83,3)**	0 (0) 6 (100)	0 (0) 6 (100)	1 (16,7) 5 (83,3)	3 (50) 3 (50)
● Control	**CTRL**	**CTRL1**	**CTRL2**	**CTRL3**	**CTRL4**
Betegek száma	***n = 24***	*n = 6*	*n = 6*	*n = 6*	*n = 6*
Életkor: Medián (tartomány) Átlag	**50,5 (20–81)** **52,9**	46,5 (26–71) 46,5	47 (20–62) 45	70,5 (49–81) 67,2	52,5 (41–69) 53
Nem (%): Férfi Nő	**9 (37,5)** **15 (62,5)**	2 (33,3) 4 (66,7)	4 (66,7) 2 (33,3)	4 (66,7) 2 (33,3)	4 (66,7) 2 (33,3)

LC-MS-alapú proteomikai vizsgálatok és aadatelemzésük: A folyamatábra (**39. ábra**) mutatja azt a munkamenetet, amely alapján a bemutatott négy betegcsoportot elválasztó fehérjemintázat azonosításra került. Ebben az esetben a daganatok csoportosítása a perifériás vérből izolált sEV-k proteomikai vizsgálata alapján történt.

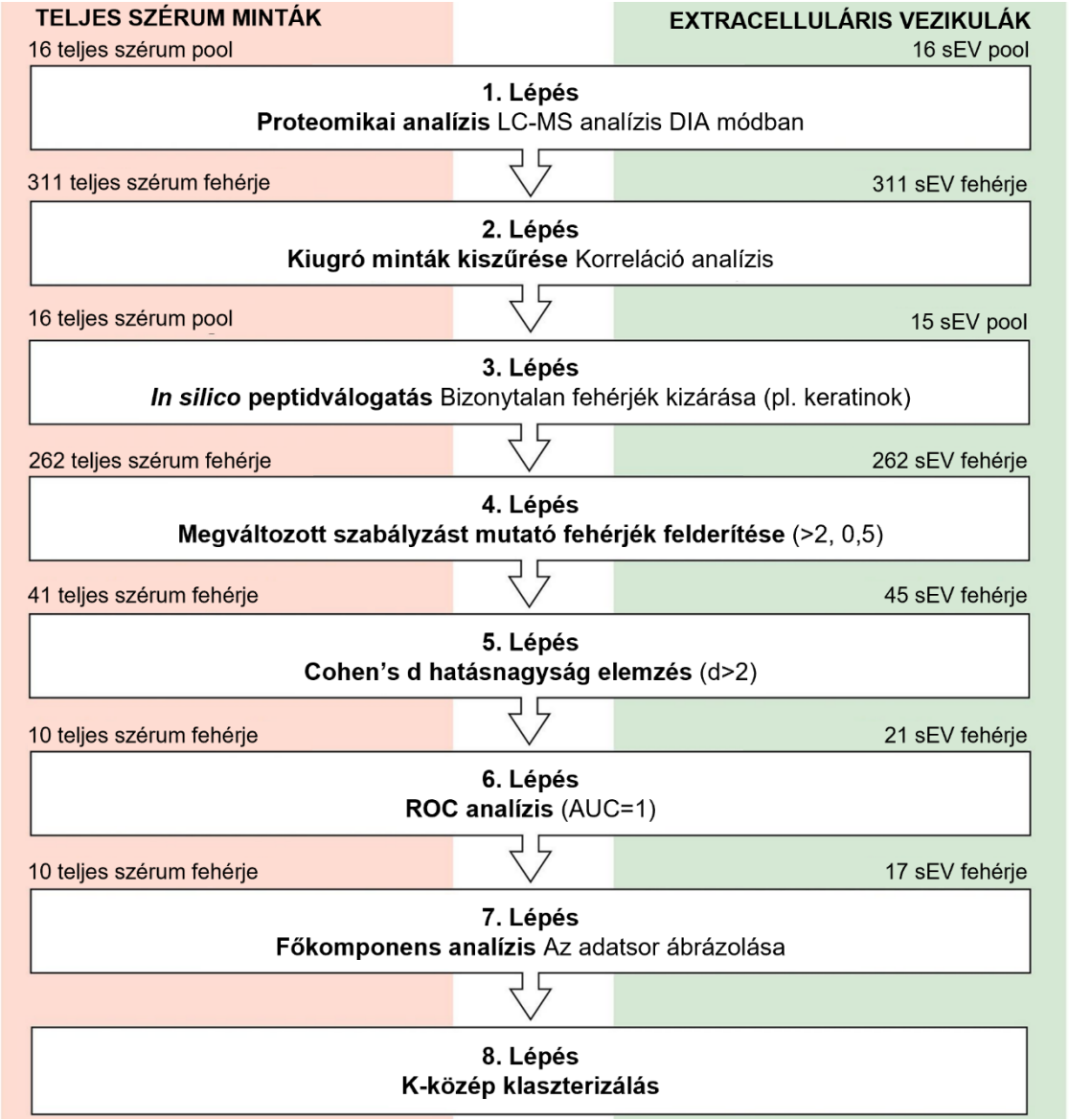

39. ábra. Proteomikai adatok elemzése a betegcsoportok klasszifikálására.

A GBM, BM, M és CTRL betegekből nyert teljes szérum- és sEV-mintákon LC-MS/MS-analízist végeztünk (1. lépés). Az egyes csoportok egyéni mintáiból (n = 24) 4-4 poolt készítettünk az egyéni eltérések kiküszöbölése, a minták számának csökkentése, az LC-MS/MS mérések idejének lerövidítése és az anyagszükséglet csökkentése érdekében.

Az adatfüggetlen adatgyűjtési (DIA) üzemmódban kimutatott 311 fehérjéből spektrumkönyvtárat építettünk fel. Az sEV kontroll csoportban a mérés során felmerülő technikai hiba miatt négyből három minta került be statisztikai elemzésekbe (2. lépés). A nem kellően alátámasztható jelenléttel mért fehérjék, valamint a hiányzó értékekkel rendelkező fehérjék kizárása után (3. lépés) összesen 262 fehérjén végeztük el a további elemzéseket.
Az adatfeldolgozás következő lépésében a felül- és alulszabályozott fehérjék azonosítása történt (4. lépés), amely 41 szérumban azonosított fehérjét és 45 sEV-fehérjét eredményezett. Az egyes CNS-tumorcsoportok és a CTRL összehasonlítása mellett a fehérjék kiválasztása során a CNS-tumorcsoportok közötti csoportközi különbségeket is értékeltük. Mivel a klinikailag releváns változás fontos szempont az azonosított fehérjék kiválasztásakor, a Cohen d hatásnagyság változást fogadtuk el a csoportok közötti különbség mutatójaként. A Cohen-féle d hatásnagyságelemzés (5. lépés) $d > 2$ küszöbértékkel 10, illetve 21 fehérjét eredményezett a teljes szérum- és az sEV-mintákban. A ROC-elemzésekben (6. lépés) 10 fehérje a teljes szérumból (MMP9, HSPB1, CASP14, HBG1, IGHG4, DEFA1, VWF, HNRNPA1, S100A8, TLN1) és 17 sEV-fehérje (MMP9, HSPB1, CASP14, HBG1, FGB, GGCT, PF4, S100A7, FN1, ANPEP, FLG2, HSPA8, IGLL1, MMRN1, S100A14, SBSN, SPRR2E) felelt meg az $AUC = 1$ kiválasztási kritériumoknak. A két mintatípus négy szignifikánsan megváltozott fehérjén osztozott, nevezetesen az MMP9, CASP14, HBG1 és HSPB1.
A fehérjék kiválasztását követően PCA-t (7. lépés) végeztünk az adathalmaz vizualizálása érdekében. Végül k-közép klaszterizálás (8. lépés) segítségével tártuk fel a különbséget a teljes szérum és a szérumból izolált vezikulák klaszterezési potenciálja között.

MMP-9 analízisekben vizsgált betegek: A Debreceni Egyetem Idegsebészeti Klinikáján kezelt 222 beteg szérummintáinak sEV izolátumát elemeztük (**7. táblázat**).

ELISA vizsgálat az sEV-k MMP-9 koncentrációjára vonatkozóan: Minden vizsgálathoz standard görbét alkalmaztunk, és az összes mintát két párhuzamosban futtattuk külön lemezeken. Az első lépésben 50 µl vizsgálati puffert és 50 µl mérési sztenderdet vagy 12-szeres hígítású mintákat adtunk a megfelelő lyukakba, majd a lemezeket lezártuk és szobahőmérsékleten 2 órán át inkubáltuk, miközben 200 fordulat/perc sebes-séggel rázattuk. Az inkubálás után a lemezeket négyszer mostuk mosópufferrel. Az első lépést további három inkubációs lépés követte, nevezetesen 100 µl humán MMP-9 detektáló antitest oldatot, 100 µl Avidin-HRP oldatot és 100 µl D szubsztrát oldatot adtunk minden egyes lyukba, és szobahőmérsékleten inkubáltuk 1 órán át, 30 percig, illetve 15 percig. A lemezeket négyszer

mostuk mosópufferrel az egyes inkubációs eljárások között. Az utolsó lépést sötétben végeztük, majd a reakciót 100 µl oldat hozzáadásával leállítottuk; az abszor-banciát azonnal leolvastuk 450 nm-en és 570 nm-en egy asztali benchtop reader-rel (Multiskan RC, Thermo Labsystems).

7. táblázat MMP-9 vizsgálatok betegcsoportjainak jellemzése

Betegcsoport megnevezése	***n* = 222**	**%**
Glioblastoma multiforme (GBM)	**121**	**54%**
szekunder glioblasztóma (GBMszek)	*18*	*15%*
preoperatív minták (GBMszek preop)	9	50%
posztoperatív minták (GBMszek posztop)	9	50%
primer glioblasztóma (GBMprim)	*103*	*85%*
preoperatív minták (GBMprim preop)	69 (10) [1]	67%
kiújulás befolyásoló hatásának vizsgálata	69	67%
elsődleges daganat	54	78%
kiújult daganat	15	22%
terápia befolyásoló hatásának vizsgálata	69	67%
terápia előtt	15	22%
terápiát követően	54	78%
túlélés vizsgálata	27	39%
>65 év	11	41%
≤65 év	16	59%
magas MMP-9 szint (≥28 ppm)	17	63%
alacsony MMP-9 szint (<28 ppm)	10	37%
posztoperatív minták (GBMprim posztop)	14 (10)[1]	33%
Agyi metasztázis (BM)	**37**	**17%**
carcinoma planocellulare (BMplano)	*13*	*35%*
adenocarcinoma (BMadeno)	*24*	*65%*
preoperatív minták (BMpreop)	27 (6)[2]	73%
posztoperatív minták (BMposztop)	10 (6)[2]	27%
Meningioma (M)	**28**	**13%**
I grádusú meningeoma (M_I)	*20*	*71%*
I grádusú meningeoma (M_II)	*8*	*29%*
Kontroll (CTRL)	**36**	**16%**
gerincvelő porckorongsérv	*36*	*16%*
férfi	16	44%
nő	20	56%

A százalékok az egyes statisztikai elemzéseken belüli részvételi arányokat jelzik; [1] A páros *t*-tesztben részt vevő GBM betegek száma; [2] A páros *t*-tesztben érintett BM betegek száma.

Statisztikai analízisek az MMP-9 vizsgálatokhoz: A statisztikai tesztek elvégzése előtt az MMP-9 szintet a szérum sEV-k fehérjetartalmára normalizáltuk, ami azt jelenti, hogy az MMP-9 koncentrációt (ng/mL) elosztottuk az EV-ben dúsított izolátumok fehérjekoncentrációjával (ng/mL) minden minta esetében. Az összes analízis eredményét milliomodrészben (ppm) adtuk meg.

Raman spektroszkópiai analízisekben vizsgált betegek: A Debreceni Egyetem Idegsebészeti Klinikáján kezelt 138 beteg vérmintáit elemeztük. A daganat-asszociált mintákat GBM, BM, M betegekből nyertük, a gerincvelő porckorongsérvben (nem daganatos CNS betegség) szenvedő betegek szolgáltak kontroll CTRL-ként (**8. táblázat**).

Minden beteg aláírta a beleegyező nyilatkozatot. A vizsgálatot a Helsinki Nyilatkozatnak megfelelően végeztük, és két független szerv etikai jóváhagyását szereztük be (51450-2/2015/EKU (0411/15), Orvosi Kutatási Tanács, Tudományos és Kutatási Etikai Bizottság, Budapest, 2015. október 30. és 121/2019-SZTE, Szegedi Tudományegyetem, Emberi Vizsgálatok Felülvizsgálati Bizottsága, Szent-Györgyi Albert Klinikai Központ, Szeged, 2019. július 19.).

8. táblázat. Spektroszkópiai vizsgálatok betegcsoportjainak jellemzése.

Beteg-csoportok	Betegek száma	Életkor (év)			Nem	
		Tartomány	Átlag	Medián	Férfi (%)	Nő (%)
CTRL	36	20–81	53,6	54	16 (44,4)	20 (55,6)
GBM	46	33–82	64,3	66	28 (60,9)	18 (39,1)
BM	28	42–82	63,5	62,6	18 (64,3)	10 (35,7)
M	28	30–79	58,6	60	5 (17,9)	23 (82,1)

Raman spektroszkópiai mérések: A sEV minták Raman spektrumának felvételét Senterra II (Bruker) mikroszkóppal végeztük visszaszórásos elrendezést alkalmazva. A mintákat centrifugáltuk, kalcium-fluorid hordozóra cseppentettük, és az elemzés előtt szobahőmérsékleten, levegőn szárítottuk rá a hordozóra. Minden mintát ugyanazokkal a konfigurációs paraméterekkel elemeztünk (névleges lézerteljesítmény: 12,5 mW; integrációs idő: 30 másodperc; interferométer felbontása: 1,5 cm^{-1}; gerjesztési hullámhossz: 532 nm.) A spektrumokat minden mintáról 50×-es optikai objektívvel (Olympus) gyűjtöttük. A spektrumokat átlagolás előtt (mintánként 5 spektrum) alapvonal korrekciónak vetettük alá a Bruker berendezéshez kapható OPUS szoftver segítségével. A 801 cm^{-1} és 3100,5 cm^{-1} közötti spektrumtartományt használtuk a további elemzésekhez (**40. ábra**).

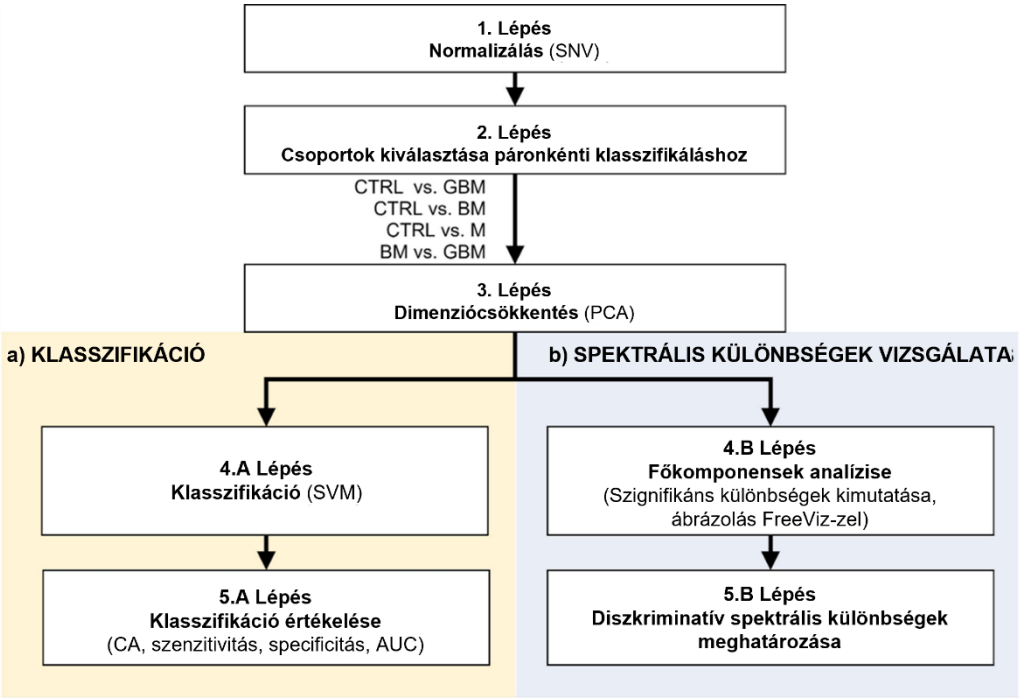

40. ábra. Az sEV-k molekuláris ujjlenyomatának spektroszkópiai megközelítése.

Az ábra a Raman spektroszkópiai adatok analízisének lépéseit mutatja be. A 3. lépést követően a munkafolyamatot a céljainknak megfelelően kétféleképpen folytattuk (a és b rész). Rövidítések: AUC: area under the curve; CA: classification accuracy; SNV: standard normal variate; SVM: support-vector machine; PCA: principal component analysis.

Az alapvonal korrekción átesett adatok normalizálását az SNV-módszerrel végeztük, amely a spektrumokat egymással összehasonlíthatóvá alakította. Az SNV-vel normalizált spektrumokat PCA-val vizsgáltuk. Az adatok transzformálását az Orange 3.27.0 szoftver segítségével végeztük (Demšar et al., 2013).

A klasszifikáció során az osztályozó modell megalkotásához és teszteléséhez a négy betegcsoportot páronként hasonlítottuk össze (minden betegcsoportot a CTRL csoporthoz, valamint a BM és GBM csoportot). A minták osztályozását a lineáris SVM algoritmus segítségével végeztük el, és minden egyes páros összehasonlításhoz osztályozási modelleket építettünk. Első lépésként az adatokat véletlenszerűen 90:10 arányban felosztottuk tanító- és teszthalmazokra. A tanító halmazon alkalmazott SVM algoritmus egy olyan hipersíkot határozott meg, amely a PCA-transzformált térben el tudja választani az összehasonlított csoportokat (a folyamat eredményeként kialakított hipersík jelentett egy betanított SVM modellt). Ezt követően az SVM a teszthalmazba tartozó mintákat – ugyanezen térbe elhelyezve – a csoporthoz tartozás pontszámával látta el (0-tó 1-ig) az elválasztó hipersíktól való helyzetük és távolságuk alapján.

Ahhoz, hogy a tesztmintákat be lehessen sorolni valamely betegcsoportba, meghatároztuk az ehhez szükséges csoporthoz tartozási pontszámok minimális küszöbértékét. A meghatározott küszöbérték feletti pontszámmal rendelkező tesztmintákat az adott célcsoportba soroltuk.

Minden páros összehasonlítás során tízszer ismételtük meg a tanító- és teszthalmaz felosztását.

Az osztályozás hatékonyságát a szenzitivitás, specificitás, és a ROC-analízisből kapott AUC értékek alapján határoztuk meg. Az osztályozást és a hatékonyság értékelését az Orange 3.27.0 és a GraphPad Prism 8.4.3 szoftverek segítségével végeztük el.

A spektrális különbségek azonosítása érdekében a kapott PC-k és a különböző betegcsoportok közötti korrelációt a FreeViz módszerrel határoztuk meg (**36. ábra**). Összefoglalva, a FreeViz módszer a többváltozós adatokat egy kétdimenziós szórásdiagramban jeleníti meg. A FreeViz ábrákon a mintákat és a PC-ket pontokkal, illetve vektorokkal ábrázoltuk.

A PC-k csoportonkénti statisztikai különbségeit Welch *t*-próbával elemeztük. Tekintettel arra, hogy a PC-k az eredeti változók (hullámszámok) lineáris kombinációja, meghatározhatók azon hullámszámok, amelyek a legnagyobb mértékben járulnak hozzá egy adott PC-hez, így a két összehasonlított csoport megkülönböztetéséhez. A $p < 0,05$ értékeket szignifikánsnak tekintettük. A FreeViz vizsgálatot az Orange 3.78.0 szoftverrel végeztük.

5. ÖSSZEFOGLALÁS ÉS ÚJ EREDMÉNYEK

Kutatásaim során munkatársaim segítségével a tumoros mikrokörnyezet különböző alkotóelemeinek a működését vizsgáltam. Mint tudjuk, a daganatok egy nagyon komplex, rendkívül hatékonyan együttműködő sejtközösséget alkotnak, amely közösség tagjai igen intenzív kommunikációt folytatnak egymás között mind a tumorokat alkotó elemekkel, mind pedig a szűkebb és tágabb értelemben vett környezetükkel. Ezek az egymással kommunikáló elemek, legyenek azok szolubilis vagy partikuláris természetűek, mind hozzájárulnak a tumorok sikeréhez. Minden egyes jelátviteli esemény része lehet annak az immunszerkesztési láncolatnak, amely az esetek jelentős részében a daganatok túléléséhez és növekedéséhez vezethet, hiszen sikerrel kerülik el az immunrendszerünk védekezésének különböző rétegeit. Ahogyan egész testünket, a daganatot is érhetik és érik is különböző hatások, amelyek időnként a tumorokon belüli egyensúly megbomlásához, illetve akár a tumorsejtek pusztulásához is vezethetnek.

A bemutatott munkánk során elsőként az immunrendszerünk olyan elemei kerültek a kísérletek középpontjába, amelyek TLR ligandumokkal, mint a külső vagy belső mikrokozmoszunk résztvevőiből származó molekulákkal befolyásolhatóak és részesei lehetnek akár az antitumorális immunválaszoknak is.

Ezen folyamatokat célzó kísérleteink során bebizonyítottuk a következőket:

- A *Chlamydophila pneumoniae* hőinaktiváció után is képes a daganatot infiltráló makrofágok polaritásának megváltoztatására.
- Az inaktivált *C. pneumoniae* által indukált változások jelentős mennyiségű M1 polarizációs állapothoz tartozó citokin és kemokin termelődését idézik elő.
- Az inaktivált *C. pneumoniae* hatására a melanóma tüdőáttéteinek csökkenése következik be az immunkompetens állatokban.

Figyelembe véve a kísérleteink dolgozatban ismertetett menetét, arra a következtetésre jutottunk, hogy a szaporodásra nem képes, hőinaktivált *C. pneumoniae* szuszpenzióban található, lázkeltésre nem alkalmas TLR ligandumok képesek a tumorokat jellemzően infiltráló, tumortámogató M2 típusú makrofágok polaritását az M1, antitumorális irányba eltolni. Ez a hatás és az intenzív antitumorális citokinek és kemokinek termelődése a már kialakult daganatok visszafejlődéséhez is vezethet az immunkompetens állatmodellekben.

A daganatellenes hatásokat tovább vizsgálva, a TLR ligandumokkal indukálható IL-24-nek az immunsejtekre gyakorolt hatásait tanulmányoztuk.

- Munkánk során megállapítottuk, hogy az IL-24 képes az immunsejtek attraktálásra mind *in vitro* mind *in vivo* körülmények között. Az IL-24-nek kemotaktikus és kemokinetikus hatását bizonyítottuk a humán monocitákra vonatkozóan.
- *In vivo* az IL-24 kemotaktikus hatással bír a monocitákra, illetve neutrofil granulocitákra vonatkozóan.
- Bizonyítottuk, hogy az IL-24 kemotaktikus jelátvitele G fehérje kapcsolt receptoron keresztül történik és egyúttal a MAPK és JAK jelátviteli útvonalak is érintettek.

A TLR ligandumok és szolubilis faktorok tumoros mikrokörnyezetben való immunmodulációs hatásainak vizsgálata során kerültek a látóterünkbe az igen élénk kommunikációs útvonalak partikuláris szereplői, az extracelluláris vezikulák.

- Bebizonyítottuk, hogy a melanóma sejtek által kibocsájtott extracelluláris vezikulák a daganatszövet résztvevőinek tekintett, illetve a testszerte megtalálható mezenchimális őssejtekben egy onkogén átprogramozást képesek elindítani.
- A melanóma sejtek extracelluláris vezikulái az MSC-kben mind mRNS, mind fehérje szinten olyan útvonalak és molekulák kifejeződését indítják el, amelyek a melanóma sejtekre jellemzőek: ilyenek a migrációs kapacitás élénkülése, a daganatszövet növekedése és áttétképzési hajlandóságának emelkedése.

Az sEV-k tehát igen hatékony információhordozók, a bennük található molekuláris összetétel változása tehát nagy valószínűséggel a befogadó sejtek biológiáját és viselkedését is képes lehet megváltoztatni. Felmerül tehát a kérdés, ha olyan kritikus változásokat képesek előidézni, mint egy szöveti őssejtben elindított onkogén program, vajon a környezeti stresszorok vagy akár a daganatterápiák milyen hatást gyakorolnak a vezikuláris tartalomra és ezáltal a kiváltott sejtes válaszokra.

- Kísérleteink során azt találtuk, hogy a környezeti stresszorok hatására nem csak a termelődő sEV-k mennyisége, de molekuláris összetétele is szignifikáns mértékben változik meg, a miRNS és fehérje tartalom tekintetében.
- A stresszorok nyomása alatt képződő sEV-k befolyásolják a sejtciklust, elősegítik a daganatsejtek migrációját, megváltoztatják a mikroszövet-képzési kapacitást.

Mivel az sEV-k minden testfolyadékban megtalálhatóak és a szolubilis biomarkerekhez képest stabilak, a napjainkban egyre nagyobb népszerűségnek örvendő folyadékbiopsziák ideális célpontjaivá válhatnak. Különösen igaz ez abban az esetben, ha a nehezen hozzáférhető központi idegrendszeri tumorokról beszélünk. Megfigyeltük, hogy az sEV-k segítségével elkülöníthetjük egymástól a daganatos betegségekben szenvedő páciensek

különböző csoportjait. Kísérleteink során arra a következtetésre jutottunk, hogy az sEV-k komplex analízisével sokkal nagyobb hatékonysággal és biztonsággal vagyunk képesek a betegcsoportok megállapítására, mintha egyedi molekulákat vizsgálnánk.

- Bizonyítottuk, hogy a CNS daganatos betegek szérumából izolált sEV-k alkalmasabbak a proteomikai elemzésen alapuló klasszifikációra, mint a teljes szérum minták.
- Szérumból izolált sEV-k vizsgálatával sikerült egy olyan fehérjét, az MMP-9-et azonosítanunk, amely a GBM-ben szenvedő betegek esetében prognosztikus értékkel bírhat.
- Az sEV-k Raman spektroszkópiája segítségével igen magas, 80% feletti szenzitivitással és specificitással tudjuk a CNS tumorokban szenvedő betegeket a szövettani diagnózison alapuló csoportokba sorolni.

Az sEV-k, illetve az extracelluláris vezikulák jelentősége az intercelluláris kommunikációban több szinten jelenik meg:

- A vezikulák nem a sejtek hulladék lerakói, a molekuláris tartalom jelentős része irányítottan kerül a membráncsomagokba.
- A molekuláris tartalom összetételét komplex sejtélettani változások határozzák meg, így az egyedi molekulák jelátvivő szerepe elveszik, helyette a különböző komponensek egymáshoz viszonyított aránya válik meghatározóvá.
- A kettős foszfolipid réteg által határolt struktúrák minden eddig ismert módozatnál hatékonyabb információtranszfert valósítanak meg, hiszen beltartalmukat megvédik az enzimatikus hasításoktól vagy roncsoló mechanikai hatásoktól.

Véleményem szerint különlegesen érdekessé teszi az EV-k útján történő molekuláris információtranszfert az a megközelítés, mely szerint a vezikuláris transzport egy lehetséges magyarázata annak, hogyan válhat egy lokális, pathológiás folyamat szisztémás betegséggé. Az sEV-k Raman spektroszkópiai vizsgálata megtanított bennünket arra, hogy a folyadékbiopsziás vizsgálatok esetében nem kizárólag az „egy betegség - egy molekula” megközelítés lehet az üdvözítő. **Munkáinkban nem az egyedi molekulákat, hanem a kisméretű extracelluláris vezikulákat tekintettük az információ új egységének.** Az sEV-k komplexitása mintegy jelerősítőként szerepel vizsgálatainkban, nem keresünk egyedi molekulákat ellenben a teljes molekuláris tartalommal és azok arányának felszínre hozásával próbáljuk meg leírni az emberi test patofiziológiai állapotát.

6. KÖSZÖNETNYILVÁNÍTÁS

Mindazok az eredmények, amelyeket ebben a dolgozatban bemutattam, csak egy kicsinyke részét képezik mindannak a sok sikernek és rengeteg kudarcnak, aminek eddigi kutatói pályafutásom során élvezője, vagy épp ellenkezőleg, elszenvedője voltam. Sem a jelenlegi doktori mű, sem a benne foglalt eredmények nem születhettek volna meg a családom, a férjem és a fiam, az édesanyám (†), az édesapám (†), a nagymamám (†) és a barátaim folyamatos, önzetlen támogatása és szeretete nélkül. Mindezekért nekik tartozom hálával.

Immunológus mentoraim közül elsőként Dr. Joost Oppenheimnek (†) és Dr. Zack Howardnak szeretném megköszönni azt, hogy megmutatták nekem, hogyan kell megalkuvás nélkül haladni a tudományos célom felé, álljon elém bármilyen természetű nehézség is. Köszönöm, hogy posztdoktori éveimet vezetésük alatt a Laboratory of Molecular Immunoregulation-ben tölthettem, a National Cancer Institute fredericki kampuszán.

Köszönöm egyetemi mentoraimnak, Prof. Mándi Yvettnek, Prof. Duda Ernőnek és Prof. Minárovits Jánosnak, hogy megmutatták nekem az immunológia szépségeit. Mind az immunológia alapjainak az elsajátítását, mind pedig a citokinek csodálatos világának a megismerését nekik köszönhetem.

Köszönettel tartozom Bíró Tamás professzor úrnak, hogy segített a saját tudományos utam keresésében, hogy mindig bíztatott és feltétel nélkül hitt bennem.

Köszönettel tartozom korábbi és jelenlegi PhD hallgatóimnak: Marton Annamáriának, Harmati Máriának, Gyukity-Sebestyén Edinának, Dobra Gabriellának, Bukva Mátyásnak és Böröczky Tímeának, akik fáradhatatlan munkájukkal megteremtették a jelenlegi munkacsoport működésének alapjait és hozzájárultak ezen dolgozat eredményeinek megszületéséhez. Külön köszönet illeti meg a technikai segítségért Pintér Lillát.

Köszönöm jelenlegi PhD hallgatóimnak, és tudományos diákköri hallgatóimnak a mindennapok apróbb és nagyobb feladatainak gyakorlati kivitelezését.

Hálás vagyok klinikus együttműködő partnereinknek, Prof. Klekner Álmosnak, Prof. Oláh Juditnak, Prof. Hideghéthy Katalinnak, Prof. Barzó Pálnak a klinikai kutatások során nyújtott segítségükért, támogatásukért.

Köszönöm Prof. Gácser Attilának és Dr. Horváth Péternek, hogy támogató, türelmes és megértő főnökeim voltak. Köszönöm Prof. Széll Márta rektorhelyettes asszony és Prof. Lázár György dékán úr támogatását az MTA doktori értekezésem elkészítéséhez. Hálával tartozom

mindazért az erőfeszítésért, amit Kemény Lajos professzor úrral közösen az Immunológiai Tanszék létrehozásáért tettek, és hogy alapító tanszékvezetőként én kaphattam lehetőséget a munkára.

Hálásan köszönöm az Immunológiai Tanszéken és a Szegedi Biológiai Kutatóközpontban dolgozó minden munkatársamnak, hogy türelmükkel és megértésükkel, vagy technikai segítségükkel támogatták a munkámat.

7. SAJÁT KÖZLEMÉNYEK, TUDOMÁNYMETRIAI ADATOK

7.1 Az értekezést megalapozó közlemények (tematikus sorrendben)

1. **Buzas, K**; Marton, A; Vizler, C; Gyukity-Sebestyen, E; Harmati, M; Nagy, K; Zvara, A; Katona, RL; Tubak, V; Endresz, V et al.
Bacterial sepsis increases survival in metastatic melanoma: Chlamydophila pneumoniae induces macrophage polarization and tumor regression.
JOURNAL OF INVESTIGATIVE DERMATOLOGY 136 : 4 pp. 862-865. , 4 p. (2016)
IF: 6,287
Összes idézettség: 9 Független idézettség: 7

2. **Buzas, K**; Oppenheim, JJ; Howard, OMZ.
Myeloid cells migrate in response to IL-24.
CYTOKINE 55 : 3 pp. 429-434. , 6 p. (2011)
IF: 3,019
Összes idézettség: 20 Független idézettség: 20

3. Marton, A; Vizler, C; Kusz, E; Temesfoi, V; Szathmary, Z; Nagy, K; Szegletes, Z; Varo, G; Siklos, L; Katona, RL; Tubak, V; Howard, OM; Duda, E; Minarovits, J; Nagy, K; **Buzas, K.**
Melanoma cell-derived exosomes alter macrophage and dendritic cell functions in vitro.
IMMUNOLOGY LETTERS 148 : 1 pp. 34-38. , 5 p. (2012)
IF: 2,337
Összes idézettség: 93 Független idézettség: 89

4. Gyukity-Sebestyén, E; Harmati, M; Dobra, G; Németh, IB; Mihály, J; Zvara, Á; Hunyadi-Gulyás, É; Katona, R; Nagy, I; Horváth, P; Bálind, Á; Szkalisity, Á; Kovács, M; Pankotai, T; Borsos, B; Erdélyi, M; Szegletes, Z; Veréb, ZJ; Buzás, EI; Kemény, L; Bíró, T; **Buzás, K.**
Melanoma-Derived Exosomes Induce PD-1 Overexpression and Tumor Progression via Mesenchymal Stem Cell Oncogenic Reprogramming.
FRONTIERS IN IMMUNOLOGY 10 Paper: 2459 , 22 p. (2019)
IF: 5,085
Összes idézettség: 32 Független idézettség: 30

5. Harmati, M; Tarnai, Z; Decsi, G; Kormondi, S; Szegletes, Z; Janovak, L; Dekany, I; Saydam, O; Gyukity-Sebestyen, E; Dobra, G; Nagy, I; Nagy, K; **Buzas, K.**
Stressors alter intercellular communication and exosome profile of nasopharyngeal carcinoma cells.
JOURNAL OF ORAL PATHOLOGY AND MEDICINE 46 : 4 pp. 259-266. , 8 p. (2017)
IF: 2,237
Összes idézettség: 39 Független idézettség: 33

6. Harmati, M; Gyukity-Sebestyen, E; Dobra, G; Janovak, L; Dekany, I; Saydam, O; Hunyadi-Gulyas, E; Nagy, I; Farkas, A; Pankotai, T; Ujfaludi, Z; Horvath, P; Piccinini, F; Kovacs, M; Biro, T; **Buzas, K.**
Small extracellular vesicles convey the stress-induced adaptive responses of melanoma cells.
SCIENTIFIC REPORTS 9 : 1 Paper: 15329 , 19 p. (2019)
IF: 3,998
Összes idézettség: 48 Független idézettség: 45

7. Dobra, G; Bukva, M; Szabo, Z; Bruszel, B; Harmati, M; Gyukity-Sebestyen, E; Jenei, A; Szucs, M; Horvath, P; Biro, T; Klekner, A; **Buzas, K.**
Small Extracellular Vesicles Isolated from Serum May Serve as Signal-Enhancers for the Monitoring of CNS Tumors.
INTERNATIONAL JOURNAL OF MOLECULAR SCIENCES 21 : 15 Paper: 5359 , 20 p. (2020)
IF: 5,924
Összes idézettség: 13 Független idézettség: 11

8. Dobra, G; Gyukity-Sebestyen, E; Bukva, M; Harmati, M; Nagy, V; Szabo, Z; Pankotai, T; Klekner, A; **Buzas, K.**
MMP-9 as Prognostic Marker for Brain Tumours: A Comparative Study on Serum-Derived Small Extracellular Vesicles.
CANCERS 15: 3 p. 712 (2023)
IF: 6,575
Összes idézettség: 0 Független idézettség: 0

9. Bukva, M; Dobra, G; Gomez-Perez, J; Koos, K; Harmati, M; Gyukity-Sebestyen, E; Biro, T; Jenei, A; Kormondi, S; Horvath, P; Konya, Z; Klekner, A; **Buzas, K.**
Raman Spectral Signatures of Serum-Derived Extracellular Vesicle-Enriched Isolates May Support the Diagnosis of CNS Tumors.
CANCERS 13 : 6 Paper: 1407 , 19 p. (2021)
IF: 6,575
Összes idézettség: 4 Független idézettség: 3

7.2 Idegennyelvű közlemények a PhD fokozat megszerzése előtt (2005 december)

1. **Buzas, K**; Megyeri, K; Miczak, A; Fekete, A; Degre, M; Mandi, Y; Rosztoczy, I.
Different staphylococcal strains elicit different levels of production of T-helper 1-inducing cytokines.
ACTA MICROBIOLOGICA ET IMMUNOLOGICA HUNGARICA 51 : 3 pp. 371-384. , 14 p. (2004)
IF: -
Összes idézettség: 8 Független idézettség: 7

2. **Buzas, K**; Megyeri, K; Hogye, M; Csanady, M; Bogats, G; Mandi, Y.
Comparative study of the roles of cytokines and apoptosis in dilated and hypertrophic cardiomyopathies.
EUROPEAN CYTOKINE NETWORK 15 : 1 pp. 53-59. , 7 p. (2004)
IF: 1,747
Összes idézettség: 21 Független idézettség: 18

3. **Buzas, K**; Miczak, A; Degre, M; Megyeri, K.
Rubella virus infection dysregulates the pattern of p63 expression.
APMIS 112 : 10 pp. 656-662. , 7 p. (2004)
IF: 1,5
Összes idézettség: 4 Független idézettség: 2

4. Hogye, M; Mandi, Y; Csanady, M; Sepp, R; **Buzas, K**.
Comparison of circulating levels of interleukin-6 and tumor necrosis factor-alpha in hypertrophic cardiomyopathy and in idiopathic dilated cardiomyopathy.
AMERICAN JOURNAL OF CARDIOLOGY 94 : 2 pp. 249-251. , 3 p. (2004)
IF: 3,14
Összes idézettség: 60 Független idézettség: 60

7.3 A PhD fokozat megszerzése óta megjelent további idegennyelvű közlemények

1. Böröczky, T; Dobra, G; Bukva, M; Gyukity-Sebestyén, E; Hunyadi-Gulyás, É; Darula, Zs; Horváth, P; **Buzás, K**; Harmati, M.
Impact of Experimental Conditions on Extracellular Vesicles' Proteome: A Comparative Study.
LIFE-BASEL 13 : 1 p. 206 (2023)
IF: 3,253
Összes idézettség: 1 Független idézettség: 1

2. Diosdi, A; Hirling, D; Kovacs, M; Toth, T; Harmati, M; Koos, K; **Buzas, K**; Piccinini, F; Horvath, P.
A quantitative metric for the comparative evaluation of optical clearing protocols for 3D multicellular spheroids.
COMPUTATIONAL AND STRUCTURAL BIOTECHNOLOGY JOURNAL 19 pp. 1233-1243. , 11 p. (2021)
IF: 6,155
Összes idézettség: 2 Független idézettség: 1

3. Diosdi, A; Hirling, D; Kovacs, M; Toth, T; Harmati, M; Koos, K; **Buzas, K**; Piccinini, F; Horvath, P.
Cell lines and clearing approaches: a single-cell level 3D light-sheet fluorescence microscopy dataset of multicellular spheroids.
DATA IN BRIEF 36 Paper: 107090 , 9 p. (2021)
IF: -
Összes idézettség: 1 Független idézettség: 0

4. Grexa, I; Diosdi, A; Harmati, M; Kriston, A; Moshkov, N; **Buzas, K**; Pietiäinen, V; Koos, K; Horvath, P.
SpheroidPicker for automated 3D cell culture manipulation using deep learning.
SCIENTIFIC REPORTS 11 : 1 Paper: 14813 , 11 p. (2021)
IF: 4,997
Összes idézettség: 6 Független idézettség: 6

5. Harmati, M; Bukva, M; Boroczky, T; **Buzas, K**; Gyukity-Sebestyen, E.
The role of the metabolite cargo of extracellular vesicles in tumor progression.
CANCER AND METASTASIS REVIEWS 40 : 4 pp. 1203-1221. , 19 p. (2021)
IF: 9,237
Összes idézettség: 9 Független idézettség: 9

6. Peirsman, A; Blondeel, E; Ahmed, T; Anckaert, J; Audenaert, D; Boterberg, T; **Buzas, K**; Carragher, N; Castellani, G; Castro, F et al.

MISpheroID: a knowledgebase and transparency tool for minimum information in spheroid identity.
NATURE METHODS 18 : 11 pp. 1294-1303. , 10 p. (2021)
IF: 47,99
Összes idézettség: 14 Független idézettség: 8

7. Jenei, S; Tiricz, H; Szolomajer, J; Timar, E; Klement, E; Al, Bouni Mohamad Anas; L Rui, M; Kata, D; Harmati, M; **Buzas, K** et al.
Potent Chimeric Antimicrobial Derivatives of the Medicago truncatula NCR247 Symbiotic Peptide
FRONTIERS IN MICROBIOLOGY 11 Paper: 270 , 10 p. (2020)
IF: 5,64
Összes idézettség: 13 Független idézettség: 8

8. Decsi, G; Soki, J; Pap, B; Dobra, G; Harmati, M; Kormondi, S; Pankotai, T; Braunitzer, G; Minarovits, J; Sonkodi, I; Urban, E; Nemeth, IB; Nagy, K; **Buzas, K.**
Chicken or the Egg: Microbial Alterations in Biopsy Samples of Patients with Oral Potentially Malignant Disorders.
PATHOLOGY AND ONCOLOGY RESEARCH 25 : 3 pp. 1023-1033. , 11 p. (2019)
IF: 2,826
Összes idézettség: 10 Független idézettség: 10

9. Körmöndi, S; Terhes, G; Pál, Z; Varga, E; Harmati, M; **Buzás, K**; Urbán, E.
Human Pasteurellosis Health Risk for Elderly Persons Living with Companion Animals.
EMERGING INFECTIOUS DISEASES 25 : 2 pp. 229-235. , 7 p. (2019)
IF: 6,259
Összes idézettség: 9 Független idézettség: 9

10. Majoros, H; Ujfaludi, Zs; Borsos, BN; Hudacsek, VV; Nagy, Z; Coin, F; **Buzas, K**; Kovács, I; Bíró, T; Boros, IM et al.
SerpinB2 is involved in cellular response upon UV irradiatio
SCIENTIFIC REPORTS 9 : 1 Paper: 2753 , 13 p. (2019)
IF: 3,998
Összes idézettség: 8 Független idézettség: 6

11. Hettmann, A; Demcsák, A; Bach, Á; Decsi, G; Dencs, Á; Pálinkó, D; Rovó, L; Terhes, G; Urbán, E**; Buzás, K** et al.
Prevalence and genotypes of human papillomavirus in saliva and tumor samples of head and neck cancer patients in Hungary.
INFECTION GENETICS AND EVOLUTION 59 pp. 99-106. , 8 p. (2018)
IF: 2,611
Összes idézettség: 6 Független idézettség: 5

12. Banati, F; Koroknai, A; Szenthe, K; Tereh, T; Hidasi, A; Bankuti, B; **Buzas, K**; Lemnitzer, F; Ruzsics, Zs; Szathmary, S et al.
Up-Regulation of Lamin A/C Expression in Epstein-Barr Virus Immortalized B Cells and Burkitt Lymphoma Cell Lines of Activated B Cell Phenotype.
JOURNAL OF MICROBIAL AND BIOCHEMICAL TECHNOLOGY 9 : 3 pp. 087-094. , 8 p. (2017)
IF: -
Összes idézettség:- Független idézettség: -

13. Harmati, M; Gyukity-Sebestyen, E; Dobra, G; Terhes, G; Urban, E; Decsi, G; Mimica-Dukic, N; Lesjak, M; Simin, N; Pap, B; Nemeth I.B; **Buzas, K**.
Binary mixture of Satureja hortensis and Origanum vulgare subsp. hirtum essential oils: in vivo therapeutic efficiency against Helicobacter pylori infection.
HELICOBACTER 22 : 2 Paper: e12350 , 7 p. (2017)
IF: 4,123
Összes idézettség: 14 Független idézettség: 13

14. Piccinini, F; Balassa, T; Szkalisity, A; Molnar, C; Paavolainen, L; Kujala, K; **Buzas, K**; Sarazova, M; Pietiainen, V; Kutay, U et al.
Advanced Cell Classifier: User-Friendly Machine-Learning-Based Software for Discovering Phenotypes in High-Content Imaging Data.
CELL SYSTEMS 4 : 6 pp. 651-655. , 5 p. (2017)
IF: 8,982
Összes idézettség: 44 Független idézettség: 32

15. Zsedenyi, A; Farkas, B; Abdelrasoul, GN; Romano, I; Gyukity-Sebestyen, E; Nagy, K; Harmati, M; Dobra, G; Kormondi, S; Decsi, G; Nemeth IB; Diaspro, A; Brandi, F; Beke, S; **Buzas, K.**
Gold nanoparticle-filled biodegradable photopolymer scaffolds induced muscle remodeling: in vitro and in vivo findings.
MATERIALS SCIENCE & ENGINEERING C-MATERIALS FOR BIOLOGICAL APPLICATIONS 72 pp. 625-630. , 6 p. (2017)
IF: 5,08
Összes idézettség: 9 Független idézettség: 8

16. Lesjak, M; Simin, N; Orcic, D; Franciskovic, M; Knezevic, P; Beara, I; Aleksic, V; Svircev, E; **Buzas, K**; Mimica-Dukic, N.
Binary and Tertiary Mixtures of Satureja hortensis and Origanum vulgare Essential Oils as Potent Antimicrobial Agents Against Helicobacter pylori.
PHYTOTHERAPY RESEARCH 30 : 3 pp. 476-484. , 9 p. (2016)
IF: 3,092
Összes idézettség: 23 Független idézettség: 20

17. Marton, A; Kusz, E; Kolozsi, C; Tubak, V; Zagotto, G; **Buzas, K**; Quintieri, L; Vizler, C.
Vanillin Analogues o-Vanillin and 2,4,6-Trihydroxybenzaldehyde Inhibit NF kappa B Activation and Suppress Growth of A375 Human Melanoma.
ANTICANCER RESEARCH 36 : 11 pp. 5743-5750. , 8 p. (2016)
IF: 1,937
Összes idézettség: 20 Független idézettség: 20

18. **Buzas, K**; Kiss, A; Vizler, C.
Current approaches of tumor immunotherapy.
ACTA BIOLOGICA SZEGEDIENSIS 59 : Suppl. 1. pp. 69-82. , 14 p. (2015)
IF: -
Összes idézettség: - Független idézettség: -

19. Farkas, B; Zsedenyi, A; Gyukity-Sebestyen, E; Romano, I; Nagy, K; Diaspro, A; Brandi, F; **Buzas, K**; Beke, S.
Excimer laser-produced biodegradable photopolymer scaffolds do not induce immune rejection in vivo.
JOURNAL OF LASER MICRO NANOENGINEERING 10 : 1 pp. 11-14. , 4 p. (2015)
IF: 0,759
Összes idézettség: 5 Független idézettség: 1

20. Yanez-Mo, M; Siljander, PR; Andreu, Z; Zavec, AB; Borras, FE; Buzas, EI; **Buzas, K**; Casal, E; Cappello, F; Carvalho, J et al.
Biological properties of extracellular vesicles and their physiological functions.
JOURNAL OF EXTRACELLULAR VESICLES 4 Paper: 27066 (2015)
IF: ekkor még nincs, jelenleg 17,377
Összes idézettség: 2861 Független idézettség: 2599

21. Nagy, Z; Kovács, I; Török, M; Tóth, D; Vereb, G; **Buzás, K**; Juhász, I; Blumberg, PM; Bíró, T; Czifra, G.
Function of RasGRP3 in the formation and progression of human breast cancer.
MOLECULAR CANCER 13 : 1 Paper: 96 (2014)
IF: 4,257
Összes idézettség: 18 Független idézettség: 18

22. Decsi, G; Tarnai, Z; Zsedényi, A; **Buzás, K**; Nagy, K; Sonkodi, I; Minárovits, J.
A szájüregi laphámrák és praeblastomatosisai: a papillomavírus-fertőzés szerepe és a korai diagnózis lehetőségei [Oral carcinoma and its preblastomatoses: The role ofpapillomavirus infection and theprospects of early diagnosis.
LEGE ARTIS MEDICINAE 24 : (3) pp. 111-119. , 9 p. (2014)
Összes idézettség: 0 Független idézettség: 0

23. Juhasz, K; **Buzas, K**; Duda, E.
Importance of reverse signaling of the TNF superfamily in immune regulation.
EXPERT REVIEW OF CLINICAL IMMUNOLOGY 9 : 4 pp. 335-348. , 14 p. (2013)
IF: 3,342
Összes idézettség: 45 Független idézettség: 45

24. Ay, E; Banati, F; Mezei, M; Bakos, A; Niller, HH; **Buzas, K**; Minarovits, J.
Epigenetics of HIV Infection: Promising Research Areas and Implications for Therapy.
AIDS REVIEWS 15 : 3 pp. 181-188. , 8 p. (2013)
IF: 4,023
Összes idézettség: 25 Független idézettség: 20

25. Niller, HH; Banati, F; Nagy, K; **Buzas, K**; Minarovits, J.
Update on microbe-induced epigenetic changes: Bacterial effectors and viral oncoproteins as epigenetic dysregulators.
FUTURE VIROLOGY 8 : 11 pp. 1111-1126. , 16 p. (2013)
IF: 1
Összes idézettség: 5 Független idézettség: 5

26. Szenthe, K; Nagy, K; **Buzas, K**; Niller, HH; Minarovits, J.
MicroRNAs as Targets and Tools in B-Cell Lymphoma Therapy.
JOURNAL OF CANCER THERAPY 4 : 3 pp. 466-474. , 9 p. (2013)
IF: -
Összes idézettség: 1 Független idézettség: 0

27. Keseru, JS; Szabó, I; Gál, Z; Massidda, O; Mingoia, M; Kaszanyitzky, E; Jánosi, S; Hulvely, J; Csorba, A; **Buzás, K** et al.
Identification of β-lactamases in human and bovine isolates of Staphylococcus aureus strains having borderline resistance to penicillinase-resistant penicillins (PRPs) with proteomic methods.
VETERINARY MICROBIOLOGY 147 : 1-2 pp. 96-102. , 7 p. (2011)
IF: 3,327
Összes idézettség: 7 Független idézettség: 5

28. Qi, J; **Buzas, K**; Fan, HT; Cohen, JI; Wang, KN; Mont, E; Klinman, D; Oppenheim, JJ; Howard, OMZ.
Painful Pathways Induced by TLR Stimulation of Dorsal Root Ganglion Neurons.
JOURNAL OF IMMUNOLOGY 186 : 11 pp. 6417-6426. , 10 p. (2011)
IF: 5,788
Összes idézettség: 130 Független idézettség: 128

29. Hutamekalin, P; Farkas, AE; Orbok, A; Wilhelm, I; Nagyoszi, P; Veszelka, S; Deli, MA; **Buzas, K**; Hunyadi-Gulyas, E; Medzihradszky, KF et al.
Effect of nicotine and polyaromtic hydrocarbons on cerebral endothelial cells.
CELL BIOLOGY INTERNATIONAL 32 : 2 pp. 198-209. , 12 p. (2008)
IF: 1,619
Összes idézettség: 45 Független idézettség: 33

30. Birko, Z; Bialek, S; **Buzas, K**; Szajli, E; Traag, BA; Medzihradszky, KF; Rigali, S; Vijgenboom, E; Penyige, A; Kele, Z et al.
The secreted signaling protein factor C triggers the A-factor responseregulon in streptomyces griseus - Overlapping signaling routes.
MOLECULAR & CELLULAR PROTEOMICS 6 : 7 pp. 1248-1256. , 9 p. (2007)
IF: 9,425
Összes idézettség: 19 Független idézettség: 9

31. Hofner, P; Seprenyi, G; Miczak, A; **Buzas, K**; Gyulai, Z; Medzihradszky, KF; Rouhiainen, A; Rauvala, H; Mandi, Y.
High mobility group box 1 protein induction by Mycobacterium Bovis BCG.
MEDIATORS OF INFLAMMATION 2007 Paper: 53805 (2007)
IF: 1,162
Összes idézettség: 11 Független idézettség: 10

32. Megyeri, K; **Buzas, K**; Miczak, A; Buzas, E; Kovacs, L; Seprenyi, G; Falus, A; Mandi, Y.
The role of histamine in the intracellular survival of Mycobacterium bovis BCG.
MICROBES AND INFECTION 8 : 4 pp. 1035-1044. , 10 p. (2006)
IF: 3,127
Összes idézettség: 11 Független idézettség: 11

33. **Buzas, K**; Megyeri, K.
Staphylococci induce the production of melanoma differentiation-associated protein-7/IL-24.
ACTA MICROBIOLOGICA ET IMMUNOLOGICA HUNGARICA 53 : (4) pp. 431-440. , 10 p. (2006)10 p. (2006)
IF: 0,870
Összes idézettség: 9 Független idézettség: 7

7.4 Öt legfontosabbnak tartott tudományos közlemény

1. **Buzas, K**; Oppenheim, JJ; Howard, OMZ.
Myeloid cells migrate in response to IL-24.
CYTOKINE 55 : 3 pp. 429-434. , 6 p. (2011)
IF: 3,019
Összes idézettség: 20 Független idézettség: 20

2. Marton, A; Vizler, C; Kusz, E; Temesfoi, V; Szathmary, Z; Nagy, K; Szegletes, Z; Varo, G; Siklos, L; Katona, RL; Tubak, V; Howard, OM; Duda, E; Minarovits, J; Nagy, K; **Buzas, K.**
Melanoma cell-derived exosomes alter macrophage and dendritic cell functions in vitro.
IMMUNOLOGY LETTERS 148 : 1 pp. 34-38. , 5 p. (2012)
IF: 2,337
Összes idézettség: 93 Független idézettség: 89

3. Gyukity-Sebestyén, E; Harmati, M; Dobra, G; Németh, IB; Mihály, J; Zvara, Á; Hunyadi-Gulyás, É; Katona, R; Nagy, I; Horváth, P; Bálind, Á; Szkalisity, Á; Kovács, M; Pankotai, T; Borsos, B; Erdélyi, M; Szegletes, Z; Veréb, ZJ; Buzás, EI; Kemény, L; Bíró, T; **Buzás, K.**
Melanoma-Derived Exosomes Induce PD-1 Overexpression and Tumor Progression via Mesenchymal Stem Cell Oncogenic Reprogramming.
FRONTIERS IN IMMUNOLOGY 10 Paper: 2459 , 22 p. (2019)
IF: 5,085
Összes idézettség: 32 Független idézettség: 30

4. Harmati, M; Gyukity-Sebestyen, E; Dobra, G; Janovak, L; Dekany, I; Saydam, O; Hunyadi-Gulyas, E; Nagy, I; Farkas, A; Pankotai, T; Ujfaludi, Z; Horvath, P; Piccinini, F; Kovacs, M; Biro, T; **Buzas, K.**
Small extracellular vesicles convey the stress-induced adaptive responses of melanoma cells.
SCIENTIFIC REPORTS 9 : 1 Paper: 15329 , 19 p. (2019)
IF: 3,998
Összes idézettség: 48 Független idézettség: 45

5. Bukva, M; Dobra, G; Gomez-Perez, J; Koos, K; Harmati, M; Gyukity-Sebestyen, E; Biro, T; Jenei, A; Kormondi, S; Horvath, P; Konya, Z; Klekner, A; **Buzas, K.**
Raman Spectral Signatures of Serum-Derived Extracellular Vesicle-Enriched Isolates May Support the Diagnosis of CNS Tumors.
CANCERS 13 : 6 Paper: 1407 , 19 p. (2021)
IF: 6,575
Összes idézettség: 4 Független idézettség: 3

7.5 Tudománymetriai adatok

In extenso közlemények száma	46
magyar nyelven:	1
angol nyelven:	45
In extenso közlemények száma a PhD előtt:	4
In extenso közlemények száma a PhD után:	42
In extenso első szerzős közlemények száma:	7
In extenso utolsó szerzős közlemények száma:	12
Összesített impakt faktor:	202,4
Független hivatkozások száma:	3373
Könyvfejezetek száma:	1
Felsőoktatási tankönyvfejezet:	0
Hirsch-index:	17

8. IRODALOMJEGYZÉK

Abbruzzese, C., Matteoni, S., Signore, M., Cardone, L., Nath, K., Glickson, J. D., & Paggi, M. G. (2017). Drug repurposing for the treatment of glioblastoma multiforme. *Journal of Experimental & Clinical Cancer Research: CR*, *36*(1), 169. https://doi.org/10.1186/s13046-017-0642-x

Adams, S. (2009). Toll-like receptor agonists in cancer therapy. *Immunotherapy*, *1*(6), 949–964. https://doi.org/10.2217/imt.09.70

Akira, S., Uematsu, S., & Takeuchi, O. (2006). Pathogen Recognition and Innate Immunity. *Cell*, *124*(4), 783–801. https://doi.org/10.1016/j.cell.2006.02.015

Aldape, K., Brindle, K. M., Chesler, L., Chopra, R., Gajjar, A., Gilbert, M. R., Gottardo, N., Gutmann, D. H., Hargrave, D., Holland, E. C., Jones, D. T. W., Joyce, J. A., Kearns, P., Kieran, M. W., Mellinghoff, I. K., Merchant, M., Pfister, S. M., Pollard, S. M., Ramaswamy, V., … Gilbertson, R. J. (2019). Challenges to curing primary brain tumours. *Nature Reviews Clinical Oncology*, *16*(8), 509–520. https://doi.org/10.1038/s41571-019-0177-5

Alix-Panabières, C., & Pantel, K. (2021). Liquid Biopsy: From Discovery to Clinical Application. *Cancer Discovery*, *11*(4), 858–873. R. https://doi.org/10.1158/2159-8290.CD-20-1311

Anderson, H. C. (1969). Vesicles associated with calcification in the matrix of epiphyseal cartilage. *The Journal of Cell Biology*, *41*(1), 59–72. https://doi.org/10.1083/jcb.41.1.59

Andoh, A., Shioya, M., Nishida, A., Bamba, S., Tsujikawa, T., Kim-Mitsuyama, S., & Fujiyama, Y. (2009). Expression of IL-24, an activator of the JAK1/STAT3/SOCS3 cascade, is enhanced in inflammatory bowel disease. *Journal of Immunology (Baltimore, Md.: 1950)*, *183*(1), 687–695. https://doi.org/10.4049/jimmunol.0804169

Azam, Z., Quillien, V., Wang, G., & To, S.-S. T. (2019). The potential diagnostic and prognostic role of extracellular vesicles in glioma: Current status and future perspectives. *Acta Oncologica*, *58*(3), 353–362. https://doi.org/10.1080/0284186X.2018.1551621

Baglio, S. R., Lagerweij, T., Pérez-Lanzón, M., Ho, X. D., Léveillé, N., Melo, S. A., Cleton-Jansen, A.-M., Jordanova, E. S., Roncuzzi, L., Greco, M., van Eijndhoven, M. A. J., Grisendi, G., Dominici, M., Bonafede, R., Lougheed, S. M., de Gruijl, T. D., Zini, N., Cervo, S., Steffan, A., … Pegtel, D. M. (2017). Blocking Tumor-Educated MSC Paracrine Activity Halts Osteosarcoma Progression. *Clinical Cancer Research: An Official Journal of the American Association for Cancer Research*, *23*(14), Article 14. https://doi.org/10.1158/1078-0432.CCR-16-2726

Balabanian, K., Foussat, A., Bouchet-Delbos, L., Couderc, J., Krzysiek, R., Amara, A., Baleux, F., Portier, A., Galanaud, P., & Emilie, D. (2002). Interleukin-10 modulates the sensitivity of peritoneal B lymphocytes to chemokines with opposite effects on stromal cell-derived factor-1 and B-lymphocyte chemoattractant. *Blood*, *99*(2), 427–436. https://doi.org/10.1182/blood.v99.2.427

Barillari, G. (2020). The Impact of Matrix Metalloproteinase-9 on the Sequential Steps of the Metastatic Process. *International Journal of Molecular Sciences*, *21*(12), Article 12. https://doi.org/10.3390/ijms21124526

Basu, B., & Ghosh, M. K. (2019). Extracellular Vesicles in Glioma: From Diagnosis to Therapy. *BioEssays: News and Reviews in Molecular, Cellular and Developmental Biology*, *41*(7), Article 7. https://doi.org/10.1002/bies.201800245

Benoit, M., Desnues, B., & Mege, J.-L. (2008). Macrophage Polarization in Bacterial Infections. *The Journal of Immunology*, *181*(6), 3733–3739. https://doi.org/10.4049/jimmunol.181.6.3733

Bernard, N. J., & O'Neill, L. A. (2013). Mal, more than a bridge to MyD88. *IUBMB Life*, *65*(9), Article 9. https://doi.org/10.1002/iub.1201

Bersanelli, M., & Buti, S. (2017). From targeting the tumor to targeting the immune system: Transversal challenges in oncology with the inhibition of the PD-1/PD-L1 axis. *World Journal of Clinical Oncology*, *8*(1), Article 1. https://doi.org/10.5306/wjco.v8.i1.37

Bhoopathi, P., Lee, N., Pradhan, A. K., Shen, X.-N., Das, S. K., Sarkar, D., Emdad, L., & Fisher, P. B. (2016). Mda-7/IL-24 Induces Cell Death in Neuroblastoma through a Novel Mechanism Involving AIF and ATM. *Cancer Research*, *76*(12), 3572–3582. https://doi.org/10.1158/0008-5472.CAN-15-2959

Bhutia, S. K., Das, S. K., Azab, B., Menezes, M. E., Dent, P., Wang, X.-Y., Sarkar, D., & Fisher, P. B. (2013). Targeting breast cancer-initiating/stem cells with melanoma differentiation-associated gene-7/interleukin-24. *International Journal of Cancer*, *133*(11), Article 11. https://doi.org/10.1002/ijc.28289

Bickels, J., Kollender, Y., Merinsky, O., & Meller, I. (2002). Coley's toxin: Historical perspective. *The Israel Medical Association Journal: IMAJ*, *4*(6), Article 6.

Boutilier, A. J., & Elsawa, S. F. (2021). Macrophage Polarization States in the Tumor Microenvironment. *International Journal of Molecular Sciences*, *22*(13), 6995. https://doi.org/10.3390/ijms22136995

Bukva, M., Dobra, G., Gomez-Perez, J., Koos, K., Harmati, M., Gyukity-Sebestyen, E., Biro, T., Jenei, A., Kormondi, S., Horvath, P., Konya, Z., Klekner, A., & Buzas, K. (2021). Raman Spectral Signatures of Serum-Derived Extracellular Vesicle-Enriched Isolates May Support the Diagnosis of CNS Tumors. *Cancers*, *13*(6), Article 6. https://doi.org/10.3390/cancers13061407

Burns, K., Janssens, S., Brissoni, B., Olivos, N., Beyaert, R., & Tschopp, J. (2003). Inhibition of interleukin 1 receptor/Toll-like receptor signaling through the alternatively spliced, short form of MyD88 is due to its failure to recruit IRAK-4. *The Journal of Experimental Medicine*, *197*(2), 263–268. https://doi.org/10.1084/jem.20021790

Buzás, K., Marton, A., Vizler, C., Gyukity-Sebestyén, E., Harmati, M., Nagy, K., Zvara, Á., Katona, R. L., Tubak, V., Endrész, V., Németh, I. B., Oláh, J., Vígh, L., Bíró, T., & Kemény, L. (2016). Bacterial Sepsis Increases Survival in Metastatic Melanoma: Chlamydophila Pneumoniae Induces Macrophage Polarization and Tumor Regression. *Journal of Investigative Dermatology*, *136*(4), Article 4. https://doi.org/10.1016/j.jid.2015.12.032

Buzas, K., & Megyeri, K. (2006). Staphylococci Induce the Production of Melanoma Differentiation-Associated Protein-7/IL-24. *Acta Microbiologica et Immunologica Hungarica*, *53*(4), Article 4. https://doi.org/10.1556/AMicr.53.2006.4.2

Buzas, K., Oppenheim, J. J., & Zack Howard, O. M. (2011). Myeloid cells migrate in response to IL-24. *Cytokine*, *55*(3), Article 3. https://doi.org/10.1016/j.cyto.2011.05.018

Caby, M.-P., Lankar, D., Vincendeau-Scherrer, C., Raposo, G., & Bonnerot, C. (2005). Exosomal-like vesicles are present in human blood plasma. *International Immunology*, *17*(7), Article 7. https://doi.org/10.1093/intimm/dxh267

Callahan, M. K., & Wolchok, J. D. (2013). At the Bedside: CTLA-4- and PD-1-blocking antibodies in cancer immunotherapy. *Journal of Leukocyte Biology*, *94*(1), 41–53. https://doi.org/10.1189/jlb.1212631

Camussi, G., Deregibus, M.-C., Bruno, S., Grange, C., Fonsato, V., & Tetta, C. (2011). Exosome/microvesicle-mediated epigenetic reprogramming of cells. *American Journal of Cancer Research*, *1*(1), 98–110.

Cappello, F., Logozzi, M., Campanella, C., Bavisotto, C. C., Marcilla, A., Properzi, F., & Fais, S. (2017). Exosome levels in human body fluids: A tumor marker by themselves? *European Journal of Pharmaceutical Sciences: Official Journal of the European*

Federation for Pharmaceutical Sciences, *96*, 93–98. https://doi.org/10.1016/j.ejps.2016.09.010

Caudell, E. G., Mumm, J. B., Poindexter, N., Ekmekcioglu, S., Mhashilkar, A. M., Yang, X. H., Retter, M. W., Hill, P., Chada, S., & Grimm, E. A. (2002). The protein product of the tumor suppressor gene, melanoma differentiation-associated gene 7, exhibits immunostimulatory activity and is designated IL-24. *Journal of Immunology (Baltimore, Md.: 1950)*, *168*(12), Article 12. https://doi.org/10.4049/jimmunol.168.12.6041

Chacón-Salinas, R., Serafín-López, J., Ramos-Payán, R., Méndez-Aragón, P., Hernández-Pando, R., Van Soolingen, D., Flores-Romo, L., Estrada-Parra, S., & Estrada-García, I. (2005). Differential pattern of cytokine expression by macrophages infected in vitro with different Mycobacterium tuberculosis genotypes. *Clinical and Experimental Immunology*, *140*(3), 443–449. https://doi.org/10.1111/j.1365-2249.2005.02797.x

Chamberlain, R. S., & Kaufman, H. (2000). Innovations and strategies for the development of anticancer vaccines. *Expert Opinion on Pharmacotherapy*, *1*(4), Article 4. https://doi.org/10.1517/14656566.1.4.603

Chambers, A. F., & Matrisian, L. M. (1997). Changing views of the role of matrix metalloproteinases in metastasis. *JNCI Journal of the National Cancer Institute*, *89*(17), Article 17. https://doi.org/10.1093/jnci/89.17.1260

Chang, A. E., & Shu, S. (1996). Current status of adoptive immunotherapy of cancer. *Critical Reviews in Oncology/Hematology*, *22*(3), Article 3. https://doi.org/10.1016/1040-8428(96)00194-1

Chen, K., Huang, J., Gong, W., Iribarren, P., Dunlop, N. M., & Wang, J. M. (2007). Toll-like receptors in inflammation, infection and cancer. *International Immunopharmacology*, *7*(10), 1271–1285. https://doi.org/10.1016/j.intimp.2007.05.016

Chen, P.-M., Yen, M.-L., Liu, K.-J., Sytwu, H.-K., & Yen, B.-L. (2011). Immunomodulatory properties of human adult and fetal multipotent mesenchymal stem cells. *Journal of Biomedical Science*, *18*(1), 49. https://doi.org/10.1186/1423-0127-18-49

Choy, C., & Jandial, R. (2016). Breast Cancer Exosomes Breach the Blood-Brain Barrier. *Neurosurgery*, *78*(6), Article 6. https://doi.org/10.1227/NEU.0000000000001242

Clish, C. B., O'Brien, J. A., Gronert, K., Stahl, G. L., Petasis, N. A., & Serhan, C. N. (1999). Local and systemic delivery of a stable aspirin-triggered lipoxin prevents neutrophil recruitment *in vivo*. *Proceedings of the National Academy of Sciences*, *96*(14), 8247–8252. https://doi.org/10.1073/pnas.96.14.8247

Codman, E. A. (1935). Symposium on the Treatment of Primary Malignant Bone Tumors. *The American Journal of Surgery*, *27*(1), Article 1. https://doi.org/10.1016/S0002-9610(35)90819-4

Coley, W. B. (1891). II. Contribution to the Knowledge of Sarcoma. *Annals of Surgery*, *14*(3), Article 3. https://doi.org/10.1097/00000658-189112000-00015

Coley, W. B. (1991). The treatment of malignant tumors by repeated inoculations of erysipelas. With a report of ten original cases. 1893. *Clinical Orthopaedics and Related Research*, *262*, Article 262.

Costa-Silva, B., Aiello, N. M., Ocean, A. J., Singh, S., Zhang, H., Thakur, B. K., Becker, A., Hoshino, A., Mark, M. T., Molina, H., Xiang, J., Zhang, T., Theilen, T.-M., García-Santos, G., Williams, C., Ararso, Y., Huang, Y., Rodrigues, G., Shen, T.-L., … Lyden, D. (2015). Pancreatic cancer exosomes initiate pre-metastatic niche formation in the liver. *Nature Cell Biology*, *17*(6), Article 6. https://doi.org/10.1038/ncb3169

Curren Smith, E. W. (2015). Macrophage Polarization and Its Role in Cancer. *Journal of Clinical & Cellular Immunology*, *06*(04). https://doi.org/10.4172/2155-9899.1000338

De Broe, M., Wieme, R., & Roels, F. (1975). Letter: Membrane fragments with koinozymic properties released from villous adenoma of the rectum. *Lancet (London, England)*, *2*(7946), 1214–1215. https://doi.org/10.1016/s0140-6736(75)92709-9

de Menezes-Neto, A., Sáez, M. J. F., Lozano-Ramos, I., Segui-Barber, J., Martin-Jaular, L., Ullate, J. M. E., Fernandez-Becerra, C., Borrás, F. E., & del Portillo, H. A. (2015). Size-exclusion chromatography as a stand-alone methodology identifies novel markers in mass spectrometry analyses of plasma-derived vesicles from healthy individuals. *Journal of Extracellular Vesicles*, *4*(1), Article 1. CD5 LGAL3. https://doi.org/10.3402/jev.v4.27378

de Visser, K. E., Eichten, A., & Coussens, L. M. (2006). Paradoxical roles of the immune system during cancer development. *Nature Reviews. Cancer*, *6*(1), 24–37. https://doi.org/10.1038/nrc1782

Dehne, N., Mora, J., Namgaladze, D., Weigert, A., & Brüne, B. (2017). Cancer cell and macrophage cross-talk in the tumor microenvironment. *Current Opinion in Pharmacology*, *35*, 12–19. https://doi.org/10.1016/j.coph.2017.04.007

Delneste, Y., Beauvillain, C., & Jeannin, P. (2007). Immunité naturelle: Structure et fonction des *Toll-like receptors*. *Médecine/Sciences*, *23*(1), 67–74. https://doi.org/10.1051/medsci/200723167

Demšar, J., Curk, T., Erjavec, A., Gorup, Č., Hočevar, T., Milutinovič, M., Možina, M., Polajnar, M., Toplak, M., Starič, A., Štajdohar, M., Umek, L., Žagar, L., Žbontar, J., Žitnik, M., & Zupan, B. (2013). Orange: Data Mining Toolbox in Python. *J. Mach. Learn. Res.*, *14*(1), 2349–2353.

Dhawan, P., & Richmond, A. (2002). Role of CXCL1 in tumorigenesis of melanoma. *Journal of Leukocyte Biology*, *72*(1), 9–18. https://doi.org/10.1189/jlb.72.1.9

Dieu-Nosjean, M. C., Massacrier, C., Vanbervliet, B., Fridman, W. H., & Caux, C. (2001). IL-10 induces CCR6 expression during Langerhans cell development while IL-4 and IFN-gamma suppress it. *Journal of Immunology (Baltimore, Md.: 1950)*, *167*(10), 5594–5602. https://doi.org/10.4049/jimmunol.167.10.5594

Dobashi, K., Aihara, M., Araki, T., Shimizu, Y., Utsugi, M., Iizuka, K., Murata, Y., Hamuro, J., Nakazawa, T., & Mori, M. (2001). Regulation of LPS induced IL-12 production by IFN-gamma and IL-4 through intracellular glutathione status in human alveolar macrophages. *Clinical and Experimental Immunology*, *124*(2), 290–296. https://doi.org/10.1046/j.1365-2249.2001.01535.x

Dobra, G., Bukva, M., Szabo, Z., Bruszel, B., Harmati, M., Gyukity-Sebestyen, E., Jenei, A., Szucs, M., Horvath, P., Biro, T., Klekner, A., & Buzas, K. (2020). Small Extracellular Vesicles Isolated from Serum May Serve as Signal-Enhancers for the Monitoring of CNS Tumors. *International Journal of Molecular Sciences*, *21*(15), Article 15. https://doi.org/10.3390/ijms21155359

Dvorak, H. F., Quay, S. C., Orenstein, N. S., Dvorak, A. M., Hahn, P., Bitzer, A. M., & Carvalho, A. C. (1981). Tumor shedding and coagulation. *Science (New York, N.Y.)*, *212*(4497), 923–924. https://doi.org/10.1126/science.7195067

Ehrt, S., Schnappinger, D., Bekiranov, S., Drenkow, J., Shi, S., Gingeras, T. R., Gaasterland, T., Schoolnik, G., & Nathan, C. (2001). Reprogramming of the macrophage transcriptome in response to interferon-gamma and Mycobacterium tuberculosis: Signaling roles of nitric oxide synthase-2 and phagocyte oxidase. *The Journal of Experimental Medicine*, *194*(8), 1123–1140. https://doi.org/10.1084/jem.194.8.1123

Ekmekcioglu, S., Ellerhorst, J., Mhashilkar, A. M., Sahin, A. A., Read, C. M., Prieto, V. G., Chada, S., & Grimm, E. A. (2001). Down-regulated melanoma differentiation associated gene (mda-7) expression in human melanomas. *International Journal of Cancer*, *94*(1), Article 1. https://doi.org/10.1002/ijc.1437

Ellerhorst, J. A., Prieto, V. G., Ekmekcioglu, S., Broemeling, L., Yekell, S., Chada, S., & Grimm, E. A. (2002). Loss of MDA-7 expression with progression of melanoma. *Journal of Clinical Oncology: Official Journal of the American Society of Clinical Oncology*, *20*(4), Article 4. https://doi.org/10.1200/JCO.2002.20.4.1069

El-Zayat, S. R., Sibaii, H., & Mannaa, F. A. (2019). Toll-like receptors activation, signaling, and targeting: An overview. *Bulletin of the National Research Centre*, *43*(1), Article 1. https://doi.org/10.1186/s42269-019-0227-2

Engelhardt, B., Carare, R. O., Bechmann, I., Flügel, A., Laman, J. D., & Weller, R. O. (2016). Vascular, glial, and lymphatic immune gateways of the central nervous system. *Acta Neuropathologica*, *132*(3), Article 3. https://doi.org/10.1007/s00401-016-1606-5

Engelhardt, B., & Ransohoff, R. M. (2012). Capture, crawl, cross: The T cell code to breach the blood-brain barriers. *Trends in Immunology*, *33*(12), 579–589. https://doi.org/10.1016/j.it.2012.07.004

ERYSIPELAS AND PRODIGIOSUS TOXINS (COLEY). (1934). *JAMA: The Journal of the American Medical Association*, *103*(14), Article 14. https://doi.org/10.1001/jama.1934.02750400038015

Fan, J. Y., Huang, Y., Li, Y., Muluh, T. A., Fu, S. Z., & Wu, J. B. (2022). Bacteria in cancer therapy: A new generation of weapons. *Cancer Medicine*, *11*(23), 4457–4468. https://doi.org/10.1002/cam4.4799

Filippidis, A. S., Zarogiannis, S. G., Ioannou, M., Gourgoulianis, K., Molyvdas, P.-A., & Hatzoglou, C. (2012). Permeability of the arachnoid and pia mater. The role of ion channels in the leptomeningeal physiology. *Child's Nervous System: ChNS: Official Journal of the International Society for Pediatric Neurosurgery*, *28*(4), Article 4. https://doi.org/10.1007/s00381-012-1688-x

Fisher, P. B., Sarkar, D., Lebedeva, I. V., Emdad, L., Gupta, P., Sauane, M., Su, Z., Grant, S., Dent, P., Curiel, D. T., Senzer, N., & Nemunaitis, J. (2007). Melanoma differentiation associated gene-7/interleukin-24 (mda-7/IL-24): Novel gene therapeutic for metastatic melanoma. *Toxicology and Applied Pharmacology*, *224*(3), Article 3. https://doi.org/10.1016/j.taap.2006.11.021

Flaherty, K. T., Hodi, F. S., & Fisher, D. E. (2012). From genes to drugs: Targeted strategies for melanoma. *Nature Reviews Cancer*, *12*(5), 349–361. https://doi.org/10.1038/nrc3218

García-Rodríguez, C. (2007). Toll-like receptor 4-dependent pathways as sensors of endogenous "danger" signals. New evidences and potential therapeutic targets. *Inmunología*, *26*(4), 210–215. https://doi.org/10.1016/S0213-9626(07)70090-2

Gillies, R. J., Verduzco, D., & Gatenby, R. A. (2012). Evolutionary dynamics of carcinogenesis and why targeted therapy does not work. *Nature Reviews. Cancer*, *12*(7), Article 7. https://doi.org/10.1038/nrc3298

Greco, A., Di Benedetto, A., Howard, C. M., Kelly, S., Nande, R., Dementieva, Y., Miranda, M., Brunetti, A., Salvatore, M., Claudio, L., Sarkar, D., Dent, P., Curiel, D. T., Fisher, P. B., & Claudio, P. P. (2010). Eradication of therapy-resistant human prostate tumors using an ultrasound-guided site-specific cancer terminator virus delivery approach. *Molecular Therapy: The Journal of the American Society of Gene Therapy*, *18*(2), Article 2. https://doi.org/10.1038/mt.2009.252

Guiducci, C., Vicari, A. P., Sangaletti, S., Trinchieri, G., & Colombo, M. P. (2005). Redirecting *In vivo* Elicited Tumor Infiltrating Macrophages and Dendritic Cells towards Tumor Rejection. *Cancer Research*, *65*(8), 3437–3446. https://doi.org/10.1158/0008-5472.CAN-04-4262

Gulei, D., Petrut, B., Tigu, A. B., Onaciu, A., Fischer-Fodor, E., Atanasov, A. G., Ionescu, C., & Berindan-Neagoe, I. (2018). Exosomes at a glance—Common nominators for

cancer hallmarks and novel diagnosis tools. *Critical Reviews in Biochemistry and Molecular Biology*, *53*(5), Article 5. https://doi.org/10.1080/10409238.2018.1508276

Gupta, P., Su, Z., Lebedeva, I. V., Sarkar, D., Sauane, M., Emdad, L., Bachelor, M. A., Grant, S., Curiel, D. T., Dent, P., & Fisher, P. B. (2006). mda-7/IL-24: Multifunctional cancer-specific apoptosis-inducing cytokine. *Pharmacology & Therapeutics*, *111*(3), Article 3. https://doi.org/10.1016/j.pharmthera.2005.11.005

Gyukity-Sebestyén, E., Harmati, M., Dobra, G., Németh, I. B., Mihály, J., Zvara, Á., Hunyadi-Gulyás, É., Katona, R., Nagy, I., Horváth, P., Bálind, Á., Szkalisity, Á., Kovács, M., Pankotai, T., Borsos, B., Erdélyi, M., Szegletes, Z., Veréb, Z. J., Buzás, E. I., … Buzás, K. (2019). Melanoma-Derived Exosomes Induce PD-1 Overexpression and Tumor Progression via Mesenchymal Stem Cell Oncogenic Reprogramming. *Frontiers in Immunology*, *10*, 2459. https://doi.org/10.3389/fimmu.2019.02459

Hall, S. S. (1997). *A commotion in the blood: Life, death, and the immune system* (1st ed). Henry Holt.

Harding, C., Heuser, J., & Stahl, P. (1983). Receptor-mediated endocytosis of transferrin and recycling of the transferrin receptor in rat reticulocytes. *Journal of Cell Biology*, *97*(2), 329–339. https://doi.org/10.1083/jcb.97.2.329

Harmati, M., Bukva, M., Böröczky, T., Buzás, K., & Gyukity-Sebestyén, E. (2021). The role of the metabolite cargo of extracellular vesicles in tumor progression. *Cancer and Metastasis Reviews*, *40*(4), Article 4. https://doi.org/10.1007/s10555-021-10014-2

Harmati, M., Gyukity-Sebestyen, E., Dobra, G., Janovak, L., Dekany, I., Saydam, O., Hunyadi-Gulyas, E., Nagy, I., Farkas, A., Pankotai, T., Ujfaludi, Z., Horvath, P., Piccinini, F., Kovacs, M., Biro, T., & Buzas, K. (2019). Small extracellular vesicles convey the stress-induced adaptive responses of melanoma cells. *Scientific Reports*, *9*(1), Article 1. https://doi.org/10.1038/s41598-019-51778-6

Harmati, M., Tarnai, Z., Decsi, G., Kormondi, S., Szegletes, Z., Janovak, L., Dekany, I., Saydam, O., Gyukity-Sebestyen, E., Dobra, G., Nagy, I., Nagy, K., & Buzas, K. (2017). Stressors alter intercellular communication and exosome profile of nasopharyngeal carcinoma cells. *Journal of Oral Pathology & Medicine*, *46*(4), Article 4. https://doi.org/10.1111/jop.12486

Hinshaw, D. C., & Shevde, L. A. (2019). The Tumor Microenvironment Innately Modulates Cancer Progression. *Cancer Research*, *79*(18), 4557–4566. https://doi.org/10.1158/0008-5472.CAN-18-3962

Ho, W. J., Jaffee, E. M., & Zheng, L. (2020). The tumour microenvironment in pancreatic cancer—Clinical challenges and opportunities. *Nature Reviews Clinical Oncology*, *17*(9), 527–540. https://doi.org/10.1038/s41571-020-0363-5

Hobohm, U. (2001). Fever and cancer in perspective. *Cancer Immunology, Immunotherapy: CII*, *50*(8), Article 8. https://doi.org/10.1007/s002620100216

Hoebe, K., Janssen, E., & Beutler, B. (2004). The interface between innate and adaptive immunity. *Nature Immunology*, *5*(10), Article 10. https://doi.org/10.1038/ni1004-971

Hoption Cann, S. A., van Netten, J. P., & van Netten, C. (2003). Dr William Coley and tumour regression: A place in history or in the future. *Postgraduate Medical Journal*, *79*(938), Article 938.

Hormigo, A., Gu, B., Karimi, S., Riedel, E., Panageas, K. S., Edgar, M. A., Tanwar, M. K., Rao, J. S., Fleisher, M., DeAngelis, L. M., & Holland, E. C. (2006). YKL-40 and Matrix Metalloproteinase-9 as Potential Serum Biomarkers for Patients with High-Grade Gliomas. *Clinical Cancer Researh*, *12*(19), Article 19. https://doi.org/10.1158/1078-0432.CCR-06-0181

Hsieh, M.-Y., Chen, W.-Y., Jiang, M.-J., Cheng, B.-C., Huang, T.-Y., & Chang, M.-S. (2006). Interleukin-20 promotes angiogenesis in a direct and indirect manner. *Genes and Immunity*, *7*(3), 234–242. https://doi.org/10.1038/sj.gene.6364291

Hu, J. L., Wang, W., Lan, X. L., Zeng, Z. C., Liang, Y. S., Yan, Y. R., Song, F. Y., Wang, F. F., Zhu, X. H., Liao, W. J., Liao, W. T., Ding, Y. Q., & Liang, L. (2019). CAFs secreted exosomes promote metastasis and chemotherapy resistance by enhancing cell stemness and epithelial-mesenchymal transition in colorectal cancer. *Molecular Cancer*, *18*(1), Article 1. https://doi.org/10.1186/s12943-019-1019-x

Huang, A. C., & Zappasodi, R. (2022). A decade of checkpoint blockade immunotherapy in melanoma: Understanding the molecular basis for immune sensitivity and resistance. *Nature Immunology*, *23*(5), 660–670. https://doi.org/10.1038/s41590-022-01141-1

Huang, E. Y., Madireddi, M. T., Gopalkrishnan, R. V., Leszczyniecka, M., Su, Z., Lebedeva, I. V., Kang, D., Jiang, H., Lin, J. J., Alexandre, D., Chen, Y., Vozhilla, N., Mei, M. X., Christiansen, K. A., Sivo, F., Goldstein, N. I., Mhashilkar, A. B., Chada, S., Huberman, E., … Fisher, P. B. (2001). Genomic structure, chromosomal localization and expression profile of a novel melanoma differentiation associated (mda-7) gene with cancer specific growth suppressing and apoptosis inducing properties. *Oncogene*, *20*(48), 7051–7063. https://doi.org/10.1038/sj.onc.1204897

Jiang, H., Lin, J. J., Su, Z. Z., Goldstein, N. I., & Fisher, P. B. (1995). Subtraction hybridization identifies a novel melanoma differentiation associated gene, mda-7, modulated during human melanoma differentiation, growth and progression. *Oncogene*, *11*(12), Article 12.

Jiang, J., Li, J., Zhou, X., Zhao, X., Huang, B., & Qin, Y. (2022). Exosomes Regulate the Epithelial–Mesenchymal Transition in Cancer. *Frontiers in Oncology*, *12*, 864980. https://doi.org/10.3389/fonc.2022.864980

Jiang, Y., Chen, M., Nie, H., & Yuan, Y. (2019). PD-1 and PD-L1 in cancer immunotherapy: Clinical implications and future considerations. *Human Vaccines & Immunotherapeutics*, *15*(5), 1111–1122. https://doi.org/10.1080/21645515.2019.1571892

Jin, S. H., Choi, D., Chun, Y.-J., & Noh, M. (2014). Keratinocyte-derived IL-24 plays a role in the positive feedback regulation of epidermal inflammation in response to environmental and endogenous toxic stressors. *Toxicology and Applied Pharmacology*, *280*(2), Article 2. https://doi.org/10.1016/j.taap.2014.08.019

Johnsen, K. B., Gudbergsson, J. M., Andresen, T. L., & Simonsen, J. B. (2019). What is the blood concentration of extracellular vesicles? Implications for the use of extracellular vesicles as blood-borne biomarkers of cancer. *Biochimica Et Biophysica Acta. Reviews on Cancer*, *1871*(1), Article 1. https://doi.org/10.1016/j.bbcan.2018.11.006

Johnston, B. J., & Novales, E. T. (1962). Clinical effect of Coley's toxin. II. A seven-year study. *Cancer Chemotherapy Reports*, *21*, 43–68.

Jouanguy, E., Döffinger, R., Dupuis, S., Pallier, A., Altare, F., & Casanova, J. L. (1999). IL-12 and IFN-gamma in host defense against mycobacteria and salmonella in mice and men. *Current Opinion in Immunology*, *11*(3), 346–351. https://doi.org/10.1016/s0952-7915(99)80055-7

Kalluri, R., & Zeisberg, M. (2006). Fibroblasts in cancer. *Nature Reviews. Cancer*, *6*(5), 392–401. https://doi.org/10.1038/nrc1877

Kaplan, R. N., Riba, R. D., Zacharoulis, S., Bramley, A. H., Vincent, L., Costa, C., MacDonald, D. D., Jin, D. K., Shido, K., Kerns, S. A., Zhu, Z., Hicklin, D., Wu, Y., Port, J. L., Altorki, N., Port, E. R., Ruggero, D., Shmelkov, S. V., Jensen, K. K., … Lyden, D. (2005). VEGFR1-positive haematopoietic bone marrow progenitors initiate the pre-metastatic niche. *Nature*, *438*(7069), 820–827. https://doi.org/10.1038/nature04186

Kee, D., & McArthur, G. (2017). Immunotherapy of melanoma. *European Journal of Surgical Oncology: The Journal of the European Society of Surgical Oncology and the British Association of Surgical Oncology*, *43*(3), Article 3. https://doi.org/10.1016/j.ejso.2016.07.014

Keller, S., Ridinger, J., Rupp, A.-K., Janssen, J. W. G., & Altevogt, P. (2011). Body fluid derived exosomes as a novel template for clinical diagnostics. *Journal of Translational Medicine*, *9*, 86. https://doi.org/10.1186/1479-5876-9-86

Kiszewski, A. E., Becerril, E., Aguilar, L. D., Kader, I. T. A., Myers, W., Portaels, F., & Hernàndez Pando, R. (2006). The local immune response in ulcerative lesions of Buruli disease. *Clinical and Experimental Immunology*, *143*(3), Article 3. https://doi.org/10.1111/j.1365-2249.2006.03020.x

Kleffel, S., Posch, C., Barthel, S. R., Mueller, H., Schlapbach, C., Guenova, E., Elco, C. P., Lee, N., Juneja, V. R., Zhan, Q., Lian, C. G., Thomi, R., Hoetzenecker, W., Cozzio, A., Dummer, R., Mihm, M. C., Flaherty, K. T., Frank, M. H., Murphy, G. F., … Schatton, T. (2015). Melanoma Cell-Intrinsic PD-1 Receptor Functions Promote Tumor Growth. *Cell*, *162*(6), Article 6. https://doi.org/10.1016/j.cell.2015.08.052

Kong, J., Tian, H., Zhang, F., Zhang, Z., Li, J., Liu, X., Li, X., Liu, J., Li, X., Jin, D., Yang, X., Sun, B., Guo, T., Luo, Y., Lu, Y., Lin, B., & Liu, T. (2019). Extracellular vesicles of carcinoma-associated fibroblasts creates a pre-metastatic niche in the lung through activating fibroblasts. *Molecular Cancer*, *18*(1), Article 1. https://doi.org/10.1186/s12943-019-1101-4

Kosaka, N., Kogure, A., Yamamoto, T., Urabe, F., Usuba, W., Prieto-Vila, M., & Ochiya, T. (2019). Exploiting the message from cancer: The diagnostic value of extracellular vesicles for clinical applications. *Experimental & Molecular Medicine*, *51*(3), Article 3. https://doi.org/10.1038/s12276-019-0219-1

Kotenko, S. V. (2002). The family of IL-10-related cytokines and their receptors: Related, but to what extent? *Cytokine & Growth Factor Reviews*, *13*(3), Article 3. https://doi.org/10.1016/s1359-6101(02)00012-6

Kotenko, S. V., & Langer, J. A. (2004). Full house: 12 receptors for 27 cytokines. *International Immunopharmacology*, *4*(5), Article 5. https://doi.org/10.1016/j.intimp.2004.01.003

Kragstrup, T. W., Otkjaer, K., Holm, C., Jørgensen, A., Hokland, M., Iversen, L., & Deleuran, B. (2008). The expression of IL-20 and IL-24 and their shared receptors are increased in rheumatoid arthritis and spondyloarthropathy. *Cytokine*, *41*(1), 16–23. https://doi.org/10.1016/j.cyto.2007.10.004

Krone, B., Kölmel, K. F., Henz, B. M., & Grange, J. M. (2005). Protection against melanoma by vaccination with Bacille Calmette-Guerin (BCG) and/or vaccinia: An epidemiology-based hypothesis on the nature of a melanoma risk factor and its immunological control. *European Journal of Cancer (Oxford, England: 1990)*, *41*(1), 104–117. https://doi.org/10.1016/j.ejca.2004.08.010

Kucharzewska, P., & Belting, M. (2013). Emerging roles of extracellular vesicles in the adaptive response of tumour cells to microenvironmental stress. *Journal of Extracellular Vesicles*, *2*. https://doi.org/10.3402/jev.v2i0.20304

Lässer, C., Eldh, M., & Lötvall, J. (2012). Isolation and characterization of RNA-containing exosomes. *Journal of Visualized Experiments: JoVE*, *59*, Article 59. https://doi.org/10.3791/3037

Lebedeva, I. V., Emdad, L., Su, Z.-Z., Gupta, P., Sauane, M., Sarkar, D., Staudt, M. R., Liu, S.-J., Taher, M. M., Xiao, R., Barral, P., Lee, S.-G., Wang, D., Vozhilla, N., Park, E. S., Chatman, L., Boukerche, H., Ramesh, R., Inoue, S., … Fisher, P. B. (2007). mda-7/IL-24, novel anticancer cytokine: Focus on bystander antitumor, radiosensitization

and antiangiogenic properties and overview of the phase I clinical experience (Review). *International Journal of Oncology*, *31*(5), 985–1007.

Lebedeva, I. V., Sarkar, D., Su, Z.-Z., Kitada, S., Dent, P., Stein, C. A., Reed, J. C., & Fisher, P. B. (2003). Bcl-2 and Bcl-x(L) differentially protect human prostate cancer cells from induction of apoptosis by melanoma differentiation associated gene-7, mda-7/IL-24. *Oncogene*, *22*(54), Article 54. https://doi.org/10.1038/sj.onc.1206891

Lebedeva, I. V., Su, Z., Chang, Y., Kitada, S., Reed, J. C., & Fisher, P. B. (2002). The cancer growth suppressing gene mda-7 induces apoptosis selectively in human melanoma cells. *Oncogene*, *21*(5), Article 5. https://doi.org/10.1038/sj.onc.1205116

Lebedeva, I. V., Su, Z. Z., Sarkar, D., & Fisher, P. B. (2003). Restoring apoptosis as a strategy for cancer gene therapy: Focus on p53 and mda-7. *Seminars in Cancer Biology*, *13*(2), Article 2. https://doi.org/10.1016/s1044-579x(02)00134-7

Leng, R.-X., Pan, H.-F., Tao, J.-H., & Ye, D.-Q. (2011). IL-19, IL-20 and IL-24: Potential therapeutic targets for autoimmune diseases. *Expert Opinion on Therapeutic Targets*, *15*(2), Article 2. https://doi.org/10.1517/14728222.2011.534461

Li, H., Fan, X., & Houghton, J. (2007). Tumor microenvironment: The role of the tumor stroma in cancer. *Journal of Cellular Biochemistry*, *101*(4), 805–815. https://doi.org/10.1002/jcb.21159

Lightman, S., Rechthand, E., Terubayashi, H., Palestine, A., Rapoport, S., & Kador, P. (1987). Permeability changes in blood-retinal barrier of galactosemic rats are prevented by aldose reductase inhibitors. *Diabetes*, *36*(11), 1271–1275. https://doi.org/10.2337/diab.36.11.1271

Lin, Q., Zhou, C.-R., Bai, M.-J., Zhu, D., Chen, J.-W., Wang, H.-F., Li, M.-A., Wu, C., Li, Z.-R., & Huang, M.-S. (2020). Exosome-mediated miRNA delivery promotes liver cancer EMT and metastasis. *American Journal of Translational Research*, *12*(3), Article 3.

Lone, S. N., Nisar, S., Masoodi, T., Singh, M., Rizwan, A., Hashem, S., El-Rifai, W., Bedognetti, D., Batra, S. K., Haris, M., Bhat, A. A., & Macha, M. A. (2022). Liquid biopsy: A step closer to transform diagnosis, prognosis and future of cancer treatments. *Molecular Cancer*, *21*(1), 79. https://doi.org/10.1186/s12943-022-01543-7

Lorger, M. (2012). Tumor microenvironment in the brain. *Cancers*, *4*(1), 218–243. https://doi.org/10.3390/cancers4010218

Lu, P., Weaver, V. M., & Werb, Z. (2012). The extracellular matrix: A dynamic niche in cancer progression. *The Journal of Cell Biology*, *196*(4), 395–406. https://doi.org/10.1083/jcb.201102147

Lv, C., Su, Q., Liang, Y., Hu, J., & Yuan, S. (2016). Oncolytic vaccine virus harbouring the IL-24 gene suppresses the growth of lung cancer by inducing apoptosis. *Biochemical and Biophysical Research Communications*, *476*(1), Article 1. https://doi.org/10.1016/j.bbrc.2016.05.088

Ma, Q., Jin, B., Zhang, Y., Shi, Y., Zhang, C., Luo, D., Wang, P., Duan, C., Song, H., Li, X., Deng, X., Chen, Z., Wang, Z., Jiang, H., & Liu, Y. (2016). Secreted recombinant human IL-24 protein inhibits the proliferation of esophageal squamous cell carcinoma Eca-109 cells in vitro and in vivo. *Oncology Reports*, *35*(5), 2681–2690. https://doi.org/10.3892/or.2016.4633

Ma, Y., Chen, H., Wang, Q., Luo, F., Yan, J., & Zhang, X.-L. (2009). IL-24 protects against Salmonella typhimurium infection by stimulating early neutrophil Th1 cytokine production, which in turn activates CD8+ T cells. *European Journal of Immunology*, *39*(12), Article 12. https://doi.org/10.1002/eji.200939678

Maarof, G., Bouchet-Delbos, L., Gary-Gouy, H., Durand-Gasselin, I., Krzysiek, R., & Dalloul, A. (2010). Interleukin-24 inhibits the plasma cell differentiation program in

human germinal center B cells. *Blood*, *115*(9), 1718–1726. https://doi.org/10.1182/blood-2009-05-220251

Maia, J., Caja, S., Strano Moraes, M. C., Couto, N., & Costa-Silva, B. (2018). Exosome-Based Cell-Cell Communication in the Tumor Microenvironment. *Frontiers in Cell and Developmental Biology*, *6*, 18. https://doi.org/10.3389/fcell.2018.00018

Mansell, A., Brint, E., Gould, J. A., O'Neill, L. A., & Hertzog, P. J. (2004). Mal interacts with tumor necrosis factor receptor-associated factor (TRAF)-6 to mediate NF-kappaB activation by toll-like receptor (TLR)-2 and TLR4. *The Journal of Biological Chemistry*, *279*(36), Article 36. https://doi.org/10.1074/jbc.C400289200

Mantovani, A., Biswas, S. K., Galdiero, M. R., Sica, A., & Locati, M. (2013). Macrophage plasticity and polarization in tissue repair and remodelling: Macrophage plasticity and polarization in tissue repair and remodelling. *The Journal of Pathology*, *229*(2), 176–185. https://doi.org/10.1002/path.4133

Mantovani, A., Bottazzi, B., Colotta, F., Sozzani, S., & Ruco, L. (1992). The origin and function of tumor-associated macrophages. *Immunology Today*, *13*(7), 265–270. https://doi.org/10.1016/0167-5699(92)90008-U

Mantovani, A., Locati, M., Vecchi, A., Sozzani, S., & Allavena, P. (2001). Decoy receptors: A strategy to regulate inflammatory cytokines and chemokines. *Trends in Immunology*, *22*(6), 328–336. https://doi.org/10.1016/s1471-4906(01)01941-x

Mantovani, A., Sica, A., & Locati, M. (2005). Macrophage Polarization Comes of Age. *Immunity*, *23*(4), 344–346. https://doi.org/10.1016/j.immuni.2005.10.001

Mantovani, A., Sica, A., Sozzani, S., Allavena, P., Vecchi, A., & Locati, M. (2004). The chemokine system in diverse forms of macrophage activation and polarization. *Trends in Immunology*, *25*(12), 677–686. https://doi.org/10.1016/j.it.2004.09.015

Mantovani, A., Sozzani, S., Locati, M., Allavena, P., & Sica, A. (2002). Macrophage polarization: Tumor-associated macrophages as a paradigm for polarized M2 mononuclear phagocytes. *Trends in Immunology*, *23*(11), Article 11. https://doi.org/10.1016/S1471-4906(02)02302-5

Martinez, F. O., & Gordon, S. (2014). The M1 and M2 paradigm of macrophage activation: Time for reassessment. *F1000Prime Reports*, *6*. https://doi.org/10.12703/P6-13

Martinez, F. O., Gordon, S., Locati, M., & Mantovani, A. (2006). Transcriptional Profiling of the Human Monocyte-to-Macrophage Differentiation and Polarization: New Molecules and Patterns of Gene Expression. *The Journal of Immunology*, *177*(10), 7303–7311. https://doi.org/10.4049/jimmunol.177.10.7303

Marton, A., Vizler, C., Kusz, E., Temesfoi, V., Szathmary, Z., Nagy, K., Szegletes, Z., Varo, G., Siklos, L., Katona, R. L., Tubak, V., Howard, O. M. Z., Duda, E., Minarovits, J., Nagy, K., & Buzas, K. (2012). Melanoma cell-derived exosomes alter macrophage and dendritic cell functions in vitro. *Immunology Letters*, *148*(1), 34–38. https://doi.org/10.1016/j.imlet.2012.07.006

Matsumoto, J., Stewart, T., Banks, W. A., & Zhang, J. (2018). The Transport Mechanism of Extracellular Vesicles at the Blood-Brain Barrier. *Current Pharmaceutical Design*, *23*(40), Article 40. https://doi.org/10.2174/1381612823666170913164738

Mattei, V., Barenco, M. G., Tasciotti, V., Garofalo, T., Longo, A., Boller, K., Löwer, J., Misasi, R., Montrasio, F., & Sorice, M. (2009). Paracrine diffusion of PrP(C) and propagation of prion infectivity by plasma membrane-derived microvesicles. *PloS One*, *4*(4), Article 4. https://doi.org/10.1371/journal.pone.0005057

Matzinger, P. (1994). Tolerance, danger, and the extended family. *Annual Review of Immunology*, *12*, 991–1045. https://doi.org/10.1146/annurev.iy.12.040194.005015

Matzinger, P. (2002). The danger model: A renewed sense of self. *Science (New York, N.Y.)*, *296*(5566), Article 5566. https://doi.org/10.1126/science.1071059

McCarthy, E. F. (1995). The Registry of Bone Sarcoma. A history. *The Iowa Orthopaedic Journal*, *15*, 74–78.

McCarthy, E. F. (2006). The toxins of William B. Coley and the treatment of bone and soft-tissue sarcomas. *The Iowa Orthopaedic Journal*, *26*, 154–158.

Melo, S. A., Luecke, L. B., Kahlert, C., Fernandez, A. F., Gammon, S. T., Kaye, J., LeBleu, V. S., Mittendorf, E. A., Weitz, J., Rahbari, N., Reissfelder, C., Pilarsky, C., Fraga, M. F., Piwnica-Worms, D., & Kalluri, R. (2015). Glypican-1 identifies cancer exosomes and detects early pancreatic cancer. *Nature*, *523*(7559), Article 7559. https://doi.org/10.1038/nature14581

Menezes, M. E., Bhoopathi, P., Pradhan, A. K., Emdad, L., Das, S. K., Guo, C., Wang, X.-Y., Sarkar, D., & Fisher, P. B. (2018). Role of MDA-7/IL-24 a Multifunction Protein in Human Diseases. In *Advances in Cancer Research* (Vol. 138, pp. 143–182). Elsevier. https://doi.org/10.1016/bs.acr.2018.02.005

Menezes, M. E., Shen, X.-N., Das, S. K., Emdad, L., Guo, C., Yuan, F., Li, Y.-J., Archer, M. C., Zacksenhaus, E., Windle, J. J., Subler, M. A., Ben-David, Y., Sarkar, D., Wang, X.-Y., & Fisher, P. B. (2015). MDA-7/IL-24 functions as a tumor suppressor gene in vivo in transgenic mouse models of breast cancer. *Oncotarget*, *6*(35), Article 35. https://doi.org/10.18632/oncotarget.6047

Mishra, P. J., Mishra, P. J., Glod, J. W., & Banerjee, D. (2009). Mesenchymal stem cells: Flip side of the coin. *Cancer Research*, *69*(4), 1255–1258. https://doi.org/10.1158/0008-5472.CAN-08-3562

Möhrmann, L., Huang, H. J., Hong, D. S., Tsimberidou, A. M., Fu, S., Piha-Paul, S. A., Subbiah, V., Karp, D. D., Naing, A., Krug, A., Enderle, D., Priewasser, T., Noerholm, M., Eitan, E., Coticchia, C., Stoll, G., Jordan, L.-M., Eng, C., Kopetz, E. S., … Janku, F. (2018). Liquid Biopsies Using Plasma Exosomal Nucleic Acids and Plasma Cell-Free DNA Compared with Clinical Outcomes of Patients with Advanced Cancers. *Clinical Cancer Research*, *24*(1), Article 1. https://doi.org/10.1158/1078-0432.CCR-17-2007

Mondal, S., Adhikari, N., Banerjee, S., Amin, S. A., & Jha, T. (2020). Matrix metalloproteinase-9 (MMP-9) and its inhibitors in cancer: A minireview. *European Journal of Medicinal Chemistry*, *194*, 112260. https://doi.org/10.1016/j.ejmech.2020.112260

Monteiro-Reis, S., Carvalho-Maia, C., Bart, G., Vainio, S. J., Pedro, J., Silva, E. R., Sales, G., Henrique, R., & Jerónimo, C. (2021). Secreted Extracellular Vesicle Molecular Cargo as a Novel Liquid Biopsy Diagnostics of Central Nervous System Diseases. *International Journal of Molecular Sciences*, *22*(6), 3267. https://doi.org/10.3390/ijms22063267

Morad, G., Carman, C. V., Hagedorn, E. J., Perlin, J. R., Zon, L. I., Mustafaoglu, N., Park, T.-E., Ingber, D. E., Daisy, C. C., & Moses, M. A. (2019). Tumor-Derived Extracellular Vesicles Breach the Intact Blood-Brain Barrier via Transcytosis. *ACS Nano*, *13*(12), Article 12. https://doi.org/10.1021/acsnano.9b04397

Morrison, B. J., Morris, J. C., & Steel, J. C. (2013). Lung cancer-initiating cells: A novel target for cancer therapy. *Targeted Oncology*, *8*(3), 159–172. https://doi.org/10.1007/s11523-012-0247-4

Murphy, J. T., Sommer, S., Kabara, E. A., Verman, N., Kuelbs, M. A., Saama, P., Halgren, R., & Coussens, P. M. (2006). Gene expression profiling of monocyte-derived macrophages following infection with Mycobacterium avium subspecies avium and Mycobacterium avium subspecies paratuberculosis. *Physiological Genomics*, *28*(1), Article 1. https://doi.org/10.1152/physiolgenomics.00098.2006

Musso, T., Cappello, P., Stornello, S., Ravarino, D., Caorsi, C., Otero, K., Novelli, F., Badolato, R., & Giovarelli, M. (2005). IL-10 enhances CCL2 release and chemotaxis

induced by CCL16 in human monocytes. *International Journal of Immunopathology and Pharmacology*, *18*(2), 339–349. https://doi.org/10.1177/039463200501800216

Nauts, H. C., & McLaren, J. R. (1990). Coley toxins—The first century. *Advances in Experimental Medicine and Biology*, *267*, 483–500. https://doi.org/10.1007/978-1-4684-5766-7_52

Negi, S., Rutman, A. K., & Paraskevas, S. (2019). Extracellular Vesicles in Type 1 Diabetes: Messengers and Regulators. *Current Diabetes Reports*, *19*(9), Article 9. https://doi.org/10.1007/s11892-019-1193-7

Nogués, L., Benito-Martin, A., Hergueta-Redondo, M., & Peinado, H. (2018). The influence of tumour-derived extracellular vesicles on local and distal metastatic dissemination. *Molecular Aspects of Medicine*, *60*, 15–26. https://doi.org/10.1016/j.mam.2017.11.012

Osti, D., Del Bene, M., Rappa, G., Santos, M., Matafora, V., Richichi, C., Faletti, S., Beznoussenko, G. V., Mironov, A., Bachi, A., Fornasari, L., Bongetta, D., Gaetani, P., DiMeco, F., Lorico, A., & Pelicci, G. (2019). Clinical Significance of Extracellular Vesicles in Plasma from Glioblastoma Patients. *Clinical Cancer Research*, *25*(1), Article 1. https://doi.org/10.1158/1078-0432.CCR-18-1941

Ott, P. A., Hodi, F. S., & Robert, C. (2013). CTLA-4 and PD-1/PD-L1 Blockade: New Immunotherapeutic Modalities with Durable Clinical Benefit in Melanoma Patients. *Clinical Cancer Research*, *19*(19), 5300–5309. https://doi.org/10.1158/1078-0432.CCR-13-0143

Paget, S. (1889). THE DISTRIBUTION OF SECONDARY GROWTHS IN CANCER OF THE BREAST. *The Lancet*, *133*(3421), 571–573. https://doi.org/10.1016/S0140-6736(00)49915-0

Pan, B. T., & Johnstone, R. M. (1983). Fate of the transferrin receptor during maturation of sheep reticulocytes in vitro: Selective externalization of the receptor. *Cell*, *33*(3), Article 3. https://doi.org/10.1016/0092-8674(83)90040-5

Parayath, N. N., Padmakumar, S., & Amiji, M. M. (2020). Extracellular vesicle-mediated nucleic acid transfer and reprogramming in the tumor microenvironment. *Cancer Letters*, *482*, 33–43. https://doi.org/10.1016/j.canlet.2020.04.009

Park, M. A., Walker, T., Martin, A. P., Allegood, J., Vozhilla, N., Emdad, L., Sarkar, D., Rahmani, M., Graf, M., Yacoub, A., Koumenis, C., Spiegel, S., Curiel, D. T., Voelkel-Johnson, C., Grant, S., Fisher, P. B., & Dent, P. (2009). MDA-7/IL-24-induced cell killing in malignant renal carcinoma cells occurs by a ceramide/CD95/PERK-dependent mechanism. *Molecular Cancer Therapeutics*, *8*(5), 1280–1291. https://doi.org/10.1158/1535-7163.MCT-09-0073

Pastushenko, I., & Blanpain, C. (2019). EMT Transition States during Tumor Progression and Metastasis. *Trends in Cell Biology*, *29*(3), 212–226. https://doi.org/10.1016/j.tcb.2018.12.001

Peinado, H., Alečković, M., Lavotshkin, S., Matei, I., Costa-Silva, B., Moreno-Bueno, G., Hergueta-Redondo, M., Williams, C., García-Santos, G., Ghajar, C., Nitadori-Hoshino, A., Hoffman, C., Badal, K., Garcia, B. A., Callahan, M. K., Yuan, J., Martins, V. R., Skog, J., Kaplan, R. N., … Lyden, D. (2012). Melanoma exosomes educate bone marrow progenitor cells toward a pro-metastatic phenotype through MET. *Nature Medicine*, *18*(6), 883–891. https://doi.org/10.1038/nm.2753

Persaud, L., De Jesus, D., Brannigan, O., Richiez-Paredes, M., Huaman, J., Alvarado, G., Riker, L., Mendez, G., Dejoie, J., & Sauane, M. (2016). Mechanism of Action and Applications of Interleukin 24 in Immunotherapy. *International Journal of Molecular Sciences*, *17*(6), Article 6. https://doi.org/10.3390/ijms17060869

Pfeffer, K., Matsuyama, T., Kündig, T. M., Wakeham, A., Kishihara, K., Shahinian, A., Wiegmann, K., Ohashi, P. S., Krönke, M., & Mak, T. W. (1993). Mice deficient for

the 55 kd tumor necrosis factor receptor are resistant to endotoxic shock, yet succumb to L. monocytogenes infection. *Cell*, *73*(3), 457–467. https://doi.org/10.1016/0092-8674(93)90134-c

Piccinini, F. (2015). AnaSP: A software suite for automatic image analysis of multicellular spheroids. *Computer Methods and Programs in Biomedicine*, *119*(1), 43–52. https://doi.org/10.1016/j.cmpb.2015.02.006

Pisitkun, T., Shen, R.-F., & Knepper, M. A. (2004). Identification and proteomic profiling of exosomes in human urine. *Proceedings of the National Academy of Sciences of the United States of America*, *101*(36), Article 36. https://doi.org/10.1073/pnas.0403453101

Poliakov, A., Spilman, M., Dokland, T., Amling, C. L., & Mobley, J. A. (2009). Structural heterogeneity and protein composition of exosome-like vesicles (prostasomes) in human semen. *The Prostate*, *69*(2), Article 2. https://doi.org/10.1002/pros.20860

Pradhan, A. K., Talukdar, S., Bhoopathi, P., Shen, X.-N., Emdad, L., Das, S. K., Sarkar, D., & Fisher, P. B. (2017). Mda-7/IL-24 Mediates Cancer Cell-Specific Death via Regulation of miR-221 and the Beclin-1 Axis. *Cancer Research*, *77*(4), Article 4. https://doi.org/10.1158/0008-5472.CAN-16-1731

Preusser, M. (2014). A step towards clinical blood biomarkers of glioblastoma. *Nature Reviews Neurology*, *10*(12), 681–682. https://doi.org/10.1038/nrneurol.2014.208

Qi, J., Buzas, K., Fan, H., Cohen, J. I., Wang, K., Mont, E., Klinman, D., Oppenheim, J. J., & Howard, O. M. Z. (2011). Painful pathways induced by TLR stimulation of dorsal root ganglion neurons. *Journal of Immunology (Baltimore, Md.: 1950)*, *186*(11), Article 11. https://doi.org/10.4049/jimmunol.1001241

Qian, W., Liu, J., Tong, Y., Yan, S., Yang, C., Yang, M., & Liu, X. (2008). Enhanced antitumor activity by a selective conditionally replicating adenovirus combining with MDA-7/interleukin-24 for B-lymphoblastic leukemia via induction of apoptosis. *Leukemia*, *22*(2), Article 2. https://doi.org/10.1038/sj.leu.2405034

Rahmani, M., Mayo, M., Dash, R., Sokhi, U. K., Dmitriev, I. P., Sarkar, D., Dent, P., Curiel, D. T., Fisher, P. B., & Grant, S. (2010). Melanoma differentiation associated gene-7/interleukin-24 potently induces apoptosis in human myeloid leukemia cells through a process regulated by endoplasmic reticulum stress. *Molecular Pharmacology*, *78*(6), 1096–1104. https://doi.org/10.1124/mol.110.068007

Ramesh, R., Mhashilkar, A. M., Tanaka, F., Saito, Y., Branch, C. D., Sieger, K., Mumm, J. B., Stewart, A. L., Boquoi, A., Dumoutier, L., Grimm, E. A., Renauld, J.-C., Kotenko, S., & Chada, S. (2003). Melanoma differentiation-associated gene 7/interleukin (IL)-24 is a novel ligand that regulates angiogenesis via the IL-22 receptor. *Cancer Research*, *63*(16), 5105–5113.

Ramirez, S. H., Andrews, A. M., Paul, D., & Pachter, J. S. (2018). Extracellular vesicles: Mediators and biomarkers of pathology along CNS barriers. *Fluids and Barriers of the CNS*, *15*(1), Article 1. https://doi.org/10.1186/s12987-018-0104-7

Rao, J. S., Yamamoto, M., Mohaman, S., Gokaslan, Z. L., Fuller, G. N., Stetler-Stevenson, W. G., Rao, V. H., Liotta, L. A., Nicolson, G. L., & Sawaya, R. E. (1996). Expression and localization of 92 kDa type IV collagenase/gelatinase B (MMP-9) in human gliomas. *Clinical & Experimental Metastasis*, *14*(1), Article 1. https://doi.org/10.1007/BF00157681

Ratajczak, J., Wysoczynski, M., Hayek, F., Janowska-Wieczorek, A., & Ratajczak, M. Z. (2006). Membrane-derived microvesicles: Important and underappreciated mediators of cell-to-cell communication. *Leukemia*, *20*(9), Article 9. https://doi.org/10.1038/sj.leu.2404296

Ratajczak, M. Z., & Ratajczak, J. (2020). Extracellular microvesicles/exosomes: Discovery, disbelief, acceptance, and the future? *Leukemia*, *34*(12), Article 12. https://doi.org/10.1038/s41375-020-01041-z

Ridge, S. M., Sullivan, F. J., & Glynn, S. A. (2017). Mesenchymal stem cells: Key players in cancer progression. *Molecular Cancer*, *16*(1), 31. https://doi.org/10.1186/s12943-017-0597-8

Ridnour, L. A., Cheng, R. Y. S., Switzer, C. H., Heinecke, J. L., Ambs, S., Glynn, S., Young, H. A., Trinchieri, G., & Wink, D. A. (2013). Molecular Pathways: Toll-like Receptors in the Tumor Microenvironment—Poor Prognosis or New Therapeutic Opportunity. *Clinical Cancer Research*, *19*(6), 1340–1346. https://doi.org/10.1158/1078-0432.CCR-12-0408

Roth, L., Prahst, C., Ruckdeschel, T., Savant, S., Weström, S., Fantin, A., Riedel, M., Héroult, M., Ruhrberg, C., & Augustin, H. G. (2016). Neuropilin-1 mediates vascular permeability independently of vascular endothelial growth factor receptor-2 activation. *Science Signaling*, *9*(425), ra42. https://doi.org/10.1126/scisignal.aad3812

Rottenberg, M. E., Gigliotti-Rothfuchs, A., & Wigzell, H. (2002). The role of IFN-gamma in the outcome of chlamydial infection. *Current Opinion in Immunology*, *14*(4), 444–451. https://doi.org/10.1016/s0952-7915(02)00361-8

Rozmyslowicz, T., Majka, M., Kijowski, J., Murphy, S. L., Conover, D. O., Poncz, M., Ratajczak, J., Gaulton, G. N., & Ratajczak, M. Z. (2003). Platelet- and megakaryocyte-derived microparticles transfer CXCR4 receptor to CXCR4-null cells and make them susceptible to infection by X4-HIV. *AIDS (London, England)*, *17*(1), Article 1. https://doi.org/10.1097/00002030-200301030-00006

Sahoo, A., Lee, C.-G., Jash, A., Son, J.-S., Kim, G., Kwon, H.-K., So, J.-S., & Im, S.-H. (2011). Stat6 and c-Jun mediate Th2 cell-specific IL-24 gene expression. *Journal of Immunology (Baltimore, Md.: 1950)*, *186*(7), Article 7. https://doi.org/10.4049/jimmunol.1002620

Sakuishi, K., Jayaraman, P., Behar, S. M., Anderson, A. C., & Kuchroo, V. K. (2011). Emerging Tim-3 functions in antimicrobial and tumor immunity. *Trends in Immunology*, *32*(8), 345–349. https://doi.org/10.1016/j.it.2011.05.003

Sarkar, D., Lebedeva, I. V., Gupta, P., Emdad, L., Sauane, M., Dent, P., Curiel, D. T., & Fisher, P. B. (2007). Melanoma differentiation associated gene-7 (mda-7)/IL-24: A 'magic bullet' for cancer therapy? *Expert Opinion on Biological Therapy*, *7*(5), Article 5. https://doi.org/10.1517/14712598.7.5.577

Sarkar, D., Su, Z.-Z., Lebedeva, I. V., Sauane, M., Gopalkrishnan, R. V., Valerie, K., Dent, P., & Fisher, P. B. (2002). Mda-7 (IL-24) Mediates selective apoptosis in human melanoma cells by inducing the coordinated overexpression of the GADD family of genes by means of p38 MAPK. *Proceedings of the National Academy of Sciences of the United States of America*, *99*(15), Article 15. https://doi.org/10.1073/pnas.152327199

Sarkar, D., Su, Z.-Z., Park, E.-S., Vozhilla, N., Dent, P., Curiel, D. T., & Fisher, P. B. (2008). A cancer terminator virus eradicates both primary and distant human melanomas. *Cancer Gene Therapy*, *15*(5), Article 5. https://doi.org/10.1038/cgt.2008.14

Sarkar, D., Su, Z.-Z., Vozhilla, N., Park, E. S., Gupta, P., & Fisher, P. B. (2005). Dual cancer-specific targeting strategy cures primary and distant breast carcinomas in nude mice. *Proceedings of the National Academy of Sciences of the United States of America*, *102*(39), Article 39. https://doi.org/10.1073/pnas.0506837102

Sarkar, S., Quinn, B. A., Shen, X., Dent, P., Das, S. K., Emdad, L., Sarkar, D., & Fisher, P. B. (2015). Reversing translational suppression and induction of toxicity in pancreatic cancer cells using a chemoprevention gene therapy approach. *Molecular Pharmacology*, *87*(2), 286–295. https://doi.org/10.1124/mol.114.094375

Sauane, M., Gopalkrishnan, R. V., Lebedeva, I., Mei, M. X., Sarkar, D., Su, Z.-Z., Kang, D.-C., Dent, P., Pestka, S., & Fisher, P. B. (2003). Mda-7/IL-24 induces apoptosis of diverse cancer cell lines through JAK/STAT-independent pathways. *Journal of Cellular Physiology*, *196*(2), 334–345. https://doi.org/10.1002/jcp.10309

Sauane, M., Gopalkrishnan, R. V., Sarkar, D., Su, Z. Z., Lebedeva, I. V., Dent, P., Pestka, S., & Fisher, P. B. (2003). MDA-7/IL-24: Novel cancer growth suppressing and apoptosis inducing cytokine. *Cytokine & Growth Factor Reviews*, *14*(1), 35–51. https://doi.org/10.1016/s1359-6101(02)00074-6

Scavo, M. P., Depalo, N., Tutino, V., De Nunzio, V., Ingrosso, C., Rizzi, F., Notarnicola, M., Curri, M. L., & Giannelli, G. (2020). Exosomes for Diagnosis and Therapy in Gastrointestinal Cancers. *International Journal of Molecular Sciences*, *21*(1), Article 1. https://doi.org/10.3390/ijms21010367

Schaefer, G., Venkataraman, C., & Schindler, U. (2001). Cutting edge: FISP (IL-4-induced secreted protein), a novel cytokine-like molecule secreted by Th2 cells. *Journal of Immunology (Baltimore, Md.: 1950)*, *166*(10), Article 10. https://doi.org/10.4049/jimmunol.166.10.5859

Sellge, G., & Kufer, T. A. (2015). PRR-signaling pathways: Learning from microbial tactics. *Seminars in Immunology*, *27*(2), 75–84. https://doi.org/10.1016/j.smim.2015.03.009

Shapiro, B. A., Vu, N. T., Shultz, M. D., Shultz, J. C., Mietla, J. A., Gouda, M. M., Yacoub, A., Dent, P., Fisher, P. B., Park, M. A., & Chalfant, C. E. (2016). Melanoma Differentiation-associated Gene 7/IL-24 Exerts Cytotoxic Effects by Altering the Alternative Splicing of Bcl-x Pre-mRNA via the SRC/PKCδ Signaling Axis. *The Journal of Biological Chemistry*, *291*(41), Article 41. https://doi.org/10.1074/jbc.M116.737569

Shaughnessy, L. M., & Swanson, J. A. (2007). The role of the activated macrophage in clearing Listeria monocytogenes infection. *Frontiers in Bioscience: A Journal and Virtual Library*, *12*, 2683–2692. https://doi.org/10.2741/2364

Sheridan, C. (2016). Exosome cancer diagnostic reaches market. *Nature Biotechnology*, *34*(4), 359–360. https://doi.org/10.1038/nbt0416-359

Shimanovsky, A., Jethava, A., & Dasanu, C. A. (2013). Immune alterations in malignant melanoma and current immunotherapy concepts. *Expert Opinion on Biological Therapy*, *13*(10), 1413–1427. https://doi.org/10.1517/14712598.2013.827658

Sica, A., Larghi, P., Mancino, A., Rubino, L., Porta, C., Totaro, M. G., Rimoldi, M., Biswas, S. K., Allavena, P., & Mantovani, A. (2008). Macrophage polarization in tumour progression. *Seminars in Cancer Biology*, *18*(5), 349–355. https://doi.org/10.1016/j.semcancer.2008.03.004

Singh, K., Kant, S., Singh, V. K., Agrawal, N. K., Gupta, S. K., & Singh, K. (2014). Toll-like receptor 4 polymorphisms and their haplotypes modulate the risk of developing diabetic retinopathy in type 2 diabetes patients. *Molecular Vision*, *20*, 704–713.

Sinha, P., Clements, V. K., & Ostrand-Rosenberg, S. (2005). Reduction of Myeloid-Derived Suppressor Cells and Induction of M1 Macrophages Facilitate the Rejection of Established Metastatic Disease. *The Journal of Immunology*, *174*(2), 636–645. https://doi.org/10.4049/jimmunol.174.2.636

Sironi, M., Guglielmotti, A., Polentarutti, N., Fioretti, F., Milanese, C., Romano, M., Vigini, C., Coletta, I., Sozzani, S., Bernasconi, S., Vecchi, A., Pinza, M., & Mantovani, A. (1999). A small synthetic molecule capable of preferentially inhibiting the production of the CC chemokine monocyte chemotactic protein-1. *European Cytokine Network*, *10*(3), Article 3.

Solinas, G., Germano, G., Mantovani, A., & Allavena, P. (2009). Tumor-associated macrophages (TAM) as major players of the cancer-related inflammation. *Journal of Leukocyte Biology*, *86*(5), 1065–1073. https://doi.org/10.1189/jlb.0609385

Sozzani, S., Ghezzi, S., Iannolo, G., Luini, W., Borsatti, A., Polentarutti, N., Sica, A., Locati, M., Mackay, C., Wells, T. N. C., Biswas, P., Vicenzi, E., Poli, G., & Mantovani, A. (1998). Interleukin 10 Increases CCR5 Expression and HIV Infection in Human Monocytes. *Journal of Experimental Medicine*, *187*(3), 439–444. https://doi.org/10.1084/jem.187.3.439

Stange, E.-L., Rademacher, F., Drerup, K. A., Heinemann, N., Möbus, L., Gläser, R., & Harder, J. (2022). ***Staphylococcus aureus*** Activates the Aryl Hydrocarbon Receptor in Human Keratinocytes. *Journal of Innate Immunity*, *14*(6), 582–592. https://doi.org/10.1159/000524033

Szebeni, G. J., Kriston-Pál, É., Blazsó, P., Katona, R. L., Novák, J., Szabó, E., Czibula, Á., Fajka-Boja, R., Hegyi, B., Uher, F., Krenács, L., Joó, G., & Monostori, É. (2012). Identification of Galectin-1 as a Critical Factor in Function of Mouse Mesenchymal Stromal Cell-Mediated Tumor Promotion. *PLoS ONE*, *7*(7), e41372. https://doi.org/10.1371/journal.pone.0041372

Talukdar, S., Emdad, L., Das, S. K., Sarkar, D., & Fisher, P. B. (2016). Evolving Strategies for Therapeutically Targeting Cancer Stem Cells. *Advances in Cancer Research*, *131*, 159–191. https://doi.org/10.1016/bs.acr.2016.04.003

Tamai, H., Miyake, K., Yamaguchi, H., Takatori, M., Dan, K., Inokuchi, K., & Shimada, T. (2012). AAV8 vector expressing IL24 efficiently suppresses tumor growth mediated by specific mechanisms in MLL/AF4-positive ALL model mice. *Blood*, *119*(1), Article 1. https://doi.org/10.1182/blood-2011-05-354050

Tao, S.-C., & Guo, S.-C. (2020). Role of extracellular vesicles in tumour microenvironment. *Cell Communication and Signaling: CCS*, *18*(1), Article 1. https://doi.org/10.1186/s12964-020-00643-5

Taylor, D. D., Homesley, H. D., & Doellgast, G. J. (1980). Binding of specific peroxidase-labeled antibody to placental-type phosphatase on tumor-derived membrane fragments. *Cancer Research*, *40*(11), 4064–4069.

Tesovnik, T., Kovač, J., Pohar, K., Hudoklin, S., Dovč, K., Bratina, N., Trebušak Podkrajšek, K., Debeljak, M., Veranič, P., Bosi, E., Piemonti, L., Ihan, A., & Battelino, T. (2020). Extracellular Vesicles Derived Human-miRNAs Modulate the Immune System in Type 1 Diabetes. *Frontiers in Cell and Developmental Biology*, *8*, 202. https://doi.org/10.3389/fcell.2020.00202

THE FAILURE OF THE ERYSIPELAS TOXINS. (1894). *JAMA: The Journal of the American Medical Association*, *XXIII*(24), Article 24. https://doi.org/10.1001/jama.1894.02421290035005

Théry, C., Witwer, K. W., Aikawa, E., Alcaraz, M. J., Anderson, J. D., Andriantsitohaina, R., Antoniou, A., Arab, T., Archer, F., Atkin-Smith, G. K., Ayre, D. C., Bach, J.-M., Bachurski, D., Baharvand, H., Balaj, L., Baldacchino, S., Bauer, N. N., Baxter, A. A., Bebawy, M., … Zuba-Surma, E. K. (2018). Minimal information for studies of extracellular vesicles 2018 (MISEV2018): A position statement of the International Society for Extracellular Vesicles and update of the MISEV2014 guidelines. *Journal of Extracellular Vesicles*, *7*(1), Article 1. https://doi.org/10.1080/20013078.2018.1535750

Tian, Y.-C., Chen, Y.-C., Chang, C.-T., Hung, C.-C., Wu, M.-S., Phillips, A., & Yang, C.-W. (2007). Epidermal growth factor and transforming growth factor-beta1 enhance HK-2 cell migration through a synergistic increase of matrix metalloproteinase and sustained activation of ERK signaling pathway. *Experimental Cell Research*, *313*(11), 2367–2377. https://doi.org/10.1016/j.yexcr.2007.03.022

Treps, L., Edmond, S., Harford-Wright, E., Galan-Moya, E. M., Schmitt, A., Azzi, S., Citerne, A., Bidère, N., Ricard, D., & Gavard, J. (2016). Extracellular vesicle-transported

Semaphorin3A promotes vascular permeability in glioblastoma. *Oncogene*, *35*(20), 2615–2623. https://doi.org/10.1038/onc.2015.317

Ueno, M., Asada, K., Toda, M., Nagata, K., Sotozono, C., Kosaka, N., Ochiya, T., Kinoshita, S., & Hamuro, J. (2016). Concomitant Evaluation of a Panel of Exosome Proteins and MiRs for Qualification of Cultured Human Corneal Endothelial Cells. *Investigative Ophthalmology & Visual Science*, *57*(10), 4393–4402. https://doi.org/10.1167/iovs.16-19805

Ugurel, S., Röhmel, J., Ascierto, P. A., Flaherty, K. T., Grob, J. J., Hauschild, A., Larkin, J., Long, G. V., Lorigan, P., McArthur, G. A., Ribas, A., Robert, C., Schadendorf, D., & Garbe, C. (2017). Survival of patients with advanced metastatic melanoma: The impact of novel therapies–update 2017. *European Journal of Cancer*, *83*, 247–257. https://doi.org/10.1016/j.ejca.2017.06.028

Vargas-Alarcón, G., Posadas-Romero, C., Villarreal-Molina, T., Alvarez-León, E., Angeles-Martinez, J., Posadas-Sanchez, R., Monroy-Muñoz, I., Luna-Fuentes, S., González-Salazar, C., Ramirez-Bello, J., Cardoso-Saldaña, G., Medina-Urrutia, A., & Kimura-Hayama, E. (2014). IL-24 gene polymorphisms are associated with cardiometabolic parameters and cardiovascular risk factors but not with premature coronary artery disease: The genetics of atherosclerotic disease Mexican study. *Journal of Interferon & Cytokine Research: The Official Journal of the International Society for Interferon and Cytokine Research*, *34*(9), 659–666. https://doi.org/10.1089/jir.2013.0081

Veziroglu, E. M., & Mias, G. I. (2020). Characterizing Extracellular Vesicles and Their Diverse RNA Contents. *Frontiers in Genetics*, *11*, 700. https://doi.org/10.3389/fgene.2020.00700

Vitale, I., Manic, G., Coussens, L. M., Kroemer, G., & Galluzzi, L. (2019). Macrophages and Metabolism in the Tumor Microenvironment. *Cell Metabolism*, *30*(1), Article 1. https://doi.org/10.1016/j.cmet.2019.06.001

Wang, C.-J., Xue, X.-B., Yi, J.-L., Chen, K., Zheng, J.-W., Wang, J., Zeng, J.-P., & Xu, R.-H. (2006). Melanoma differentiation-associated gene-7, MDA-7/IL-24, selectively induces growth suppression, apoptosis in human hepatocellular carcinoma cell line HepG2 by replication-incompetent adenovirus vector. *World Journal of Gastroenterology*, *12*(11), 1774–1779. https://doi.org/10.3748/wjg.v12.i11.1774

Wang, H., Jiang, D., Li, W., Xiang, X., Zhao, J., Yu, B., Wang, C., He, Z., Zhu, L., & Yang, Y. (2019). Evaluation of serum extracellular vesicles as noninvasive diagnostic markers of glioma. *Theranostics*, *9*(18), 5347–5358. https://doi.org/10.7150/thno.33114

Wang, H., Wei, H., Wang, J., Li, L., Chen, A., & Li, Z. (2020). MicroRNA-181d-5p-Containing Exosomes Derived from CAFs Promote EMT by Regulating CDX2/HOXA5 in Breast Cancer. *Molecular Therapy. Nucleic Acids*, *19*, 654–667. https://doi.org/10.1016/j.omtn.2019.11.024

Wang, L., Yang, G., Zhao, D., Wang, J., Bai, Y., Peng, Q., Wang, H., Fang, R., Chen, G., Wang, Z., Wang, K., Li, G., Yang, Y., Wang, Z., Guo, P., Peng, L., Hou, D., & Xu, W. (2019). CD103-positive CSC exosome promotes EMT of clear cell renal cell carcinoma: Role of remote MiR-19b-3p. *Molecular Cancer*, *18*(1), Article 1. https://doi.org/10.1186/s12943-019-0997-z

Wang, M., & Liang, P. (2005). Interleukin-24 and its receptors. *Immunology*, *114*(2), Article 2. https://doi.org/10.1111/j.1365-2567.2005.02094.x

Wang, M., Tan, Z., Zhang, R., Kotenko, S. V., & Liang, P. (2002). Interleukin 24 (MDA-7/MOB-5) signals through two heterodimeric receptors, IL-22R1/IL-20R2 and IL-20R1/IL-20R2. *The Journal of Biological Chemistry*, *277*(9), 7341–7347. https://doi.org/10.1074/jbc.M106043200

Wang, X., Ye, Z., Zhong, J., Xiang, J., & Yang, J. (2007). Adenovirus-mediated Il-24 expression suppresses hepatocellular carcinoma growth via induction of cell apoptosis and cycling arrest and reduction of angiogenesis. *Cancer Biotherapy & Radiopharmaceuticals*, *22*(1), 56–63. https://doi.org/10.1089/cbr.2006.370

Wang, Z., Xie, Z., Lu, Q., Chang, C., & Zhou, Z. (2017). Beyond Genetics: What Causes Type 1 Diabetes. *Clinical Reviews in Allergy & Immunology*, *52*(2), Article 2. https://doi.org/10.1007/s12016-016-8592-1

Waters, C. M., & Bassler, B. L. (2005). Quorum sensing: Cell-to-cell communication in bacteria. *Annual Review of Cell and Developmental Biology*, *21*, 319–346. https://doi.org/10.1146/annurev.cellbio.21.012704.131001

Weis, S. M., & Cheresh, D. A. (2011). Tumor angiogenesis: Molecular pathways and therapeutic targets. *Nature Medicine*, *17*(11), 1359–1370. https://doi.org/10.1038/nm.2537

Whitaker, E. L., Filippov, V. A., & Duerksen-Hughes, P. J. (2012). Interleukin 24: Mechanisms and therapeutic potential of an anti-cancer gene. *Cytokine & Growth Factor Reviews*, *23*(6), Article 6. https://doi.org/10.1016/j.cytogfr.2012.08.004

Wiemann, B., & Starnes, C. O. (1994). Coley's toxins, tumor necrosis factor and cancer research: A historical perspective. *Pharmacology & Therapeutics*, *64*(3), 529–564. https://doi.org/10.1016/0163-7258(94)90023-X

Willsmore, Z. N., Coumbe, B. G. T., Crescioli, S., Reci, S., Gupta, A., Harris, R. J., Chenoweth, A., Chauhan, J., Bax, H. J., McCraw, A., Cheung, A., Osborn, G., Hoffmann, R. M., Nakamura, M., Laddach, R., Geh, J. L. C., MacKenzie-Ross, A., Healy, C., Tsoka, S., … Karagiannis, S. N. (2021). Combined anti-PD-1 and anti-CTLA-4 checkpoint blockade: Treatment of melanoma and immune mechanisms of action. *European Journal of Immunology*, *51*(3), 544–556. https://doi.org/10.1002/eji.202048747

Wolf, P. (1967). The nature and significance of platelet products in human plasma. *British Journal of Haematology*, *13*(3), 269–288. https://doi.org/10.1111/j.1365-2141.1967.tb08741.x

Yacoub, A., Mitchell, C., Hong, Y., Gopalkrishnan, R. V., Su, Z.-Z., Gupta, P., Sauane, M., Lebedeva, I. V., Curiel, D. T., Mahasreshti, P. J., Rosenfeld, M. R., Broaddus, W. C., James, C. D., Grant, S., Fisher, P. B., & Dent, P. (2004). MDA-7 regulates cell growth and radiosensitivity in vitro of primary (non-established) human glioma cells. *Cancer Biology & Therapy*, *3*(8), Article 8. https://doi.org/10.4161/cbt.3.8.968

Yáñez-Mó, M., Siljander, P. R.-M., Andreu, Z., Bedina Zavec, A., Borràs, F. E., Buzas, E. I., Buzas, K., Casal, E., Cappello, F., Carvalho, J., Colás, E., Cordeiro-da Silva, A., Fais, S., Falcon-Perez, J. M., Ghobrial, I. M., Giebel, B., Gimona, M., Graner, M., Gursel, I., … De Wever, O. (2015). Biological properties of extracellular vesicles and their physiological functions. *Journal of Extracellular Vesicles*, *4*(1), Article 1. https://doi.org/10.3402/jev.v4.27066

Yang, E., Wang, X., Gong, Z., Yu, M., Wu, H., & Zhang, D. (2020). Exosome-mediated metabolic reprogramming: The emerging role in tumor microenvironment remodeling and its influence on cancer progression. *Signal Transduction and Targeted Therapy*, *5*(1), Article 1. https://doi.org/10.1038/s41392-020-00359-5

Ye, D., Gong, M., Deng, Y., Fang, S., Cao, Y., Xiang, Y., & Shen, Z. (2022). Roles and clinical application of exosomal circRNAs in the diagnosis and treatment of malignant tumors. *Journal of Translational Medicine*, *20*(1), 161. https://doi.org/10.1186/s12967-022-03367-x

Zarember, K. A., & Godowski, P. J. (2002). Tissue Expression of Human Toll-Like Receptors and Differential Regulation of Toll-Like Receptor mRNAs in Leukocytes in Response

to Microbes, Their Products, and Cytokines. *The Journal of Immunology*, *168*(2), Article 2. https://doi.org/10.4049/jimmunol.168.2.554

Zeng, Z., Li, Y., Pan, Y., Lan, X., Song, F., Sun, J., Zhou, K., Liu, X., Ren, X., Wang, F., Hu, J., Zhu, X., Yang, W., Liao, W., Li, G., Ding, Y., & Liang, L. (2018). Cancer-derived exosomal miR-25-3p promotes pre-metastatic niche formation by inducing vascular permeability and angiogenesis. *Nature Communications*, *9*(1), Article 1. https://doi.org/10.1038/s41467-018-07810-w

Zhao, Z., Fan, J., Hsu, Y.-M. S., Lyon, C. J., Ning, B., & Hu, T. Y. (2019). Extracellular vesicles as cancer liquid biopsies: From discovery, validation, to clinical application. *Lab on a Chip*, *19*(7), Article 7. https://doi.org/10.1039/C8LC01123K

Zhuo, B., Shi, Y., Qin, H., Sun, Q., Li, Z., Zhang, F., Wang, R., & Wang, X. (2017). Interleukin-24 inhibits osteosarcoma cell migration and invasion via the JNK/c-Jun signaling pathways. *Oncology Letters*, *13*(6), 4505–4511. https://doi.org/10.3892/ol.2017.5990

9. A DOLGOZATBAN TÁRGYALT CIKKEK MÁSOLATAI

***Nicholas G. Martin*[1] *and Sarah E. Medland*[1]**

[1]*QIMR Berghofer Medical Research Institute, Brisbane, Australia;* [2]*School of Psychology, University of Queensland, Brisbane, Australia;* [3]*MRC Integrative Epidemiology Unit, School of Social and Community Medicine, University of Bristol, Bristol, UK;* [4]*University of Queensland Diamantina Institute, Translational Research Institute, Brisbane, Australia;* [5]*School of Social & Community Medicine, University of Bristol, Oakfield House, Oakfield Grove, Bristol, UK;* [6]*Max Planck Institute for Psycholinguistics, Nijmegen, The Netherlands;* [7]*Department of Psychiatry, Washington University, St. Louis, Missouri, USA;* [8]*Department of Psychology, La Trobe University, Melbourne, Australia;* [9]*National Centre for Forensic Studies, Faculty of Education, Science, Technology and Mathematics, University of Canberra, Canberra, Australia; and* [10]*Office of the Chief Forensic Scientist, Forensic Services Department, Victoria Police, Australia*
**Corresponding author e-mail: Yvonne.Ho@qimrberghofer.edu.au or d.evans1@uq.edu.au*

SUPPLEMENTARY MATERIAL

Supplementary material is linked to the online version of the paper at www.jidonline.org, and at http://dx.doi.org/10.1016/j.jid.2015.10.062.

REFERENCES

Abecasis GR, Cherny SS, Cookson WO, et al. Merlin-rapid analysis of dense genetic maps using sparse gene flow trees. Nat Genet 2002; 30:97–101.

Boker S, Neale M, Maes H, et al. OpenMx 1.2 User Guide. Charlottesville, VA: Department of Psychology, University of Virginia; 2012.

Boyd A, Golding J, Macleod J, et al. Cohort profile: the "children of the 90s"—the index offspring of the Avon Longitudinal Study of Parents and Children. Int J Epidemiol 2013;42: 111–27.

Holt S. The genetics of dermal ridges. Springfield, IL: Charles C. Thomas; 1968.

Li M, Gui H, Kwan J, et al. GATES: a rapid and powerful gene-based association test using extended Simes procedure. Am J Hum Genet 2011;88:283–93.

Machado J, Fernandes P, Roquetti R, et al. Digital dermatoglyphic heritability differences as evidenced by a female twin study. Twin Res Hum Genet 2010;13:482–9.

Martin N, Eaves L, Loesch D. A genetical analysis of covariation between finger ridge counts. Ann Hum Biol 1982;9:539–52.

Medland S, Loesch D, Mdzewski B, et al. Linkage analysis of a model quantitative trait in humans: finger ridge count shows significant multivariate linkage to 5q14.1. PLoS Genet 2007a;3: 1736–44.

Medland S, Park D, Loesch D, et al. Ridgecounter: a program for obtaining semi-automated finger ridge counts. Ann Hum Biol 2007b;34: 504–17.

Medland S, Zayats T, Glaser B, et al. A variant in LIN28B is associated with 2D:4D finger-length ratio, a putative retrospective biomarker of prenatal testosterone exposure. Am J Hum Genet 2010;86:519–25.

Mulvihill J, Smith D. The genesis of dermatoglyphics. J Pediatr 1969;75:579–89.

Penrose L. Memorandum on dermatoglyphic nomenclature, Birth Defects Original Article Series, vol. 4. NY: National Foundation-March of Dimes; 1968.

Willer C, Li Y, Abecasis G. METAL: fast and efficient meta-analysis of genomewide association scans. Bioinformatics 2010;26: 2190–1.

Yao J, Zhou B, Zhang J, et al. A new tumor suppressor LncRNA ADAMTS9-AS2 is regulated by DNMT1 and inhibits migration of glioma cells. Tumour Biol 2014;35:1–10.

Zhang J, Rubio V, Zheng S, et al. Knockdown of OLA1, a regulator of oxidative stress response, inhibits motility and invasion of breast cancer cells. J Zhejiang Univ Sci B 2009;10:796–804.

Bacterial Sepsis Increases Survival in Metastatic Melanoma: *Chlamydophila Pneumoniae* Induces Macrophage Polarization and Tumor Regression

Journal of Investigative Dermatology (2016) **136,** 862–865; doi:10.1016/j.jid.2015.12.032

TO THE EDITOR

The initiative of this study was the unexpected complete tumor regression in a patient with stage IV cutaneous metastatic melanoma, who suffered multifactorial sepsis syndrome during BOLD (bleomycin, oncovin, lomustine, and dacarbazine) chemotherapy (see Supplementary Figure S1 online). After targeted antibiotic treatment and combined complication-free chemotherapy, the patient's physical condition improved, and the metastases unexpectedly disappeared. The patient has been asymptomatic and metastasis-free since the end of BOLD therapy. A significant decrease in the volume of the previously palpable axillary and abdominal metastases had already been observed when BOLD therapy was interrupted because of sepsis. A timeline of events is given in Table 1.

Molecular genetics research in the last decade assisted in the development of BRAF inhibitors and immuno-oncological agents, which resulted in significant improvement in the life expectancy of melanoma patients. Dacarbazine-based chemotherapies, once the gold standard (Hobohm, 2001; Wiemann and Starnes, 1994), are still approved and widely applied in melanoma therapy, but their efficacy is relatively low (Garbe et al., 2011). Therefore, the fact that clinical improvement was observed quite early during the chemotherapy suggested other factors behind the outcome, and the concurrent sepsis seemed to offer a potential explanation.

It has long been recognized that cancer patients might recover after bacterial infections (Hobohm, 2001). The hypothesis was that fever and tumor necrosis factor-α induced by the

Abbreviations: BOLD, bleomycin, oncovin, lomustine, and dacarbazine; COX, cyclooxygenase; CP, Chlamydophila pneumoniae; LM, lung metastasis

Accepted manuscript published online 29 December 2015; corrected proof published online 11 February 2016

Table 1. Timeline of clinical case report

Day	
−360	The patient herself detected a bleeding nevus-like lesion on the back and an enlarged axillary lymph node. No steps were taken.
120	Hospital visit. X-ray, mammography, and abdominal Doppler seem to be negative. Axillary lymph node biopsy was proposed. The patient was temporarily lost to follow-up.
0	Hospital visit for abdominal pain. Gastritis was diagnosed, and a gastric polyp was removed. Tumor masses were discovered in the retroperitoneal lymph nodes (15−20 mm), spleen (67 mm), and bladder (40 × 68 mm). Another tumor was detected in the brain by computerized tomography (40 mm).
4	The intracranial tumor mass was removed surgically and diagnosed as amelanotic melanoma metastasis.
24	Cranial radiotherapy was initiated.
30	Leukocytosis, fever. Amoxicillin + clavulanic acid treatment.
32	Radiotherapy completed.
35	BOLD (bleomycin, oncovin, lomustine, and dacarbazine) chemotherapy initiated.
37	Chemotherapy was suspended on the third day because of vomiting and fever. Gastric fluid contained *Escherichia coli* and *Candida albicans*. *Clostridium difficile* toxin also was detected. Fluconazole and ceftriaxone (later metronidazole) treatment was initiated.
52	Central venous catheter was removed because of putative *Pseudomonas aeruginosa* infection, which was later confirmed by blood test.
59	The primary tumor was excised and analyzed (melanoma malignum, Br 1.52 mm, C1. III., pT2b).
77	BOLD, second treatment cycle. Decrease of axillary and abdominal metastases was detected.
120	BOLD, third cycle. Further improvement of the axillary and intra-abdominal metastases was recorded. No intra-abdominal lymphadenomegaly was seen, and a single liver metastasis and shrinking splenic metastasis were detected.
162	BOLD, fourth cycle. Complete remission of the axillary and abdominal metastases was observed.
210	BOLD, fifth cycle. Complete remission of the axillary and abdominal metastases was observed.
255	BOLD, sixth cycle. The patient was asymptomatic, verified by positron emission tomography/computerized tomography to be metastases-free.
>1,500	The patient is asymptomatic, verified by positron emission tomography/computerized tomography to be metastases-free.

infectious agents caused tumor regression, but this could not be reproduced by administration of tumor necrosis factor-α or by hyperthermia (Nauts et al., 1946; Tsung and Norton, 2006). It has been observed that an attenuated form of *Listeria monocytogenes* can infect cancer cells but not normal cells, and this phenomenon resulted in a potentially effective experimental cancer therapy (Quispe-Tintaya et al., 2013).

Vaccination with intracellular pathogens such as bacille Calmette-Guérin or vaccinia virus significantly decreased the incidence of melanoma (Krone et al., 2005). However, a convincing explanation is still missing.

Although it is generally accepted that antitumor immune mechanisms overlap with antibacterial immune responses (Adams, 2009; Chen et al., 2007), the exact mechanism induced by microbes is not understood.

Because immune responses also appear to be decisive factors in the outcome of melanoma (Ridnour et al., 2013; Shimanovsky et al., 2013), we hypothesized that sepsis, by triggering polarized, "joint" antibacterial and antitumor immune responses, could induce tumor regression. This hypothesis was tested in our experimental model.

To clarify the role of the adaptive immune system in the antitumor immune mechanisms induced by *Chlamydophila pneumoniae* (CP; successfully identified in the primary melanoma after our patient recovered from sepsis; see Supplementary Figure S1f), lung metastases (LMs) were induced in immunocompetent C57BL/6 mice or immunodeficient NSG mice. Animals were then CP- or mock-treated (see Supplementary Materials online). To assess the effects of treatment, histological, immunological, and molecular analyses were performed.

In immunocompetent, CP-treated animals, the number of LMs significantly decreased ($P = 0.003$) (Figure 1a) and survival (Figure 1t) significantly increased ($P = 0.04$) compared to mock treatment. This was not observed in immunodeficient mice, and the treated animals did not develop fever (33.2 °C ± 1.0 °C mock vs. 34.8 °C ± 0.5 °C CP) or high plasma levels of tumor necrosis factor-α, which is against the "fever hypothesis" (Hobohm, 2001; Wiemann and Starnes, 1994).

Histological analysis of slices from the lungs of mock-treated melanoma-bearing immunocompetent mice showed a high number of LMs, with frequent intratumor necrosis (Figure 1e). In contrast, fewer and smaller foci of regressive LMs were observed in the CP-treated immunocompetent animals (Figure 1f). Moreover, in this group, high numbers of tumor-infiltrating mononuclear histiocytes and lymphoid cells were identified in the LMs. The LMs did not exhibit significant intratumor immune reactions in the immunodeficient mice, regardless of treatment type (Figure 1g and h). Markedly increased immune reaction in the lungs of the CP-treated mice was also verified by immunolabeling of the cell surface activation markers CD11b and CD80 (Figure 1i−l). Immune cell invasion was not detected after mock treatment; the immune cells were concentrated in the marginal zones of the tumors (Figure 1i and k). In contrast, after CP treatment, marked infiltration by activated lymphocytes was seen in the internal tumor stroma (Figure 1j and l), and the differences were significant ($P = 0.0001$) (Figure 1m and n).

To assess macrophage polarization, M1 (antitumor) or M2 (protumor) macrophage-specific cytokine and chemokine transcriptome profiling was performed (Mantovani et al., 2004). Macrophage markers were detected with quantitative PCR from pooled lung samples 2, 4, and 12 hours after mock or CP treatment. Four hours after CP application, markedly increased levels of M1-specific mRNA transcripts for CCL2, CCL3, IL-6, CXCL10, CCL7, CD80, CXCL11, CXCL9, IL-23, and tumor necrosis factor-α were detected. In line with this, mRNA expression of

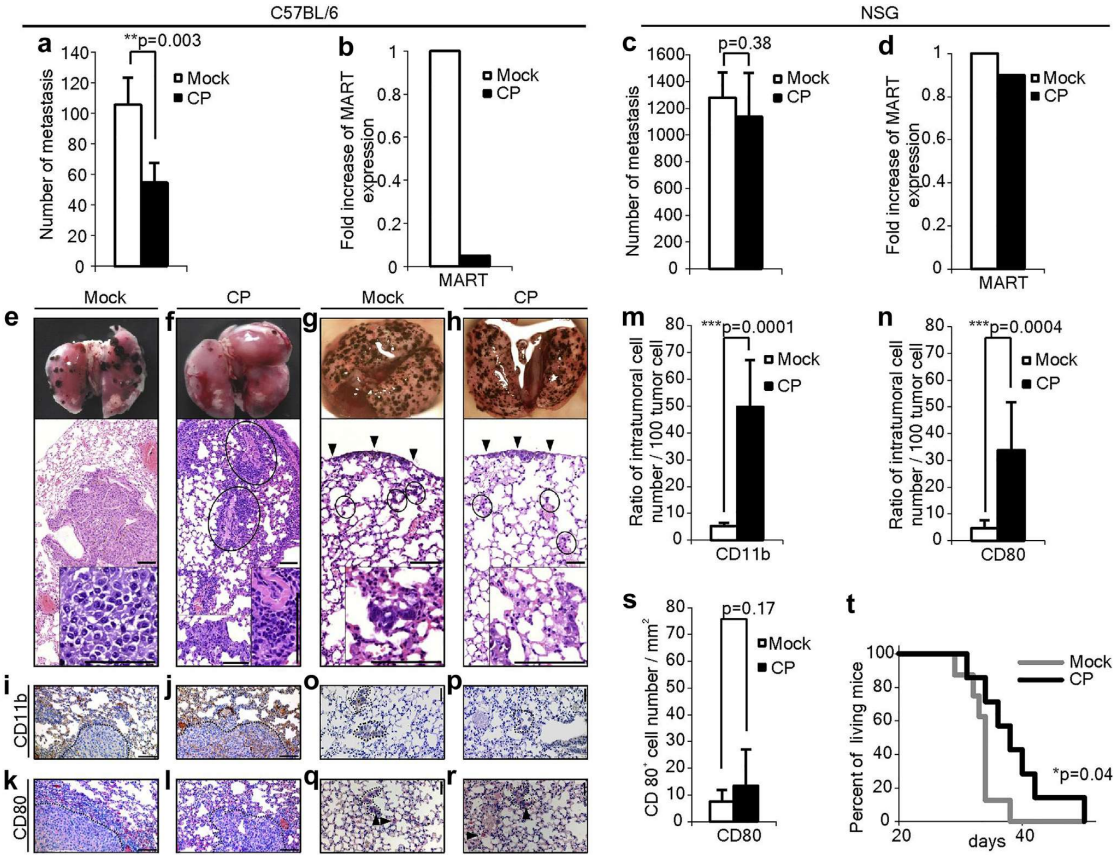

Figure 1. *Chlamydophila pneumoniae* treatment results in melanoma metastasis regression and increases survival of animals as well as of CD11b$^+$ and CD80$^+$ immune cell infiltration of tumor tissues. (**a, c**) Number of lung metastases, (**b, d**) melanoma antigen MART, and (**t**) survival rate of mock or *Chlamydophila pneumoniae* (CP)-treated immunocompetent C57BL/6 and immunodeficient NSG mice. (**e—h**) Representative images and hematoxylin and eosin-stained histological sections of dissected lungs of (**e**) mock and (**f**) CP-treated immunocompetent mice, as well as of (**g**) mock and (**h**) CP-treated immunodeficient (NSG) animals. Note that subpleural metastasis formation is extensive in diameter but not in thickness in NSG mice (arrowheads). Bars = 100 μm. (**e**) Trophical necroses indicate high tumor burden. Inset: atypical tumor cells and regions of necrosis. (**f**) Circles and right inset: foci of regressive metastases. Left inset: areas of residual pneumonitis after CP treatment. (**g, h**) In both mock and CP-treated NSG mice, miliary metastases were developed subpleurally (arrowheads) and intraparenchymally (circles) without significant inflammatory reactions (insets: higher magnification of intraparenchymal metastases). (**i—l**) Immunohistochemistry of (**i, j**) CD11b (diaminobenzidine, brown) and (**k, l**) CD80 (Fast red, red) on lungs of (**i, k**) mock or (**j, l**) CP-treated C57BL/6 mice. Dashed lines indicate tumor border. (**i—r**) Arrows indicate infiltrating immune cells. Intratumoral number of (**m**) CD11b$^+$ and (**n**) CD80$^+$ cells determined as a ratio of 100 tumor cells in C57BL/6 mice. (**s**) CD80$^+$ cells in NSG lungs counted by square millimeter. Data are given as mean ± standard deviation.

most M2-specific markers decreased. Interestingly, the levels of some important M2 markers (CXCL13, IL1Ra) were actually increased (see Supplementary Figure S2a and b online). Upon CP administration, the quantity of M1-specific cytokine and chemokine mRNA was significantly increased ($P = 0.014$) after 4 hours in comparison to M2 markers.

Alteration in the expression pattern of cyclooxygenase (COX)-1 and COX-2 is one of the key markers of macrophage polarization (Mantovani et al., 2013; Martinez et al., 2006). Western blot analysis revealed that 12 hours after CP treatment, protein expression of the M2-specific COX-1 decreased by half, whereas protein expression of the M1-specific COX-2 increased more than twofold (see Supplementary Figure S2c and d).

Two hours after CP treatment but not after mock treatment, CXCL1 melanoma growth factor immunoreactivity become undetectable (see Supplementary Figure S3a and b online). To assess whether this in vivo phenomenon was due to a direct CP-CXCL1 interaction, equal amounts of recombinant CXCL1 were incubated in vitro (in the presence of protease inhibitors) with increasing quantities of CP. CXCL1 levels were determined by western blotting. CP depleted CXCL1 in a dose-dependent manner, suggesting strong and direct binding by CP (see Supplementary Figure S3c and d).

Our results seem to indicate that CP treatment does indeed induce a complex antitumor response. We showed that CP treatment can suppress LM formation in immunocompetent (but not in immunodeficient) mice. M1-type macrophage polarization was

demonstrated, which is associated with antitumor effects (Sica et al., 2008). The antitumor immune polarization/activation was further supported by the profound enrichment of CD80- and CD11b-expressing immune cells in the lungs of CP-treated animals (Prebeck et al., 2001). Of special importance, the melanoma growth factor CXCL1 was completely depleted by CP, both in vivo and in vitro.

Because (i) CXCL1-induced NF-κB activity was shown to facilitate melanoma transformation by allowing melanocytes to escape apoptosis and (ii) IκB-α ΔN (super-repressor of NF-rκB) reduced tumor growth and metastatic potential of melanoma cells (Dhawan et al., 2002), we consider the possible scenario not only that CP induced M1-type macrophage polarization but that CXCL1-induced depletion could significantly contribute to tumor regression. Evidently, results of the animal study strongly support our assumption about the role of sepsis in the observed outcome; however, these data cannot exclude the role of the BOLD therapy. The conclusion that can be safely drawn at this point is that sepsis, in the context of BOLD therapy, resulted in dramatic improvement, otherwise not seen in uncomplicated therapy, which suggests that the occurrence of sepsis was an event of key importance.

CONFLICT OF INTEREST

The authors state no conflict of interest.

ACKNOWLEDGMENTS

This work was approved by The Medical Ethics Committee of University of Szeged and was conducted in accordance with the Declaration of Helsinki Principles. Written informed consent was obtained from our patient. This project has been funded by Hungarian Scientific Research Fund-OTKA PD 84064, OTKA 112493, TAMOP-4.2.2-A-11/1/KONV-2012-0025, IPA HUSRB/1203/214/230. We thank Zoltan Kis and Laszlo Puskas for PCR, Gabriella Dobra for technical assistance; Erno Duda, Janos Minarovits, and Gabor Braunitzer for helpful discussions; and Biocenter Ltd for the RNA purification kit.

***Krisztina Buzás*[1,2,9,*], *Annamária Marton*[2,9], *Csaba Vizler*[2], *Edina Gyukity-Sebestyén*[2], *Mária Harmati*[2], *Katalin Nagy*[1], *Ágnes Zvara*[3], *Róbert L. Katona*[3], *Vilmos Tubak*[4], *Valéria Endrész*[5], *István B. Németh*[6], *Judit Oláh*[6], *László Vígh*[2], *Tamás Bíró*[7] and *Lajos Kemény*[6,8]**

[1]University of Szeged, Faculty of Dentistry, Szeged, Hungary; [2]Hungarian Academy of Sciences, Biological Research Centre, Institute of Biochemistry, Szeged, Hungary; [3]Hungarian Academy of Sciences, Biological Research Centre, Institute of Genetics, Szeged, Hungary; [4]Creative Laboratory Ltd, Szeged, Hungary; [5]Department of Medical Microbiology and Immunobiology, University of Szeged, Szeged, Hungary; [6]Department of Dermatology and Allergology, University of Szeged, Szeged, Hungary; [7]DE-MTA "Lendület" Cellular Physiology Research Group, Departments of Immunology and Physiology, University of Debrecen, Medical Faculty, Debrecen, Hungary; and [8]MTA-SZTE Dermatological Research Group, University of Szeged, Szeged, Hungary
[9]These authors contributed equally to this work.
[*]Corresponding author e-mail: kr.buzas@gmail.com or buzask@brc.hu

SUPPLEMENTARY MATERIAL

Supplementary material is linked to the online version of the paper at www.jidonline.org, and at http://dx.doi.org/10.1016/j.jid.2015.12.032.

REFERENCES

Adams S. Toll-like receptor agonists in cancer therapy. Immunotherapy 2009;1:949–64.

Chen K, Huang J, Gong W, Iribarren P, Dunlop NM, Wang JM. Toll-like receptors in inflammation, infection and cancer. Int Immunopharmacol 2007;7:1271–85.

Dhawan P, Richmond A. Role of CXCL1 in tumorigenesis of melanoma. J Leukoc Biol 2002;72:9–18.

Garbe C, Eigentler TK, Keilholz U, Hauschild A, Kirkwood JM. Systematic review of medical treatment in melanoma: current status and future prospects. Oncologist 2011;16:5–24.

Hobohm U. Fever and cancer in perspective. Cancer Immunol Immunother 2001;50:391–6.

Krone B, Kolmel KF, Henz BM, Grange JM. Protection against melanoma by vaccination with Bacille Calmette-Guerin (BCG) and/or vaccinia: an epidemiology-based hypothesis on the nature of a melanoma risk factor and its immunological control. Eur J Cancer 2005;41:104–17.

Mantovani A, Biswas SK, Galdiero MR, Sica A, Locati M. Macrophage plasticity and polarization in tissue repair and remodelling. J Pathol 2013;229:176–85.

Mantovani A, Sica A, Sozzani S, Allavena P, Vecchi A, Locati M. The chemokine system in diverse forms of macrophage activation and polarization. Trends Immunol 2004;25:677–86.

Martinez FO, Gordon S, Locati M, Mantovani A. Transcriptional profiling of the human monocyte-to-macrophage differentiation and polarization: new molecules and patterns of gene expression. J Immunol 2006;177:7303–11.

Nauts HC, Swift WE, Coley BL. The treatment of malignant tumors by bacterial toxins as developed by the late William B. Coley, M.D., reviewed in the light of modern research. Cancer Res 1946;6:205–16.

Prebeck S, Kirschning C, Dürr S, da Costa C, Donath B, Brand K, et al. Predominant role of toll-like receptor 2 versus 4 in Chlamydia pneumoniae-induced activation of dendritic cells. J Immunol 2001;167:3316–23.

Quispe-Tintaya W, Chandra D, Jahangir A, Harris M, Casadevall A, Dadachova E, et al. Nontoxic radioactive Listeria(at) is a highly effective therapy against metastatic pancreatic cancer. Proc Natl Acad Sci U S A 2013;110:8668–73.

Ridnour LA, Cheng RY, Switzer CH, Heinecke JL, Ambs S, Glynn S, et al. Molecular pathways: toll-like receptors in the tumor microenvironment—poor prognosis or new therapeutic opportunity. Clin Cancer Res 2013;19:1340–6.

Shimanovsky A, Jethava A, Dasanu CA. Immune alterations in malignant melanoma and current immunotherapy concepts. Expert Opin Biol Ther 2013;13:1413–27.

Sica A, Larghi P, Mancino A, Rubino L, Porta C, Totaro MG, et al. Macrophage polarization in tumour progression. Semin Cancer Biol 2008;18:349–55.

Tsung K, Norton JA. Lessons from Coley's toxin. Surg Oncol 2006;15:25–8.

Wiemann B, Starnes CO. Coley's toxins, tumor necrosis factor and cancer research: a historical perspective. Pharmacol Ther 1994;64:529–64.

Supplementary information

Materials and methods

The mouse model

B16F1 melanoma cells (ECACC, Salisbury, UK) were administered intravenously ($1x10^5$ cell/100 µl) to 6-8 week old female immunocompetent C57BL/6 or immuno-deficient NOD/Scid IL2rg null (NSG) mice (Charles River Laboratories, Budapest, Hungary). One week after the tumor cell administration, mice were treated with *C. pneumoniae* strain CWL-029 (VR-029, ATCC, Wesel, Germany) propagated in Hep2 cells (CCL-23, ATCC, Wesel, Germany) (Mantovani *et al.*, 2004). *C. pneumoniae* and the mock control (processed Hep2 cells) were heat-inactivated at 90˚C for 30 minutes. Mice were mildly sedated with sodium pentobarbital (7.5 mg/ml) and treated intranasally with 1×10^6 IFU *C. pneumoniae* 7, 9, 11, 14, and 16 days after tumor implantation. In the case of immune-deficient mice, since physical conditions of NSG mice deteriorated extremely rapidly, animals were euthanized at day 14 after the third *C. pneumoniae* treatment. The special advantages of this model are: (i) with intravenous injection of melanoma cells, visible lung tumor metastases develop within 7 days after injection without significant spreading into other organs; and (ii) *C. pneumoniae* is a lung-specific intracellular pathogen with a significant invasion rate even to the lung metastases. Two hours after the 1st inhalation (day 7), 4 hours after 2nd, 12 hours after 3rd and 24 hours after 5th inhalation, 3 animals/group were anaesthetized and their lungs were harvested for protein, mRNA and histological analysis. The remaining mice received the 4th (day 14) and the 5th (day 16) treatments and were followed for survival. At the end-point, the animals were euthanized, their lungs were removed and 3 independent persons counted the number of surface metastases in a blind fashion.

All animal experiments were performed in accordance with national (1998. XXVIII; 40/2013) and European (2010/63/EU) animal ethics guidelines. The experimental protocols

were approved by the Animal Experimentation and Ethics Committee of the Biological Research Centre of the Hungarian Academy of Sciences and the Hungarian National Animal Experimentation and Ethics Board (clearance number: XVI./03521/2011.). Informed consent was obtained from all subjects.

Survival

For the survival experiments, groups of mice (n=15) were treated as described 5 times after melanoma implantation. Kaplan-Meier survival curves were analyzed by a log-rank statistical test and $p \leq 0.05$ was regarded as statistically significant. The body temperatures of 3 animals/group were measured using an AMA Digital AD 15 TH thermometer 2 hours after the 1st treatment and 4 hours after the 2nd inhalation (day 7 and 9). All animal experiments were authorized by the institutional and national animal welfare committees.

Cytokine and Chemokine Expression Analysis by Quantitative Real-time PCR

Total RNA was purified using a NucleoSpin RNA II RNA isolation kit (Macherey-Nagel, Düren, Germany); first-strand cDNA was synthesized and Q-PCR reactions were performed of M1 type (CCL2, CCL3, CD86, IL12, IL6, IL10, CXCL16, CCL7, CD80, CXCL11, CXCL9, IL23, TNFα) and M2 type (CD163, CXCL13, TGFβ, IL1Ra, CD23, CCL1, CCL22, IL4, CCL17, CCL24, CD150, IL10, CXCL1) markers on pooled samples (n=3) on a RotorGene 3000 instrument (Corbett Research) with gene-specific primers and SYBR Green protocol to monitor gene expression. Each individual Ct value was normalized to the average Ct values of four internal control genes (ΔCt values). The final relative gene expression ratios (fold change) were calculated as comparisons of ΔCt values (ΔΔCt values). Non-template control sample was used for each PCR run to check the primer-dimer formation. Primer sequences are available upon request.

C. pneumoniae detection from the primary tumor of patient by PCR

DNA was extracted from the formalin fixed paraffin-embedded (FFPE) samples using Nucleospin® FFPE DNA kit (Macherey-Nagel, Düren, Germany) according to the manufacturer's instruction. For experiments involving a human subject were performed in accordance with National and Regional Ethics Comitte VI-R-039/01840-2/2012; 25363/2012/EKU; 448/PI/2012. The experimental protocols were approved by the National and Regional Ethics Comitte (clearance number: MCC-INTER-001.)

Histology, immunohistochemistry

Lung specimens were fixed in 4% buffered formaldehyde; then routine HE histology as wells as standardized immunohistochemistry tissue microarray were performed using anti-CD11b (clone M1/70; R&D Systems, Minneapolis, MN) and CD80 (B7-1; R&D Systems, Minneapolis, MN) antibodies.

Cytokine and chemokine detection by proteome profiling

Expression levels of different cytokines in pooled lung specimens were determined using Mouse Cytokine Array Panel A (R&D Systems, Minneapolis, MN), according to the manufacturer's instructions.

Western blot analysis of COX-1 and COX-2

To determine COX-1/COX-2 balance, Western blot analysis was performed using the lung lysates. Samples of total proteins were resolved on NuPAGE 4-12% Bis-Tris Gel, and then transfered to a nitrocellulose membrane. The membrane was incubated with anti-COX-1 (1:250, R&D, Minneapolis, MN) mouse monoclonal antibody and anti-COX-2 (1:200, R&D,

Minneapolis, MN) goat polyclonal antibody. After overnight incubation, the membranes were washed with 1 x TRIS Buffer supplemented with 0,05% Tween20 (Sigma, St. Louis, MO) and incubated for one hour with peroxidase conjugated anti-mouse (1:1000, R&D, Minneapolis, MN) and anti-goat IgG (1:10000, Sigma, St. Louis, MO) and developed using Odyssey Fc chemiluminescence detection system (LiCor Bioscience, Lincoln, NE).

Western blot analysis of CXCL1

Recombinant mouse CXCL1 protein (0.5 μg, R&D Systems, Minneapolis, MN) was mixed and incubated (37°C, 30 min) with different 10-fold (10-10000) dilutions of *C. pneumoniae* solutions (3.6 μg-0.00036 μg). CXCL1 protein amounts were then detected by Western blot analysis using an anti-CXCL1 antibody (1:1000, R&D Systems, Minneapolis, MN).

Statistical analysis

Kaplan-Meier survival curves were analyzed by a log-rank statistical test and $p \leq 0.05$ was regarded as statistically significant. Analyses of other data were performed using two-tailed Student's *t* test.

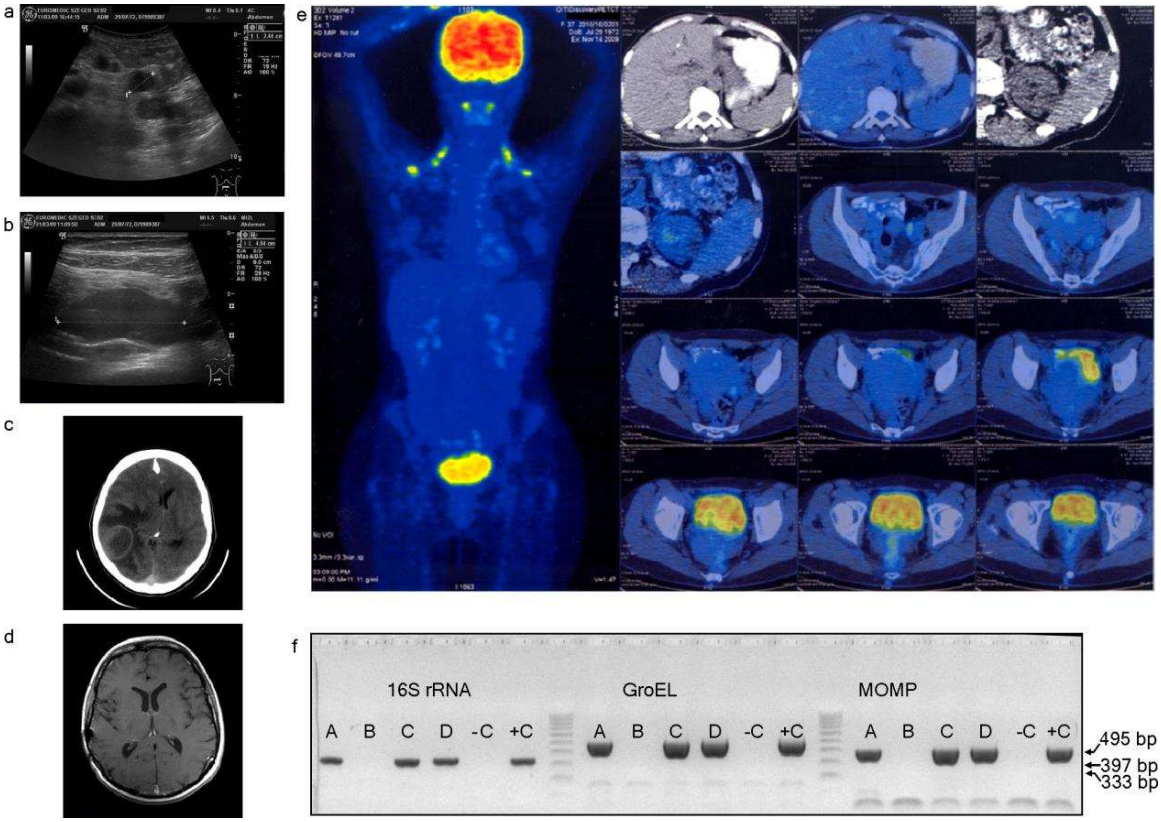

Supplementary Figure 1:

Data obtained with the patient: Complete melanoma metastasis regression verified by PET-CT and retrospective PCR analysis-based detection of *C. pneumoniae*

(**a, b**) Ultrasonography; high tumor burden in the abdominal cavity. (**c, d**) CT and MRI scans; preoperational brain metastasis in the temporooccipital lobe and postoperational tumor-free brain status, respectively. (**e**) PET-CT scans; complete tumor regression in the body shortly after the septic event and BOLD treatment. (**f**) Retrospective detection of *C. pneumoniae* (C. pn.)-specific genes by RT-PCR. 16S rRNA: a housekeeping gene of C. pn. GroEL: Heat shock protein 60 of C. pn., a group I chaperonin expressed on the surface of elementary bodies. MOMP: Major Outer Membrane Protein gene of C. pn. A-D: FFPE samples from different sections of primary melanoma; -C: PCR negative control (uninfected Hep2 cells); +C: PCR positive control (Hep2 cells infected by C. pn. strain TW183).

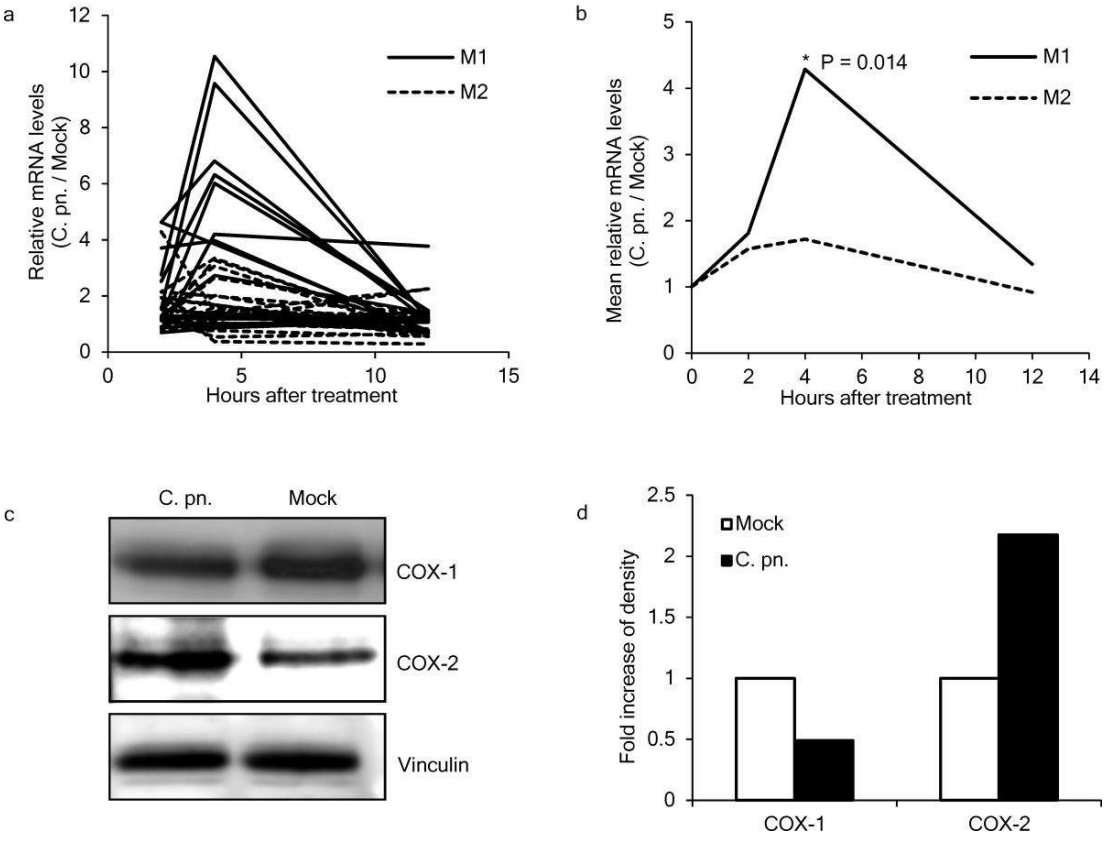

Supplementary Figure 2:

***C. pneumoniae* treatment induces M1 type macrophage polarization**

(**a**) Relative alterations in the levels of individual M1 type and M2 type cytokine/chemokine specific mRNA transcripts in lung samples of *C. pneumoniae* (C. pn.) vs. mock-treated tumor-bearing C57BL/6 mice, as determined by real-time PCR. (**b**) Mean values of relative M1 and M2 cytokine mRNA expressions; at 4 hours after treatment, M1 and M2 levels are significantly different (two-tailed t-test). (**c**) Representative Western blot. Expressions of COX-1 and COX-2 were determined in lung samples 12 hours after *C. pneumoniae* or mock treatment of melanoma-bearing C57BL/6 mice (**d**) Densitometry analysis. Intensity of immunoreactive bands of COX-1 and COX-2 were determined and then normalized to that of vinculin. Data are presented as fold increase compared to values of the mock-treated group (regarded as 1). A minimum of three experiments yielded similar results.

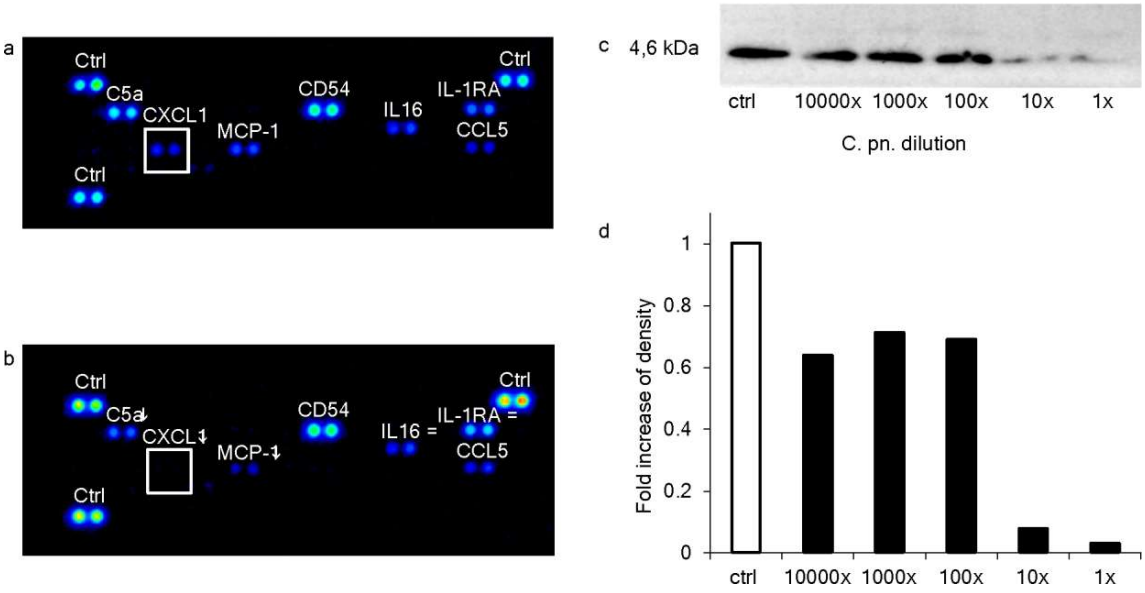

Supplementary Figure 3:

CXCL1 is depleted by *C. pneumoniae* both *in vivo* and *in vitro*

Assessment of cytokine/chemokine protein levels (Proteome profiler) in lungs of melanoma-bearing C57BL/6 mice 2 hours after mock (**a**) or *C. pneumoniae* (**b**) treatment. Squares indicate CXCL1 which disappeared 2 hours after *C. pneumoniae* treatment (**c**) Representative Western blot. Recombinant mouse CXCL1 protein (0.5 μg) was *in vitro* incubated with 500 IUFU/μl (1x) *C. pneumoniae*, (C. pn.) or its 10x, 100x, 1,000x, and 10,000x dilutions and then Western blotting was performed. (**d**) Densitometry analysis of immunoreactive bands shown in panel **c**. Values of the control (ctrl, vehicle treated) group were regarded as 1. Two experiments yielded similar results.

Supplementary Discussion:

The blots of the Proteome Profiler (Suppl. Fig. 3a, b) in the upper left lower left and lower right positions are the so-called assay controls, they merely indicate that the test was technically successful. The rest of the proteins –which could be relevant in the anti-tumoral immune response-are as follows (from left to right and from top to bottom): C5a, CD54, CXCL1, MCP-1, IL-16, IL-1Ra, CCL5.

- **C5a** is a complement protein that has been implicated in tumorigenesis. C5a accelerates tumor progression, can directly activate myeloid-derived suppressor cells, stimulate angiogenesis and cell migration. C5a increases VEGF level, prevents the activation of apoptotic caspase 3 and DNA fragmentation, and may function as an anti-apoptotic molecule (Kim *et al.*, 2005; Gunn *et al.*, 2012). We found decreased levels of this protein after treatment.

- **CD54** (ICAM-1) expresses with a dose- and time-dependent increase in human malignant melanoma cells on stimulation of TNF-alpha. Inhibition of ICAM-1 expression on melanoma cells reduces the metastatic ability of the melanoma cells, indicating an important role of ICAM-1 in metastasis (Miele *et al*., 1994). B. Cava et al. described that metastasis reduction of B16 cells is correlated to the reduction of plasma gelatinolitic activity and to the decrease of cells expressing CD44, CD54, and integrin-β_3 adhesion molecules.

- **CXCL1** is a melanoma growth factor and known as M2 marker. Our results suggest that the depletion of CXCL1 could play a role in the reduction of metastasis formation.

- **MCP-1** (decreased in our model) is produced by a variety of tumors, including B16F1 and plays an important role in tumor progression, especially in angiogenesis (Kim *et al*., 2005;

Koga *et al.*, 2008). Tumor cell-activated macrophages release TNFα, which facilitates the MCP-1 production of tumor cells. Thus, disruption of tumor-stromal cell interaction may inhibit tumor progression by reducing the production of tumor-promoting proinflammatory mediators, such as MCP-1 (Yoshimura *et al.,* 2015).

- **IL-16**: it is a pleiotropic cytokine that functions as a chemoattractant, hence a modulator of T cell activation. The cytokine function is exclusively attributed to the secreted C-terminal peptide, while the N-terminal product may play a role in cell cycle control. Caspase 3 is reported to be involved in the proteolytic processing of this protein (http://www.cancerindex.org/geneweb/IL16.htm). IL-16 appears in the literature remarkably scarcely in connection with cancer, and we could not detect alteration in its level either; therefore, we do not know the relevance of this protein to the discussed observation.

- **IL-1Ra** (moderately decreased or unchanged in our model) is the receptor antagonist of IL-1 and it has been described as pleiotropic (Aubie *et al.*, 2015; Di Mitri *et al.*, 2014). Although IL-1Ra has been described to inhibit subcutaneus B16 melanoma growth *in vivo* (McKenzie et al., 1996) we did not observe significant changes in its level upon treatment; therefore, similar to IL-16, the relevance of this finding is still unknown.

- **CCL5** is a chemokine with tumor supportive properties (Adler *et al.*, 2003; Sugasawa *et al.*, 2008). In rectal cancer, significant decrease of CCL5 was associated with a favorable response to chemoradiation therapy (Tada *et al.*, 2014). Moreover, Mdr2 and CCR5 (CCL5 receptor) double knock-out mice exhibited significant decrease in tumor incidence and size of hepatocellular carcinoma (Barashi *et al.*, 2013). Finally, CCL5 was found to enhance cytotoxicity of regulatory T cells against CD8+ cells (Chang *et al.*, 2012).

Supplementary References

Adler EP, Lemken CA, Katchen NS *et al.* (2003) A dual role for tumor-derived chemokine RANTES (CCL5). *Immunol Lett* 90:187-94

Aubie K. Shaw, Michael W. Pickup, Anna Chytil *et al.* (2015) TGFβ Signaling in Myeloid Cells Regulates Mammary Carcinoma Cell Invasion through Fibroblast Interactions. *PLoS One* 10:e0117908

Barashi N, Weiss ID, Wald O *et al.* (2013) Inflammation-induced hepatocellular carcinoma is dependent on CCR5 in mice. *Hepatology* 58:1021-30

Chang LY, Lin YC, Mahalingam J *et al.* (2012) Tumor-derived chemokine CCL5 enhances TGF-β-mediated killing of CD8(+) T cells in colon cancer by T-regulatory cells. *Cancer Res* 72:1092-102

Di Mitri D, Toso A, Chen JJ *et al.* (2014) Tumour-infiltrating Gr-1+ myeloid cells antagonize senescence in cancer. *Nature* 515:134-7

Gava B, Zorzet S, Spessotto P *et al.* (2006) Inhibition of B16 melanoma metastases with the ruthenium complex imidazolium trans-imidazoledimethylsulfoxide-tetrachlororuthenate and down-regulation of tumor cell invasion. *J Pharmacol Exp Ther* 317:284-91

Gunn L, Ding C, Liu M *et al.* (2012) Opposing roles for complement component C5a in tumor progression and the tumor microenvironment. *J Immunol* 189:2985-94

Kim DY, Martin CB, Lee SN *et al.* (2005) Expression of complement protein C5a in a murine mammary cancer model: tumor regression by interference with the cell cycle. *Cancer Immunol Immunother* 54:1026-37

Kim MY, Byeon CW, Hong KH *et al*. (2005) Inhibition of the angiogenesis by the MCP-1 (monocyte chemoattractant protein-1) binding peptide. *FEBS Lett* 579:1597-601

Koga M, Kai H, Egami K *et al.* (2008) Mutant MCP-1 therapy inhibits tumor angiogenesis and growth of malignant melanoma in mice. *Biochem Biophys Res Commun* 365:279-84

McKenzie RC, Oran A, Dinarello CA *et al.* (1996) Interleukin-1 receptor antagonist inhibits subcutaneous B16 melanoma growth in vivo. *Anticancer Res* 16:437-41

Miele ME, Bennett CF, Miller BE *et al.* (1994) Enhanced metastatic ability of TNF-alpha-treated malignant melanoma cells is reduced by intercellular adhesion molecule-1 (ICAM-1, CD54) antisense oligonucleotides. *Exp Cell Res* 214 :231-41

Sugasawa H, Ichikura T, Kinoshita M *et al.* (2008) Gastric cancer cells exploit CD4+ cell-derived CCL5 for their growth and prevention of CD8+ cell-involved tumor elimination. *Int J Cancer* 122:2535-41

Tada N, Tsuno NH, Kawai K *et al.* (2014) Changes in the plasma levels of cytokines/chemokines for predicting the response to chemoradiation therapy in rectal cancer patients. *Oncol Rep* 31:463-71

Tsung K, Norton JA (2006) Lessons from Coley's Toxin. *Surg Oncol* 15:25-8.

Yoshimura T, Liu M, Chen X *et al.* (2015) Crosstalk between tumor cells and macrophages in stroma renders tumor cells as the primary source of MCP-1/CCL2 in Lewis lung carcinoma. *Front Immunol* 6:332

Wiemann B, Starnes CO (1994) Coley's toxins, tumor necrosis factor and cancer research: a historical perspective. *Pharmacol Ther* 64:529-64.

Published in final edited form as:
Cytokine. 2011 September ; 55(3): 429–434. doi:10.1016/j.cyto.2011.05.018.

Myeloid cells Migrate in Response to IL-24

Krisztina Buzas[a,b], **Joost J. Oppenheim**[a], and **O. M. Zack Howard**[a,*]
[a] Laboratory of Molecular Immunoregulation, Cancer and Inflammation Program, National Cancer Institute-Frederick, Center for Cancer Research, Frederick MD, USA 21702

Abstract

IL-24 (melanoma differentiation associated gene 7 product) is a member of the IL-10 cytokine family that has been reported to possess anti-tumor activity. IL-24 is produced by immune tissues and its expression can be induced in human peripheral blood mononuclear cells by pathogen-associated molecules. While immune cells are known to produce IL-24, the response of immune cells to IL-24 is unclear. Using recombinant human IL-24, we demonstrated that IL-24 induces human monocyte and neutrophil migration, in vitro. An in vivo chemotaxis model showed that IL-24 attracted CD11b positive myeloid cells. To further characterize the chemotactic IL-24 response and type(s) of receptor(s) utilized by IL-24, we treated monocytes with signaling pathway inhibitors. IL-24-induced migration was reduced by pertussis toxin treatment, thus implicating G-protein coupled receptors in this process. Additionally, MEK and JAK inhibitors markedly decreased monocyte migration toward IL-24. These results suggest that IL-24 activates several signaling cascades in immune cells eliciting migration of myeloid cells, which may contribute to the known anti-cancer effects of IL-24.

Keywords

IL-24; Mda-7; monocyte; neutrophil; migration

1. Introduction

IL-24 (or melanoma differentiation associated gene 7 product, mda-7) is best known as a tumor suppressor. It is a member of the IL-10 cytokine family, other family members include IL-20, IL-22, IL-26, IL-28 and IL-29. Further it is produced by immune cells and keratinocytes [1, 2]. Expression of IL-24 can be induced by stimulating peripheral blood mononuclear cells (PBMC) with phytohaemagglutinin (PHA), lipopolysaccharide (LPS), IL-4 or influenza A virus infection [3, 4]. IL-24 induces the expression of proinflammatory cytokines such as IL-6, IFN-γ and TNF-α suggesting a Th1 bias despite its amino acid sequence homology to the classic Th2 cytokine, IL-10 [5].

*Corresponding author: O. M. Zack Howard, 1050 Boyles St, P. O. Box B, Bld 560 Rm 31-19, Frederick MD 21702-1201, howardz@mail.nih.gov, +1 301 846 1348 (P), +1 301 846 6789 (F).
[b]current address National Center for Epidemiology, Microbiological Research Group, Hungary

Conflict of Interest - None

Two heterodimeric receptors have been identified for IL-24 on epithelial and stromal cells [6, 7]: IL-20R2/IL-20R1 and IL-20R2/IL-22R. IL-24 binds to IL-20R2 alone, but heterodimerization with IL-20R1 or IL-22R increases the binding affinity and is necessary for receptor mediated signal transduction. IL-20R1, IL-20R2 and IL-22R1 are not expressed by immune cells[7]. Nevertheless, treating peripheral blood mononuclear cells with IL-24 induces those cells to produce many pro-inflammatory cytokines, suggesting that IL-24 interacts with as yet unidentified receptors on PBMC [5].

Adenovirus delivery of IL-24 (Ad-24) to the intracellular compartment, which circumvents receptor utilisation, induces selective apoptosis in cancer cells, but not normal somatic cells; the exact mechanisms of selective tumor cell death are not fully understood [8–12]. Ad-24 administration to most tumors, including solid tumor e.g., pancreatic, prostate, melanoma, non-small cell lung carcinoma and [13] leukemia cell lines, leads to cell-specific apoptosis. Ad-24 results in the activation of a number of cellular signaling molecules including the caspase cascade, PKR, p38, STAT3, PI3K, GSK-3, ILK-1, BAX, BAK, Fas, DR4, TRAIL, iNOS, IRF-1 and IRF-2 [13–16] and can result in arrest at the G2/M cell cycle phase [17]. Importantly, these signaling molecules are not uniformly expressed by neoplastic and normal cells, suggesting that the tumor selective apoptotic activity of IL-24 is due to the level of signal not presence of signal [18].

IL-10 and IL-20 have been demonstrated to induce cell migration by both direct and indirect methods [19–23]. IL-10 has been shown to enhance Langerhans cell migration from skin, however the molecular mechanism for this effect was not demonstrated [19]. Several indirect mechanisms for IL-10 induced cell migration have been reported, including IL-10-induced increase in CCL2 (MCP-1) expression by human monocytes [23], CCR6 expression by Langerhans cells [21] and cytoskeletal reorganization subsequent to CXCL12 (SDF-1) treatment of B-cells[22]. IL-20 signals through IL-20R1 and IL-20R2 on endothelial cells to induce phosphorylation of MAP kinase family members, which correlated with HUVEC migration and vascular tube formation [20]. IL-24, by stimulating IL-22R on endothelial cells, has been shown to inhibit endothelial cell differentiation and migration [24]. Further, IL-24 (at ng/ml concentrations) has been shown to inhibit TGFalpha-induced keratinocyte proliferation and migration through the IL-20R1/IL-20R2 complex [25]. The effect of IL-24 on immune cell migration has not been reported.

In this study, we investigated the ability of IL-24 to induce leukocyte migration both in vitro and in vivo. We further evaluated the signaling cascade(s) initiated by IL-24 stimulation of monocytes in an effort to elucidate the class of receptor(s) utilized by IL-24 on PBMCs.

2. Materials and Methods

Unless otherwise indicted supplies were obtained from Sigma-Aldrich St. Louis, MO. Recombinant human IL-24 (R&D systems), recombinant human CCL2 (Peprotech, Rocky Hill, NJ).

2.1 Human monocytes and neutrophils

Primary human leukocytes were isolated from fresh normal donor leukapheresis packs under an approved human subjects protocol as previously reported [26]. The blood was centrifuged (600 x gravity for 30 minutes) through Ficoll-Hypaque (Sigma), and peripheral blood mononuclear cells (PBMCs) collected at the interface were washed with PBS and centrifuged through a one step 23% isoosmotic Percoll (Pharmacia, Uppsala, Sweden) gradient (900 x gravity for 30 minutes). The enriched monocyte population was recovered from top of the percoll cushion. The monocyte population is >85% pure based on non-specific esterase stain. The pellet from the Ficoll-Hypaque separation is mixed with 3%

dextran-500 (Pharmacia) and allowed to settle for 30 minutes, the contaminating red blood cells settle leaving 95% granulocytes at the top of the dextran cushion. Following isolation, neutrophils were used for in vitro chemotaxis assays immediately while monocytes were stored overnight at 4ºC in DMEM containing 10% FCS.

2.2 Migrations assays

In vitro chemotaxis assays were performed as described previously [26]. Micro-Boyden chambers were supplied by Neuro Probe (Gaithersburg, MD). Briefly, cells were resuspended at 1 million/ml in chemotaxis media (RPMI containing 1% bovine serum albumin (Sigma) and 25 mM HEPES pH 8 (Gibco)). Standard polycarbonate track-etch (PCTE) membranes (5 um size) were used to separate resupended cells in the upper wells from chemoattractants diluted chemotaxis media. Neutrophils were incubated for 60 minutes at 37°C in the micro-Boyden chambers while monotyces were incubated for 90 minutes. After the cell specific migration time, the membrane was removed from the micro-Boyden chamber, the cell side wiped to remove the cells that did not migrate through the membrane and the membrane with migrated cells was H&E stained. The number of cells migrating was determined by microscopy of the H&E stained membrane at 400 X power. Chemotactic Index was calculated by dividing number of cells counted in the induced migration by number of cells counted in the spontaneous migration. A minimum of 6 determinations were made for each condition. Mean values and standard errors of the mean (SEM) are reported. Graphics were produced and statistical analysis performed using GraphPad Prism. For the “checkerboard” chemokinesis assay, monocytes were pretreated at 37°C with recombinant IL-24 at the indicated concentrations for 30 minutes before being added to the upper wells of the micro-Boyden chamber. To inhibit the signaling of GiCPR we used 100 ng/ml pertussis toxin (List Biological Laboratories, Campbell, CA). 50 μM AG 490 (Calbiochem, La Jolla, CA) was used as a JAK family inhibitor and 50 μM U0126 (Sigma) as a MEK1 and MEK2 inhibitor. Cells suspended in medium were treated with inhibitors at the specific concentrations for 30 min at 37ºC in a water bath.

2.3 In vivo chemotaxis assay - Air Pouch

C57BL/6 mice were provided by Animal Production Area of the NCI (Frederick, MD). NCI-Frederick is accredited by AAALAC International and follows the Public Health Service Policy for the Care and Use of Laboratory Animals. Animal care was provided in accordance with the procedures outlined in the “Guide for Care and Use of Laboratory Animals” (National Research Council; 1996; National Academy Press; Washington, D.C.) The method was adapted from Sironi et al [27, 28]; 3 ml of air was injected subcutaneously into the dorsal surface of the test mouse on day one to form an air pouch. On day three, 2.5 mls of sterile air were be injected into the same site to re-enforce the air pouch. On day six, 1 ml of sterile eliciting agent diluted in HBSS w/o Ca^{2+} and Mg^{2+} was injected into the air pouch. The eliciting agent concentrations were either HBSS or 1000 ng/ml CCL2, 10, 1.0, 0.1 ng/ml IL-24. After 24 hours the test animals were be euthanized by CO_2 and the elicited leukocytes collected for further analysis. Each treatment group contained 5 mice. 5 experiments were conducted with HBSS and 1000 ng/ml CCL2. 4 experiments were conducted with either 10, 1.0 or 0.1 ng/ml IL-24. Mean values and standard errors of the mean (SEM) are reported as are two-tailed Student t-test values comparing test samples to HBSS control samples. Graphics were produced and statistical analysis performed using GraphPad Prism.

2.4 FACS analysis

The cells were fixed by 1% w/v paraformaldehyde in PBS and stained with 0.5μg/ml antibodies against CD3ε (B&D, cat# 553062), CD11b (B&D, cat # 557397), CD45 (BioScience, cat# 48-0451-82), Ly6C (Biolegend, cat#128006), Ly6g (Biolegend, cat#

127614) and F4/80 (eBioscience, cat # 48-4801). Cells were handled in FACS buffer (DPBS without calcium and magnesium, 1% Fetal calf serum, 1% goat sera, 0.02% sodium azide). FACS analysis was performed on Canto II (BD Biosciences) using Diva software. Analysis was performed using FlowJO (Tree Star, Inc.). Mean values and standard errors of the mean (SEM) are reported as are two-tailed Student t-test values comparing test samples to HBSS control samples. The number of repeats was at least 4 for each eliciting agent.

3. Results

3.1 IL-24 induces human monocyte and neutrophil migration in vitro

Using a recombinant human IL-24, we set up in vitro cell migration assays. By using log dilutions of cytokine; we observed maximal migration in the range of 0.125–0.0125 ng/ml. (Fig. 1). One mechanism to demonstrate the difference between directed migration or chemotaxis and increased random movement or chemokinesis is to add IL-24 to the cells before performing a migration assay. If the migration is directional then when cells are exposed to concentrations at or below the migratory maximum concentration (0.125 ng/ml), the cells should migrate without significant changes from the media control. Also, if the migration is directional then when the cells are mixed with IL-24 concentrations higher than the migratory maximum concentration the cells should not migrate toward lower concentrations of IL-24. Shown in Table I, monocyte migration induced by IL-24 is not exclusively directional but contains both chemotactic and chemokinetic migration. This is indicated by the increase in migration observed when the cells are pretreated with 0.001 ng/ml IL-24 followed by exposure to 0.12 ng/ml of IL-24 and the fact that pretreatment with 1.2 ng/ml did not completely block migration although spontaneous migration was reduced. Our results demonstrate the ability of IL-24 to induce human monocytes and neutrophils migration *in vitro*.

3.2 IL-24 induces leukocyte migration in vivo

We next evaluated whether IL-24 recruited cells *in vivo*. Based on earlier studies showing a need for 10 fold more chemoattractant *in vivo* than that needed for maximal *in vitro* activity [28], we evaluated a range of IL-24 from 0.1 ng to 10 ng per mouse. As shown in figure 2, The 0.1 ng dose of IL-24 induced a 2-fold increase in total cells recovered while a 1000 ng dose of CCL2 induced a 1.5-fold increase, both increases are statistically significant. These results indicate that IL-24 can induce cell migration *in vivo* and *in vitro*.

3.3 IL-24 induces subsets of Leukocytes to migrate

In an effort to evaluate the subsets of leukocytes recruited by IL-24 into the mouse air pouch, we performed FACS analysis. Proportionally, there fewer CD3 positive CD45 positive leukocytes recruited by IL-24 than by CCL2, see figures 3A and B. While the majority of the cells recruited by either CCL2 or IL-24 are CD11b positive myeloid cells, IL-24 recruits statistically more CD11b positive F4/80 positive resident macrophage, see figures 3C and D. Both IL-24 and CCL2 recruited similar proportions of CD11b positive, Ly6G high, neutrophils (data not shown).

3.4 Classes of IL-24 migratory receptors on leukocytes

To categorize the classes of receptors used by IL-24 on leukocytes, we treated monocytes with signal cascade inhibitors. Because the majority of chemoattractant receptors are G protein-linked receptors that are sensitive to inhibition by pertussis toxin, we investigated the effect of pertussis toxin on IL-24-induced migration. As shown in Fig. 4A the migration induced by IL-24 was sensitive to pertussis toxin treatment, thus, a G protein-linked receptor of the Gialpha subfamily is implicated in IL-24-induced cell migration.

Many growth factor receptors that have secondary migratory effects are known to activate members of the MAPK family[29]. The receptors for IL-24 expressed by endothelial cells, IL-20R2/IL-20R1 and IL-20R2/IL-22R, are know to signal through the JAK/STAT pathway activation [8, 11, 12, 30]. We therefore tested inhibitors of these pathways and found that MEK, hatched bars compared to solid bars, (Fig. 3B) and JAK, hatched bars compared to solid bars, (Fig. 3C) inhibitors significantly decrease monocyte migration induced by IL-24.

4.0 Discussion

IL-24 induces human monocyte and neutrophil migration in vitro and leukocyte migration in vivo

We have observed that IL-24 attracts monocytes and neutrophils at very low (0.0125ng/ml) concentration *in vitro*. This indicates that IL-24 is a potent *in vitro* chemoattractant of myeloid cells and that the effect of IL-24 is likely to be due to its direct action on myeloid cells since the in vitro assay, at most, requires 90 minutes of exposure to the IL-24 to be complete. Using the murine air pouch migration model, we observed that injection of recombinant IL-24 increased leukocyte infiltration 2-fold *in vivo*. FACS analyses of attracted cells showed that the majority of the cells recruited into a mouse air pouch are CD45 positive and CD11b positive myeloid cells (≈ 80%) regardless of the eliciting agent, however, double the total cell number of cells was recruited by IL-24 vs. buffered saline indicating that IL-24 recruited myeloid cells *in vivo*. IL-24 attracts 10% more CD11b positive, F4/80 positive cells than either CCL2 or buffered saline. Expression of F4/80 is reported to identify a more mature, connective tissue, resident macrophage [31], like the macrophage found in the skin. Others have shown that over expressing IL-24 in mouse skin increased CCL2 expression and macrophage infiltration into the dermis [32]. Our data is in agreement with He and Liang's observation that over expressing IL-24 in mouse skin did not increase lymphocyte recruitment [32]. Taken together, these observations suggest that IL-24 both directly and indirectly contributes to the recruitment of macrophages.

Both CCL2 and IL-24 recruit equal numbers of CD11b positive Ly6G high granulocytes. This observation in conjunction with an earlier observation that IL-24 stimulates granulocytes to produce IFN-gamma, IL-12 and nitric oxide, which leads to an innate response restricting salmonella infection and contributes to activation of CD8 responses [33], suggests that IL-24 might both recruit and activate neutrophils. Further, our data permits the speculation that localized production or administration of IL-24 could drive myeloid cell invasion of tumor sites. Together these findings lead us to propose an additional basis for the anti-tumor effect of IL-24, namely recruitment of neutrophils and macrophage by IL-24 not only promotes a Th1 response, but may also promote cytotoxic T-cell activation [5, 33].

Classes of IL-24 migratory receptors on leukocytes

In this study we show that the oncolytic cytokine, IL-24, can induce monocyte migration at low concentrations (pg/ml) and this migration is sensitive to inhibition by Gialpha-protein, JAK and MEK inhibitors. No single chain receptor utilizes all these pathways, suggesting that multiple IL-24 receptor types are expressed on myeloid cells or that the IL-24 receptor on myeloid cells is a multi-component receptor. Our observation that an inhibitor of JAK kinases blocks monocyte movement toward IL-24 suggests that an IL-10R family member could be involved in cell migration [34] since IL-10R1 and R2, IL-20R1 and R2, IL-22R1, and IFN-λR1 each utilize different JAK kinases to transmit signals to the STATs. IL-10R2 is a common low affinity ligand binding and signaling chain in IL-10, IL-22, IL-26, IL-28A (IFN-λ2), IL28B (IFN-λ3) and IL-29 (IFN-λ1) cell activation and it is expressed by most cell types [35]. This is in contrast to other members of the IL-10R family, which have more

restricted expression profiles. It is appealing to hypothesize that IL-10R2 is also a component of the IL-24 signaling receptor on leukocytes, but as it is unlikely to be the high affinity receptor we are unable to confirm this. Earlier studies to characterize the viral IL-10 receptor complex illustrated the need for at least two components of the receptor in order to obtain both binding and signal transduction [36]. At this time we do not have a candidate for the high affinity IL-24 receptor on myeloid cells. Further, our data showed that inhibiting MEK, which is common to both the Gialpha-protein and IL10R signal cascade, also inhibited the IL-24 induced migration of monocytes. Taken together, our data suggests that the IL-24 receptor complex on myeloid cells is a multi-component receptor using G-protein, JAK and MEK signaling pathways. This is distinct from the characterized IL-24 receptor complexes expressed by endothelial cells, which are composed of IL-20R1/R2 or IL-22R1/IL-20R2 and do not depend on G-protein signal transduction. The fact that IL-24 appears to have a leukocyte specific receptor complex is not unique among the IL-10 family of cytokines. IL-19, and IL-20, [32, 34] use the same promiscuous receptor complex as IL-24 (IL-20R1/R2) on keratinocytes, but leukocytes don't express those receptors. However, IL-19 induces monocytes to express TNF and IL-6 [37] and IL-20 induces neutrophil migration [38], suggesting that a leukocyte specific receptor complex may exist for a subset of the IL-10 family of cytokines. We therefore hypothesize the existence of a novel receptor complex consisting of IL10R2 plus a novel high affinity binding receptor for IL-24, IL19 and IL-20 on leukocytes, which is responsible for the leukocyte activation and migration induced by these cytokines.

5.0 Conclusion

Our studies demonstrate that IL-24 induces myeloid cell migration both in vitro and in vivo.

Acknowledgments

This Research was supported by the Intramural Research Program of the NIH, National Cancer Institute, Center for Cancer Research

In vivo chemotaxis assays has been supported by a UICC International Cancer Technology Transfer Fellowship

References

1. Kunz S, Wolk K, Witte E, Witte K, Doecke WD, Volk HD, Sterry W, Asadullah K, Sabat R. Interleukin (IL)-19, IL-20 and IL-24 are produced by and act on keratinocytes and are distinct from classical ILs. Exp Dermatol. 2006; 15:991–1004. [PubMed: 17083366]
2. Commins S, Steinke JW, Borish L. The extended IL-10 superfamily: IL-10, IL-19, IL-20, IL-22, IL-24, IL-26, IL-28, and IL-29. J Allergy Clin Immunol. 2008; 121:1108–11. [PubMed: 18405958]
3. Buzas K, Megyeri K. Staphylococci induce the production of melanoma differentiation-associated protein-7/IL-24. Acta Microbiol Immunol Hung. 2006; 53:431–40. [PubMed: 17278711]
4. Garn H, Schmidt A, Grau V, Stumpf S, Kaufmann A, Becker M, Gemsa D, Siese A. IL-24 is expressed by rat and human macrophages. Immunobiology. 2002; 205:321–34. [PubMed: 12182458]
5. Caudell EG, Mumm JB, Poindexter N, Ekmekcioglu S, Mhashilkar AM, Yang XH, Retter MW, Hill P, Chada S, Grimm EA. The protein product of the tumor suppressor gene, melanoma differentiation-associated gene 7, exhibits immunostimulatory activity and is designated IL-24. J Immunol. 2002; 168:6041–6. [PubMed: 12055212]
6. Zheng M, Bocangel D, Doneske B, Mhashilkar A, Ramesh R, Hunt KK, Ekmekcioglu S, Sutton RB, Poindexter N, Grimm EA, Chada S. Human interleukin 24 (MDA-7/IL-24) protein kills breast cancer cells via the IL-20 receptor and is antagonized by IL-10. Cancer Immunol Immunother. 2007; 56:205–15. [PubMed: 16710719]

7. Nagalakshmi ML, Murphy E, McClanahan T, de Waal Malefyt R. Expression patterns of IL-10 ligand and receptor gene families provide leads for biological characterization. Int Immunopharmacol. 2004; 4:577–92. [PubMed: 15120644]
8. Wang M, Liang P. Interleukin-24 and its receptors. Immunology. 2005; 114:166–70. [PubMed: 15667561]
9. Sarkar D, Lebedeva IV, Gupta P, Emdad L, Sauane M, Dent P, Curiel DT, Fisher PB. Melanoma differentiation associated gene-7 (mda-7)/IL-24: a 'magic bullet' for cancer therapy? Expert Opin Biol Ther. 2007; 7:577–86. [PubMed: 17477796]
10. Fisher PB, Sarkar D, Lebedeva IV, Emdad L, Gupta P, Sauane M, Su ZZ, Grant S, Dent P, Curiel DT, Senzer N, Nemunaitis J. Melanoma differentiation associated gene-7/interleukin-24 (mda-7/IL-24): novel gene therapeutic for metastatic melanoma. Toxicol Appl Pharmacol. 2007; 224:300–7. [PubMed: 17208263]
11. Gupta P, Su ZZ, Lebedeva IV, Sarkar D, Sauane M, Emdad L, Bachelor MA, Grant S, Curiel DT, Dent P, Fisher PB. mda-7/IL-24: multifunctional cancer-specific apoptosis-inducing cytokine. Pharmacol Ther. 2006; 111:596–628. [PubMed: 16464504]
12. Kotenko SV, Langer JA. Full house: 12 receptors for 27 cytokines. Int Immunopharmacol. 2004; 4:593–608. [PubMed: 15120645]
13. Qian W, Liu J, Tong Y, Yan S, Yang C, Yang M, Liu X. Enhanced antitumor activity by a selective conditionally replicating adenovirus combining with MDA-7/interleukin-24 for B-lymphoblastic leukemia via induction of apoptosis. Leukemia. 2007
14. Kotenko SV. The family of IL-10-related cytokines and their receptors: related, but to what extent? Cytokine Growth Factor Rev. 2002; 13:223–40. [PubMed: 12486876]
15. Sarkar D, Su ZZ, Lebedeva IV, Sauane M, Gopalkrishnan RV, Valerie K, Dent P, Fisher PB. mda-7 (IL-24) Mediates selective apoptosis in human melanoma cells by inducing the coordinated overexpression of the GADD family of genes by means of p38 MAPK. Proc Natl Acad Sci U S A. 2002; 99:10054–9. [PubMed: 12114539]
16. Yacoub A, Mitchell C, Hong Y, Gopalkrishnan RV, Su ZZ, Gupta P, Sauane M, Lebedeva IV, Curiel DT, Mahasreshti PJ, Rosenfeld MR, Broaddus WC, James CD, Grant S, Fisher PB, Dent P. MDA-7 regulates cell growth and radiosensitivity in vitro of primary (non-established) human glioma cells. Cancer Biol Ther. 2004; 3:739–51. [PubMed: 15197348]
17. Wang CJ, Xue XB, Yi JL, Chen K, Zheng JW, Wang J, Zeng JP, Xu RH. Melanoma differentiation-associated gene-7, MDA-7/IL-24, selectively induces growth suppression, apoptosis in human hepatocellular carcinoma cell line HepG2 by replication-incompetent adenovirus vector. World J Gastroenterol. 2006; 12:1774–9. [PubMed: 16586551]
18. Lebedeva IV, Emdad L, Su ZZ, Gupta P, Sauane M, Sarkar D, Staudt MR, Liu SJ, Taher MM, Xiao R, Barral P, Lee SG, Wang D, Vozhilla N, Park ES, Chatman L, Boukerche H, Ramesh R, Inoue S, Chada S, Li R, De Pass AL, Mahasreshti PJ, Dmitriev IP, Curiel DT, Yacoub A, Grant S, Dent P, Senzer N, Nemunaitis JJ, Fisher PB. mda-7/IL-24, novel anticancer cytokine: focus on bystander antitumor, radiosensitization and antiangiogenic properties and overview of the phase I clinical experience (Review). Int J Oncol. 2007; 31:985–1007. [PubMed: 17912425]
19. Halliday GM, Le S. Transforming growth factor-beta produced by progressor tumors inhibits, while IL-10 produced by regressor tumors enhances, Langerhans cell migration from skin. Int Immunol. 2001; 13:1147–54. [PubMed: 11526095]
20. Hsieh MY, Chen WY, Jiang MJ, Cheng BC, Huang TY, Chang MS. Interleukin-20 promotes angiogenesis in a direct and indirect manner. Genes Immun. 2006; 7:234–42. [PubMed: 16511554]
21. Dieu-Nosjean MC, Massacrier C, Vanbervliet B, Fridman WH, Caux C. IL-10 induces CCR6 expression during Langerhans cell development while IL-4 and IFN-gamma suppress it. J Immunol. 2001; 167:5594–602. [PubMed: 11698430]
22. Balabanian K, Foussat A, Bouchet-Delbos L, Couderc J, Krzysiek R, Amara A, Baleux F, Portier A, Galanaud P, Emilie D. Interleukin-10 modulates the sensitivity of peritoneal B lymphocytes to chemokines with opposite effects on stromal cell-derived factor-1 and B-lymphocyte chemoattractant. Blood. 2002; 99:427–36. [PubMed: 11781221]

23. Musso T, Cappello P, Stornello S, Ravarino D, Caorsi C, Otero K, Novelli F, Badolato R, Giovarelli M. IL-10 enhances CCL2 release and chemotaxis induced by CCL16 in human monocytes. Int J Immunopathol Pharmacol. 2005; 18:339–49. [PubMed: 15888256]
24. Ramesh R, Mhashilkar AM, Tanaka F, Saito Y, Branch CD, Sieger K, Mumm JB, Stewart AL, Boquoi A, Dumoutier L, Grimm EA, Renauld JC, Kotenko S, Chada S. Melanoma differentiation-associated gene 7/interleukin (IL)-24 is a novel ligand that regulates angiogenesis via the IL-22 receptor. Cancer Res. 2003; 63:5105–13. [PubMed: 12941841]
25. Poindexter NJ, Williams RR, Powis G, Jen E, Caudle AS, Chada S, Grimm EA. IL-24 is expressed during wound repair and inhibits TGFalpha-induced migration and proliferation of keratinocytes. Exp Dermatol. 2010; 19:714–22. [PubMed: 20545760]
26. Howard OM, Dong HF, Su SB, Caspi RR, Chen X, Plotz P, Oppenheim JJ. Autoantigens signal through chemokine receptors: uveitis antigens induce CXCR3- and CXCR5-expressing lymphocytes and immature dendritic cells to migrate. Blood. 2005; 105:4207–14. [PubMed: 15713799]
27. Clish CB, O'Brien JA, Gronert K, Stahl GL, Petasis NA, Serhan CN. Local and systemic delivery of a stable aspirin-triggered lipoxin prevents neutrophil recruitment in vivo. Proc Natl Acad Sci U S A. 1999; 96:8247–52. [PubMed: 10393980]
28. Sironi M, Guglielmotti A, Polentarutti N, Fioretti F, Milanese C, Romano M, Vigini C, Coletta I, Sozzani S, Bernasconi S, Vecchi A, Pinza M, Mantovani A. A small synthetic molecule capable of preferentially inhibiting the production of the CC chemokine monocyte chemotactic protein-1. Eur Cytokine Netw. 1999; 10:437–42. [PubMed: 10477401]
29. Tian YC, Chen YC, Chang CT, Hung CC, Wu MS, Phillips A, Yang CW. Epidermal growth factor and transforming growth factor-beta1 enhance HK-2 cell migration through a synergistic increase of matrix metalloproteinase and sustained activation of ERK signaling pathway. Exp Cell Res. 2007; 313:2367–77. [PubMed: 17467690]
30. Wang M, Tan Z, Thomas EK, Liang P. Conservation of the genomic structure and receptor-mediated signaling between human and rat IL-24. Genes Immun. 2004; 5:363–70. [PubMed: 15175645]
31. Schaller E, Macfarlane AJ, Rupec RA, Gordon S, McKnight AJ, Pfeffer K. Inactivation of the F4/80 glycoprotein in the mouse germ line. Mol Cell Biol. 2002; 22:8035–43. [PubMed: 12391169]
32. He M, Liang P. IL-24 transgenic mice: in vivo evidence of overlapping functions for IL-20, IL-22, and IL-24 in the epidermis. J Immunol. 2010; 184:1793–8. [PubMed: 20061404]
33. Ma Y, Chen H, Wang Q, Luo F, Yan J, Zhang XL. IL-24 protects against Salmonella typhimurium infection by stimulating early neutrophil Th1 cytokine production, which in turn activates CD8+ T cells. Eur J Immunol. 2009; 39:3357–68. [PubMed: 19830736]
34. Trivella DB, Ferreira-Junior JR, Dumoutier L, Renauld JC, Polikarpov I. Structure and function of interleukin-22 and other members of the interleukin-10 family. Cell Mol Life Sci. 2010; 67:2909–35. [PubMed: 20454917]
35. Diegelmann J, Beigel F, Zitzmann K, Kaul A, Goke B, Auernhammer CJ, Bartenschlager R, Diepolder HM, Brand S. Comparative Analysis of the Lambda-Interferons IL-28A and IL-29 regarding Their Transcriptome and Their Antiviral Properties against Hepatitis C Virus. PLoS One. 2010; 5:e15200. [PubMed: 21170333]
36. Ding Y, Qin L, Zamarin D, Kotenko SV, Pestka S, Moore KW, Bromberg JS. Differential IL-10R1 expression plays a critical role in IL-10-mediated immune regulation. J Immunol. 2001; 167:6884–92. [PubMed: 11739506]
37. Liao YC, Liang WG, Chen FW, Hsu JH, Yang JJ, Chang MS. IL-19 induces production of IL-6 and TNF-alpha and results in cell apoptosis through TNF-alpha. J Immunol. 2002; 169:4288–97. [PubMed: 12370360]
38. Hsu YH, Li HH, Hsieh MY, Liu MF, Huang KY, Chin LS, Chen PC, Cheng HH, Chang MS. Function of interleukin-20 as a proinflammatory molecule in rheumatoid and experimental arthritis. Arthritis Rheum. 2006; 54:2722–33. [PubMed: 16947773]

- IL-24 induces human monocyte and neutrophil migration, in vitro.
- IL-24 attracted CD11b positive murine myeloid cells, in vivo.
- Pertussis toxin, MEK and JAK inhibitors reduced IL-24-induced migration.
- IL-24 activates several nonredundant signaling cascades in immune cells.

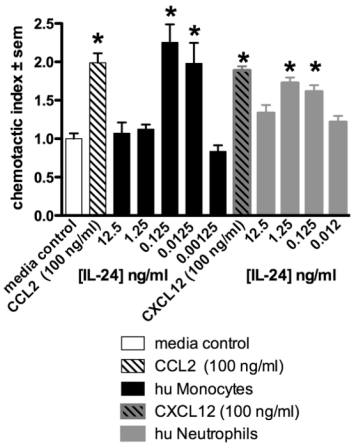

Figure 1. IL-24 induced human monocyte and neutrophil migration – In vitro

Human monocytes were assayed for chemotactic activity using a micro-Boyden chamber. Recombinant human IL-24 was acquired from R&D Systems and diluted in chemotaxis media. Chemotactic Index is shown on the y-axis and is relative to spontaneous migration, mean and sem are reported. Migration of human monocytes are shown with right hatched and black bars, while migration of human neutrophils is shown with gray bars. * indicate a p-value < 0.001 relative to spontaneous migration, determined by unpaired T-test. N>6

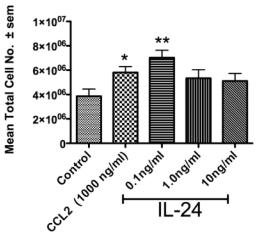

Figure 2. IL-24 induced leukocyte migration - in vivo

Recombinant IL-24 in HBSS was injected into air pouches formed on the back of C57BL/6 mice. Twenty-four hours later, cells were recovered from the air pouches and counted. Mean cell numbers in millions ± sem are reported for each treatment condition, with the control being HBSS containing no chemoattractant. * p= 0.01 student-T two tailed compared to control ** p=0.003 student-T two tailed compared to control. N≥4.

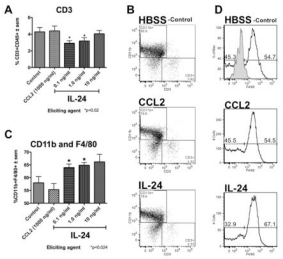

Figure 3. FACS analysis of in vivo recruited leukocytes

A. Mean proportion or percentage of all recruited leukocytes staining positive for both CD45 and CD3 is shown, along with ± sem, compared to different eliciting agents injected into the air pouch N≥4. **B.** Representative dot plot graphic of recruited CD45 gated cells stained for CD3 on the x-axis or CD11b on the y-axis. Percentage of CD45 gated cells staining positive for either CD3 or CD11b are reported in the inset. **C.** Mean percentage of recruited CD11b positive cells also staining positive for F4/80 is shown ± sem, compared to different eliciting agents injected into the air pouch N≥4 **D.** Representative histograms of CD11b+ cells that are also F4/80 positive. Percentage positive (to the right) or negative (to the left) is shown by inset numbers. The shaded histogram shows an isotype control for F4/80. *p≤0.024 compared to control HBSS injected into the air pouch

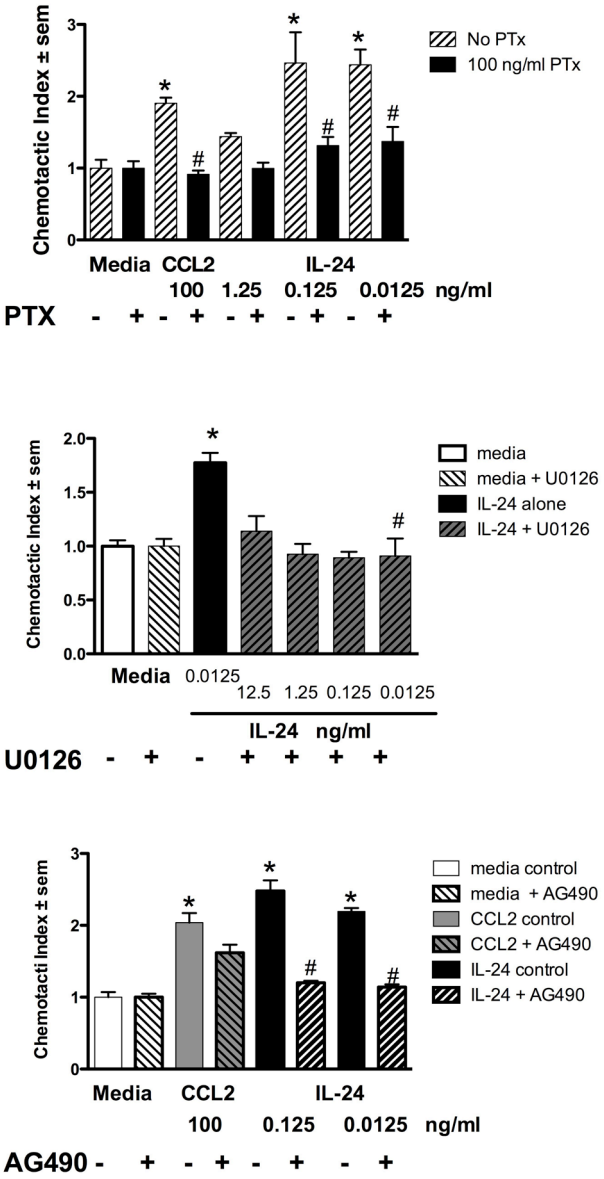

Figure 4. IL-24-induced human monocyte migration can be inhibited

A. Pertussis toxin pretreatment inhibits IL-24 induced monocyte chemotaxis. Chemotaxis to media, CCL2 or IL-24 is shown in hatched bars. The chemotaxis of monocytes pretreated for 30 minutes with 100ng/ml pertussis toxin is shown in solid black bars. * indicates increases in migration with p-values >0.001 compared to media control # indicates decreases in migration with p-values >0.01 compared to no pertussis toxin at the same concentration of chemoattractant. **B: Pretreatment of monocytes with U0126 inhibits IL-24-induced monocyte chemotaxis.** Human monocytes were pretreated for 30 minutes with 50μM U0126 (MEK inhibitor) prior to being placed in a micro-Boyden chamber. Media alone is shown in white bars. IL-24 is shown with black bars. U0126 treatment is indicted in hatched bars. * indicates increases in migration with p-values >0.001 compared to media control # indicates decreases in migration with p-values > 0.001 compared to no U0126 treatment **C: Pretreatment of monocytes with AG 490 inhibits IL-24-induced monocyte chemotaxis** Human monocytes were incubated with 50 μM AG

490 (JAK inhibitor) for 30 minutes prior to being placed in a chemotaxis chamber. Media is shown with white bars, CCL2 (100 ng/ml) is shown with gray bars, IL-24 is shown with black bars. AG-490 treated cells are shown with hatched bars. * indicates increases in migration with p-values >0.001 compared to media control # indicates decreases in migration with p-values > 0.001 compared to no AG-490 treatment. N > 6

Table I

Checkerboard analysis of IL-24 induced monocyte migration

Human monocytes were pretreated with media (0), 1.2 ng/ml, 0.12 ng/ml or 0.001 ng/ml of IL-24 for 30 minutes prior to being placed in a micro Boyden chemotaxis chamber. Across the top of the table are the pretreatment conditions and along the left hand side of the table are the lower well chemoattractant concentrations. Reported in this table are the mean cell number and SEM for each of the conditions. N>3 The mean cell no. per high powered field ± sem from 3 donors is reported

Upper wells pretreatment/lower wells	1.2 ng/ml	0.12 ng/ml	0.001 ng/ml	0
0 ng/ml	5.9 ± 1.0#	7.0 ± 1.0	10.18 ± 1.5	8.8 ± 1.1
.001	7.7 ± 1.0	15.4 ± 1.6**	7.3 ± 0.7	6.7 ± 1.2
.12	12.6 ± 1.8*	18.4 ± 2.6**	20.9 ± 3.9**	18.4 ± 3.0**
1.2	10.4 ± 1.9	10.4 ± 2.2	n.d.	12.4 ± 2.1

p=0.01 reduced

* p=0.05 increased

** P•0.006 increased

n.d = not determined for all donors

Immunology Letters 148 (2012) 34–38

Contents lists available at SciVerse ScienceDirect

Immunology Letters

journal homepage: www.elsevier.com/locate/immlet

Melanoma cell-derived exosomes alter macrophage and dendritic cell functions *in vitro*

Annamaria Marton[a], Csaba Vizler[a], Erzsebet Kusz[a], Viktoria Temesfoi[a], Zsuzsa Szathmary[b], Krisztina Nagy[c], Zsolt Szegletes[c], Gyorgy Varo[c], Laszlo Siklos[c], Robert L. Katona[d], Vilmos Tubak[a], O.M. Zack Howard[e], Erno Duda[a], Janos Minarovits[f], Katalin Nagy[g], Krisztina Buzas[a,g,*]

[a] *Institute of Biochemistry, Biological Research Center of the Hungarian Academy of Sciences, Szeged, Hungary*
[b] *Galenbio Kft, Mosonmagyaróvár, Hungary*
[c] *Institute of Biophysics, Biological Research Center of the Hungarian Academy of Sciences, Szeged, Hungary*
[d] *Institute of Genetics, Biological Research Center of the Hungarian Academy of Sciences, Szeged, Hungary*
[e] *National Cancer Institute-Frederick, Laboratory of Molecular Immunoregulation, Frederick, MD 21702-1201, United States*
[f] *National Center for Epidemiology, Microbiological Research Group, Budapest, Hungary*
[g] *Faculty of Dentistry, University of Szeged, Hungary*

ARTICLE INFO

Article history:
Received 23 December 2011
Received in revised form 6 July 2012
Accepted 30 July 2012
Available online 8 August 2012

Keywords:
Melanoma
Tumor immunity
Exosomes
Cytokine profile

ABSTRACT

To clarify controversies in the literature of the field, we have purified and characterized B16F1 melanoma cell derived exosomes (mcd-exosomes) then we attempted to dissect their immunological activities. We tested how mcd-exosomes influence CD4+ T cell proliferation induced by bone marrow derived dendritic cells; we quantified NF-κB activation in mature macrophages stimulated with mcd-exosomes, and we compared the cytokine profile of LPS-stimulated, IL-4 induced, and mcd-exosome treated macrophages. We observed that mcd-exosomes helped the maturation of dendritic cells, enhancing T cell proliferation induced by the treated dendritic cells. The exosomes also activated macrophages, as measured by NF-κB activation. The cytokine and chemokine profile of macrophages treated with tumor cell derived exosomes showed marked differences from those induced by either LPS or IL-4, and it suggested that exosomes may play a role in the tumor progression and metastasis formation through supporting tumor immune escape mechanisms.

1. Introduction

Previous studies showed that cultured human tumor cells release exosomes, *i.e.*, microvesicles of 20–100 nm diameters. Exosomes bear the molecular markers of the originating tumor cells' plasma membrane. Among others, exosomes contain structural proteins, MHC molecules and cell surface molecules typically associated with apoptosis; therefore they are possible inducers of anti-tumor immune responses [1]. The immunomodulatory activities of tumor exosomes are poorly understood, with reported activating [2] and inhibitory effects [3]. The wide range of observed biological effects seems to depend on tumor type and staging.

The size of exosomes may facilitate their *in vivo* penetration and interaction with different host cell types, even distant from the tumor mass. Exosomes have been shown to participate in cell-to-cell communication by various mechanisms. The most obvious mechanism involves membrane proteins, partially identical with those of the originating tumor cells. Upon endocytosis, exosomes may deliver their active components, proteins and RNA, directly into the cytoplasm of bystander cells. These transport processes can influence invasion of tumor cells, stimulate antigen specific T-cell responses, modulate cell polarity and have a role in the developmental patterning of tissues [4]. Exosomes may also have an important role in tumor immune evasion by direct suppression of immune cell activation.

By dissecting the immunomodulatory effects of melanoma cell derived exosomes we wished to clarify some of the controversies in the literature of the field. We tested how mcd-exosomes influence the CD4+ T cell proliferation induced by bone marrow derived dendritic cells (DCs). We quantified the NF-κB activation in mature macrophages stimulated with mcd-exosomes. We qualified the production pattern of inflammatory cytokines and chemokines that have previously been identified as mediators or regulators of anti-cancer responses. Our findings suggest that, in spite of their immune activating effects detectable in our model, the concomitant

* Corresponding author at: Biological Research Centre of the Hungarian Academy of Sciences, Szeged and at the Faculty of Dentistry, University of Szeged, Hungary.
E-mail addresses: kr.buzas@gmail.com, buzask@brc.hu (K. Buzas).

0165-2478/$ – see front matter © 2012 Elsevier B.V. All rights reserved.
http://dx.doi.org/10.1016/j.imlet.2012.07.006

immune suppressive activity of tumor-derived exosomes could contribute to tumor immune escape.

2. Materials and methods

2.1. Isolation of exosomes

mcd-exosomes were prepared according to an earlier protocol [5]. B16 supernatants were centrifuged at 3900 × *g* for 10 min at 4 °C to remove cells, than filtered through a 0.2 μm membrane (Millipore, Billerica, MA) to remove cell debris. Exosomes were pelleted by ultracentrifugation at 150,000 RCF (Ti 70 rotor 38,200 rpm for 1 h, Optima LE-80K ultracentrifuge, Beckman/T1270 rotor at 40,500 rpm for 1 h, Sorvall Discovery 90SE ultracentrifuge, Hitachi) at 4 °C. Pellet was washed twice and resuspended in DPBS and stored at −80 °C.

2.2. Exosome characterization

Exosomes were let to adsorb to the freshly cleaved muscovite mica (SPI-Chem™ Mica Sheets, Structure Probe, Inc., West Chester, PA, USA) surface directly from buffer solution (20 mM Tris, 130 mM NaCl, pH = 7). All AFM measurements were carried out with an Asylum MFP-3D head and Molecular Force Probe Controller (Asylum Research, Santa Barbara, CA), using MFP-3D Xop driver program written in Igor Pro software (version 6.2.2, Wavemetrics, Lake Oswego, OR). Image procession and data calculation were made in the same software. Silicon nitride rectangular cantilevers with "V" shaped tips (Bio-Lever BL-RC150VB-C1, Olympus Optical Co., Ltd., Tokyo, Japan with the typical spring constant of 0.03 N/m in liquid) were used for the experiments. Typically 512 × 512 points was taken at 1 line/s scan rate in AC mode under buffer solution. The measurements presented here are 1 μm × 1 μm flattened height and amplitude images, and height profile.

For transmission electron microscopy, the pelleted exosomes were washed in 0.1 M PBS then fixed overnight in a fixative containing 2% paraformaldehyde and 2.5% glutaraldehyde in 0.1 M phosphate buffer (PB). Samples were then washed in 0.1 M PB with two rinses, 30 min in each, and postfixed in 1% aqueous OsO_4 for 1 h. After 3× 30′ wash in distilled water, pellets were dehydrated in graded series of ethanol, processed through propylene oxide and embedded in plastic (Durcupan ACM). Blocks were polymerized at 56 °C for 2 days. Plastic blocks were trimmed then sectioned with a Leica Ultracut S ultramicrotome at a nominal thickness of 60 nm. Ultrathin sections were mounted on formvar coated 150 mesh copper grids, stained with uranyl acetate and lead citrate and examined under the electron microscope (Zeiss CEM 902). Digital images were taken at 85,000× and 140,000× instrumental magnification using a 4 M pixel monochrome CCD camera (Diagnostic Instruments, model #14).

2.3. Cell cultures and cell lines

Murine immature DCs were generated from bone marrow (BM). C57BL/6 mice were provided by the Animal Production Area of the NCI (Frederick, MD). NCI-Frederick is accredited by AAALAC International and follows the Public Health Service Policy for the Care and Use of Laboratory Animals. Animal care was provided in accordance with the procedures outlined in the "Guide for Care and Use of Laboratory Animals" (National Research Council, 1996; National Academy Press; Washington, D.C.). BM was obtained by aspirating cells from the femurs and tibias of 8–10-week-old female C57BL/6 mice followed by culture in RPMI-1640 medium (Mediatech, Herndon, VA) containing 10% fetal bovine serum (HyClone, Logan, Utah), 2 mM glutamine, 100 U/ml penicillin and streptomycin (Quality Biological, Gaithersburg, MD) and murine recombinant GM-CSF at 20 ng/ml. 6 days old cell cultures were induced by exosomes (5 μg/ml total protein), recombinant RANTES (1 μg/ml) (Peprotech) and anti-CD3+ anti-CD28 (2.5 μg/ml each) (BD Biosciences, San Jose, CA).

2.3.1. B16F1 melanoma cell line

Murine melanoma cell line, obtained from DTP, DCTP Tumor Repository, were cultured in Dulbecco's modified Eagle's medium (DMEM, Mediatech) containing 10% fetal bovine serum (HyClone), 1% sodium pyruvate, 1% MEM non-essential amino acids, 1% MEM vitamin solution (Invitrogen) 2 mM glutamine, 100 U/mL each penicillin and streptomycin (Quality Biological).

2.3.2. CD4+ cells

Spleens from 8- to 10-week-old female C57BL/6 mice were dissected and CD4+ cells were purified using R&D Systems (Minneapolis, MN), Mouse T Cell CD4 Subset Column Kit following the manufacturer's instruction.

2.3.3. RAW 264.7 macrophage cell line

The RAW 264.7 murine macrophages were cultured in MIX MEM [1:1 mixture of Dulbecco's modified Eagle's medium and Ham's F-12 plus 10% (v/v) FCS (all from Sigma)].

2.3.4. Transfection of cell lines

RAW 264.7 macrophages were transfected with pNF-κB-luc4 plasmid as described previously [6].

2.4. Luciferase assay

One-day-old cultures RAW 264.7 cells, grown on luminoplates (Corning-Costar; Zenon Biotechnology Ltd., Szeged, Hungary) were used. Cells (5×10^5 cells/well in MIX MEM, 10% FCS) were induced by mcd-exosomes and 100 ng/ml LPS (*E. coli* 055:B5; Sigma). After 6 h of incubation with inducers, the medium was removed, and the cells were washed and lysed for 10 min at room temperature in Cell Culture Lysis Reagent (20 μl/well; Promega Bio-Science Hungary, Budapest). Substrate was added (20 μl/well; Promega, Bio-Science Hungary, Budapest), and luciferase activity was measured in a Luminoskan Ascent (Thermo Electron Corporation, Waltham, MA) scanning luminometer. Cell viability was routinely determined using trypan blue exclusion test during the assays to make sure that assays were always carried out on viable cells.

2.5. Proteoma profiling of mcd-exosomes induced macrophages

10^6/sample mature macrophages were induced by 100 ng/ml LPS (Sigma), 20 ng/ml IL-4 (R&D Systems, Minneapolis, MN) and mcd-Exosomes (total protein content adjusted for 600 μg/ml) for 24 h. To define basal cytokine and chemokine production of the mature macrophages, they were cultured in absence of the stimulators. After induction, supernatants were collected and analyzed with R&D Systems Proteomes Profiler Assay following the manufacturer's instruction.

3. Results

3.1. B16 murine melanoma cells produce exosomes

At the first step, we established a standardized protocol of melanoma cell culture for exosome production. For an optimal exosome recovery, 2×10^7 melanoma cells were seeded at T75 flasks and cultured for 2–4 (typically 3) days. Melanin content of the supernatants was used as a surrogate marker of copious exosome production. Size and form distribution of the exosomes was determined by atomic force microscopy (Fig. 1a, b, and d). Fig. 1 shows

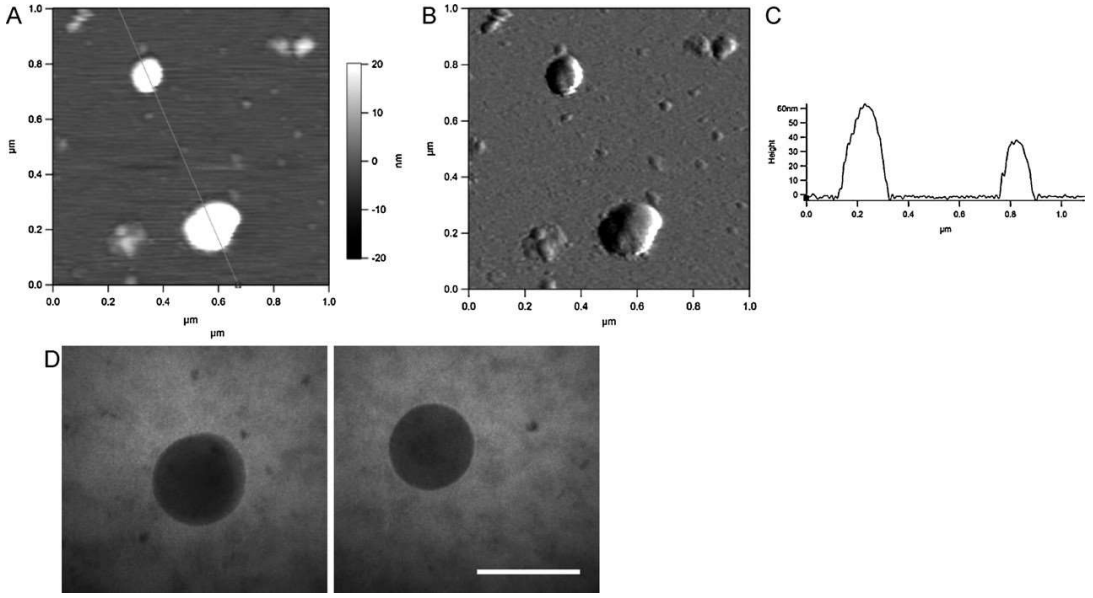

Fig. 1. B16F1 melanoma cells release exosomes into the culture medium. Exosomes prepared from the supernatants of cultured melanoma cells were visualized by two different methods. (A–C) Height and amplitude image, and height profile of exosomes measured in buffer by AFM. The size of the exosomes was found to be well defined and characteristic. (D) Transmission electron microscopic images of B16 exosomes. While the diameter of the particles is comparable to those seen by atomic force microscopy, no internal structure is noticeable. The scale bar represents 100 nm.

that the diameter of the exosomes (indicated in the AFM height image section) is in the range of 30–70 nm, respectively. This data corresponds to the typical size range of exosomes found in literature [1]. Transmission electron microscopy images showed no internal structure, thus ruling out contamination of our samples with viral particles (Fig. 1c and d).

3.2. Melanoma cell derived exosomes enhance T cell proliferation induced by DCs

Immature murine DCs were generated from bone marrow of 8–10-week-old female C57BL/6 mice. In the next step, the DCs cultures were stimulated with B16 exosomes. LPS served as a positive control for DC activation.

$CD4^+$ T cells (5×10^5 cells/well) were seeded in U-bottom 96-well plates together with 10^4 cells/well of induced or control DCs as described below. Anti-CD3 and anti-CD28 antibodies (2.5 μg/ml) were added as positive controls for inducing T cell proliferation and RANTES (1 μg/ml) as a negative control. The proliferation was determined after 72 h of incubation. Cells were pulsed with 1 μCi [^{3}H] thymidine per well for the last 6 h of culture period. We found that the mcd-exosome pretreatment significantly increased the T cell proliferation inducing capacity of DCs. As shown in Fig. 2, $CD4^+$ T cells from B6 mice were highly responsive to DC induced by purified exosomes, LPS or CD3/CD28 antibody stimulation, indicating that mcd-exosome stimulated DCs were indeed activated. In contrast, DCs pretreated by RANTES were hyporesponsive.

To assess the eventual differences between the different stimuli, effect of mcd-exosomes on T cell proliferation, bone marrow derived DCs were incubated with exosomes, LPS (100 ng/ml) or IL-4 (20 ng/ml IL-4) for 24 h. Splenic T cells separated with CD4+ T cell selection columns were co-cultured with the induced DCs. After incubation, T cell surface markers were analyzed by flow cytometry. We have found that the stimuli induced significant T cell proliferation, but no differences were detected in the ratio of the activated T cells (CD4+CD44+CD25+), neither resting T cells between the different treatment groups. We concluded that mcd-exosomes, just like LPS or IL-4, could induce T cell proliferation, but no signs of different types of polarization were detected in this model (data not shown). These results, however, again underlined that melanoma derived exosomes are not immunologically inert particles.

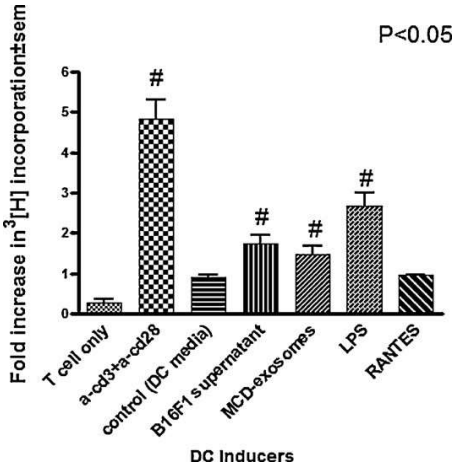

Fig. 2. B16F1 melanoma exosomes enhance T cell proliferation induced by dendritic cells. Purified T cells were stimulated with bone marrow derived C57Bl6 CD4+ dendritic cells in the presence of exosomes, positive control (LPS 100 ng/ml) or negative control (RANTES). The background T cell proliferation was determined by using T cells only, while the maximal T cell proliferation was measured after stimulation with anti-CD3 and anti-CD28 antibodies.

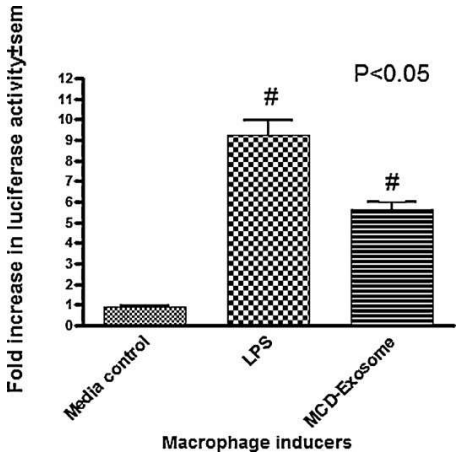

Fig. 3. B16F1 melanoma exosomes activate macrophages. B16F1 exosomes induced the activation of pNF-κB-luc4 reporter gene in RAW 264.7 mouse macrophages treated for 6 h. LPS (100 ng/ml) was applied as positive control.

3.3. Melanoma cell derived exosomes activate NF-κB in macrophages

Mature RAW 264.7 reporter macrophages stably transfected by the pNF-κB-luc4 reporter plasmid were induced with purified melanoma cell derived exosomes; the total protein concentration of the exosome suspension was adjusted to 600 μg/ml. *E. coli* LPS was used as a positive control (Fig. 3). We have found that the mcd-exosomes increased the luciferase activity ($P < 0.05$). NF-κB activation in macrophages is involved in immune activation leading to inflammatory cytokine gene transcription. The activation of this central pathway supports our hypothesis that tumor derived exosomes are able to stimulate elements of immune system. Though the increased T cell proliferation and macrophage activation verified the immunological activity of mcd-exosomes, the type of activation, *i.e.*, the contribution of M1 type, inflammatory activation that leads to tumor rejection, or M2 type activation leading to tumor progression, was not clear at this point.

3.4. Melanoma cell derived exosomes alter the cytokine and chemokine profile of macrophages

To investigate the possible type 1/type 2 bias after exosome induction, we screened the cytokine profile of mature murine macrophages. We induced 10^6 RAW 267.4 murine macrophages with B16F1 exosomes (600 μg/ml total protein), 100 ng/ml LPS (Sigma) and 20 ng/ml IL-4 (R&D Systems, Minneapolis, MN) then the supernatants were harvested and tested by a cytokine and chemokine profiling assay. The proteoma analysis of the supernatants was performed by a multi-dot blot assay (Proteome Profiler Array, R&D Systems); the areas of maximal density were quantified by the ImageJ 1.45s, NIH, USA software. Fig. 4 shows a representative result of four experiments that gave similar results. From the cytokines quantified only those that showed the most characteristic changes are plotted at the figure. Since the used RAW 264.7 murine macrophage cell line is of a mature phenotype, we detected a basal production of numerous cytokines and chemokines in absence of stimuli. After different types of induction, we found that mcd-exosomes reduced the level of TIMP1, IFN-g and IL-16, as compared with non-stimulated controls. In contrast, we detected a marked increase in the levels of IL-8, CCL2, MIP2 and IL-1Ra. The mcd-exosome induced protein pattern was distinctly different both from the LPS- and the IL-4-induced profile. IL-4 induction decreased the level of CCL2, IL-1RA and MIP2, while mcd-exosomes increased it. In contrast to LPS induction, mcd exosomes induced IL-13 and MIP2 production of the macrophages.

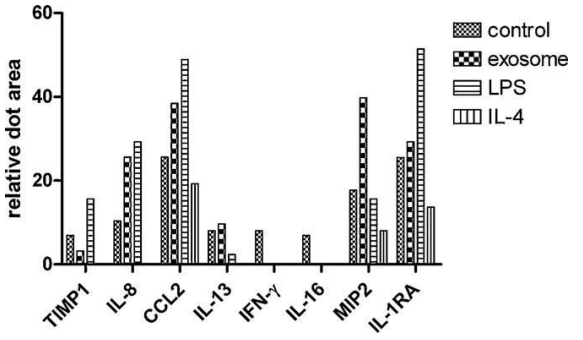

Fig. 4. B16F1 exosomes alter the cytokine and chemokine profile of mature macrophages. The basal levels of MIP2, IL-8, CCL2, IL-13 and IL-1RA proteins were increased by the treatment with melanoma cell derived exosomes, while the levels of TIMP1, IFNγ and IL-16 decreased. The mcd-exosome induced protein pattern was distinctly different both from the LPS- and the IL-4 induced profile.

Beside the cytokines mentioned above, we analyzed the expression of further cytokines and chemokines, taken together, 40 proteins, including CXCL13, IL-3, CXCL17, C5a, IL-4, CXCL11, TIMP1, G-CSF, IL-5, IL-8, TNFα, GM-CSF, IL-6, M-CSF, TREM1, CCL-1, IL-7, CCL2, CCL11, IL-10, CCL12, CD54, IL-13, CXCL9, IFNγ, IL-12p70, CCL3, IL-1α, IL-16, CCL4, IL-1β, IL-17, MIP2, IL-1Ra, IL-23, CCL5, IL-2, IL-27 and CXCL12. The levels of IL-3, CXCL17, CXCL11, IL-5, IL-6, CCL11, IL10, IL-12p70, IL-2 and CXCL12 were below the detection limit of our assay. In repeated experiments we did not find consequent, markedly differences between effect of different types of inductions in case of CXCL13, CXCL10, C5a, IL-4, G-CSF, TNFα, GM-CSF, M-CSF, TREM1, CCL-1, IL-7, CCL12, CD54CXCL9, CCL3, CCL4, IL-23, CCL5 and IL-27.

4. Discussion

In the first step of our studies we have set up a standardized method of reproducible *in vitro* production of exosomes, then their purification by differential filtration and ultracentrifugation steps. The surface composition of exosomes is generally identical to the cell membrane of the originating cells, thus no specific surface markers are available for their identification. Because of that, we turned to ultrastructural and AFM methods for quality control of the exosome suspensions. As it was expected based on literature data, the obtained exosomes had a diameter of 20–100 nm, and the lack of their internal structure showed that they are not contaminated with viral particles; a fact that could have resulted in misinterpretation of the obtained data.

Then we showed that melanoma cell derived exosomes promoted the maturation of dendritic cells, after which they induced an enhanced T cell proliferation. These results are in contrast to several earlier papers suggesting that exosomes suppress, rather than promote DC maturation, therefore they might not enhance anti cancer immunity [7,8]. Other publications suggested that tumor exosomes do enhance tumor immunity [1]. Multhoff et al. found that exosomes originating from Hsp70/Bag-4 membrane-positive pancreas and colon tumor cells stimulate migration and reactivity in NK cells [9]. These NK cells activated with exosomes effectively lysed autologous colon tumor cells. Since tumor cell derived exosomes are formed from the cell membrane of the originating cells, these discrepancies might reflect the inherent genetic instability of tumors as reflected in different molecular patterns of plasma membranes of different tumors. Based on these data, B16F1 melanomas

seem to activate, rather than suppress DC maturation and by that induction of T cell proliferation, however the phenotype of the activated T cell is not clear yet.

Although slightly less effectively than the positive control LPS, exosomes induced NF-κB activation in RAW macrophages, demonstrating that they have activatory effect in this model also. The transcription factor NF-κB is known to regulate the expression of a number of crucial genes in macrophages. Activation of these cells in response to M1 stimuli, such as TLR ligands, TNF-α and IL-1β, is regulated primarily by NF-κB [10,11]. In addition, transcription of several tumor-promoting genes, such as VEGF, IL-6, TNF- α, and COX2, is also regulated, in part, by NF-κB, pointing to its key role in the activation of tumor infiltrating macrophages [12–14].

On the other hand, Feng-Hua Wu at al described that the activated NF-κB not only promoted the proliferation of B16 cells, but also enhanced apoptosis resistance of B16 cells by up-regulating Bcl-2 and Bcl-xL and down-regulating Bax [15].

All these data suggest that the development of malignant processes is supported by exosome-induced activation of NF-κB.

The chemokine/cytokine expression changes induced by the exosome treatment are complex and more difficult to interpret.

The exosome induction resulted in a "mixed" macrophage cytokine and chemokine profile, different both from Th1 and Th2 type responses. The cytokine profile detected might be in connection with the malignant phenotype of the tumors. The reduced TIMP1 matrix metalloproteinase inhibitor level could support metastasis formation. The decreased level of IFNγ and IL-16 might reflect a reduced anti-tumoral Th1 type response, together with the IL-1Ra and IL-13, both well known suppressors of the Th1 type immune response.

CCL2 and MIP-2, expressed in higher quantities in our model, have been shown to be involved in the process of inflammation, angiogenesis, tumorigenesis, and wound healing [16,17].

TIMP-1 has also multi-faceted role in tumor growth and rejection. Although it blocks the matrix metalloproteinases, essential for tumor invasion and metastasis, it also possesses an array of tissue specific metalloproteinase-independent activities, including mitogenic and anti-apoptotic effects [18,19]. To summarize our findings, we can state that exosomes produced by B16F1 are immunologically active. They are capable of transforming dendritic cell and macrophage functions, inducing T cell proliferation and NF-κB activation *in vitro*. mcd-exosomes can trigger the secretion of cytokines and chemokines by macrophages, some of which may have anti-tumor and tumor-supporting properties, depending on the circumstances, while others may facilitate tumor progression.

In conclusion, our observations suggest that nanometer-sized exosomes produced by tumor cells may play a role in the tumor progression and metastasis formation of malignant diseases through supporting tumor escape mechanisms.

Taken together, our observations suggest that melanoma derived exosomes interact with macrophages as well as dendritic cells, although the mixed biological effects observed in our experiments may contribute not only to anti-tumor immune response but also to tumor immune escape. The fact that, in the absence of therapeutical interventions, the tumor microenvironment harbors mostly type 2 tumor associated macrophages and suppressive dendritic cells indicates that melanoma derived exosomes might typically skew the balance in the direction of immune suppressive mechanisms.

Acknowledgements

This work was supported by the National Science Fund of Hungary OTKA PD 84064, OTKA K 81180 and GOP-1.1.1-11-2011-0003 and TAMOP-4.2.2/B-10/1-2010-0012. C. Vizler was the recipient of a Bolyai fellowship of the Hungarian Academy of Sciences.

References

[1] Wieckowski E, Whiteside TL. Human tumor-derived vs dendritic cell-derived exosomes have distinct biologic roles and molecular profiles. Immunol Res 2006;36:247–54.
[2] Gastpar R, Gehrmann M, Bausero M, Asea A, Gross C, Schroeder JA, et al. Heat shock protein 70 surface-positive tumor exosomes stimulate migratory and cytolytic activity of natural killer cells. Cancer Res 2005;65:5238–47.
[3] Liu C, Yu S, Zinn K, Wang J, Zhang L, Jia Y, et al. Murine mammary carcinoma exosomes promote tumor growth by suppression of NK cell function. J Immunol 2006;176:1375–85.
[4] Camussi G, Deregibus MC, Bruno S, Cantaluppi V, Biancone L. Exosomes/microvesicles as a mechanism of cell-to-cell communication. Kidney Int 2010;78(November (9)):838–48.
[5] Thery C, Regnault A, Garin J, Wolfers J, Zitvogel L, Ricciardi-Castagnoli P, et al. Molecular characterization of dendritic cell-derived exosomes. Selective accumulation of the heat shock protein hsc73. J Cell Biol 1999;147:599–610.
[6] Eder K, Vizler C, Kusz E, Karcagi I, Glavinas H, Balogh GE, et al. The role of lipopolysaccharide moieties in macrophage response to *Escherichia coli*. Biochem Biophys Res Commun 2009;389(November (1)):46–51 [Epub 2009 August 20].
[7] Li XB, Zhang ZR, Schluesener HJ, Xu SQ. Role of exosomes in immune regulation. J Cell Mol Med 2006;10:364–75.
[8] Yu S, Liu C, Su K, Wang J, Liu Y, Zhang L, et al. Tumor exosomes inhibit differentiation of bone marrow dendritic cells. J Immunol 2007;178:6867–75.
[9] Gastpar R, Gehrmann M, Bausero MA, Asea A, Gross C, Schroeder JA, et al. Heat shock protein 70 surface-positive tumor exosomes stimulate migratory and cytolytic activity of natural killer cells. Cancer Res 2005;65:5238–47.
[10] Mantovani A, Sica A, Sozzani S, Allavena P, Vecchi A, Locati M. The chemokine system in diverse forms of macrophage activation and polarization. Trends Immunol 2004;25:677–86.
[11] Kawai T, Akira S. Signaling to NF-κB by Toll-like receptors. Trends Mol Med 2007;13:460–9.
[12] Hagemann T, Biswas SK, Lawrence T, Sica A, Lewis CE. Regulation of macrophage function in tumors: the multifaceted role of NF-κB. Blood 2009;113:3139–46.
[13] Karin M, Greten FR. NF-κB: linking inflammation and immunity to cancer development and progression. Nat Rev Immunol 2005;5:749–59.
[14] Biswas SK, Lewis CE. NF-κB as a central regulator of macrophage function in tumors. J Leukoc Biol 2010;88(November (5)):877–84 [Epub 2010 June 23].
[15] Wu FH, Yuan Y, Li D, Lei Z, Song CW, Liu YY, et al. Endothelial cell-expressed Tim-3 facilitates metastasis of melanoma cells by activating the NF-kB pathway. Oncol Rep 2010;24(September (3)):693–9.
[16] Dhawan P, Richmond A. Role of CXCL1 in tumorigenesis of melanoma. J Leukoc Biol 2002;72(July (1)):9–18.
[17] Yang J, Luan J, Yu Y, Li C, DePinho RA, Chin L, et al. Induction of melanoma in murine macrophage inflammatory protein 2 transgenic mice heterozygous for inhibitor of kinase/alternate reading frame. Cancer Res 2001;61(November (22)):8150–7.
[18] Stetler-Stevenson WG. Tissue inhibitors of metalloproteinases in cell signaling: metalloproteinase-independent biological activities. Sci Signal 2008;1(July (27)):re6.
[19] Hornebeck W, Lambert E, Petitfrère E, Bernard P. Beneficial and detrimental influences of tissue inhibitor of metalloproteinase-1 (TIMP-1) in tumor progression. Biochimie 2005;87(March–April (3–4)):377–83.

frontiers in Immunology

ORIGINAL RESEARCH
published: 18 October 2019
doi: 10.3389/fimmu.2019.02459

Melanoma-Derived Exosomes Induce PD-1 Overexpression and Tumor Progression via Mesenchymal Stem Cell Oncogenic Reprogramming

*Edina Gyukity-Sebestyén[1,2], Mária Harmati[1,2], Gabriella Dobra[1,2], István B. Németh[3], Johanna Mihály[4], Ágnes Zvara[5], Éva Hunyadi-Gulyás[6], Róbert Katona[7], István Nagy[8], Péter Horváth[1], Árpád Bálind[1], Ábel Szkalisity[1], Mária Kovács[1,9], Tibor Pankotai[10], Barbara Borsos[10], Miklós Erdélyi[11], Zsolt Szegletes[12], Zoltán J. Veréb[3], Edit I. Buzás[13], Lajos Kemény[3], Tamás Bíró[4] and Krisztina Buzás[1,14]**

[1] Laboratory of Microscopic Image Analysis and Machine Learning, Institute of Biochemistry, Biological Research Centre of Hungarian Academy of Sciences, Szeged, Hungary, [2] Doctoral School of Interdisciplinary Sciences, Faculty of Medicine, University of Szeged, Szeged, Hungary, [3] Department of Dermatology and Allergology, University of Szeged, Szeged, Hungary, [4] Department of Immunology, Faculty of Medicine, University of Debrecen, Debrecen, Hungary, [5] Laboratory of Functional Genomics, Institute of Genetics, Biological Research Centre of Hungarian Academy of Sciences, Szeged, Hungary, [6] Laboratory of Proteomics Research, Institute of Biochemistry, Biological Research Centre of Hungarian Academy of Sciences, Szeged, Hungary, [7] Artificial Chromosome and Stem Cell Research Laboratory, Institute of Genetics, Biological Research Centre of Hungarian Academy of Sciences, Szeged, Hungary, [8] Sequencing Platform, Institute of Biochemistry, Biological Research Centre of Hungarian Academy of Sciences, Szeged, Hungary, [9] Department of Pharmacology and Pharmacotherapy, Faculty of Medicine, University of Szeged, Szeged, Hungary, [10] Department of Biochemistry and Molecular Biology, Faculty of Science and Informatics, University of Szeged, Szeged, Hungary, [11] Advanced Optical Imaging Group, Department of Optics and Quantum Electronics, Faculty of Science and Informatics, University of Szeged, Szeged, Hungary, [12] Atomic Force Microscope Laboratory, Institute of Biophysics, Biological Research Centre of Hungarian Academy of Sciences, Szeged, Hungary, [13] MTA-SE Immuno-proteogenomics Extracellular Vesicle Research Group, Department of Genetics, Cell- and Immunobiology, Faculty of Medicine, Semmelweis University, Budapest, Hungary, [14] Department of Oral Biology and Experimental Dental Research, Faculty of Dentistry, University of Szeged, Szeged, Hungary*

Recently, it has been described that programmed cell death protein 1 (PD-1) overexpressing melanoma cells are highly aggressive. However, until now it has not been defined which factors lead to the generation of PD-1 overexpressing subpopulations. Here, we present that melanoma-derived exosomes, conveying oncogenic molecular reprogramming, induce the formation of a melanoma-like, PD-1 overexpressing cell population (mMSC$^{PD\text{-}1+}$) from naïve mesenchymal stem cells (MSCs). Exosomes and mMSC$^{PD\text{-}1+}$ cells induce tumor progression and expression of oncogenic factors *in vivo*. Finally, we revealed a characteristic, tumorigenic signaling network combining the upregulated molecules (e.g., PD-1, MET, RAF1, BCL2, MTOR) and their upstream exosomal regulating proteins and miRNAs. Our study highlights the complexity of exosomal communication during tumor progression and contributes to the detailed understanding of metastatic processes.

Keywords: PD-1, exosome, melanoma/tumor progression, stem cell, reprogramming, signalization pattern, metastasis

OPEN ACCESS

Edited by:
Fabrizio Mattei,
National Institute of Health (ISS), Italy

Reviewed by:
Kawaljit Kaur,
University of California, Los Angeles, United States
Fatemeh Momen-Heravi,
Columbia University, United States

***Correspondence:**
Krisztina Buzás
kr.buzas@gmail.com

Specialty section:
This article was submitted to Cancer Immunity and Immunotherapy, a section of the journal Frontiers in Immunology

Received: *21 March 2019*
Accepted: *01 October 2019*
Published: *18 October 2019*

Citation:
Gyukity-Sebestyén E, Harmati M, Dobra G, Németh IB, Mihály J, Zvara Á, Hunyadi-Gulyás É, Katona R, Nagy I, Horváth P, Bálind Á, Szkalisity Á, Kovács M, Pankotai T, Borsos B, Erdélyi M, Szegletes Z, Veréb ZJ, Buzás EI, Kemény L, Bíró T and Buzás K (2019) Melanoma-Derived Exosomes Induce PD-1 Overexpression and Tumor Progression via Mesenchymal Stem Cell Oncogenic Reprogramming. Front. Immunol. 10:2459. doi: 10.3389/fimmu.2019.02459

INTRODUCTION

Heterogeneous tumor tissue is comprised of a wide variety of collocated cells. Their spatiotemporal co-existence facilitates direct communication between them. Cancer cells contribute to tumor niche formation not only by soluble factor production and receptor-ligand interactions (1), but also by releasing vesicles whose molecular contents add up to a complex information package. Previous studies demonstrated that cultured human tumor cells release extracellular vesicles such as exosomes of 20–120 nm diameters (2). Among others, exosomes carry structural and signaling proteins, MHC molecules, cell surface molecules typically associated with apoptosis, and mRNAs/miRNAs with multiple functions (3). Therefore, these exosomal-molecular-patterns, as unique entities of the complex intercellular communication, are not independent of the quality or state of the mother cell (4, 5). Exosomes have been recognized long ago, but their identification, characterization, and isolation are still under intense investigation. Further, whereas the definition of exosomes is based on the pathway of biogenesis, oncosomes form a functional class of extracellular vesicles. Indeed, oncosomes are suggested being capable of carrying and conveying tumor-related information (6) and might have a significant role in formation of tumor microenvironment (7).

Mesenchymal stem cells (MSCs) were first described as stromal cells of the bone marrow with multipotent differentiation potential and characteristic immunomodulatory effects (8). In relation to their immunological and differentiation properties, there is a debate about the role of MSCs in tumor progression (9). Indeed, the cellular fate could depend on the cancer type and also on the status of the affected MSCs. Activated MSCs can secrete pro-angiogenic soluble factors and are able to differentiate to vessel wall associated cells (10) or to cancer associated fibroblasts (CAFs) (11). Furthermore, Baglio et al. showed that tumor secreted extracellular vesicles promote osteosarcoma progression via TGFβ signaling induced IL-6 production by MSCs (12). Moreover, Peinado et al. demonstrated that exosomes from highly metastatic melanomas increase the metastatic behavior of primary tumors by permanently educating bone marrow progenitors through the receptor tyrosine kinase MET (13).

Malignant melanoma is a highly invasive, metastatic cancer with poor prognosis and survival rate. Since melanoma has been long recognized as a highly immunogenic tumor, therapeutic approaches target different immunological mechanisms to treat patients with this aggressive skin cancer. In the past decade, besides IL-2 and CTLA-4 therapies, the PD-1:PD-L1 blockade proved to be an effective treatment in metastatic melanoma (14). Programmed cell death protein 1 (PD-1), mainly expressed by immune cells such as activated T cells, dendritic cells and macrophages is a cell surface receptor with a central role in modulation of T cell responses. PD-1 binding to its ligand, PD-L1, can result in apoptosis and anergy of immune cells.

Notably, PD-1 expression is not a default property of melanoma cells. Of further importance, recently Kleffel et al. demonstrated that PD-1 overexpressing melanoma cell subpopulations are especially aggressive, and that melanoma PD-1:PD-L1 interactions modulate mTOR signaling, whereby they interfere with programmed cell death (15). This work is remarkably instrumental with respect to the consequences of PD-1 overexpression and experimental inhibition of PD-1 functions (Pdcd1-shRNA or anti-PD-1 antibody). However, it does not define the factors the activation of which lead to the generation of PD-1 overexpressing subpopulations. This question, though, is an especially intriguing one, if one considers that one of the most effective immunotherapies available today is based on the blockade of the aforementioned PD-1:PD-L1 interaction (16).

Based on the above, in the current study, we aimed at specifically and systematically addressing the following questions:

1. Can we unambiguously define the cellular and molecular signs of melanoma-derived exosome-induced, intercellular communication-mediated malignant transformation of MSC cultures?
2. Can we detect the melanoma-derived exosome-induced tumor progression *in vivo*?
3. What alteration can be detected in the expression of PD-1, a melanoma progression marker and therapeutic target, upon exposure to melanoma-derived exosomes?

Here, we present the first piece of evidence that melanoma exosomes, by conveying a complex oncogenic molecular reprogramming, induce the formation of a PD-1 overexpressing cell population (melanoma-like $MSC^{PD\text{-}1+}$; $mMSC^{PD\text{-}1+}$) from naïve MSCs. These $mMSC^{PD\text{-}1+}$ cells represent a new entity with melanoma-like gene expression profile and phenotypic properties. Further, exosomes and exosome-activated $mMSC^{PD\text{-}1+}$ cells induce rapid tumor progression *in vivo*, due to their strong expression of oncogenic dominance factors and decreased susceptibility to programmed cell death.

MATERIALS AND METHODS

Cell Culture and Cell Line

B16F1 mouse melanoma cell line was obtained from ECACC and cultured in Dulbecco's modified Eagle's medium (DMEM, Lonza, Basel, Switzerland) containing 10% fetal bovine serum (FBS) (Euroclone, Milano, Italy), 1% sodium pyruvate, 1% MEM non-essential amino acids, 1% MEM vitamin solution, 2 mM L-glutamine, and 1% Penicillin-Streptomycin-Amphotericin B Mixture (all from Lonza).

Murine MSCs were isolated from C57BL/6N (Charles River Laboratories, Sulzfeld) 8 week-old male mice (17). Abdominal inguinal fat pads were excised, rinsed with RPMI 1640 medium, transferred to sterile tissue culture dishes and mechanically dissociated. The dissociated tissue was resuspended in RPMI 1640 containing 100 μg/ml collagenase (Sigma-Aldrich, St. Louis, MO) and incubated at 37°C for 50 min. Collagenase was neutralized with a growth medium containing 10% FBS. After centrifugation at 470 g for 15 min, cell pellets were resuspended and washed in the culture medium. After the centrifugation, cell pellets were resuspended in complete MesenCult medium (Stemcell Technologies, Vancouver, British Columbia, Canada) and filtered through a 100 μm cell strainer (BD Biosciences,

Franklin Lakes, NJ) to tissue culture dishes, and cultured for 48 h at 37°C in 5% CO_2 and 90% humidity. Unattached cells and debris were then removed and fresh medium was added to the adherent cells. The cells were cultured to 80% confluence before being released with trypsin–EDTA and sub-cultured.

Purity of MSC cultures were checked by flow cytometry analysis using the Mouse Multipotent Mesenchymal Stromal Cell Marker Antibody Panel (R&D Systems, Minneapolis, MN) according to the manufacturer's instructions.

Isolation and Characterization of the Melanoma-Derived Exosomes

Exosome Isolation by Filtration and Differential Centrifugation

Exosomes were isolated by adapting the protocol of Peinado et al. (13) from melanoma cell culture supernatant. B16F1 supernatants were harvested, supplemented by complete protease inhibitor cocktail (Roche, Mannheim, Germany) and centrifuged at 780 g for 5 min at 4°C to remove intact cells. Then, the supernatants were centrifuged at 3,900 g for 15 min at 4°C and filtered through a 0.2 μm membrane (Millipore, Billerica, MA) to remove larger cell fragments and microvesicles. Exosomes were pelleted by ultracentrifugation at 150,000 g (T-1270 rotor at 40,500 rpm) for 1 h at 4°C. The pellet was washed twice and resuspended in DPBS and stored at −80°C.

The concentration of exosomal proteins was determined using a Pierce BCA Protein assay kit (Thermo Fisher Scientific, Waltham, MA) and a Benchmark Microplate Reader (Bio-Rad, Hercules, CA) according to the manufacturer's instructions.

Determination of Shape and Size of the Isolated Vesicles

Scanning electron microscopy (SEM)

Five microliters of isolated exosomes in DPBS were spotted on glass coverslips coated with 0.01% Poly-L-Lysine (Sigma-Aldrich) and incubated overnight at 4°C. Using sterile forceps, coverslips were transferred into a plastic plate. Exosomes were fixed by gently adding 2% paraformaldehyde buffer pH 7.2 diluted in DPBS for 30 min. The coverslips were washed twice with DPBS and dehydrated with a graded ethanol series (40, 60, 80, and 100% ethanol, each for 5 min). The samples were dried with a critical point dryer (QUORUM K850, Quorum Technologies Ltd, Laughton, UK) and the coverslips were mounted onto a microscope stub at a time using carbon tape, followed by 7 nm gold coating (QUORUM Q150, Quorum Technologies Ltd) and observed under a field-emission scanning electron microscope (JEOL JSM-7100F/LV).

Atomic force microscopy (AFM)

Exosomes were let to adsorb to the freshly cleaved muscovite mica (SPI-ChemTM Mica Sheets, Structure Probe, Inc., West Chester, PA) surface directly from DPBS. All AFM measurements were carried out with an Asylum MFP-3D head and Molecular Force Probe Controller (Asylum Research, Santa Barbara, CA), using Asylum Research MFP-3D program (version 15.09.112) written in Igor Pro software (version 6.37, Wavemetrics, Lake Oswego, OR). Image procession and data calculation were made using the same software. Silicon rectangular cantilevers (OMLC-AC240TS, Olympus Optical Co., Ltd., Tokyo, Japan) with the typical spring constant of 2 N/m were used in dry condition and silicon nitride rectangular cantilevers with "V" shaped tips (Bio-Lever BL-RC150VB, Olympus Optical Co. Ltd.) with the typical spring constant of 0.03 N/m in buffer solution. Typically, 512 × 512 points was taken at 1 line/s scan rate. The measurements presented here are amplitude images and height profile.

Detection of Exosomal Markers by Western Blotting

Protein samples were resuspended in 4x sample buffer (NuPAGE LDS Sample Buffer (4X), NuPAGE Sample Reducing Agent (10X), Thermo Fisher Scientific), boiled at 96°C for 10 min, and immediately cooled on ice. Electrophoresis of the proteins was performed using 4–12% Bis-Tris Protein Gels (NuPAGE Novex, Thermo Fisher Scientific), ProSieve Color Protein Markers (Lonza), and electrophoresis buffer (NuPAGE MOPS SDS Running Buffer, Thermo Fisher Scientific) at 200 V and 0.03 A for 40 min.

The proteins of electrophoresed gels were transferred to Immobilon transfer membrane (Millipore, Darmstadt, Germany) using transfer buffer [NuPAGE Transfer Buffer (20X)] at 30 V and 170–110 mA for 60 min. Membranes were blocked in TBST buffer (25 mM Tris-HCl, 150 mM NaCl, 0.05% Tween-20, pH 7.2) containing 5% non-fat milk for 60 min at room temperature (RT). After blocking, membranes were incubated with each primary antibody in TBST buffer containing 1% non-fat milk overnight at 4°C. Membranes were washed three times for 10 min with TBST buffer and incubated for 60 min at room temperature with secondary antibody in TBST buffer containing 1% non-fat milk. Membranes were washed three times for 10 min with TBST buffer.

For exosomal marker identification western blot analyses were performed with an anti-CD63 polyclonal antibody (1:250 dilution; Biorbyt, Cambridge, UK) anti-CD9 monoclonal antibody (clone EPR2949, 1:500 dilution, LifeSpan Biosciences, Seattle, WA), anti-CD81 monoclonal antibody (clone: EAT2, 1:1,000 dilution, LifeSpan Biosciences, Seattle, WA), and anti-HSP70 monoclonal antibody (clone: C92F3A-5, 1:8,000 dilution; Enzo Life Sciences, Farmingdale, NY), anti-rabbit IgG HRP-Conjugated antibody (1:1,000 dilution, R&D Systems), anti-Hamster IgG HRP-Conjugated antibody (1:30,000 dilution, Thermo Fisher Scientific). Bound antibodies were visualized by chemiluminescence using an ECL Plus Western Blotting detection system (Advansta, Menlo Park, CA). Immunoreactive signals were detected by using LI-COR ODYSSEY Fc (Dual-mode imaging system) imager followed by analysis with Odyssey v1.2, Image Studio Lite v5.2.

Identification of Exosomal Proteins by Mass Spectrometry

Exosomal proteins (24 μg) were separated in 4–12% Bis-Tris Protein Gels and stained with Coomassie blue (0.1% Coomassie Brilliant Blue R-250, 50% methanol and 10% acetic acid).

Each lane was cut to 12–12 equal bands and subjected to in-gel digestion. Gel bands were diced to smaller pieces, and the SDS and CBB dyes were washed out with 3 × 50 μl 25 mM

ammonium-bicarbonate (ABC)/50% Acetonitrile (AcN). After reduction with DTT (1,4-dithiothreitol, Sigma-Aldrich; 20 μl, 10 mM DTT in 25 mM ABC) at 56°C for 30 min, and alkylation with IAM (iodoacetamide, Sigma- Aldrich; 20 μl, 55 mM IAM in 25 mM ABC) at RT in the dark for 30 min, the gel samples were dried in a vacuum centrifuge and after that rehydrated in 20 μl of trypsin (Sequencing Grade Modified Trypsin, Promega, Fitchburg, WI; 5 ng/μl in 25 mM ABC) and incubated at 37°C. The digestion was stopped after 4 h by lowering the pH of the buffer below 3, by adding 2 μl of 10% formic acid. Tryptic peptides were extracted from the gel with 3 × 50 μl of 2% formic acid in 50% AcN and dried. Prior mass spectrometric analysis, all samples were redissolved in 50–50 μl of 0.1% formic acid (FA).

Samples were analyzed on an LTQ-Orbitrap Elite (Thermo Fisher Scientific) mass spectrometer on-line coupled with a nanoHPLC (nanoAcquity, Waters, Milford, MA) system. 5–5 μl of the in-gel digests were loaded (for 3 min at 8 μl/min flow, using 0.1% FA in 3% Acetonitrile—97% water) onto a reversed phase trap column (Waters, Symmetry C18, 0.180 × 20 mm) and separated on a C18 reversed phase (Waters, Milford, MA, BEH300C18 1.7 μm) nanocolumn (0.075 × 200 mm). The flow rate was 330 nl/min and a linear gradient was used from 3 to 40% B in 37 min (solvent A was 0.1% FA in water and solvent B was 0.1% FA in Acetonitrile).

The high voltage (1.2 kV) was applied through liquid junction between the chromatographic column and the non-coated silica nanospray emitter (NewObjective, Woburn, MA, 10 μm tip ID). The mass spectrometer operated in data-dependent mode: the survey mass spectra were detected in the orbitrap with high resolution (R = 60 k @ m/z: 400, mass range m/z: 380–1,400) and the most abundant multiply charged 20 peaks were selected for ion-trap fragmentation (NCE: 35%; activation q: 0.25; activation time: 10 ms; minimum signal intensity: 5,000 counts). The MSMS spectra were detected in the ion trap. Dynamic exclusion was used, the precursors were excluded for 15 s after the first fragmentation event.

Data analysis: searchable peaklists (mgf format) were extracted using ProteomeDiscoverer (ver:1.4 Thermo Fisher Scientific) and subjected to database search on our in-house ProteinProspector (ver: 5.14.1) search engine using the following parameters: parent ion tolerant: 5 ppm; fragment ion tolerant: 0.6 Da; Cys carbamidomethylation was set as constant and Met oxidation, cyclisation of peptide N-terminal Glu to pyroglutamic acid, protein N terminal acetylation were set as variable modifications. Only fully tryptic peptides were considered with maximum of 2 missed cleavage sites. The *Mus musculus* and *Bos taurus* protein sequences of the Uniprot (UniProtKB.06.11.2014) database completed with human keratins and pig trypsin, altogether 106,330 protein sequences were searched. For the false discovery rate (FDR) estimation, the searches were performed on the database concatenated with the randomized sequences. Protein identification was accepted if the ProteinProspector expectation value was <0.01 and the protein was identified with at least 2 unique peptides (expectation value <0.05 and score higher than 15). FDR values were <1% in all cases.

For functional validation, the resulted protein list was analyzed by the "Core Analysis" function included in Ingenuity Pathway Analysis (IPA, Quiagen Bioinformatics) software.

Isolation and Detection of Exosomal miRNAs

miRNA sequencing was performed using SOLiD Total RNA-Seq lit for Small RNA Libraries (Applied Biosystems now part of Thermo Fisher Scientific) according to the manufacturer's instructions. Purification was performed on 10% TBE-Urea gels stained with Sybr Gold nucleic acid gel stain (both from Invitrogen now part of Thermo Fisher Scientific). Final purification was performed using PureLink PCR Micro Kit (Invitrogen). Final libraries were quality checked using High Sense DNA kit on Bioanalyzer (all from Agilent, Santa Clara, CA). Concentration of each library was determined using the SOLID Library TaqMan Quantitation Kit (Life Technologies now part of Thermo Fisher Scientific). Each library was clonally amplified on SOLiD P1 DNA Beads by emulsion PCR (ePCR). Emulsions were broken with butanol, and ePCR beads enriched for template-positive beads by hybridization with magnetic enrichment beads. Template-enriched beads were extended at the 3′ end in the presence of terminal transferase and 3′ bead linker. Beads with the clonally amplified DNA were deposited onto SOLiD sequencing slide and sequenced on SOLiD 5500 Instrument using the 50-base sequencing chemistry.

Bioinformatic Analysis Raw data quality assessment, read trimming read mapping and miRNA expression profiling were carried out in CLC Genomics Workbench tool version 8.0.2 (CLC Bio now part of Qiagen, Venlo, Netherlands) using annotated *Mus musculus* miRNA sequences according to the miRBase release 21 as a mapping reference.

In vitro Experiments

Cell Cultures

6×10^4 cell/ml passage 2 MSCs were plated in cell culture dishes ($1.5 \times 10^4/cm^2$). After 24 h incubation, MSC cultures were exposed to B16F1-derived exosomes (40 μg/ml exosomal proteins; 1.5×10^{11} exosomes) at every 24 h. Samples were exposed to exosomes for 24, 48, 72, and 96 h and then harvested in method-competent buffers.

Visualization of Labeled Exosome Internalization in MSCs

To examine the uptake of exosomes by MSCs, cells were plated to black 24-well Visiplates (1×10^4 cells/well) and incubated for 24 h. The exosomes were labeled with Dil dye (1,1′-dioctadecyl-3,3,3′,3′-tetramethylindocarbocyanine perchlorate, PromoKine, Heidelberg, Germany) and the MSC cultures were labeled with DiO dye (3,3′-dioctadecyloxacarbo-cyanine perchlorate, PromoKine) according to the manufacturer's instructions. Dil-labeled exosomes were washed in DPBS by ultracentrifugation (at 150,000 g for 1 h at 4°C). Forty micrograms per milliliter DiL-labeled exosomes were added to DiO-labeled MSC cultures and the exosome uptake was followed for 24 h in the Celldiscoverer 7 automated live cell imaging system (Zeiss, Oberkochen, Germany). After 24 h, the cells were fixed with 4% paraformaldehyde solution and a nucleus staining was performed

using DAPI (Life Technologies now part of Thermo Fisher Scientific). Then, 5 image z-stacks were acquired for both channels by Operetta High Content Screening System (Perkin Elmer, Waltham, MA). The stacks were maximum intensity projected and then analyzed automatically using a customized version of CellProfiler (18). Nuclei were detected with Otsu-adaptive threshold combined with diameter based filtering, then cytoplasms were identified with propagation method seeded from the nuclei and using the exosome channel. Exosomes were located with a customized version of A-trous wavelet transform based spot detection (19). Several wavelet levels were used to ensure the detection of exosomes with various size and then the overlaps were removed based on circularity measures. Finally, the exosome numbers per cell were identified using MATLAB programming, the diagrams were created in Microsoft Excel.

Cell Proliferation

After 72 h incubation, exosome-exposed and control MSC cultures were dissociated with trypsin from the culture surface. Cells were washed in medium and counted in a Bürker chamber and a cell counter (Bio-Rad, TC10 Automated Cell Counter).

Detection of Apoptosis

Exosome-exposed MSCs and control cells were treated with 100 ng/ml mouse TNFα (R&D Systems). After 24 h incubation, cell death was determined by the Annexin V Apoptosis Detection Kit with PI (Biolegend, San Diego, CA) according to the manufacturer's recommendations. Samples were measured by FACS Calibur flow cytometer (BD Biosciences), data were analyzed by Flowing Software (Cell Imaging Core, Turku Center for Biotechnology, Finland) where percent of positive cells was determined by relative fluorescence intensity and the results were expressed as mean of percentage of positive cells (%) ±SD. Cells that are annexin-V/PI double positive show the sign of late apoptosis, while cells that are annexin-V positive and PI negative indicate early apoptosis. Annexin-V negative and PI positive cells are necrotic, viable cells are both annexin-V, and propidium iodide (PI) negative.

RNA Preparation, Melan-A, and Mitf Quantitative Real-Time PCR (QRT-PCR)

Total RNA of biological samples was purified using the Quick-RNA MiniPrep isolation kit of #R1054S (Zymo Research Irvine, CA). All the preparation steps were carried out according the manufacturer's instructions. RNA samples were stored at −80°C in the presence 30 U of Prime RNAse inhibitor (Fermentas, part of Thermo Fisher Scientific) for further analysis. The quantity of isolated RNA samples was checked by spectrophotometry (NanoDrop 3.1.0, Rockland, DE).

QRT-PCR was performed on a RotorGene 3000 instrument (Corbett Research, Sydney, Australia) with gene-specific primers and SybrGreen protocol to monitor gene expression. One microgram of total RNA was reverse transcribed with random primers using the High-Capacity cDNA Archive Kit (Applied Biosystems) according to the manufacturer's instructions in final volume of 30 μl. The temperature profile of the reverse transcription was the following: 10 min at room temperature, 2 h at 37°C, 5 min on ice, and finally 10 min at 75°C for enzyme inactivation. These steps were carried out in a Thermal Cycler machine (MJ Research, Marshall Scientific, Hampton, NH). After dilution with 30 μl of water, 1 μl of the diluted reaction mix was used as template in the QRT-PCR. Reactions were done with FastStart SYBR Green Master mix (Roche) according to the manufacturer's instructions at a final primer concentration of 250 nM under the following conditions: 15 min at 95°C, 40 cycles of 95°C for 15 s, 60°C for 25 s, and 72°C for 25 s. The fluorescence intensity of SybrGreen dye was detected after each amplification step. Melting temperature analysis was done after each reaction to check the quality of the products. Primers were designed using the online Roche Universal Probe Library Assay Design Center. The quality of the primers was verified by MS analysis provided by Bioneer (Daejeon, Republic of Korea). Relative expression ratios were calculated as normalized ratios to MmRpl27 (*Mus musculus* ribosomal protein L27) gene. Non-template control sample was used for each PCR run to check the primer-dimer formation. The final relative gene expression ratios were calculated as delta-delta Ct values. Information about the genes and the primers is collected in **Table S1**.

RNA Isolation, Reverse Transcription, and TaqMan Panel

RNAs were isolated from MSC cells with Qiagen RNeasy mini kit (Qiagen) based on the manufacturer's instruction. RNA concentrations were measured by NanoDrop spectrophotometer (NanoDrop). cDNAs were reverse transcribed with TaqMan Reverse Transcription Reagents (Thermo Fisher Scientific) following the manufacturer's instruction. For the TaqMan QRT-PCR panel, cDNA mixture of three parallel samples was used in case of each condition: control, 6, 24, and 72 h exosome treatment applied on MSC cells derived from four mice. Eighty nanogram cDNA and TaqMan Gene Expression Master Mix (Thermo Fisher Scientific) were used for the qPCR experiment. Expression of the examined 44 genes was calculated by ΔΔCt method and normalized to the average Ct values of 4 internal controls (PPIA, 18S RNA, ACTB, and GAPDH).

PD-1 Detection

PD-1 detection by Western blotting

The cells were washed three times in PBS, then were lysed in TENT Buffer (50 mM Tris-HCl, 2 mM EDTA, 150 mM NaCl, 1% TritonX-100, completed with 1x protease inhibitor cocktail (Roche). Protein samples were separated and blotted as described above.

For PD-1 protein level detection, anti-PD-1 (clone: RMO1-14, Biolegend) antibody was used in 1:1,000 dilution. Anti-rat horseradish peroxidase (HRP)-conjugated secondary antibody (R&D Systems) was used in 1:500 dilution.

PD-1 detection by Immunofluorescence microscopy

MSC cultures were fixed with 4% paraformaldehyde for 10 min, and blocked in PBS buffer containing 5% BSA (Sigma-Aldrich) for 60 min at room temperature. After blocking, cells were incubated with primary antibody in DPBS buffer containing

1.2% BSA overnight at 4°C. As primary antibodies, 1:200 anti-PD-1 (clone: RMO1-14, Biolegend,) and 1:200 anti-MLANA (Byorbit) were used. After incubation, cells were washed three times in PBS, and incubated for 1 h at room temperature with 1:100 Alexa Fluor 647-conjugated anti-rat antibody (Jackson ImmunoResearch Laboratories, Baltimore, PA) or 1:500 Alexa Fluor 555-conjugated anti-rabbit antibody (Thermo Fisher Scientific). Tubulin was stained with 1:500 Alexa Fluor 488-conjugated anti-tubulin-α antibody (clone: 10D8, Biolegend). Nucleus staining was performed using DAPI (Life Technologies). Slides were washed three times with DPBS between each step. Images were obtained at 60x magnification using an Olympus confocal laser scanning microscope.

PD-1 detection by STORM super-resolution imaging

All dSTORM super-resolution experiments were performed on a custom-made inverted microscope based on a Nikon Eclipse Ti-E frame. After being conditioned (through spatial filtering via fiber coupling and beam expansion) the applied laser beams were focused into the back focal plane of the microscope objective (Nikon CFI Apo 100x, NA = 1.49), which produced a collimated beam on the sample. The angle of illumination was set via a tilting mirror mounted into a motorized gimbal holder and placed into the conjugate plane of the sample. All the dSTORM images were captured under EPI illumination at an excitation wavelength of 647 nm (Nikon: 647 nm, 300 mW). The laser power, controlled via an acousto-optic tunable filter (AOTF), was set to 4 kW/cm^2 on the sample plane. An additional laser (Nichia, Anan, Tokushima, Japan, 405 nm, 60 mW) was used for both reactivation and reference measurements. Images were captured by an Andor iXon3 897 BV EMCCD digital camera (512 × 512 pixels with pixel size of 16 μm). The size of the illuminated region of the sample was matched to the size of the detector, which determined the field of view (FOV = 80 × 80 μm^2). Frame stacks for dSTORM super-resolution imaging were typically captured at a reduced image size (crop mode), when only the central 128 × 128 pixel region was selected. A fluorescence filter set (Semrock, Rochester, NY, LF405/488/561/635-A-000) was used to select and separate the excitation and emission lights in the microscope. Additional emission filters (Semrock, BLP01-647R-25) were used in the detection path to further clean the fluorescent light spectrally for the reduction of spectral crosstalk.

During the measurements, the perfect focus system of the microscope was used to keep the sample in focus with a precision of <30 nm. The storage buffer on the sample was replaced with a special switching buffer (20). Typically, 10,000 frames were captured with an exposure time of 30 ms. Reference images with full size FOV were captured at low intensity when the majority of fluorescent molecules were still active and the overall structure of the labeled sample could be visualized.

The captured and stored image stacks were evaluated and analyzed by rainSTORM localization software (21). The individual images of single molecules were fitted with a Gaussian point spread function and their center positions were associated with the position of the fluorescent molecule. Localizations were filtered via their intensity, ellipticity and standard deviation values. Localizations with precisions of <45 nm were only used to form the final image. The estimated mean precision of the accepted localizations was 19 nm. Mechanical drift introduced by either the mechanical movement of the sample or thermal effects was analyzed and reduced by means of a blind drift correction algorithm. Spatial coordinates of the localized molecules were stored and the final super-resolved image was visualized. The multicolor merged images were generated by ImageJ software.

In vivo Experiments

Mouse Model

B16F1 melanoma cells were administrated intravenously (1 × 10^5 cell/100 μl) to 6–8 week old female C57BL/6N mice (Charles River Laboratories). One week later, tumor bearing mice were randomized and divided into 3 groups (n = 10/group). Mice were injected intravenously with control buffer (100 μl), exosome exposed MSCs (1 × 10^5 cell/100 μl) or exosomes (40 μg/100 μl) 7, 8, 9, 10, 11 days after the tumor injection (**Table S2**). One week after the first MSC administration, 3 animals/group were euthanized, their lungs were removed, photographed and stored at −80°C for further protein, mRNA and histological analyses. The remained mice were observed for 10 more days. At the end point, the animals were euthanized, and the tumor metastases were investigated not only in their lung, but also in their entire body and removed for histological analysis. Experiments were repeated 3 times. All animal experiments were performed in accordance with national (1998. XXVIII; 40/2013) and European (2010/63/EU) animal ethics guidelines. The experimental protocols were approved by the Animal Experimentation and Ethics Committee of the Biological Research Centre of the Hungarian Academy of Sciences and the Hungarian National Animal Experimentation and Ethics Board (clearance number: XVI./03521/2011 and XV./78/2018).

Tumor Coverage

Tumor coverage of lungs was determined by the analysis of acquired images using the ImageJ software. The area of tumors and the healthy regions was measured and the mean percentage, SD, and p values were calculated in Microsoft Excel.

Quantification of Metastases Associated Vessel Diameters

From native animal lungs 4 μm criostat sections were made on silanized slides, than fixed and retrieved by Fix and Perm A-B solution (Thermo Fisher Scientific, USA) for 20 min. Sections were counterstained by conventional hematoxilin for 30 min than washed in tap water and coverslipped. Sections were digitalized by automatic slide-scanner (3DHistech, Hungary), using the software 3DHISTECH Pannoramic Viewer (3DHistech, Hungary). Strict tumor border was carefully marked then vessel diameters were measured.

Cytokine and Chemokine Array

Lung samples were lysed in NP40 cell lysis buffer (Thermo Fisher Scientific, USA) and protein content was measured by the Pierce BCA Protein Assay kit (Thermo Fisher Scientific, USA). Expression levels of different cytokines in pooled lung specimens were determined using Mouse Cytokine Array Panel A (R&D

Systems, Cat. no. ARY006), according to the manufacturer's instructions. Immunoreactive signals were detected by using LI-COR ODYSSEY Fc (Dual-mode imaging system) imager followed by analysis with Image Studio Lite v5.2.

Custom TaqMan Array Panels

QRT-PCR was performed on an ABI Prism 7000 sequence detection system (Applied Biosystems) using specific pre-designed customized 96-well TaqMan Array oncogene panels (Thermo Fisher Scientific) containing 44 specifically selected primers and probes according to extensive literature work. Total RNA was isolated using TRIzol (Thermo Fisher Scientific), DNase treatment was performed according to the manufacturer's protocol, and then total RNA was transcribed into cDNA using High Capacity cDNA Kit (Thermo Fisher Scientific). PCR amplification was performed using TaqMan primers and probes and thermal cycle conditions were set as follows: 2 min at 50°C, 10 min at 95°C, and 40 cycles of 15 s at 95°C and 1 min at 60°C. As internal control transcripts of ACTB (Assay ID: Mm00607939_s1), GAPDH (Assay ID: Mm99999915_g1), and PPIA (Assay ID: Mm02342430_g1) were determined. The amount of the transcripts was normalized to those of the housekeeping genes using the ΔCt method. Finally the results were normalized to the expression of the vehicle control (ΔΔCt method).

For relationship discovery Hierarchical Cluster Analysis was performed by R software. In detail, the "bottom up" agglomerative hierarchical clustering strategy was used and results represented in a tree-based dendrogram [For refer the R software: (22)].

Network Representation by Ingenuity Pathway Analysis

According to literature data, we established a protein network from the *in vivo* overexpressed genes. A custom graphical representation of this network was generated using the Path Explorer tool of the IPA Path Designer. Genes are represented as red nodes, using various shapes that represent the functional class of the gene product. In a few cases proteins are substituted with the complex, which they are involved in. To identify the potential exosomal factors, which can induce the activation of the network, a list was generated from the exosomal proteins detected by LC-MS/MS and the exosomal miRNAs identified by SOLiD sequencing. The Grow tool in the IPA Path Designer revealed significant interactions between the network and the generated list (the interacting exosomal factors are listed in gray boxes and the types of relationships are indicated in parentheses). During construction in the IPA, the significance level was set to "experimentally observed" data to avoid the representation of predicted, unproven interactions.

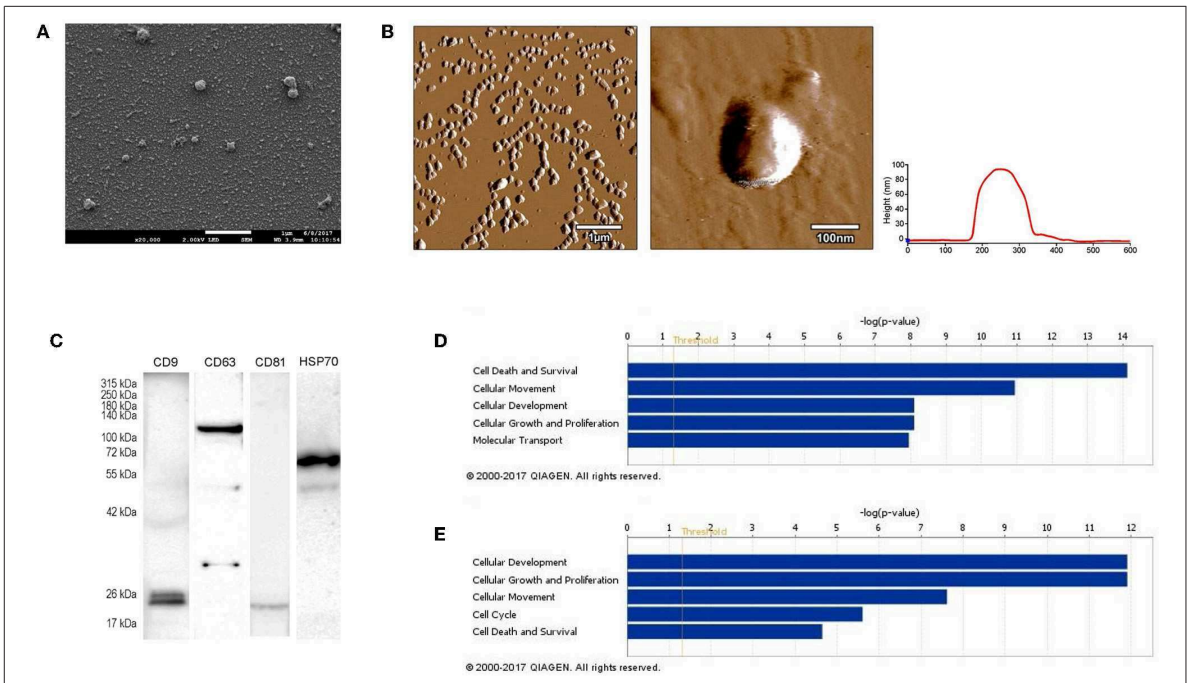

FIGURE 1 | Characterization of B16F1 melanoma cell culture-derived exosomes. **(A)** Scanning electron micrograph of melanoma exosomes. **(B)** Atomic force microscopy images of exosomes. Left and middle pictures represent the shape and surface topography of vesicles, right graph represents height profile. **(C)** Western blot analysis of common exosome markers (CD9, CD63, CD81, and HSP70). **(D,E)** Top 5 molecular and cellular functions identified by Ingenuity Pathway Analysis of exosomal proteins and miRNAs.

TABLE 1 | List of exosomal proteins identified by LC-MS/MS.

ID	Symbol	Entrez gene name
P97857	ADAMTS1	ADAM metallopeptidase with thrombospondin type 1 motif 1
Q3TNX8	ADAMTS4	ADAM metallopeptidase with thrombospondin type 1 motif 4
Q640N1	AEBP1	AE binding protein 1
P05064	ALDOA	Aldolase, fructose-bisphosphate A
P97429	ANXA4	Annexin A4
P48036	ANXA5	Annexin A5
P08226	APOE	Apolipoprotein E
Q3TWT5	ASAH1	N-acylsphingosine amidohydrolase 1
Q3TXF9	ATP1A1	ATPase Na^+/K^+ transporting subunit alpha 1
P97370	ATP1B3	ATPase Na^+/K^+ transporting subunit beta 3
Q1XID4	ATP6AP2	ATPase H^+ transporting accessory protein 2
Q9JL18	BACE2	Beta-site APP-cleaving enzyme 2
O55107	BSG	Basigin (Ok blood group)
Q8R2Q8	Bst2	Bone marrow stromal cell antigen 2
Q9WVT6	CA14	Carbonic anhydrase 14
P41731	CD63	CD63 molecule
P35762	CD81	CD81 molecule
P10605	CTSB	Cathepsin B
P18242	CTSD	Cathepsin D
P29812	DCT	Dopachrome tautomerase
P57776	EEF1D	Eukaryotic translation elongation factor 1 delta
Q3UAM9	ENG	Endoglin
P17182	ENO1	Enolase 1
P19096	FASN	Fatty acid synthase
P30416	FKBP4	FK506 binding protein 4
P11276	FN1	Fibronectin 1
P09528	FTH1	Ferritin heavy chain 1
P16858	GAPDH	Glyceraldehyde-3-phosphate dehydrogenase
P08752	GNAI2	G protein subunit alpha i2
Q3TAV1	GPNMB	Glycoprotein nmb
P19157	GSTP1	Glutathione S-transferase pi 1
P11499	HSP90AB1	Heat shock protein 90 alpha family class B member 1
B1B0C7	HSPG2	Heparan sulfate proteoglycan 2
Q9CQW9	IFITM3	Interferon induced transmembrane protein 3
G3UYZ1	IGSF8	Immunoglobulin superfamily member 8
Q91VK4	ITM2C	Integral membrane protein 2C
P02468	LAMC1	Laminin subunit gamma 1
Q60961	LAPTM4A	Lysosomal protein transmembrane 4 alpha
P35951	LDLR	Low density lipoprotein receptor
Q07797	LGALS3BP	Galectin 3 binding protein
Q3U2W5	LGALS8	Galectin 8
P16056	MET	MET proto-oncogene, receptor tyrosine kinase
P21956	MFGE8	Milk fat globule-EGF factor 8 protein
Q2TA50	MLANA	Melan-A
Q6NVG5	MREG	Melanoregulin
Q9EPX2	PAPLN	Papilin, proteoglycan like sulfated glycoprotein
Q3UIP2	PCOLCE	Procollagen C-endopeptidase enhancer
Q811J2	LOC72520	LOC72520 protein
Q80Y09	PDCD6IP	Programmed cell death 6 interacting protein
P62962	PFN1	Profilin 1
P09411	PGK1	Phosphoglycerate kinase 1
P52480	PKM	Pyruvate kinase, muscle
Q9CZB2	PMEL	Premelanosome protein
P17742	PPIA	Peptidylprolyl isomerase A
P35700	PRDX1	Peroxiredoxin 1
Q61171	PRDX2	Peroxiredoxin 2
Q543S0	PRELP	Proline and arginine rich end leucine rich repeat protein
P53994	RAB2A	RAB2A, member RAS oncogene family
Q8CCG5	RALB	RAS like proto-oncogene B
O89086	RBM3	RNA binding motif (RNP1, RRM) protein 3
P35980	RPL18	Ribosomal protein L18
Q3U5P4	SCPEP1	Serine carboxypeptidase 1
O08992	SDCBP	Syndecan binding protein
Q0VGP2	SEMA3B	Semaphorin 3B
P32261	SERPINC1	Serpin family C member 1
P10852	SLC3A2	Solute carrier family 3 member 2
Q3UQM7	SLC7A5	Solute carrier family 7 member 5
O09044	SNAP23	Synaptosome associated protein 23
Q64337	SQSTM1	Sequestosome 1
Q8CI59	STEAP3	STEAP3 metalloreductase
Q3TDG9	STX12	Syntaxin 12
O70439	STX7	Syntaxin 7
P40749	SYT4	Synaptotagmin 4
O88968	TCN2	Transcobalamin 2
Q542D9	TFRC	Transferrin receptor
P39876	TIMP3	TIMP metallopeptidase inhibitor 3
Q4FJX7	TINAGL1	Tubulointerstitial nephritis antigen like 1
Q9DCS1	TMEM176A	Transmembrane protein 176A
Q9R1Q6	TMEM176B	Transmembrane protein 176B
Q9CZX7	TMEM55A	Transmembrane protein 55A
Q9QY73	TMEM59	Transmembrane protein 59
O88746	TOM1	Target of myb1 membrane trafficking protein
O89023	TPP1	tripeptidyl peptidase 1
Q3UCW0	TSG101	Tumor susceptibility 101
Q4FJW7	TSPAN4	Tetraspanin 4
Q8BJU2	TSPAN9	Tetraspanin 9
P11344	TYR	Tyrosinase
P07147	TYRP1	Tyrosinase related protein 1
O70404	VAMP8	Vesicle associated membrane protein 8
Q8R0J7	VPS37B	VPS37B, ESCRT-I subunit
Q8R105	VPS37C	VPS37C, ESCRT-I subunit
O88384	VTI1B	Vesicle transport through interaction with t-SNAREs 1B
A8DUQ1	HBBT1	Beta-globin
P70356	MELA	Gag-pol poliprotein
P70355	MELA	Envelope protein

(Continued)

Statistical Analysis

All of the data are presented as the mean ± SD or SEM and represent minimum of three independent experiments. Statistical parameters including statistical analysis, statistical significance, and n value are reported in the figure legends. For *in vivo* experiments n = number of animals. For statistical comparison, we performed two-tailed Student's t-test. A value of $p < 0.05$ was considered significant [represented as $^{*}p < 0.05$, not significant (n.s.)].

RESULTS

Isolated Vesicles Show Exosomal Properties

First, we isolated extracellular vesicles from B16F1 mouse melanoma cells. As it was shown by SEM and AFM (**Figures 1A,B**), the isolated fraction indeed contained exosomes as the particles were cap-shaped, and their size was within the 40–120 nm range. Then, presence of molecules (CD9, CD63, CD81, and HSP70), characteristic for exosomes (4, 17) was assessed by Western blotting (**Figure 1C**).

Exosomes were then subjected to large-scale analysis to determine their protein and miRNA profiles. Whole proteome analysis (using LC-MS/MS) and bioinformatics tools (used to identify elements of the exosome's proteomics spectrum in the UniProt database, and to compare the findings with entries of the ExoCarta database) revealed that 95 distinct proteins were identified in melanoma exosomes (**Table 1**). These proteins exhibited 86.3% overlap with molecules listed as characteristic exosome protein markers in ExoCarta. Further, miRNA sequencing (using SOLiD 5500xl technology) identified 168 known miRNA elements (**Table 2**) which, similarly to the proteomics data, exhibited a large (93.5%) overlap with molecules listed as characteristic exosome miRNA markers in ExoCarta.

To uncover the functional significance of the proteomics and miRNA sequencing data, IPA was employed. This analysis has shown that the identified proteins most probably participated in cellular and molecular processes such as "Cell Death and Survival," "Cellular Movement," "Cell-to-Cell Signaling and Interaction," "Cellular Growth and Proliferation," and "Cell Morphology" ($P_{range} = 7.53 \times 10^{-15}$-$9.32 \times 10^{-4}$ significance range) (**Figure 1D**). Very similarly to these data, functions of the identified miRNAs were suggested to be linked to mechanisms of "Cellular Development," "Cellular Growth and Proliferation," "Cellular Movement," "Cell Cycle," and "Cell Death and Proliferation" ($P_{range} = 1.25 \times 10^{-12}$-$4.88 \times 10^{-2}$ significance range) (**Figure 1E**).

Tumor Exosome Exposure Resulted in Oncogenic Reprogramming of MSCs *in vitro*

Then, we investigated the effect of exosomes on biological processes (e.g., proliferation, survival, malignant transformation, etc.) of MSCs, which are generally considered as proper *in vitro* models of tumor stroma (12). For these experiments, MSC

TABLE 2 | List of exosomal miRNAs identified by SOLiD 5500xl technology.

Symbol	Seed regio	ID
let-7a-3p	UAUACAA	mmu-let-7a-1-3p
		mmu-let-7b-3p
		mmu-let-7c-2-3p
		mmu-let-7f-1-3p
let-7a-5p	GAGGUAG	mmu-let-7a-5p
		mmu-let-7b-5p
		mmu-let-7c-5p
		mmu-let-7d-5p
		mmu-let-7e-5p
		mmu-let-7f-5p
		mmu-let-7g-5p
		mmu-mir-98-5p
let-7d-3p	UAUACGA	mmu-let-7d-3p
let-7i-3p	UGCGCAA	mmu-let-7i-3p
miR-100-5p	ACCCGUA	mmu-mir-99a-5p
		mmu-mir-99b-5p
miR-101-3p	ACAGUAC	mmu-mir-101a-3p
miR-103-1-5p	GCUUCUU	mmu-mir-107-5p
miR-103-3p	GCAGCAU	mmu-mir-103-3p
		mmu-mir-107-3p
miR-10a-5p	ACCCUGU	mmu-mir-10a-5p
		mmu-mir-10b-5p
miR-1191a	AGUCUUA	mmu-mir-1191a
miR-1249-3p	CGCCCUU	mmu-mir-1249-3p
miR-125b-5p	CCCUGAG	mmu-mir-125a-5p
		mmu-mir-125b-5p
		mmu-mir-351-5p
miR-126a-5p	AUUAUUA	mmu-mir-126a-5p
miR-128-3p	CACAGUG	mmu-mir-128-3p
miR-129-1-3p	AGCCCUU	mmu-mir-129-1-3p
		mmu-mir-129-2-3p
miR-129b-5p	CUUUUUG	mmu-mir-129b-5p
miR-130a-3p	AGUGCAA	mmu-mir-130a-3p
		mmu-mir-130b-3p
		mmu-mir-301a-3p
		mmu-mir-301b-3p
miR-130a-5p	CUCUUUU	mmu-mir-130a-5p
miR-130b-5p	CUCUUUC	mmu-mir-130b-5p
miR-132-3p	AACAGUC	mmu-mir-132-3p
miR-132-5p	ACCGUGG	mmu-mir-132-5p
miR-135a-5p	AUGGCUU	mmu-mir-135a-5p
miR-138-5p	GCUGGUG	mmu-mir-138-5p
miR-139-5p	CUACAGU	mmu-mir-139-5p
miR-140-3p	ACCACAG	mmu-mir-140-3p
miR-140-5p	AGUGGUU	mmu-mir-140-5p
miR-142-3p	GUAGUGU	mmu-mir-142a-3p
miR-143-5p		mmu-mir-143-5p
miR-144-3p	ACAGUAU	mmu-mir-144-3p
miR-144-5p	GAUAUCA	mmu-mir-144-5p
miR-145-5p	UCCAGUU	mmu-mir-145a-5p

(Continued)

TABLE 2 | Continued

Symbol	Seed regio	ID
miR-146a-5p	GAGAACU	mmu-mir-146a-5p
miR-148a-3p	CAGUGCA	mmu-mir-148b-3p
miR-151-3p	UAGACUG	mmu-mir-151-3p
miR-15a-3p	AGGCCAU	mmu-mir-15a-3p
miR-15b-3p	GAAUCAU	mmu-mir-15b-3p
miR-16-2-3p	CCAAUAU	mmu-mir-16-2-3p
miR-16-5p	AGCAGCA	mmu-mir-15a-5p
		mmu-mir-15b-5p
		mmu-mir-16-5p
		mmu-mir-195a-5p
		mmu-mir-322-5p
		mmu-mir-497a-5p
miR-17-3p	CUGCAGU	mmu-mir-17-3p
miR-17-5p	AAAGUGC	mmu-mir-106b-5p
		mmu-mir-17-5p
		mmu-mir-20a-5p
		mmu-mir-93-5p
miR-181a-1-3p	CCAUCGA	mmu-mir-181a-1-3p
miR-181a-5p	ACAUUCA	mmu-mir-181a-5p
		mmu-mir-181b-5p
		mmu-mir-181c-5p
		mmu-mir-181d-5p
miR-1827	GAGGCAG	mmu-mir-709
miR-1839-3p	GACCUAC	mmu-mir-1839-3p
miR-185-5p	GGAGAGA	mmu-mir-185-5p
miR-186-5p	AAAGAAU	mmu-mir-186-5p
miR-187-3p	CGUGUCU	mmu-mir-187-3p
miR-188-3p	UCCCACA	mmu-mir-188-3p
miR-188-5p	AUCCCUU	mmu-mir-188-5p
miR-18a-5p	AAGGUGC	mmu-mir-18a-5p
miR-191-5p	AACGGAA	mmu-mir-191-5p
miR-193a-3p	ACUGGCC	mmu-mir-193a-3p
miR-1981-3p	AUCUAAC	mmu-mir-1981-3p
miR-199a-3p	CAGUAGU	mmu-mir-199a-3p
		mmu-mir-199b-3p
miR-199a-5p	CCAGUGU	mmu-mir-199a-5p
		mmu-mir-199b-5p
miR-19b-3p	GUGCAAA	mmu-mir-19a-3p
		mmu-mir-19b-3p
miR-204-5p	UCCCUUU	mmu-mir-211-5p
miR-21-5p	AGCUUAU	mmu-mir-21a-5p
miR-210-3p	UGUGCGU	mmu-mir-210-3p
miR-210-5p	GCCACUG	mmu-mir-210-5p
miR-219a-5p	GAUUGUC	mmu-mir-219a-5p
miR-22-3p	AGCUGCC	mmu-mir-22-3p
miR-22-5p	GUUCUUC	mmu-mir-22-5p
miR-221-3p	GCUACAU	mmu-mir-222-3p
miR-223-3p	GUCAGUU	mmu-mir-223-3p
miR-224-5p	AAGUCAC	mmu-mir-224-5p
miR-23a-3p	UCACAUU	mmu-mir-23a-3p
		mmu-mir-23b-3p

(Continued)

TABLE 2 | Continued

Symbol	Seed regio	ID
miR-24-1-5p	UGCCUAC	mmu-mir-24-2-5p
miR-24-3p	GGCUCAG	mmu-mir-24-3p
miR-26a-5p	UCAAGUA	mmu-mir-26a-5p
miR-26a-5p	UCAAGUA	mmu-mir-26a-5p
		mmu-mir-26b-5p
miR-27a-3p	UCACAGU	mmu-mir-27a-3p
		mmu-mir-27b-3p
miR-29a-5p	CUGAUUU	mmu-mir-29a-5p
miR-29b-1-5p	CUGGUUU	mmu-mir-29b-1-5p
miR-29b-3p	AGCACCA	mmu-mir-29a-3p
		mmu-mir-29b-3p
		mmu-mir-29c-3p
miR-3065-5p	CAACAAA	mmu-mir-3065-5p
miR-30c-5p	GUAAACA	mmu-mir-30a-5p
		mmu-mir-30b-5p
		mmu-mir-30c-5p
		mmu-mir-30d-5p
		mmu-mir-30e-5p
miR-31-3p	GCUAUGC	mmu-mir-31-3p
miR-31-5p	GGCAAGA	mmu-mir-31-5p
miR-3176	CUGGCCU	mmu-mir-378d
miR-324-5p	GCAUCCC	mmu-mir-324-5p
miR-328-3p	UGGCCCU	mmu-mir-328-3p
miR-329-3p	ACACACC	mmu-mir-362-3p
miR-33-5p	UGCAUUG	mmu-mir-33-5p
miR-330-5p	CUCUGGG	mmu-mir-326-3p
miR-331-3p	CCCCUGG	mmu-mir-331-3p
miR-339-5p	CCCUGUC	mmu-mir-339-5p
miR-340-3p	CCGUCUC	mmu-mir-340-3p
miR-344a-5p	CAGGCUC	mmu-mir-484
miR-345-5p	CUGACCC	mmu-mir-345-5p
miR-3473b	GGCUGGA	mmu-mir-3473b
		mmu-mir-3473e
miR-34a-5p	GGCAGUG	mmu-mir-34a-5p
		mmu-mir-34b-5p
		mmu-mir-34c-5p
miR-34c-3p	AUCACUA	mmu-mir-34b-3p
miR-350	UCACAAA	mmu-mir-350-3p
miR-361-5p	UAUCAGA	mmu-mir-361-5p
miR-362-5p	AUCCUUG	mmu-mir-362-5p
miR-374b-5p	UAUAAUA	mmu-mir-374b-5p
miR-378a-3p	CUGGACU	mmu-mir-378a-3p
		mmu-mir-378c
miR-378a-5p	UCCUGAC	mmu-mir-378a-5p
miR-3909	GUCCUCU	mmu-mir-877-3p
miR-423-3p	GCUCGGU	mmu-mir-423-3p
miR-423-5p	GAGGGGC	mmu-mir-423-5p
miR-425-5p	AUGACAC	mmu-mir-425-5p
miR-451a	AACCGUU	mmu-mir-451a
miR-501-5p	AUCCUUU	mmu-mir-501-5p
miR-503-5p	AGCAGCG	mmu-mir-503-5p

(Continued)

TABLE 2 | Continued

Symbol	Seed regio	ID
miR-532-5p	AUGCCUU	mmu-mir-532-5p
miR-542-3p	GUGACAG	mmu-mir-542-3p
miR-574-5p	GAGUGUG	mmu-mir-574-5p
miR-582-5p	UACAGUU	mmu-mir-582-5p
miR-652-3p	AUGGCGC	mmu-mir-652-3p
miR-670-5p	UCCCUGA	mmu-mir-670-5p
miR-700-5p	AAGGCUC	mmu-mir-700-5p
miR-744-3p	UGUUGCC	mmu-mir-744-3p
miR-744-5p		mmu-mir-744-5p
miR-7a-5p	GGAAGAC	mmu-mir-7a-5p
miR-872-3p	GAACUAU	mmu-mir-872-3p
miR-872-5p	AGGUUAC	mmu-mir-872-5p
miR-9-5p	CUUUGGU	mmu-mir-9-5p
miR-92a-3p	AUUGCAC	mmu-mir-25-3p
		mmu-mir-32-5p
		mmu-mir-92a-3p

cultures were initiated from mouse abdominal adipose tissue (17) and were subjected to melanoma exosome treatment.

First, we assessed whether exosomes were internalized by MSCs. High-throughput microscopy showed that MSCs [labeled green by the $DiOC_{18}(3)$ lipid dye] indeed took up exosomes [labeled red by the $DilC_{18}(3)$ lipid dye] as early as 1–2 h after application (**Figure S1**). Importantly, after 24 h, the majority of MSCs were loaded by exosomes (**Figures 2A,B**). Indeed, image analysis and statistical evaluation revealed a 91% internalization efficacy. This suggests that functional alterations demonstrated by this study were due to exosome-induced cell-population, and not individual cell level effects.

Then, we determined whether the internalized exosomes could induce a melanoma-like malignant transformation of the MSCs. By employing two complementary cell-counting methods, we found that proliferation rate of the MSCs significantly accelerated 72 h after exosome exposure (**Figure 2C**). By flow cytometry, we also showed that the exosome-treated MSCs exhibited a partial resistance to the cell death-inducing effects of 100 ng/ml tumor necrosis factor-α (TNFα) as the fraction of the dead cells was significantly decreased in these cultures (**Figure 2D**).

Since the exosomes were isolated from melanoma cells, we were then intrigued to uncover whether the above alterations (which all argue for the malignant transformation of the susceptible cells) also resulted in *de novo* appearance of melanoma-specific features in the transformed MSCs. To answer this question, expression of the melanoma-specific markers MLANA and MITF were investigated. By QRT-PCR, we found that mRNA transcript levels of both markers elevated markedly in MSCs upon exosome treatment (**Figure 2E** and **Figure S2**), albeit the kinetics of elevation of the two molecules were slightly different. Moreover, in good accordance with the mRNA data, immunofluorescence labeling showed that exosome exposure markedly increased the expression of MLANA at the protein level as well (**Figure 2F**).

Next, we assessed whether the above effects of exosomes inducing a malignant-like transformation of the MSCs was accompanied by a cellular-molecular oncogenic reprogramming of the target cells. Naïve MSCs were exposed to a standardized volume of exosomes for various time intervals (to avoid the experimental fluctuations, we collected pooled samples from multiple independent *in vitro* experiments). Then, samples were subjected to QRT-PCR analysis using a self-designed panel of 40 oncogenes and tumor suppressor genes which were previously suggested to play a role in melanoma progression (**Table 3**).

As shown in **Figure 3A**, gene expression pattern of MSCs exposed to melanoma exosomes, exhibited a clear oncogenic dominance (compared to the non-exposed cells). This was verified by statistical analysis of the mean relative gene expression levels of all molecules investigated. Statistically higher values were obtained in the case of exosome-treated cells ($p = 1.9 \times 10^{-5}$, $p = 0.031$ and $p = 2.3 \times 10^{-8}$ for the 6, 24, and 72 h time points, respectively).

As mentioned above, Kleffel et al. has recently shown that melanoma cell subpopulations which overexpress PD-1, quite intriguingly exhibit remarkably increased invasiveness and aggressive growth properties (15). However, the authors did not define the factor(s) which induced the above PD-1 overexpression. Since the above finding strongly suggested an "MSC re-education" capacity of melanoma exosomes to induce malignant-like behavior, we next assessed the expression of PD-1 in MSC cultures.

As expected, only insignificant PD-1 expression (both at the mRNA and protein levels) could be identified in control, non-treated MSCs. In contrast, a marked, significant, and time-dependent elevation of PD-1 expression was detected upon exosome treatment by QRT-PCR (**Figure 3B**), Western blot and an immunocytochemical analysis (**Figures 3C,D**). Further, by employing super-resolution microscopy, we were able to identify a dramatic upregulation of PD-1 at the single molecular level in exosome-treated MSCs (**Figure 3E**).

Importantly, since proteomics analysis did not identify the presence of PD-1 in exosomes, these data suggest that the high PD-1 protein content in exosome-exposed MSCs was a result of *de novo* induction and not of exosome-mediated molecular transfer. Our findings therefore suggest that melanoma exosome-mediated "re-education" of the cells resulted in a novel MSC population which could be identified as $MSC^{PD\text{-}1+}$.

B16F1 Exosomes Augment *in vivo* Tumorigenesis and Tumor Progression

After presenting evidence for the *in vitro* tumorigenic induction potential of exosomes on cultured MSCs, we hypothesized that this phenomenon could be identified *in vivo* as well. To probe this assumption, we employed the well-known animal model, routinely used in our laboratories (46), in which tumors, developed mostly in the lungs, are induced in mice by intravenous administration of mouse B16F1 melanoma cells (to the tail vein). Then, tumor-bearing mice received buffer, or exosomes isolated from the same B16F1 melanoma cells, or exosome-induced $MSC^{PD\text{-}1+}$ cells.

Notably, the exosome-related groups (i.e., exosome, $MSC^{PD\text{-}1+}$) were characterized by a markedly increased size of tumor-covered lung tissues (the increase proved to be significant in the $MSC^{PD\text{-}1+}$ group) (**Figure 4A**). Of further

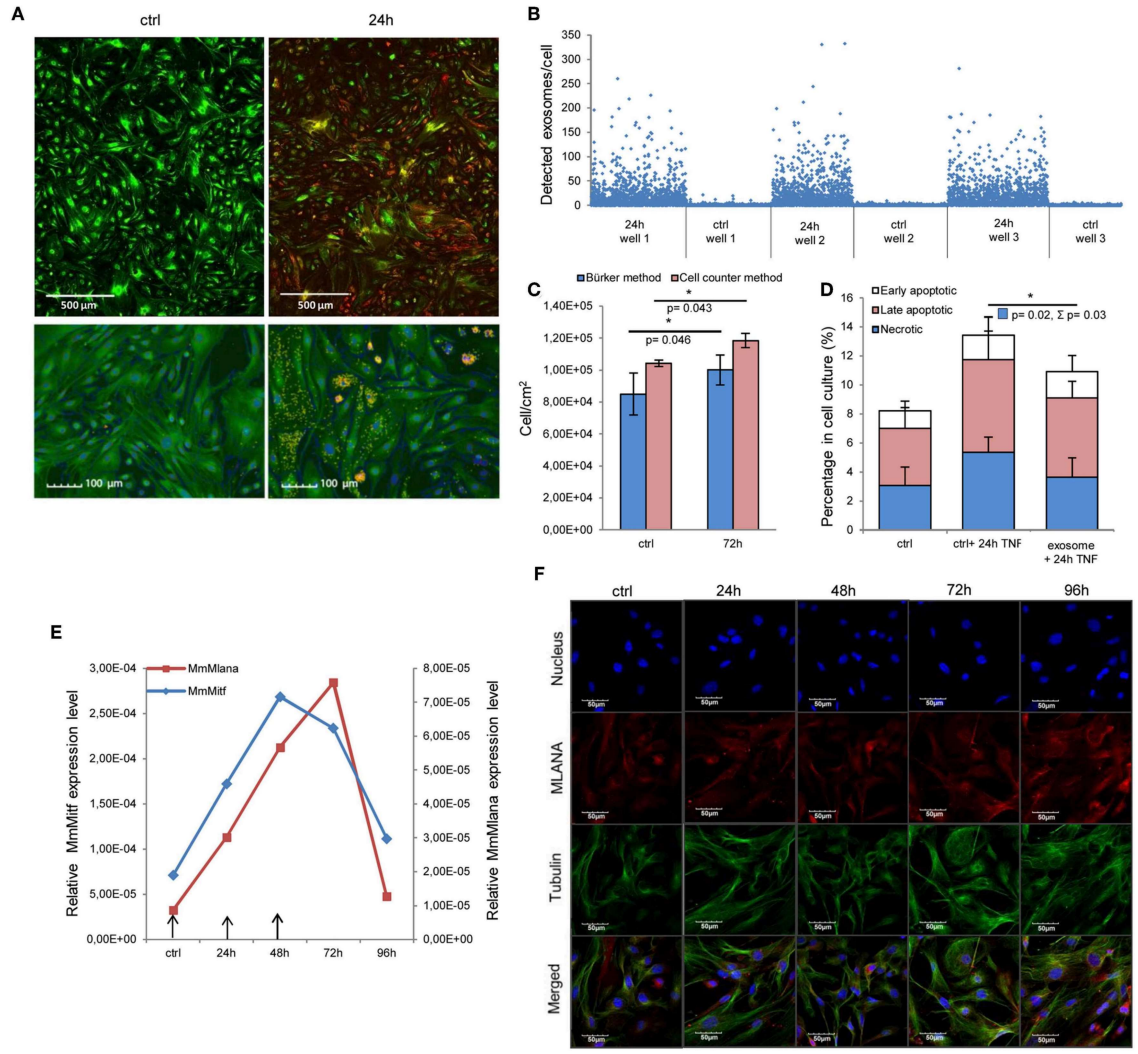

FIGURE 2 | Internalized melanoma exosomes induce malignant transformation of the recipient MSCs. **(A)** Fluorescent images of exosome uptake by MSCs. DiO (green lipid dye)-labeled cells were exposed to DiI (red lipid dye)-labeled exosomes for 24 h and fixed in 4% PFA. Control cells were treated in the same manner without exosomes. Pictures were acquired by an Operetta high content screening system (Perkin Elmer). Lower two images represent an experiment, where nuclei were counterstained with DAPI. Exosomes were detected with a customized version of A-trous wavelet transform, and were highlighted with yellow. **(B)** Quantitative analysis of exosome uptake. The graph shows the number of detected exosomes (Y axis) in each cell (X axis) in three exosome-exposed (24 h) and three control cell cultures (ctrl). **(C)** Cell proliferation assay of exosome-exposed MSCs. Cells were plated at 1×10^4 cell/cm^2 density in control and exosome-exposed cultures, and 72 h after the exosome treatment, the cell number was determined by manual counting and by an automated cell counter. Both methods showed a significantly increased cell proliferation of exosome-treated cells. Results are presented as mean ± SD ($n = 3$). **(D)** Apoptosis analysis of exosome-exposed MSCs by flow cytometry. Exosome-pre-exposed cells were treated by 100 ng/ml TNFα for 24 h, stained with Annexin V-FITC and propidium iodide. They were analyzed by flow cytometry both in the case of the TNFα-treated and the untreated control cell cultures. The graph represents the percentage of early apoptotic, late apoptotic and necrotic cells. Both TNFα-induced total cell death (Σ) and necrosis were significantly lower ($\Sigma p = 0.03$ and $p = 0.02$, respectively) in exosome-pretreated cell cultures compared to the corresponding control cells. Results are presented as mean + SD ($n = 3$). **(E)** QRT-PCR analysis of Mlana and Mitf in MSC cultures treated by exosomes in every 24 h indicated by arrows in the graph. The expression of both mRNAs increased after exosome exposure, but they showed different kinetics. **(F)** Fluorescent immunocytochemistry of MLANA in exosome-exposed MSC cultures using a primary rabbit antibody to MLANA and a secondary AlexaFluor555-conjugated antibody to rabbit IgG (red). α-tubulin network of cells was directly labeled by an AlexaFluor488-conjugated antibody (green) and the nuclei were stained with DAPI (blue).

TABLE 3 | List of genes investigated by a self-designed oncopanel.

Gene	Protein	Function	References
Alcam	ALCAM (CD166) Activated leukocyte cell adhesion molecule	Plays an important role in human malignant melanoma progression and formation of locoregional and distant metastases	(23)
Bmi1	BMI1 B cell-specific Moloney murine leukemia virus integration site 1	Induces an invasive signature in melanoma that promotes metastasis and chemoresistance	(24)
Cd44	CD44	Is a CD44s interaction with HA plays a crucial role in cell invasiveness	(25)
Eng	ENG Endoglin (CD105)	Has a crucial role in angiogenesis, important protein for tumor growth, survival, and metastasis of cancer cells to other locations in the body	(26)
Flot2	FLOT1 Flotillin-2	Is associated with melanoma progression	(27)
Itga2	ITGA2 Integrin alpha2	Is associated with increased risk of melanoma	(28)
Itga4	ITGA4 Integrin alpha 4	α4β1 integrin plays an important role in metastasis of malignant melanoma	(28)
Itga6	ITGA6 Integrin alpha 6	α6β1 integrin as a laminin receptor expression is associated with invasive potential in a highly metastatic melanoma cell line	(28)
Itgb1	ITGB1 Integrin beta-1 (CD29)	α4β1 integrin plays an important role in metastasis of malignant melanoma	(28)
Kit	KIT (CD117) Mast/stem cell growth factor receptor (SCFR)	c-Kit signaling activates the MAPK and PI3K signaling cascades	(29)
Muc1	MUC1 Mucin1 cell surface associated	Promotes melanoma migration through the Akt signaling pathway	(29)
Pecam1	PECAM1 Platelet endothelial cell adhesion molecule (CD31)	Can play multiple roles in diverse processes related to melanoma development, dormancy, migration/invasion, and angiogenesis	(30)
Prom1	Prominin-1 (CD133)	Is a melanoma stem cell marker	(31)
Thy	CD90	Is a cell adhesion molecule. Melanoma cells use Thy-1 on endothelial cells for metastasis formation	(32)
Cdc42	CDC42 Cell division control protein 42 homolog	Is vital for the transforming Ras signal emanating from endomembranes	(33)
Tiam1	TIAM1 T-cell lymphoma invasion and metastasis 1	Has crucial roles in regulation of the actin cytoskeleton, cell migration, cell cycle progression, gene transcription, and cell adhesion	(34)
Bcl2	BCL-2 B-cell lymphoma 2	Plays a pivotal role in the regulation of molecules associated with the migratory and invasive phenotype, contributing, in cooperation to hypoxia, to tumor progression	(29)
Bax	BAX Bcl-2-associated X protein	Plays a crucial role in apoptotic cell death induced, the Bax/Bcl-2 ratio determines the susceptibility of melanoma cells	(35)
Casp9	CASP9 Caspase-9	Is linked to the mitochondrial death pathway	(35)
Casp8	CASP8 Caspase-8	Plays a central role in the execution-phase of cell apoptosis	(36)
Cdk4	CDK4 Cyclin-dependent kinase 4	Promotes cell-cycle progression and inhibit both cell senescence and apoptosis	(29)
Elk1	ELK1 ETS domain-containing protein Elk-1	Is a member of ETS oncogene family, transcription activator	(37)
Ets1	ETS1 E26 transformation-specific	Is required for migration in cell lines with an active RAS/ERK signaling pathway	(29)
Hgf	HGF Hepatocyte growth factor	Can activate the MAP-kinase pathway, which is upregulated in the majority of melanoma, through the proto-oncogene c-MET	(38)
Jak2	JAK2 Janus kinase 2	Is an activator of transcription (STAT) pathway is thought to play a central role in melanoma cell biology	(39)
Met	MET Hepatocyte growth factor receptor	Induces several biological responses that collectively give rise to a program known as invasive growth	(40)
Myb	MYB transcriptional activator Myb	Is a transcription factor. Among other genes, MYB regulates the transcription of the Kit, Bcl2, Ets-2, and N-Ras	(41)
Nras	NRAS Neuroblastoma RAS viral oncogene homolog	Recruits and stimulates a number of intracellular signaling pathways including the Raf/MEK/ERK mitogen activated protein kinase (MAPK) pathway, the PI3K/AKT pathway	(29)
Stat3	STAT3 Signal transducer and activator of transcription 3	Promotes transcription of many genes that involve in melanoma metastasis	(42)
Kitl	KIT-ligand Stem cell factor (CD117)	Is a cytokine that binds to the c-KIT receptor. This cytokine plays an important role in melanogenesis	(29)
Rb1	RB1 Retinoblastoma 1 protein	Is a tumor suppressor protein that is dysfunctional in several major cancers	(43)
Pik3ca	PI3K Phosphatidylinositide 3-kinases	Is a PI3K/AKT pathway play a pivotal role in tumor development, growth, and metastasis of melanoma	(29)
Raf1	RAF1 Proto-oncogene serine/threonine-protein kinase	Is a crucial regulators of the ERK MAP kinase signaling cascade	(44)

(Continued)

TABLE 3 | Continued

Gene	Protein	Function	References
Mtor	mTOR Serine/threonine-protein kinase	Mechanistic target of rapamycin, is a serine/threonine protein kinase that regulates cell growth, cell proliferation, cell motility, cell survival	(29)
Akt1	AKT Protein kinase B	Plays a key role in multiple cellular processes such as glucose metabolism, apoptosis, cell proliferation, transcription, and cell migration	(29)
Map2k1	MEK1 Dual specificity mitogen-activated protein kinase kinase 1	Is an essential component of the MAP kinase signal transduction pathway, this kinase is involved in many cellular processes such as proliferation, differentiation, transcription regulation, and development	(29)
Map2k2	MEK2 Dual specificity mitogen-activated protein kinase kinase 2	Plays a critical role in mitogen growth factor signal transduction. It phosphorylates and thus activates MAPK1/ERK2 and MAPK2/ERK3	(29)
Mapk3	ERK1 Extracellular-signal-regulated kinases	Ras-Erk1/2 is a key regulator pathway in melanoma cell proliferation	(29)
Mapk1	ERK2 Mitogen-activated protein kinase 1	Ras-Erk1/2 is a key regulator pathway in melanoma cell proliferation	(29)
Rac1	RAC1 Ras-related C3 botulinum toxin substrate 1	Functions in multiple signaling pathways are leading to cell adhesion, migration, proliferation, and transformation	(45)

importance, we also found that in both exosome-related groups, the numbers of distant metastases were significantly elevated when compared to the control (**Figure 4B**), and diameter of metastases associated blood vessels significantly increased in exosome and $MSC^{PD\text{-}1+}$ injected groups of tumor bearing mice (**Figure S3**). Using of cytokine and chemokine arrays, tumor supportive cytokine and chemokine levels were elevated in exosome related groups (**Figure S4**). As we have seen during our previous studies (46), these metastases were mostly localized to the ovaries and kidneys (and very rarely to the lymph nodes) of control tumor-bearing animals. However, besides these sites, the presence of exosomes resulted in frequent metastases in the lymph nodes and, as a new location, in the liver. Interestingly, in $MSC^{PD\text{-}1+}$ treated mice, exosome-transformed MSCs could be identified in the para-aortic lymph nodes by FISH (**Figure 4C**) verifying the successful *in vivo* adherence of $MSC^{PD\text{-}1+}$ cells.

Lung tissues of the different groups were then subjected to in-depth expressional profiling 14 days after injection of exosomes or $MSC^{PD\text{-}1+}$ cells. Namely, QRT-PCR analysis was performed using a self-designed panel of 40 genes; besides housekeeping genes, we assessed expression of (i) proto-oncogenes; (ii) genes reportedly involved in malignant transformation; and/or (iii) genes found to be involved in melanoma development and progression.

Hierarchical cluster analysis (HCA) of the gene expression patterns clearly showed a robust proto-oncogenic dominance in lung samples of the exosome-related groups when compared to the control tissues. Indeed, we identified significant *de novo* induction of 26 and 23 genes: Alcam1, Eng, Flot2, Itga4, Itga6, Kit, Pecam1, Prom1, Thy, Cdc42, Tiam1, Bcl2, Bax, Casp9, Casp8, Ets1, Hgf, Jak2, Met, Myb, Map2k1, Map2k2, Mapk1 in both group and Elk1, Rb1, Itga2 in the exosome group. An additional six and three genes were identified with at least 10-fold increase (Cd44, Itgb1, Muc1, Pik3ca, Akt1, Rac1 in the exosome group and Cd44, Itgb1, Rac1 in the $MSC^{PD\text{-}1+}$ group). Furthermore, six and eight genes showed at least two-fold mRNA level elevations (Bmi1, Cdk4, Stat3, Kitl, Raf1, Mtor and Bmi1, Muc1, Cdk4, Stat3, Kitl, Pik3ca, Mtor, Akt1, respectively). **Figure 4D** presents a heatmap of indicative data of overexpressed genes induced by exosome exposure.

Furthermore, we showed that, besides the above genes, expression of PD-1 was also significantly increased in both exosome-related groups (**Figure 4E**). Notably, although mRNA transcript level of PD-1 was close to two-fold in $MSC^{PD\text{-}1+}$ lung tissues in comparison to samples in the exosome group, the difference was not significant (most probably due to the large inter-animal variability and standard error).

We constructed a Venn-diagram (**Figure 4F**) to show all possible logical connections between the various gene expression patterns presented in **Figure 4D**. Importantly, according to cluster analysis, we could not identify a single gene which was missing from the exosome-related groups in comparison to the control tumor-bearing mice. In other words, whereas these exosome-related groups did exhibit gene expression profiles which were characteristic only for them, such individual profiles could not be detected in the control group.

Specifically, the following gene expression patterns were defined:

- three genes (Elk1, Rb1, Igta2) were exclusively induced only in the exosome-treated group;
- twenty-three genes (Prom1, Tiam1, Bcl2, Bax, Casp9, Hgf, Jak2, Met, Mapk2k2, Alcam1, Eng, Flot2, Itga4, Itga6, Kit, Pecam1, Thy, Cdc42, Casp8, Ets1, Myb, Map2k1, Mapk1) were found to be upregulated both in the exosome and $MSC^{PD\text{-}1+}$ cell treated groups;
- fourteen genes (Bmi1, Cd44, Itgb1, Muc1, Cdk4, Nras, Sat3, Kitl, Raf1, Mtor, Akt1, Mapk3, Pik3ca, Rac1) were found to be upregulated in all three groups.

Finally, it should be noted that the dramatic gene expression alterations seen in the exosome-related groups were exclusively due to the presence of the exosomes as the "$MSC^{PD\text{-}1+}$ only" cluster contained no genes (**Figure 4F**).

Melanoma-Derived Exosomes Promote Tumorigenic and Cell Survival Signaling Pathway(s)

Figure 5 shows the map of interaction pathways based on overexpressed molecules (red symbols) in *in vivo* experiments. We detected overexpressed elements of three main pathways

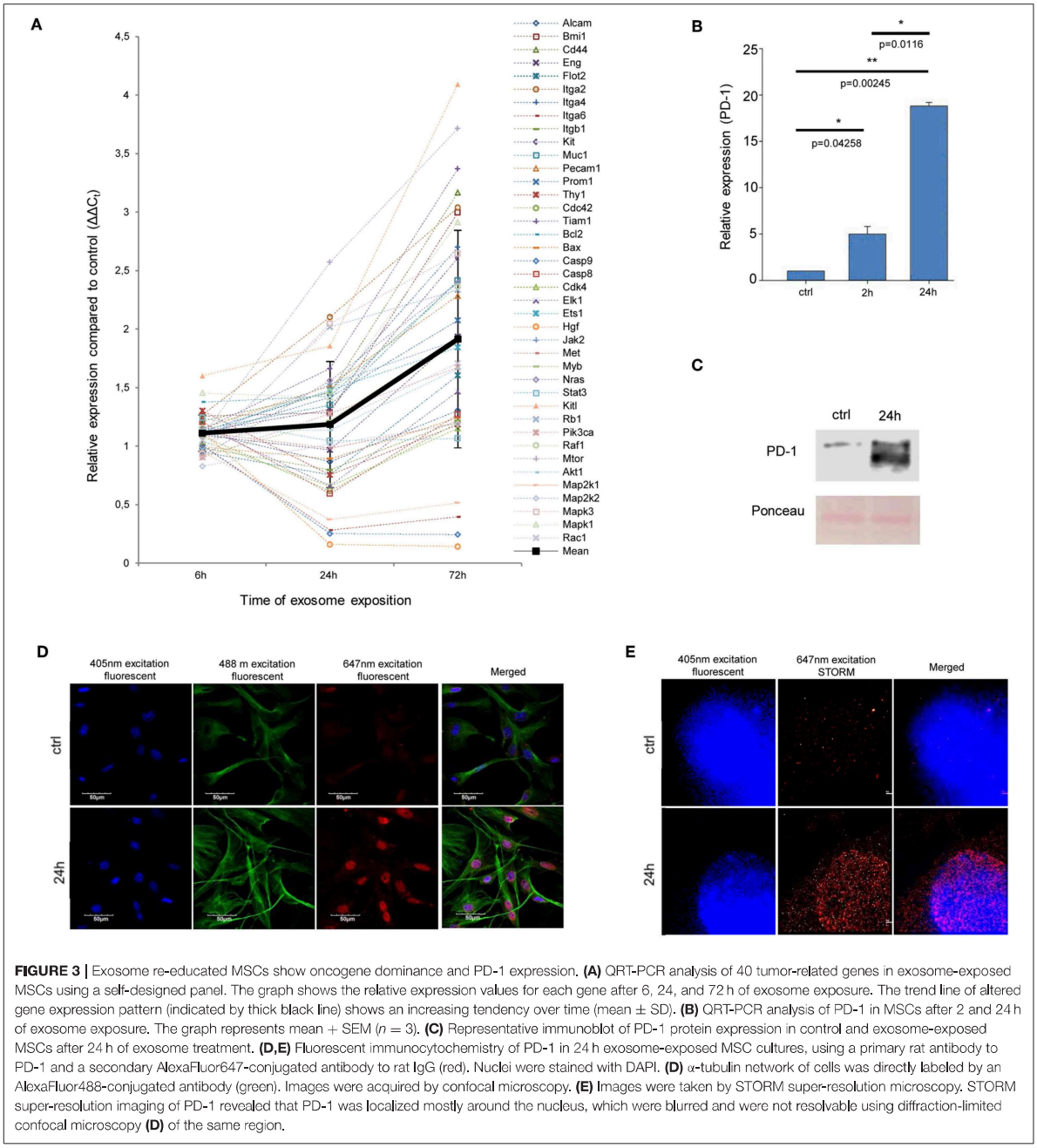

FIGURE 3 | Exosome re-educated MSCs show oncogene dominance and PD-1 expression. **(A)** QRT-PCR analysis of 40 tumor-related genes in exosome-exposed MSCs using a self-designed panel. The graph shows the relative expression values for each gene after 6, 24, and 72 h of exosome exposure. The trend line of altered gene expression pattern (indicated by thick black line) shows an increasing tendency over time (mean ± SD). **(B)** QRT-PCR analysis of PD-1 in MSCs after 2 and 24 h of exosome exposure. The graph represents mean + SEM ($n = 3$). **(C)** Representative immunoblot of PD-1 protein expression in control and exosome-exposed MSCs after 24 h of exosome treatment. **(D,E)** Fluorescent immunocytochemistry of PD-1 in 24 h exosome-exposed MSC cultures, using a primary rat antibody to PD-1 and a secondary AlexaFluor647-conjugated antibody to rat IgG (red). Nuclei were stained with DAPI. **(D)** α-tubulin network of cells was directly labeled by an AlexaFluor488-conjugated antibody (green). Images were acquired by confocal microscopy. **(E)** Images were taken by STORM super-resolution microscopy. STORM super-resolution imaging of PD-1 revealed that PD-1 was localized mostly around the nucleus, which were blurred and were not resolvable using diffraction-limited confocal microscopy **(D)** of the same region.

which do participate in tumor progression and metastasis formation (47). Using the IPA Path Designer Grow tool, we generated an interaction map which contains proteins (or their established complexes) encoded by the overexpressed genes, and exosomal miRNAs and proteins (gray boxes) which were previously shown to control or affect the marked signaling molecules.

To demonstrate these results and to explore the potential causative exosomal factors, we again performed an IPA. The analysis allowed further refinement of the underlying molecular

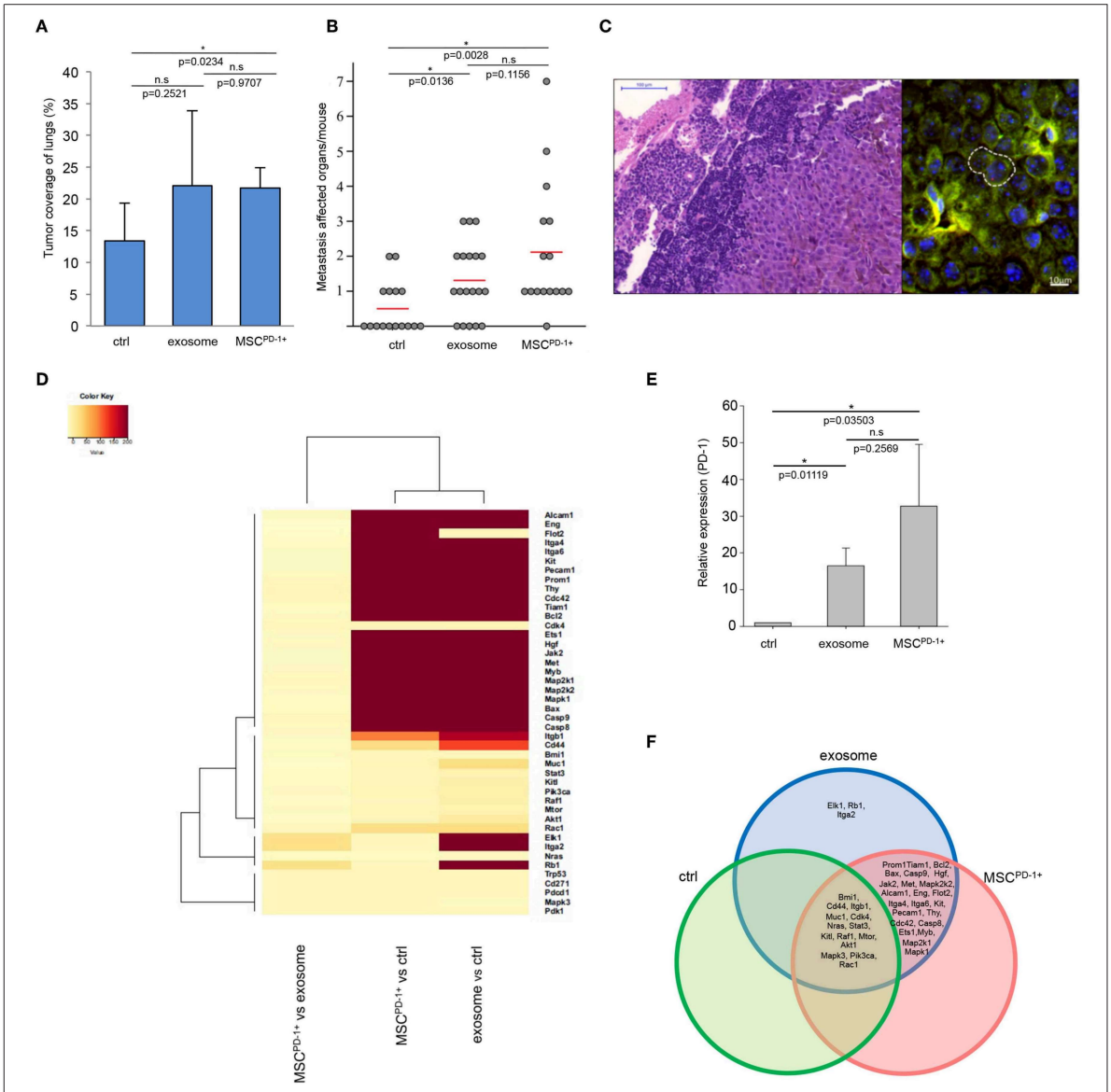

FIGURE 4 | Melanoma exosomes promote tumor progression and metastasis formation *in vivo*. **(A)** Tumor coverage of lungs on day 15 in different animal groups. The graph represents mean + SD ($n = 3$). **(B)** Number of distant metastases on day 25. One dot represents one animal in each group, red lines show the average number of metastases per animal. **(C)** FISH analysis of a paraortic lymph node metastases, which showed the presence of exosome-exposed MSC. Y chromosome (red dot) of the male mouse-derived MSC was detected in the metastases of a female mouse. **(D)** Heatmap and cluster analysis of gene expression pattern, which show protooncogenic dominance in exosome or MSC^{PD-1+} groups. Robust hierarchical clustering based on fold changes in the gene expression data between selected groups divide the treated groups into several upper classes. Groups treated by exosomes or MSC^{PD-1+} were compared to untreated controls. Exosomes MSC^{PD-1+} treatments were closely related. **(E)** QRT-PCR analysis of PD-1 in the lung samples using TaqMan probes ($n = 3$). **(F)** The Venn diagram shows possible relations between a finite collections of different sets of genes measured during gene expression profiling **(D)**.

processes and pathways involved in the summarized effect of this gene expression profile. The previously described 40-gene QRT-PCR panel was enriched in genes related to cellular movement and migration, cell survival and connective tissue development and function, involving tumor cells. Additional processes included growth and proliferation of tumor cells as well as the PD-1:PD-L1 interaction (and its consequences). Focusing on PD-1 and mTOR pathway, a network was

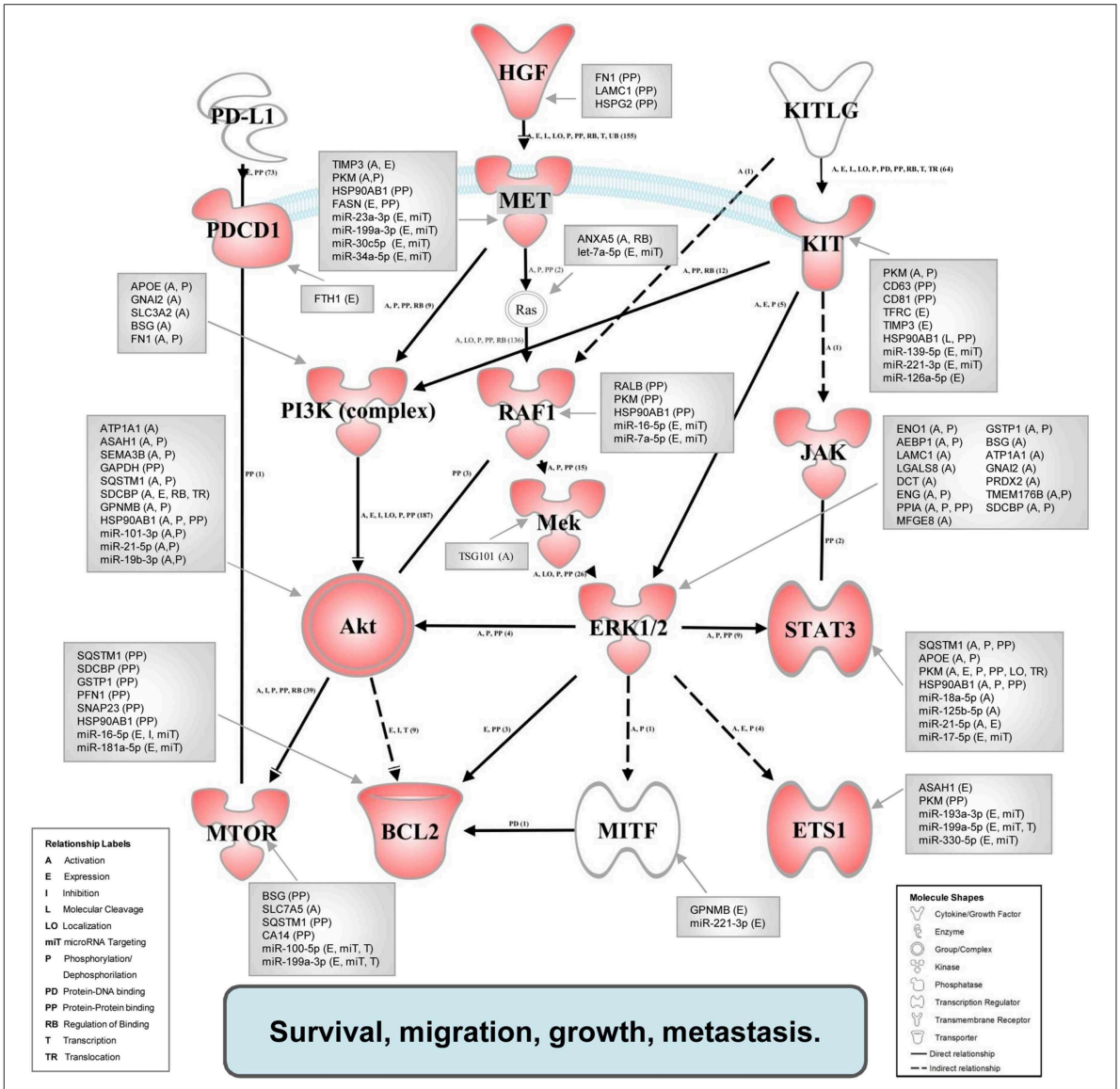

FIGURE 5 | Integrated associative network of the *in vivo* overexpressed genes supplemented with the interacting exosomal factors. The network of overexpressed genes (red symbols) was conceived by us based on literature data. The relationships between molecules were supported also by the IPA knowledge base. Network visualization was performed using the Path Explorer tool of the IPA Path Designer. The exosomal proteins and miRNAs (gray boxes) were connected to elements of the network by the Grow tool of the IPA Path Designer based on experimental data of the IPA knowledge base. Activation of the established network by exosomal components may support the survival, migration, growth, and metastasis of tumor cells.

built from the overexpressed genes, and their complexes known to be related to tumor progression using the Path Explorer tool in the IPA Path Designer. Then a list was generated that contained the exosomal proteins detected by MS and the exosomal miRNAs identified by SOLiD sequencing. The Grow tool in the IPA Path Designer revealed significant interactions between the exosome-induced expression network and the molecular content of these vesicles. The resulting interaction network shows both direct and indirect interactions, but it contains only experimentally observed relationships based on the Ingenuity Knowledge Base. This network demonstrates that 61 exosomal molecules (**Table 4**)

TABLE 4 | List of exosomal proteins and miRNAs connected to the integrated associative network by IPA Path Designer.

ID	Symbol	Entrez gene name	Symbol	Seed regio	ID
Q640N1	AEBP1	AE binding protein 1	let-7a-3p	UAUACAA	mmu-let-7a-1-3p, mmu-let-7b-3p
P48036	ANXA5	Annexin A5			mmu-let-7c-2-3p, mmu-let-7f-1-3p
P08226	APOE	Apolipoprotein E	let-7a-5p	GAGGUAG	mmu-let-7a-5p, mmu-let-7b-5p
Q3TWT5	ASAH1	N-acylsphingosine amidohydrolase 1			mmu-let-7c-5p, mmu-let-7d-5p
Q3TXF9	ATP1A1	ATPase Na^+/K^+ transporting subunit alpha 1			mmu-let-7e-5p, mmu-let-7f-5p
C55107	BSG	Basigin (Ok blood group)			mmu-let-7g-5p, mmu-mir-98-5p
Q9WVT6	CA14	Carbonic anhydrase 14	miR-100-5p	ACCCGUA	mmu-mir-99a-5p, mmu-mir-99b-5p
P41731	CD63	CD63 molecule	miR-125b-5p	CCCUGAG	mmu-mir-125a-5p, mmu-mir-125b-5p
P35762	CD81	CD81 molecule			mmu-mir-351-5p
P29812	DCT	Dopachrome tautomerase	miR-126a-5p	AUUAUUA	mmu-mir-126a-5p
Q3UAM9	ENG	Endoglin	miR-139-5p	CUACAGU	mmu-mir-139-5p
P17182	ENO1	Enolase 1	miR-16-5p	AGCAGCA	mmu-mir-15a-5p, mmu-mir-15b-5p
P19096	FASN	Fatty acid synthase			mmu-mir-16-5p, mmu-mir-195a-5p
P11276	FN1	Fibronectin 1			mmu-mir-322-5p, mmu-mir-497a-5p
P09528	FTH1	Ferritin heavy chain 1	miR-17-5p	AAAGUGC	mmu-mir-106b-5p, mmu-mir-17-5p
P16858	GAPDH	glyceraldehyde-3-phosphate dehydrogenase			mmu-mir-20a-5p, mmu-mir-93-5p
P08752	GNAI2	G protein subunit alpha i2	miR-181a-5p	ACAUUCA	mmu-mir-181a-5p, mmu-mir-181b-5p
Q3TAV1	GPNMB	Glycoprotein nmb			mmu-mir-181c-5p, mmu-mir-181d-5p
P19157	GSTP1	glutathione S-transferase pi 1	miR-18a-5p	AAGGUGC	mmu-mir-18a-5p
P11499	HSP90AB1	Heat shock protein 90 alpha family class B member 1	miR-193a-3p	ACUGGCC	mmu-mir-193a-3p
B1B0C7	HSPG2	Heparan sulfate proteoglycan 2	miR-199a-3p	CAGUAGU	mmu-mir-199a-3p, mmu-mir-199b-3p
P02468	LAMC1	Laminin subunit gamma 1	miR-199a-5p	CCAGUGU	mmu-mir-199a-5p, mmu-mir-199b-5p
Q3U2W5	LGALS8	Galectin 8	miR-19b-3p	GUGCAAA	mmu-mir-19a-3p,
P21956	MFGE8	Milk fat globule-EGF factor 8 protein			mmu-mir-19b-3p
P62962	PFN1	Profilin 1	miR-21-5p	AGCUUAU	mmu-mir-21a-5p
P52480	PKM	Pyruvate kinase, muscle	miR-221-3p	GCUACAU	mmu-mir-222-3p
P17742	PPIA	Peptidylprolyl isomerase A	miR-223-3p	GUCAGUU	mmu-mir-223-3p
Q61171	PRDX2	Peroxiredoxin 2	miR-23a-3p	UCACAUU	mmu-mir-23a-3p
Q8CCG5	RALB	RAS like proto-oncogene B			mmu-mir-23b-3p
O08992	SDCBP	Syndecan binding protein	miR-30c-5p	GUAAACA	mmu-mir-30a-5p
Q0VGP2	SEMA3B	Semaphorin 3B			mmu-mir-30b-5p
P10852	SLC3A2	Solute carrier family 3 member 2			mmu-mir-30c-5p
Q3UQM7	SLC7A5	Solute carrier family 7 member 5			mmu-mir-30d-5p
O09044	SNAP23	Synaptosome associated protein 23			mmu-mir-30e-5p
Q64337	SQSTM1	Sequestosome 1	miR-330-5p	CUCUGGG	mmu-mir-326-3p
Q542D9	TFRC	Transferrin receptor	miR-34a-5p	GGCAGUG	mmu-mir-34a-5p
P39876	TIMP3	TIMP metallopeptidase inhibitor 3			mmu-mir-34b-5p
Q9R1Q6	TMEM176B	Transmembrane protein 176B			mmu-mir-34c-5p
Q3UCW0	TSG101	Tumor susceptibility 101	miR-7a-5p	GGAAGAC	mmu-mir-7a-5p

may affect tumor progression through pathways controlled by key components including MET, Ras, RAF1, Mek, ERK1/2, MITF, BCL2, PI3K, Akt, mTOR, PD-1, KIT, JAK STAT3, or ETS1.

Taken together, these findings demonstrate that interaction between exosomes and MSCs induces a tumor-like phenotype with PD-1 overexpression of naïve MSC *in vitro* and a fast tumor progression *in vivo*.

DISCUSSION

Considering the fact that metastatic complications are responsible for almost 90% of cancer-driven mortality (48), a deep understanding of tumor metastatic processes is one of the most important challenges in both fundamental and applied research directions in tumor biology. Whilst certain organotropic aspects of tumor cells were addressed by Paget's

"seed-and-soil" hypothesis in the early nineteenth century (49), the detailed description of the spatiotemporal characteristics of the metastatic processes requires an extended model. MSCs, as multipotent stromal cells, are important players in dynamic tumor microenvironment (12). MSCs could stimulate angiogenesis via paracrine signaling and participate in metastasis formation to promote the epithelial-mesenchymal transition (12). Consequently, in the last decade, numerous studies suggested the importance of soluble and vesicle-like components of the tumor microenvironment in epithelial-mesenchymal transition as crucial factors in the metastatic establishment (50). Among these, recent findings of intercellular communication mechanisms unquestionably highlighted the crucial role of EVs (e.g., exosomes) serving as "information packages" within the coordinated cell-to-cell signaling (51).

In the current study, we demonstrate that MSCs, widely abundant in solid tumors as well as in healthy tissues, undergo a marked re-education process upon communication with metastatic cancer cells via exosome-mediated information transfer. This transformation process results in characteristic response-patterns corresponding to a given cancerous cell lines (12).

First, we intended to precisely define the EV population which we later employed via *in vitro* and *in vivo* experimental approaches. Besides applying the experimental requirements of the International Society for Extracellular Vesicles (ISEV) (i.e., determination of shape, size distribution and protein markers) (52), we thoroughly defined the miRNA and protein content of melanoma exosomes. These systematic assays concluded that the isolated vesicles contained factors, which may regulate signaling pathways related to cell death and survival, cellular movement, development and cell proliferation. Given the appropriate uptake of these vesicles by the targeted, multipotent recipient cells, it is highly probable that most signaling pathways mentioned above were significantly affected. In accordance with previous results in the literature, we showed successful internalization of exosomes by recipient MSCs. As expected, following 72 h of exposure, MSCs displayed accelerated proliferation presumably initiated by the transforming exosome cargo. Moreover, melanoma exosomes were able to hinder the induction of the cell death response commonly triggered by TNFα. TNFα is a frequently identified, soluble, tumor-suppressing factor in cancerous microenvironments (53). This inhibition strongly suggested that exosomes initialize and sustain malignant transformation of MSCs.

Further, we described numerous, exosome-induced phenotypic manifestation of the above malignant re-education process in the recipient cells. Apart from identifying tumor markers, the transformation of exposed cells is characterized by markedly modified gene expression patterns. As discussed previously, specific gene expression alterations are often associated with specific steps of cancerous transformation. Malignant cell lines possess altered expression of genes responsible for apoptotic regulation (Bax, Bcl2, caspases), regulating metastasis (integrins, ITGA2-6, ITGB1, KIT) or various growth factors (ETS1, HGF, MET, etc.). Importantly, we successfully identified two melanoma-specific markers, i.e., MITF (Microphthalmia-associated transcription factor) and MLANA (Melanoma antigen recognized by T-cells) in the exosome-exposed MSCs. MLANA and its regulator MITF play a fundamental role in melanocyte development, tumor progression and are overexpressed in melanoma cells (54). The presence of these markers in exosome-exposed MSCs shows effective transfer of the encoded tumorigenic information, and may have a pivotal role in disease progression. Besides, we also identified a characteristic set of genes, belonging mostly to proto-oncogenes, whose expression was significantly elevated upon exosome treatment. Among these molecules, we emphasize the increased expression of CD44 which was previously assigned as cancer stem cell marker and of mTOR, a characteristic indicator of the engagement of the PD-1:PD-L1 pathway (15). Indeed, activation of mTOR signaling is particularly important. As it was previously demonstrated by Kleffel et al., overexpression of PD-1 in exceptionally aggressive melanoma subpopulations facilitated tumor progression by activating the mTOR signaling pathway (actually, this response was highly unexpected compared to that of the classic PD-1:PD-L1 dependent T-cell anergy, a crucial aspect of immunotherapy in the clinics) (15). Quite strikingly, in exosome treated MSCs, we detected a significant induction of PD-1 and mTOR. These novel data strongly support that these vesicles might trigger the formation of an aggressive, melanoma-like subpopulation of re-educated recipient MSCs.

Our findings therefore propose that the re-educated melanoma-like $MSC^{PD\text{-}1+}$ subpopulation, originating from multipotent tissue-derived MSCs, is an autonomous entity. It is characterized by typical properties of cancerous transformation such as hyperproliferation, resistance to apoptosis, expression of melanoma markers, proto-oncogenic gene expression patterns, and PD-1 over-expression. Indeed, those melanoma exosomes that induced *in vitro* generation of the melanoma-like $MSC^{PD\text{-}1+}$ cells, also facilitated *in vivo* metastasis formation in the lungs or other distant organs of treated animals. Actually, our findings that melanoma exosomes or exosome re-educated $MSC^{PD\text{-}1+}$ promote tumor progression, are in good accordance with previous finding of Kleffel et al. describing that shRNA or antibody mediated inhibition of PD-1 signaling inhibits metastasis formation and tumor progression in experimental animals (15). Assessment of the expression patterns of genes related to tumor progression in the exposed animal tissues revealed numerous cases of exosome-induced overexpression; this supports our hypothesis that melanoma exosomes should be considered as oncosomes (6).

Our results also demonstrated that melanoma exosomes also generated a characteristic signaling pattern in $MSC^{PD\text{-}1+}$ recipient population. As it was shown in numerous studies PI3K/Akt, Ras/MAPK, and STAT3 pathways are commonly activated in tumor cells (47, 55). In this study, based on our *in vitro* and *in vivo* results and literature data, we introduce a novel, comprehensive network of common tumor-related proteins, such as PD-1, MET, RAF1, STAT3, BCL2, or mTOR. The network highlights not only the relationship of these elements, but also contains upstream exosomal regulating factors which may contribute to the activation of tumorigenic signaling, and hence, fast tumor progression.

According to our best knowledge, this associative network between overexpressed genes and the potential exosomal inducers, is the first tumor progression signaling pattern which connected experimental response-patterns with experimentally detected exosomal-molecular-patterns. Further, our data also indicate that the above complexity of exosomal communication requires system-level approaches.

Finally, it is important to note that our conclusions are not based on *in silico* predictions exclusively, but rather on carefully designed and systematically executed *in vitro* and *in vivo* experiments, all suggesting that the specific, robust, molecular content of the isolated exosomes can indeed generate a unique intercellular niche responsible for the re-education of neighboring cells via oncogenic transformation. These re-educated melanoma-like MSC^{PD-1+} cells, in turn, facilitate metastatic disease progression via ignition of a complex series of subsequent events both locally and systematically. Thus, based on our results and recently published, additional evidences about exosomes, there is an urgent demand to supplement and extend the outdated "seed-and-soil" hypothesis with the oncosome-driven re-education process.

DATA AVAILABILITY STATEMENT

All datasets generated for this study are included in the manuscript/**Supplementary Files**.

ETHICS STATEMENT

All animal experiments were performed in accordance with national (1998. XXVIII; 40/2013) and European (2010/63/EU) animal ethics guidelines. The experimental protocols were approved by the Animal Experimentation and Ethics Committee of the Biological Research Centre of the Hungarian Academy of Sciences and the Hungarian National Animal Experimentation and Ethics Board (clearance number: XVI./03521/2011 and XVI./78/2018).

AUTHOR CONTRIBUTIONS

EG-S: acquisition, analysis and interpretation of data (*in vitro* and *in vivo* experiments), drafting or revising the article. MH and GD: acquisition, analysis and interpretation of data, drafting or revising the article. IBN: histology. JM: acquisition, analysis and interpretation of data-*in vivo* QRT-PCR. ÁZ: acquisition, analysis and interpretation of data (MLANA, MITF). ÉH-G: acquisition, analysis and interpretation of Proteomics data. RK: providing and supervising of stem cell protocols. IN: acquisition, analysis and interpretation of miRNA data. PH: supervising of machine learning. ÁB: high content screening. ÁS: acquisition, analysis and interpretation of machine learning data. MK: acquisition, analysis and interpretation of confocal data. TP: drafting or revising the article, PD-1 QRT-PCR. BB: acquisition, analysis of data (*in vitro* QRT-PCR). ME: STORM microscopy. ZS: AFM microscopy. ZV: acquisition, analysis and interpretation of apoptosis data. EB: drafting or revising the article. LK: clinical relevance and drafting or revising the article. TB: conception and design and drafting or revising the article. KB: conception and design, acquisition of data, analysis and interpretation of data, drafting or revising the article and founding acquisition.

FUNDING

This work was in part supported by the National Research, Development and Innovation Fund of Hungary, financed under the NKFI-6-K funding scheme (11493 project), GINOP-2.3.2-15-2016-00015, GINOP-2.2.1-15-2017-00052, János Bolyai Research Scholarship of the Hungarian Academy of Sciences ÚNKP-19-4 New National Excellence Program of the Ministry for Innovation and Technology and University of Szeged Open Access Fund. The dSTORM experiments were funded by the Hungarian Brain Research Program (KTIA_13_NAP-A-I/14) and the GINOP-2.3.2-15-2016-00036.

ACKNOWLEDGMENTS

The authors wish to thank Gábor Braunitzer and Csaba Vizler, for scientific discussion, Annamária Marton for technical issues and adaptation of MSC isolation protocol, Lilla Pintér for technical support.

SUPPLEMENTARY MATERIAL

The Supplementary Material for this article can be found online at: https://www.frontiersin.org/articles/10.3389/fimmu.2019.02459/full#supplementary-material

REFERENCES

1. Li HLL, Fan X, Houghton J. Tumor microenvironment: the role of the tumor stroma in cancer. *J Cell Biochem.* (2007) 101:805–15. doi: 10.1002/jcb.21159
2. Yang C, Robbins PD. The roles of tumor-derived exosomes in cancer pathogenesis. *Clin Dev Immunol.* (2011) 2011:842849. doi: 10.1155/2011/842849
3. Braicu C, Tomuleasa C, Monroig P, Cucuianu A, Berindan-Neagoe I, Calin GA. Exosomes as divine messengers: are they the Hermes of modern molecular oncology? *Cell Death Differ.* (2015) 22:34–45. doi: 10.1038/cdd.2014.130
4. Yáñez-Mó M, Siljander PR, Andreu Z, Zavec AB, Borràs FE, Buzas E, et al. Biological properties of extracellular vesicles and their physiological functions. *J Extracell Vesicles.* (2015) 4:27066. doi: 10.3402/jev.v4.27066
5. Harmati M, Tarnai Z, Decsi G, Kormondi S, Szegletes Z, Janovak L, et al. Stressors alter intercellular communication and exosome profile of nasopharyngeal carcinoma cells. *J Oral Pathol Med.* (2017) 46:259–66. doi: 10.1111/jop.12486
6. Meehan B, Rak J, Di Vizio D. Oncosomes - large and small: what are they, where they came from? *J Extracell Vesicles.* (2016) 5:33109. doi: 10.3402/jev.v5.33109

7. Minciacchi VR, Freeman MR, Di Vizio D. Extracellular vesicles in cancer: exosomes, microvesicles and the emerging role of large oncosomes. *Semin Cell Dev Biol.* (2015) 40:41–51. doi: 10.1016/j.semcdb.2015.02.010
8. Chen PM, Yen ML, Liu KJ, Sytwu HK, Yen BL. Immunomodulatory properties of human adult and fetal multipotent mesenchymal stem cells. *J Biomed Sci.* (2011) 18:49. doi: 10.1186/1423-0127-18-49
9. Ridge SM, Sullivan FJ, Glynn SA. Mesenchymal stem cells: key players in cancer progression. *Mol Cancer.* (2017) 16:31. doi: 10.1186/s12943-017-0597-8
10. Suzuki K, Sun R, Origuchi M, Kanehira M, Takahata T, Itoh J, et al. Mesenchymal stromal cells promote tumor growth through the enhancement of neovascularization. *Mol Med.* (2011) 17:579–87. doi: 10.2119/molmed.2010.00157
11. Mishra PJ, Mishra PJ, Glod JW, Banerjee D. Mesenchymal stem cells: flip side of the coin. *Cancer Res.* (2009) 69:1255–8. doi: 10.1158/0008-5472.CAN-08-3562
12. Baglio SR, Lagerweij T, Pérez-Lanzón M, Ho XD, Léveillé N, Melo SA, et al. Blocking tumor-educated MSC paracrine activity halts osteosarcoma progression. *Clin Cancer Res.* (2017) 23:3721–33. doi: 10.1158/1078-0432.CCR-16-2726
13. Peinado H, Alečković M, Lavotshkin S, Matei I, Costa-Silva B, Moreno-Bueno G, et al. Melanoma exosomes educate bone marrow progenitor cells toward a pro-metastatic phenotype through MET. *Nat Med.* (2012) 18:883–91. doi: 10.1038/nm.2753
14. Kee D, McArthur G. Immunotherapy of melanoma. *Eur J Surg Oncol.* (2017) 43:594–603. doi: 10.1016/j.ejso.2016.07.014
15. Kleffel S, Posch C, Barthel SR, Mueller H, Schlapbach C, Guenova E, et al. Melanoma cell-intrinsic PD-1 receptor functions promote tumor growth. *Cell.* (2015) 162:1242–56. doi: 10.1016/j.cell.2015.08.052
16. Bersanelli M, Buti S. From targeting the tumor to targeting the immune system: transversal challenges in oncology with the inhibition of the PD-1/PD-L1 axis. *World J Clin Oncol.* (2017) 8:37–53. doi: 10.5306/wjco.v8.i1.37
17. Szebeni GJ, Kriston-Pál É, Blazsó P, Katona RL, Novák J, Szabó E, et al. Identification of galectin-1 as a critical factor in function of mouse mesenchymal stromal cell-mediated tumor promotion. *PLoS ONE.* (2012) 7:411372. doi: 10.1371/journal.pone.0041372
18. Carpenter AE, Jones TR, Lamprecht MR, Clarke C, Kang I, Friman O, et al. CellProfiler: image analysis software for identifying and quantifying cell phenotypes. *Genome Biol.* (2006) 7:R100. doi: 10.1186/gb-2006-7-10-r100
19. Olivo-Marin JC. Extraction of spots in biological images using multiscale products. *Pattern Recognit.* (2002) 35:1989–96. doi: 10.1016/S0031-3203(01)00127-3
20. van de Linde S, Löschberger A, Klein T, Heidbreder M, Wolter S, Heilemann M, et al. Direct stochastic optical reconstruction microscopy with standard fluorescent probes. *Nat Protoc.* (2011) 6:991–1009. doi: 10.1038/nprot.2011.336
21. Rees EJ, Erdelyi M, Kaminski-Schierle GS, Knight AE, Kaminski CF. Elements of image processing in localisation microscopy. *J Opt.* (2013) 15:094012. doi: 10.1088/2040-8978/15/9/094012
22. R Development Core Team. *R: A Language and Environment for Statistical Computing*. R Foundation for Statistical Computing, Vienna, Austria (2008).
23. Donizy P, Zietek M, Halon A, Leskiewicz M, Kozyra C, Matkowski R. Prognostic significance of ALCAM (CD166/MEMD) expression in cutaneous melanoma patients. *Diagn Pathol.* (2015) 10:86. doi: 10.1186/s13000-015-0331-z
24. Ferretti R, Bhutkar A, McNamara MC, Lees JA. BMI1 induces an invasive signature in melanoma that promotes metastasis and chemoresistance. *Genes Dev.* (2016) 30:18–33. doi: 10.1101/gad.267757.115
25. Mummert ME, Mummert DI, Ellinger L, Takashima A. Functional roles of hyaluronan in B16-F10 melanoma growth and experimental metastasis in mice. *Mol Cancer Ther.* (2003) 2:295–300.
26. Muñoz R, Arias Y, Ferreras JM, Jiménez P, Langa C, Rojo MA, et al. *In vitro* and *in vivo* effects of an anti-mouse endoglin (CD105)-immunotoxin on the early stages of mouse B16MEL4A5 melanoma tumours. *Cancer Immunol Immunother.* (2013) 62:541–51. doi: 10.1007/s00262-012-1357-7
27. Hazarika P, McCarty MF, Prieto VG, George S, Babu D, Koul D, et al. Up-regulation of Flotillin-2 is associated with melanoma progression and modulates expression of the thrombin receptor protease activated receptor 1. *Cancer Res.* (2004) 64:7361–9. doi: 10.1158/0008-5472.CAN-04-0823
28. Lee N, Barthel SR, Schatton T. Melanoma stem cells and metastasis: mimicking hematopoietic cell trafficking? *Lab Investig.* (2014) 94:13–30. doi: 10.1038/labinvest.2013.116
29. Ahmed KBR, Davies AM. New molecular targets for the systemic therapy of melanoma. In: Murph M, editor. *Research on Melanoma - A Glimpse into Current Directions and Future Trends*. London, UK: Intech (2011). p. 161–80.
30. Dunleavey JM, Xiao L, Thompson J, Kim MM, Shields JM, Shelton SE, et al. Vascular channels formed by subpopulations of PECAM1+ melanoma cells. *Nat Commun.* (2014) 5:5200. doi: 10.1038/ncomms6200
31. Madjd Z, Erfani E, Gheytanchi E, Moradi-Lakeh M, Shariftabrizi A, Asadi-Lari M. Expression of CD133 cancer stem cell marker in melanoma: a systematic review and meta-analysis. *Int J Biol Markers.* (2016) 31:118–25. doi: 10.5301/jbm.5000209
32. Schubert K, Gutknecht D, Köberle M, Anderegg U, Saalbach A. Melanoma cells use Thy-1 (CD90) on endothelial cells for metastasis formation. *Am J Pathol.* (2013) 182:266–76. doi: 10.1016/j.ajpath.2012.10.003
33. Stengel K, Zheng Y. Cdc42 in oncogenic transformation, invasion, and tumorigenesis. *Cell Signal.* (2011) 23:1415–23. doi: 10.1016/j.cellsig.2011.04.001
34. Minard ME, Kim LS, Price JE, Gallick GE. The role of the guanine nucleotide exchange factor Tiam1 in cellular migration, invasion, adhesion and tumor progression. *Breast Cancer Res Treat.* (2004) 84:21–32. doi: 10.1023/B:BREA.0000018421.31632.e6
35. Raisova M, Hossini AM, Eberle J, Riebeling C, Wieder T, Sturm I, et al. The Bax/Bcl-2 ratio determines the susceptibility of human melanoma cells to CD95/Fas-mediated apoptosis. *J Invest Dermatol.* (2001) 117:333–40. doi: 10.1046/j.0022-202x.2001.01409.x
36. Stupack DG. Caspase-8 as a therapeutic target in cancer. *Cancer Lett.* (2013) 332:133–40. doi: 10.1016/j.canlet.2010.07.022
37. Chen J, Zhang XD. Nanodelivery of anticancer agents in melanoma: encouraging, but a long way to go. In: Hamblin M, Avci P, Prow T, editors. *Nanoscience in Dermatology*. Cambridge: Academic Press (2016). p. 189–202. doi: 10.1016/B978-0-12-802926-8.00015-X
38. Hügel R, Muendlein A, Volbeding L, Drexel H, Richtig E, Wehkamp U, et al. Serum levels of hepatocyte growth factor as a potential tumor marker in patients with malignant melanoma. *Melanoma Res.* (2016) 26:354–60. doi: 10.1097/CMR.0000000000000269
39. Nicholas C, Lesinski GB. The Jak-STAT signal transduction pathway in melanoma. In: Tanaka Y, editor. *Breakthroughs in Melanoma Research*. London, UK: IntechOpen. (2011). p. 283–306. doi: 10.5772/18876
40. Al-U'datt DGF, Al-Husein BAA, Qasaimeh GR. A mini-review of c-Met as a potential therapeutic target in melanoma. *Biomed Pharmacother.* (2017) 88:194–202. doi: 10.1016/j.biopha.2017.01.045
41. Ramsay RG, Gonda TJ. MYB function in normal and cancer cells. *Nat Rev Cancer.* (2008) 8:523–34. doi: 10.1038/nrc2439
42. Cao HH, Chu JH, Kwan HY, Su T, Yu H, Cheng CY, et al. Inhibition of the STAT3 signaling pathway contributes to apigenin-mediated anti-metastatic effect in melanoma. *Sci Rep.* (2016) 6:21731. doi: 10.1038/srep21731
43. Roesch A, Becker B, Meyer S, Hafner C, Wild PJ, Landthaler M, et al. Overexpression and hyperphosphorylation of retinoblastoma protein in the progression of malignant melanoma. *Mod Pathol.* (2005) 18:565–72. doi: 10.1038/modpathol.3800324
44. Kyriakis JM, App H, Zhang XF, Banerjee P, Brautigan DL, Rapp UR, et al. Raf-1 activates MAP kinase-kinase. *Nature.* (1992) 358:417–21. doi: 10.1038/358417a0
45. Li A, Machesky L. Rac1 cycling fast in melanoma with P29S.M. *Pigment Cell Melanoma Res.* (2013) 26:289–90. doi: 10.1111/pcmr.12074
46. Buzás K, Marton A, Vizler C, Gyukity-Sebestyén E, Harmati M, Nagy K, et al. Bacterial sepsis increases survival in metastatic melanoma: *Chlamydophila pneumoniae* induces macrophage polarization and tumor regression. *J Invest Dermatol.* (2016) 136:862–5. doi: 10.1016/j.jid.2015.12.032
47. Flaherty KT, Hodi FS, Fisher DE. From genes to drugs: targeted strategies for melanoma. *Nat Rev Cancer.* (2012) 12:349–61. doi: 10.1038/nrc3218
48. Chaffer CL, Weinberg RA. A perspective on cancer cell metastasis. *Science.* (2011) 331:1559–64. doi: 10.1126/science.1203543

49. Paget S. The distribution of secondary growths in cancer of the breast. *Lancet*. (1889) 1:571–3. doi: 10.1016/S0140-6736(00)49915-0
50. Gopal SK, Greening DW, Rai A, Chen M, Xu R, Shafiq A, et al. Extracellular vesicles: their role in cancer biology and epithelial-mesenchymal transition. *Biochem J*. (2017) 474:21–45. doi: 10.1042/BCJ20160006
51. Tkach M, Théry C. Communication by extracellular vesicles: where we are and where we need to go. *Cell*. (2016) 164:1226–32. doi: 10.1016/j.cell.2016.01.043
52. Lötvall J, Hill AF, Hochberg F, Buzás E, Di Vizio D, Gardiner C, et al. Minimal experimental requirements for definition of extracellular vesicles and their functions: a position statement from the International Society for Extracellular Vesicles. *J Extracell Vesicles*. (2014) 3:26913. doi: 10.3402/jev.v3.26913
53. Balkwill F. Tumour necrosis factor and cancer. *Nat Rev Cancer*. (2009) 9:361–71. doi: 10.1038/nrc2628
54. Schepsky A, Bruser K, Gunnarsso GJ, Goodall J, Hallsson JH, Goding CR, et al. The microphthalmia-associated transcription factor Mitf interacts with beta-catenin to determine target gene expression. *Mol Cell Biol*. (2006) 26:8914–27. doi: 10.1128/MCB.02299-05
55. Chen J, Shao R, Zhang XD, Chen C. Applications of nanotechnology for melanoma treatment, diagnosis, and theranostics. *Int J Nanomedicine*. (2013) 8:2677–88. doi: 10.2147/IJN.S45429

Conflict of Interest: The authors declare that the research was conducted in the absence of any commercial or financial relationships that could be construed as a potential conflict of interest.

Journal of
Oral Pathology & Medicine

doi: 10.1111/jop.12486

J Oral Pathol Med

wileyonlinelibrary.com/journal/jop

Stressors alter intercellular communication and exosome profile of nasopharyngeal carcinoma cells

Maria Harmati[1], Zsofia Tarnai[2], Gabor Decsi[2], Sandor Kormondi[3], Zsolt Szegletes[4], Laszlo Janovak[5], Imre Dekany[6], Okay Saydam[7], Edina Gyukity-Sebestyen[1], Gabriella Dobra[1], Istvan Nagy[8], Katalin Nagy[2], Krisztina Buzas[1,2]

[1]*Laboratory of Microscopic Image Analysis and Machine Learning, Institute of Biochemistry, Biological Research Centre of the Hungarian Academy of Sciences, Szeged, Hungary;* [2]*Department of Oral Biology and Experimental Dental Research, Faculty of Dentistry, University of Szeged, Szeged, Hungary;* [3]*Department of Traumatology, Faculty of Medicine, University of Szeged, Szeged, Hungary;* [4]*Biological Application of the Atomic Force Microscope Research Group, Institute of Biophysics, Biological Research Centre of the Hungarian Academy of Sciences, Szeged, Hungary;* [5]*Department of Physical Chemistry and Materials Sciences, University of Szeged, Szeged, Hungary;* [6]*MTA-SZTE Supramolecular and Nanostructured Materials Research Group, University of Szeged, Szeged, Hungary;* [7]*Molecular Neuro-Oncology Research Unit, Medical University of Vienna, Vienna, Austria;* [8]*Sequencing Platform, Institute of Biochemistry, Biological Research Centre of the Hungarian Academy of Sciences, Szeged, Hungary*

BACKGROUND: Head and neck cancers comprise the sixth most common cancer type worldwide. One of the most remarkable malignancies of the head and neck is the cancer of the nasopharynx, with a strong metastatic tendency already in the early stage. Besides the conventional pathways of metastasis formation, the information content of exosomes produced by the cancer cells may play a key role in metastatic transformation. The aim of this study was to investigate how stressors alter the characteristic of tumor derived exosomes.

METHODS: In our experimental model, we compared the quantity and content of exosomes produced by a nasopharyngeal carcinoma cell line (5-8F) under conventional (chemotherapy) and alternative (Ag–TiO_2-catalyzed reactive oxygen species generation) cytostatic treatment. After isolation, exosomes were identified by atomic force microscopy and quantified with Nanosight NS500 device. MicroRNA content of them was analyzed using SOLiD 5500xl technology. The sequences were annotated in CLC Genomics Workbench version 5.5.1.

RESULTS: Beyond the classic chemotherapeutic agent (doxorubicin), Ag–TiO_2 in a photo-catalytic process also showed cytostatic activity. Tumor cell damage induced by the cytostatic treatments significantly altered the number of released exosomes and led to the predominance of tumor suppressors in the exosomal miRNA profile.

CONCLUSIONS: Our results suggest that the intercellular communication between tumor cells and surrounding stroma cells can be altered by microenvironment which increased quantity of exosomes and diversity of miRNAs in this study. Imbalance of oncogenic and tumor suppressor miRNAs caused by cytostatic treatments may influence the antiproliferative and metastasis inhibitory effect of cytostatic agents.

J Oral Pathol Med (2016)

Keywords: cytostatic agents; exosomes; microRNAs; nanoparticles; nasopharyngeal carcinoma

Correspondence: Krisztina Buzas, Hungarian Academy of Sciences, Biological Research Center, Temesvári krt. 62., Szeged H-6726, Hungary. Tel: +3662599600, Fax: +3662433506, E-mail: kr.buzas@gmail.com
Accepted for publication July 19, 2016

Introduction

Exosomes and microvesicles (MVs) are nanometer-sized membrane vesicles secreted from various cell types (including tumor cells) into the extracellular milieu and body fluids. MVs and exosomes contain different kinds of biomolecules, such as proteins, lipids, and nucleic acids, whereby EVs are suggested to modulate the immune function, angiogenesis, cell proliferation, cell-to-cell communication, and tumor invasion (1, 2).

An increasing number of publications highlight the role of exosomes and microRNA carried by extracellular vesicles in tumor progression, metastatic activity, and also in tumor response under suboptimal conditions, for example, chemotherapy-induced cell damage (3, 4).

Head and neck cancers are a heterogeneous group of epithelial cancers (including the tumors of the larynx, hypopharynx, oropharynx, nasopharynx, the paranasal sinuses, and the oral and nasal cavity) that evolve from the oral and pharyngeal squamous epithelium.

Head and neck squamous cell carcinoma with an incidence of more than 600 000 per year is the sixth most common cancer worldwide (5). The five-year survival rate

for these patients is 50–60%, which has not decreased in the last thirty years (6).

Nasopharyngeal carcinoma (NPC) is a distinct cancer type of the head and neck region, differing from other cancers in terms of its epidemiology, etiology, clinical behavior, and response to treatment.

The prognosis of NPC depends on the metastatic activity and loco-regional spread (7). Unfortunately, NPC has an early metastatic tendency (8). The metastatic potential is considerably high: 60–90% of the patients develop metastases in the regional lymphatic nodes (9).

In the background of this high metastatic activity may stand an additional mechanism of metastasis formation mediated by the exosomes produced by cancer cells (1).

NPC-derived exosomes contain a variety of bioactive molecules, such as proteins, lipids, and nucleic acids like microRNAs (miRNAs). The latter are small, non-coding post-transcriptional regulators which are considered to play a key role in biological processes and tumor development. MiRNAs have been found to regulate many kinds of genes including development, proliferation, differentiation, and stress response (10).

MicroRNAs might also be good biomarkers for cancer detection, as miRNAs are remarkably stable in blood and it seems that each malignant disease has its own, specific miRNA expression profile (11). Being able to offer a reliable prognosis of NPC by miRNA characteristics would be a significant improvement in the battle against the disease.

The purpose of this study was to investigate how exosomal miRNAs might assist metastasis formation in NPC and how cytostatic therapies as stressors influence the characteristics of the tumor-derived exosomes.

In our experimental model, we examined the exosome-producing capacity of an NPC cell line under different cytostatic treatments. The miRNA content of the exosomes was also examined. We sought to answer whether cytostatic therapy could alter the quantity and contents of the tumor-derived exosomes. 5-8F NPC cells were exposed to two different types of cytostatic treatment, namely the classical chemotherapy with doxorubicin and a new method for the inhibition of cell proliferation, in which we utilized the photocatalytic activity of Ag–TiO_2. The effects of these treatments were compared in terms of exosome output and miRNA profile.

Doxorubicin—the antracycline antibiotic widely used in the chemotherapy of several cancer types—exerts its cytostatic effect by intercalating the DNA.

Ag–TiO_2 photocatalyst particles irradiated with exciting wavelength light show photocatalytic activity. Photocatalysis is a photo-induced reaction, in which the photons are exiting the photocatalyst particles. During the photocatalytic process, the irradiated photocatalyst particles produce highly reactive oxygen species such as superoxide (O_2^-), hydrogen peroxide (H_2O_2), or hydroxyl radical ($^{\cdot}HO$) (12). Due to these reactive radicals, the photocatalyst particles can degrade many organic compounds and inactivate microorganisms via destroying the cell wall and the DNA (12, 13). However, TiO_2 needs high-energy (UV) photons to be activated, and has a low quantum efficiency due to the TiO_2 wide band gap (E_g = 3.2 eV for anatase) and fast recombination rate of photo-generated electron and hole pairs. Silver nanoparticles-functionalized TiO_2 photocatalysts (Ag–TiO_2) enhance the light absorbance of the catalyst in the visible range and significantly improve the photocatalytic activity of the metal oxide semiconductor under UV–visible light (14).

We found that tumor cell damage induced by the cytostatic treatments significantly increased the quantity of the exosomes and altered their miRNA content. This significantly increased quantity of the exosomes may potentiate the information transfer of tumor cells to the surrounding stroma cells and affect the mechanisms of metastasis formation.

Materials and methods

Synthesis of Ag–TiO_2 photocatalyst particles

Commercially available TiO_2 (Degussa P25 from Evonik Gmbh) photocatalyst with a specific surface area of ~50 m^2/g was used as a standard photocatalyst without any treatment. Plasmonic Ag nanoparticles were prepared on the surface of TiO_2 to enhance the photocatalytic efficiency of the prepared Ag–TiO_2 sample. The prepared Ag–TiO_2 photocatalyst contained 0.5 wt.% surface silver nanoparticles. The detailed process of the Ag–TiO_2 nanoparticle synthesis was published in our earlier publications (13, 14).

Cell line and culture conditions

5-8F human NPC cell line was kindly provided by Ji Ming Wang (NCI-Frederick, MD, USA). Cell cultures were stored at 37°C in a humidified incubator with 5% CO_2, in Dulbecco's modified Eagle's medium (DMEM) supplemented with 10% fetal bovine sera depleted of contaminating vesicles, 1% MEM non-essential amino acids, 1% MEM vitamin solution, and 100 U/ml penicillin–streptomycin (all from Lonza, Basel, Switzerland).

There was no ethical approval required for this study.

Cell culture treatments and exosome isolation

To investigate the changes of exosome production under suboptimal conditions, cell cultures were treated at 90% confluency in three different ways: The medium was replaced with (i) fresh media, (ii) fresh media supplemented by 0.6 μM doxorubicin, and (iii) fresh media supplemented by light-induced 2.5 μg/ml Ag–TiO_2 aqueous nanodispersion (this concentration was chosen based on the *in vitro* tests as well as limitation of *in vivo* application). The photoreactive Ag–TiO_2 nanoparticles were induced by a low-pressure mercury lamp (GCL303T5/4 type, LightTech, Dunakeszi, Hungary) mostly emitting light wavelength $\lambda \geq 360$ nm, for 10 min from a 10-cm distance in one-third medium volume. After the light induction, the medium was supplemented to the total volume. This step was necessary because of the light absorption and reflection of the medium layer in the dishes which would otherwise prevent the induction of Ag–TiO_2. After 72 h, supernatants were collected and the exosomes were isolated by differential filtration and ultracentrifugation as described previously (15).

Cell viability assay

To characterize the effects of suboptimal conditions regarding viability, the cells were treated with different

concentrations of doxorubicin and light-induced photoreactive Ag–TiO_2 dispersion. After 72 h, cell viability was determined by trypan blue exclusion.

Identification of exosomes

Atomic force microscopic (AFM) measurements were carried out with an Asylum MFP-3D head and controller (Asylum Research, Santa Barbara, CA, USA). The driver program MFP-3D Xop was written in IGOR Pro Software (Wavemetrics, Lake Oswego, OR, USA). For imaging, gold-coated silicon nitride rectangular cantilevers were used with a typical spring constant of 0.03 N/m in air (BL-RC150 VB, Olympus Optical Co. Ltd., Tokyo, Japan). The spring constant for each cantilever was determined by thermal calibration followed by Sader's method (16–19). For the measurements, freshly cleaved 1 × 1 cm mica (SPI-Chem Mica Sheets) surfaces were used as supports for exosomes and microvesicles. The negatively charged mica surfaces were incubated in 2% APTES ((3-aminopropyl) triethoxysilan, Sigma, St. Louis, MO, USA) dissolved in isopropanol for 90 min in shaking condition at RT to create free amine groups on their surface (18, 20, 21). Exosomes and microvesicles were attached to the modified surface with glutaraldehyde. Measurements were carried out in tapping (AC) mode in PBS solution. Typically, 512 × 512 point scans were taken at 0.4 Hz scan rate. Both the trace and retrace images were recorded and compared. The measurements presented here are 1.5 × 1.5 μm^2 flattened heights. Experiments were repeated three to five times.

Measurement of the number distribution of exosomes

Nanoparticle tracking analysis (NTA) was used to compare the number and size of the exosomes isolated from the three different supernatants. NTA is the commercial name of an optical particle tracking which is an accepted method for obtaining concentration and size distribution of EV populations, including exosomes (22). These measurements were performed by the NanoSight's NS500 device.

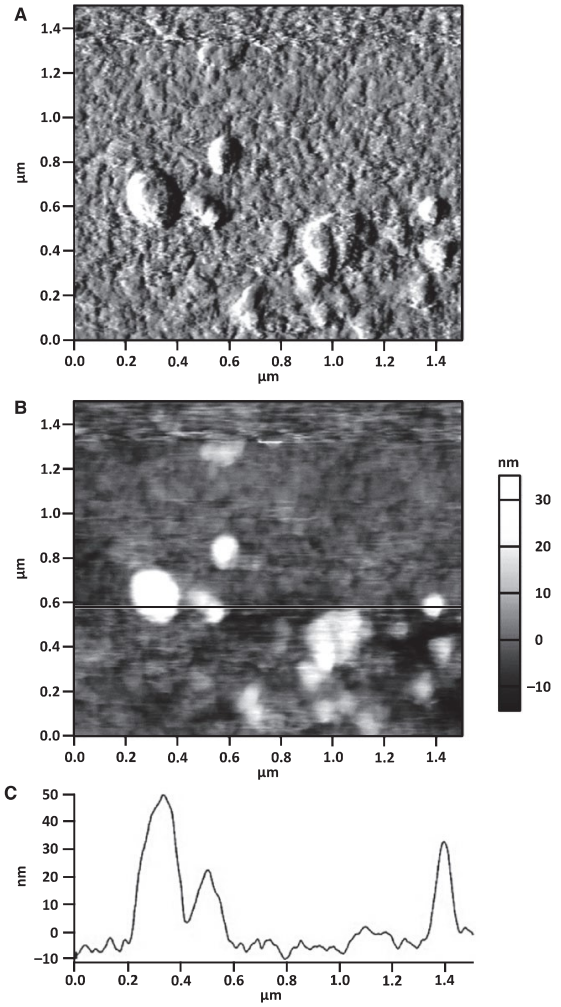

Figure 1 High-resolution AFM images of intact exosomes. Height (A) and amplitude (B) images (1.5 × 1.5 μm^2) are shown together with height profiles (C) corresponding to the horizontal line assigned on the height images. Exosomes were attached to the APTES-covered mica surface with glutaraldehyde.

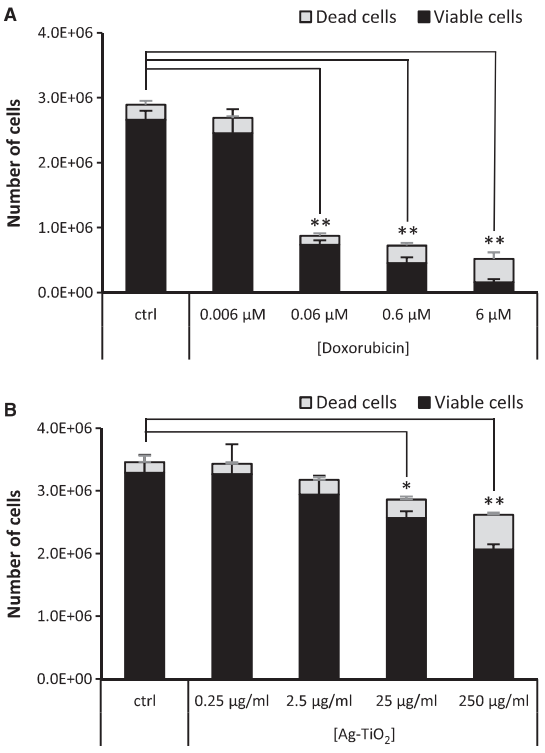

Figure 2 Cytostatic and antiproliferative effects of doxorubicin and Ag–TiO_2 treatments on 5-8F NPC cell cultures. Number of viable cells significantly decreased 72 h after (A) 0.06-6 µM doxorubicin (**$P < 0.001$) and (B) 25-250 µg/ml Ag–TiO_2 treatments (25 µg/ml Ag–TiO_2: *$P = 0.003$; 250 µg/ml Ag–TiO_2: **$P < 0.001$).

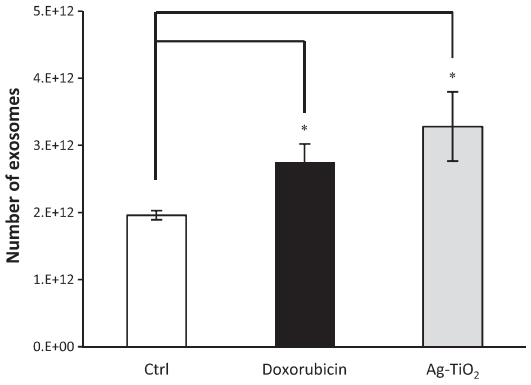

Figure 3 5-8F human NPC cell-derived exosome production under suboptimal conditions. 0.6 μM doxorubicin and 2.5 μg/ml Ag–TiO_2 treatments significantly increased the exosome production in number (*$P < 0.001$).

MiRNA analysis of exosomes

In order to determine differences of the miRNA content of exosomes derived from the control, doxorubicin- or Ag–TiO_2-treated cell culture supernatants, six parallel but independent experiments were performed to collect supernatant and isolate exosomes. MiRNA was isolated from all samples by the NucleoSpin miRNA kit (Macherey-Nagel, Düren, Germany) according to the manufacturer's instructions and analyzed using the SOLiD 5500xl technology. The sequences were annotated in CLC Genomics Workbench version 5.5.1 as described previously (23).

Statistical analysis

Data analyses were performed using two-tailed Student's *t*-test by Microsoft Excel, and $P \leq 0.05$ was regarded as statistically significant.

Results

Exosome identification

In situ AFM measurements were used to characterize the size and shape distribution of exosomes. This method is suitable to define the size and mechanical properties of the particles; therefore, the exosomes can be distinguished from viruses or other contaminations. We have found the appropriate shape and size of exosomes in 30–70 nm (Fig. 1).

Cell viability changes under suboptimal conditions

To characterize the effects of suboptimal conditions for the viability of cells, we treated the cell cultures with doxorubicin or light-induced Ag–TiO_2. Our results verified the already established concentration-dependent cytotoxicity

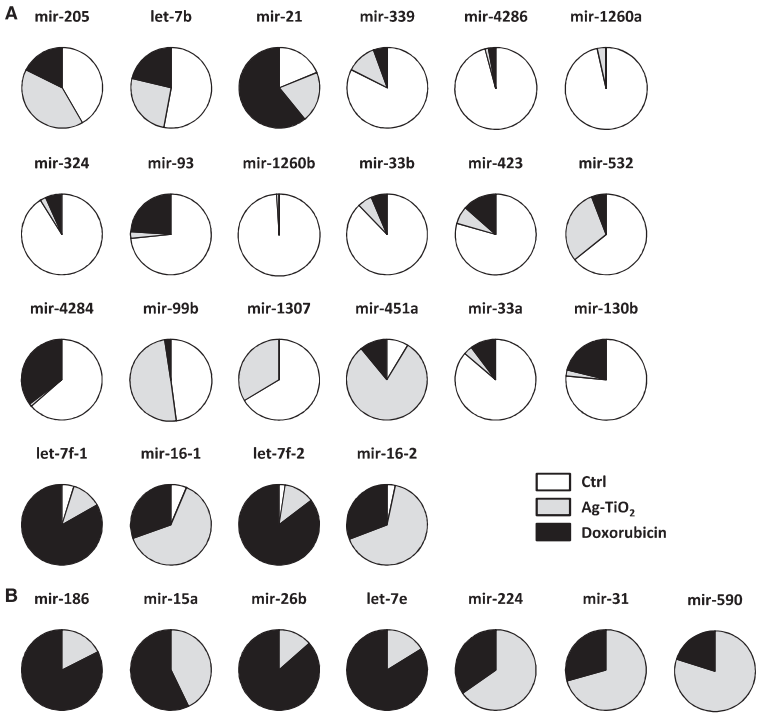

Figure 4 Ratio of miRNAs carried by the different exosomes. (A) miRNAs that markedly (tenfold increase or 0.1-fold decrease) changed during cell culturing under cytostatic treatment. (B) The most abundant miRNAs that were exclusively detected in one or both group of the treated 5-8F NPC cell-derived exosomes.

Table 1 Normalized expression values of miRNAs and their previously described oncogenic potential in NPC or other cancer types

				miRNAs previously described				
miRNA	*Ctrl*	*Doxo*	*Ag–TiO_2*	*Cancer type*	*Specimen*	*Effect*	*Targets*	*Ref*
mir-205	217 933	92 055	213 069	NPC	Clinical specimens and cell lines: CNE2, 6-10B and 9-4E	O	TP53INP1	(S1)
				NPC	Cell lines: CNE-2R, CNE-2	O	PTEN	(S2)
let-7b	108 344	43 337	52 824	NPC	Cell lines: HK1, HONE1, NP69, NP460	TS	c-Myc	(S3)
mir-21	48 568	156 766	52 607	NPC	Clinical samples and cell lines: CNE-1, CNE-2, TWO3, and C666-1	O	PTEN	(S4)
					Clinical samples and NPC cell line	O	BCL2	(S5)
					NP69. C666-1, CNE2, HONE1, 6-10B Akata(+), Akata(−), Ramos, Namalwa, Raji, B95-8	O	PDCD4, Fas-L	(S6)
mir-339	28 643	1916	4188	BC	Clinical samples and cell lines: MCF-7, MDA-MB-231, MDA-MB-468	TS	BCL-6	(S7)
				CRC	Clinical samples and cell lines: HCT116, HT29, LS174T, SW480, SW620, LOVO	TS	PRL-1	(S8)
				NSCLC	Clinical samples and cell lines: 95D, 95C	TS	BCL-6, VCP	(S9)
mir-4286	23 661	737	325	GBM	Clinical samples and cell lines: U-87 MG, U-118 MG, LN18	NA	C2ORF21, LRRC4, VAMP1, ERO1L, PDE4A	(S10)
mir-1260a	17 435	0	631	NBL	Cell line: SH-SY5Y, animal model	O	ADAMTS-1 and CREB	(S11)
mir-324	17 435	1253	453	Glioma	Cell lines: U87, LN229	TS	GLI1	(S12)
mir-93	17 435	5675	625	NPC	Clinical samples and cell lines: CNE1, CNE2	O	TGFβR2	(S13)
mir-1260b	11 208	0	108	PC	Clinical samples and cell line: PC-3	O	sFRP1, Smad4	(S14)
mir-33b	11 208	811	752	CRC	Clinical samples and cell lines: HT-29, HCT 116, SW480	TS	CDK6, CCND1, Pim-1	(S15)
				OSA	Clinical samples and cell lines: MG-63, U2OS, SOSP-9607, SAOS-2	TS	c-Myc	(S16)
mir-423	11 208	1916	982	HCC	Cell lines: HEK-293T, HepG2	O	p21Cip1/Waf1	(S17)
mir-532	11 208	1032	5214	MM	Clinical samples and cell lines: M1–M11	O	RUNX3	(S18)
mir-4284	9963	5528	172	GBM	GBM neurosphere cultures and U87 cell line	TS		(S19)
mir-99b	7472	369	7764	HNSCC	Meta-analysis and cell lines: 1386Ln, UM1	TS	IGF1R	(S20)
				NSCLC	Clinical samples and cell lines: H1299, H522, HCC95, HCC1438	TSr	FGFR3	(S21)
				PC	Clinical samples and cell lines: LNCaP, C4-2, and WPE1-NB26	TS	SMARCA5, SMARCD1, mTOR	(S22)
mir-1307	6227	0	3149	CRC	Clinical samples and cell lines: Caco-2, CHO, DLD-1, HCT116, LoVo, and SW620	O	Bcl2	(S23)
mir-451a	6227	7886	57 356	NPC	Clinical samples and cell lines: NP69 CNE-1, CNE-2, C666-1, HNE-1, HONE-1, SUNE-1, 5-8F, and 6-10B	TS	MIF	(S24)
				HSCC	Clinical samples and cell lines: FaDu, SAS	TS	ESDN	(S25)
mir-33a	3736	442	153	LC	Cell lines: A549, H1299, BEAS-2B, NCI-H460, HOS	TS	PTHrP	(S26)
mir-130b	3736	1032	115	CRC	Clinical samples and cell line: CHO	O	PTEN	(S27)
				GC	Clinical samples and cell lines: AGS, SNU1, SNU5, SNU16, AZ521, MKN7, MKN28, MKN45	O	RUNX3	(S28)
				PC	Clinical samples and cell lines: ANC-1, ASPC-1, Miapaca-2, BXPC-3, SW1990	TS	STAT3	(S29)
let-7f-1	2491	42 821	6189	NPC	Cell lines: HK1, HONE1, NP69, NP460	TS	c-Myc	(S3)
mir-16-1	2491	11 940	24 822	NPC	Cell line: CNE-2Z	TS	Bcl2	(S30)
				NPC	Cell lines: BL41, BL41/B95.8, Jijoye, EREB2.5	TS	BRCA-1	(S31)

(continued)

Table 1 (continued)

miRNAs previously described								
miRNA	*Ctrl*	*Doxo*	*Ag–TiO$_2$*	*Cancer type*	*Specimen*	*Effect*	*Targets*	*Ref*
let-7f-2	1245	43 485	6196	NPC	Cell lines: HK1, HONE1, NP69, NP460	TS	c-Myc	(S3)
mir-16-2	1245	11 498	24 586	NPC	Cell line: CNE-2Z	TS	Bcl2	(S30)
				NPC	Cell lines: BL41, BL41/B95.8, Jijoye, EREB2.5	TS	BRCA-1	(S31)
mir-186	0	32 650	6980	BCA	Clinical samples and cell lines: J82, HT1376, RT4, T24, and TCCSUP HCV29	TS	NSBP1	(S32)
				NSCLC	Clinical samples and cell lines: A549, NCI-H358, H157, H1299, 16HBE	TS	ROCK1	(S33)
mir-15a	0	19 679	14 750	NPC	Cell line: CNE-2Z	TS	Bcl2	(S30)
				NPC	Cell lines: BL41, BL41/B95.8, Jijoye, EREB2.5	TS	BRCA-1	(S31)
mir-26b	0	15 920	2486	NPC	Cell line: 293	TS	COX-2	(S34)
let-7e	0	10 540	2033	NPC	Cell lines: HK1, HONE1, NP69, NP460	TS	c-Myc	(S3)
mir-224	0	7591	14 266	NSCLC	Clinical samples and cell lines: H1299, H3122, H2228, A549	O	TNFAIP1, SMAD4	(S35)
				ESCC	Clinical samples and cell lines: TE13, Eca109	O	PHLPP1 PHLPP2	(S36)
mir-31	0	6412	15 388	NPC	Cell lines: C666-1, NP69	TS	FIH1, MCM2	(S37)
mir-590	0	1695	6699	NPC	Clinical samples and cell lines:CNE1, CNE2, C666-1	TS	CD44	(S38)

NPC, nasopharyngeal carcinoma; O, oncogene; TS, tumor suppressor; BC, breast cancer; CRC, colorectal cancer; NSCLC, non-small cell lung cancer; GBM, glioblastoma; NBL, neuroblastoma; PC, prostate cancer; OSA, osteosarcoma; HCC, hepatocellular carcinoma; MM, malignant melanoma; HNSCC, head and neck squamous cell carcinoma; HSCC, hypopharyngeal squamous cell carcinoma; LC, lung cancer; GC, gastric cancer; BCA, bladder cancer; ESCC, esophageal squamous cell carcinoma.

and antiproliferative effect of doxorubicin (Fig. 2). A new observation was that photogenerated reactive free radicals produced by the Ag–TiO_2 photocatalyst particles as a result of photocatalysis reduced cell proliferation. Number of viable cells significantly decreased after treatment with 25 μg/ml ($P = 0.003$) and 250 μg/ml ($P < 0.001$) Ag–TiO_2.

Distribution of exosomes

Changes of the size and number distribution of exosomes derived from the differently treated cell cultures were determined by nanoparticle tracking analysis (NTA). We found that the size distribution did not significantly change after either doxorubicin or Ag–TiO_2 treatments (data not shown). In contrast, the quantity of produced exosomes exhibited a significant change under suboptimal conditions. Ag–TiO_2 treatment resulted in a remarkably increased exosome production ($P = 0.0023$) after 72 h of treatment. Similarly, the DNA damage induced by doxorubicin resulted in significantly ($P = 0.001$) elevated exosome production (Fig. 3).

Altered exosomal miRNA content

The qualitative analysis of exosome content targeted the miRNAs carried by the NPC-derived exosomes. The SOLiD 5500xl technology and the bioinformatics supported the high-quality screening of miRNA content.

MicroRNA diversity impressively increased under sub-optimal conditions. In the control samples, 71 different types of miRNA were identified. This increased to 121 types in the doxorubicin-treated samples and to 223 in the Ag–TiO_2-treated ones.

Fourteen types of exosomal miRNA showed more than tenfold decrease after either doxorubicin or Ag–TiO_2 treatment (Fig. 4). More than half of these have oncogenic potential in NPC or other cancer types (Table 1). Although some of them (mir-33a, the let-7 family) have tumor suppressor functions, their role in the chemoresistance is also proven (24).

Fifty-seven and 152 miRNAs were detected exclusively in the doxorubicin-treated cell-derived exosomes and in the Ag–TiO_2-treated cell-derived exosomes, respectively (Fig. 4). Let-7e, mir-15a, mir-186, mir-26b, mir-224, mir-31, and mir-590 were the most abundant miRNA types among them. In addition, five other miRNA types (let-7f-2, let-7f-1, mir-16-2, mir-16-1, and mir-451a) showed tenfold or higher increase in one or both types of stress induced exosomes (Fig. 4). Most of these were previously described as tumor suppressors in NPC (Table 1).

Based on data from the literature (summarized in Table 1) about potential functions of listed miRNAs, NPC cells release tumor suppressor miRNA types via exosomes and retain the oncogenic and resistance-enhancing ones under stress to maintain their tumorigenecity. In contrast, under normal conditions, cells produce and release miRNA types that promote progression and metastasis formation *in vivo*.

The various types of miRNA can have different targets and functions depending on the tumor type, clinical stage, therapy, or other specific regulatory factors and conditions. For example, mir-130b has oncogenic functions in

colorectal and gastric cancer (S27, S28), but in pancreatic cancer, its tumor suppressor role was proven (S29).

Discussion

Exosomes are the smallest class of extracellular vesicles by size, secreted via an evolutionally conserved, endosomal pathway. The content and function of exosomes are variable, defined by the structure of the mother cells and the microenvironment (25). In the present study, we characterized the 5-8F NPC cell line-derived exosomes by size and by microRNA content as the potent information packages of intercellular communication. While the size and shape distribution of the nanovesicles turned out to be unchanged by treatment, we observed significant changes in the quantity and quality of exosomes under suboptimal conditions.

Doxorubicin is a well-known anthracycline chemotherapeutic agent. Its therapeutic effect can be traced back to its ability to intercalate adjacent DNA base pairs, the inhibition of topoisomerase II, and the production of hydroxyl free radicals (26). Doxorubicin can also induce histone eviction from open chromatin (27). These effects lead to the inhibition of cell proliferation and apoptosis initiation in the rapidly replicating cells. However, we could detect significantly increased exosome production parallel with reduced cell viability. The DNA stress changed not only the number of secreted exosomes but induced marked changes in the microRNA profile.

Reactive oxygen species (ROS) generation by Ag–TiO_2 photocatalysis is a known phenomenon (13), and ROS-induced cell damage is not a new phenomenon either (28). However, their effects on exosome production have not been examined so far. Similar to doxorubicin exposure, the cell damage caused by Ag–TiO_2 photocatalysis-related ROS generation resulted in significantly increased exosome production and markedly altered miRNA profile.

Increased exosome production of stress exposed tumor cells has been observed in several studies (29–32). Kucharzewska and Belting conceptualized that different stress factors cause cellular accumulation of ceramide, which triggers increased production and secretion of exosomes as an adaptation to microenvironmental stress (33).

As for the miRNA profiles, the quantitative change of a specific miRNA type was defined as marked when the expression level of that specific type exhibited a tenfold change compared to its original (control) level. Marked change of 30 different miRNA types was observed. The tumor suppressor-like to oncogenic-like ratio was 20:10. Based on our observations, both stress conditions, Ag–TiO_2 and doxorubicin, also elevated exosome responses.

Although alterations of exosomal characteristics had similar trends under Ag–TiO_2 and doxorubicin stress, there are several miRNAs, such as mir-1260, mir-93, or mir-16-1 that showed different intensity or opposite changes compared to control miRNA levels. A plausible explanation for this, that the tested cytostatic agents have distinct mode of action in the cells resulting in different miRNA regulatory effects. Our data suggest that these stressors, besides their antiproliferative effect, may influence the intercellular communication of tumor cells. Increases in exosome release and imbalance of oncogenic and tumor suppressor exosomal miRNAs could have an additional effect on tumor development. For instance, the process of metastasis formation that depends on the microenvironment of the tumor cells (34,35) can be influenced by doxorubicin or Ag–TiO_2 treatments, as tumor-derived exosomes internalized by stromal cells have an altered information content.

References

1. Kahlert C, Kalluri R. Exosomes in tumor microenvironment influence cancer progression and metastasis. *J Mol Med (Berl)* 2013; **91**: 431–7.
2. Muralidharan-Chari V, Clancy JW, Sedgwick A, D'Souza-schorley C. Microvesicles: mediators of extracellular communication during cancer progression. *J Cell Sci* 2010; **123**: 1603–11.
3. Salido-Guadarrama I, Romero-Cordoba S, Peralta-Zaragoza O, Hidlago-Miranda A, Rodrigez-Dorantes M. MicroRNAs transported by exosomes in body fluids as mediators of intercellular communication in cancer. *Onco Targets Ther* 2014; **7**: 1327–38.
4. Hayes J, Peruzzi PP, Lawler S. MicroRNAs in cancer: biomarkers, functions and therapy. *Trends Mol Med* 2014; **20**: 460–9.
5. Leemans CR, Braakhuis BJM, Brakenhoff RH. The molecular biology of head and neck cancer. *Nat Rev Cancer* 2011; **11**: 9–22.
6. Pulte D, Brenner H. Changes in survival in head and neck cancers in the late 20th and early 21st century: a period analysis. *Oncologist* 2010; **15**: 994–1001.
7. Arango BA, Castrellon AB, Perez CA, et al. Nasopharyngeal carcinoma: alternative treatment options after disease progression. *Expert Rev Anticancer Ther* 2010; **10**: 377–86.
8. Vokes EE, Liebowitz DN, Weichselbaum RR. Nasopharyngeal carcinoma. *Lancet* 1997; **350**: 1087–91.
9. Wang X, Li L, Hu C, et al. Patterns of level II node metastasis in nasopharyngeal carcinoma. *Radiother Oncol* 2008; **89**: 28–32.
10. Bartel DP. MicroRNAs: genomics, biogenesis, mechanism, and function. *Cell* 2004; **116**: 281–97.
11. Liu N, Chen NY, Ciu RX, et al. Prognostic value of a microRNA signature in nasopharyngeal carcinoma: a microRNA expression analysis. *Lancet Oncol* 2012; **13**: 633–41.
12. Fujishima A, Honda K. Electrochemical photolysis of water at a semiconductor electrode. *Nature* 1972; **238**: 37–8.
13. Tallósy SP, Janovák L, Ménesi J, et al. Investigation of the antibacterial effects of silver-modified TiO_2 and ZnO plasmonic photocatalysts embedded in polymer thin films. *Environ Sci Pollut Res Int* 2014; **21**: 11155–67.
14. Veres Á, Rica T, Janovák L, et al. Silver and gold modified plasmonic TiO_2 hybrid films for photocatalytic decomposition of ethanol under visible light. *Catal Today* 2012; **181**: 156–62.
15. Marton A, Vizler C, Kusz E, et al. Melanoma cell-derived exosomes alter macrophage and dendritic cell functions in vitro. *Immunol Lett* 2012; **148**: 34–8.
16. Hutter JL, Bechhoefer J. Calibration of atomic-force microscope tips. *Rev Sci Instrum* 1993; **64**: 1868–73.
17. Sader JE, Chon JWM, Mulvaney P. Calibration of rectangular atomic force microscope cantilevers. *Rev Sci Instrum* 1999; **70**: 3967–9.
18. Higgins MJ, Proksch R, Sader JE, et al. Noninvasive determination of optical lever sensitivity in atomic force microscopy. *Rev Sci Instrum* 2006; **77**: 013701.

19. Sader JE, Sanelli JA, Adamson BD, et al. Spring constant calibration of atomic force microscope cantilevers of arbitrary shape. *Rev Sci Instrum* 2012; **83**: 103705.
20. Ebner A, Hinterdorfer P, Gruber HJ. Comparison of different aminofunctionalization strategies for attachment of single antibodies to AFM cantilevers. *Ultramicroscopy* 2007; **107**: 922–7.
21. Aekbote BL, Jacak J, Schütz GJ, et al. Aminosilane-based functionalization of two-photon polymerized 3D SU-8 microstructures. *Eur Polym J* 2012; **48**: 1745–54.
22. Witwer KW, Buzas EI, Bemis LT, et al. Standardization of sample collection, isolation and analysis methods in extracellular vesicle research. *J Extracell Vesicles* 2013; **27**: 2.
23. Wirth R, Kovács E, Maróti G, Bagi Z, Rákhely G, Kovács KL. Characterization of a biogas-producing microbial community by short-read next generation DNA sequencing. *Biotechnol Biofuels* 2012; **5**: 41.
24. Zhou Y, Huang Z, Wu S, et al. miR-33a is up-regulated in chemoresistant osteosarcoma and promotes osteosarcoma cell resistance to cisplatin by down-regulating TWIST. *J Exp Clin Cancer Res* 2014; **33**: 12.
25. Yáñez-Mó M, Siljander PR, Andreu Z, et al. Biological properties of extracellular vesicles and their physiological functions. *J Extracell Vesicles* 2015; **4**: 27066.
26. Hortobagyi GN. Anthracyclines in the treatment of cancer. An overview. *Drugs* 1997; **54**(Suppl 4): 1–7.
27. Pang B, Qiao X, Janssen L, et al. Drug-induced histone eviction from open chromatin contributes to the chemotherapeutic effects of doxorubicin. *Nat Commun* 2013; **4**: 1908.
28. Filomeni G, De Zio D, Cecconi F. Oxidative stress and autophagy: the clash between damage and metabolic needs. *Cell Death Differ* 2015; **22**: 377–88.
29. King HW, Michael MZ, Gleadle JM. Hypoxic enhancement of exosome release by breast cancer cells. *BMC Cancer* 2012; **12**: 421.
30. Eldh M, Ekström K, Valadi H, et al. Exosomes communicate protective messages during oxidative stress; possible role of exosomal shuttle RNA. *PLoS One* 2010; **5**: e15353.
31. Hedlund M, Nagaeva O, Kargl D, Baranov V, Mincheva-Nilsson L. Thermal- and oxidative stress causes enhanced release of NKG2D ligand-bearing immunosuppressive exosomes in leukemia/lymphoma T and B cells. *PLoS One* 2011; **6**: e16899.
32. Lv LH, Wan YL, Lin Y, et al. Anticancer drugs cause release of exosomes with heat shock proteins from human hepatocellular carcinoma cells that elicit effective natural killer cell antitumor responses in vitro. *J Biol Chem* 2012; **287**: 15874–85.
33. Kucharzewska P, Belting M. Emerging roles of extracellular vesicles in the adaptive response of tumour cells to microenvironmental stress. *J Extracell Vesicles* 2013; **5**: 2.
34. Spano D, Zollo M. Tumor microenvironment: a main actor in the metastasis process. *Clin Exp Metastasis* 2012; **29**: 381–95.
35. Quail DF, Joyce JA. Microenvironmental regulation of tumor progression and metastasis. *Nat Med* 2013; **19**: 1423–37.

Acknowledgements

This research was funded by OTKA PD 84064, OTKA K 112493, TAMOP-4.2.2-A-11/1/KONV-2012-0025, and IPA HUSRB/1203/214/230. The authors would like to thank Gábor Braunitzer and János Minarovits for their helpful comments.

Conflict of interest

The authors declare no conflict of interest.

Supporting Information

Additional Supporting Information may be found in the online version of this article:

Data S1 References.

www.nature.com/scientificreports

SCIENTIFIC REPORTS
nature research

OPEN

Small extracellular vesicles convey the stress-induced adaptive responses of melanoma cells

Maria Harmati[1,2], Edina Gyukity-Sebestyen[1,2], Gabriella Dobra[1,2], Laszlo Janovak[3], Imre Dekany[3], Okay Saydam[4], Eva Hunyadi-Gulyas[5], Istvan Nagy[6], Attila Farkas[7], Tibor Pankotai[8,9], Zsuzsanna Ujfaludi[8,9], Peter Horvath[1,10], Filippo Piccinini[11], Maria Kovacs[1], Tamas Biro[12,13] & Krisztina Buzas[1,9*]

Exosomes are small extracellular vesicles (sEVs), playing a crucial role in the intercellular communication in physiological as well as pathological processes. Here, we aimed to study whether the melanoma-derived sEV-mediated communication could adapt to microenvironmental stresses. We compared B16F1 cell-derived sEVs released under normal and stress conditions, including cytostatic, heat and oxidative stress. The miRNome and proteome showed substantial differences across the sEV groups and bioinformatics analysis of the obtained data by the Ingenuity Pathway Analysis also revealed significant functional differences. The *in silico* predicted functional alterations of sEVs were validated by *in vitro* assays. For instance, melanoma-derived sEVs elicited by oxidative stress increased Ki-67 expression of mesenchymal stem cells (MSCs); cytostatic stress-resulted sEVs facilitated melanoma cell migration; all sEV groups supported microtissue generation of MSC-B16F1 co-cultures in a 3D tumour matrix model. Based on this study, we concluded that (i) molecular patterns of tumour-derived sEVs, dictated by the microenvironmental conditions, resulted in specific response patterns in the recipient cells; (ii) *in silico* analyses could be useful tools to predict different stress responses; (iii) alteration of the sEV-mediated communication of tumour cells might be a therapy-induced host response, with a potential influence on treatment efficacy.

Exosomes are small (30–200 nm)[1] endosome-derived vesicles that are actively secreted into the extracellular environment from most cell types. Initially, exosomes were proposed to eliminate cellular waste, but it has been proven that they also play a key role in the intercellular communication between adjacent as well as distal cells through the horizontal transfer of lipids, proteins and nucleic acids. Over the past three decades, exosomes have surged to the forefront of cell biology research, and recently an increasing body of evidence indicates that this exosomal communication is a deliberate and highly orchestrated process. Clinical relevance of exosomes is also considerable, since they are associated with numerous physiological and pathological conditions, including cancer diseases[2].

[1]Laboratory of Microscopic Image Analysis and Machine Learning, Institute of Biochemistry, Biological Research Centre of the Hungarian Academy of Sciences, Szeged, Hungary. [2]Doctoral School of Interdisciplinary Medicine, Faculty of Medicine, University of Szeged, Szeged, Hungary. [3]Interdisciplinary Excellence Centre, Department of Physical Chemistry and Materials Science, University of Szeged, Szeged, Hungary. [4]Department of Pediatrics, University of Minnesota, Minneapolis, USA. [5]Laboratory of Proteomics Research, Institute of Biochemistry, Biological Research Centre of the Hungarian Academy of Sciences, Szeged, Hungary. [6]Sequencing Platform, Institute of Biochemistry, Biological Research Centre of the Hungarian Academy of Sciences, Szeged, Hungary. [7]Laboratory of Microbial Genomics, Institute of Plant Biology, Biological Research Centre of the Hungarian Academy of Sciences, Szeged, Hungary. [8]Department of Biochemistry and Molecular Biology, Faculty of Science and Informatics, University of Szeged, Szeged, Hungary. [9]Department of Oral Biology and Experimental Dental Research, Faculty of Dentistry, University of Szeged, Szeged, Hungary. [10]Institute for Molecular Medicine Finland, University of Helsinki, Helsinki, Finland. [11]Laboratorio di Bioscienze, Istituto Scientifico Romagnolo per lo Studio e la Cura dei Tumori (IRST) IRCCS, Meldola, Italy. [12]Department of Immunology, Faculty of Medicine, University of Debrecen, Debrecen, Hungary. [13]Hungarian Centre of Excellence for Molecular Medicine, Szeged, Hungary. *email: kr.buzas@gmail.com

Conditions	Control 1	Cytostatic stress	Heat stress	Control 2	Oxidative stress
sEV donor cell cultures	Ctrl	Doxo	Hs	Ag Ctrl	Ag-TiO_2
Treatment	—	0.6 μM doxorubicin	3 × 2 h at 42°C	illuminated medium	light-induced 2.5 μg/ml Ag-TiO_2
Released sEV groups	Ctrl sEV	Doxo sEV	Hs sEV	Ag Ctrl sEV	Ag-TiO_2 sEV

Table 1. Treatment schedule of tumour cell cultures and the isolated sEV groups.

Tumours are not just insular masses of proliferating cancer cells; they are also complex tissues composed of cellular components, such as mesenchymal stem cells (MSCs), cancer-associated fibroblasts (CAFs), endothelial cells, immune cells as well as extracellular matrix (ECM) components, which establish the so-called tumour microenvironment (TME) surrounding the tumour cells. The TME does not only surround the tumour cells, it also actively contributes to tumour progression, which requires a continuous paracrine communication[3,4]. One of the possible candidates for intercellular communication might be exosomes, since several recent papers have emphasized the mediating role of exosomes in the tumour macro- and microenvironment[4–6]. Upon contact with recipient cells, tumour-derived exosomes alter their phenotypic and functional properties conveying molecular and genetic messages[7].

Since malignant melanoma is one of the most aggressive cancers, the B16F1 mouse melanoma cell line was chosen as a tumour cell model for this study. Melanoma cells potentially disseminate from a relatively small primary tumour and form metastases in multiple sites, including the lung, liver, brain, bone and lymph nodes[8]. This high metastatic potential can be explained by the unique features of melanoma. For instance, melanoma cells are mesenchymal in nature ensuring that a larger percentage of cells can act as stem cells with self-renewal capacity. They share many antigens with vascular endothelial cells (vasculogenic mimicry) which enables them to survive in the circulation, and increases their migration and invasion capacity as well. Furthermore, melanoma-derived extracellular vesicles also have a crucial role in the rapid tumour progression[8–12]. They are capable to induce a tumour-favourable phenotype in the EV-recipient cells in the TME[13] and the metastatic sites[14,15]. For instance, after re-education by exosomes, MSCs may promote tumour growth and metastasis[16,17]; fibroblast[18] and endothelial cells[19] can promote angiogenesis. There are also a few papers about intrinsic stresses, such as low pH[20]- or hypoxia[21]-induced alterations of melanoma exosomes, and their ability to transfer drug resistance[22]. However, different extrinsic stress-elicited changes have not been elucidated yet.

Using a unique approach, this study compared changes in the vesicular information transfer of melanoma cells under different inducible stress conditions. Exosomes are complex information packages, and we consider them as message delivering units with specific molecular patterns, rather than putting emphasis on a few exosomal signal molecules. Following the guideline recommended by ISEV (International Society for Extracellular Vesicles), called MISEV2018 (Minimal information for studies of extracellular vesicles 2018)[23], we refer to the isolated vesicles based on their size by using the term 'small extracellular vesicles' (sEVs), even though their exosomal characteristics are demonstrated.

To gain insights into the plasticity and role of sEVs under suboptimal conditions, we investigated cytostatic, heat and oxidative stress-induced alterations of the B16F1 mouse melanoma cell-derived sEVs. Clinical relevance of this study is highlighted by previous papers, since chemo- or radiotherapy were shown to increase the amount of circulating tumour-derived EVs[24,25]. Although chemotherapy provides long-term clinical benefits to patients, it may induce tumour-promoting host responses as well[26]. Furthermore, Keklikoglou *et al.* have shown that paclitaxel and doxorubicin elicit the production of pro-metastatic breast cancer-derived EVs[27]. Hyperthermia treatment involves increasing the target site temperature to induce thermic stress, which results in cancer cell cytotoxicity and immune response stimulation via immune cell activation. Therefore, hyperthermia may enhance the therapeutic efficacy in combined therapies[28,29], but its impact on tumour exosome-mediated intercellular communication has not been described yet. To induce oxidative stress, we used Ag-TiO_2 photocatalyst particles, which represent a high potential for therapeutic applications through antibacterial[30,31], antifungal[32] and anticancer[33] activities. However, the effects of Ag-TiO_2-based therapies on the vesicular communication have not been investigated yet.

Results and Discussion

In order to study the adaptive sEV-mediated communication under microenvironmental stress, we investigated cytostatic, heat and oxidative stress-induced alterations of the B16F1 mouse melanoma cell-derived sEVs. After verification the exosomal characteristics of our sEV isolates, we optimized the cytostatic and oxidative stress treatment conditions by proliferation assay and established the protocol for heat stress based on literature data[34] to expose the melanoma cells to sublethal stress conditions. Then, for the sEV production, we cultured the B16F1 cells under five different conditions in EV-depleted FBS-containing media; control cultures (Ctrl) received culture medium, cytostatic stressed cultures (Doxo) were treated with 0.6 μM doxorubicin, heat stressed cultures (Hs) were incubated at 42°C for 3 × 2 h, oxidative stressed cultures (Ag-TiO_2) were treated with 2.5 μg/ml light-induced Ag-TiO_2, and as a control of the oxidative stress (Ag Ctrl), additional cultures were treated with illuminated media (Table 1). After a 72 h stress exposure period of B16F1 cultures, sEVs were isolated from their supernatants, quantified by nanoparticle tracking analysis (NTA) and analysed by SOLiD sequencing and LC-MS/MS to determine the miRNome and proteome of sEVs. Functional differences between sEV groups were predicted first *in silico* using the Ingenuity Pathway Analysis (IPA) based on the protein and miRNA data, and then verified by *in vitro* experiments targeting tumour-related cellular functions, such as Ki-67 expression, cell cycle dynamics, migration capacity and microtissue generation of the recipient cells (Fig. 1).

Our oxidative stress model is based on the photocatalytic activity of the Ag-TiO_2 particles[31,35]. During the process of photocatalysis under appropriate (exciting) wavelength, reactive hydroxyl radicals (OH·) are produced, which are primarily responsible for photooxidation of organic materials or inactivating bacteria[36]. Hydroxyl radicals are the most reactive oxygen species and cause irreversible DNA damages which could lead to DNA degradation in bacteria[36]. In our previous work, the amount of reactive hydroxyl radicals formed on Ag-TiO_2 particles was determined by the hydrogen peroxide-induced luminol-dependent chemiluminescence reaction[30]. It was presented that concentration of the Ag-TiO_2-produced OH· radicals was equivalent to 0.33 mM H_2O_2 after 20 min visible light illumination.

Descriptive statistics of sEVs released under different microenvironmental conditions. *Isolated EVs fulfil the minimal experimental requirements for small extracellular vesicles (sEVs).* First, to fulfil the minimal experimental requirements for extracellular vesicles, suggested in the MISEV2018[23], we characterised the B16F1 cell-derived extracellular vesicles isolated from conditioned media by differential filtration and ultracentrifugation. Presence of the vesicles in the sEV isolates was verified by atomic force microscopy (AFM), and size distribution of the isolated vesicle population was described by dynamic light scattering (DLS) with a Z-average of 78 nm. EV markers, such as CD63 and CD9 (transmembrane proteins), HSP70, Alix and TSG101 (cytosolic proteins), Calnexin (negative sEV marker) were investigated in the vesicle isolates and the donor cell lysates by Western blot (Supplementary Fig. S1).

Vesicle production of melanoma cells is elevated under stress conditions. Scanning electron microscopy (SEM) revealed spectacular morphological changes of the B16F1 cells in each stressed group (Doxo, Hs and Ag-TiO_2) 24 h after treatments (Fig. 2a, top panels). Taking advantage of the high magnification capacity of SEM, we were able to observe the surface structures of the cells as well (Fig. 2a, bottom panels). At a 20,000 × magnification, we discovered spherical, exosome-sized vesicles, which were present in higher numbers on the stressed cells compared to the untreated Ctrl cells ($p_{Doxo} = 0.00297$, $p_{Hs} = 0.03928$, $n = 5$; Fig. 2b).

Then, we isolated sEVs from conditioned media of the five groups of cell cultures and quantified by the NTA-based NanoSight Analysis. There was a significant increase in vesicle number per cell in the Doxo ($20.2 \pm 0.4 \times 10^3$; $p = 0.00021$) and the Hs ($12.7 \pm 3.8 \times 10^3$; $p = 0.03006$) groups compared to the Ctrl one ($5.35 \pm 0.7 \times 10^3$). The Ag-TiO_2-treated cultures produced $13 \pm 1.8 \times 10^3$ sEVs per cell, while production of the Ag Ctrl group was only $7.9 \pm 1.6 \times 10^3$ sEVs per cell ($n = 3$, Fig. 2c). At the same time, stress conditions did not affect the size distribution of sEVs.

Other reports also demonstrated that cells, including tumour cells, release a higher amount of exosomes in response to different types of stresses[37], such as hypoxia[38], acidosis[39], oxidative stress[40], thermal stress[40], radiation[41] and cytotoxic drugs[42–44].

Concentration of the encapsulated doxorubicin under cytostatic stress is less than 10% of median lethal dose. To reveal if doxorubicin, used for cytostatic stress in 0.6 µM concentration, could be encapsulated into the vesicles, Doxo sEV isolates were analysed by fluorescence spectroscopy. Using the Ctrl sEVs as a background, the calculated doxorubicin concentration of the Doxo sEVs was 14.735 nM.

Based on the measurements, the Doxo sEV suspensions – used for treatment of recipient cells – contained only 8 ng/ml doxorubicin. Therefore, it cannot be excluded that sEVs may transfer doxorubicin to the recipient cells, but the doxorubicin content of Doxo sEVs is less than 10% of the median lethal dose (LD50 = 100 ng/ml) for mouse melanoma cells[45].

Encapsulation of Ag-TiO_2 nanoparticles into sEVs cannot be proven. To investigate the possibility of Ag-TiO_2 encapsulation into sEVs, we measured the size distribution of the nanoparticles by DLS. The mean particle size was around 255 nm during the whole studied time interval (Supplementary Fig. S2). This means that the initial Ag-TiO_2 photocatalyst particles form aggregates because the primer size of the Ag-TiO_2 particles is around 25 nm as seen in the TEM image in our previous paper[46]. Thus, DLS measurements did indicate particle aggregation in the used medium; however, it also can be seen that the size of these particle aggregates did not change during the experiments. These results suggest that the Ag-TiO_2 particles cannot be transferred into the recipient cells in this aggregated form and they cannot contaminate the sEV isolates, since particles over 220 nm were eliminated during the isolation process.

We also tried to detect disaggregated Ag-TiO_2 nanoparticles in the sEV isolates using chemiluminescence (CL) method and transmission electron microscopy (TEM). After photoirradiation of the Ag-TiO_2, generated ROS can be detected by adding luminol, which emit light upon oxidation[30]. We compared the CL intensity of Ag-TiO_2 sEV lysates to an Ag-TiO_2 calibration curve prepared in Ag Ctrl sEV lysate, but it was under the detection limit (0.25 µg/ml; Supplementary Fig. S2). Moreover, on TEM images we could not observe any internal structures of the sEVs or contaminating electron-dense nanoparticles in the Ag-TiO_2 sEV isolate (Supplementary Fig. S2).

miRNome and proteome of the melanoma sEVs strongly depend on the microenvironmental conditions of the donor cells. Exosomes deliver a wide range of RNAs and proteins to convey messages to the recipient cells. Their molecular content correlates with the type and state of the donor cell[2]. In this study, we compared the miRNA and protein patterns of the sEV groups to show the influence of the microenvironment on these information packages.

A total of 254 miRNAs were identified by SOLiD sequencing with more than ten read counts; 35.04% of these miRNAs were detected in each sEV group, while 6.30%, 1.18% and 0.79% were exclusively detected in the Ag-TiO_2, Ctrl and Doxo sEVs, respectively. Hs and Ag Ctrl sEV-specific miRNAs were not found (Fig. 3a, left panel). The proportion of the over- and underrepresented miRNAs under stress conditions was the highest in the Ag-TiO_2 sEVs, where 53.41% of the detected miRNAs showed more than twofold changes compared to the

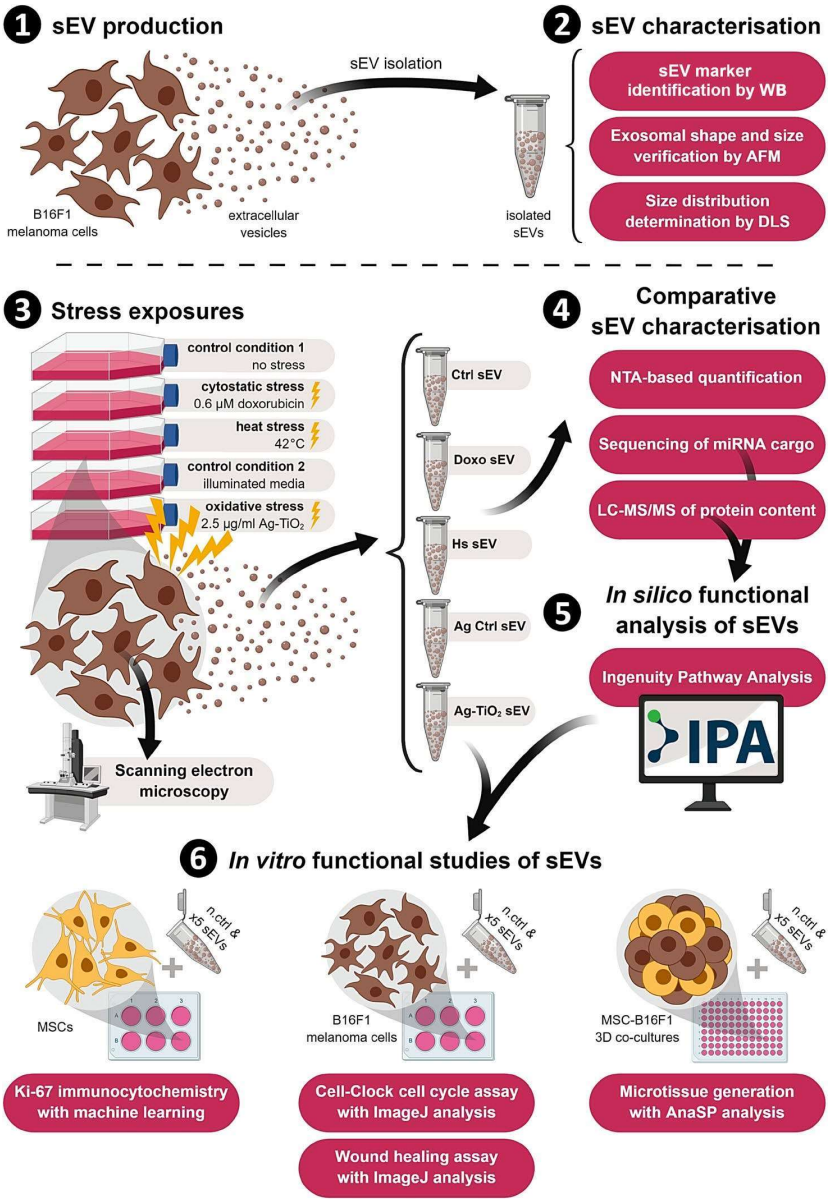

Figure 1. Schematic illustration of the experimental workflow in six steps. B16F1 mouse melanoma cell-derived sEVs were isolated and characterised by Western Blot (WB), atomic force microscopy (AFM) and dynamic light scattering (DLS). Then B16F1 cultures were treated in five different ways, and 72 h supernatants were harvested for sEV isolation. Vesicle samples were then analysed by nanoparticle tracking analysis (NTA) to determine the number of released sEVs, sequencing and LC-MS/MS to describe their miRNome and proteome. Ingenuity Pathway Analysis (IPA) was used to analyse data and predict the functional differences between sEV groups. This *in silico* predictions were tested *in vitro* on mesenchymal stem cell (MSC) and melanoma cell cultures and MSC-B16F1 3D co-cultures as well using Ki-67-specific immunocytochemistry, Cell-Clock cell cycle assay, wound healing assay, and 3D hanging drop technology. Abbreviation: n.ctrl-negative control. Figure was created with BioRender.com.

corresponding control (Fig. 3a, right panel). Results of the sequencing data were validated by qPCR on three major miRNAs of this study, *i.e.* mmu-miR-16-5p, mmu-miR-125b-5p and mmu-miR-29a-3p (Supplementary Fig. S3).

Using LC-MS/MS, a total of 216 proteins were detected with three or more peptides; 59.72% of these proteins were common to all sEV groups, and only a few unique proteins were found (Fig. 3b, left panel). Eight Hs sEV-specific

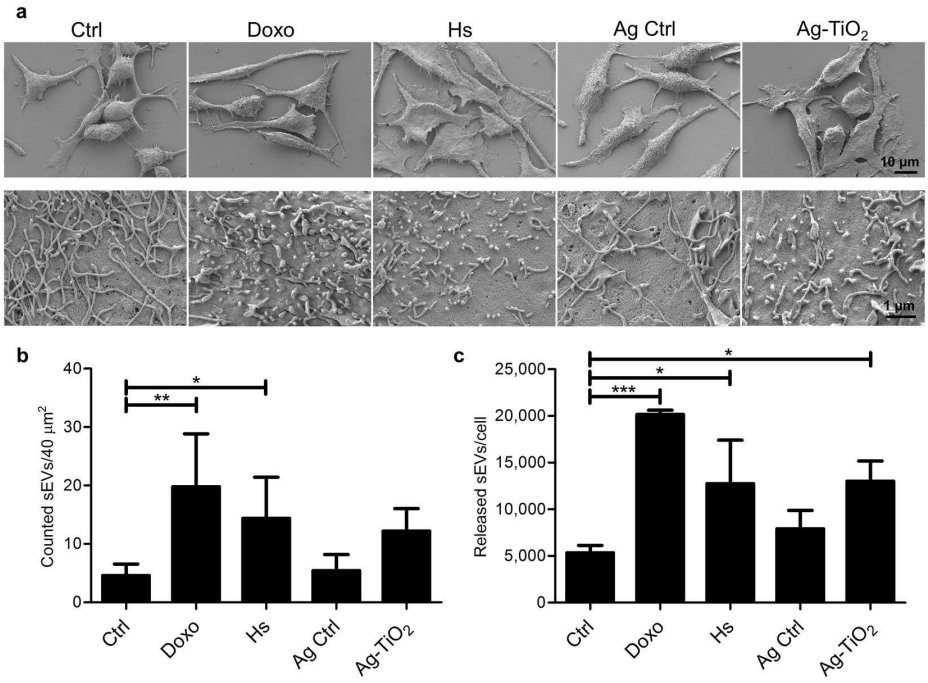

Figure 2. Microenvironmental stress factors resulted in morphological changes and elevated vesicle production of melanoma cells. (**a**) Scanning electron micrograph of the differently treated melanoma cells. The top row of pictures was taken in 1,500 × magnification showing the different cell morphology after 24 h treatments. The bottom row of pictures was taken in 20,000 × magnification showing the distinct cell surface structures. (**b**) The number of counted exosome-sized vesicles on the surface of cells using ImageJ (n = 5). (**c**) Number of released vesicles/cell based on NanoSight measurements (n = 3). Each bar represents mean + SD; *p < 0.05, **p < 0.01 and ***p < 0.001 indicate statistical significance.

proteins were identified; half of these had a chaperone function (HSBP1, SERPINH1, CCT5, CLU). The major impact of heat stress on the protein composition of sEVs was also evidenced by the high proportion of the over- and under-represented proteins (52.21%) compared to the Ctrl sEV group. Cytostatic stress also resulted in dramatic and distinct changes in the protein content of vesicles. For instance, the proportion of proteins, which decreased below the detectable level was the highest (15.34%) in Doxo sEVs (Fig. 3b, right panel). Many of the commonly found proteins have a function in vesicular trafficking, membrane fusion or MVB biology which suggests they have a role in exosome biogenesis. There are also melanocyte-specific molecules, such as some melanin biosynthesis elements (DCT, MLANA, PMEL, TYR or TYRP1), and we found a several metabolism-, cytoskeletal organisation-, extracellular matrix remodelling-related proteins, adhesion molecules, receptors and transporters, which may have a crucial role in tumour progression (Fig. 3c). Proteomics data were validated by Western blot, where a vesicular marker, the HSP70 and the MLANA showed similar signal intensity patterns to the LC-MS/MS data (Supplementary Fig. S4).

Our findings about the molecular cargo of sEVs are in accordance with previous studies, which also showed changes in the exosomal content upon exposure of the donor cells to external stimuli and stress conditions[41,44,47,48]. Furthermore, Peinado *et al.*[17] and Lazar *et al.*[49], analysing protein composition of different melanoma cell line-derived exosomes, also found melanocyte-specific proteins, transmembrane proteins, such as tetraspanins, transporters and receptors as well as MVB and endosomal pathway-related proteins, for instance ESCRT-associated proteins, annexins, cytoskeletal and small GTP-binding proteins[17,49].

Comprehensive *in silico* analysis of functional differences between sEV groups. Since the exosomal cargo is a complex information package containing a large number and wide variety of molecules, it may act on several biological processes in the recipient cells. In this study, we aimed to identify these biological processes even for normal (Ctrl) B16F1 sEVs and also for the stress-exposed cell-derived ones. We performed bioinformatics analyses to interpret the biological context of the obtained miRNA and protein data applying the IPA. This software is based on computer algorithms that analyse the functional connectivity of the molecules using the Ingenuity Knowledge Base. For these *in silico* analyses, we set the confidence level to 'Experimentally observed' that enables literature data-based analysis, but not unproven predictions. Phrases between apostrophes are 'IPA-specific terms' in this paper.

Using the 'Core analysis' feature, we found a huge overlap in the 'Top 5 canonical pathways' between sEV groups. Namely, 'Gycolysis I', 'Gluconeogenesis I', 'Eumelanin Biosynthesis' and 'Phagosome maturation' was listed

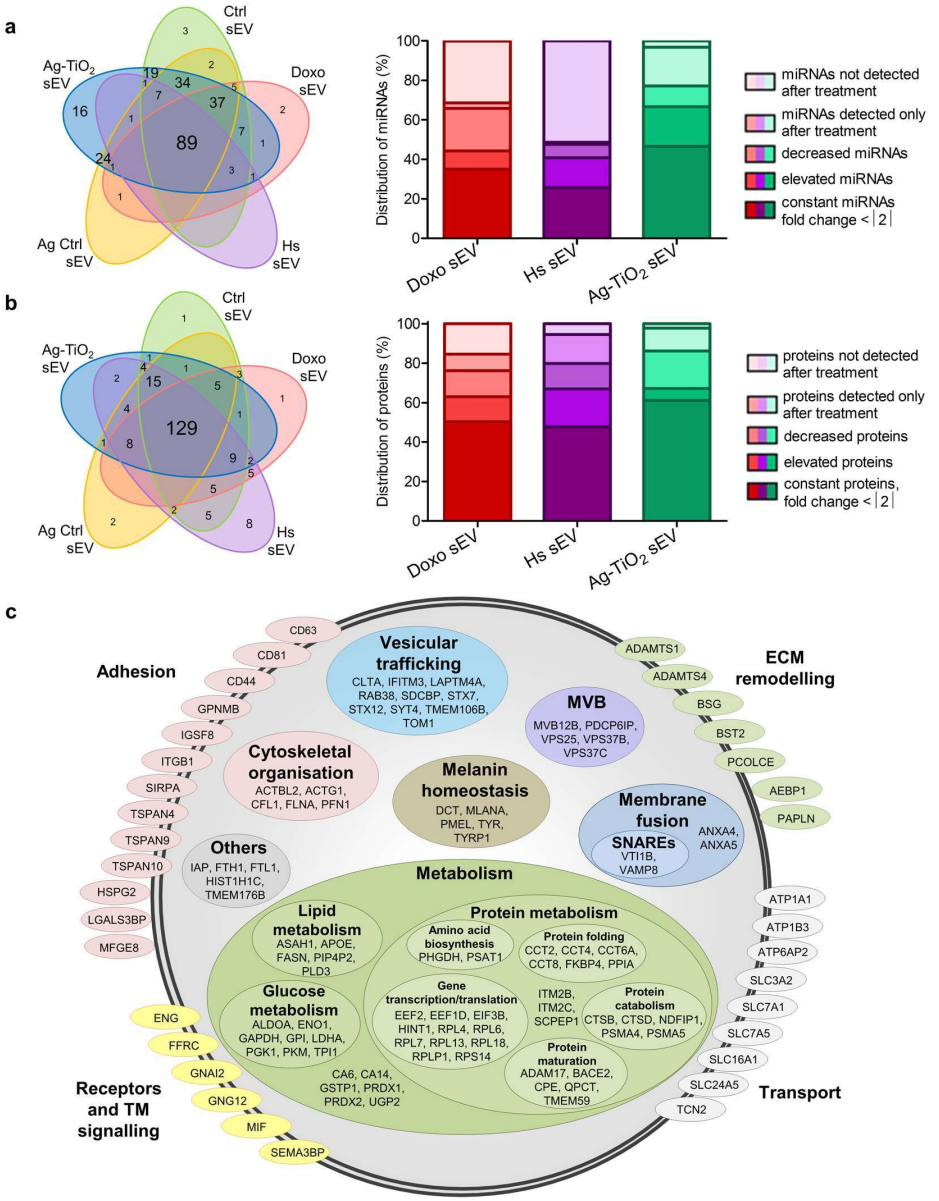

Figure 3. Stress factors caused unique molecular patterns of the melanoma-derived sEVs. (**a**,**b**) Results of the miRNA sequencing and whole proteome analysis by LC-MS/MS. Venn diagrams show the number of common and unique molecules of the different sEVs. Stacked bar graphs show the distribution of sEV molecules based on their changes compared to the appropriate control. (**c**) Classification of the common proteins for each sEV group based on their function and localisation in vesicles.

in all five cases, while 'Inhibition of matrix metalloproteinases' (MMPs) was only found in Ctrl sEVs, and 'EIF2 signalling' was listed in the four other sEV groups (Fig. 4a). As it was shown in the previous section, beside the remarkable differences, sEVs contain many donor cell-specific molecules, which helps to interpret these results. For instance, the Warburg effect, which means, that cancer cells may prefer metabolism via aerobic glycolysis rather than oxidative phosphorylation[50,51] gives a possible explanation for the strong presence of glycolysis and glyconeogenesis-related molecules in sEVs. Since the investigated B16F1 is a melanin-producing cell line, the reason for the presence of the eumelanin biosynthesis-related molecules is obvious. Vesicular processes of exosome biogenesis[52] account for the high number of phagosome maturation-related molecules in the isolated vesicles. Presence of the MMP- and EIF2 signalling-related molecules in the sEVs can also be explained by the tumour cell origin[53–55].

a

Top 5 biological pathways	p-value				
	Ctrl sEV	Doxo sEV	Hs sEV	Ag Ctrl sEV	Ag-TiO_2 sEV
Glycolysis I	3.22E-08	9.50E-09	1.37E-08	2.33E-08	5.50E-08
Gluconeogenesis I	1.93E-05	8.21E-06	1.06E-05	1.54E-05	2.81E-05
Eumelanin biosynthesis	2.17E-05	1.27E-05	1.50E-05	1.88E-05	2.74E-05
Phagosome maturation	1.48E-04	3.80E-05	5.75E-05	5.52E-04	5.02E-05
Inhibition of matrix metalloproteinases	1.64E-03	6.79E-02	1.04E-03	1.38E-03	2.18E-03
EIF2 signalling	1.02E-02	4.36E-05	4.32E-07	1.09E-06	4.68E-06

b

Top 5 molecular and cellular functions	p-range				
	Ctrl sEV	Doxo sEV	Hs sEV	Ag Ctrl sEV	Ag-TiO_2 sEV
Cellular development	4.45E-04-5.35E-20	3.08E-04-3.60E-19	1.67E-04-2.51E-19	4.09E-04-8.18E-20	5.60E-04-3.52E-20
Cellular growth and proliferation	4.45E-04-5.35E-20	3.08E-04-3.60E-19	1.67E-04-2.51E-19	4.09E-04-8.18E-20	5.60E-04-3.52E-20
Cell death and survival	4.82E-04-7.73E-20	2.47E-04-2.40E-21	1.73E-04-7.89E-25	3.89E-04-3.15E-19	5.92E-04-1.53E-18
Cellular movement	4.45E-04-3.58E-15	3.08E-04-5.11E-14	1.81E-04-5.03E-12	4.31E-04-5.97E-14	5.88E-04-3.58E-14-
Cell-to-cell signalling and interaction	4.81E-04-2.71E-07	3.05E-04-1.12E-07	1.77E-04-2.40E-08	4.02E-04-3.77E-08	5.92E-04-3.99E-07
Protein synthesis	1.53E-04-4.69E-06	3.12E-04-4.21E-08	1.96E-04-1.55E-12	9.31E-05-5.51E-07	9.89E-05-1.00E-06

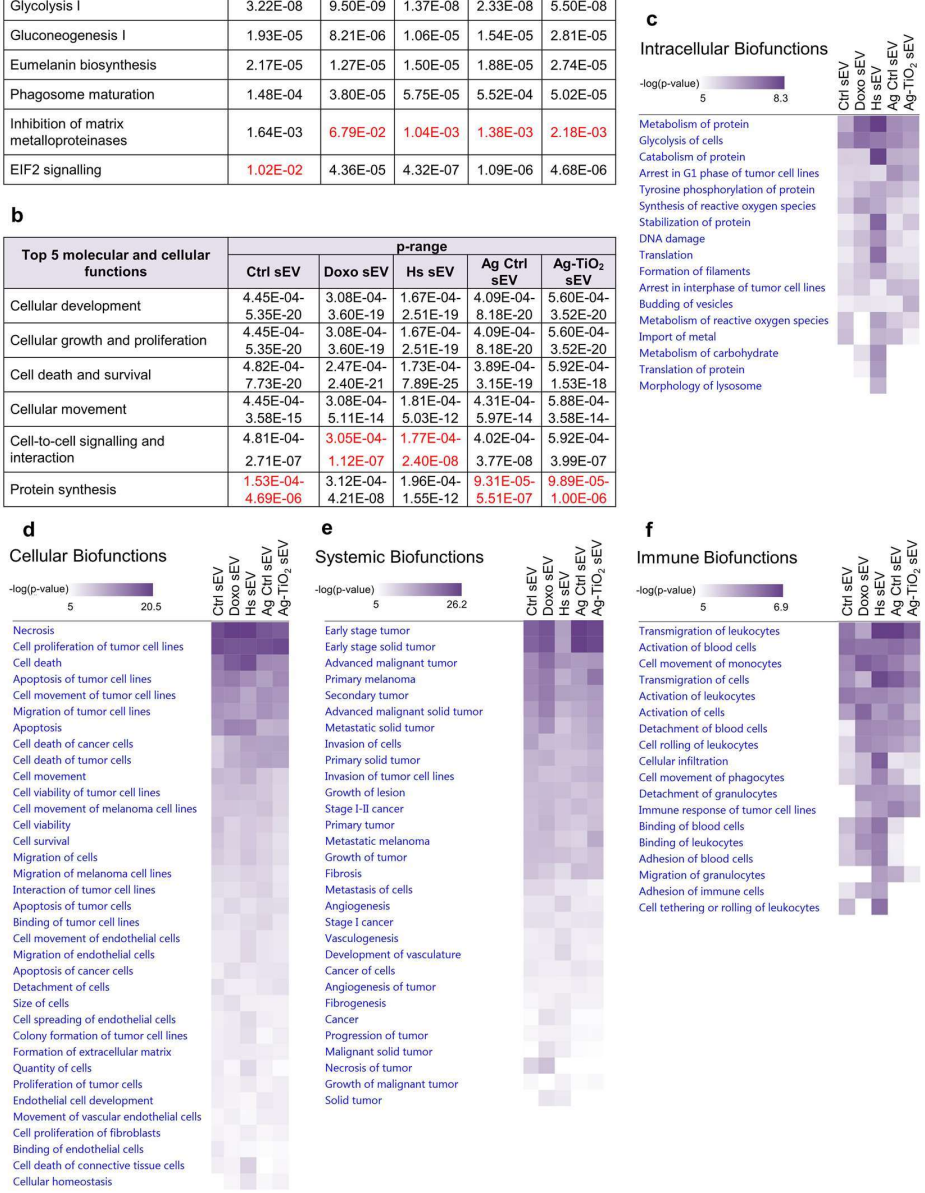

Figure 4. IPA showed that sEVs may influence many biological pathways and functions with different significance via their miRNA and protein content. (**a**) 'Top 5 canonical pathways' for each sEV group. Red values label the significance of pathways, which were not included in the Top 5. (**b**) 'Top 5 molecular and cellular functions' for each sEV group. Red values label the significance ranges of functions, which were not included in the Top 5. (**c–f**) Heatmaps from the 'Comparison analysis' of the molecular content of vesicles. Relevant 'Biofunctions' with -log(p-value) > 5 were organised into four groups, namely intracellular, cellular, systemic and immune processes.

'Top 5 molecular and cellular functions' also showed similarities across the sEV groups. 'Cellular development', 'Cellular growth and proliferation', 'Cell death and survival' and 'Cellular movement' were shared between each sEV group; 'Protein synthesis' was listed in Doxo and Hs sEVs and 'Cell-to-cell signalling and interaction'

in Ctrl, Ag Ctrl and Ag-TiO_2 ones (Fig. 4b). All of these cellular functions are involved in tumour progression, which highlights the role and diverse effects of vesicles in recipient cell reprogramming in the tumour matrix and the metastatic sites[4–7,56–58].

Performing 'Comparison analysis' in the IPA, we built a heatmap of the melanoma-related 'Diseases and Biofunctions', significantly influenced by any sEV group (-log(p-value) > 5). This *in silico* analysis revealed that the sEVs may play a role not only in intracellular and cellular, but in systemic and immunological processes as well (Fig. 4c–f). Focusing on the activation and inhibitory effects, we identified many 'Biofunctions', which may be regulated differently by the sEVs, highlighting the role of the releasing conditions in the vesicular communication of melanoma cells. In order to prove the tumour-associated functional differences between sEV groups, some 'Biofunctions' related to stem cell proliferation, cell cycle, migration of tumour cells and aggregation of cells were selected for *in vitro* investigations.

In silico predictions-based _in vitro_ analyses of sEV-induced cellular responses in tumour matrix cells. In regulation-focused examinations using the LC-MS/MS and SOLiD sequencing data, the 'Grow tool' of IPA enabled to identify the interacting vesicular molecules for the investigated 'Biofunctions'. Then, the 'Molecule Activity Predictor' (MAP) feature of IPA predicted their overall regulatory effects for each sEV group. Following these *in silico* studies, predicted alterations of the sEV-induced cell responses were analysed experimentally by *in vitro* methods. Proliferation, cell cycle dynamics, migration capacity and microtissue generation of the sEV recipient cells were investigated by Ki-67 immunocytochemistry, Cell-Clock cell cycle assay, wound healing assay and hanging drop technology, respectively.

Ag-TiO_2 sEVs facilitate proliferation of mesenchymal stem cells. As an important element of the TME, the MSCs can be targeted by the tumour-derived extracellular vesicles. Therefore, we investigated the effects of the different sEVs on stem cells. First, the *in silico* analyses predicted activation of Ki-67 expression for the Ctrl, Hs and Ag-TiO_2 sEVs, and activation of 'Proliferation of stem cells' for each sEV group. These predictions suggest that after internalisation by stem cells, each of the investigated sEV groups may induce cell divisions and three of them could result in Ki-67 upregulation, if the delivered vesicular cargo is active in the recipient cells (Fig. 5a). According to the IPA analyses, the key B16F1 vesicular regulator of the Ki-67 expression may be the aldo-keto reductase family 1 member B1 (AKR1B1), which is known to be involved in glucose metabolism, osmoregulation, detoxication of lipid aldehydes[59], oxidative stress signalling, activation of NF-κB and expression of adhesion molecules, such as ICAM or VCAM. It has recently been shown that inhibition of AKR1B1 prevented proliferation and expression of Ki-67 in the human umbilical vein endothelial cells (HUVEC)[60]. The IPA-predicted activation of 'Proliferation of stem cells' might be enhanced for instance by fibronectin (FN1)[61], which was previously described by Sharma *et al.* to increase the growth of embryonic stem cells[61] (Fig. 5a).

To test the differences in the Ki-67 regulation across sEV groups, we treated MSC cultures with 200 µg/ml sEV suspensions or PBS buffer as a negative control. After 24 h or 72 h of vesicle exposures, the Ki-67 expression was investigated by immunocytochemistry. For the quantitative evaluation of the experiment, the Operetta high-content imaging system and an image analysis and machine learning software (SCT Analyzer 1.0)[62] was applied, which enabled to analyse almost 1.6×10^5 cells within a few hours. Our computer-assisted image analysis pipeline was comprised of cell segmentation, feature extraction and machine learning modules, where we had a training set with two classes for the Ki-67 positive and the negative cells. Compared to the negative control group, Ag-TiO_2 sEVs significantly increased the proportion of Ki-67 positive cells after 72 h ($p = 0.03572$, $n = 4$; Fig. 5b,c).

Proliferation of MSCs was also tested by direct cell counting, where all of the cells in the sEV-exposed cell cultures were counted using DAPI staining, imaging and machine learning. Results showed increased proliferation of cells upon exposure to Hs and Ag-TiO_2 sEVs as early as 24 h, but different sEVs each had a distinct influence on this cell function (Fig. 5d).

Our *in vitro* results suggest that melanoma sEVs released under different microenvironmental conditions may have distinct effect on stem cell proliferation. However, beside the IPA predicted interactions, additional molecules and factors, such as the encapsulated doxorubicin, may also be involved in this process.

Previously, tumour exosomes derived from melanoma cells[17], osteosarcoma cells[63] or breast cancer cells[64] have been shown to re-educate MSCs and provide them tumour-promoting properties. The tumour-educated stem cells may go through an oncogenic reprogramming resulting in increased proliferation capacity *in vitro*, and tumour growth- and metastasis progression-supporting effects *in vivo*. Here, we also observed an increase in the proliferation and Ki-67 expression upon the normal (Ctrl) sEV exposure. However, our results suggest that the stem cell re-education capacity of vesicles strongly depends on the microenvironmental conditions of the releasing tumour cells.

Doxo and Ctrl sEVs affect the cell cycle of melanoma cells. IPA analyses predicted inhibition of 'G1 phase of tumour cell lines' and 'G1/S phase transition of tumour cell lines' upon exposure to Ctrl, Doxo and Hs sEVs (Fig. 6a). In other words, the molecular content of these vesicles may cause an arrest in the G1 phase in recipient tumour cells. As displayed on Fig. 6a, IPA found a total of 15 sEV molecules in our B16F1 data, which may influence the G1 phase of tumour cell lines. Hypothetically, the key player of their inhibitory effect may be the aspartyl-tRNA synthetase (DARS). In 1999, Yamashita *et al.*[65] investigated T24 bladder carcinoma cells and showed that DARS causes a retinoblastoma-independent downregulation of cyclin A, which is required for S phase entry[65]. Another component of the B16F1 vesicles, the p53 inducible miR-34a may lead to apoptosis and cell cycle arrest in the G1 phase, thereby suppressing tumour cell proliferation[66]. Ji *et al.*[67] showed that restoration of miR-34 expression in pancreatic cancer cells inhibited cell growth and invasion, induced apoptosis, arrested cell cycle in G1 and G2/M phases and sensitized the cells to chemotherapy and radiation[67].

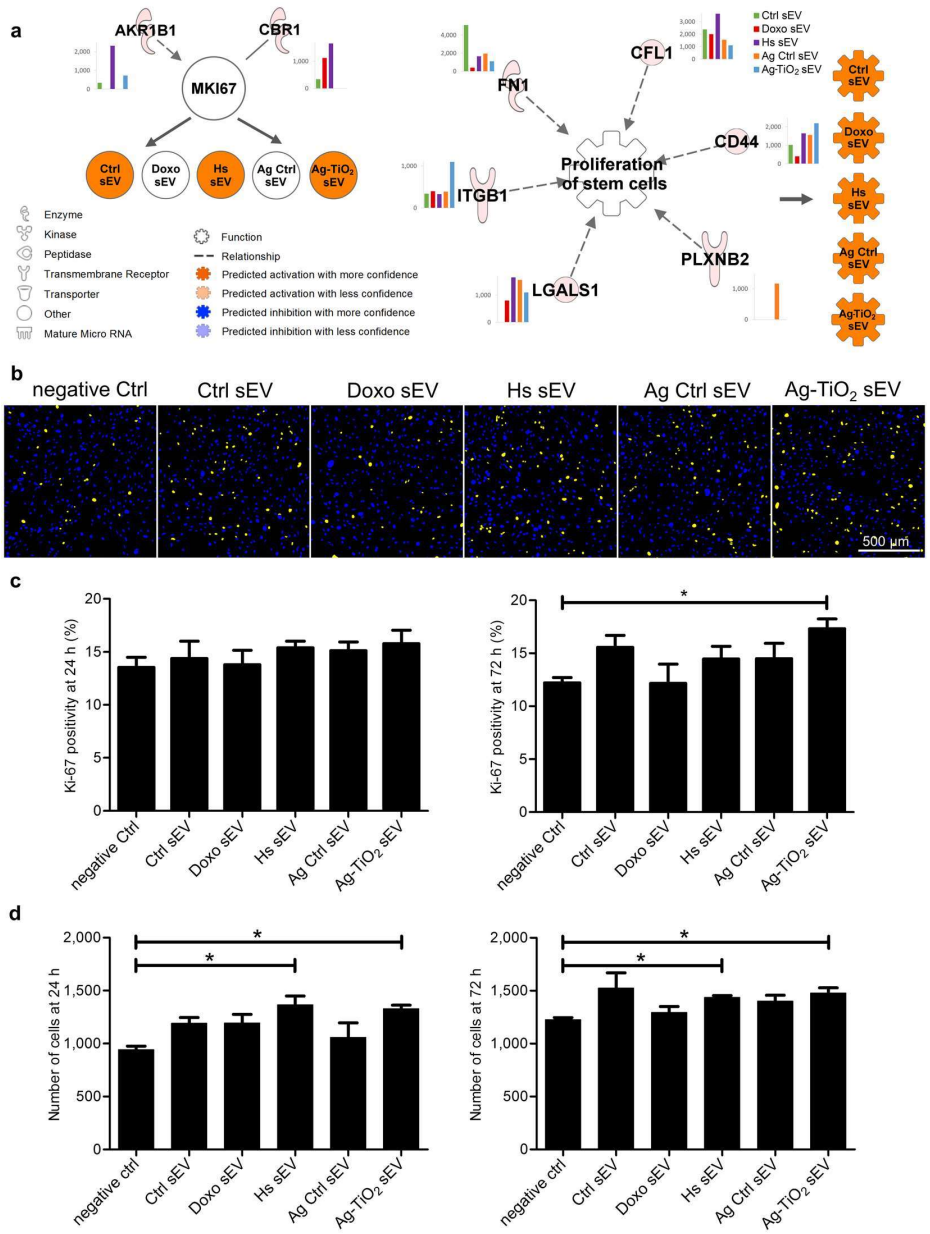

Figure 5. Stress-exposed melanoma cell-derived vesicles affected the proliferation of MSCs. (**a**) IPA predictions for the regulatory effects of sEV molecules on Ki-67 expression and 'Proliferation of stem cells'. Networks show every upstream regulator proteins accompanied by a bar graph, which represents the normalised expression values of the molecule for each sEV group. Coloured symbols, named as the sEV groups, display the expected regulation changes of the analysed 'Molecule' and 'Biofunction' upon exposure to the vesicles. (**b**,**c**) Evaluation of the Ki-67-specific immunocytochemistry using an image analysis and machine learning software. (**b**) Images are representatives of the classified ones. Yellow and blue dots show the Ki-67 positive and negative nuclei, respectively. (**c**) Bar graphs show percentages of the Ki-67 positive cells 24 h (left panel) and 72 h (right panel) after sEV exposures. Each bar represents mean + SD (n = 4). (**d**) Cell numbers of the sEV-exposed cells after 24 h and 72 h incubation time. Bar graphs represent mean + SD values (n = 3), *$p < 0.05$ indicates statistical significance.

To test the *in silico* predicted effects of sEVs on tumour cell cycle, we performed a Cell-Clock cell cycle assay on B16F1 melanoma cells exposed to sEVs for 24 h, 48 h and 72 h along with a PBS-treated negative control group. This assay utilizes a vital redox dye that changes colour based on the cell cycle phase. It becomes yellow in G1,

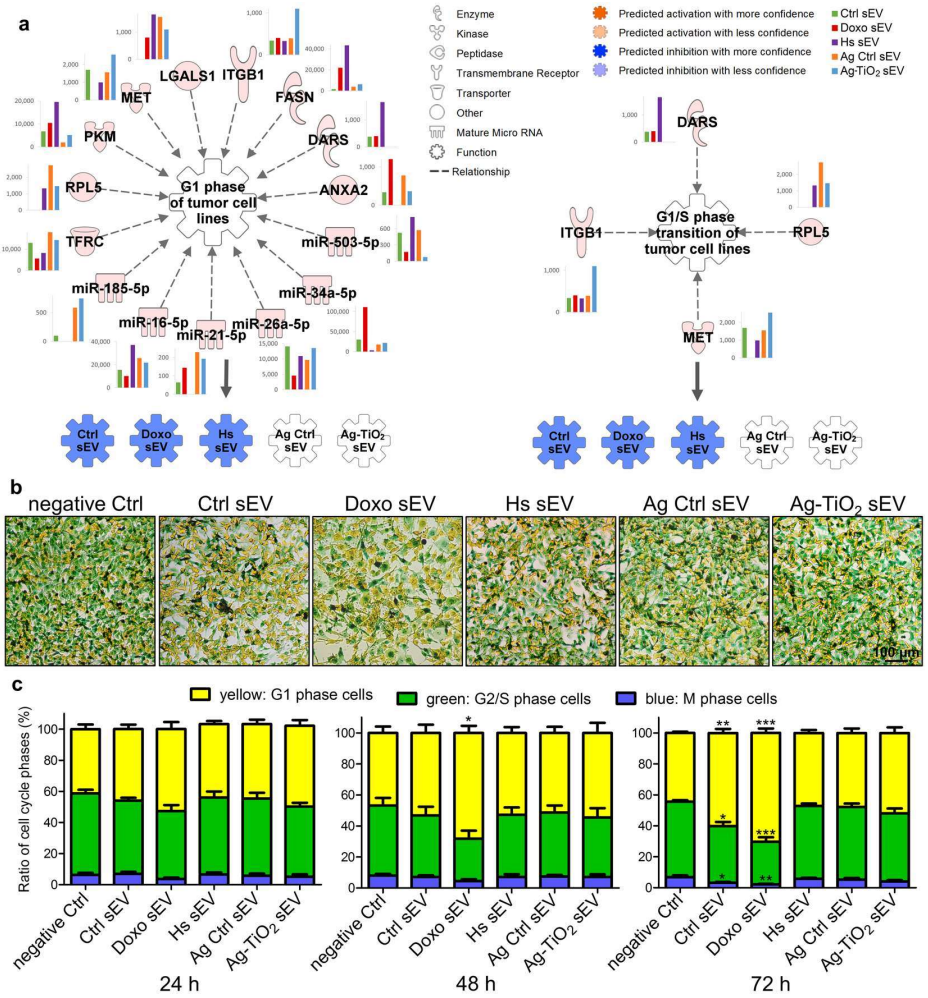

Figure 6. Ctrl and Doxo sEVs caused an arrest in G1 phase of melanoma cells. (**a**) IPA predictions for the regulatory effects of sEV molecules on the 'G1 phase of tumour cell lines' and 'G1/S phase transition of tumour cell lines'. Networks show every upstream regulator proteins and miRNAs accompanied by a bar graph, which represents the normalised expression values of the molecule for each sEV group. Coloured symbols, named as the sEV groups, display the expected regulation changes of the analysed 'Biofunctions' upon exposure to the vesicles. (**b**,**c**) Cell-Clock cell cycle assay of sEV-exposed B16F1 cell cultures. (**b**) Representative images of the cell clock dye-labelled cultures. (**c**) Distribution of the yellow, green and blue cells in the cell cultures, which labels the G1, G2/S and M phase cells, respectively. Each bar represents mean + SD ($n = 4$), *$p < 0.05$, **$p < 0.01$ and ***$p < 0.001$ indicate statistical significance.

green in S/G2 and blue in M phase. In the negative Ctrl group, cells were present in the G1, S/G2, and M phases in average proportions of $44.84 \pm 2.68\%$, $47.80 \pm 3.34\%$ and $7.35 \pm 0.81\%$, respectively ($n = 12$). Ctrl and Doxo sEVs led to an increase in the proportion of the yellow, *i.e.* G1 phase, cells in a time dependent manner. After 72 h, these cells represented $59.20 \pm 4.06\%$ of the Ctrl sEV-exposed cultures ($p = 0.00346$, $n = 4$) and $70.32 \pm 7.24\%$ of Doxo sEV-exposed cultures ($p = 4.28 \times 10^{-6}$, $n = 4$) (Fig. 6b,c). These results confirmed the IPA predicted arrest in G1 phase by the Ctrl and Doxo, but not by the Hs sEVs.

It has been previously demonstrated that tumour cells can efflux drugs through exosome secretion[43,68]. Yang *et al.* showed that doxorubicin-treated MCF-7 breast carcinoma cells produced drug-containing exosomes. Doxorubicin that was encapsulated in the MCF-7 exosomes had more potent cytotoxicity against the parental MCF-7 cells than the free drug[43]. Furthermore, doxorubicin arrest the cell cycle of tumour cells at G1/S and G2/M checkpoints[69,70]. Based on these literature data and our fluorescence spectroscopy measurements, we hypothesize that encapsulated doxorubicin might contribute to the enhanced cell cycle arrest effect of Doxo sEVs.

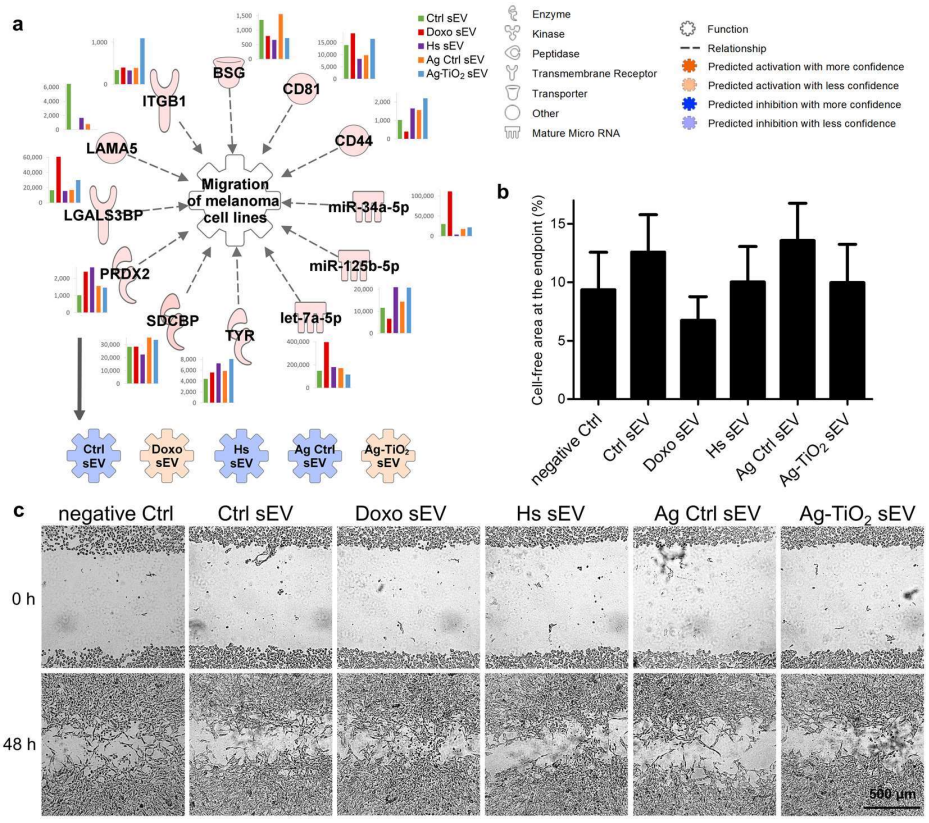

Figure 7. Doxo sEVs enhanced the migration of melanoma cells. (**a**) IPA predictions for the regulatory effects of sEV molecules on the 'Migration of melanoma cell lines'. Network shows every upstream regulator proteins and miRNAs accompanied by a bar graph, which represents the normalised expression values of the molecule for each sEV group. Coloured symbols, named as the sEV groups, display the expected regulation changes of the analysed 'Biofunction' upon exposure to the vesicles. (**b**,**c**) Wound healing assay of sEV-exposed B16F1 cell cultures. (**b**) The bar graph shows the result of the analysis of wound closures by the ImageJ wound healing tool. It represents mean + SD values (n = 8). (**c**) Representative images of the wounds after 48 h of sEV exposures.

Migration capacity of melanoma cells is differently altered by the sEVs. From many cell movement-related 'Biofunctions', which were predicted to be targeted by sEVs (Fig. 4d–f), we chose the 'Migration of melanoma cell lines' for further IPA and *in vitro* investigations. The *in silico* analyses showed varying sEV effects. More specifically, Doxo and Ag-TiO_2 sEVs are predicted to facilitate the melanoma cell migration, while the three other ones may inhibit this function (Fig. 7a). According to the IPA analyses, negative B16F1 sEV regulators may include the laminin subunit alpha-5 (LAMA5), peroxiredoxin-2 (PRDX2), tyrosinase (TYR), let-7a-5p, miR-125b-5p and the miR-34a-5p. Listed positive regulators include the CD44 antigen (CD44), CD81 antigen (CD81), basigin (BSG), integrin beta-1 (ITGB1) and the galectin-3-binding protein (LGALS3BP) (Fig. 7a). Using attachment and pulmonary metastases assays, Hibino *et al.*[71] identified four peptides of LAMA5, which showed activity *in vitro* and also *in vivo*. These peptides reduced migration and invasion of B16F10 melanoma cells[71]. Lee *et al.*[72] showed that the PRDX2 enzyme is a selective antioxidant suppressor for proliferation and migration of melanoma cell lines (SK-MEL-5, SK-MEL-28, A375, G361, B16F10)[72]. Stampolidis *et al.* demonstrated that LGALS3BP promotes cell viability and facilitates cell motility of the human C8161 melanoma cell line[73].

Using wound healing assay, we investigated the effect of sEVs on migration of B16F1 cells, which approximated to the IPA predicted tendency. Migration of cells into the wounded area was slightly decreased in the presence of Ctrl and Ag Ctrl sEVs, compared to migration of the negative Ctrl cells. Acceleration of wound closure was observed in response to Doxo sEVs (n = 8). However, Hs and Ag-TiO_2 sEVs had no effect on tumour cell migration (Fig. 7b,c).

The importance of migration capacity in tumour progression is unquestionable, since the process of tumour cell invasion and metastasis is conventionally understood as the migration of individual cells, which detach from the primary tumour, enter lymphatic vessels or the bloodstream and seed in distant organs[74]. This cancer cell migration is typically regulated by integrins, matrix-degrading enzymes, cell-cell adhesion molecules and cell-cell communication[74]. Direct and indirect effects of stress-elicited sEVs on tumour cell migration and metastasis

have been demonstrated in some studies[27,47,75]. Here, we amended literature data by showing that the cytostatic stress-exposed cell-derived sEVs enhance the migration of the recipient melanoma cells. This can be interpreted as an adaptive escape mechanism: Doxo sEVs, delivering a warning message, induce the migration of the neighbouring melanoma cells. In a recent study[27], breast cancer cells also showed an sEV-mediated escape mechanism under doxorubicin and paclitaxel exposures, by releasing pro-metastatic exosomes[27].

Each sEV group enhances the migration of endothelial cells. IPA predicted the activation of 'Cell migration of endothelial cells' and 'Cell spreading of endothelial cells' upon exposure to each sEV group labelling a large number of potentially contributing sEV molecules (Supplementary Fig. S5). Therefore, we repeated the wound healing assays on bEnd.3 mouse endothelial cells, where we could verify the IPA predictions. However, Ctrl sEVs showed the highest migration enhancing effect (Supplementary Fig. S5).

Endothelial cell migration is an essential component of angiogenesis, which is a key process of tumour progression[76]. These results demonstrate that some type of stress conditions may slightly decrease the endothelial cell migration promoting effects of sEVs. At the same time, they highlight that sEVs may have target cell-specific functional effects in the recipients, which further increases the diversity of the sEV-mediated communication of melanoma cells.

Microtissue generation is facilitated independently of the sEV groups. IPA predicted that each of the five sEV groups may activate many 'Biofunctions' related to the formation of a 3D cell interaction matrix, *e.g.* 'Aggregation of cells', 'Formation of ECM' (Fig. 8a), 'Cell-cell contact' or 'Interaction of tumour cell lines' (Supplementary Fig. S6). The intensity of these activations is variable between sEV groups, for example activation of the 'Aggregation of cells' is predicted to be the strongest upon Doxo and Hs sEV exposures. *In silico* analyses revealed a large number of contributing B16F1 sEV molecules. For instance, it is worth to mention the programmed cell death 6-interacting protein (PDCD6IP, Alix). It has an important role not only in the exosome biogenesis[52], but Pan *et al.*[77], who investigated fibroblast morphology, demonstrated that a sub-population of Alix localises extracellularly and regulates integrin-mediated cell adhesions and fibronectin matrix assembly[77].

In order to mimic *in vivo* conditions, we established a simplified 3D tumour matrix model co-culturing MSCs and B16F1 cells in hanging drop plates. By definition, multicellular cell aggregates, which produce their own ECM and are comprised of more than one cell types are termed as microtissues[78]. Applying an equal number of the two cell types (a total of 5,000 cells/well), microtissue generation was followed under sEV exposures and PBS treatment as a negative control for 72 h. The created microtissues were photographed and analysed by the AnaSP software developed for automatic image analysis of multicellular spheroids[79]. Each group of sEVs resulted in smaller and more compact microtissues, since the average values of the measured area, perimeter, diameter and volume was lower, compared to the negative Ctrl samples (Fig. 8b–d). These results were validated using mouse embryonic fibroblasts (MEFs) co-cultured with B16F1 cells, where each sEV group facilitated the microtissue generation, except the Hs sEVs (Supplementary Fig. S7).

In videomicroscopy studies, Crawford *et al.*[80] observed that microvesicles attaching to the cell membranes promoted cell-to-cell interactions and spheroid formation of glioblastoma, breast carcinoma and osteosarcoma cells. They also showed that elevated extracellular Ca^{2+} levels promote microvesicle production and result in smaller and less dense spheroids, which might seem paradoxical. However, they interpreted their results as a pathophysiological adaptation, since increasing spheroid surface to volume ratio, thereby increasing the surface area enhances the uptake of oxygen, growth factors and nutrients by tumour cells that make up the spheroid mass[80]. In our experimental setup, sEV exposures resulted in smaller microtissues from the same number of cells suggesting the generation of more compact structures, which may be explained by the role of vesicles in generation of cell-cell associations, and may also indicate an adaptation mechanism.

Tumours exist in a 3D microenvironment, in which morphological and functional properties, such as the ECM, cell-cell interactions, oxygen gradient and acid gradient create transport barriers for drug delivery[81]. In this study, Doxo sEV exposure resulted in the most compact structures, which may reduce penetration of drugs. Previously, tumour-derived extracellular vesicles have been shown to transfer drug resistance into other tumour cells[82,83] suggesting that the Doxo sEVs might convey protective messages resulting in more compact microtissues.

Conclusions

In this study, we compared different inducible cellular stress conditions, and we found that cytostatic, heat and oxidative stresses resulted in changes in the vesicular cargo composition, leading to distinct functional alterations of the melanoma-derived sEVs in the TME recipient cells.

We showed that sEVs, being complex information packages may participate in a wide range of signalling pathways. The fact that a vesicular molecular pattern with a large number of molecules can influence the activation of the cellular homeostasis network at several points, suggests a huge diversity of sEV functions, which sometimes seem to be paradoxical in the *in vitro* experiments. In conclusion, hundreds of vesicular molecules may have thousands of functional effects in the recipient cells leading to an unconceivable outcome. Here, we successfully predicted the functional effects of the investigated sEV molecular patterns – induced by five treatment conditions – by bioinformatics analyses using unique combinations of the IPA approaches. Based on our knowledge, our experimental setup was suitable to model the transfer and functional activity of the vesicular cargo in the recipient cells. Here, we demonstrated, that pathway analyses may provide a good approximation to the prediction of different inducible stress-elicited responses, suggesting that *in silico* analyses may be useful tools not only in the field of research, but in a therapeutic approach as well.

Our paper not only provides a detailed characterisation of the doxorubicin-, heat- and Ag-TiO_2-induced molecular patterns of melanoma-derived sEVs and the resulted response patterns in the recipient cells, it also increases our knowledge about the molecular and functional complexity as well as condition-dependent variability

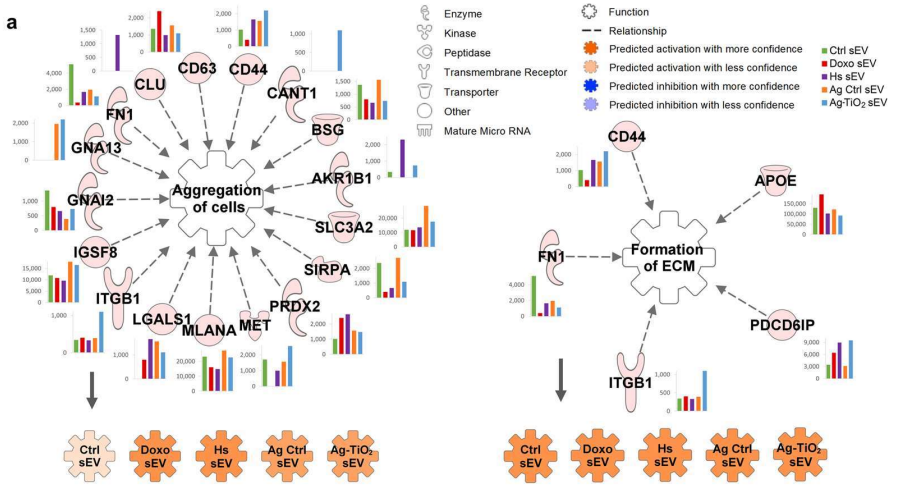

b

Group name	negative Ctrl	Ctrl sEV	Doxo sEV	Hs sEV	Ag Ctrl sEV	Ag-TiO_2 sEV
Eq. diameter (µm)	445 ±3	315 ±7	244 ±3	351 ±11	371 ±5	338 ±7
Major diameter (µm)	521 ±21	370 ±7	275 ±15	430 ±31	440 ±7	393 ±3
Minor diameter (µm)	307 ±56	221 ±16	204 ±14	242 ±61	287 ±20	254 ±8
Convexity	0.801 ±0.033	0.799 ±0.015	0.911 ±0.024	0.808 ±0.035	0.779 ±0.013	0.759 ±0.053
Solidity	0.885 ±0.022	0.849 ±0.014	0.942 ±0.019	0.867 ±0.03	0.859 ±0.019	0.839 ±0.061
Sphericity	0.731 ±0.044	0.701 ±0.011	0.865 ±0.038	0.727 ±0.052	0.694 ±0.020	0.667 ±0.061

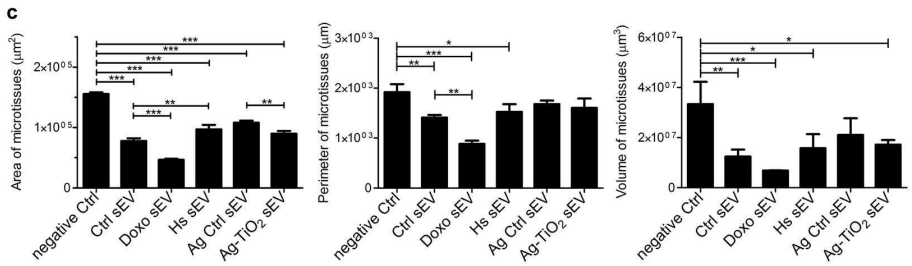

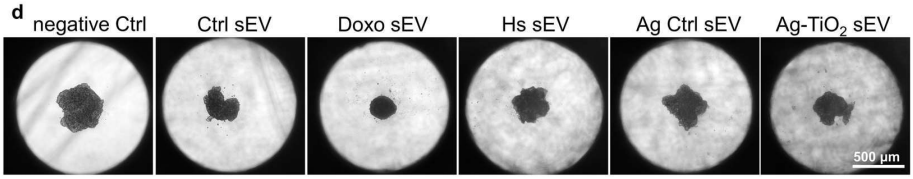

Figure 8. All sEV groups facilitated microtissue generation. (**a**) IPA predictions for the regulatory effects of sEV molecules on the 'Aggregation of cells' and the 'Formation of extracellular matrix'. Networks show every upstream regulator proteins and miRNAs accompanied by a bar graph, which represents the normalised expression values of the molecule for each sEV group. Coloured symbols, named as the sEV groups, display the expected regulation changes of the analysed 'Biofunctions' upon exposure to the vesicles. (**b**,**c**) Descriptive statistics of the 72 h B16F1-MSC microtissues resulted from image analysis using the AnaSP software. Eq. diameter means equivalent diameter, major and minor diameters are measured through centroid. Table contains mean ± SD values. Bar graphs show the area, perimeter and volume statistics of the generated microtissues (mean + SD, n = 3). Statistical evaluation was performed by Welch's ANOVA test with Tukey's HSD post-hoc test; *$p < 0.05$, **$p < 0.01$ and ***$p < 0.001$ indicate statistical significance. (d) Representative images of the generated microtissues after 72 h of sEV exposures.

of the melanoma-derived sEVs. This study contributes to a better understanding of the pathogenesis and therapeutic responses of melanoma. It also highlights that indirect effects of any therapy, such as a chemotherapy, may have a great influence on the intercellular communication of the affected cells.

Based on this study, we conclude that the molecular pattern of these highly protected information packages is dictated by the microenvironmental conditions, including the therapeutic stress factors. The altered cargo of sEVs is able to not only enhance or suppress existing signalisation pathways, but even trigger *de novo* pathway activations, resulting a unique target cell-specific response pattern in the sEV recipient cells. Recent literature data[24,25,27,47] along with this study suggest that alteration of this complex sEV-mediated intercellular communication of tumour cells deserves special attention among the therapy-induced host responses, which may have a potential influence on the treatment efficacy.

Methods

Cell cultures. B16F1 (ECACC 92101203) mouse melanoma cell line was obtained from ECACC and cultured in DMEM supplemented by 10% FBS (EuroClone), 2 mM L-glutamine and 1% Penicillin-Streptomycin-Amphotericin B mixture (P/S/A; all from Lonza); mouse embryonic fibroblasts (MEFs; ATCC SCRC-1040) were obtained from ATCC and cultured in DMEM supplemented by 15% FBS and 1% P/S/A; bEnd.3 mouse endothelial cell line (ATCC CRL-2299) was obtained from ATCC and cultured in DMEM supplemented by 10% FBS and 1% P/S/A. Primary mouse mesenchymal stem cells (MSCs) were isolated from adipose tissue of 6-8 week old male C57BL/6N mice (Charles River Laboratories) and cultured using the MesenCult Expansion Kit (STEMCELL Technologies). All cell cultures were maintained in a humidified incubator at 37°C and 5% CO_2. Purity of MSC cultures was checked by flow cytometry using the Mouse Multipotent Mesenchymal Stromal Cell Marker Antibody Panel (R&D Systems) according to the manufacturer's instructions and a FACSCalibur instrument coupled with CellQuest Pro 6.0 (BD Biosciences). Animal experiments were performed in accordance with the national and European animal ethics guidelines. The animal experimental protocols were approved by the Animal Experimentation and Ethics Committee of the Biological Research Centre of the Hungarian Academy of Sciences and the Hungarian National Animal Experimentation and Ethics Board (clearance number: XVI./78/2018).

Ag-TiO_2 photocatalyst particles. Synthesis of Ag-TiO_2 nanoparticles was performed as published earlier[31,35]. Briefly, the silver particles were strongly attached on the surface of metal oxide by photodeposition. A commercially available TiO_2 (Degussa P25, Evonik Gmbh) with a specific surface area of ~50 m^2/g was used for this purpose. The prepared Ag-TiO_2 photocatalyst contained 0.5 wt% surface silver nanoparticles. Dispersion of particles was made in PBS at a concentration of 10 mg/ml and sonicated for 30 min directly before use.

Stress conditions. B16F1 cell cultures were treated at 70% confluency in five different ways in EV-depleted FBS-containing media for 72 h (Table 1). The Control 1 group received only fresh medium. Cytostatic stressed cells were treated with 0.6 μM doxorubicin, heat stressed cells were incubated at 42°C for 2 h in every 24 h (a total of 3 times), oxidative stressed cells were treated with light-induced 2.5 μg/ml Ag-TiO_2. In detail, the photoreactive Ag-TiO_2 nanoparticles were induced by a low-pressure mercury lamp ($\lambda \geq 360$ nm, GCL303T5/4 type, LightTech) for 60 min from 3 cm distance in a 75% medium volume to avoid the light absorption and reflection of the medium layer. After the illumination, the medium was adjusted to the final volume. To eliminate the effect of illumination itself, we established another control group, which received medium illuminated in the same way as described above. Parameters of the cytostatic and oxidative stresses were based on previous optimization by proliferation assay. Heat stress conditions were adapted from literature data[34]. In each group, 72 h supernatants of 6 parallel cell cultures were harvested, pooled and subjected to sEV isolation.

Scanning electron microscopy (SEM). B16F1 cells seeded to poly-L-lysine-coated 5 mm cover glasses were treated as described above. After 24 h incubation, cells were washed with PBS and fixed for overnight in 2.5% glutaraldehyde and 0.05 M cacodylate buffer diluted in PBS (pH 7.2). Then, cells were washed with PBS, dehydrated with a graded ethanol series (30%, 50%, 70%, 80% EtOH, each for 1 h and 100% EtOH, for 3 × 1 h) and dried with a critical point dryer (Quorum Technologies Ltd, K850). Cover glasses were mounted onto microscope stubs using carbon tape, followed by 15 nm gold coating (Quorum Technologies Ltd, Q150) and observed under a field-emission scanning electron microscope (JEOL Ltd, JSM-7100F/LV). Images were taken in 1,500 × and 20,000 × magnification.

sEV isolation and characterisation. Vesicles were isolated by differential filtration and ultracentrifugation. Briefly, 72 h supernatants from the stress-exposed B16F1 cultures were centrifuged at 780 g for 5 min, and at 3,900 g for 15 min at 4°C, then filtered by a 0.2 μm membrane to remove cells, debris and larger vesicles. Small EVs were pelleted by ultracentrifugation at 150,000 g for 60 min at 4°C using a T-1270 fixed-angle rotor and a WX + ultracentrifuge (Sorvall). The pellet was washed twice and resuspended in PBS. Protein concentrations of sEV isolates were measured by the Pierce BCA Protein assay kit (Thermo Scientific) on a benchtop microplate reader (Multiskan RC, Thermo Labsystems) coupled with the Ascent Software 2.6. Small EVs were characterised by atomic force microscopy as described previously[44], dynamic light scattering using a Zetasizer Nano S instrument (Malvern Panalytical Ltd) and Western blot analysis (described in the Supplementary Methods). Quantification of sEVs was performed by nanoparticle tracking analysis using a NanoSight NS500 instrument (Malvern Panalytical Ltd).

Fluorescence spectroscopy. The emission and excitation spectra of doxorubicin were measured by a FluoroLog-3 spectrofluorometer (Horiba Ltd). The maximum wavelengths for excitation ($\lambda_{ex} = 492$ nm) and emission ($\lambda_{em} = 592$ nm) were then used for measuring the fluorescence intensity of Doxo sEVs and Ctrl sEVs as a background. A calibration curve of doxorubicin covering a concentration range of 0-1,000 nM was applied to determine the encapsulated doxorubicin concentration of the sEV samples.

Dynamic light scattering (DLS) measurements of Ag-TiO_2 particles. The particle size values of the Ag-TiO_2 photocatalyst particles were determined DLS with a Zetasizer Nano ZS ZEN 4003 apparatus (Malvern Panalytical Ltd) equipped with a He-Ne laser ($\lambda = 633$ nm). The measurements were performed in B16F1 culture medium for a 72 h time interval. Size distribution measurements were carried out in triplicate, and mean ± SD values are reported.

Chemiluminescence detection of Ag-TiO_2 nanoparticles. Isolated Ag Ctrl and Ag-TiO_2 sEVs were lysed by TENT buffer and freeze-thaw cycle, then a 10-fold, 5-step Ag-TiO_2 nanoparticle dilution series (0–2.5 µg/ml) was prepared in Ag Ctrl sEV suspension for calibration. Protein concentration of sEV lysates was 200 µg/ml. After 30 min illumination on 96-well plates, 50 µl 3.38 mM luminol solution was added to 50 µl of samples and light emission was immediately detected by a Luminoskan Ascent Microplate Luminometer (Thermo Scientific). Each sample was measured in triplicates.

Transmission electron microscopy (TEM). The morphology of Ag-TiO_2 sEVs and Ag-TiO_2 sEVs mixed with Ag-TiO_2 nanoparticles was examined using a Tecnai G2 20 × -Twin type instrument (FEI), operating at an acceleration voltage of 200 kV. For TEM measurements the samples were dropped on a grid (carbon film with 200 Mesh coper grids; CF200-Cu, Electron Microscopy Sciences) and dried.

miRNA analysis of sEVs. Pellets of sEVs were subjected to miRNA isolation using the NucleoSpin miRNA isolation kit (Macherey-Nagel) according to the manufacturer's instructions. Sequencing was performed using SOLiD Total RNA-Seq lit for Small RNA Libraries (Applied Biosystems) based on the manufacturer's protocol. Purification was performed on 10% TBE-Urea gels stained with Sybr Gold nucleic acid gel stain (both from Invitrogen). Final purification was performed using PureLink PCR Micro Kit (Invitrogen). Final libraries were quality checked using High Sensitivity DNA kit on Bioanalyzer (Agilent Technologies). Concentration of the libraries was determined by the SOLiD Library TaqMan Quantitation Kit (Life Technologies). Each library was clonally amplified on SOLiD P1 DNA Beads by emulsion PCR (ePCR). Emulsions were broken using butanol, and ePCR beads were enriched for template-positive beads by hybridization with magnetic enrichment beads. Template-enriched beads were extended at the 3' end in the presence of terminal transferase and 3' bead linker. Beads with the clonally amplified DNA were deposited onto SOLiD sequencing slide and sequenced on SOLiD 5500xl instrument using the 50-base sequencing chemistry.

Bioinformatics analysis of raw data, quality assessment, read trimming, read mapping and miRNA expression profiling was carried out in CLC Genomics Workbench 8.0.2 (Qiagen Bioinformatics) using annotated *Mus musculus* miRNA sequences according to the miRBase release 21 as a mapping reference. Only miRNAs with ≥10 read counts were accepted.

Results of sequencing were validated by qPCR on 3 selected miRNAs, mmu-miR-16-5p, mmu-miR-125b-5p, mmu-miR-29a-3p. Intact total RNA – including miRNA – were prepared from sEV isolates by miRNA Miniprep System (Promega) according to the manufacturer's instructions. Then, 70 ng of each sample were reverse transcribed using microRNA cDNA synthesis kit (Sigma-Aldrich). The qPCR reactions were performed on PikoReal Real-Time PCR System (Thermo Scientific) using SYBR Green chemistry and commercially available miRNA specific primers (Sigma-Aldrich). Cq values of each miRNA were normalized by U6 endogenous controls in all samples and expression levels were calculated using -ddCt method.

Proteome analysis of sEVs. Detailed LC-MS/MS analysis of sEVs is described in the Supplementary Methods. Briefly, 25 µg of vesicular proteins were separated by SDS-PAGE and stained with Coomassie blue. Then, each lane was cut to 12 equal bands and subjected to an in-gel trypsinisation procedure. The extracted peptides were analysed on an LTQ-Orbitrap Elite (Thermo Scientific) mass spectrometer on-line coupled with a nanoHPLC (nanoAcquity, Waters) system. Searchable peaklists were extracted using Proteome Discoverer 1.4 (Thermo Scientific) and subjected to database search on our in-house Protein Prospector 5.14.1 search engine against the *Mus musculus* and *Bos taurus* protein sequences of the Uniprot (UniProtKB.06.11.2014) database completed with human keratins and pig trypsin, altogether 106,330 protein sequences were searched. Protein identification was accepted if the protein was identified with ≥3 unique peptides, but peptides with identical bovine and mouse sequence were excluded. FDR values were less than 1% in all cases. Results were validated by Western blot (described in the Supplementary Methods).

Bioinformatics analysis. Normalised miRNA and protein data derived from the LC-MS/MS and SOLiD sequencing were analysed by the Ingenuity Pathway Analysis (IPA, Qiagen Bioinformatics). First, we used the 'Core Analysis' feature to reveal functional differences between the five sEV groups, where 'Top 5 canonical pathways' and 'Top 5 molecular and cellular functions' (Fig. 4a,b) were obtained. Secondly, using the 'Comparison Analysis' feature, we created a heatmap containing 'Biofunctions', which had relevance in melanoma and >5 -log(p-value). This heatmap was divided into four parts based on biological relevance; intracellular, cellular, systemic and immune processes are displayed in separated panels (Fig. 4c–f). Thirdly, some 'Biofunctions' were chosen for further investigation to reveal the regulatory effects of sEVs on them. Using the 'Grow tool', the upstream interacting vesicular molecules were identified for the selected 'Biofunctions' for each sEV group. Then, using the 'Molecule Activity Predictor' (MAP) tool, we could reveal the activation or inhibitory effects of each sEV group for each 'Biofunction' (Figs. 5–8a). Through these *in silico* analysis, we could model the effects of the different sEVs in the recipient cells in spite of their molecular complexity. Figures were edited in the IPA 'Path Designer' and completed with Excel diagrams. For all IPA analyses, the confidence level was set to 'Experimentally observed' enabling literature data-based analysis, but not unproven predictions.

Exposures of MSCs and B16F1 cells to the sEVs. To avoid additional effects of changing conditions, cells were exposed to sEVs in their standard, complete media before each of the following functional assays. Briefly, cells were treated with 200 µg/ml sEV suspensions, or PBS as a negative control for 24 h, 48 h or 72 h. For longer incubation times, treatments were repeated in every 24 h.

Ki-67 expression analysis of MSCs. MSCs exposed to sEVs for 24 h and 72 h were fixed in 4% paraformaldehyde for 10 min at room temperature (RT) for immunocytochemistry. Then, cells were permeabilised with 0.1% Triton X-100 and non-specific antibody binding was blocked with 5% BSA. We applied direct labelling using anti-mouse/rat Ki-67 monoclonal antibody conjugated to eFluor 615 dye (1:400, eBioScience) in 1.2% BSA overnight at 4°C. Nuclear counterstaining was performed with DAPI for 15 min at RT. Cells were washed 3 times with PBS for 5 min between each step. Finally, the cells were covered by Fluoromount-G (SouthernBiotech) and cover glasses. Fluorescent images were taken by the Operetta high content screening system (PerkinElmer) and analysed by an image analysis and machine learning software (SCT Analyzer 1.0) developed by the Single-Cell Technologies Ltd[62]. Our pipeline was comprised of cell segmentation, feature extraction and machine learning modules. K-means algorithm was used for the nuclei segmentation based on the DAPI signal, then we extracted the eFluor 615 signal-related features, *i.e.* max intensity, min intensity, mean intensity, median intensity, SD intensity for the generated nuclei masks. We established a training set with two classes for the Ki-67 positive and the negative cells. This training set, containing 100 objects in both classes was validated by the implemented k-fold cross-validation. For machine learning, we used the Multi-Layer Perceptron (MLP) method. The Ki-67 expression analysis was repeated 4 times and the applied methods enabled to analyse a total of 159,596 cells.

Cell counting. MSC cultures in 384-well plates were exposed to sEVs for 24 h and 72 h, then fixed in 4% paraformaldehyde for 10 min at RT and stained with 1 µg/ml DAPI for 15 min at RT. Images were acquired from whole wells using a TCS SP8 microscope (Leica Microsystems) in fluorescent mode, followed by an analysis using the SCT Analyzer 1.0 machine learning software. The experiment was repeated 3 times.

Cell cycle analysis. Changes in the cell cycle dynamics of sEV-exposed B16F1 cells were analysed using the Cell-Clock cell cycle assay (Biocolor Ltd) according to the assay protocol. This assay can be used to distinguish the four major phases of the mammalian cell cycle using a vital redox dye, which is yellow, green or dark blue in G1, S/G2, and M phase cells, respectively. After staining, cells were photographed using an Axiovert S100 microscope (Zeiss) equipped by a Nikon D5000 camera. Images were analysed by the ImageJ software to determine the percentage of cells in each cell cycle phase. The experiment was performed with 4 repeats.

Wound healing assay. Alterations of the migration capabilities of sEV-exposed B16F1 and bEnd.3 cells were assessed by scratch assay. Nearly confluent monolayers of cells were scratch wounded using a sterile 200 µl pipette tip, washed 3 times with culture media to remove cellular debris, then treated with 200 µg/ml sEV suspensions or PBS in fresh complete media. Wound closure was followed until the cell-free area decreased below 10% in at least 1 sample, when images were taken by an inverted microscope (Zeiss, Axiovert S100) equipped by a Nikon D5000 camera. Grey-scaled images were analysed using the MRI Wound Healing Tool in the ImageJ software. The experiment was repeated 8 times for B16F1 cells, and 4 times for bEnd.3 cells.

Analysis of microtissue generation. Effects of different sEVs on cell-cell contact and cell-ECM interactions was examined on MSC-B16F1 and MEF-B16F1 co-cultures using a simplified 3D tumour matrix model to better represent the *in vivo* conditions, than 2D cultures. Equal number of MSCs or MEFs and B16F1 cells were seeded to 96-well GravityPLUS hanging drop plates (InSphero AG) in sEV- or PBS-containing media (5,000 cell/40 µl/well). Microtissue generation was followed for 72 h and images were acquired in every 24 h using an Axiovert S100 microscope (Zeiss) equipped by a Nikon D5000 camera. To quantify differences in size and shape between the microtissues, 72 h images were grey scaled and analysed by the AnaSP software[79]. Measured parameters of microtissues were the equivalent diameter, major diameter through centroid, minor diameter through centroid, convexity, solidity, sphericity, area, perimeter and volume. The experiments were repeated 3 times.

Statistical analysis. Since the homogeneity of variances assumption of the ANOVA had not met with our data, statistical analyses were performed by the Welch's ANOVA test with Tukey's HSD post-hoc test (Alpha = 0.05) using a Microsoft Excel add-in, the Real Statistics Resource Pack software (Release 5.4). Copyright (2013–2018) Charles Zaiontz (www.real-statistics.com). Diagrams were prepared in GraphPad Prism 5.03. All average values represent mean ± SD and number of asterisk denote minimum statistical significance, *i.e.* *$p < 0.05$, **$p < 0.01$ and ***$p < 0.001$ on figures. Exact p-values are indicated in the text, when it is necessary. Figure 1 was created with BioRender.com.

Data availability

All datasets generated during the current study are available from the corresponding author upon reasonable request.

Received: 26 March 2019; Accepted: 23 September 2019;
Published online: 25 October 2019

References

1. Kotrbová, A. *et al.* TEM Exosome Analyzer: a computer-assisted software tool for quantitative evaluation of extracellular vesicles in transmission electron microscopy images. *J Extracell Vesicles.* **8**, 1560808, https://doi.org/10.1080/20013078.2018.1560808 (2019).
2. Yáñez-Mó, M. *et al.* Biological properties of extracellular vesicles and their physiological functions. *J Extracell Vesicles.* **4**, 27066, https://doi.org/10.3402/jev.v4.27066 (2015).

3. Kolenda, T. *et al.* Tumor microenvironment - Unknown niche with powerful therapeutic potential. *Rep Pract Oncol Radiother.* **23**, 143–153, https://doi.org/10.1016/j.rpor.2018.01.004 (2018).
4. Meehan, K. & Vella, L. J. The contribution of tumour-derived exosomes to the hallmarks of cancer. *Crit Rev Clin Lab Sci.* **53**, 121–131, https://doi.org/10.3109/10408363.2015.1092496 (2016).
5. Javeed, N. & Mukhopadhyay, D. Exosomes and their role in the micro-/macro-environment: a comprehensive review. *J Biomed Res.* **31**, 386–394, https://doi.org/10.7555/JBR.30.20150162 (2017).
6. Tkach, M. & Théry, C. Communication by Extracellular Vesicles: Where We Are and Where We Need to Go. *Cell.* **164**, 1226–1232, https://doi.org/10.1016/j.cell.2016.01.043 (2016).
7. Whiteside, T. L. Tumor-Derived Exosomes and Their Role in Cancer Progression. *Adv Clin Chem.* **74**, 103–141, https://doi.org/10.1016/bs.acc.2015.12.005 (2016).
8. Braeuer, R. R. *et al.* Why is melanoma so metastatic? *Pigment Cell Melanoma Res.* **27**, 19–36, https://doi.org/10.1111/pcmr.12172 (2014).
9. Matsumoto, A. *et al.* Accelerated growth of B16BL6 tumor in mice through efficient uptake of their own exosomes by B16BL6 cells. *Cancer Sci.* **108**, 1803–1810, https://doi.org/10.1111/cas.13310 (2017).
10. Guo, D. *et al.* RAB27A promotes melanoma cell invasion and metastasis via regulation of pro-invasive exosomes. *Int J Cancer.* **144**, 3070–3085, https://doi.org/10.1002/ijc.32064 (2019).
11. Li, J. *et al.* Blockage of transferred exosome-shuttled miR-494 inhibits melanoma growth and metastasis. *J Cell Physiol.* **234**, 15763–15774, https://doi.org/10.1002/jcp.28234 (2019).
12. Isola, A. L., Eddy, K., Zembrzuski, K., Goydos, J. S. & Chen, S. Exosomes released by metabotropic glutamate receptor 1 (GRM1) expressing melanoma cells increase cell migration and invasiveness. *Oncotarget.* **9**, 1187–1199, https://doi.org/10.18632/oncotarget.23455 (2017).
13. Xiao, D. *et al.* Melanoma cell-derived exosomes promote epithelial-mesenchymal transition in primary melanocytes through paracrine/autocrine signaling in the tumor microenvironment. *Cancer Lett.* **376**, 318–327, https://doi.org/10.1016/j.canlet.2016.03.050 (2016).
14. Hood, J. L., San, R. S. & Wickline, S. A. Exosomes released by melanoma cells prepare sentinel lymph nodes for tumor metastasis. *Cancer Res.* **71**, 3792–3801, https://doi.org/10.1158/0008-5472.CAN-10-4455 (2011).
15. Shu, S. L. *et al.* Metabolic reprogramming of stromal fibroblasts by melanoma exosome microRNA favours a pre-metastatic microenvironment. *Sci Rep.* **8**, 12905, https://doi.org/10.1038/s41598-018-31323-7 (2018).
16. Lin, L. Y. *et al.* Tumour cell-derived exosomes endow mesenchymal stromal cells with tumour-promotion capabilities. *Oncogene.* **35**, 6038–6042, https://doi.org/10.1038/onc.2016.131 (2016).
17. Peinado, H. *et al.* Melanoma exosomes educate bone marrow progenitor cells toward a pro-metastatic phenotype through MET. *Nat Med.* **18**, 883–891, https://doi.org/10.1038/nm.2753 (2012).
18. Zhou, X. *et al.* Melanoma cell-secreted exosomal miR-155-5p induce proangiogenic switch of cancer-associated fibroblasts via SOCS1/JAK2/STAT3 signaling pathway. *J Exp Clin Cancer Res.* **37**, 242, https://doi.org/10.1186/s13046-018-0911-3 (2018).
19. Hood, J. L. Melanoma exosome induction of endothelial cell GM-CSF in pre-metastatic lymph nodes may result in different M1 and M2 macrophage mediated angiogenic processes. *Med Hypotheses.* **94**, 118–122, https://doi.org/10.1016/j.mehy.2016.07.009 (2016).
20. Boussadia, Z. *et al.* Acidic microenvironment plays a key role in human melanoma progression through a sustained exosome mediated transfer of clinically relevant metastatic molecules. *J Exp Clin Cancer Res.* **37**, 245, https://doi.org/10.1186/s13046-018-0915-z (2018).
21. Wozniak, M., Peczek, L., Czernek, L. & Düchler, M. Analysis of the miRNA Profiles of Melanoma Exosomes Derived Under Normoxic and Hypoxic Culture Conditions. *Anticancer Res.* **37**, 6779–6789, https://doi.org/10.21873/anticanres.12138 (2017).
22. Cesi, G. *et al.* A new ALK isoform transported by extracellular vesicles confers drug resistance to melanoma cells. *Mol Cancer.* **17**, 145, https://doi.org/10.1186/s12943-018-0886-x (2018).
23. Théry, C. *et al.* Minimal information for studies of extracellular vesicles 2018 (MISEV2018): a position statement of the International Society for Extracellular Vesicles and update of the MISEV2014 guidelines. *J Extracell Vesicles.* **7**, 1535750, https://doi.org/10.1080/20013078.2018.1535750 (2018).
24. König, L. *et al.* Elevated levels of extracellular vesicles are associated with therapy failure and disease progression in breast cancer patients undergoing neoadjuvant chemotherapy. *Oncoimmunology.* **7**, e1376153, https://doi.org/10.1080/2162402X.2017.1376153 (2017).
25. Osti, D. *et al.* Clinical Significance of Extracellular Vesicles in Plasma from Glioblastoma Patients. *Clin Cancer Res.* **25**, 266–276, https://doi.org/10.1158/1078-0432.CCR-18-1941 (2019).
26. Shaked, Y. Balancing efficacy of and host immune responses to cancer therapy: the yin and yang effects. *Nat Rev Clin Oncol.* **13**, 611–626, https://doi.org/10.1038/nrclinonc.2016.57 (2016).
27. Keklikoglou, I. *et al.* Chemotherapy elicits pro-metastatic extracellular vesicles in breast cancer models. *Nat Cell Biol.* **21**, 190–202, https://doi.org/10.1038/s41556-018-0256-3 (2019).
28. Lee, S. *et al.* Immunogenic Effect of Hyperthermia on Enhancing Radiotherapeutic Efficacy. *Int J Mol Sci.* **19**, E2795, https://doi.org/10.3390/ijms19092795 (2018).
29. Mahmood, J. *et al.* Immunotherapy, Radiotherapy, and Hyperthermia: A Combined Therapeutic Approach in Pancreatic Cancer Treatment. *Cancers (Basel).* **10**, E469, https://doi.org/10.3390/cancers10120469 (2018).
30. Tallósy, S. P. *et al.* Adhesion and inactivation of Gram-negative and Gram-positive bacteria on photoreactive TiO_2/polymer and Ag–TiO_2/polymer nanohybrid films. *Appl Surf Sci.* **371**, 139–150, https://doi.org/10.1016/j.apsusc.2016.02.202 (2016).
31. Tallósy, S. P. *et al.* Investigation of the antibacterial effects of silver-modified TiO_2 and ZnO plasmonic photocatalysts embedded in polymer thin films. *Environ Sci Pollut Res Int.* **21**, 11155–11167, https://doi.org/10.1007/s11356-014-2568-6 (2014).
32. Szweda, P. *et al.* Essential Oils, Silver Nanoparticles and Propolis as Alternative Agents Against Fluconazole Resistant *Candida albicans, Candida glabrata* and *Candida krusei* Clinical Isolates. *Indian J Microbiol.* **55**, 175–183, https://doi.org/10.1007/s12088-014-0508-2 (2015).
33. Ahamed, M., Khan, M. A. M., Akhtar, M. J., Alhadlaq, H. A. & Alshamsan, A. Ag-doping regulates the cytotoxicity of TiO_2 nanoparticles via oxidative stress in human cancer cells. *Sci Rep.* 7, 17662, https://doi.org/10.1038/s41598-017-17559-9 (2017).
34. Tani, F. *et al.* Surface expression of a C-terminal alpha-helix region in heat shock protein 72 on murine LL/2 lung carcinoma can be recognized by innate immune sentinels. *Mol Immunol.* **46**, 1326–1339, https://doi.org/10.1016/j.molimm.2008.11.020 (2009).
35. Veres, Á. *et al.* Silver and gold modified plasmonic TiO_2 hybrid films for photocatalytic decomposition of ethanol under visible light. *Catal Today.* **181**, 156–162, https://doi.org/10.1016/j.cattod.2011.05.028 (2012).
36. Hawley R.J., Kozlovac J.P. Decontamination. In: Lindler L.E., Lebeda F. J., Korch G. W. (eds) Biological Weapons Defense. Infectious Disease. Humana Press, https://doi.org/10.1385/1-59259-764-5:333 (2005).
37. Kucharzewska, P. & Belting, M. Emerging roles of extracellular vesicles in the adaptive response of tumour cells to microenvironmental stress. *J Extracell Vesicles.* **2**, 10.3402/jev.v2i0.20304, https://doi.org/10.3402/jev.v2i0.20304, (2013).
38. King, H. W., Michael, M. Z. & Gleadle, J. M. Hypoxic enhancement of exosome release by breast cancer cells. *BMC Cancer.* **12**, 421, https://doi.org/10.1186/1471-2407-12-421 (2012).
39. Parolini, I. *et al.* Microenvironmental pH is a key factor for exosome traffic in tumor cells. *J Biol Chem.* **284**, 34211–34222, https://doi.org/10.1074/jbc.M109.041152 (2009).

40. Hedlund, M., Nagaeva, O., Kargl, D., Baranov., V. & Mincheva-Nilsson, L. Thermal- and oxidative stress causes enhanced release of NKG2D ligand-bearing immunosuppressive exosomes in leukemia/lymphoma T and B cells. *PLoS One* **6**, e16899, https://doi.org/10.1371/journal.pone.0016899 (2011).
41. Jelonek, K., Widlak, P. & Pietrowska, M. The Influence of Ionizing Radiation on Exosome Composition, Secretion and Intercellular Communication. *Protein Pept Lett.* **23**, 656–663, https://doi.org/10.2174/0929866523666160427105138 (2016).
42. Lv, L. H. *et al.* Anticancer drugs cause release of exosomes with heat shock proteins from human hepatocellular carcinoma cells that elicit effective natural killer cell antitumor responses *in vitro*. *J Biol Chem.* **287**, 15874–15885, https://doi.org/10.1074/jbc.M112.340588 (2012).
43. Yang, Y., Chen, Y., Zhang, F., Zhao, Q. & Zhong, H. Increased anti-tumour activity by exosomes derived from doxorubicin-treated tumour cells via heat stress. *Int J Hyperthermia.* **31**, 498–506, https://doi.org/10.3109/02656736.2015.1036384 (2015).
44. Harmati, M. *et al.* Stressors alter intercellular communication and exosome profile of nasopharyngeal carcinoma cells. *J Oral Pathol Med.* **46**, 259–266, https://doi.org/10.1111/jop.12486 (2017).
45. Zapata-Benavides, P. *et al.* WT1 silencing by RNAi synergizes with chemotherapeutic agents and induces chemosensitization to doxorubicin and cisplatin in B16F10 murine melanoma cells. *Oncology letters.* **3**, 751–755, https://doi.org/10.3892/ol.2012.578 (2012).
46. Veres, Á. *et al.* Photocatalytic performance of silver-modified TiO_2 embedded in poly(ethyl-acrylate-co-methyl metacrylate) matrix. *Colloid Polym Sci.* **292**, 207–217, https://doi.org/10.1007/s00396-013-3063-1 (2014).
47. Mutschelknaus, L. *et al.* Radiation alters the cargo of exosomes released from squamous head and neck cancer cells to promote migration of recipient cells. *Sci Rep.* **7**, 12423, https://doi.org/10.1038/s41598-017-12403-6 (2017).
48. Wozniak, M., Peczek, L., Czernek, L. & Düchler, M. Analysis of the miRNA Profiles of Melanoma Exosomes Derived Under Normoxic and Hypoxic Culture Conditions. *Anticancer Res.* **37**, 6779–6789, https://doi.org/10.21873/anticanres.12138 (2017).
49. Lazar, I. *et al.* Proteome characterization of melanoma exosomes reveals a specific signature for metastatic cell lines. *Pigment Cell Melanoma Res.* **28**, 464–475, https://doi.org/10.1111/pcmr.12380 (2015).
50. Warburg, O. On the origin of cancer cells. *Science* **123**, 309–314, https://doi.org/10.1126/science.123.3191.309 (1956).
51. Vazquez, A., Liu, J., Zhou, Y. & Oltvai, Z. N. Catabolic efficiency of aerobic glycolysis: the Warburg effect revisited. *BMC Syst Biol.* **4**, 58, https://doi.org/10.1186/1752-0509-4-58 (2010).
52. Hessvik, N. P. & Llorente, A. Current knowledge on exosome biogenesis and release. *Cell Mol Life Sci.* **75**, 193–208, https://doi.org/10.1007/s00018-017-2595-9 (2018).
53. Alaseem, A. *et al.* Matrix Metalloproteinases: A challenging paradigm of cancer management. *Semin Cancer Biol.* **56**, 100–115, https://doi.org/10.1016/j.semcancer.2017.11.008 (2019).
54. Jabłońska-Trypuć, A., Matejczyk, M. & Rosochacki, S. Matrix metalloproteinases (MMPs), the main extracellular matrix (ECM) enzymes in collagen degradation, as a target for anticancer drugs. *J Enzyme Inhib Med Chem.* **31**, 177–183, https://doi.org/10.3109/14756366.2016.1161620 (2016).
55. Zheng, Q., Ye, J. & Cao, J. Translational regulator eIF2α in tumor. *Tumour Biol.* **35**, 6255–6264, https://doi.org/10.1007/s13277-014-1789-0 (2014).
56. Tai, Y. L., Chen, K. C., Hsieh, J. T. & Shen, T. L. Exosomes in cancer development and clinical applications. *Cancer Sci.* **109**, 2364–2374, https://doi.org/10.1111/cas.13697 (2018).
57. Saleem, S. N. & Abdel-Mageed, A. B. Tumor-derived exosomes in oncogenic reprogramming and cancer progression. *Cell Mol Life Sci.* **72**, 1–10, https://doi.org/10.1007/s00018-014-1710-4 (2014).
58. Becker, A. *et al.* Extracellular Vesicles in Cancer: Cell-to-Cell Mediators of Metastasis. *Cancer Cell* **30**, 836–848, https://doi.org/10.1016/j.ccell.2016.10.009 (2016).
59. Penning, T. M. & Drury, J. E. Human aldo-keto reductases: Function, gene regulation, and single nucleotide polymorphisms. *Arch Biochem Biophys.* **464**, 241–250, https://doi.org/10.1016/j.abb.2007.04.024 (2007).
60. Tammali, R., Reddy, A. B., Srivastava, S. K. & Ramana, K. V. Inhibition of aldose reductase prevents angiogenesis *in vitro* and *in vivo*. *Angiogenesis.* **14**, 209–221, https://doi.org/10.1007/s10456-011-9206-4 (2011).
61. Sharma, M. *et al.* Developmental Competence of Buffalo (*Bubalus bubalis*) Pluripotent Embryonic Stem Cells Over Different Homologous Feeder Layers and the Comparative Evaluation with Various Extracellular Matrices. *Int J Stem Cells.* **6**, 26–36, https://doi.org/10.15283/ijsc.2013.6.1.26 (2013).
62. Toth, T. *et al.* Environmental properties of cells improve machine learning-based phenotype recognition accuracy. *Sci Rep.* **8**, 10085, https://doi.org/10.1038/s41598-018-28482-y (2018).
63. Baglio, S. R. *et al.* Blocking Tumor-Educated MSC Paracrine Activity Halts Osteosarcoma Progression. *Clin Cancer Res.* **23**, 3721–3733, https://doi.org/10.1158/1078-0432.CCR-16-2726 (2017).
64. Cho, J. A., Park, H., Lim, E. H. & Lee, K. W. Exosomes from breast cancer cells can convert adipose tissue-derived mesenchymal stem cells into myofibroblast-like cells. *Int J Oncol.* **40**, 130–138, https://doi.org/10.3892/ijo.2011.1193 (2012).
65. Yamashita, A., Hakura, A. & Inoue, H. Suppression of anchorage-independent growth of human cancer cell lines by the drs gene. *Oncogene* **18**, 4777–4787, https://doi.org/10.1038/sj.onc.1202852 (1999).
66. Tarasov, V. *et al.* Differential regulation of microRNAs by p53 revealed by massively parallel sequencing: miR-34a is a p53 target that induces apoptosis and G1-arrest. *Cell Cycle.* **6**, 1586–1593, https://doi.org/10.4161/cc.6.13.4436 (2007).
67. Ji, Q. *et al.* MicroRNA miR-34 inhibits human pancreatic cancer tumor-initiating cells. *PLoS One.* **4**, e6816, https://doi.org/10.1371/journal.pone.0006816 (2009).
68. Zhao, L., Liu, W., Xiao, J. & Cao, B. The role of exosomes and "exosomal shuttle microRNA" in tumorigenesis and drug resistance. *Cancer Lett.* **356**, 339–346, https://doi.org/10.1016/j.canlet.2014.10.027 (2015).
69. Bar-On, O., Shapira, M. & Hershko, D. D. Differential effects of doxorubicin treatment on cell cycle arrest and Skp2 expression in breast cancer cells. *Anticancer Drugs.* **18**, 1113–1121 https://doi.org/10.1097/CAD.0b013e3282ef4571 (2007).
70. Lüpertz, R., Wätjen, W., Kahl, R. & Chovolou, Y. Dose- and time-dependent effects of doxorubicin on cytotoxicity, cell cycle and apoptotic cell death in human colon cancer cells. *Toxicology.* **271**, 115–121, https://doi.org/10.1016/j.tox.2010.03.012 (2010).
71. Hibino, S. *et al.* Identification of an active site on the laminin alpha5 chain globular domain that binds to CD44 and inhibits malignancy. *Cancer Res.* **64**, 4810–4816, https://doi.org/10.1158/0008-5472.CAN-04-0129 (2004).
72. Lee, D. J. *et al.* Peroxiredoxin-2 represses melanoma metastasis by increasing E-Cadherin/β-Catenin complexes in adherens junctions. *Cancer Res.* **73**, 4744–4757, https://doi.org/10.1158/0008-5472.CAN-12-4226 (2013).
73. Stampolidis, P., Ullrich, A. & Iacobelli, S. LGALS3BP, lectin galactoside-binding soluble 3 binding protein, promotes oncogenic cellular events impeded by antibody intervention. *Oncogene.* **34**, 39–52, https://doi.org/10.1038/onc.2013.548 (2015).
74. Friedl, P. & Wolf, K. Tumour-cell invasion and migration: diversity and escape mechanisms. *Nat Rev Cancer.* **3**, 362–374, https://doi.org/10.1038/nrc1075 (2003).
75. Huang, Z., Yang, M., Li, Y., Yang, F. & Feng, Y. Exosomes Derived from Hypoxic Colorectal Cancer Cells Transfer Wnt4 to Normoxic Cells to Elicit a Prometastatic Phenotype. *Int J Biol Sci.* **14**, 2094–2102, https://doi.org/10.7150/ijbs.28288 (2018).
76. Lamalice, L., Le Boeuf, F. & Huot, J. Endothelial cell migration during angiogenesis. *Circ Res.* **100**, 782–794, https://doi.org/10.1161/01.RES.0000259593.07661.1e (2007).
77. Pan, S. *et al.* Extracellular Alix regulates integrin-mediated cell adhesions and extracellular matrix assembly. *EMBO J.* **27**, 2077–2090, https://doi.org/10.1038/emboj.2008.134 (2008).

78. Piccinini, F., Santis, I. & Bevilacqua, A. Advances in cancer modeling: fluidic systems for increasing representativeness of large 3D multicellular spheroids. *Biotechniques.* **65**, 312–314, https://doi.org/10.2144/btn-2018-0153 (2018).
79. Piccinini, F. AnaSP: a software suite for automatic image analysis of multicellular spheroids. *Comput Methods Programs Biomed.* **119**, 43–52, https://doi.org/10.1016/j.cmpb.2015.02.006 (2015).
80. Crawford, S., Diamond, D., Brustolon, L. & Penarreta, R. Effect of increased extracellular Ca^{++} on microvesicle production and tumor spheroid formation. *Cancer Microenviron.* **4**, 93–103, https://doi.org/10.1007/s12307-010-0049-0 (2010).
81. Huang, B. W. & Gao, J. Q. Application of 3D cultured multicellular spheroid tumor models in tumor-targeted drug delivery system research. *J Control Release.* **270**, 246–259, https://doi.org/10.1016/j.jconrel.2017.12.005 (2018).
82. Samuel, P. *et al.* Cisplatin induces the release of extracellular vesicles from ovarian cancer cells that can induce invasiveness and drug resistance in bystander cells. *Philos Trans R Soc Lond B Biol Sci.* **373**, 20170065, https://doi.org/10.1098/rstb.2017.0065 (2018).
83. Santos, J. C. *et al.* Exosome-mediated breast cancer chemoresistance via miR-155 transfer. *Sci Rep.* **8**, 829, https://doi.org/10.1038/s41598-018-19339-5 (2018).

Acknowledgements
The authors thank for any help of other researchers in the Biological Research Centre of the Hungarian Academy of Sciences, namely Lilla Pinter, Ede Migh and Arpad Balind for their technical assistance, Ferenc Kovacs, Andras Kriston, Norbert Bara for developing the SCT Analyzer 1.0, Zsolt Szegletes for the AFM images, Andras Kincses for the DLS measurements of sEVs, Maria Deli for providing the bEnd.3 cell line and members of the Laboratory of Tumor Immunology and Pharmacology for making available their tissue culture facility. We would like to thank Zoltan Arpad Varadi for the IT support. This work was supported by GINOP-2.3.2-15-2016-00015; GINOP-2.2.1-15-2017-00052 and NKFI-6-K funding scheme (11493 project). The Ministry of Human Capacities, Hungary grant 20391-3/2018/FEKUSTRAT and the University of Szeged Open Access Fund is also acknowledged. Krisztina Buzas and Tibor Pankotai are supported by János Bolyai Research Scholarship of the Hungarian Academy of Sciences, Krisztina Buzas is also supported by the ÚNKP-19-4 New National Excellence Program of the Ministry for Innovation and Technology.

Author contributions
K.B. supervised the research, conceived and designed the experiments and contributed to the writing of the paper; K.B. and P.H. provided resources to this study; M.H. contributed to the experimental design; performed most of the experiments; analysed data and wrote the manuscript. E.Gy.-S. contributed to the experimental work, including the Western blot analyses and miRNA isolation, G.D. contributed to the experimental work, including the Cell-Clock cell cycle assay, fluorescence spectroscopy and to the data analysis, L.J. and I.D. synthetized the Ag-TiO_2 photocatalyst particles and performed their DLS measurements and TEM, O.S. performed the NTA, E.H.-G. performed the proteomic analysis, I.N performed the miRNA analysis, A.F. performed the SEM, Zs.U. performed the qPCR analyses of miRNAs, M.K. performed the high-content screening and contributed to the data analysis, F.P. contributed to the developing of the 3D cell culture model and the data analysis, T.P. and T.B. provided critical feedback to the study; all authors revised the manuscript.

Competing interests
The authors declare no competing interests.

Additional information
Supplementary information is available for this paper at https://doi.org/10.1038/s41598-019-51778-6.

Correspondence and requests for materials should be addressed to K.B.

Reprints and permissions information is available at www.nature.com/reprints.

Publisher's note Springer Nature remains neutral with regard to jurisdictional claims in published maps and institutional affiliations.

International Journal of
Molecular Sciences

MDPI

Article

Small Extracellular Vesicles Isolated from Serum May Serve as Signal-Enhancers for the Monitoring of CNS Tumors

Gabriella Dobra [1,2], Matyas Bukva [1,2], Zoltan Szabo [3], Bella Bruszel [3], Maria Harmati [1], Edina Gyukity-Sebestyen [1], Adrienn Jenei [4], Monika Szucs [5,6], Peter Horvath [1], Tamas Biro [7], Almos Klekner [4] and Krisztina Buzas [1,8,9,*]

1 Laboratory of Microscopic Image Analysis and Machine Learning, Institute of Biochemistry, Biological Research Centre, H-6726 Szeged, Hungary; dobragab@yahoo.co.uk (G.D.); bukvamatyas@gmail.com (M.B.); harmatimarcsi@gmail.com (M.H.); e.gyukity.sebestyen@gmail.com (E.G.-S.); horvath.peter@brc.hu (P.H.)
2 Department of Medical Genetics, Doctoral School of Interdisciplinary Medicine, University of Szeged, H-6720 Szeged, Hungary
3 Department of Medical Chemistry, Faculty of Medicine, University of Szeged, H-6720 Szeged, Hungary; szabo.zoltan@med.u-szeged.hu (Z.S.); bruszel.bella@med.u-szeged.hu (B.B.)
4 Department of Neurosurgery, Clinical Centre, University of Debrecen, H-4032 Debrecen, Hungary; jenei.adrienn@med.unideb.hu (A.J.); aklekner@yahoo.com (A.K.)
5 Department of Medical Physics and Informatics, Faculty of Medicine, University of Szeged, H-6720 Szeged, Hungary; szucs.monika@med.u-szeged.hu
6 Department of Medical Physics and Informatics, Faculty of Science and Informatics, University of Szeged, H-6720 Szeged, Hungary
7 Department of Immunology, Faculty of Medicine, University of Debrecen, H-4032 Debrecen, Hungary; biro.lcmp@gmail.com
8 Department of Immunology, Faculty of Medicine, University of Szeged, H-6720 Szeged, Hungary
9 Department of Immunology, Faculty of Science and Informatics, University of Szeged, H-6720 Szeged, Hungary
* Correspondence: kr.buzas@gmail.com; Tel.: +36-62-432-340

Received: 26 June 2020; Accepted: 24 July 2020; Published: 28 July 2020

Abstract: Liquid biopsy-based methods to test biomarkers (e.g., serum proteins and extracellular vesicles) may help to monitor brain tumors. In this proteomics-based study, we aimed to identify a characteristic protein fingerprint associated with central nervous system (CNS) tumors. Overall, 96 human serum samples were obtained from four patient groups, namely glioblastoma multiforme (GBM), non-small-cell lung cancer brain metastasis (BM), meningioma (M) and lumbar disc hernia patients (CTRL). After the isolation and characterization of small extracellular vesicles (sEVs) by nanoparticle tracking analysis (NTA) and atomic force microscopy (AFM), liquid chromatography -mass spectrometry (LC-MS) was performed on two different sample types (whole serum and serum sEVs). Statistical analyses (ratio, Cohen's d, receiver operating characteristic; ROC) were carried out to compare patient groups. To recognize differences between the two sample types, pairwise comparisons (Welch's test) and ingenuity pathway analysis (IPA) were performed. According to our knowledge, this is the first study that compares the proteome of whole serum and serum-derived sEVs. From the 311 proteins identified, 10 whole serum proteins and 17 sEV proteins showed the highest intergroup differences. Sixty-five proteins were significantly enriched in sEV samples, while 129 proteins were significantly depleted compared to whole serum. Based on principal component analysis (PCA) analyses, sEVs are more suitable to discriminate between the patient groups. Our results support that sEVs have greater potential to monitor CNS tumors, than whole serum.

Keywords: extracellular vesicles; cancer biomarker; proteomics

1. Introduction

According to the World Health Organization (WHO), cancer is the second leading cause of death, accounting for an estimated 9.6 million cases in 2018. Globally, 1 in 6 deaths is due to cancer [1]. The cancer burden continues to grow worldwide, exerting tremendous physical, emotional and financial strain on individuals, families, communities and on health systems [2].

The diagnosis of central nervous system (CNS) tumors is based on CT and MRI scans, as well as on the histopathological analysis of samples obtained by biopsy or via surgical resection. However, these procedures are highly invasive, uncomfortable for the patient, bear a considerable risk of complications and provide limited information on tumor status. Therefore, biomarkers appropriate for monitoring disease progression and response to treatment are eagerly required. While repeated MRI scans serve as the standard method to follow patients, it has little prognostic value for long-term recurrence [3]. Thus, neuro-oncological research aims to identify novel biomarkers suitable for monitoring CNS tumors in clinical practice [4].

Liquid biopsy is in the spotlight of biomarker-focused research, as body fluids are easily accessible sources of biomarkers and are available with minimally invasive and low cost sampling procedures. Also, multiple sampling allows the monitoring of disease progression and therapeutic response [5]. Every cell, including neoplastic cells, release molecular markers into the circulation. Tumor-derived biomarkers include proteins, nucleic acids, circulating tumor cells, platelets and tumor-derived extracellular vesicles that accumulate in urine, cerebrospinal fluid, saliva and blood [6].

Blood is the most easily accessible source for biomarkers, thus it is frequently used to assess disease status in malignancies such as prostate, liver and ovarian cancers based on the serum concentrations of PSA, AFP and CA125, respectively. In neuro-oncology, blood-based biomarkers are mainly used to evaluate toxicity and safety of treatments to guide patient management. For example, myelosuppression is a common risk associated with temozolomide treatment and radiotherapy, thus standard practice dictates weekly tests of complete blood count, including whole blood cell differential and platelet counts during definitive chemoradiotherapy [7]. Finding biomarkers for blood-based CNS tumor monitoring is more challenging, as the blood-brain barrier (BBB) prevents the release of tumor-related biomarkers into peripheral blood. However, it would have outstanding benefits in clinical patient management, thus efforts to identify blood based biomarkers, including proteins, nucleic acids, circulating tumor cells and extracellular vesicles are currently in the forefront of neuro-oncological research [8].

Extracellular vesicles (EVs) are promising cancer biomarkers accessible via liquid biopsy, because they are cell-secreted, nano-sized and stably exist in all types of body fluids. EVs contain a sample of the cytosolic milieu, including an abundance of DNA, RNA, proteins and other analytes, while externally they also resemble their cell of origin [9]. EVs are small, lipid bilayer-enclosed vesicles released by both cancer and non-cancerous cells into the extracellular space [10].

EVs secreted by cancer cells communicate with neighboring stromal cells or even with cells at distant sites, inducing an alteration of the cell program [11,12]. Pre-metastatic niche formation has been shown in several tumors, for example, in pancreatic, lung, colorectal and ovarian cancers [13–16]. Also, EVs may be taken up by immune cells, leading to immunosuppression [17]. More recently, EVs have even gained a role in cancer diagnosis and therapy [18–20] as biomarker molecules that may be identified in different primary tumors with high sensitivity and specificity [21]. Regarding pancreatic cancer, Kalluri and colleagues found that glypican-1 (GPC1), a cell surface proteoglycan, is specifically enriched in circulating exosomes (30–200 nm endosome-derived EVs). GPC1 is suitable to differentiate early- and late-stage pancreatic cancer from benign diseases of the pancreas, with an accuracy of 100% [22]. The available evidence also supports that tumor-derived EVs can cross the BBB [23,24], however, currently no clinically relevant EV biomarkers are accepted for the monitoring of CNS tumors.

Several studies report on gene or protein expression analyses of CNS tumor tissue (specifically, glioblastoma), allowing to identify biomarkers that could be secreted into the blood and thus could be detected from serum samples. Recent studies have aimed to identify one and two specific biomarkers

for the reliable evaluation of actual tumor status [25–27] but none of these proteins alone was found to be sufficiently specific and sensitive to serve as a monitoring marker.

Regarding that previous attempts to find surrogate serum markers for brain tumors have failed when based on a single or only few candidate factors, we made an attempt to identify a characteristic protein fingerprint of 10–20 candidate markers associated with CNS tumors.

For this purpose, 96 serum samples were collected from four patient groups according to the criteria of the National Ethical Committee and proteomics analysis was performed using liquid chromatography and mass spectrometry (LC-MS). The serum samples were obtained from patients diagnosed with the two most common types of brain tumors [28], namely malignant glioblastoma multiforme (GBM) and benign meningioma (M), as well as from patients with a prevalent brain metastasis [29] originating from non-small-cell lung cancer (BM). Patients with lumbar disc herniation served as controls (CTRL). Following a statistical selection, these four patient groups were compared with respect to the identified proteins. In parallel, small extracellular vesicles (sEVs) were isolated from the serum samples by differential centrifugation and proteomics and statistical analyses were also performed on these sEV samples, allowing to compare the suitability of these two different sample types. According to the best of our knowledge, this is the first study that compares the proteome of whole serum and serum-derived sEV samples. Results from the proteomics analysis indicate that using a protein fingerprint of serum-derived sEVs instead of analyzing whole serum increases the accuracy of distinguishing between the clinical samples, that is, between the patient groups. Our results support that sEVs have a greater potential for the proteomics-based monitoring of CNS tumors compared to whole serum analysis.

2. Results

2.1. EV Samples Show sEV Properties with Similar Concentration and Size Distribution in the Different Patient Groups

To verify the value of circulating extracellular vesicles as potential biomarkers for CNS tumors, EVs were isolated from the serum of patients with glioblastoma multiforme (GBM), single brain metastasis originating from non-small-cell lung cancer (BM) and meningioma (M), as well as from control patients with lumbar disc herniation (CTRL). Each group included 24 individuals of both genders with various ages. Extracellular vesicles were isolated from the sera by differential centrifugation and were characterized by atomic force microscopy (AFM) and nanoparticle tracking analysis (NTA). Pools of 6 samples were formed in all groups, allowing four parallel samples to be tested per group (see in Section 4.1). Western blot analyses were also performed to demonstrate the EV nature (Figure S1).

EVs were divided into subtypes based on their size range, separating small EVs (sEVs) and medium/large EVs (m/lEVs) [30]. AFM analysis revealed that the small EV subtype includes various structures. Mean and mode diameters of the particles, represented by an average of the 16 sample pools, were measured as 112 nm and 86 nm by NTA, respectively (Figure 1A).

The quantitative characterization of serum sEVs by NTA (Figure 1B) revealed no significant differences between the four patient groups regarding the size and concentration of circulating sEVs. However, within the groups high individual differences were observed in the measured parameters of the sEVs.

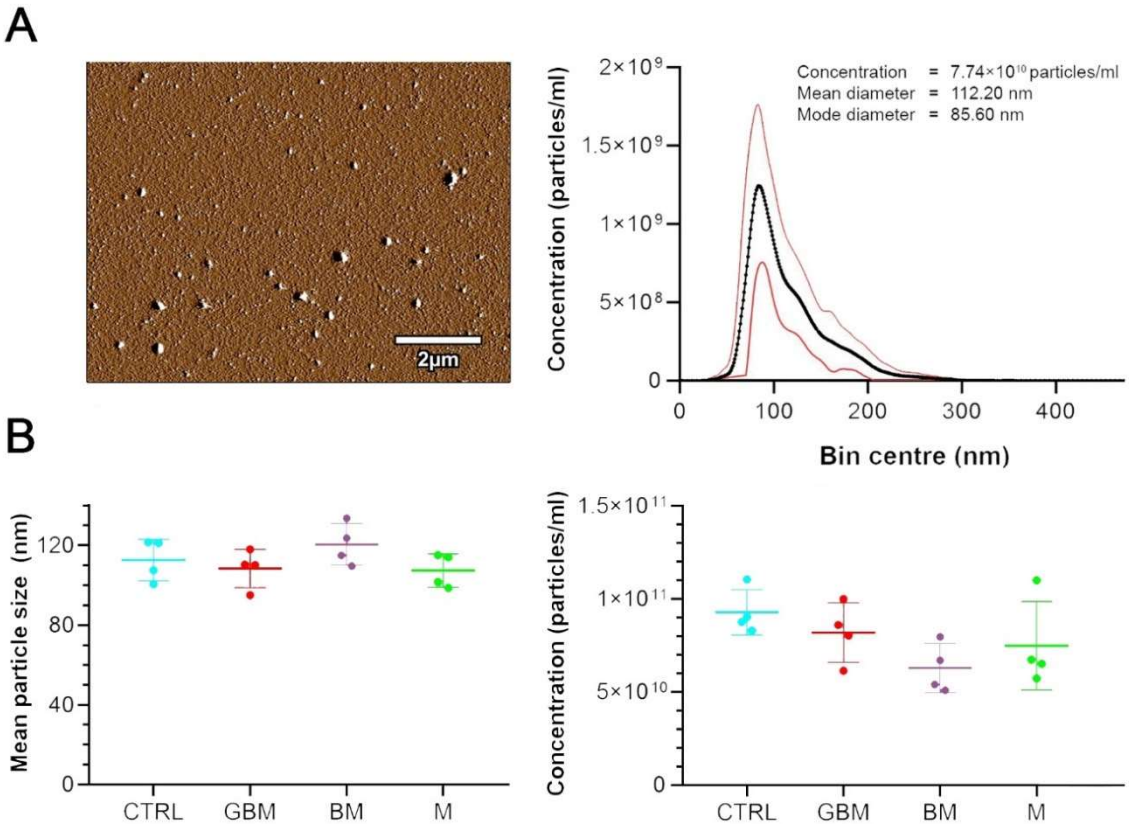

Figure 1. Characterization and quantitative properties of the small extracellular vesicle (sEV) samples. (**A**) Atomic force microscopy (AFM) image of sEV isolates displays vesicles with diameters within the range of 50–140 nm. The diagram shows the size distribution of the 96 sEV samples isolated from the serum, presenting the mean +/−95% CI values measured by nanoparticle tracking analysis (NTA). (**B**) Dot plots show the number and size distribution of small extracellular vesicles (sEVs) displayed in mean size (left) and concentration (right) values for each sample pools (4 samples/group).

2.2. Statistical Analysis of LC-MS Data Reveals Characteristic Proteomic Fingerprints for Each Patient Group and Informs on the Suitability of the Two Different Sample Types in Distinguishing CNS Tumors

We aimed to identify the differences between the four patient groups to reveal the characteristic protein profiles associated with the CNS tumors in point. Using an intensity ratio of >2 or <0.5 with Cohen's d effect size of 2 as a cut-off, we investigated which proteins show reliable intensity difference and which proteins can separate at least one group from the others based on a receiver operating characteristic (ROC) analysis. Moreover, utilizing principal component analysis (PCA) with k-means clustering, we were able to compare the suitability of the two different sample types to distinguish between the CNS tumors in point. Figure 2 shows the flowchart of LC-MS data processing and the results of the statistical analyses.

Proteomics analyses by LC-MS (Step 1) were performed on whole serum and sEV samples obtained from patients with GBM, BM, M and CTRL. Individual samples (n = 24) in each group were arranged into 4 pools (see in Section 4.1) to eliminate individual variances, reduce sample number, shorten the time of LC-MS measurements and reduce the need for materials. The Data independent acquisition (DIA) mode constructed spectral library revealed 311 proteins (see Table S1). Based on Pearson's correlation analyses (Step 2), one of the sEV control samples had to be excluded from further statistical analyses (Table S2). After excluding unreliable proteins, as well as proteins with missing values (Step 3), a total of 262 proteins remained for the final analysis.

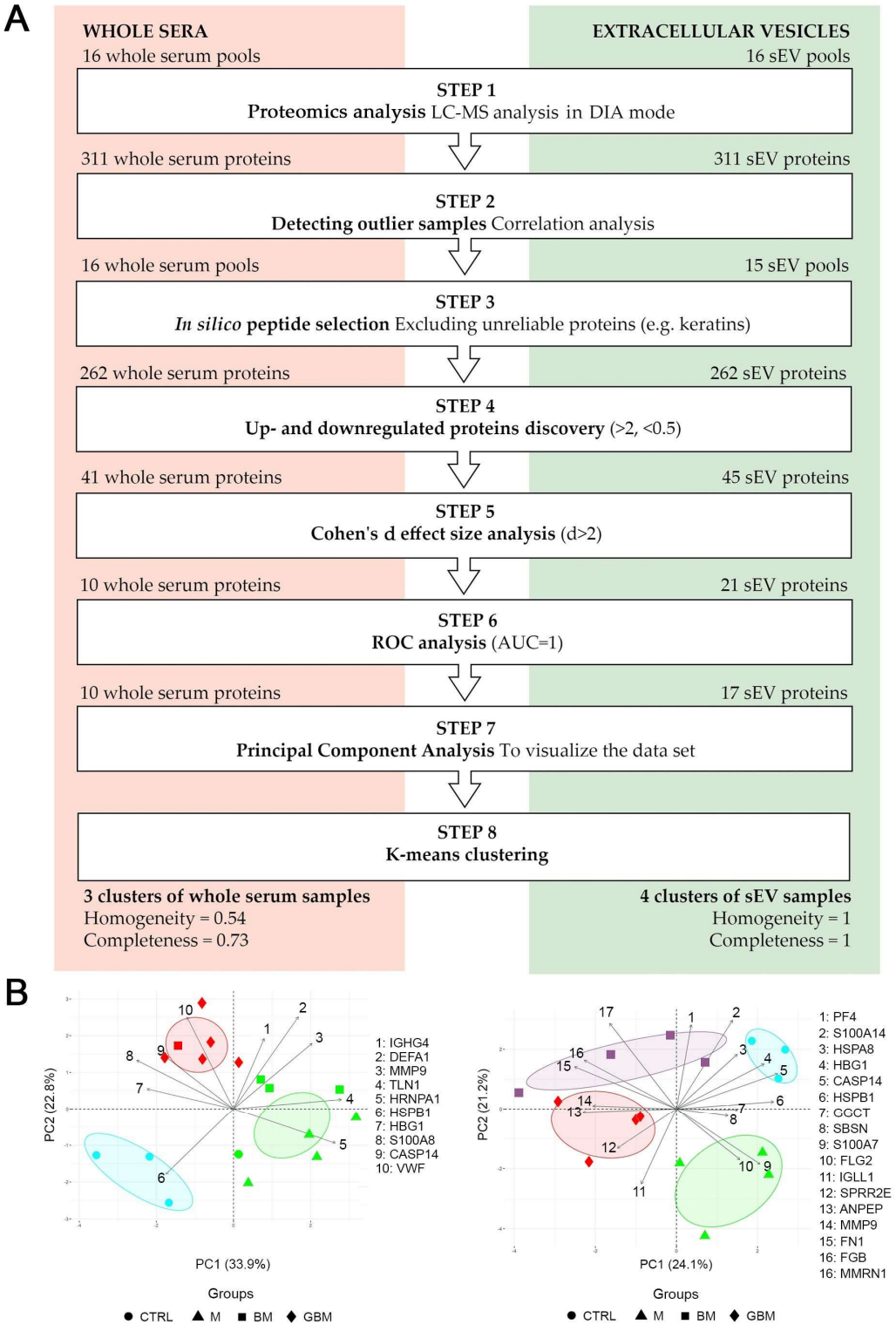

Figure 2. Statistical analysis of the proteome of whole serum (left) and sEV samples (right). (**A**) The flowchart shows the steps of selecting the proteins revealed by liquid chromatography and mass spectrometry (LC-MS) (**B**) The diagrams visualize the results of the principal component analysis (PCA) and k-means clustering. X and Y axes of PCA biplots show principal component 1 (PC1) and principal component 2 (PC2) with explained variances. Arrows represent the coefficients of each protein for PC1 versus the coefficients for PC2, showing the significance of each protein in influencing PCs. Different dots represent the 4 patient groups. Colors indicate the clusters formed by k-means clustering; ellipses indicating the 95% confidence interval were constructed around the barycenters of the clusters.

Following basic processing, up- and down-regulated protein discovery (Step 4) resulted in 41 whole serum proteins and 45 sEV proteins. In addition to comparing each CNS tumor group to CTRL, between-group differences among the CNS tumor groups were also assessed in the protein selection process. As clinically relevant incidence is an important consideration for selecting the proteins identified, Cohen's d effect size was adopted as an indicator of between-groups difference. The Cohen's d effect size analysis (Step 5) with a threshold of d > 2 yielded 10 and 21 proteins in the whole serum and sEV samples, respectively. In the ROC analyses (Step 6) 10 whole serum proteins (MMP9, HSPB1, CASP14, HBG1, IGHG4, DEFA1, VWF, HNRNPA1, S100A8, TLN1) and 17 sEV proteins (MMP9, HSPB1, CASP14, HBG1, FGB, GGCT, PF4, S100A7, FN1, ANPEP, FLG2, HSPA8, IGLL1, MMRN1, S100A14, SBSN, SPRR2E) were found to meet the AUC = 1 selection criteria. Table S3 includes the UniProt ID, Gene symbol, ratio of intensity means > 2 or < 0.5 and Cohen's d effect size > 2 parameters for the selected proteins. The two sample groups shared four significantly altered proteins (highlighted in Table S3), namely MMP9, CASP14, HBG1 and HSPB1.

Following protein selection, PCA (Step 7) was performed to visualize the dataset, where several potentially correlated proteins were projected into a smaller number of variables. K-means clustering (Step 8) on the whole serum PCA biplot resulted in 3 inhomogeneous or incomplete clusters. Calculated cluster homogeneity and completeness scores are 0.56 and 0.73, respectively. In contrast to whole serum samples, the clustering of sEV samples formed homogeneous and complete clusters, with homogeneity and completeness scores of 1. The results of the PCA analyses and k-means clustering indicate considerable differences between the whole serum and sEV samples (Figure 2B). We found that the accuracy of distinguishing between various CNS tumors can be increased using a protein panel from serum-derived sEVs, compared to analyzing whole serum samples.

2.3. Statistical Evaluation and IPA of LC-MS Data Revealed the Background of Suitability Differences between Whole Serum and sEV Samples

2.3.1. Quantitative Changes of the Proteome May Affect the Suitability of sEV Samples to Provide Biomarkers for CNS Tumor Status Monitoring

Statistical comparison of the proteome of sEV and whole serum samples was performed to reveal quantitative differences affecting the suitability of different sample types to provide biomarkers for CNS tumor status monitoring. Pairwise statistical comparison (Welch's test) was used to identify proteins significantly enriched or depleted in sEV samples compared to whole serum samples (Figure 3). Sixty-five proteins were found to be significantly enriched in sEV samples, while 129 proteins were significantly depleted ($p < 0.05$). Using our sEV purification protocol detailed in the Section 4, we obtained a uniform particle size range of sEVs but the magnitude of quantitative changes in the sEV versus whole serum proteome suggested the possible presence of lipoprotein and serum protein contaminations. The level of apolipoproteins was decreased in sEV enriched samples (sEV/serum mean ratio is 0.66), however this fraction could not be completely eliminated. Besides, well known high abundance serum proteins (e.g., ALB) dominated the protein content of sEV enriched samples too. However, the enrichment of non-tissue specific (ITGA2B, ITGB3, LGALS3BP), epithelial cell (CD5L) and platelet related (STOM, TSPAN9) EV marker proteins [31] confirms sEV enrichment (sEV/serum mean ratio is 26.58), while it also demonstrates the presence of sEVs produced during clotting.

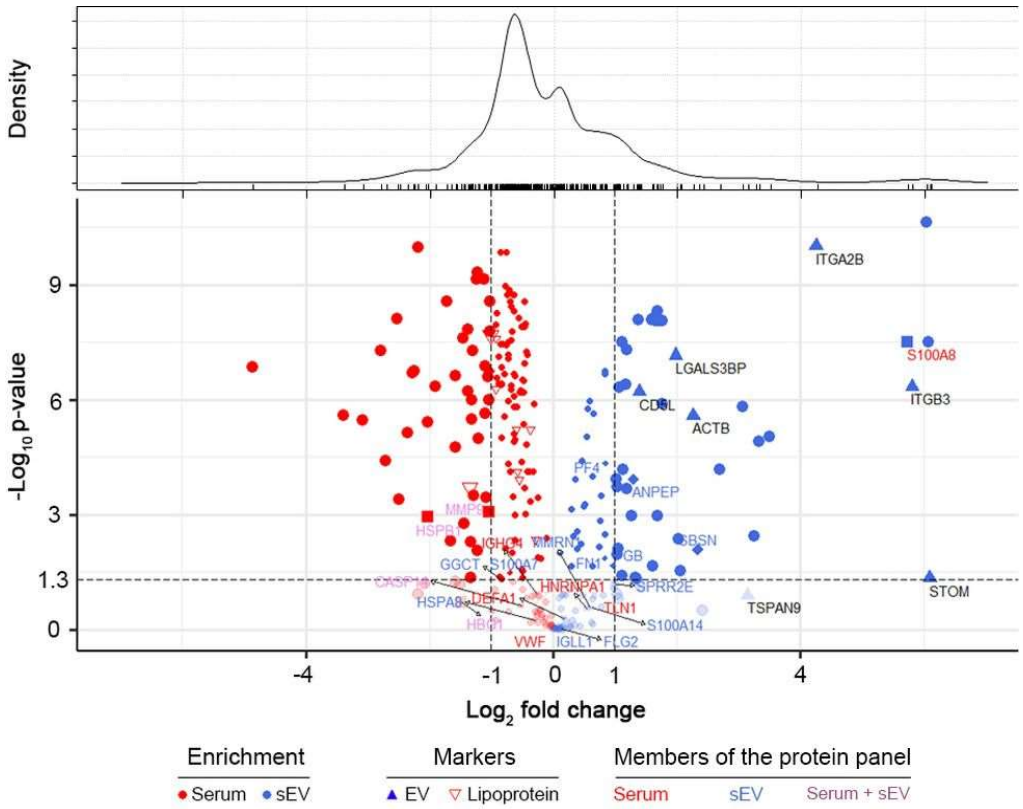

Figure 3. Quantitative comparison of the proteome of sEV and whole serum samples. Volcano plot represents the observed changes in average MS intensities in paired sEV vs. serum comparisons. Protein enrichment is marked with red and blue colored symbols in whole serum and sEVs, respectively. Lipoproteins (empty red upside-down triangles), elements of our whole serum protein panel (red letters, square symbols), sEV protein panel (blue letters, diamond symbols) and common members of the two protein panels (purple letters) are highlighted. Values of –log (p) were obtained from paired Welch's test in sEV/serum comparisons. Density estimation of log2 (fold change) values is shown on top.

Among the 17 proteins of the sEV marker panel described in Section 2.2 only 6 were significantly enriched in the sEV samples and 5 of the 10 proteins comprising the specific serum panel had higher abundance in whole serum (Figure 3). These findings suggest that the better suitability of sEV enriched samples to serve a biomarker source is not explained by a total increase in the abundance of specific proteins. (Detailed proteomics findings, protein annotation and sEV enrichment data are available in Table S1).

Additional sample processing (sEV isolation) may introduce higher technical variance in case of sEV samples, thus it may reduce the analytical suitability of this sample type. Our analysis revealed a similar level of variance for proteins quantified in each sample type (excluding contaminants)—median coefficients of variation within each patient group were in the ranges of 20.78–23.87% for sEV and 20.21–24.45% for serum samples (see Figure S2 for CV distributions).

2.3.2. Biological Background Might Be Responsible for the Increased Suitability of sEV Samples to Provide Biomarkers for CNS Tumor Status Monitoring

To gain insight into the biological background of the obtained proteomics data, IPAwas applied. We performed 'Core Analyses' for whole serum and sEV data separately, yielding a list of significantly influenced 'Diseases and Functions' in each patient group ($p < 0.05$). Using 'Comparison Analysis,' we were able to develop heatmaps covering the relevant systemic and tumor-related functions, as well as the activated or inhibited immune functions (Figure 4A). Regarding whole serum samples, many of the significantly influenced functions identified are related to CNS involvement and active immune

regulatory processes but the patient groups are not clearly distinguished on the heatmaps (Figure 4A, left panels). In contrast, on two of the three sEV proteome-based heatmaps M was evidently separated from the malignant tumor groups (Figure 4A, right panels), where tumor progression-related functions (e.g., angiogenesis, proliferation and migration of tumor cells) were detected to be highly activated and the activated immune functions (e.g., cell movement or activation of myeloid cells) predominate over inhibited immune functions (e.g., phagocytosis).

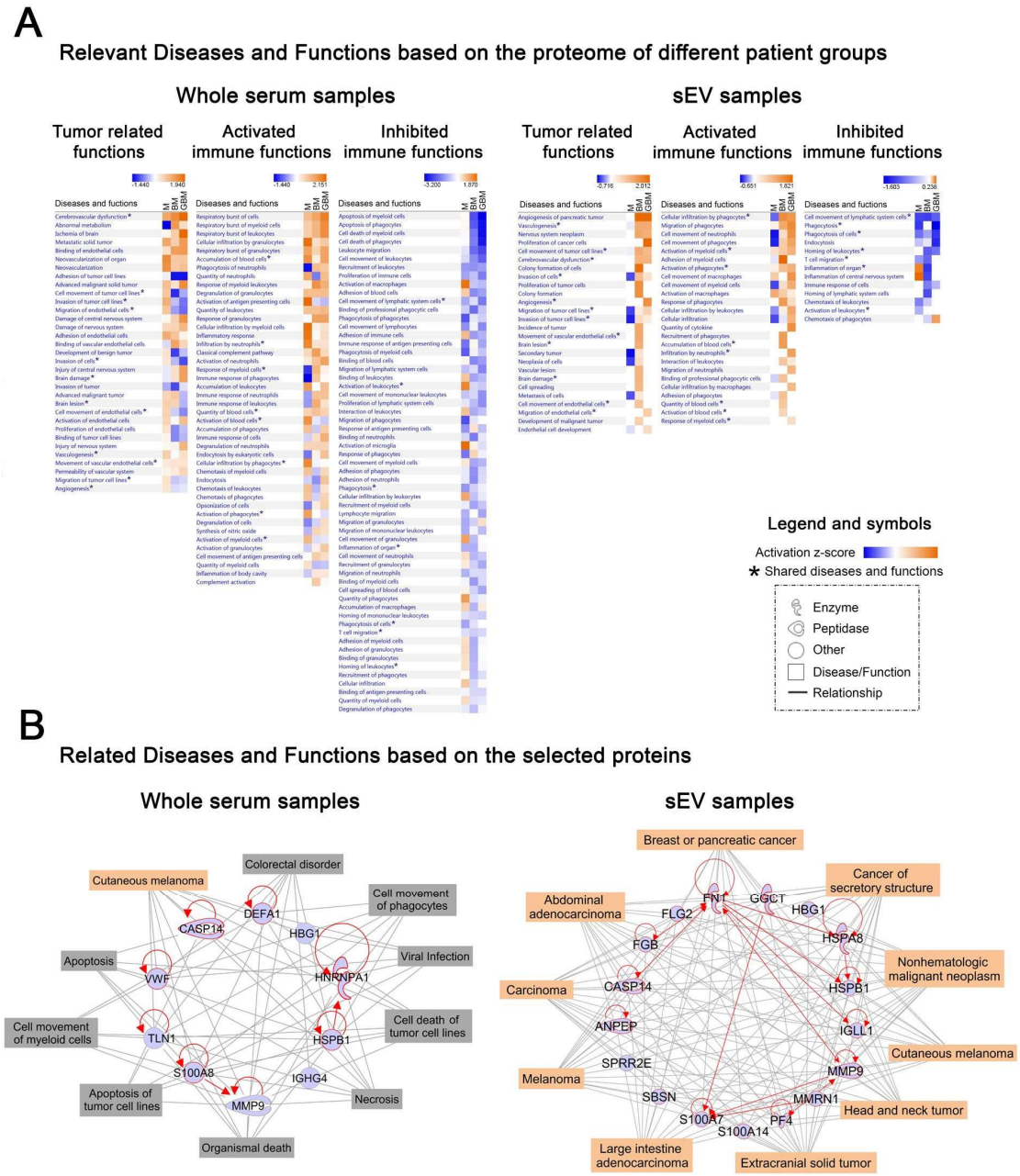

Figure 4. Ingenuity Pathway Analysis (IPA) analyses of whole serum (left) and sEV (right) data derived from the LC-MS analysis. (**A**) Heatmaps show relevant 'Diseases and Functions' in three separated panels related to systemic and tumor-related functions, as well as activated and inhibited immune functions. Z-score indicates activation or inhibition rates of the relevant 'Diseases and Functions' in the three tumorous patient groups compared to the control group. * symbol indicates the shared diseases and functions in whole serum and sEVs. (**B**) Networks display the selected 10 whole serum or 17 sEV proteins (blue symbols) and their relationships (red lines). Top ten related 'Diseases (highlighted in orange symbols) and Functions (highlighted in grey)' are connected by grey lines.

Next, we attempted to specify the common biological role of the characteristic protein profiles identified. Therefore, we elaborated two networks containing the selected 10 and 17 proteins identified based on whole serum and the sEV data, respectively (Figure 4B). Using the 'Grow tool,' the top ten influenced 'Diseases and Functions' were integrated into the networks. In case of the whole serum network (Figure 4B, left panel), nine different related 'Diseases and Functions' were identified, including viral infection, apoptosis, necrosis or cell movement of phagocytes and myeloid cells and only one was cancer-related. In contrast, the top ten influenced diseases identified on the sEV network based on the identified 17 proteins (Figure 4B, right panel) were all tumor-associated, suggesting their potential involvement in the pathophysiology of cancers.

3. Discussion

Non-invasive diagnostic tests are of outstanding clinical importance because of their minimal burden and risk to the patient, their repeatability, low cost, high information content and easy accessibility. In CNS tumors, a minimally invasive technique for describing the actual tumor status should be particularly important. Conventional MRI tests commonly used for the monitoring of CNS tumors are not absolutely appropriate for discriminating between various tumor types (e.g., cannot differentiate between glioblastomas and solitary metastases, CNS lymphomas or other glioma grades [32]) and cannot distinguish recurrence from pseudoprogression. Brain biopsies, as another option, are highly challenging and risky, especially when multiple sampling is required for long-term follow-up [33]. For several cancer types, blood-based tumor markers, such as PSA, AFP and CA125 have been introduced into clinical practice and research for the identification of further noninvasive biomarkers applicable for monitoring a wider scale of malignant diseases is ongoing [34]. However, regarding CNS tumors these studies have generally failed, presumably explained by several reasons, including (1) the barrier function of BBB (releasing less tumor 'information' into the systemic circulation), (2) the presence of molecules released into the blood from other sources and (3) possibly because of the complexity of tumor tissues (such as glioblastoma multiforme). These issues hamper attempts to use a single or only a few biomarkers to diagnose and monitor CNS tumors.

Based on these considerations, we aimed to detect the characteristic protein fingerprint of some common CNS tumors, trying to amplify the signal/information that brain tumors release into the circulation. For this purpose, the protein content of 96 clinical serum samples and related sEV samples isolated from the whole serum was measured by LC-MS. Serum samples were collected from three brain tumor groups considered as the most common malignant, benign and metastatic brain tumors (glioblastoma multiforme, meningioma [28] and brain metastasis of non-small-cell lung cancer [29]) and a control group (lumbar disc herniation).

To examine whether the proteomes of serum and sEV samples are suitable for differentiating between the CNS tumors in point, that is, whether they are applicable to diagnose and monitor the disease, the proteomes of these four patient groups were compared. The effectiveness of tumor type distinction may be increased if the analysis is restricted to proteins which exhibit significant between-group differences. Protein selection was carried out as described in literature [35] (using ratio of intensity means; Cohen's d effect size; ROC) but much stricter thresholds were applied (>2, <0.5; d > 2; AUC = 1, respectively). Statistical selection yielded a collection of proteins whose intensity showed significant between-group differences and thus these proteins could be reckoned as the most suitable molecules for distinguishing between the tumor types examined. Specifically, protein selection yielded a 10- and 17-membered protein panel for whole serum and sEV samples, respectively. While none of these proteins appeared to be able to distinguish between the patient groups individually, their combination was found to reliably discriminate between the different patient groups suggesting that instead of a few candidates, a specific protein panel is required for a perfect differentiation between various tumor types.

To evaluate group distinction efficiency, PCA with k-means clustering was carried out according to literature [36]. Homogeneity and completeness scores of the clusters were calculated to measure the

performance of k-means clustering. Cluster homogeneity and completeness mean that each cluster contains only samples from the same group and all samples of a given group are assigned to the same cluster. Both scores are bounded below by 0 and above by 1. A score of 1 indicates perfect homogeneity or completeness. PCA revealed that sEV samples were more suitable for group distinction. Despite carefully selected and perfectly identical statistical analyses for the two sample types, the homogeneity and completeness scores for the whole serum analysis were 0.56 and 0.73, respectively, compared to scores 1 and 1 for the analysis of sEV samples. The explanation for these findings is illustrated on a PCA biplot (Figure 2). Regarding serum samples, the proteins that can separate two given groups by the appropriate ratio and effect size may have similar intensities in other groups as well. For example, DEFA1 is important in distinguishing the CTRL group from the BM and GBM groups, however, it shows similar intensities in the GBM and BM groups, hampering the separation of these groups (see DEFA1 arrow pointing between the BM and GBM groups in the whole serum PCA plot). Still, DEFA1 cannot be removed, because it plays a key role in separating the CTRL group from malignant tumors. In contrast, the majority of the proteins identified in the sEV samples were able to separate any given group from all the others.

To check whether the poorer performance of whole serum proteins in distinguishing between the patient groups is attributed to the number of the proteins considered, we performed another PCA analysis including only up- and down-regulated proteins selected from the whole identified panel (see Figure 2, Step 4), yielding a similar number of proteins for the two sample types. The PCA analysis of these 41 whole serum and 45 sEV proteins yielded similar results as the previous analysis of carefully selected proteins only and the sEV sample type proved to perform better again. Although the sEV sample was far from being perfect in this case (4 groups were recognized with a homogeneity score of 0.66 and a completeness score of 0.66), the results for the whole serum analysis indicated that not even the sample groups can be recognized based on these proteins only 2 groups were recognized, homogeneity—0.07, completeness: 0.40) (Figure S3). These findings support that sEVs have a better efficiency in distinguishing between various patient groups, irrespective of the order of magnitude of proteins analyzed for the comparison of sEV and whole serum samples.

To investigate the background of our observations, we performed a quantitative proteomics comparison of the two sample types. A quantitative evaluation of sEV purification protocols was suggested based on quantitative LC-MS based proteomics approach, using enrichment analysis of carefully selected sEV markers along with medium specific contamination marker proteins (e.g., lipoproteins and serum). To the best of our knowledge, we are the first group to quantitatively compare the proteome of serum derived small extracellular vesicles with that of the original whole serum samples. sEV enrichment may increase the relative abundance of proteins present in higher concentration within sEVs and the increased signal-to-noise ratio may be beneficial for the quantitative LC-MS analysis of such proteins. On the other hand, proteins in serum are originating from different sources of the human body. Any fractionation (e.g., enrichment of a specific sEV population) may decrease the suppressing effect of the uninformative protein fraction released from sources not specific for the target disease. No association was revealed between being a sEV marker and sEV enrichment, suggesting that it not the overall enrichment process that should be responsible for the increased suitability of sEV samples to provide biomarkers for CNS tumor monitoring. Instead, the removal of an uninformative protein fraction, providing a more specific sample, may explain why the sEV sample is more applicable for distinguishing between various CNS cancer patient groups. Compared to whole serum samples, EVs may be more suitable for investigating tumor related molecular patterns, as the characteristic fingerprint molecules are present in higher concentrations in sEV samples and are accompanied by less contaminating molecules that may bias the analytical findings.

To understand the biological background for our proteomics-based data, IPA was used for the separate analyses of whole serum and sEV data. 'Core Analyses' were performed, yielding a list of significantly influenced 'Diseases and Functions' comprising tumor-related functions as well as activated or inhibited immune functions in each patient group ($p < 0.05$). 'Comparison Analysis' was

carried out to compare the affected 'Diseases and Functions' in the different patient groups. Regarding whole serum samples, many of the significantly influenced functions identified were associated with CNS involvement and active immune regulatory processes but the patient groups were not clearly distinguished on the heatmaps. In contrast, on the sEV proteome-based heatmaps the benign M was clearly separated from the malignant tumors, for which numerous tumor progression-related functions (e.g., angiogenesis, proliferation and migration of tumor cells) were found to be highly activated. The generated IPA heatmaps also revealed that the proteome of sEV samples may provide more specific information on the immune reactions characteristic to the patient groups. We assume that activated immune functions (e.g., cellular infiltration and migration of phagocytes) may play a crucial role in the development of an immune-suppressive microenvironment, while antitumoral immune responses (e.g., phagocytosis, inflammation) might be inhibited.

Serum is a dual source of biomolecular information on cancer, as it contains the molecules released by cancer cells, as well as those released during the immune system's tumor-specific responses [37]. Therefore, the differences observed in the serum vesicles isolated from different patient groups may not only mirror tumor-specific processes but also those related to the associated immune responses [38,39]. Samples enriched in sEVs can offer an amplified source of relevant information, representing not only the specific tumor tissue but also the associated immune responses. Thus, an appropriate protein panel, covering both sources, may have improved efficiency for CNS tumor classification and monitoring.

In addition, the networks developed based on the IPA 'Grow tool' demonstrated that the biological background of the sEV-based characteristic protein profile is more specifically associated with the tumor types compared with the whole serum based protein profile. The role of some of the proteins included in the sEV-based characteristic protein profile has already been described, for example in GBM biology, making these proteins promising targets for extracellular vesicle-based biomarker development [25].

In addition to the proteomics-based comparison of EV samples, we also examined the EV concentration of individual serum samples. Interestingly, no significant differences were detected between the four patient groups regarding the concentration of serum sEVs, with a mean size of 112.2 nm. Osti et al. observed higher EV plasma levels in GBM patients, brain metastases and extra-axial brain tumors compared to healthy controls. Other researchers also demonstrated higher EV concentration in tumorous patients, when unfractionated EV isolates [40] or a wider spectra of EVs were analyzed [41,42]. However, other non-neoplastic diseases of the central nervous system may also increase the number of small-sized circulating EVs, as it was demonstrated in acute ischemic stroke [43] or multiple sclerosis patients [44]. Our vesicle number measurement results, as well as the findings detailed above suggest that the elevated sEV concentration cannot be clearly attributed to the presence of the tumor as immune responses or other systemic responses also contribute to the circulating EV population. Our proteomics-based findings, coupled with the available literature data, suggest that circulating small-sized EVs show important qualitative but not quantitative differences between benign or malignant brain tumors and spinal disc herniation.

Liu and colleagues highlighted that serum is not the perfect choice for a representative sampling of circulating EVs [45], as a high fraction of EVs may be lost during coagulation and also blood components (e.g., platelets) may release microvesicles (MV) during clotting, altering the original MV content of blood samples. However, serum is still the preferred sample form for blood-based clinical diagnoses and it is a practical choice for future clinical developments. It should be noted that co-purification of proteins [46] and lipoprotein particles [47] in EV isolation methods is a common and well known challenge [31]. The presence of protein aggregates [48] and lipoproteins in sEV isolates may provide additional explanation for the lack of increase in the concentration of enriched sEV particles in cancer patients' serum, contrary to literature data on plasma [49] or serum samples [40]. Efforts to eliminate lipoproteins are described in numerous papers reporting on attempts to introduce more sophisticated methods (e.g., combination of ultracentrifugation and size-exclusion chromatography) [50]. In fact, these laborious and instrumentation demanding methods are of high importance in scientific research of the molecular contents of EVs but they may not be applicable in routine clinical practice. Our sEV

isolation protocol has several advantages, as it does not require expensive equipment or highly trained professionals and the entire procedure (along with characterization) is performed within 4 h, therefore, this technique could be easily incorporated into clinical practice.

Our quantitative proteomics results demonstrate that even a simple sEV enrichment protocol can increase the diagnostic potential of serum samples for the identification and classification of patients with different CNS cancers. This finding also supports that even a low-efficacy sEV enrichment/purification method may be appropriate to enhance the analytical applicability of serum samples for CNS cancer monitoring, however, in such cases a quantitative description of enrichment efficiency is definitely required for the right interpretation of the analytical results [51].

In conclusion, our findings support that extracellular vesicles have a greater potential for the monitoring of CNS tumors compared to whole serum samples. Using EV samples is a possible way to amplify the signals released by brain tumors into the circulation. Given the easy-to-implement isolation and enrichment protocol established in this study, the introduction of EV analysis would be beneficial in clinical practice.

4. Materials and Methods

4.1. Patients

Blood samples of 96 patients treated between March 2015 and January 2018 in the Department of Neurosurgery, University of Debrecen were analyzed. Samples were obtained from patients with primary glioblastoma multiforme (GBM), meningioma (M) and single brain metastasis originating from non-small-cell lung cancer (BM). Control samples (CTRL) were collected from patients with spinal disc herniation without evidence of cancer. This non-tumor patient group served as control group in comparison to the patients having different intracranial tumor to distinguish the effects of tumorous processes from the CNS involvement on circulating sEVs. Each group contained 24 individuals with mixed ages and genders. As shown in the Table 1, six-sample-pools were created from the individuals, allowing four parallel samples to be tested per group. Blood samples were collected one day prior to neurosurgical procedure in each tumor case. None of the patients received radio- or chemotherapy before tumor resection. Blood samples were stored by the Neurosurgical Brain Tumor and Tissue Bank of Debrecen according to the criteria of the National Research Ethics Committee. An informed consent form was signed by each patient; the study was conducted in accordance with the Declaration of Helsinki. This study was carried out according to two ethical approvals, namely 51450-2/2015/EKU (0411/15), Medical Research Council, Scientific and Research Ethics Committee, Budapest, October 30, 2015 and 121/2019-SZTE, University of Szeged, Human Investigation Review Board, Albert Szent-Györgyi Clinical Centre, Szeged, 19 July 2019.

Table 1. Patient cohort [1].

♦ Glioblastoma Multiforme	GBM	GBM1	GBM2	GBM3	GBM4
Total No. of patients	***n* = 24**	*n* = 6	*n* = 6	*n* = 6	*n* = 6
Age, Median (range)	**67 (33–82)**	64.5 (38–82)	69.5 (33–76)	67.5 (49–74)	66.5 (63–77)
Mean	**64.9**	62.7	63.8	64.7	68.5
Sex (%), Male	**13 (54.2)**	3 (50)	3 (50)	5 (83.3)	2 (33.3)
Female	**11 (45.8)**	3 (50)	3 (50)	1 (16.7)	4 (66.7)
■ Brain Metastasis	**BM**	**BM1**	**BM2**	**BM3**	**BM4**
Total No. of patients	***n* = 24**	*n* = 6	*n* = 6	*n* = 6	*n* = 6
Age, Median (range)	**64 (42–82)**	66.5 (51–82)	68 (62–71)	63.5 (42–81)	59.5 (53–64)
Mean	**64**	67.7	67.5	59.7	59.5
Sex (%), Male	**13 (54.2)**	2 (33.3)	3 (50)	4 (66.7)	4 (66.7)
Female	**11 (45.8)**	4 (66.7)	3 (50)	2 (33.3)	2 (33.3)
▲ Meningioma	**M**	**M1**	**M2**	**M3**	**M4**

Table 1. *Cont.*

♦ Glioblastoma Multiforme	GBM	GBM1	GBM2	GBM3	GBM4
Total No. of patients	***n* = 24**	*n* = 6	*n* = 6	*n* = 6	*n* = 6
Age, Median (range)	**60 (30–79)**	54.5 (39–69)	62 (30–66)	61.5 (44–75)	66.5 (52–79)
Mean	**58.0**	53.5	53	59.3	66
Sex (%), Male	**4 (16.7)**	0 (0)	0 (0)	1 (16.7)	3 (50)
Female	**20 (83.3)**	6 (100)	6 (100)	5 (83.3)	3 (50)
• **Control**	**CTRL**	**CTRL1**	**CTRL2**	**CTRL3**	**CTRL4**
Total No. of patients	***n* = 24**	*n* = 6	*n* = 6	*n* = 6	*n* = 6
Age, Median (range)	**50.5 (20–81)**	46.5 (26–71)	47 (20–62)	70.5 (49–81)	52.5 (41–69)
Mean	**52.9**	46.5	45	67.2	53
Sex (%), Male	**9 (37.5)**	2 (33.3)	4 (66.7)	4 (66.7)	4 (66.7)
Female	**15 (62.5)**	4 (66.7)	2 (33.3)	2 (33.3)	2 (33.3)

[1] The table summarizes the main characteristics of the patient groups examined. Each group (average values highlighted in bald) included 24 individuals, converted into six-sample-pools to yield four samples per group for further analysis.

4.2. Preparation of Serum Samples, sEV Isolation and Characterization

Blood samples were collected into BD Vacutainer SST II Advance Tubes (Becton, Dickinson and Company, Franklin Lakes, NJ, USA), allowed to clot for at least 1 h at room temperature and centrifuged for 20 min at 3000× *g*, 10 °C to remove cells. Following the 3000× *g* centrifugation, the supernatant serum was transferred to new Eppendorf tubes and centrifuged for 30 min at 10,000× *g*, 4 °C to remove debris and large vesicles. One milliliter serum aliquot was diluted with DPBS (Ca^{2+}-free, Mg^{2+}-free, Lonza Group Ltd., Basel, Switzerland) to 8 mL and ultracentrifuged for 70 min, at 100,000× *g*, 4 °C (polycarbonate tubes, fixed angle T-1270 rotor, Thermo Fisher Scientific, Waltham, MA, USA). The pellet was resuspended in 100 uL DPBS and stored at −80 °C until further processing. This sEV isolation protocol served to reach intermediate recovery and intermediate specificity according to MISEV2018 [31].

SEVs were characterized by AFM (Oxford Instruments Asylum Research, Abingdon, UK), as described previously [52] and NTA using a NanoSight NS300 instrument (Malvern Panalytical Ltd., Malvern, UK) as it described below. Classical EV markers were presented by Western blot analyses using NuPAGE reagents and an XCell SureLock Mini-Cell System (Thermo Fisher Scientific, Waltham, MA, USA) according to manufacturer's protocols. For detection of the CD81 and Alix markers, we used rabbit anti-human CD81 (1:1000, Sigma-Aldrich, St. Louis, MO, USA) and rabbit anti-human Alix (1:1000, Sigma-Aldrich, St. Louis, MO, USA) primary antibody and HRP-conjugated anti-rabbit IgG (1:1000, R&D Systems, Minneapolis, MN, USA) secondary antibody.4.3. Quantitative analysis of sEVs by NTA.

As suggested by a recent study [53], sEVs were diluted in particle free DPBS and analyzed using a NanoSight NS300 instrument with 532 nm laser (Malvern Panalytical Ltd., Malvern, UK). The measurements were performed on the 16 sEV sample pools (described in 4.1). Six videos of 60 s were recorded for each sample under constant settings (Camera level: 15; Treshold: 4, 25 °C; 60–80 particles/frame) and analyzed to obtain data on size distribution and particle concentration.

4.3. Proteomic Analysis by LC-MS

4.3.1. 'In Solution' Digestion

Individual samples containing 20 µg protein were diluted to 10 µL with 0.1 M NH_4HCO_3 (pH = 8.0) buffer; 12 µL 0.1% RapiGest SF (Waters, Milford, MA, USA) and 2 µL 55 mM dithioeritritol solution was added and kept at 60 °C for 30 min to unfold and reduce proteins. A volume of 2 µL 200 mM iodo acetamide solution was added to alkylate the proteins which were kept for an additional 30 min in the dark at room temperature. The samples were digested overnight at 37 °C with trypsin (Thermo

Scientific, Waltham, MA, USA, enzyme/protein ratio: 0.4 to 1). The digestion was stopped by addition of 1 µL of concentrated formic acid.

4.3.2. LC-MS

The separation of the digested samples was carried out on a nanoAcquity UPLC, (Waters, Milford, MA, USA) using Waters ACQUITY UPLC M-Class Peptide C18 (130 Å, 1.78 µm, 75 µm × 250 mm) column with a nonlinear 90 min gradient. Eluents were water (A) and acetonitrile (B) containing 0.1 *V*/*V*% formic acid and the separation of the peptide mixture was performed at 45 °C with 0.35 µL/min flow rate using an optimized nonlinear LC gradient (3–40% B). The LC was coupled to a high-resolution Q Exactive Plus quadrupole-orbitrap hybrid mass spectrometer (Thermo Scientific, Waltham, MA, USA). The quantitative measurements of digested individual samples were performed in DIA mode. The survey scan for DIA method operated with 35,000 resolution. The full scan was performed between 380 to 1020 *m*/*z*. The AGC target was set to 5 × 106 or 120 ms maximum injection time. In the 400–1000 *m*/*z* region 22 *m*/*z* wide overlapping windows were acquired at 17,500 resolution (AGC target: 3 × 106 or 100 ms injection time, normalized collision energy: 27 for charge 2). The quantitative analysis was performed in Encyclopedia 0.81 [54] using default settings after deconvolution, peak picking and conversion of raw MS files to mzML format in Proteowizard [55]. A comprehensive spectral library [56] of 10,000 human proteins was used for peptide identification. Protein quantities calculated by the Encyclopedia software based on summed intensities of the automatically filtered peptides were used in further statistical evaluations.

4.4. Statistical Analysis

The collected data about the whole serum and extracellular vesicles were reduced and analyzed using statistical methods. Pearson's correlation analysis was used to investigate the outlier samples [57], contaminating proteins (cytokeratins) and proteins with missing values were excluded from the proteomic data [58]. Data were log-transformed to reduce skewness and increase linearity [59]. Cohen's d effect size was calculated to measure the difference between the protein intensity means, outcomes in two different groups [60,61]. Pairwise ROC analysis allowed us to find those proteins which can separate at least one group to the others [62]. The calculated ROC AUC (area under the ROC curve) values are accepted if it equals to 1. In order to transform several (potentially) correlated proteins into a (smaller) number of uncorrelated variables and visualize the dataset, PCA with k-means clustering was performed [63–66]. Homogeneity and completeness scores of the clusters were calculated to measure the performance of k-means clustering [67]. Two-tailed Welch's *t*-test was performed to identify the significantly enriched or depleted proteins in sEV samples. The statistical analyses were performed using R statistical program (version 3.6.3 with pROC, FactoMineR, factoextra and ggplot2 packages; Vienna, Austria), Python programming language (version 3.8, Scotts Valley, CA, USA) and Perseus (MaxQuant, Munich, Germany). Values of $p < 0.05$ were considered significant (see in Appendix A more detailed). GraphPad Prism 8 (San Diego, CA, USA) was used for further data visualization.

4.5. In Silico Analysis of LC-MS Data

Protein data derived from the LC-MS were analyzed by the IPA (Qiagen Bioinformatics, Hilden, Germany). Using fold change values, 'Core Analysis' were performed for whole serum and sEV data separately to identify 'Diseases and Functions,' which can be significantly influenced by the described proteomes ($p < 0.05$). After 'Comparison Analysis,' we created heatmaps of the relevant 'Diseases and Functions,' that is, tumor-related and immunological functions showing regulatory differences between the three CNS tumor groups. Activation z-score calculated by IPA indicates the extent and direction of the effect that given proteins have on function/disease.

The selected 10 whole serum proteins and 17 sEV proteins were introduced to custom pathways as well. Then, 'Connect tool' of IPA was used to reveal the relationships between these molecules and

'Grow tool' was applied to search the top ten 'Diseases and Functions' assigned to the 10 whole serum proteins or 17 sEV proteins. Results are displayed in two networks created by the IPA Path Designer.

Confidence level was set to 'Experimentally observed' for all IPA procedures, which enables literature data-based analysis but excludes unproven predictions.

4.6. Data Availability

All datasets generated during the current study are available from the corresponding author upon reasonable request.

We have submitted all relevant data of our experiments to the EV-TRACK [68] knowledgebase EV-TRACK ID: EV200080.

5. Conclusions

Our study aimed to detect the characteristic protein fingerprint of the most common CNS tumors. Intending to amplify the signal that brain tumors release into the circulation, in addition to the whole serum's, the protein content of the small extracellular vesicles isolated from the serum was also examined.

Comparative proteomic analysis suggests that sEVs may be more suitable for investigating tumor related molecular patterns, because these molecules are present in higher concentrations in sEV samples compared to whole serum samples and have less 'noise' that may bias the analytical findings. In silico analyses revealed that the biological background of the sEV-based characteristic protein profile of the samples is more specifically associated with the tumor types compared with the whole serum based protein profile. Samples enriched in sEVs can offer an amplified source of relevant information, representing not only the specific tumor tissue but also the associated immune responses.

These findings revealed that circulating small-sized extracellular vesicles were more suitable for separating different patient groups. The number of proteins applied for monitoring cannot be reduced to a few individual molecules, instead, a specific protein panel is required for perfect differentiation. To the best of our knowledge, we are the first group to quantitatively compare the proteome of serum derived small extracellular vesicles with that of the original whole serum samples.

In conclusion, our findings support that extracellular vesicles have a greater potential for monitoring CNS tumors, compared to whole serum samples. Considering that analyzing sEVs can be performed easily, incorporating our method into clinical practice would be of great benefit.

Supplementary Materials: Supplementary materials can be found at http://www.mdpi.com/1422-0067/21/15/5359/s1. Figure S1: Western blot analyses of classical EV markers, Figure S2: Intragroup Coefficients of variation (CV) distributions, Figure S3: PCA dotplot constructed after statistical selection based on the means of intensity ratio; Table S1: 311 membered protein table of DIA mode constructed spectral library; Table S2: Sample correlation matrix; Table S3: List of the selected proteins.

Author Contributions: Conceptualization, K.B.; methodology, G.D. and K.B.; validation, G.D., B.B. and A.J.; formal analysis G.D., M.B., Z.S., M.H., M.S.; investigation, G.D., M.B. and E.G.-S.; resources, A.K., P.H., T.B. and K.B.; writing—original draft preparation, G.D., M.B., Z.S. and M.H.; writing—review and editing, G.D. and K.B.; visualization, G.D, M.B., Z.S. and M.H.; supervision, A.K. and K.B.; project administration, G.D. and K.B.; funding acquisition, K.B. All authors have read and agreed to publish the final version of the manuscript.

Funding: This study was founded by the following research grants: GINOP-2.3.2-15-2016-00015 (K.B.); GINOP-2.2.1-15-2017-00052 (K.B.), 2017-1.2.1-NKP-2017-00002 "National Brain Research Program NAP 2.0" (A.K.), UNKP-19-4-SZTE-63 (K.B.), Janos Bolyai Research Scholarship of the Hungarian Academic of Sciences (K.B.).

Acknowledgments: The authors thank Lilla Pinter for her technical assistance and Zsolt Szegletes for taking the AFM images. The authors thank Dora Bokor, PharmD, for proofreading the manuscript.

Conflicts of Interest: The authors declare no conflict of interest. The funders had no role in the design of the study; in the collection, analyses, or interpretation of data; in the writing of the manuscript, or in the decision to publish the results.

Abbreviations

AFM	Atomic force microscopy
BBB	Blood brain barrier
BM	Brain metastasis originating from non-small-cell lung cancer
CNS	Central nervous system
CTRL	Controls – lumbar disc hernia patients
DIA	Data independent acquisition
EVs	Extracellular Vesicles
GBM	Primary glioblastoma multiforme
IPA	Ingenuity Pathway Analysis
LC-MS	Liquid chromatography - mass spectrometry
M	Meningioma
NTA	Nanoparticle tracking analysis
PCA	Principal component analysis
ROC	Receiver operating characteristic
sEVs	small extracellular vesicles

Appendix A. Detailed Description of the Statistical Analyses.

The collected data about the whole serum and extracellular vesicles were reduced and analyzed using statistical methods. Pearson's correlation analysis was used to investigate the outlier samples [57]. Contaminating proteins (cytokeratins) and proteins with missing values were excluded from the proteomic data [58]. Data were log-transformed to reduce skewness and increase linearity [59].

Cohen's d effect size was calculated to measure the difference between the protein intensity mean, outcomes in two different groups. The formula of the Cohen's d effect size

$$d = \frac{\left|\overline{X}_1 - \overline{X}_2\right|}{\sqrt{\frac{(n_1-1)SD_1^2+(n_2-1)SD_2^2}{n_1+n_2-2}}}$$

where X is the mean protein intensity in a given group, SD is standard deviation and n is sample size [60]. In this study we say at least 2 effect size is necessary. It indicates that the mean of group 1 is at the 97.7 percentile of group 2, and the nonoverlapping area of the two distributions at least is 81.1% [61].

Pairwise ROC analysis allowed us to find those proteins which can separate at least one group to the others [62]. The ROC analysis use the true positive rate (sensitivity) and the true negative rate (specificity) at various threshold settings. Plotting the sensitivity against the 1-specificity we get the ROC curve, under the area under this curve measure the separability of the given variable (protein). AUC = 0.5 represents an unsuitable variable to the separate two groups. If AUC = 1, the separation using the actual variable is error-free. In our study the calculated AUC (area under the curve) values are accepted if it equals to 1.

In order to transform several (potentially) correlated proteins into a (smaller) number of uncorrelated variables, and visualize the dataset, principal component analysis (PCA) with k-means clustering was performed. The goal of PCA is to reduce a large number of correlated variables with a set of uncorrelated principal components. These components can be thought of as linear combinations of the original variables that are optimally weighted and derived from the correlation matrix of the data [63].

K-means clustering was performed on the obtained PCA score plots by Hartigan-Wong algorithm [64,65]. Optimal numbers of clusters were determined with Silhouette method and these recommended values were used for clustering [66].

Homogeneity and completeness scores of the clusters were calculated to measure the performance of k-means clustering Cluster homogeneity and completeness mean that each cluster contains only

samples from the same group, and all samples of a given group are assigned to the same cluster. Both scores are bounded below by 0 and above by 1. A score of 1 indicates the perfect homogeneity or completeness. [67].

Two-tailed Welch's t-test was performed to identify significantly enriched or depleted proteins in sEV samples.

The statistical analyses were performed using R statistical program (version 3.6.3 with pROC, FactoMineR, factoextra and ggplot2 packages), Python programming language (version 3.8) and Perseus (MaxQuant). Values of $p < 0.05$ were considered significant. GraphPad Prism 8 was used for further data visualization.

References

1. World Health Organization. *WHO Guidelines for the Pharmacological and Radiotherapeutic Management of Cancer Pain in Adults and Adolescents*; World Health Organization, 2018; License: CC BY-NC-SA 3.0 IGO. Available online: https://apps.who.int/iris/handle/10665/279700 (accessed on 1 June 2020).
2. World Health Organization. *Guide to Cancer Early Diagnosis*; World Health Organization, 2017; License: CC BY-NC-SA 3.0 IGO. Available online: https://apps.who.int/iris/handle/10665/254500 (accessed on 1 June 2020).
3. Garden, G.A.; Campbell, B.M. Glial biomarkers in human central nervous system disease. *Glia* **2016**, *64*, 1755–1771. [CrossRef] [PubMed]
4. Staedtke, V.; Dzaye, O.; Holdhoff, M. Actionable molecular biomarkers in primary brain tumors. *Trends Cancer* **2016**, *2*, 338–349. [CrossRef] [PubMed]
5. Good, D.M.; Thongboonkerd, V.; Novak, J.; Bascands, J.L.; Schanstra, J.P.; Coon, J.J.; Dominiczak, A.; Mischak, H. Body fluid proteomics for biomarker discovery: Lessons from the past hold the key to success in the future. *J. Proteome Res.* **2007**, *6*, 4549–4555. [CrossRef] [PubMed]
6. Best, M.G.; Sol, N.; Zijl, S.; Reijneveld, J.C.; Wesseling, P.; Wurdinger, T. Liquid biopsies in patients with diffuse glioma. *Acta Neuropathol.* **2015**, *129*, 849–865. [CrossRef] [PubMed]
7. Gerber, D.E.; Grossman, S.A.; Zeltzman, M.; Parisi, M.A.; Kleinberg, L. The impact of thrombocytopenia from temozolomide and radiation in newly diagnosed adults with high-grade gliomas. *Neuro Oncol.* **2007**, *9*, 47–52. [CrossRef]
8. Cagney, D.N.; Sul, J.; Huang, R.Y.; Ligon, K.L.; Wen, P.Y.; Alexander, B.M. The FDA NIH Biomarkers, EndpointS and other Tools (BEST) resource in neuro-oncology. *Neuro Oncol.* **2018**, *20*, 1162–1172. [CrossRef]
9. Sheridan, C. Exosome cancer diagnostic reaches market. *Nat. Biotechnol.* **2016**, *34*, 359–360. [CrossRef]
10. Colombo, M.; Raposo, G.; Théry, C. Biogenesis, secretion and intercellular interactions of exosomes and other extracellular vesicles. *Annu. Rev. Cell Dev. Biol* **2014**, *30*, 255–289. [CrossRef] [PubMed]
11. Nogués, L.; Benito-Martin, A.; Hergueta-Redondo, M.; Peinado, H. The influence of tumour-derived extracellular vesicles on local and distal metastatic dissemination. *Mol. Asp. Med.* **2018**, *60*, 15–26. [CrossRef]
12. Hoshino, A.; Costa-Silva, B.; Shen, T.L.; Rodrigues, G.; Hashimoto, A.; Tesic Mark, M.; Molina, H.; Kohsaka, S.; Di Giannatale, A.; Ceder, S.; et al. Tumour exosome integrins determine organotropic metastasis. *Nature* **2015**, *527*, 329–335. [CrossRef] [PubMed]
13. Costa-Silva, B.; Aiello, N.M.; Ocean, A.J.; Singh, S.; Zhang, H.; Thakur, B.K.; Becker, A.; Hoshino, A.; Mark, M.T.; Molina, H.; et al. Pancreatic cancer exosomes initiate pre-metastatic niche formation in the liver. *Nat. Cell Biol.* **2015**, *17*, 816–826. [CrossRef] [PubMed]
14. Liu, Y.; Gu, Y.; Han, Y.; Zhang, Q.; Jiang, Z.; Zhang, X.; Huang, B.; Xu, X.; Zheng, J.; Cao, X. Tumor Exosomal RNAs Promote Lung Pre-metastatic Niche Formation by Activating Alveolar Epithelial TLR3 to Recruit Neutrophils. *Cancer Cell* **2016**, *30*, 243–256. [CrossRef] [PubMed]
15. Zeng, Z.; Li, Y.; Pan, Y.; Lan, X.; Song, F.; Sun, J.; Zhou, K.; Liu, X.; Ren, X.; Wang, F.; et al. Cancer-derived exosomal miR-25-3p promotes pre-metastatic niche formation by inducing vascular permeability and angiogenesis. *Nat. Commun.* **2018**, *9*, 5395. [CrossRef] [PubMed]
16. Feng, W.; Dean, D.C.; Hornicek, F.J.; Shi, H.; Duan, Z. Exosomes promote pre-metastatic niche formation in ovarian cancer. *Mol. Cancer* **2019**, *18*, 124. [CrossRef] [PubMed]
17. Chen, G.; Huang, A.C.; Zhang, W.; Zhang, G.; Wu, M.; Xu, W.; Yu, Z.; Yang, J.; Wang, B.; Sun, H.; et al. Exosomal PD-L1 contributes to immunosuppression and is associated with anti-PD-1 response. *Nature* **2018**, *560*, 382–386. [CrossRef] [PubMed]

18. Scavo, M.P.; Depalo, N.; Tutino, V.; De Nunzio, V.; Ingrosso, C.; Rizzi, F.; Notarnicola, M.; Curri, M.L.; Giannelli, G. Exosomes for Diagnosis and Therapy in Gastrointestinal Cancers. *Int. J. Mol. Sci.* **2020**, *21*, 367. [CrossRef] [PubMed]
19. Basu, B.; Ghosh, M.K. Extracellular Vesicles in Glioma: From Diagnosis to Therapy. *Bioessays* **2019**, *41*, e1800245. [CrossRef]
20. Kosaka, N.; Kogure, A.; Yamamoto, T.; Urabe, F.; Usuba, W.; Prieto-Vila, M.; Ochiya, T. Exploiting the message from cancer: The diagnostic value of extracellular vesicles for clinical applications. *Exp. Mol. Med.* **2019**, *51*, 31. [CrossRef]
21. Möhrmann, L.; Huang, H.J.; Hong, D.S.; Tsimberidou, A.M.; Fu, S.; Piha-Paul, S.A.; Subbiah, V.; Karp, D.D.; Naing, A.; Krug, A. Liquid biopsies using plasma exosomal nucleic acids and plasma cell-free DNA compared with clinical outcomes of patients with advanced cancers. *Clin. Cancer Res.* **2018**, *24*, 181–188. [CrossRef]
22. Melo, S.A.; Luecke, L.B.; Kahlert, C.; Fernandez, A.F.; Gammon, S.T.; Kaye, J.; LeBleu, V.S.; Mittendorf, E.A.; Weitz, J.; Rahbari, N.; et al. Glypican-1 identifies cancer exosomes and detects early pancreatic cancer. *Nature* **2015**, *523*, 177–182. [CrossRef]
23. Choy, C.; Jandial, R. Breast Cancer Exosomes Breach the Blood-Brain Barrier. *Neurosurgery* **2016**, *78*, N10-1. [CrossRef] [PubMed]
24. García-Romero, N.; Carrión-Navarro, J.; Esteban-Rubio, S.; Lázaro-Ibáñez, E.; Peris-Celda, M.; Alonso, M.M.; Guzmán-De-Villoria, J.; Fernández-Carballal, C.; de Mendivil, A.O.; García-Duque, S.; et al. DNA sequences within glioma-derived extracellular vesicles can cross the intact blood-brain barrier and be detected in peripheral blood of patients. *Oncotarget* **2017**, *8*, 1416–1428. [CrossRef] [PubMed]
25. Gollapalli, K.; Ray, S.; Srivastava, R.; Renu, D.; Singh, P.; Dhali, S.; Bajpai Dikshit, J.; Srikanth, R.; Moiyadi, A.; Srivastava, S. Investigation of serum proteome alterations in human glioblastoma multiforme. *Proteomics* **2012**, *12*, 2378–2390. [CrossRef] [PubMed]
26. Gállego Pérez-Larraya, J.; Paris, S.; Idbaih, A.; Dehais, C.; Laigle-Donadey, F.; Navarro, S.; Capelle, L.; Mokhtari, K.; Marie, Y.; Sanson, M.; et al. Diagnostic and prognostic value of preoperative combined GFAP, IGFBP-2 and YKL-40 plasma levels in patients with glioblastoma. *Cancer* **2014**, *120*, 3972–3980. [CrossRef] [PubMed]
27. Figueroa, J.M.; Carter, B.S. Detection of glioblastoma in biofluids. *J. Neurosurg.* **2018**, *129*, 334–340. [CrossRef] [PubMed]
28. Ostrom, Q.T.; Gittleman, H.; Truitt, G.; Boscia, A.; Kruchko, C.; Barnholtz-Sloan, J.S. CBTRUS Statistical Report: Primary Brain and Other Central Nervous System Tumors Diagnosed in the United States in 2011-2015. *Neuro Oncol.* **2018**, *20*, iv1–iv86. [CrossRef]
29. Fox, B.D.; Cheung, V.J.; Patel, A.J.; Suki, D.; Rao, G. Epidemiology of Metastatic Brain Tumors. *Neurosurg. Clin. N. Am.* **2011**, *22*, 1–6. [CrossRef]
30. Théry, C.; Witwer, K.W.; Aikawa, E.; Alcaraz, M.J.; Anderson, J.D.; Andriantsitohaina, R.; Antoniou, A.; Arab, T.; Archer, F.; Atkin-Smith, G.K.; et al. Minimal information for studies of extracellular vesicles 2018 (MISEV2018): A position statement of the International Society for Extracellular Vesicles and update of the MISEV2014 guidelines. *J. Extracell. Vesicles* **2018**, *7*, 1535750. [CrossRef]
31. de Menezes-Neto, A.; Sáez, M.J.; Lozano-Ramos, I.; Segui-Barber, J.; Martin-Jaular, L.; Ullate, J.M.; Fernandez-Becerra, C.; Borrás, F.E.; Del Portillo, H.A. Size-exclusion chromatography as a stand-alone methodology identifies novel markers in mass spectrometry analyses of plasma-derived vesicles from healthy individuals. *J. Extracell. Vesicles* **2015**, *4*, 27378. [CrossRef]
32. Weber, M.A.; Zoubaa, S.; Schlieter, M.; Jüttler, E.; Huttner, H.B.; Geletneky, K.; Ittrich, C.; Lichy, M.P.; Kroll, A.; Debus, J.; et al. Essig Diagnostic performance of spectroscopic and perfusion MRI for distinction of brain tumors. *Neurology* **2006**, *66*, 1899–1906. [CrossRef]
33. Shankar, G.M.; Balaj, L.; Stott, S.L.; Nahed, B.; Carter, B.S. Liquid biopsy for brain tumors. *Expert Rev. Mol. Diagn.* **2017**, *17*, 943–947. [CrossRef] [PubMed]
34. Marrugo-Ramírez, J.; Mir, M.; Samitier, J. Blood-Based Cancer Biomarkers in Liquid Biopsy: A Promising Non-Invasive Alternative to Tissue Biopsy. *Int. J. Mol. Sci.* **2018**, *21*, 2877. [CrossRef] [PubMed]
35. Miyauchi, E.; Furuta, T.; Ohtsuki, S.; Tachikawa, M.; Uchida, Y.; Sabit, H.; Obuchi, W.; Baba, T.; Watanabe, M.; Terasaki, T.; et al. Identification of blood biomarkers in glioblastoma by SWATH mass spectrometry and quantitative targeted absolute proteomics. *PLoS ONE* **2018**, *13*, e0193799. [CrossRef] [PubMed]

36. Rhie, S.K.; Perez, A.A.; Lay, F.D.; Schreiner, S.; Shi, J.; Polin, J.; Farnham, P.J. A high-resolution 3D epigenomic map reveals insights into the creation of the prostate cancer transcriptome. *Nat. Commun.* **2019**, *10*, 4154. [CrossRef] [PubMed]
37. Anderson, K.S.; LaBaer, J. The sentinel within: Exploiting the immune system for cancer biomarkers. *J. Proteome Res.* **2005**, *4*, 1123–1133. [CrossRef] [PubMed]
38. Wen, C.; Seeger, R.C.; Fabbri, M.; Wang, L.; Wayne, A.S.; Jong, A.Y. Biological roles and potential applications of immune cell-derived extracellular vesicles. *J. Extracell. Vesicles* **2017**, *6*, 1400370. [CrossRef] [PubMed]
39. Veerman, R.E.; Güçlüler Akpinar, G.; Eldh, M.; Gabrielsson, S. Immune Cell-Derived Extracellular Vesicles –Functions and Therapeutic Applications. *Trends Mol. Med.* **2019**, *25*, 382–394. [CrossRef]
40. Gercel-Taylor, C.; Atay, S.; Tullis, R.H.; Kesimer, M.; Taylor, D.D. Nanoparticle analysis of circulating cell-derived vesicles in ovarian cancer patients. *Anal. Biochem.* **2012**, *428*, 44–53. [CrossRef]
41. Lázaro-Ibáñez, E.; Sanz-Garcia, A.; Visakorpi, T.; Escobedo-Lucea, C.; Siljander, P.; Ayuso-Sacido, A.; Yliperttula, M. Different gDNA content in the subpopulations of prostate cancer extracellular vesicles: Apoptotic bodies, microvesicles and exosomes. *Prostate* **2014**, *74*, 1379–1390. [CrossRef]
42. König, L.; Kasimir-Bauer, S.; Bittner, A.K.; Hoffmann, O.; Wagner, B.; Santos Manvailer, L.F.; Kimmig, R.; Horn, P.A.; Rebmann, V. Elevated levels of extracellular vesicles are associated with therapy failure and disease progression in breast cancer patients undergoing neoadjuvant chemotherapy. *Oncoimmunology* **2017**, *27*, e1376153. [CrossRef]
43. Ji, Q.; Ji, Y.; Peng, J.; Zhou, X.; Chen, X.; Zhao, H.; Xu, T.; Chen, L.; Xu, Y. Increased Brain-Specific MiR-9 and MiR-124 in the Serum Exosomes of Acute Ischemic Stroke Patients. *PLoS ONE* **2016**, *11*, e0163645. [CrossRef] [PubMed]
44. Galazka, G.; Mycko, M.P.; Selmaj, I.; Raine, C.S.; Selmaj, K.W. Multiple sclerosis: Serum-derived exosomes express myelin proteins. *Mult. Scler.* **2018**, *24*, 449–458. [CrossRef] [PubMed]
45. Liu, M.-L.; Werth, V.P.; Williams, K.J. Blood plasma versus serum: Which is right for sampling circulating membrane microvesicles in human subjects? *Ann. Rheum. Dis.* **2020**, *79*, e73. [CrossRef] [PubMed]
46. Smolarz, M.; Pietrowska, M.; Matysiak, N.; Mielańczyk, Ł.; Widłak, P. Proteome Profiling of Exosomes Purified from a Small Amount of Human Serum: The Problem of Co-Purified Serum Components. *Proteomes* **2019**, *7*, 18. [CrossRef]
47. Sódar, B.W.; Kittel, Á.; Pálóczi, K.; Vukman, K.V.; Osteikoetxea, X.; Szabó-Taylor, K.; Németh, A.; Sperlágh, B.; Baranyai, T.; Giricz, Z.; et al. Low-density lipoprotein mimics blood plasma-derived exosomes and microvesicles during isolation and detection. *Sci. Rep.* **2016**, *6*, 24316. [CrossRef] [PubMed]
48. Filipe, V.; Hawe, A.; Jiskoot, W. Critical evaluation of Nanoparticle Tracking Analysis (NTA) by NanoSight for the measurement of nanoparticles and protein aggregates. *Pharm. Res.* **2010**, *27*, 796–810. [CrossRef] [PubMed]
49. Osti, D.; Del Bene, M.; Rappa, G.; Santos, M.; Matafora, V.; Richichi, C.; Faletti, S.; Beznoussenko, G.V.; Mironov, A.; Bachi, A.; et al. Clinical Significance of Extracellular Vesicles in Plasma from Glioblastoma Patients. *Clin. Cancer Res.* **2019**, *25*, 266–276. [CrossRef]
50. Karimi, N.; Cvjetkovic, A.; Jang, S.C.; Crescitelli, R.; Hosseinpour Feizi, M.A.; Nieuwland, R.; Lötvall, J.; Lässer, C. Detailed analysis of the plasma extracellular vesicle proteome after separation from lipoproteins. *Cell Mol. Life Sci.* **2018**, *75*, 2873–2886. [CrossRef]
51. Xu, R.; Greening, D.W.; Zhu, H.J.; Takahashi, N.; Simpson, R.J. Extracellular vesicle isolation and characterization: Toward clinical application. *J. Clin. Investig.* **2016**, *126*, 1152–1162. [CrossRef]
52. Harmati, M.; Tarnai, Z.; Decsi, G.; Kormondi, S.; Szegletes, Z.; Janovak, L.; Dekany, I.; Saydam, O.; Gyukity-Sebestyen, E.; Dobra, G.; et al. Stressors alter intercellular communication and exosome profile of nasopharyngeal carcinoma cells. *J. Oral Pathol. Med.* **2017**, *46*, 259–266. [CrossRef]
53. Parsons, M.E.M.; McParland, D.; Szklanna, P.B.; Guang, M.H.Z.; O'Connell, K.; O'Connor, H.D.; McGuigan, C.; Ní Áinle, F.; McCann, A.; Maguire, P.B. A Protocol for Improved Precision and Increased Confidence in Nanoparticle Tracking Analysis Concentration Measurements between 50 and 120 nm in Biological Fluids. *Front. Cardiovasc. Med.* **2017**, *4*, 68. [CrossRef] [PubMed]
54. Searle, B.C.; Pino, L.K.; Egertson, J.D.; Ting, Y.S.; Lawrence, R.T.; MacLean, B.X.; Villén, J.; MacCoss, M.J. Chromatogram libraries improve peptide detection and quantification by data independent acquisition mass spectrometry. *Nat. Commun.* **2018**, *9*, 5128. [CrossRef] [PubMed]

55. Chambers, M.; Maclean, B.; Burke, R.; Amodei, D.; Ruderman, D.L.; Neumann, S.; Gatto, L.; Fischer, B.; Pratt, B.; Egertson, J.; et al. A cross-platform toolkit for mass spectrometry and proteomics. *Nat. Biotechnol.* **2012**, *30*, 918–920. [CrossRef] [PubMed]
56. Rosenberger, G.; Koh, C.C.; Guo, T.; Röst, H.L.; Kouvonen, P.; Collins, B.C.; Heusel, M.; Liu, Y.; Caron, E.; Vichalkovski, A.; et al. A repository of assays to quantify 10,000 human proteins by SWATH-MS. *Sci. Data* **2014**, *1*, 140031. [CrossRef] [PubMed]
57. Metz, T.O.; Qian, W.J.; Jacobs, J.M.; Gritsenko, M.A.; Moore, R.J.; Polpitiya, A.D.; Monroe, M.E.; Camp, D.G., 2nd; Mueller, P.W.; Smith, R.D. Application of proteomics in the discovery of candidate protein biomarkers in a diabetes autoantibody standardization program sample subset. *J. Proteome Res.* **2008**, *7*, 698–707. [CrossRef] [PubMed]
58. Hodge, K.; Have, S.T.; Hutton, L.; Lamond, A.I. Cleaning up the masses: Exclusion lists to reduce contamination with HPLC-MS/MS. *J. Proteom.* **2013**, *88*, 92–103. [CrossRef] [PubMed]
59. Curran-Everett, D. Explorations in statistics: The log transformation. *Adv. Physiol. Educ.* **2018**, *42*, 343–347. [CrossRef]
60. Lakens, D. Calculating and reporting effect sizes to facilitate cumulative science: A practical primer for t-tests and ANOVAs. *Front. Psychol.* **2013**, *4*, 863. [CrossRef]
61. Cohen, J. *Statistical Power Analysis for the Behavioral Sciences*, 2nd ed.; Routledge: New York, NY, USA, 1988. [CrossRef]
62. Fawcett, T. An introduction to ROC analysis. *Pattern Recognit. Lett.* **2006**, *27*, 861–874. [CrossRef]
63. Husson, F.; Le, S.; Pagès, J. *Exploratory Multivariate Analysis by Example Using R*, 2nd ed.; Chapman and Hall/CRC: New York, NY, USA, 2017. [CrossRef]
64. Hartigan, J.A.; Wong, M.A. Algorithm AS 136: A K-Means Clustering Algorithm. *J. Appl. Stat.* **1979**, *28*, 100. [CrossRef]
65. Ding, C.; He, X. K-means clustering via principal component analysis. In Proceedings of the Twenty-First International Conference on Machine Learning, Banff, AB, Canada, 4–8 July 2004; Association for Computing Machinery: New York, NY, USA, 2004. [CrossRef]
66. Rousseeuw, P.J. Silhouettes: A graphical aid to the interpretation and validation of cluster analysis. *J. Comput. Appl. Math.* **1987**, *20*, 53–65. [CrossRef]
67. Pedregosa, F.; Varoquaux, G.; Gramfort, A.; Michel, V.; Thirion, B.; Grisel, O.; Blondel, M.; Prettenhofer, P.; Weiss, R.; Dubourg, V.; et al. Scikit-learn: Machine Learning in Python. *J. Mach. Learn. Res.* **2012**, *12*, 2825–2830.
68. Van Deun, J.; Mestdagh, P.; Agostinis, P.; Akay, Ö.; Anand, S.; Anckaert, J.; Martinez, Z.A.; Baetens, T.; Beghein, E.; Bertier, L.; et al. EV-TRACK: Transparent reporting and centralizing knowledge in extracellular vesicle research. *Nat. Methods* **2017**, *14*, 228–232. [CrossRef] [PubMed]

cancers

MDPI

Article

MMP-9 as Prognostic Marker for Brain Tumours: A Comparative Study on Serum-Derived Small Extracellular Vesicles

Gabriella Dobra [1,2,3], Edina Gyukity-Sebestyén [1,3], Mátyás Bukva [1,2,3], Mária Harmati [1,3], Valentina Nagy [1,3], Zoltán Szabó [4], Tibor Pankotai [5,6], Álmos Klekner [7] and Krisztina Buzás [1,3,*]

1 Laboratory of Microscopic Image Analysis and Machine Learning, Institute of Biochemistry, Biological Research Centre, Eötvös Loránd Research Network (ELKH), H-6726 Szeged, Hungary
2 Doctoral School of Interdisciplinary Medicine, Albert Szent-Györgyi Medical School, University of Szeged, H-6720 Szeged, Hungary
3 Department of Immunology, Albert Szent-Györgyi Medical School, Faculty of Science and Informatics, University of Szeged, H-6720 Szeged, Hungary
4 Department of Medical Chemistry, Albert Szent-Györgyi Medical School, University of Szeged, H-6720 Szeged, Hungary
5 Institute of Pathology, Albert Szent-Györgyi Medical School, University of Szeged, H-6720 Szeged, Hungary
6 Genome Integrity and DNA Repair Group, Hungarian Centre of Excellence for Molecular Medicine (HCEMM), University of Szeged, H-6720 Szeged, Hungary
7 Department of Neurosurgery, Faculty of Medicine, University of Debrecen, H-4032 Debrecen, Hungary
* Correspondence: buzas.krisztina@brc.hu; Tel.: +36-62-432-340

Simple Summary: The invasive nature of brain tumours, particularly glioblastoma, severely limits its therapy. Matrix-metalloproteinases (MMPs), enzymes involved in the degradation of the extracellular matrix, are associated with the invasiveness of brain tumours; hence, the determination of MMPs is critical for the monitoring of cancer patients. The aim of our comparative study was to evaluate the possible additional utility of the MMP-9 level of serum-derived small extracellular vesicles (sEVs) for characterising brain tumours. We established a relationship between low MMP-9 content in sEVs and improved survival, and discovered that MMP-9 levels considerably differed between tumour types and stages, showing a positive correlation with aggressiveness. We demonstrated on a large number of samples that the high MMP-9 level of serum-sEVs may serve as a negative prognostic marker for brain tumours.

Abstract: Matrix metalloproteinase-9 (MMP-9) degrades the extracellular matrix, contributes to tumour cell invasion and metastasis, and its elevated level in brain tumour tissues indicates poor prognosis. High-risk tissue biopsy can be replaced by liquid biopsy; however, the blood–brain barrier (BBB) prevents tumour-associated components from entering the peripheral blood, making the development of blood-based biomarkers challenging. Therefore, we examined the MMP-9 content of small extracellular vesicles (sEVs)—which can cross the BBB and are stable in body fluids—to characterise tumours with different invasion capacity. From four patient groups (glioblastoma multiforme, brain metastases of lung cancer, meningioma, and lumbar disc herniation as controls), 222 serum-derived sEV samples were evaluated. After isolating and characterising sEVs, their MMP-9 content was measured by ELISA and assessed statistically (correlation, paired *t*-test, Welch's test, ANOVA, ROC). We found that the MMP-9 content of sEVs is independent of gender and age, but is affected by surgical intervention, treatment, and recurrence. We found a relation between low MMP-9 level in sEVs (<28 ppm) and improved survival (8-month advantage) of glioblastoma patients, and MMP-9 levels showed a positive correlation with aggressiveness. These findings suggest that vesicular MMP-9 level might be a useful prognostic marker for brain tumours.

Keywords: liquid biopsy; small extracellular vesicles; matrix metalloproteinase-9; central nervous system diseases; brain tumour; prognostic marker; survival; glioblastoma

Citation: Dobra, G.; Gyukity-Sebestyén, E.; Bukva, M.; Harmati, M.; Nagy, V.; Szabó, Z.; Pankotai, T.; Klekner, Á.; Buzás, K. MMP-9 as Prognostic Marker for Brain Tumours: A Comparative Study on Serum-Derived Small Extracellular Vesicles. *Cancers* **2023**, *15*, 712. https://doi.org/10.3390/cancers15030712

Academic Editor: Maxim V. Berezovski

Received: 19 December 2022
Revised: 15 January 2023
Accepted: 21 January 2023
Published: 24 January 2023

1. Introduction

In tumour diagnostics, computed tomography (CT) and magnetic resonance imaging (MRI) scans are used to determine disease status, as well as to evaluate the response to treatments [1]; however, these techniques have well-known limitations [2]. MRI, for instance, can only detect tumour masses of sufficient size, and the treatment-related changes may overlap with residual or recurrent tumours [3]. Furthermore, it is also difficult to distinguish between central nervous system (CNS) malignancies such as glioblastoma multiforme and brain metastases [4], and MRI has limited applicability to identify long-term recurrence [5].

Further standard methods for profiling tumours require obtaining tumour samples through invasive surgical procedures. In addition to carrying a high risk of complications, the limitations of such invasive procedures include difficulty in acquiring tumour samples with high heterogeneity or in inaccessible positions and taking multiple biopsies in the occurrence of metastases, as well as monitoring tumour response or relapse. Thus, neuro-oncological research aims to discover novel methods suitable for monitoring CNS tumours in clinical practice [6].

Considering the challenges associated with traditional biopsies, recent oncology research has turned its focus from analysing whole tissues to analysing various biological fluids for tumour-derived components [7–9]; this technique is known as liquid biopsy (LB). LBs have drastically revolutionised the field of clinical oncology, offering ease in tumour sampling, continuous monitoring by repeated sampling, devising personalised therapeutic regimens, and screening for therapeutic resistance [10]. Tumour tissues release proteins, nucleic acids, circulating tumour cells, platelets, and tumour-derived extracellular vesicles into the bloodstream [11]; all these may serve as cancer biomarkers accessible via LB.

Extracellular vesicles (EVs) are small, lipid bilayer-enclosed vesicles released by both normal and neoplastic cells into the extracellular space [12] which enter into the circulation [13–15]. EVs are promising cancer biomarkers accessible through LB because they are cell-secreted, nano-sized, and stable in all body fluids [16,17]. Evs contain a sample of cytosolic milieu of the donor cells, including an abundance of DNA, RNA, proteins, and other analytes [18–21], while externally they also resemble their cell of origin [22]. Mounting evidence indicates that EVs contain a wealth of information that can be used to improve cancer diagnosis and prognostic evaluation [23–25]. The majority of the studies mainly focused on nucleic acids [26], but EV proteins are also receiving more and more attention in cancer diagnostics [27,28].

Finding blood–based biomarkers for CNS tumour monitoring is more challenging, as the blood–brain barrier (BBB) may prevent the release of tumour-related biomarkers into peripheral blood. The available evidence supports that tumour-derived EVs can cross the BBB [29,30]. However, currently no clinically relevant EV biomarkers are accepted for the monitoring of CNS tumours.

In a previous study, we analysed the protein content of whole serum as well as serum-derived small extracellular vesicles (sEVs)—EVs with a diameter of 30–200 nm size [31], theoretically called exosomes—of 96 patients suffering from CNS diseases. Comparative proteomic analysis by liquid chromatography–mass spectrometry (LC-MS) revealed that samples enriched in sEVs can provide an amplified source of relevant information; thus, sEVs may be more suitable than whole sera for separating patients with distinct CNS diseases using a protein panel [32]. Among the proteins of the determined panel, the matrix metalloproteinase-9 (MMP-9) was the most effective candidate in the separation of the patient groups.

Matrix metalloproteinases (MMPs) are zinc-dependent endopeptidases that play an essential role in the physiology of cells by degrading the extracellular matrix (ECM) [33]. It has been found that ECM has an important role also in cancer progression [34]. Some ECM proteins, such as fibronectin, thrombospondin-1, laminin, and osteopontin influence the phenotype of the tumour by affecting cell migration or angiogenesis. Interaction between cancer cells and ECM components is essential for cell transformation as well as

carcinogenesis [35]. In addition to the ECM degradation, MMPs have multiple biological functions in all stages of cancer, from initiation to the development of metastases [36–38]. Although they are associated with cancer cell survival and tumour spread, MMPs are synthetised by cancer cells in a very small amount. By secreting interleukin, interferon, growth factors, and extracellular MMP inductors, cancer cells stimulate surrounding host cells to produce MMPs in a paracrine manner [39]. MMPs secreted by normal cells can be bound to the cancer cell surface and can be utilised by the tumour cells [34].

Matrix metalloproteinase-9 (also known as 92 kDa type IV collagenase or gelatinase B) is one of the most complex forms of MMPs [33]. The role of MMP-9 in tumour tissue invasion and metastasis formation was already described in 1990 [40], and the elevated levels of MMP-9 in human brain tumours was also been reported in the 1990's [41]. Rao et al. also showed that the expression of MMP-9 is significantly upregulated in highly malignant gliomas and correlates with the progression, suggesting a role for MMP-9 in promoting the observed invasiveness [42].

In recent decades, several studies reported the upregulation of MMP-9 in the source of tumour tissue, which provides the opportunity to identify MMP-9 in the serum as well. In the case of some peripheral tumours, elevated MMP-9 levels in plasma were detected and associated with cancer development, invasion, and poorer survival [43]; however, according to other research, MMP-9 in blood samples cannot be considered useful in estimating the invasive capacity of cancer [44]. In the case of brain tumours, specifically for glioblastoma, serum and plasma MMP-9 content analyses yielded conflicting results [45–48].

Based on the findings of our previous study [32], we hypothesised that the contradictions in the literature could be resolved by subjecting the serum-derived sEVs instead of whole serum to the MMP-9 analysis, since EVs are stable in the blood and can cross the BBB, thereby allowing the identification of the tumour-specific distinctive biomolecules using a non-invasive, simple blood test.

For this purpose, in this study, 222 serum samples were collected from four patient groups according to the criteria of the National Ethical Committee, and MMP-9 analysis was performed on serum-derived sEV samples using enzyme-linked immunosorbent assay (ELISA). According to our knowledge, this was the first study that investigated the MMP-9 level of serum sEVs in human brain tumours. The large sample size allowed us to demonstrate the factors influencing the MMP-9 level (age, gender, surgical resection, recurrence, therapy), and was suitable for determining a measurable, significant difference in the sEV MMP-9 level associated with different diseases and patient survival outcomes. Calculating the MMP-9 concentrations of serum-derived sEVs enabled us to establish the cut-off values and the specificity and sensitivity of the analysis required in clinical practice.

2. Materials and Methods

2.1. Patients

Blood samples of 222 patients treated at the Department of Neurosurgery, of the University of Debrecen were analysed. Samples were obtained from patients with glioblastoma multiforme (GBM), meningioma (M), and brain metastasis originating from non-small cell lung cancer (BM). Control samples (CTRL) were collected from patients with lumbar disc herniation without evidence of cancer. In addition to the four main groups, subgroups were also distinguished based on histopathology, sampling time (prior or after to surgery), grading, recurrence, and treatment (Table 1). Detailed patient characteristics can be found in Table S1.

Table 1. Patient cohort and participation in the statistical analyses.

Characteristics	*n* = 222	%
Glioblastoma multiforme (GBM)	**121**	**54%**
secondary glioblastoma (GBMsec)	*18*	*15%*
preoperative samples (GBMsec preop)	9	50%
postoperative samples (GBMsec postop)	9	50%
primary glioblastoma (GBMprim)	*103*	*85%*
preoperative samples (GBMprim preop)	69 (10) [1]	67%
recurrence-related analysis	69	67%
original tumour	54	78%
recurrence	15	22%
therapy involvement analysis	69	67%
patients before therapy	54	78%
patients with therapy	15	22%
survival analysis	27	39%
>65 Years	11	41%
≤65 Years	16	59%
high MMP-9 level (≥28 ppm)	17	63%
low MMP-9 level (<28 ppm)	10	37%
postoperative samples (GBMprim postop)	14 **(10)** [1]	33%
Brain Metastasis (BM)	**37**	**17%**
carcinoma planocellulare (BMplano)	*13*	*35%*
adenocarcinoma (BMadeno)	*24*	*65%*
preoperative samples (BMpreop)	27 (6) [2]	73%
postoperative samples (BMpostop)	10 (6) [2]	27%
Meningioma (M)	**28**	**13%**
meningioma Grade I (M_I)	*20*	*71%*
meningioma Grade II (M_II)	*8*	*29%*
Control (CTRL)	**36**	**16%**
lumbar disc herniation	*36*	*16%*
male	16	44%
female	20	56%

Percentages indicate the participation rates within each statistical analyses; [1] Number of GBM patients involved in paired *t*-test; [2] Number of BM patients involved in paired *t*-test.

Blood samples were collected, processed to serum, and stored by the Neurosurgical Brain Tumour and Tissue Bank of Debrecen according to the criteria of the National Research Ethics Committee. An informed consent form was signed by each patient; the study was conducted in accordance with the Declaration of Helsinki. This study was carried out according to two ethical approvals, namely 51450-2/2015/EKU (0411/15), Medical Research Council, Scientific and Research Ethics Committee, Budapest, 30 October 2015 and 121/2019-SZTE, University of Szeged, Human Investigation Review Board, Albert Szent-Györgyi Clinical Centre, Szeged, 19 July 2019.

2.2. Preparation of Serum Samples

Blood samples were collected into BD Vacutainer SST II Advance Tubes, allowed to clot for at least 1 h at room temperature, and centrifuged for 20 min at 3000× *g*, 10 °C. The serum samples were stored at −80 °C until further processing.

2.3. sEV Isolation and Characterization

sEVs were isolated from the sera via differential centrifugation as described previously [32]. Briefly, after thawing on ice, sera were centrifuged for 30 min at 10,000× *g*, 4 °C, then for 70 min at 110,000 g, 4 °C, using a fixed-angle rotor (T-1270, Thermo Fisher Scientific, Waltham, MA, USA). The pellet was resuspended in particle-free Dulbecco's phosphate-buffered saline (DPBS, Lonza Group Ltd., Basel, Switzerland) and stored at −80 °C until further processing. This sEV isolation protocol served to reach intermediate

recovery and intermediate specificity according to the guideline 'Minimal Information for Studies of Extracellular Vesicles 2018' (MISEV2018) [31].

Following the main suggestions and requirements included in MISEV2018, sEVs were characterised by transmission electron microscopy (TEM), Western blot analysis (WB), and nanoparticle tracking analysis (NTA). The TEM and WB measurements were performed on a representative sample of each main group.

In order to examine sEV morphology, TEM analysis was performed using a Tecnai G2 20 X-Twin type instrument (FEI, Hillsboro, OR, USA), operating at an acceleration voltage of 200 kV. The samples were dropped on a grid (carbon film with 200 mesh copper grids (CF200-Cu, Electron Microscopy Sciences, Hatfield, PA, USA)) and dried without staining or other fixation procedure.

Confirming the presence of sEVs, CD81, CD5L, and calnexin markers were presented by Western blot analyses using NuPAGE reagents and an XCell SureLock Mini-Cell System (Thermo Fisher Scientific, Waltham, MA, USA) according to the manufacturer's protocols. The protein content of sEV samples was determined using a Pierce BCA Protein assay kit (Thermo Fisher Scientific, Waltham, MA, USA) and a benchtop microplate reader (Multiskan RC, Thermo Labsystems, Waltham, MA, USA) according to the manufacturer's instructions. For detection of the sEV markers in the four main groups, rabbit anti-human Alix (1:1000), rabbit anti-human CD5L (1:2000), and rabbit anti-human Calnexin (1:10,000) primary antibodies (all from Sigma-Aldrich, St. Louis, MO, USA), and HRP-conjugated anti-rabbit IgG (1:1000, R&D Systems, Minneapolis, MN, USA) secondary antibody were used. THP-1 cell line (ATCC, Manassas, VA, USA) lysate was used for the positive control for Calnexin.

Determining the nanoparticle size distribution and concentration of the tested samples, sEVs were diluted in particle free DPBS and analysed using a NanoSight NS300 instrument with 532 nm laser (Malvern Panalytical Ltd., Malvern, UK). Six videos of 60 s were recorded for each sample under constant settings (Camera level: 15; Threshold: 4, 25 °C; 60–80 particles/frame).

2.4. MMP-9 Analysis by LC-MS

The LC-MS analysis was performed in a previous study [32] based on the serum sEV samples of 96 from the total of 222 patients. Samples presented the four main groups, namely GBM, BM, M, and CTRL. Each group contained 24 individuals with mixed ages and genders; six-sample-pools were created from the individuals, allowing four parallel samples to be tested per group. Blood samples were collected one day prior to neurosurgical procedure in each tumour case. None of the patients received radio- or chemotherapy before tumour resection.

The detailed methodology of LC-MS measurements was described in the named article [32]. Briefly, for 'in solution' digestion, individual samples containing 20 µg protein were diluted to 26 µL and kept at 60 °C for 30 min to unfold and reduce the proteins, and then kept at RT for 30 min to alkylate the proteins. The samples were digested overnight at 37 °C with trypsin, then stopped by formic acid. The separation of the digested samples was carried out on a nanoAcquity UPLC (Waters, Milford, MA, USA), using Waters ACQUITY UPLC M-Class Peptide C18 column. The LC was coupled to a high-resolution Q Exactive Plus quadrupole-orbitrap hybrid MS (Thermo Scientific, Waltham, MA, USA). The quantitative measurements of digested individual samples were performed in DIA mode, and the analysis was conducted in Encyclopedia 0.81. A comprehensive spectral library of 10,000 human proteins was used for peptide identification.

2.5. MMP-9 Analysis by ELISA

To accurately measure MMP-9 content of sEVs, LEGEND MAX Human MMP-9 ELISA Kit (Biolegend, San Diego, CA, USA) was used according to the manufacturer's protocol. sEV isolates of 222 serum samples were measured individually, and the vesicles were disrupted in a detergent-free manner by five repeated freeze–thaw cycles to expose the

entire protein content. As we examined sEV isolates, potential interferences—observed in clinical immunoassays of sera [49]—are avoided. The assay procedures are briefly summarised below.

A standard curve was applied for each assay, and all samples were run in duplicate on separate plates. In the first step, 50µL assay buffer and 50 uL standard dilutions or 12× diluted samples were added to the appropriate wells, and the plates were sealed and incubated at room temperature for 2 h while shaking at 200 rpm. After the incubation, plates were washed four times with 1× wash buffer. The first step was followed by three more incubation steps, namely 100 µL of human MMP-9 detection antibody solution, 100 µL of Avidin-HRP solution, and 100 µL of substrate solution D were added to each well and incubated at room temperature for 1 h, 30 min, and 15 min, respectively. The plates were washed four times with 1× wash buffer between each incubation procedure. The last step was performed in the dark, and then the reaction was stopped by adding 100 µL of stop solution; the absorbance was immediately read at 450 nm and 570 nm on a benchtop microplate reader (Multiskan RC, Thermo Labsystems, Waltham, MA, USA).

2.6. Statistical Analyses

Before conducting any statistical tests, the MMP-9 level was normalised to the protein content of serum sEVs, meaning that MMP-9 concentration (ng/mL) was divided by protein concentration of the EV-enriched isolates (ng/mL) for every sample. The results of all the analyses are notated in parts-per-million (ppm), describing the individual values of MMP-9 in patients.

Outliers from the analysed groups were always excluded using the ROUT (robust regression followed by outlier identification) method with the Q parameter set to 1%. Then we examined the assumptions of normal distribution utilising the Shapiro–Wilk test and the homogeneity of variances by using the F test (comparing two groups) and the Brown–Forsythe test (comparing more than two groups).

The MMP-9 ppm concentrations of independent groups and matched samples were compared with Welch's test and the paired *t*-test, respectively. One-way ANOVA was used to examine differences between more than two groups.

To determine the relationship between continuous variables, linear regression analyses were conducted. To improve linearity in regression, skewed data were logarithmised.

The diagnostic potential of the MMP-9 ppm was evaluated using receiver operating characteristic (ROC) analyses. Kaplan–Meier analyses with log-rank tests were used to compare the overall survival rates of different groups.

The collected data about the MMP-9 content of sEVs were analysed statistically using GraphPad Prism 8.3.4.

2.7. Data Availability

All datasets generated during the current study are available from the corresponding author upon reasonable request. All relevant data of our experiments had been submitted to the EV-TRACK [50] knowledgebase (EV-TRACK ID: EV230005).

3. Results

3.1. The sEVs' MMP-9 Content Measured by ELISA Is Consistent with the Previous LC-MS Results

Our main goal was to compare the MMP-9 content of serum-derived small extracellular vesicle (sEV) samples from 222 patients with different CNS diseases. The four main investigated groups were glioblastoma (GBM), brain metastasis originated from non-small cell lung cancer (BM), meningioma (M), and lumbar disc hernia patients as controls (CTRL).

In a previous study, following the isolation and characterisation of sEV samples, LC-MS analysis was performed on 96 sEV samples. Each of the four groups (GBM, BM, M, and CTRL) contained 24 individuals, and six sample pools were created from the individuals allowing four parallel samples to be tested per group. As a result of the analysis, a 17 membered protein panel was constructed from the identified proteins which were able to

separate the four groups with 100% efficacy [32]. In this study, we investigated which of the 17 sEV proteins were the most suitable for distinguishing patients, and found MMP-9 to be the most significant ($p = 0.0065$, multi ROC AUC = 0.86).

Following the candidate selection, in the current study, the MMP-9 content of the 96 sEV samples was measured by ELISA, and the MMP-9 intensities (from LC-MS) were compared with the averaged MMP-9 concentrations (from ELISA) of the six-sample-pools to ascertain that ELISA is also capable of distinguishing the groups. The correlation analysis confirmed that the MMP-9 concentrations measured by ELISA were highly comparable to LC-MS measurements ($r = 0.7264$; $p = 0.0022$) (Figure 1).

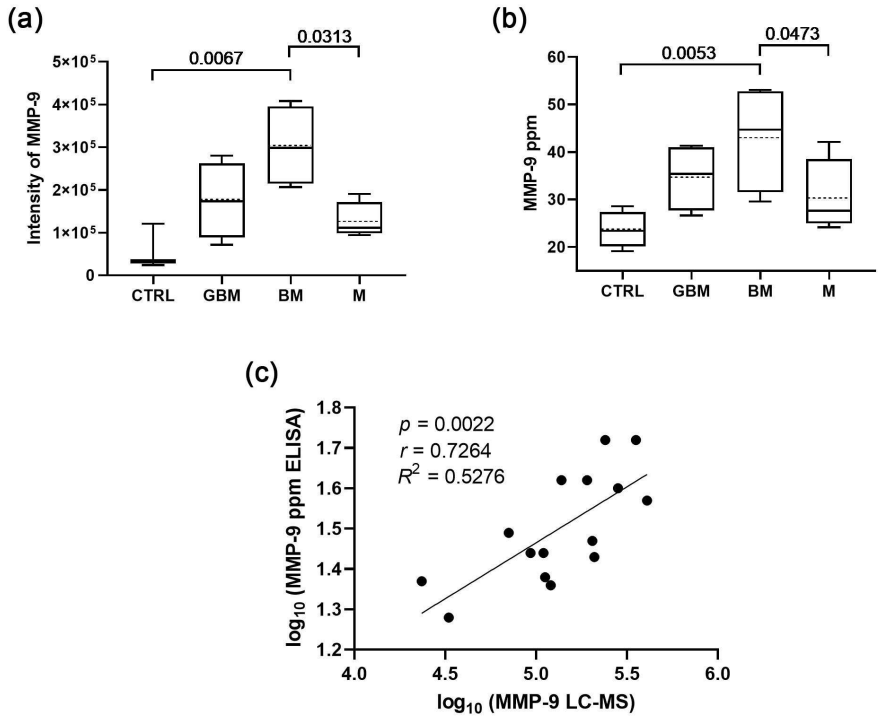

Figure 1. Comparison of the sEV MMP-9 content measured by ELISA with the LC-MS results. (**a**) MMP-9 levels of serum-derived sEVs based on LC-MS data (boxplot shows median with interquartile range, mean with dotted line, error bars range from the 5th–95th percentiles (nCTRL = 3, nGBM = 4, nBM = 4, nM = 4). (**b**) MMP-9 levels of serum-derived sEVs based on ELISA data (nCTRL = 4, nGBM = 4, nBM = 4, nM = 4). Dotted lines indicate mean values. (**c**) Correlation between the MMP-9 levels measured by LC-MS and ELISA.

Therefore, we aimed to perform ELISA measurements on the larger cohort; the MMP-9 concentrations and sEV characteristics can be found in Table S1 and Figure S1, respectively. The large sample size allows us to investigate factors influencing the MMP-9 level, and is suitable for examining whether there is a measurable, significant difference in the sEV MMP-9 level associated with different diseases and patient survival outcome. Measuring the MMP-9 concentrations of serum EVs instead of MMP-9 intensities enables the determination of the cut-off values required in the clinic, as well as the specificity and sensitivity of the test.

3.2. Several Factors Might Influence the MMP-9 Level of the Serum-Derived sEVs

Performing comparative studies between different tumours requires examining what factors (e.g., age, gender, surgical resection, recurrence, and therapy) may influence MMP-9 levels of serum-derived sEVs (Figure 2).

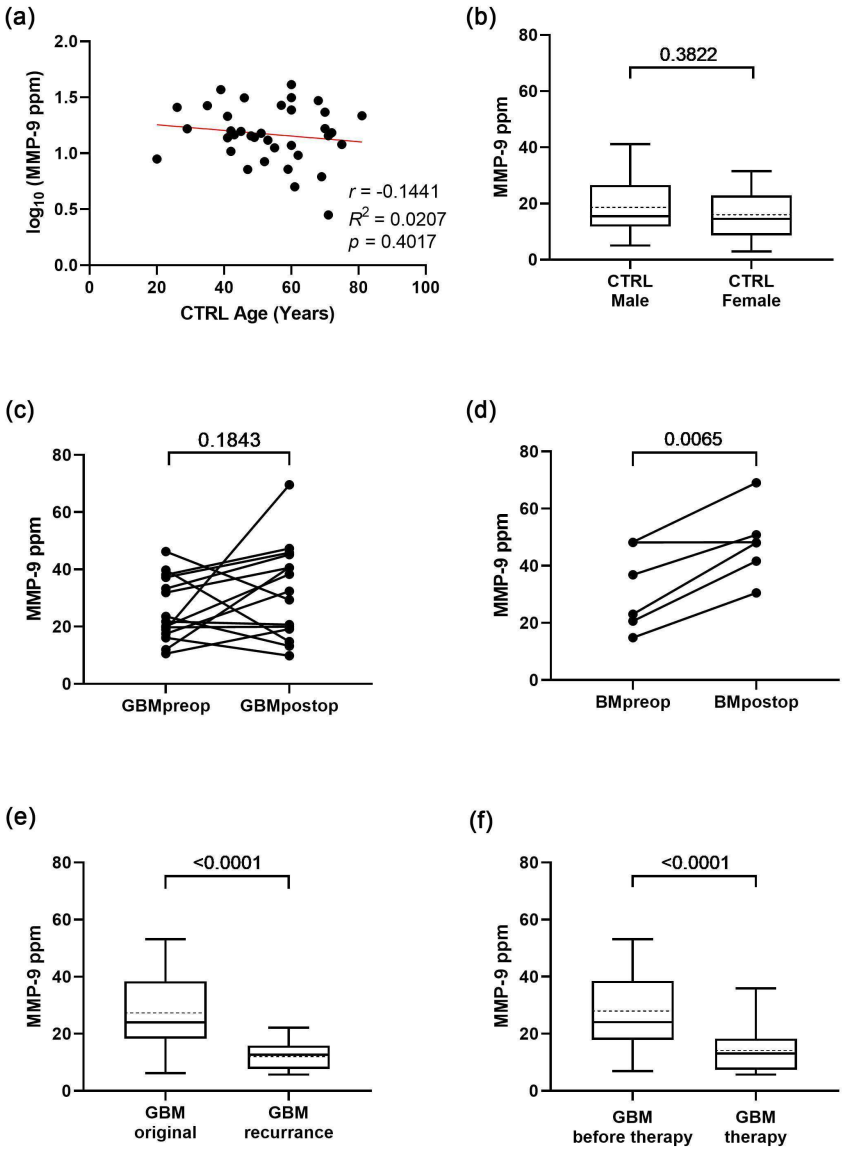

Figure 2. Factors influencing MMP-9 level of serum-derived sEVs. (**a**) Relationship between age and MMP-9 levels in the control group. (nCTRL = 36). (**b**) MMP-9 levels of the two genders in the control group (boxplots show the median with interquartile range, mean with dotted line, error bars range from the 5th–95th percentiles; nCTRL male = 16, nCTRL female = 20). (**c**,**d**) Changes in individual patient's MMP-9 levels before and after surgical resection for the GBM and BM groups, respectively (nGBM preop-postop = 14, nBM preop-postop = 6). (**e**) MMP-9 levels of serum-derived sEVs regarding the original tumour and the recurrence in GBM group before surgical resection (nGBM original = 52, nGBM recurrence = 14). (**f**) MMP-9 levels in GBM group to treatment status (nGBM before therapy = 52, nGBM therapy = 15).

The MMP-9 level was normalised to the total protein content of serum sEVs, meaning that MMP-9 concentration (ng/mL) was divided by protein concentration of the EV-enriched isolates (ng/mL) for every sample. The results of all the analyses are notated in parts-per-million (ppm) describing the individual values of MMP-9 in patients (Table S1).

Age and gender analyses were carried out in the control group, eliminating the possible MMP-9-modifying effect of any tumour disease. Correlation analysis revealed that there is no distinct relationship between age and MMP-9 levels (Figure 2a). The MMP-9 level of serum-derived extracellular vesicles shows no significant difference between male and female patients, as determined by Welch's test (Figure 2b). Based on these findings, further data analyses were conducted regardless of the age or gender of the patients.

Examining the effects of surgical resection on the MMP-9 level of sEVs, paired *t*-tests were completed in the GBM and BM groups (Figure 2c,d, respectively). The MMP-9 levels were similar ($p = 0.1843$, fold change = 15%) before and after the surgical resection in the case of primary GBM patients, while BM samples showed marked increase ($p = 0.0065$, fold change = 209%) after resection.

Further examination on preoperative GBM samples found a distinct difference between the original tumour and the recurrence based on MMP-9 levels of serum sEVs (Figure 2e), and the recurrence showed a lower level of MMP-9 on average ($p < 0.0001$).

Determining the influence of the administered therapy, MMP-9 levels were also compared based on whether or not GBM patients had received treatment at the time of sampling. Our result ($p < 0.0001$) indicates that therapy might decrease the MMP-9 levels of the circulating sEVs (Figure 2f).

In addition to the paired *t*-test shown in Figure 2c,d, unpaired *t*-tests (Welch's tests) were performed on all primary and secondary GBM samples, as well as on all BM samples to determine the effect of surgical resection on a broader cohort (Figure S2). First, all the preoperative and postoperative samples were evaluated; then, subsequent exclusions were made for individuals who had relapsed or received therapy. The unpaired *t*-tests on primary GBM and BM samples (Figure S2a,c) yielded the same results as the paired *t*-tests (Figure 2c,d); however, for the secondary GBM samples, the significant differences were erased when the recurrent or treated samples were excluded from the statistical analysis (Figure S2b).

Based on our findings, we can conclude that in addition to the disease types, surgical resection, recurrence, and therapy might influence the MMP-9 level of the serum-derived sEVs. Due to these findings, all subsequent analyses were conducted exclusively on samples obtained prior to surgical resection and therapy administration.

3.3. MMP-9 Level of Serum sEVs Differs in Various CNS Tumours Showing a Positive Correlation with Tumour Aggressiveness

Further statistical analyses were performed in order to identify if there is a difference between the serum sEV MMP-9 levels of the patient groups (Figure 3).

As a first step, Welch's test was used to compare the control group with all the tumour patients (Figure 3a). Based on ROC analysis, the two groups were significantly distinguishable ($p = 0.0002$) using a cut-off point of 16 MMP-9 ppm with 74% sensitivity, 61% specificity, and an AUC of 0.70 (Figure 3b).

The tumour patients then were divided into M, GBM, and BM, and we found that the differences remained significant between controls and malignant tumours, as well as between the benign and malignant tumours (Figure 3c). Separate comparison resulted in increased specificity, sensitivity values, and AUC scores in the case of control-malignant tumour comparisons at the expense of control-benign comparisons (Figure 3d).

In the last step, the patients were divided into further subgroups based on histopathology. In the subgroup analysis, primary and secondary GBM, patients with grade I and II meningiomas, and brain metastases from patients with adenocarcinoma and carcinoma planocellulare were distinguished. The detailed results are presented in Figure S3. The

comparisons of the patient groups showing significant differences in MMP-9 levels resulted in AUC scores up to 0.77.

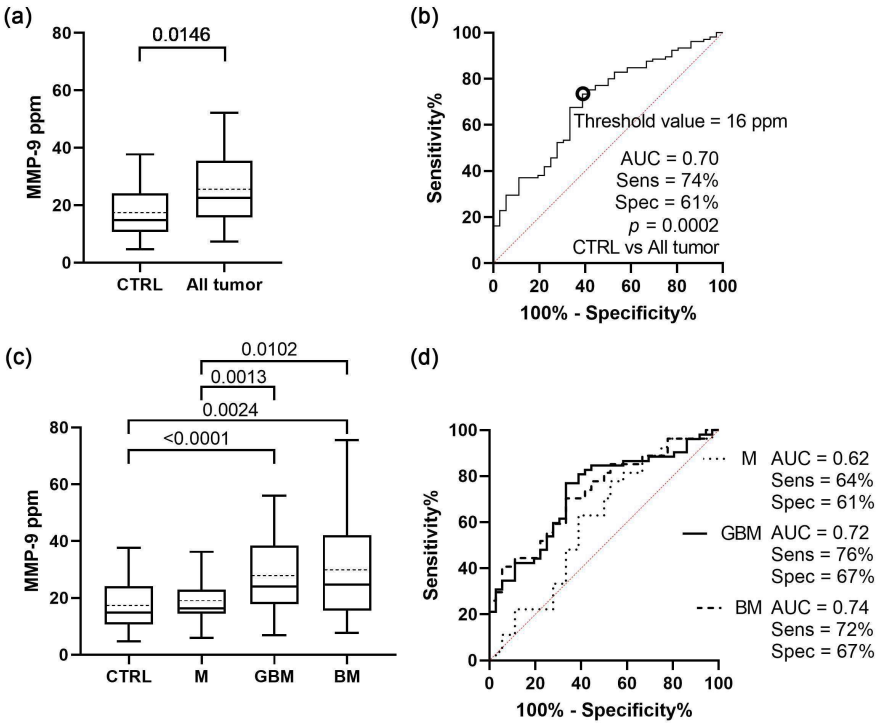

Figure 3. Comparative analyses of MMP-9 level of serum sEVs on the four main groups. (**a**) Graph shows the MMP-9 level of the control group comparing all the tumour patients (median with interquartile range, mean with dotted line, error bars range from the 5th–95th percentiles; nCTRL = 36, nAll tumour = 105). (**b**) ROC curves for exploring the differences between the MMP-9 level of the control group and all the tumour patients (nCTRL = 36, nAll tumour = 109). (**c**) Diagram shows the MMP-9 level of serum sEVs among the four patient groups (nCTRL = 36, nM = 27, nGBM = 52, nBM = 27). (**d**) ROC curves for comparing the three tumour groups to controls (nCTRL = 36, nM = 27, nGBM = 52, nBM = 27).

Our data indicate that patients suffering from malignant, but not benign brain tumours can be distinguished from CTRL patients based on the MMP-9 level of serum sEVs, and that the MMP-9 level of serum sEVs differs between CNS tumour types, showing a positive correlation with tumour aggressiveness.

3.4. The sEVs' MMP-9 Level Might Be a Prognostic Marker for Overall Survival in GBM Patients

After analysing the influencing factors, we aimed to determine whether MMP-9 levels correlate with disease progression/patient survival. To assess the prognostic value of MMP-9 levels in serum sEVs, we analysed the preoperative serum samples from 27 GBM patients. Patients in this study were not administered by any treatment at the time of sampling (Figure 4).

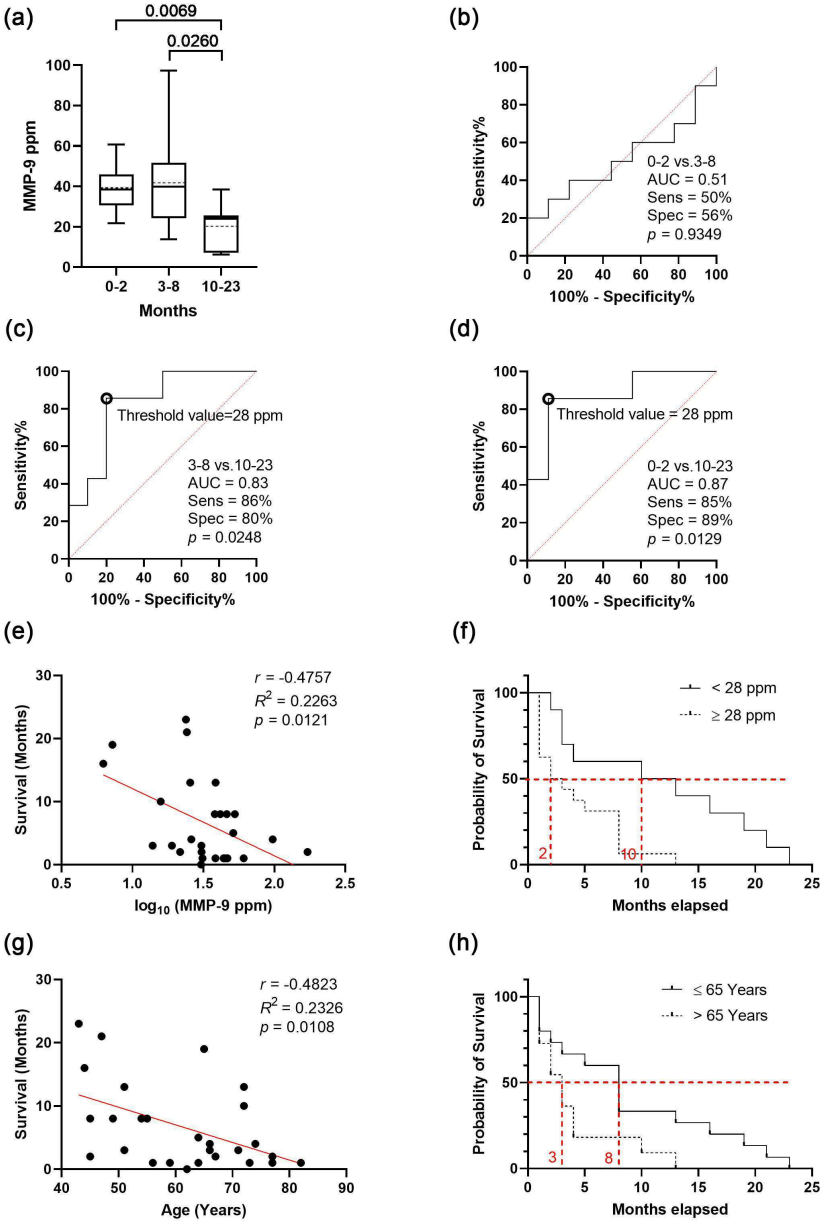

Figure 4. Investigation of survival in GBM patients. (**a**) Differences among the short-, medium- and long-term survival based on MMP-9 level of serum derived sEVs of GBM patients (median with interquartile range, mean with dotted line, error bars range from the 5th–95th percentiles, dotted lines indicate mean values). (**b–d**) Receiver operating characteristic (ROC) curves for comparing the short- (0–2 months), medium- (3–8 months) and long-term (10–23 months) survival groups (threshold values of the group-membership score are marked with black circles). (**e**) Correlation between MMP-9 level and survival in the GBM group (nGBM = 27). (**f**) Overall survival according to low and high (n < 28 ppm = 10 and $n \geq$ 28 ppm = 17) MMP-9 level. (**g**) Relationship between age and survival in the GBM group (nGBM = 27); (**h**) Overall survival according to the age ($n \leq$ 65 years = 16 and $n >$ 65 years = 11).

To reveal the prognostic value of sEVs' MMP-9 level on survival, subjects were divided into three groups based on their survival time (short-, medium- and long-term) using 0–2, 3–8, 10–23 months as the cut-offs (Figure 4a). Long-term survival was found to be associated with a significantly lower MMP-9 level compared to the MMP-9 levels of the other two groups (Figure 4b–d). These differences represent a high specificity and sensitivity of 80–89% at a threshold of 28 MMP-9 ppm, and AUC values of 0.83–0.87 in ROC analyses allow efficient distinction of these survival groups.

These results suggest that there should be a correlation between the MMP-9 level of serum sEVs and overall survival (OS), so we performed an analysis where we observed that lower survival time was associated with higher MMP-9 level (Figure 4e). To determine the extent of the influencing effect of MMP-9 levels on survival, patients were separated into two groups, with the previously established threshold of 28 ppm. Based on the Kaplan–Meier chart, patients with low MMP-9 level (<28 ppm) presented with a significant OS benefit (HR 2.401, 95%CI 1.095 to 5.261, $p = 0.0063$), which represents an eight-month increase in the median OS (Figure 4f).

The probability of survival also decreased with age; therefore, we repeated the examination with a cut-off of 65 years. According to the Kaplan–Meier chart, patients under the age of 65 had a five-month increase (HR 2.037, 95%CI 0.8524 to 4.869, $p = 0.0340$) in median survival (Figure 4c). It is crucial to note that age and MMP-9 level are independent (see Figure 2a); we can conclude that the MMP-9 level of serum sEVs may influence survival regardless of age.

To summarise the main findings, analysis of samples taken prior to surgical resection and the administration of therapy revealed a negative correlation between higher MMP-9 levels and the survival, and long-term (10–23 months) survival found to be associated with low MMP-9 level (<28 ppm). Our results support that the high level of MMP-9 in serum-derived sEVs might be a negative prognostic marker of the probability of survival in GBM patients.

4. Discussion

In recent years, oncology research has turned its focus from analysing whole tumour tissues to analysing various biological fluids for tumour-derived components [7,9]. Although several attempts have been made to identify GBM-specific biomarkers in serum [11,51,52], to the best of our knowledge, serum/plasma biomarkers are not routinely used for clinical monitoring of glioblastoma. The lack of reliable non-invasive serum-based biomarkers for GBM can be explained by several reasons, including (1) the extremely high complexity of tumour tissues (hence the name glioblastoma multiforme), (2) the barrier function of BBB that prevents the 'tumour information' from entering the circulation, and (3) the presence of abundant molecules that can 'mask' the potential biomarker candidates.

Using EV samples instead of whole sera, it is possible to amplify the signals released by brain tumours into the circulation [32]. Extracellular vesicles are stable in the blood [12], and can cross the BBB [29,30]; moreover, EVs may contain tumour-related molecules in higher concentrations and are accompanied by less contaminating molecules that may bias the analytical findings. These advantageous properties of EVs increase the possibility of identifying molecules that provide valuable information regarding tumours.

Due to the priority of living-cell secretion, large amounts and stable circulation compared to circulating tumour cells and ctDNA, exosome-based liquid biopsy has been tested in clinical trials and several of them have been approved and reached the market. In 2016, Exosome Diagnostics proposed the first exosome-based liquid biopsy in the world [22], ExoDx™ Lung (ALK), for the isolation and analysis of exosomal RNA from blood samples. In addition, the ExoDx Prostate IntelliScore (EPI) has been certified by FDA [53], and 26% of unnecessary needle biopsies were avoided with an appropriate threshold [54]. High sensitivity was achieved in prospective studies; therefore, they could be used to assist in the early diagnosis of cancer and eliminate unnecessary prostate biopsy [55].

According to Lihares et al., screening for gliomas has no clinical relevance at this time [48]. This is due to the low incidence, absence of sensitive biomarkers in plasma, and the observation that gliomas can develop apparently de novo in a matter of weeks or months. However, a non-invasive biomarker that can be used to estimate tumour state and patient survival would be of great assistance to physicians.

Based on these considerations, we sought to determine whether the MMP-9 (an endopeptidase involved in ECM degradation, thus having a role in tumour invasion) level of serum-derived sEVs can provide information about patient survival. ELISA was used to measure the MMP-9 content of 222 sEV samples isolated from whole serum for this purpose. Serum samples were collected from patients with the most common malignant, benign, and metastatic brain tumours, namely glioblastoma multiforme, meningioma [56], and brain metastasis of non-small cell lung cancer [57], and from control patients with lumbar disc herniation.

Following the measurements, comparative analyses on the MMP-9 level of sEVs were conducted. We determined that surgical resection, recurrence, and therapy can modify the MMP-9 level, but neither age nor gender can. We also detected statistically significant differences in the sEVs' MMP-9 levels associated with various diseases, as well as a correlation between low MMP-9 level and longer survival time, which highlighted the prognostic value of vesicular MMP-9 level. However, functional studies, including MMP-9 activity measurements, would be needed to explore the causal relationship between tumour progression and the MMP-9 level of serum sEVs.

We hypothesise that the higher MMP-9 level of sEVs observed in patients with a poor prognosis is due to the tumour itself. However, there is a debate surrounding the source of the tumour-specific EVs in the blood. Osti et al., as a confirmation of the tumour origin of extracellular vesicles, employed an orthotopic transplantation of tumour-initiating cells (TICs) isolated from human GBM. GBM TICs expressing the exosomal marker CD9 coupled with the GFP protein were produced using lentiviral transduction. Because GBM-derived extracellular vesicles express CD9 on their surface, they were distinguished from natural GFP-negative mouse extracellular vesicles by following the GFP signal. According to their data, nearly half of the extracellular vesicles in the peripheral circulation of transplanted mice were tumour-derived [58]. However, using EV capture and staining techniques that allow differentiation of host cell and GBM-derived EVs, Fraser et al. demonstrated that tumoral EVs often present less than 10% of all EVs with extensive heterogeneity in tumour marker expression in GBM patient plasma [59]. The proportion of tumour-derived sEVs in the blood is a very interesting issue, although its clarification is beyond the scope of our study.

To the best of our knowledge, this study was the first one that analyses the MMP-9 content of serum sEVs; nevertheless, a few serum MMP-9 investigations have been published with contradictory findings. Hormingo et al. found that YKL-40 and MMP-9 could be monitored in patients' serum and help confirm the absence of active disease in GBM [45]. However, after five years, the same group (Iwamoto et al.) conducted a longitudinal prospective study of MMP-9 as a serum marker in gliomas, and the larger cohort could not confirm the previous findings. Serum MMP-9 showed no utility in determining glioma disease status and was not a clinically relevant prognostic marker of survival. There was no statistically significant correlation between serum MMP-9 levels and radiographic disease status. Longitudinal increases in MMP-9 were weakly associated with shorter survival in glioblastoma patients, but they were not independently associated with survival after adjusting for age, extent of resection, and performance status [46]. In contrast, Ricci et al. confirm that MMP-9 levels are significantly higher in high-grade glioma, in low- and high-grade meningioma samples, as well as in metastasis specimens compared to healthy individuals ($p < 0.001$) [47]. This latter research of serum MMP-9 levels is in line with our sEV-based findings.

Several technical issues may have contributed to the poor and contradictory serum/plasma results. It is important to note that the measurement of MMPs in body fluids can be in-

fluenced by the type of fluid and method of collection and storage. EDTA or heparin, for instance, can affect the baseline serum/plasma concentrations of MMP-9 [60]. To solve this issue, for instance, Ricci et al. prepared native serum using plastic tubes without coagulation accelerators, to prevent the release of gelatinases during platelet activation [47]. We used BD Vacutainer SST II Advance Tubes acril gel with only silica particles as clot activators.

Another difficulty is that plasma MMP-9 may be unstable and degrades rapidly even when stored at −80 °C [61,62]. This problem can be alleviated by using sEVs instead of serum, as the high biological stability allows long-term storage of specimens for exosome isolation and detection [63]. Diagnostic analytes, RNA, DNA, or protein cargo in exosomes maintain this informative profile's stability during sample storage, which is essential for the development of biomarkers using retrospective samples [64]. This raises the possibility of monitoring MMP-9 not only at the protein, but also at the mRNA level.

Recently, several research groups have studied vesicular mRNA that can be isolated from body fluids [65–68]. However, the majority of MMP-9 mRNA investigations are conducted on tissue samples [69–71], and there are only a few studies assessing MMP-9 mRNA and MMP-9 protein in serum [72–74]. Although these are not comparative studies of cancer patients, they indicate that increase in MMP-9 is detectable with similar efficiency at both mRNA and protein levels. At the same time, due to the complex regulation of translation and protein degradation, there is no strict correlation between mRNA and protein abundances [75–77]. Thus, we assume that vesicular MMP-9 could be measured at the mRNA level as well, but its prognostic value would need further investigation.

It is also important to note that there is no gold standard method for sEV isolation, which may impede the reproducibility of experimental findings in EV research. The applied technique impacts the isolation efficacy in terms of yield, purity, and EV composition, which may interfere with downstream analyses, including the molecular cargo profiling [78–81]. Another technical issue in EV research is that storage at −80 °C and freeze–thaw cycles may affect stability of EV membranes leading to EV disruption and subsequent fusion phenomena, which may influence the EV characteristics, including biological activity [82–85], but enable the use of repeated freeze-thaw cycles to expose the entire EV cargo prior to downstream analyses (as it was done here and previous studies [86,87], or to load therapeutic cargo into vesicles [88,89]. To enhance the reliability, transparency, and reproducibility of EV studies, the ISEV published the MISEV guidelines, which discuss all technical issues and provide help to set up the experimental protocols best fit to the research question [31,90].

Prior studies have suggested that MMP-9 measurements in serum do not reliably reflect circulating MMP-9 levels and may be artificially high compared to results obtained from plasma samples [43,91–93], but Iwamoto et al. showed that serum and plasma MMP-9 samples were highly correlated in their large sample size, so serum, and thus serum-derived sEV samples, could be used appropriately [46].

In order to find the putative source of the MMP-9 as biomarker, Ricci et al. correlated the expression of serum MMP-9 with the expression of the same protein in the tumour tissue. To address this aim, glioma tissues were subjected to immunohistochemistry with MMP-9 antibody. They discovered that the delocalisation of the MMP-9 signal from glioma cells to endothelial cells of neoplastic blood arteries is directly associated with tumour malignancy. In line with these findings, previous immunohistochemical and in situ hybridization studies demonstrated that, in high-grade glioma, MMP-9 expression is primarily restricted to perivascular regions at the infiltrating borders of the tumour and, in the majority of cases, to endothelial cells, with a close association to tumour malignant behaviour [94,95]. To determine the origin of MMP9 in GBM, Jiguet-Jiglaire et al. analysed its expression by immunohistochemistry. According to their findings, MMP-9 staining was mainly located in the microvascular proliferation, and also in inflammatory cells and circulating intravascular cells. No staining was observed in glioblastoma cells or in the extracellular matrix [39].

The successiveness of a biomarker candidate can be determined by comparing its efficacy to that of existing clinical procedures. We were unable to correlate the sEVs' MMP-9

level of the patients with their MRI status; nevertheless, contradictory findings exist in the literature. Hormigo et al. observed that levels of MMP-9 were higher in the serum samples of patients with high-grade glioma after surgery, while the MMP-9 concentrations were significantly lower in glioblastoma patients with no radiographic evidence of disease in comparison to the subjects with active tumour [45]. In contrast, Iwamoto et al. found that there was no statistically significant correlation between serum MMP-9 levels and radiographic disease status [46]. Moreover, in a very recent study by Jiguet-Jiglaire et al., MMP-9 did not correlate with glioblastoma tumour volume, invasion, or angiogenesis assessed by neuro-imaging [39].

In addition to disease status, other patient characteristics may influence MMP-9 levels in the patient sera. Otero-Estévez et al. found that MMP-9 was significantly correlated with gender and age when examining the serum of colorectal cancer patients [44]. In contrast, in our study on serum-derived sEVs, there was no distinct relationship between age and MMP-9 levels, and there was no significant difference between male and female patients in terms of MMP-9 level (Figure 2). Based on our findings, data analyses on serum-derived sEVs can be conducted regardless of the age or gender of the patients.

The surgical resection also can affect the extracellular vesicle concentration and the MMP-9 content of serum/plasma EVs. Osti et al. measured a significant drop ($p < 0.001$) in plasma extracellular vesicle concentration after surgery [58]. Hormigo et al. observed that levels of MMP-9 were higher in the sera samples of patients with high-grade glioma after surgery, suggesting that increases in the serum level of this protein may be associated with brain inflammation and breakdown of the blood–brain barrier, rather than be a true measure of tumour burden [45]. In our study, the MMP-9 level of serum sEVs were similar before and after the surgical resection in the case of primary GBM patients ($p = 0.1843$; $n = 14$), while BM samples showed marked increase ($p = 0.0116$; fold change = 209%) after resection. This intriguing phenomenon relies on the basis of a few BM samples ($n = 6$), and therefore should be supported by further measurements.

Determining the influence of the administered therapy, MMP-9 levels were also compared based on whether or not GBM patients had received treatment at the time of sampling. Our result ($p < 0.0001$) indicated that therapy might decrease the MMP-9 level of circulating sEVs (Figure 2f). Further examination on preoperative GBM samples found a distinct difference between the original tumour and the recurrence based on the MMP-9 level of serum sEVs (Figure 3e). Although recurrence shows a lower level of MMP-9 on average ($p < 0.0001$), the majority of these GBM patients received treatment, therefore the decrease in MMP-9 cannot be attributed solely to relapse. Tabouret et al. reported that urine protein levels of MMP-2 also decreased and were considered to be related to treatment response, although this was not confirmed in an additional patient cohort [96].

One of the main findings of our study relies on the correlation analysis of samples taken prior to surgical resection and the administration of therapy on MMP-9 level and survival. A negative correlation was revealed between higher MMP-9 levels and the survival, and the long-term (10–23-month) survival was found to be associated with a low MMP-9 level (<28 ppm). Our results support that the high level of MMP-9 in serum-derived sEVs might be a negative prognostic marker of the probability of survival in GBM patients. Osti et al. tested for possible associations between plasma extracellular vesicle concentration and patient outcomes. Patients with GBM were ranked according to their extracellular vesicle content and divided into high-content or low content groups; no significant differences in PFS or OS were found [58]. Jiguet-Jiglaire tested patients with recurrent glioblastoma prior to treatment and found decreased plasma levels of MMP-9 associated with increased OS [39].

By measuring the level of MMP-9, we may determine the efficacy of the treatment. For instance, the majority of patients with GBM will experience relapse despite surgery and standard first-line treatment consisting of radiotherapy with concurrent and adjuvant temozolomide. In certain cases, therapeutic options at the time of recurrence include surgery or reirradiation, whereas in other cases, bevacizumab is the preferred option worldwide. Jiguet-Jiglaire et al. demonstrated that low baseline plasma levels of MMP-9

were associated with a high response rate and a prolonged PFS and OS in patients with recurrent GBM treated with bevacizumab but not cytotoxic chemotherapy. In addition, they observed that MMP-9 plasma levels decreased during treatment with bevacizumab and tended to rise with disease progression. In a retrospective analysis performed in the Avaglio trial (a randomised phase III trial that compared bevacizumab versus placebo in addition to standard of care in newly diagnosed glioblastoma patients), a low plasma level of MMP-9 at baseline consistently predicted PFS and OS gain associated to bevacizumab [39].

Unmet medical need exists for biomarkers able to predict response to antiangiogenic agents. According to the ClinicalTrials.gov database, only a few studies are currently being conducted to determine the predictive value of MMP-9 level on cancer treatment response. One study aims to investigate the predictive impact of circulating MMP-2 and MMP-9 on the progression-free survival of patients with metastatic kidney cancer treated with anti-angiogenic agents (Sunitinib or Pazopanib) in comparison with two untreated cohorts (NCT03185039). Another study evidenced the role for MMP-9 in the primary or acquired resistance to bevacizumab; therefore, in their trial they use monoclonal antibody GS5745 that may overcome resistance to bevacizumab through a specific inhibition of MMP-9. The phase I study is the first step to analyse the tolerance, determine the recommended dose of the combination, and explore the impact of GS5745 on MMP-9 plasma levels and multimodal imaging in patients with recurrent glioblastoma (NCT03631836).

On the other hand, Farina and Mackay draw attention to the Janus-faced nature of MMP-9. This important molecule plays an essential role in tumour biology, from initiation/promotion to angiogenesis, dissemination, immune surveillance, and metastatic growth. However, MMP-9 also possesses antitumour activity and serves essential physiological functions [97]. In order to determine the potential therapeutic efficacy of inhibiting MMP-9 function in cancer therapy, it is necessary to develop specific inhibitors of MMP-9, to inhibit the tumour promoting function of MMP-9 instead of suppressing the anti-tumour effect. Validation of MMP-9's predictive value in a prospective study is a crucial step toward its possible routine therapeutic application. In addition, it may be advantageous to (i) investigate the invasion- and angiogenesis-related molecules co-expressed with MMP-9, or (ii) develop strategies for inhibiting tumour-specific activators of MMP-9 instead of using direct inhibitors.

In summary, we have demonstrated that sEVs' MMP-9 content is suitable for estimating the probability of patient survival and it allows us to obtain information about CNS tumour aggressiveness. This biomarker's benefits include its accessibility (a simple blood test), affordability, fast detectability, ease of implementation, and reproducibility. Collectively, these advantageous characteristics would permit the application of serum sEVs' MMP-9 for non-invasive patient monitoring.

5. Conclusions

Glioblastoma is the most prevalent primary brain tumour in adults, comprising 45.2% of all malignant primary CNS tumours, with a median survival time of 15 months. On average, 5.5% of patients live five years after their diagnosis [98].

The link between the survival of glioblastoma patients and their MMP-9 level of serum-derived sEVs is revealed in our article; hence, the identification of sEVs' MMP-9 is of great importance. Our presented fast-to-perform and non-invasive method can support clinical decision making.

Supplementary Materials: The following supporting information can be downloaded at: https://www.mdpi.com/article/10.3390/cancers15030712/s1, Figure S1: Characterisation of isolated particles; Figure S2: Comparison of all the preoperative and the postoperative GBM and BM samples in terms of MMP-9 level; Figure S3: Differences among controls and various CNS tumour patients based on MMP-9 level of sEVs originated from preoperative serum samples; Table S1: Detailed patient characteristics.

Author Contributions: Conceptualization, G.D. and K.B.; methodology, G.D. and E.G.-S.; validation, M.H.; formal analysis, G.D. and M.B.; investigation, E.G.-S., V.N., M.H., Z.S. and G.D.; resources, Á.K., T.P. and K.B.; writing—original draft preparation, G.D.; writing—review and editing, K.B.; visualisation, G.D. and M.B.; supervision, K.B.; funding acquisition, K.B.; All authors have read and agreed to the published version of the manuscript.

Funding: This study was supported by the following research grants: GINOP-2.2.1-15-2017-00052 (K.B.), TKP-2021-EGA-09 (K.B.), OTKA-K143255 (K.B.), Szent-Györgyi Albert Research Fund provided by University of Szeged (K.B.), "National Brain Research Program NAP 2.0" (Á.K.), ÚNKP-22-5-SZTE-318 (T.P.). The project has received funding from the EU's Horizon 2020 research and innovation program under grant agreement No. 739593. (T.P.), ÚNKP-22-3-New National Excellence Program of the Ministry for Innovation and Technology from the source of the National Research, Development and Innovation Fund (M.B., V.N.) Project no. TKP-2021-EGA-09 has been implemented with the support provided by the Ministry of Culture and Innovation of Hungary from the National Research, Development and Innovation Fund, financed under the TKP2021-EGA funding scheme (K.B.).

Institutional Review Board Statement: The study was conducted in accordance with the Declaration of Helsinki, and ethical approval was obtained from two independent bodies (51450-2/2015/EKU (0411/15), Medical Research Council, Scientific and Research Ethics Committee, Budapest, 30 October 2015, and 121/2019-SZTE, University of Szeged, Human Investigation Review Board, Albert Szent-Györgyi Clinical Centre, Szeged, 19 July 2019).

Informed Consent Statement: Informed consent was obtained from all subjects involved in the study.

Data Availability Statement: All datasets generated during the current study are available from the corresponding author upon reasonable request.

Acknowledgments: The authors thank László Janovák for transmission electron microscopy measurements, Lilla Pintér and Tímea Böröczky for their technical assistance, and Adrienn Jenei and László Szivos for organising serum samples and providing patient data.

Conflicts of Interest: The authors declare no conflict of interest. The funders had no role in the design of the study; in the collection, analyses, or interpretation of data; in the writing of the manuscript, or in the decision to publish the results.

References

1. Macdonald, D.R.; Cascino, T.L.; Schold, S.C.; Cairncross, J.G. Response criteria for phase II studies of supratentorial malignant glioma. *J. Clin. Oncol.* **1990**, *8*, 1277–1280. [CrossRef]
2. Van den Bent, M.J.; Vogelbaum, M.A.; Wen, P.Y.; Macdonald, D.R.; Chang, S.M. End Point Assessment in Gliomas: Novel Treatments Limit Usefulness of Classical Macdonald's Criteria. *J. Clin. Oncol.* **2009**, *27*, 2905–2908. [CrossRef]
3. Pope, W.B.; Brandal, G. Conventional and advanced magnetic resonance imaging in patients with high-grade glioma. *Q. J. Nucl. Med. Mol. Imaging* **2018**, *62*, 239–253. [CrossRef]
4. Neska-Matuszewska, M.; Bladowska, J.; Sąsiadek, M.; Zimny, A. Differentiation of glioblastoma multiforme, metastases and primary central nervous system lymphomas using multiparametric perfusion and diffusion MR imaging of a tumor core and a peritumoral zone—Searching for a practical approach. *PLoS ONE* **2018**, *13*, e0191341. [CrossRef] [PubMed]
5. Garden, G.A.; Campbell, B.M. Glial biomarkers in human central nervous system disease: Glial Biomarkers in Human CNS Disease. *Glia* **2016**, *64*, 1755–1771. [CrossRef]
6. Staedtke, V.; Dzaye, O.D.; Holdhoff, M. Actionable Molecular Biomarkers in Primary Brain Tumors. *Trends Cancer* **2016**, *2*, 338–349. [CrossRef] [PubMed]
7. Cohen, J.D.; Li, L.; Wang, Y.; Thoburn, C.; Afsari, B.; Danilova, L.; Douville, C.; Javed, A.A.; Wong, F.; Mattox, A.; et al. Detection and localization of surgically resectable cancers with a multi-analyte blood test. *Science* **2018**, *359*, 926–930. [CrossRef] [PubMed]
8. Watson, Z.L.; Bitler, B.G. Type I Protein Arginine Methyltransferases Overexpression Promotes Transformation and Potentiates Her2/Neu–Driven Tumorigenesis. *Cancer Res.* **2019**, *79*, 3–4. [CrossRef]
9. Alix-Panabières, C.; Pantel, K. Liquid Biopsy: From Discovery to Clinical Application. *Cancer Discov.* **2021**, *11*, 858–873. [CrossRef]
10. Lone, S.N.; Nisar, S.; Masoodi, T.; Singh, M.; Rizwan, A.; Hashem, S.; El-Rifai, W.; Bedognetti, D.; Batra, S.K.; Haris, M.; et al. Liquid biopsy: A step closer to transform diagnosis, prognosis and future of cancer treatments. *Mol. Cancer* **2022**, *21*, 79. [CrossRef]
11. Best, M.G.; Sol, N.; Zijl, S.; Reijneveld, J.C.; Wesseling, P.; Wurdinger, T. Liquid biopsies in patients with diffuse glioma. *Acta Neuropathol.* **2015**, *129*, 849–865. [CrossRef]
12. Colombo, M.; Raposo, G.; Théry, C. Biogenesis, Secretion, and Intercellular Interactions of Exosomes and Other Extracellular Vesicles. *Annu. Rev. Cell Dev. Biol.* **2014**, *30*, 255–289. [CrossRef] [PubMed]

13. Janowska-Wieczorek, A.; Wysoczynski, M.; Kijowski, J.; Marquez-Curtis, L.; Machalinski, B.; Ratajczak, J.; Ratajczak, M.Z. Microvesicles derived from activated platelets induce metastasis and angiogenesis in lung cancer. *Int. J. Cancer* **2005**, *113*, 752–760. [CrossRef]
14. Théry, C.; Ostrowski, M.; Segura, E. Membrane vesicles as conveyors of immune responses. *Nat. Rev. Immunol.* **2009**, *9*, 581–593. [CrossRef] [PubMed]
15. Ostrowski, M.; Carmo, N.B.; Krumeich, S.; Fanget, I.; Raposo, G.; Savina, A.; Moita, C.F.; Schauer, K.; Hume, A.N.; Freitas, R.P.; et al. Rab27a and Rab27b control different steps of the exosome secretion pathway. *Nat. Cell Biol.* **2010**, *12*, 19–30. [CrossRef] [PubMed]
16. Hu, T.; Wolfram, J.; Srivastava, S. Extracellular Vesicles in Cancer Detection: Hopes and Hypes. *Trends Cancer* **2021**, *7*, 122–133. [CrossRef]
17. Hergenreider, E.; Heydt, S.; Tréguer, K.; Boettger, T.; Horrevoets, A.J.G.; Zeiher, A.M.; Scheffer, M.P.; Frangakis, A.S.; Yin, X.; Mayr, M.; et al. Atheroprotective communication between endothelial cells and smooth muscle cells through miRNAs. *Nat. Cell Biol.* **2012**, *14*, 249–256. [CrossRef] [PubMed]
18. Skog, J.; Würdinger, T.; van Rijn, S.; Meijer, D.H.; Gainche, L.; Curry, W.T.; Carter, B.S.; Krichevsky, A.M.; Breakefield, X.O. Glioblastoma microvesicles transport RNA and proteins that promote tumour growth and provide diagnostic biomarkers. *Nat. Cell Biol.* **2008**, *10*, 1470–1476. [CrossRef]
19. Kahlert, C.; Melo, S.A.; Protopopov, A.; Tang, J.; Seth, S.; Koch, M.; Zhang, J.; Weitz, J.; Chin, L.; Futreal, A.; et al. Identification of Double-stranded Genomic DNA Spanning All Chromosomes with Mutated KRAS and p53 DNA in the Serum Exosomes of Patients with Pancreatic Cancer. *J. Biol. Chem.* **2014**, *289*, 3869–3875. [CrossRef]
20. Al-Nedawi, K.; Meehan, B.; Micallef, J.; Lhotak, V.; May, L.; Guha, A.; Rak, J. Intercellular transfer of the oncogenic receptor EGFRvIII by microvesicles derived from tumour cells. *Nat. Cell Biol.* **2008**, *10*, 619–624. [CrossRef]
21. Demory Beckler, M.; Higginbotham, J.N.; Franklin, J.L.; Ham, A.-J.; Halvey, P.J.; Imasuen, I.E.; Whitwell, C.; Li, M.; Liebler, D.C.; Coffey, R.J. Proteomic Analysis of Exosomes from Mutant KRAS Colon Cancer Cells Identifies Intercellular Transfer of Mutant KRAS. *Mol. Cell. Proteom.* **2013**, *12*, 343–355. [CrossRef]
22. Sheridan, C. Exosome cancer diagnostic reaches market. *Nat. Biotechnol.* **2016**, *34*, 359–360. [CrossRef]
23. Kosaka, N.; Kogure, A.; Yamamoto, T.; Urabe, F.; Usuba, W.; Prieto-Vila, M.; Ochiya, T. Exploiting the message from cancer: The diagnostic value of extracellular vesicles for clinical applications. *Exp. Mol. Med.* **2019**, *51*, 1–9. [CrossRef]
24. Scavo, M.P.; Depalo, N.; Tutino, V.; De Nunzio, V.; Ingrosso, C.; Rizzi, F.; Notarnicola, M.; Curri, M.L.; Giannelli, G. Exosomes for Diagnosis and Therapy in Gastrointestinal Cancers. *Int. J. Mol. Sci.* **2020**, *21*, 367. [CrossRef]
25. Hoshino, A.; Kim, H.S.; Bojmar, L.; Gyan, K.E.; Cioffi, M.; Hernandez, J.; Zambirinis, C.P.; Rodrigues, G.; Molina, H.; Heissel, S.; et al. Extracellular Vesicle and Particle Biomarkers Define Multiple Human Cancers. *Cell* **2020**, *182*, 1044–1061.e18. [CrossRef]
26. Möhrmann, L.; Huang, H.J.; Hong, D.S.; Tsimberidou, A.M.; Fu, S.; Piha-Paul, S.A.; Subbiah, V.; Karp, D.D.; Naing, A.; Krug, A.; et al. Liquid Biopsies Using Plasma Exosomal Nucleic Acids and Plasma Cell-Free DNA Compared with Clinical Outcomes of Patients with Advanced Cancers. *Clin. Cancer Res.* **2018**, *24*, 181–188. [CrossRef]
27. Tao, S.-C.; Guo, S.-C. Role of extracellular vesicles in tumour microenvironment. *Cell Commun. Signal. CCS* **2020**, *18*, 163. [CrossRef]
28. Ruhen, O.; Meehan, K. Tumor-Derived Extracellular Vesicles as a Novel Source of Protein Biomarkers for Cancer Diagnosis and Monitoring. *Proteomics* **2019**, *19*, 1800155. [CrossRef]
29. Choy, C.; Jandial, R. Breast Cancer Exosomes Breach the Blood-Brain Barrier. *Neurosurgery* **2016**, *78*, N10–N11. [CrossRef]
30. García-Romero, N.; Carrión-Navarro, J.; Esteban-Rubio, S.; Lázaro-Ibáñez, E.; Peris-Celda, M.; Alonso, M.M.; Guzmán-De-Villoria, J.; Fernández-Carballal, C.; de Mendivil, A.O.; García-Duque, S.; et al. DNA sequences within glioma-derived extracellular vesicles can cross the intact blood-brain barrier and be detected in peripheral blood of patients. *Oncotarget* **2017**, *8*, 1416–1428. [CrossRef]
31. Théry, C.; Witwer, K.W.; Aikawa, E.; Alcaraz, M.J.; Anderson, J.D.; Andriantsitohaina, R.; Antoniou, A.; Arab, T.; Archer, F.; Atkin-Smith, G.K.; et al. Minimal information for studies of extracellular vesicles 2018 (MISEV2018): A position statement of the International Society for Extracellular Vesicles and update of the MISEV2014 guidelines. *J. Extracell. Vesicles* **2018**, *7*, 1535750. [CrossRef] [PubMed]
32. Dobra, G.; Bukva, M.; Szabo, Z.; Bruszel, B.; Harmati, M.; Gyukity-Sebestyen, E.; Jenei, A.; Szucs, M.; Horvath, P.; Biro, T.; et al. Small Extracellular Vesicles Isolated from Serum May Serve as Signal-Enhancers for the Monitoring of CNS Tumors. *Int. J. Mol. Sci.* **2020**, *21*, 5359. [CrossRef] [PubMed]
33. Mondal, S.; Adhikari, N.; Banerjee, S.; Amin, S.A.; Jha, T. Matrix metalloproteinase-9 (MMP-9) and its inhibitors in cancer: A minireview. *Eur. J. Med. Chem.* **2020**, *194*, 112260. [CrossRef] [PubMed]
34. Noel, A.; Jost, M.; Maquoi, E. Matrix metalloproteinases at cancer tumor–host interface. *Semin. Cell Dev. Biol.* **2008**, *19*, 52–60. [CrossRef]
35. Jabłońska-Trypuć, A.; Matejczyk, M.; Rosochacki, S. Matrix metalloproteinases (MMPs), the main extracellular matrix (ECM) enzymes in collagen degradation, as a target for anticancer drugs. *J. Enzyme Inhib. Med. Chem.* **2016**, *31*, 177–183. [CrossRef]
36. Chambers, A.F.; Matrisian, L.M. Changing views of the role of matrix metalloproteinases in metastasis. *JNCI J. Natl. Cancer Inst.* **1997**, *89*, 1260–1270. [CrossRef]

37. Mannello, F.; Tonti, G.; Papa, S. Matrix Metalloproteinase Inhibitors as Anticancer Therapeutics. *Curr. Cancer Drug Targets* **2005**, *5*, 285–298. [CrossRef]
38. Barillari, G. The Impact of Matrix Metalloproteinase-9 on the Sequential Steps of the Metastatic Process. *Int. J. Mol. Sci.* **2020**, *21*, 4526. [CrossRef]
39. Jiguet-Jiglaire, C.; Boissonneau, S.; Denicolai, E.; Hein, V.; Lasseur, R.; Garcia, J.; Romain, S.; Appay, R.; Graillon, T.; Mason, W.; et al. Plasmatic MMP9 released from tumor-infiltrating neutrophils is predictive for bevacizumab efficacy in glioblastoma patients: An AVAglio ancillary study. *Acta Neuropathol. Commun.* **2022**, *10*, 1. [CrossRef]
40. Stetler-Stevenson, W.G. Type IV collagenases in tumor invasion and metastasis. *Cancer Metastasis Rev.* **1990**, *9*, 289–303. [CrossRef]
41. Rao, J.S.; Steck, P.A.; Mohanam, S.; Stetler-Stevenson, W.G.; Liotta, L.A.; Sawaya, R. Elevated levels of M(r) 92,000 type IV collagenase in human brain tumors. *Cancer Res.* **1993**, *53*, 2208–2211.
42. Rao, J.S.; Yamamoto, M.; Mohaman, S.; Gokaslan, Z.L.; Fuller, G.N.; Stetler-Stevenson, W.G.; Rao, V.H.; Liotta, L.A.; Nicolson, G.L.; Sawaya, R.E. Expression and localization of 92 kDa type IV collagenase/gelatinase B (MMP-9) in human gliomas. *Clin. Exp. Metastasis* **1996**, *14*, 12–18. [CrossRef] [PubMed]
43. Wu, C.-Y.; Wu, M.-S.; Chiang, E.-P.; Chen, Y.-J.; Chen, C.-J.; Chi, N.-H.; Shih, Y.-T.; Chen, G.-H.; Lin, J.-T. Plasma Matrix Metalloproteinase-9 Level Is Better than Serum Matrix Metalloproteinase-9 Level to Predict Gastric Cancer Evolution. *Clin. Cancer Res.* **2007**, *13*, 2054–2060. [CrossRef] [PubMed]
44. Otero-Estévez, O.; Chiara, L.D.; Rodríguez-Girondo, M.; Rodríguez-Berrocal, F.J.; Cubiella, J.; Castro, I.; Hernández, V.; Martínez-Zorzano, V.S. Serum matrix metalloproteinase-9 in colorectal cancer family-risk population screening. *Sci. Rep.* **2015**, *5*, 13030. [CrossRef]
45. Hormigo, A.; Gu, B.; Karimi, S.; Riedel, E.; Panageas, K.S.; Edgar, M.A.; Tanwar, M.K.; Rao, J.S.; Fleisher, M.; DeAngelis, L.M.; et al. YKL-40 and Matrix Metalloproteinase-9 as Potential Serum Biomarkers for Patients with High-Grade Gliomas. *Clin. Cancer Res.* **2006**, *12*, 5698–5704. [CrossRef]
46. Iwamoto, F.M.; Hottinger, A.F.; Karimi, S.; Riedel, E.; Dantis, J.; Jahdi, M.; Panageas, K.S.; Lassman, A.B.; Abrey, L.E.; Fleisher, M.; et al. Longitudinal prospective study of matrix metalloproteinase-9 as a serum marker in gliomas. *J. Neurooncol.* **2011**, *105*, 607–612. [CrossRef]
47. Ricci, S.; Guadagno, E.; Bruzzese, D.; Del Basso De Caro, M.; Peca, C.; Sgulò, F.G.; Maiuri, F.; Di Carlo, A. Evaluation of matrix metalloproteinase type IV-collagenases in serum of patients with tumors of the central nervous system. *J. Neurooncol.* **2017**, *131*, 223–232. [CrossRef] [PubMed]
48. Linhares, P.; Carvalho, B.; Vaz, R.; Costa, B.M. Glioblastoma: Is There Any Blood Biomarker with True Clinical Relevance? *Int. J. Mol. Sci.* **2020**, *21*, 5809. [CrossRef]
49. Luong, J.H.T.; Vashist, S.K. Chemistry of Biotin-Streptavidin and the Growing Concern of an Emerging Biotin Interference in Clinical Immunoassays. *ACS Omega* **2020**, *5*, 10–18. [CrossRef]
50. EV-TRACK Consortium; Van Deun, J.; Mestdagh, P.; Agostinis, P.; Akay, Ö.; Anand, S.; Anckaert, J.; Martinez, Z.A.; Baetens, T.; Beghein, E.; et al. EV-TRACK: Transparent reporting and centralizing knowledge in extracellular vesicle research. *Nat. Methods* **2017**, *14*, 228–232. [CrossRef]
51. Preusser, M. A step towards clinical blood biomarkers of glioblastoma. *Nat. Rev. Neurol.* **2014**, *10*, 681–682. [CrossRef]
52. Kros, J.M.; Mustafa, D.M.; Dekker, L.J.M.; Sillevis Smitt, P.A.E.; Luider, T.M.; Zheng, P.-P. Circulating glioma biomarkers. *Neuro-Oncol.* **2014**, *17*, 343–360. [CrossRef] [PubMed]
53. McKiernan, J.; Donovan, M.J.; O'Neill, V.; Bentink, S.; Noerholm, M.; Belzer, S.; Skog, J.; Kattan, M.W.; Partin, A.; Andriole, G.; et al. A Novel Urine Exosome Gene Expression Assay to Predict High-grade Prostate Cancer at Initial Biopsy. *JAMA Oncol.* **2016**, *2*, 882. [CrossRef] [PubMed]
54. McKiernan, J.; Donovan, M.J.; Margolis, E.; Partin, A.; Carter, B.; Brown, G.; Torkler, P.; Noerholm, M.; Skog, J.; Shore, N.; et al. A Prospective Adaptive Utility Trial to Validate Performance of a Novel Urine Exosome Gene Expression Assay to Predict High-grade Prostate Cancer in Patients with Prostate-specific Antigen 2–10 ng/ml at Initial Biopsy. *Eur. Urol.* **2018**, *74*, 731–738. [CrossRef] [PubMed]
55. Margolis, E.; Brown, G.; Partin, A.; Carter, B.; McKiernan, J.; Tutrone, R.; Torkler, P.; Fischer, C.; Tadigotla, V.; Noerholm, M.; et al. Predicting high-grade prostate cancer at initial biopsy: Clinical performance of the ExoDx (EPI) Prostate Intelliscore test in three independent prospective studies. *Prostate Cancer Prostatic Dis.* **2022**, *25*, 296–301. [CrossRef]
56. Ostrom, Q.T.; Gittleman, H.; Truitt, G.; Boscia, A.; Kruchko, C.; Barnholtz-Sloan, J.S. CBTRUS Statistical Report: Primary Brain and Other Central Nervous System Tumors Diagnosed in the United States in 2011–2015. *Neuro-Oncology* **2018**, *20*, iv1–iv86. [CrossRef]
57. Fox, B.D.; Cheung, V.J.; Patel, A.J.; Suki, D.; Rao, G. Epidemiology of Metastatic Brain Tumors. *Neurosurg. Clin. N. Am.* **2011**, *22*, 1–6. [CrossRef]
58. Osti, D.; Del Bene, M.; Rappa, G.; Santos, M.; Matafora, V.; Richichi, C.; Faletti, S.; Beznoussenko, G.V.; Mironov, A.; Bachi, A.; et al. Clinical Significance of Extracellular Vesicles in Plasma from Glioblastoma Patients. *Clin. Cancer Res.* **2019**, *25*, 266–276. [CrossRef]
59. Fraser, K.; Jo, A.; Giedt, J.; Vinegoni, C.; Yang, K.S.; Peruzzi, P.; Chiocca, E.A.; Breakefield, X.O.; Lee, H.; Weissleder, R. Characterization of single microvesicles in plasma from glioblastoma patients. *Neuro-Oncology* **2019**, *21*, 606–615. [CrossRef]

60. Jung, K.; Laube, C.; Lein, M.; Lichtinghagen, R.; Tschesche, H.; Schnorr, D.; Loening, S.A. Kind of sample as preanalytical determinant of matrix metalloproteinase 2 and 9 and tissue inhibitor of metalloproteinase 2 in blood. *Clin. Chem.* **1998**, *44*, 1060–1062. [CrossRef]
61. Rouy, D.; Ernens, I.; Jeanty, C.; Wagner, D.R. Plasma storage at −80°C does not protect matrix metalloproteinase-9 from degradation. *Anal. Biochem.* **2005**, *338*, 294–298. [CrossRef] [PubMed]
62. Zucker, S.; Cao, J. Measurement of Matrix Metalloproteinases in Serum of Patients with Melanoma: Snarled in Technical Pitfalls. *Clin. Cancer Res.* **2005**, *11*, 5069–5070. [CrossRef]
63. Yu, D.; Li, Y.; Wang, M.; Gu, J.; Xu, W.; Cai, H.; Fang, X.; Zhang, X. Exosomes as a new frontier of cancer liquid biopsy. *Mol. Cancer* **2022**, *21*, 56. [CrossRef] [PubMed]
64. Yu, W.; Hurley, J.; Roberts, D.; Chakrabortty, S.K.; Enderle, D.; Noerholm, M.; Breakefield, X.O.; Skog, J.K. Exosome-based liquid biopsies in cancer: Opportunities and challenges. *Ann. Oncol.* **2021**, *32*, 466–477. [CrossRef] [PubMed]
65. Lai, H.; Li, Y.; Zhang, H.; Hu, J.; Liao, J.; Su, Y.; Li, Q.; Chen, B.; Li, C.; Wang, Z.; et al. exoRBase 2.0: An atlas of mRNA, lncRNA and circRNA in extracellular vesicles from human biofluids. *Nucleic Acids Res.* **2022**, *50*, D118–D128. [CrossRef]
66. Li, Y.; Zhao, J.; Yu, S.; Wang, Z.; He, X.; Su, Y.; Guo, T.; Sheng, H.; Chen, J.; Zheng, Q.; et al. Extracellular Vesicles Long RNA Sequencing Reveals Abundant mRNA, circRNA, and lncRNA in Human Blood as Potential Biomarkers for Cancer Diagnosis. *Clin. Chem.* **2019**, *65*, 798–808. [CrossRef]
67. Bracht, J.W.P.; Gimenez-Capitan, A.; Huang, C.-Y.; Potie, N.; Pedraz-Valdunciel, C.; Warren, S.; Rosell, R.; Molina-Vila, M.A. Analysis of extracellular vesicle mRNA derived from plasma using the nCounter platform. *Sci. Rep.* **2021**, *11*, 3712. [CrossRef]
68. Kumar, S.R.; Kimchi, E.T.; Manjunath, Y.; Gajagowni, S.; Stuckel, A.J.; Kaifi, J.T. RNA cargos in extracellular vesicles derived from blood serum in pancreas associated conditions. *Sci. Rep.* **2020**, *10*, 2800. [CrossRef]
69. Taran, K.; Wnęk, A.; Kobos, J.; Andrzejewska, E.; Przewratil, P. Tissue and serum mRNA profile of MMPs-2/9 as a potential novel biomarker for the most individual approach in infantile hemangiomas and cancer disease. *Immunobiology* **2017**, *222*, 1035–1042. [CrossRef]
70. Wu, Z.-S.; Wu, Q.; Yang, J.-H.; Wang, H.-Q.; Ding, X.-D.; Yang, F.; Xu, X.-C. Prognostic significance of MMP-9 and TIMP-1 serum and tissue expression in breast cancer. *Int. J. Cancer* **2008**, *122*, 2050–2056. [CrossRef]
71. Guo, C.-B.; Wang, S.; Deng, C.; Zhang, D.-L.; Wang, F.-L.; Jin, X.-Q. Relationship between matrix metalloproteinase 2 and lung cancer progression. *Mol. Diagn. Ther.* **2007**, *11*, 183–192. [CrossRef] [PubMed]
72. Zhou, L.; Kou, D.-Q. Correlation between acute myocardial infarction complicated with cerebral infarction and expression levels of MMP-2 and MMP-9. *Eur. Rev. Med. Pharmacol. Sci.* **2019**, *23*, 297–302. [CrossRef] [PubMed]
73. Vira, H.J.; Pradhan, V.D.; Umare, V.D.; Chaudhary, A.K.; Rajadhyksha, A.G.; Nadkar, M.Y.; Ghosh, K.; Nadkarni, A.H. Expression of the matrix metalloproteinases MMP-2 and MMP-9 and their inhibitors TIMP-1 and TIMP-2 in systemic lupus erythematosus patients. *Neth. J. Med.* **2020**, *78*, 261–268. [PubMed]
74. Prasetyo, E.; Asadul Islam, A.; Hatta, M.; Widodo, D.; Pattelongi, I. The Profile of MMP-9, MMP-9 mRNA Expression, -1562 C/T Polymorphism and Outcome in High-risk Traumatic Brain Injury: The Effect of Therapeutic Mild Hypothermia. *Neurol. Med. Chir.* **2017**, *57*, 612–619. [CrossRef]
75. Liu, Y.; Beyer, A.; Aebersold, R. On the Dependency of Cellular Protein Levels on mRNA Abundance. *Cell* **2016**, *165*, 535–550. [CrossRef]
76. Mund, A.; Brunner, A.-D.; Mann, M. Unbiased spatial proteomics with single-cell resolution in tissues. *Mol. Cell* **2022**, *82*, 2335–2349. [CrossRef]
77. Buccitelli, C.; Selbach, M. mRNAs, proteins and the emerging principles of gene expression control. *Nat. Rev. Genet.* **2020**, *21*, 630–644. [CrossRef]
78. Jia, Y.; Yu, L.; Ma, T.; Xu, W.; Qian, H.; Sun, Y.; Shi, H. Small extracellular vesicles isolation and separation: Current techniques, pending questions and clinical applications. *Theranostics* **2022**, *12*, 6548–6575. [CrossRef]
79. Freitas, D.; Balmaña, M.; Poças, J.; Campos, D.; Osório, H.; Konstantinidi, A.; Vakhrushev, S.Y.; Magalhães, A.; Reis, C.A. Different isolation approaches lead to diverse glycosylated extracellular vesicle populations. *J. Extracell. Vesicles* **2019**, *8*, 1621131. [CrossRef]
80. Clos-Sansalvador, M.; Monguió-Tortajada, M.; Roura, S.; Franquesa, M.; Borràs, F.E. Commonly used methods for extracellular vesicles' enrichment: Implications in downstream analyses and use. *Eur. J. Cell Biol.* **2022**, *101*, 151227. [CrossRef]
81. Veerman, R.E.; Teeuwen, L.; Czarnewski, P.; Güclüler Akpinar, G.; Sandberg, A.; Cao, X.; Pernemalm, M.; Orre, L.M.; Gabrielsson, S.; Eldh, M. Molecular evaluation of five different isolation methods for extracellular vesicles reveals different clinical applicability and subcellular origin. *J. Extracell. Vesicles* **2021**, *10*, e12128. [CrossRef] [PubMed]
82. Gelibter, S.; Marostica, G.; Mandelli, A.; Siciliani, S.; Podini, P.; Finardi, A.; Furlan, R. The impact of storage on extracellular vesicles: A systematic study. *J. Extracell. Vesicles* **2022**, *11*, e12162. [CrossRef] [PubMed]
83. Wu, Y.; Deng, W.; Klinke II, D.J. Exosomes: Improved methods to characterize their morphology, RNA content, and surface protein biomarkers. *Analyst* **2015**, *140*, 6631–6642. [CrossRef] [PubMed]
84. Bosch, S.; de Beaurepaire, L.; Allard, M.; Mosser, M.; Heichette, C.; Chrétien, D.; Jegou, D.; Bach, J.-M. Trehalose prevents aggregation of exosomes and cryodamage. *Sci. Rep.* **2016**, *6*, 36162. [CrossRef] [PubMed]
85. Cheng, Y.; Zeng, Q.; Han, Q.; Xia, W. Effect of pH, temperature and freezing-thawing on quantity changes and cellular uptake of exosomes. *Protein Cell* **2019**, *10*, 295–299. [CrossRef]

86. Sallai, I.; Marton, N.; Szatmári, A.; Kittel, Á.; Nagy, G.; Buzás, E.I.; Khamari, D.; Komlósi, Z.; Kristóf, K.; Drahos, L.; et al. Activated polymorphonuclear derived extracellular vesicles are potential biomarkers of periprosthetic joint infection. *PLoS ONE* **2022**, *17*, e0268076. [CrossRef]
87. Yang, J.E.; Rossignol, E.D.; Chang, D.; Zaia, J.; Forrester, I.; Raja, K.; Winbigler, H.; Nicastro, D.; Jackson, W.T.; Bullitt, E. Complexity and ultrastructure of infectious extracellular vesicles from cells infected by non-enveloped virus. *Sci. Rep.* **2020**, *10*, 7939. [CrossRef]
88. Zhang, Y.-F.; Shi, J.-B.; Li, C. Small extracellular vesicle loading systems in cancer therapy: Current status and the way forward. *Cytotherapy* **2019**, *21*, 1122–1136. [CrossRef]
89. Antimisiaris, S.; Mourtas, S.; Marazioti, A. Exosomes and Exosome-Inspired Vesicles for Targeted Drug Delivery. *Pharmaceutics* **2018**, *10*, 218. [CrossRef]
90. Lötvall, J.; Hill, A.F.; Hochberg, F.; Buzás, E.I.; Di Vizio, D.; Gardiner, C.; Gho, Y.S.; Kurochkin, I.V.; Mathivanan, S.; Quesenberry, P.; et al. Minimal experimental requirements for definition of extracellular vesicles and their functions: A position statement from the International Society for Extracellular Vesicles. *J. Extracell. Vesicles* **2014**, *3*, 26913. [CrossRef]
91. Jung, K.; Lein, M.; Laube, C.; Lichtinghagen, R. Blood specimen collection methods influence the concentration and the diagnostic validity of matrix metalloproteinase 9 in blood. *Clin. Chim. Acta* **2001**, *314*, 241–244. [CrossRef] [PubMed]
92. Gerlach, R.F.; Uzuelli, J.A.; Souza-Tarla, C.D.; Tanus-Santos, J.E. Effect of anticoagulants on the determination of plasma matrix metalloproteinase (MMP)-2 and MMP-9 activities. *Anal. Biochem.* **2005**, *344*, 147–149. [CrossRef] [PubMed]
93. Souza-Tarla, C.D.; Uzuelli, J.A.; Machado, A.A.; Gerlach, R.F.; Tanus-Santos, J.E. Methodological issues affecting the determination of plasma matrix metalloproteinase (MMP)-2 and MMP-9 activities. *Clin. Biochem.* **2005**, *38*, 410–414. [CrossRef] [PubMed]
94. Forsyth, P.A.; Wong, H.; Laing, T.D.; Rewcastle, N.B.; Morris, D.G.; Muzik, H.; Leco, K.J.; Johnston, R.N.; Brasher, P.M.A.; Sutherland, G.; et al. Gelatinase-A (MMP-2), gelatinase-B (MMP-9) and membrane type matrix metalloproteinase-1 (MT1-MMP) are involved in different aspects of the pathophysiology of malignant gliomas. *Br. J. Cancer* **1999**, *79*, 1828–1835. [CrossRef]
95. Vince, G.H.; Wagner, S.; Pietsch, T.; Klein, R.; Goldbrunner, R.H.; Roosen, K.; Tonn, J.C. Heterogeneous regional expression patterns of matrix metalloproteinases in human malignant gliomas. *Int. J. Dev. Neurosci.* **1999**, *17*, 437–445. [CrossRef] [PubMed]
96. Tabouret, E.; Boudouresque, F.; Barrie, M.; Matta, M.; Boucard, C.; Loundou, A.; Carpentier, A.; Sanson, M.; Metellus, P.; Figarella-Branger, D.; et al. Association of matrix metalloproteinase 2 plasma level with response and survival in patients treated with bevacizumab for recurrent high-grade glioma. *Neuro-Oncol.* **2014**, *16*, 392–399. [CrossRef] [PubMed]
97. Farina, A.; Mackay, A. Gelatinase B/MMP-9 in Tumour Pathogenesis and Progression. *Cancers* **2014**, *6*, 240–296. [CrossRef] [PubMed]
98. Kanderi, T.; Gupta, V. Glioblastoma Multiforme. In *StatPearls*; StatPearls Publishing: Treasure Island, FL, USA, 2022.

cancers

MDPI

Article

Raman Spectral Signatures of Serum-Derived Extracellular Vesicle-Enriched Isolates May Support the Diagnosis of CNS Tumors

Matyas Bukva [1,2], Gabriella Dobra [1,2], Juan Gomez-Perez [3], Krisztian Koos [1], Maria Harmati [1], Edina Gyukity-Sebestyen [1], Tamas Biro [4,5], Adrienn Jenei [6], Sandor Kormondi [7], Peter Horvath [1], Zoltan Konya [3], Almos Klekner [6] and Krisztina Buzas [1,8,*]

1 Laboratory of Microscopic Image Analysis and Machine Learning, Biological Research Centre, Institute of Biochemistry, Eötvös Loránd Research Network (ELKH), H-6726 Szeged, Hungary; bukva.matyas@brc.hu (M.B.); dobra.gabriella@brc.hu (G.D.); koos.krisztian@brc.hu (K.K.); harmati.maria@brc.hu (M.H.); sebestyen.edina@brc.hu (E.G.-S.); horvath.peter@brc.hu (P.H.)
2 Department of Medical Genetics, Doctoral School of Interdisciplinary Medicine, University of Szeged, H-6720 Szeged, Hungary
3 Department of Applied and Environmental Chemistry, University of Szeged, H-6720 Szeged, Hungary; juan.gomez@chem.u-szeged.hu (J.G.-P.); konya@chem.u-szeged.hu (Z.K.)
4 Department of Immunology, Faculty of Medicine, University of Debrecen, H-4032 Debrecen, Hungary; biro.tamas@med.unideb.hu
5 Monasterium Laboratory, D-48149 Münster, Germany
6 Clinical Centre, Department of Neurosurgery, University of Debrecen, H-4032 Debrecen, Hungary; jenei.adrienn@med.unideb.hu (A.J.); klekner.almos@med.unideb.hu (A.K.)
7 Department of Traumatology, University of Szeged, H-6720 Szeged, Hungary; kormondi.sandor.pal@med.u-szeged.hu
8 Department of Immunology, University of Szeged, H-6720 Szeged, Hungary
* Correspondence: buzas.krisztina@brc.hu; Tel.: +36-62-432-340

check for updates

Citation: Bukva, M.; Dobra, G.; Gomez-Perez, J.; Koos, K.; Harmati, M.; Gyukity-Sebestyen, E.; Biro, T.; Jenei, A.; Kormondi, S.; Horvath, P.; et al. Raman Spectral Signatures of Serum-Derived Extracellular Vesicle-Enriched Isolates May Support the Diagnosis of CNS Tumors. *Cancers* **2021**, *13*, 1407. https://doi.org/10.3390/cancers13061407

Academic Editors: Brigitta G. Baumert and Janusz Rak

Received: 22 January 2021
Accepted: 16 March 2021
Published: 19 March 2021

Simple Summary: The conventional central nervous system (CNS) tumor diagnostic methods, especially the invasive intracranial surgical tissue sample collecting, imposes a heavy burden on both patients and healthcare providers. We aimed to explore the potential role of serum-derived small extracellular vesicles (sEVs) in diagnosing CNS tumors through Raman spectroscopic analyses. A relevant number of clinical samples (138) were obtained from four patient groups, namely glioblastoma multiforme, brain metastasis of non-small-cell lung cancer, meningioma, and lumbar disc herniation as controls. After the isolation and Raman measurements of sEV-sized particles, the Principal Component Analysis–Support Vector Machine algorithm was performed on the Raman spectra for pairwise classifications. The groups compared were distinguishable with 80–95% sensitivity and 80–90% specificity. Our results support that Raman spectroscopic analysis of sEV-sized particles is a promising liquid-biopsy-based method that could be further developed in order to be applicable in the diagnosis of CNS tumors.

Abstract: Investigating the molecular composition of small extracellular vesicles (sEVs) for tumor diagnostic purposes is becoming increasingly popular, especially for diseases for which diagnosis is challenging, such as central nervous system (CNS) malignancies. Thorough examination of the molecular content of sEVs by Raman spectroscopy is a promising but hitherto barely explored approach for these tumor types. We attempt to reveal the potential role of serum-derived sEVs in diagnosing CNS tumors through Raman spectroscopic analyses using a relevant number of clinical samples. A total of 138 serum samples were obtained from four patient groups (glioblastoma multiforme, non-small-cell lung cancer brain metastasis, meningioma and lumbar disc herniation as control). After isolation, characterization and Raman spectroscopic assessment of sEVs, the Principal Component Analysis–Support Vector Machine (PCA–SVM) algorithm was performed on the Raman spectra for pairwise classifications. Classification accuracy (CA), sensitivity, specificity and the Area Under the Curve (AUC) value derived from Receiver Operating Characteristic (ROC) analyses were used to evaluate the performance of classification. The groups compared were distinguishable with

82.9–92.5% CA, 80–95% sensitivity and 80–90% specificity. AUC scores in the range of 0.82–0.9 suggest excellent and outstanding classification performance. Our results support that Raman spectroscopic analysis of sEV-enriched isolates from serum is a promising method that could be further developed in order to be applicable in the diagnosis of CNS tumors.

Keywords: small extracellular vesicles; Raman spectroscopy; glioblastoma multiforme; brain metastasis; meningioma; CNS tumors; liquid biopsy

1. Introduction

In recent decades, secreted extracellular vesicles (EVs) have been recognized as a pathway for intercellular communication in both eukaryotes and prokaryotes [1]. Furthermore, several studies demonstrate the role of EVs in maintaining cellular homeostasis and integrity by compensating for the stress condition [2–4]. Their involvement in different pathophysiological processes has already been highlighted, especially in malignant diseases [5,6]. EVs released by tumor cells are involved in both stromal and distant cell communication, metastatic niche formation, and immune cell suppression [7–13].

Recent clinical research has highlighted that EVs could serve as novel tools for various therapeutic approaches, including oncotherapy, vaccination, immune-modulatory or regenerative therapies, and drug delivery [14]. Furthermore, EVs are gaining increasing popularity in biomarker research as their potential in liquid biopsy has been recognized [15].

Secreted EVs are stably present in body fluids, and represent a concentrated sample of the cytosolic milieu (proteins, nucleic acids, and lipids) of the donor cells [16–18]. It has been shown that EVs isolated from the serum and plasma offer a useful tool to improve the signal-to-noise ratio in analytics by assuring to abundant protein depletion (such as albumin and lipoproteins) and enriching the tumor-specific molecular composition [19,20]. Moreover, EVs can cross various biological barriers, such as the blood–brain barrier (BBB), and easily enter the peripheral blood [21,22].

Examining the protein, nucleic acid, or lipid contents of EVs has revealed several molecules as promising diagnostic markers for different tumor types. For example, glypican-1 glycoprotein enriched in circulating EVs has been shown to be suitable for distinguishing malignant pancreatic cancer from benign malformations with 100% classification accuracy [23,24].

Given their favorable biological properties, serum-derived EVs are being evaluated in the diagnosis and monitoring of central nervous system (CNS) tumors which represent a major challenge in oncology [25].

Today, the diagnosis of CNS tumors mainly relies on neuroimaging techniques (e.g., magnetic resonance imaging (MRI) or computer tomography (CT)) and tissue biopsy. However, all of these methods have numerous limitations [26]. Among others, MRI can only detect tumor masses of sufficient magnitude, and has little prognostic value in terms of long-term recurrence [27]. Distinguishing between different CNS malignancies, such as glioblastoma multiforme and brain metastases, is also challenging using neuroimaging techniques [28]. In addition, treatment-related changes can overlap with residual or recurrent tumors, making tumor monitoring highly challenging [29].

Many brain tumors are particularly difficult to be sampled or are inaccessible for tissue biopsy. Even in cases of biopsy, the procedure harbors significant risks for the patient (e.g., hemorrhage, or impairment of neurological functions). These risks and difficulties hamper not only the diagnosis, but also the monitoring of treatment response or distinguishing tumor recurrence from pseudoprogression [30]. In addition, in some cases, such as in glioblastoma multiforme, the focal sampling of small and localized tumor tissues may not fully capture intratumoral heterogeneity [31,32].

Liquid biopsy has remarkable advantages over conventional methods, offering a minimally invasive, safer, faster, and cheaper way to diagnose and monitor malignant

diseases. Tumor tissues release various types of biomarkers, such as proteins, nucleic acids or lipids, and EVs that accumulate in body fluids (including the blood, urine, cerebrospinal fluid and saliva) are accessible for sampling [33–35].

Tumor markers determined from blood samples, such as the prostate-specific antigen (PSA), alpha-fetoprotein and cancer antigen 125 (CA-125), have already been introduced into clinical practice to support the diagnosis and/or monitoring of prostate, liver and ovarian cancers. Research is underway to identify other non-invasive biomarkers for the monitoring of a broader range of malignant diseases [36].

However, identifying blood-based CNS tumor markers is more challenging, presumably explained by several reasons. BBB can prevent tumor-derived molecules (tumor "information") from entering the peripheral blood, therefore molecules released by other tissues/cells at high concentrations can impede the detection of potential tumor biomarkers present in lower concentrations. Abundant serum proteins (such as albumin or lipoproteins) also appear as a significant analytical noise [19,37]. Nevertheless, investigations for blood-based CNS tumor markers are in the spotlight of neuro-oncological research, as they would have outstanding advantages in patient care [38].

Due to their beneficial properties detailed above, EVs are promising tools in the research for CNS tumor biomarkers. Several published studies aimed to examine the nucleic acid and protein contents of blood samples or EVs derived from CNS tumor patients (specifically, from patients with gliomas). However, these studies attempted to identify one or two biomarkers of nucleic acid or protein types, and these molecules did not prove to be sufficiently specific or sensitive to serve as diagnostic markers, and thus they were not validated with blinded samples [39–41].

Analyzing the whole molecular composition of tumor-related EVs isolated from blood samples may provide a solution to overcome the difficulties encountered in CNS tumor biomarker research. Raman spectroscopy is a suitable approach for this purpose, since it provides information on the entire molecular content of a sample. Raman spectroscopy is a non-destructive, label-free vibrational technique that measures the non-elastic scattering effect induced by a radiating laser. The energy of this inelastically scattered light is reduced by the vibrational energy of the chemical bonds present in the molecules within a sample [42]. The difference is proportional to, and thus specifically refers to, the chemical composition of the sample. Therefore Raman spectroscopy can reveal a specific spectral signature that describes the whole chemical composition, and thus avoids the need for identifying any specific protein, nucleic acid, or lipid biomarkers [43]. In addition, Raman spectroscopy may be suitable for the characterization of EVs by identifying different subtypes by origin and function, which is an important and long-standing challenge for EV-based biomarker research [44].

Recent studies suggest that Raman spectroscopic analysis of the whole molecular composition of various sample types may be suitable to develop promising diagnostic methods for clinical practice [45–47]. Some of these in vitro studies focused on EVs and demonstrated their outstanding diagnostic efficiency. For example, using this technique, Parks and colleagues distinguished EVs released by lung cancer cells from those secreted by normal cells with 95.3% sensitivity and 97.3% specificity. Meanwhile, discriminatory spectral differences were also identified using principal component analysis (PCA) [48]. Charmichael and colleagues revealed that EVs originating from pancreatic cancer cells were distinguishable from those released by normal pancreatic epithelial cells with 90% accuracy [49].

However, no studies to date have investigated the diagnostic efficiency of Raman spectroscopic analysis of serum-derived EVs with regard to CNS tumors. Thus, we aimed to explore the potential role of serum-derived EVs in diagnosing CNS tumors through Raman spectroscopic analyses on a relevant number of clinical samples.

For this purpose, 138 serum samples were obtained from four patient groups. The serum samples were collected from patients diagnosed with the two most common types of brain tumors, namely malignant glioblastoma multiforme (GBM) and the typically benign

meningioma (M), as well as from patients with a prevalent brain metastasis originating from non-small-cell lung cancer (BM). Patients with lumbar disc herniation without evidence of neurological cancer served as controls (CTRL) [20,50,51]. Particles within the size range of small EVs (sEVs) were isolated from serum samples via differential centrifugation, and were assessed by a Raman microscope. Multivariate analyses, including Principal Component Analysis–Support Vector Machine (PCA–SVM) and FreeViz, as well as conventional statistical methods, such as Receiver Operating Characteristic (ROC) analysis, were carried out on spectroscopic data to develop and evaluate a classification model.

Our results support that analyzing the serum-derived sEV-enriched isolates by Raman spectroscopy, which captures the whole molecular composition, may be suitable to develop a method with a possible diagnostic value for CNS tumors, and thus it may have the potential to be introduced into clinical practice in the future.

2. Results

2.1. Particles Isolated from Serum Show sEV Properties

Particles were isolated by differential centrifugation from 138 serum samples of patients with GBM, BM), M and CTRL. Isolated sEVs were characterized by transmission electron microscopy (TEM) and nanoparticle tracking analysis (NTA), as well as by examining characteristic sEV markers (Alix, CD81 and calnexin) by Western blotting (WB) (Figure 1). Average concentration, mean and mode diameter of the particles were measured as 7.41×10^{10} particles/mL, 111.20 nm and 83.32 nm, respectively. Alix, CD81 positivity and calnexin negativity was determined (see Figure S1 for the original WB images).

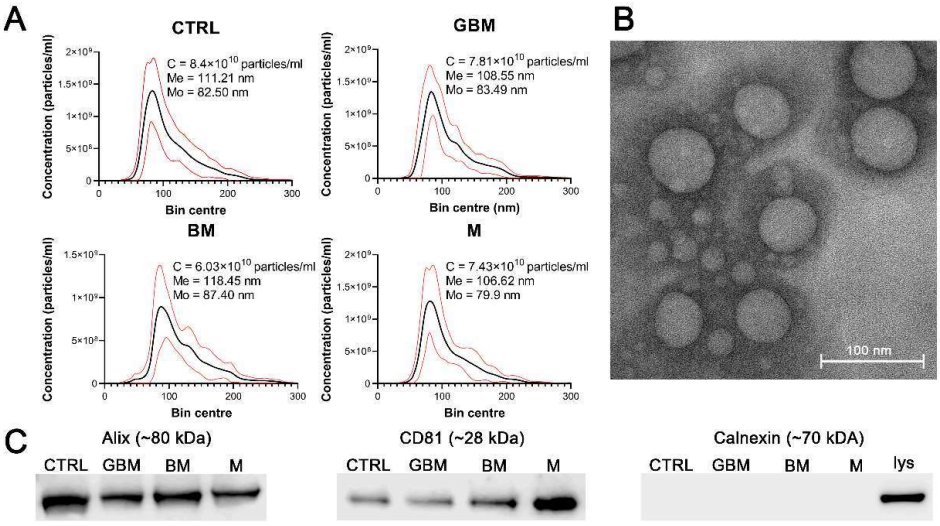

Figure 1. Characterization of the particles. The figure represents the results of the particle characterization: size distribution of the sEV samples isolated from the four patient groups (black and red lines represent the mean and the standard deviation of the concentration, respectively) (**A**), a representative TEM image of the sEVs (**B**), and the Western blot analysis of the sEV markers (**C**). (Abbreviations: CTRL, control; GBM, glioblastoma multiforme; BM, brain metastasis; M, meningioma; C, particle concentration; lys, cell lysate; Me, mean diameter size; Mo, mode diameter size.)

No statistically significant differences were identified among the patient groups in any of the parameters of the isolated particles.

2.2. Patient Groups Can Be Distinguished Using the PCA–SVM Algorithm with High Classification Efficiency

Raman spectroscopic analyses of the isolated 138 samples yielded 5 spectra per sample. The spectral range between 801 cm^{-1} and 3100.5 cm^{-1} was investigated. After standard

normal variate (SNV) normalization and PCA transformation, the classification of samples was performed using the SVM algorithm. Classification efficiency was evaluated by classification accuracy (CA), sensitivity, specificity and the area under the curve (AUC) value derived from the ROC analysis. Relevant spectral differences were revealed by PCA. Figure 2 shows the flowchart of Raman spectroscopy data processing.

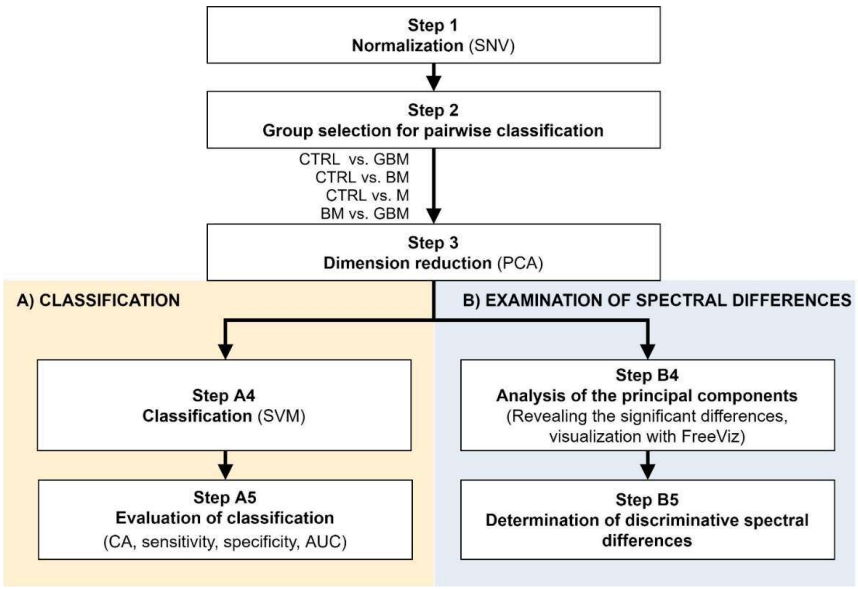

Figure 2. Workflow of Raman spectroscopic data processing. The figure shows the analysis step by step. After Step 3, the workflow separates (parts **A** and **B**) according to the purpose of the analysis. (Abbreviations: AUC, area under the curve; CA, classification accuracy; SNV, standard normal variate; SVM, support-vector machine; PCA, principal component analysis).

After averaging the spectra, row normalization was performed using the SNV method (Step 1) (Figure 3).

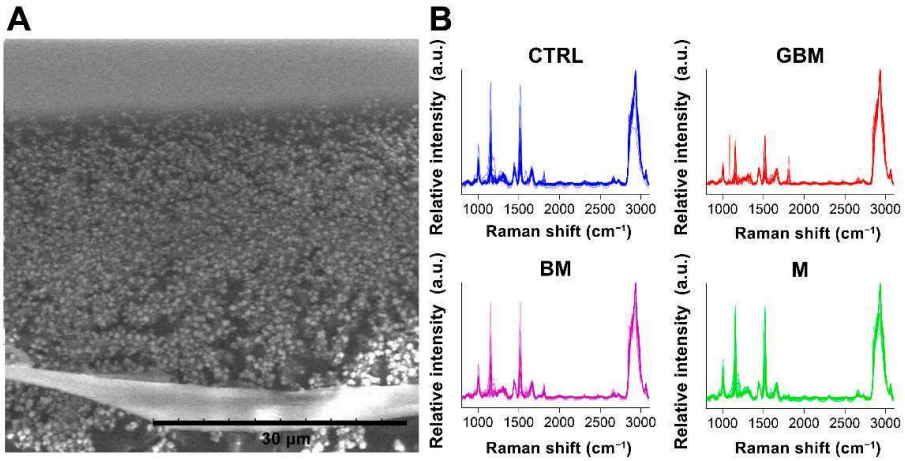

Figure 3. Particles on a calcium fluoride substrate (scanning electron microscope image) (**A**). Averaged and SNV-normalized spectra of the four patient groups (**B**). (Abbreviations: a.u., arbitrary unit).

Following SNV-normalization, the spectra for the samples of the four patient groups were compared pairwise (each patient group was compared to the control, and BM vs. GBM was compared) for two purposes: first, to develop and test a classification algorithm, and second, to identify relevant spectral differences. PCA applied on the pairwise comparisons reduced multivariate data dimensions by transforming the original variables (wavenumbers) into a smaller number of new variables, i.e., principal components (PCs) (Step 3).

Pairwise comparisons were conducted using the linear SVM (Step A4) algorithm, yielding classification models for each paired group. To make predictions for the test samples, a minimum threshold for the group-membership score was determined. Test samples with scores above this threshold were classified into the target group of interest. The optimal score thresholds were automatically set to correspond to the highest classification accuracy (CA, the ratio of correctly classified samples per all samples).

CA was 85.6% for CTRL vs. GBM, 91.4% for CTRL vs. BM, 82.9% for CTRL vs. M and 92.5% for BM vs. GBM. The best classification performance was achieved when a certain number of PCs were included in the models: 30 PCs for CTRL vs. GBM, 38 PCs for CTRL vs. BM, 27 PCs for CTRL vs. M, and 26 PCs for BM vs. GBM (Figure 4).

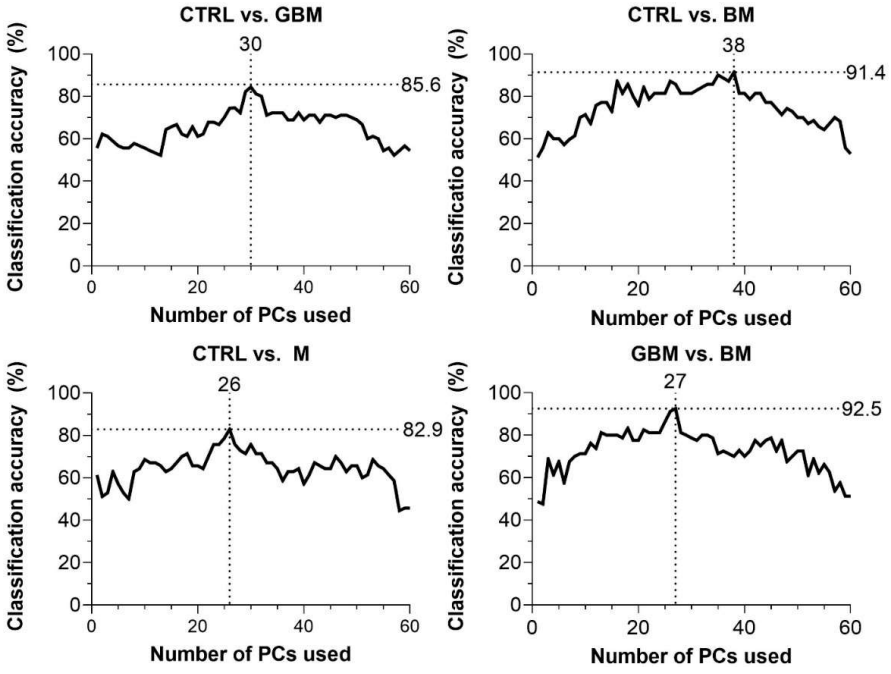

Figure 4. Classification accuracy (CA) scores with respect to the number of PCs included in the model (60 PCs at a maximum). Black dotted lines show the highest CA peaks with the corresponding number of PCs. (Abbreviations: PC, principal component).

Sensitivity and specificity were evaluated as further metrics of classification performance. ROC analyses of the pairwise classification models yielded four graphs showing the automatically set optimal thresholds (having the highest CA value), with related sensitivity, specificity and AUC values, as well as *p*-value (Figure 5).

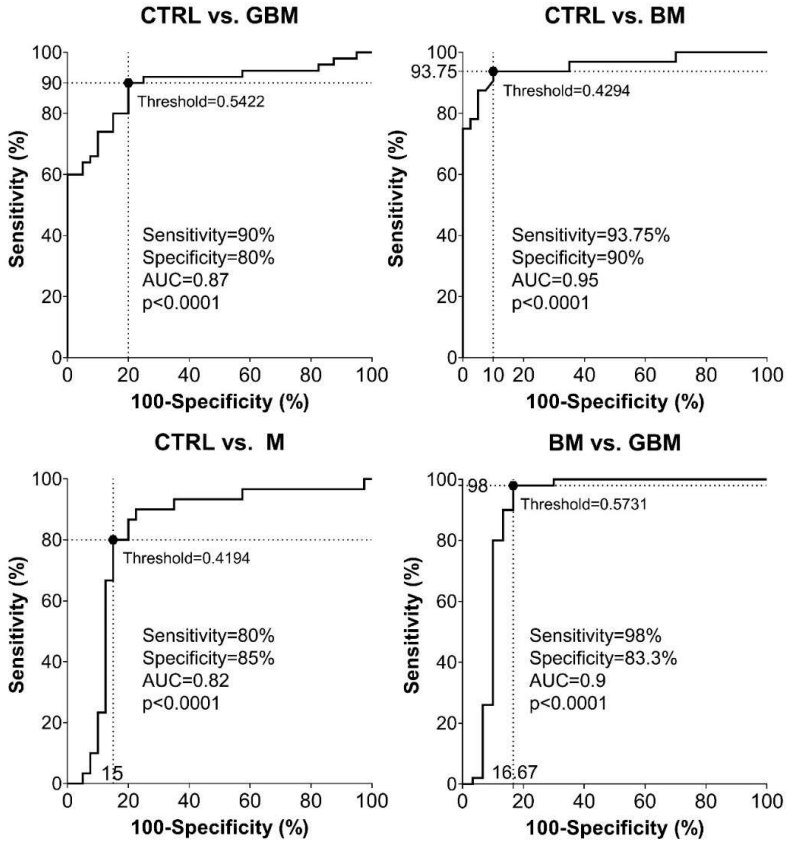

Figure 5. Receiver Operating Characteristic (ROC) curves for the classification models. Intersecting black dotted lines show sensitivity, specificity and corresponding threshold values of the group-membership score, with black filled circles at their intersections.

As shown in the graphs in Figure 5, using the optimal thresholds, the classification models were able to distinguish GBM, BM and M patients from CTRL patients with a sensitivity and specificity of 90% and 80%, 93.75% and 90%, 80% and 85%, respectively (Step A5). Using the classification model, the two malignancies, BM and GBM, could be distinguished from each other with a sensitivity of 98% and a specificity of 83.3%. In the same order of pairwise comparisons (GBM, BM and M patients vs. CTRL, and BM vs. GBM), the AUC values were 0.87, 0.95, 0.82 and 0.9, respectively ($p < 0.0001$ in all cases).

2.3. Analysis of the PCs Revealed Discriminative Spectral Differences

Next, differences in the molecular content of serum-derived sEV-enriched isolates from each group were investigated to reveal the spectral differences relevant with regard to the classification. SNV-normalized spectra and the PCs obtained from PCA were analyzed using the FreeViz method, in order to reveal and visualize relevant spectral differences.

The FreeViz method (Step B4) displayed the optimized projections of the multivariate data sets in a 2-dimensional scatterplot (Figure 6). Based on the length and direction of PC vectors, two PCs that were revealed to play the most important role in distinguishing each paired group (marked with a yellow background in Figure 6) were further assessed to determine discriminative spectral signatures.

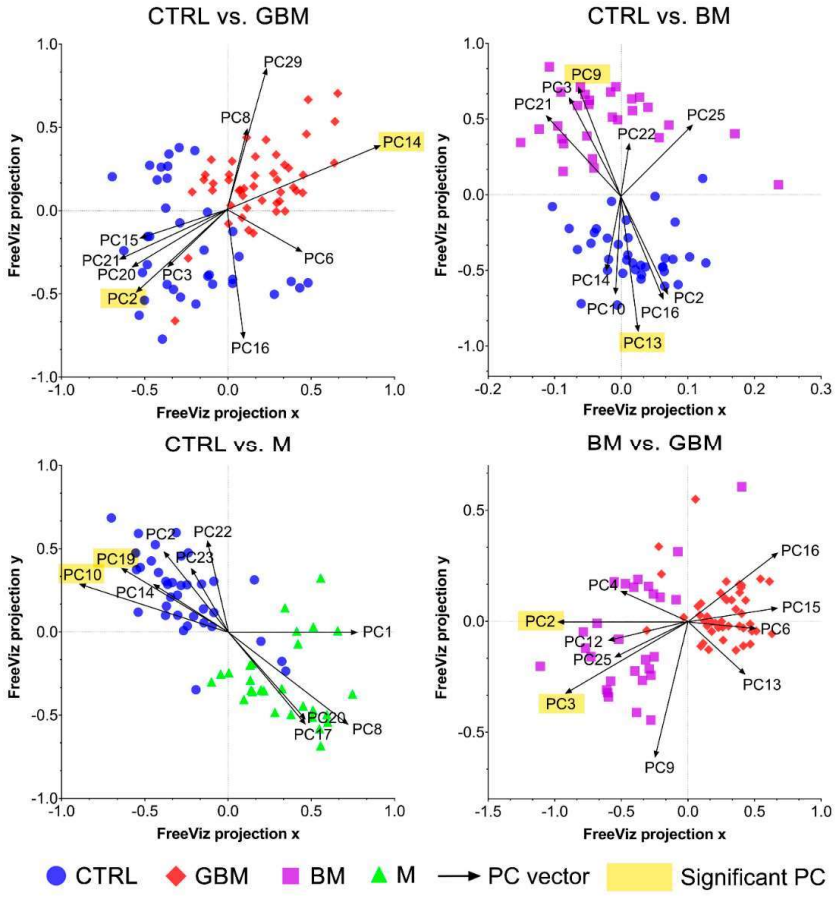

Figure 6. FreeViz projections of pairwise comparisons. Analysis of the PCA-transformed data using the FreeViz method yielded four graphs. Different dots and colors represent the patient groups and healthy controls. Black vectors represent the PCs. In each graph, only the 10 most relevant PC vectors were plotted. For each comparison, PCs marked with a yellow background indicate the 2 most significant PCs.

Based on the results of the FreeViz method and p-values from Welch's *t*-test, PC14 and PC2, PC9 and PC13, P10 and PC19, and PC2 and PC3 explained most of the discriminative differences in the CTRL vs. GBM, CTRL vs. BM, CTRL vs. M and BM vs. GBM comparisons, respectively ($p < 0.05$ in all cases) (see Figure S2 for the score plots of the selected PCs).

Evaluating the selected PCs, we attempted to find the chemical bonds and functional groups corresponding to the spectral differences found to have an important role in distinguishing the compared groups (Step B5).

Regarding the CTRL vs. GBM comparison, most of the discriminative spectral differences were characteristic for carbohydrates, such as bands associated with a pyranose ring (800–975 cm^{-1}), O-H deformation vibrations (1030–1080 cm^{-1}) and C-O stretching vibrations (1030–1290 cm^{-1}). These bands largely overlap with the region's characteristic for nucleic acids, including the bands associated with the vibrations of the phosphate-sugar backbone (800–1000 cm^{-1}), symmetric and asymmetric phosphate group stretching vibrations (1000–1250 cm^{-1}), glycosidic bond vibrations (1250–1550 cm^{-1}), and in-plane double bond vibrations of bases (1530–1780 cm^{-1}) (Figure 7).

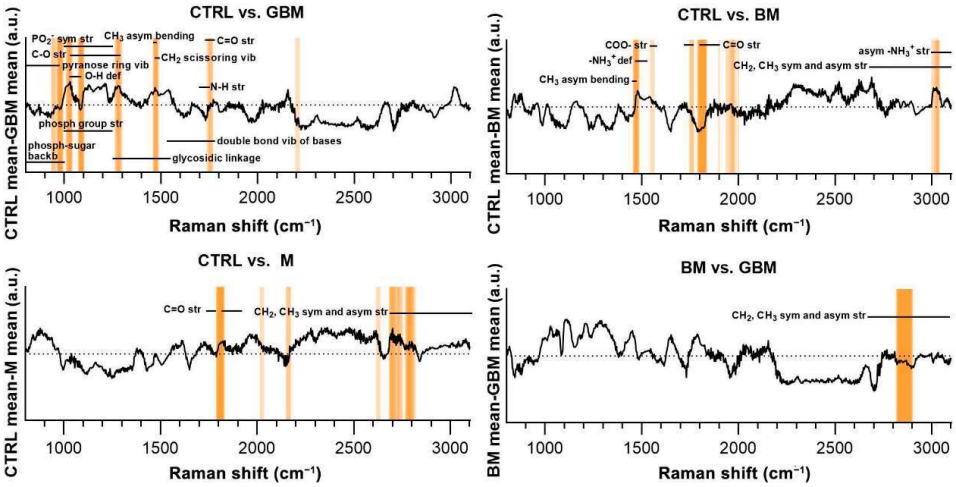

Figure 7. Subtraction spectra for the pairwise comparisons. Subtraction spectra were produced by subtracting the mean signal intensities for the groups compared. Spectral regions having a higher-than-average contribution to significant PCs were marked with orange bars. The more saturated a bar is, the more that region is represented on the selected PCs. The dotted horizontal line represents zero difference at y = 0. (Abbreviations: asym, asymmetric; backb, backbone; def, deformation; phosph, phosphate; str, stretching; sym, symmetric; vib, vibration).

Regarding the CTRL vs. BM comparison, the wavenumbers found to have an important role in distinguishing the BM group from the control mainly correlated with lipids (CH_3 asymmetrical bending (1470–1490 cm^{-1}), CH_2 and CH_3 symmetrical and asymmetrical stretching vibrations (2700–3100 cm^{-1})) and amino acids ($–NH_3^+$ deformation band (1485–1150 cm^{-1}), $–NH_3^+$ asymmetrical stretching (3000–3100 cm^{-1}), carboxylate ion stretching (1560–1600 cm^{-1}) and C=O stretching vibrations of the carboxyl group (1700–1755 cm^{-1})). Regarding the CTRL vs. M and BM vs. GBM comparisons, the wavenumbers highly correlated with vibrations originating from acyl chains of lipids, such as CH_3 and CH_2 symmetric and asymmetric stretching vibrations (2700–3100 cm^{-1}) (see Table S1 for the tabular form of the discriminative spectral differences).

3. Discussion

Circulating sEVs are considered as promising sources of CNS tumor markers. Several studies have investigated the nucleic acid and protein contents of blood samples or EVs from CNS tumor patients. These studies have generally attempted to identify one or two biomarkers targeting the proteome, genome or lipidome. However, these molecules alone do not have sufficient diagnostic or prognostic value, thus they cannot be used as single biomarkers, and none of these have been validated on blinded clinical samples [26,39–41,52,53].

Analyzing the entire molecular composition of tumor-related EVs could provide a solution to overcome the difficulties encountered in CNS tumor biomarker research. Raman spectroscopy is a suitable approach for this purpose, as it provides information on the total molecular content, yielding a specific spectral signature that describes the chemical composition of a sample. Thus, it has the potential to avoid the need for identifying any specific protein, nucleic acid or lipid biomarkers [43].

Based on these considerations, we have attempted to explore the potential role of serum-derived sEVs in the diagnosis of CNS tumors through Raman spectroscopic analyses on a clinically relevant cohort. According to our knowledge, this is the first study that aims to classify CNS tumors based on the Raman spectra of sEV-enriched isolates from serum samples.

For this purpose, 138 serum samples obtained from four patient groups were analyzed. Serum samples were collected from three brain tumor groups considered as the most common malignant, benign and metastatic brain tumors (GBM, BM, M) and from a control group (CTRL) [20,50,51]. sEV-sized particles from serum samples were isolated by differential centrifugation.

The particles found in the isolates show sEV properties (CD81, Alix positivity and calnexin negativity). However, since abundant serum protein aggregates and lipoproteins (LPs) are able to mimic sEVs in terms of size (mean and mode diameter of 111.20 nm and 83.32 nm), we cannot state that only sEVs are present in the isolates. In our previously published proteomic-based study on the same patient groups, we have shown that, although contaminants are still present in the isolates, differential centrifugation significantly enriched the sEV-specific markers and reduced the level of LPs. Since LPs and abundant serum protein aggregates are certainly present in addition to sEVs, the isolates should be considered only as sEV-enriched rather than purified sEVs. In light of these, Raman spectra may characterize a circulating particle profile, part of which is sEVs assumed as biomarkers.

No significant differences were found between the four patient groups in the concentration, mean and mode diameter of sEV-sized particles. Osti et al. observed higher EV concentration in the plasma samples of GBM patients, brain metastases and extra-axial brain tumors compared to healthy controls [54]. Other researchers also showed higher EV concentration in tumor patients when unfractionated EV isolates or a broader spectrum of EVs were analyzed [55–57]. However, other non-neoplastic diseases of the central nervous system can also increase the number of sEVs, as has been shown in acute ischemic stroke or multiple sclerosis patients [58,59]. These findings suggest that the elevated sEV concentration cannot be clearly attributed to the presence of the tumor as immune responses or other systemic responses also contribute to the circulating EV population. Therefore, the intense inflammation associated with lumbar disc herniation (CTRL) may explain why no statistical difference was identified between tumorous and non-tumorous patient groups [60].

In the light of the above, we hypothesize that the isolates contain not only tumor tissue-derived vesicles but also other circulating vesicles, including vesicles released by red blood cells, platelets and immune cells. Therefore, the differences observed in the Raman spectra of the different patient groups may not only reflect tumor-specific processes but other host responses, i.e., the tumor-associated immune responses or different coagulant phenotypes as well [61–63].

After the Raman spectroscopic measurements, multivariate analyses and conventional statistical methods were applied on the spectroscopic data to develop and evaluate a classification model, and find the characteristic spectral signatures distinguishing between the patient groups and healthy controls, as well as between the glioblastoma multiforme and brain metastasis groups.

PCA was applied to all the SNV-normalized spectra. PCA is a standard way to reduce data dimensionality and obtain characteristic spectral signatures [48,64].

Classification was performed by applying the SVM algorithm on PCA-transformed data. Classification performance was evaluated by CA, sensitivity (rate of true positive samples), specificity (rate of true negative samples), and the AUC value derived from ROC analysis, which are all commonly used and accepted metrics in clinical practice.

The GBM, BM and M groups proved to be distinguishable from CTRL with 85.6%, 91.4%, 82.9% of CA, respectively. Interestingly, maximal classification accuracy depended on the number of PCs used for classification, showing an increasing trend towards a specific number of PCs (Figure 4). The relationship between the number of PCs included and CA achieved is probably explained by the complexity of these biological samples.

In most studies, the first two PCs (PC1 and PC2) were able to describe the complete data set and revealed distinctive patterns [64]. However, as Lyng and colleagues' findings show, the first two components may not sufficiently explain the information included in

the complete Raman spectrum for biological samples, due to their complex molecular composition [65]. Using combinations of PCA and various discriminant analyses, Lyng and colleagues found that 20 PCs were required to separate breast tumor tissue samples from healthy controls with 80% CA. Our results also support that including two PCs, only one cannot develop an accurate classification model capable of spectrally discriminating between different ex vivo biological sample groups. However, classification performance can be improved by increasing the number of PCs included in the model, although above a certain number of PCs used, the information they explain may be meaningless or may account for noise, leading to decreased classification accuracy (Figure 4). This suggests that the spectra for biological samples show a high degree of overlap due to their complexity. Hence, accurate classification can be performed only when one correctly uses several dimensions, taking small spectral differences into account.

Although sensitivity and specificity can be calculated by regarding each value of the group-membership scores as a threshold, the ROC curves, including all possible decision thresholds, plus AUC together, offer a more comprehensive assessment [66,67].

According to the ROC analyses, sensitivity and specificity values were as follows: 90% and 80% for CTRL vs. GBM, 93.75 and 90% for CTRL vs. BM, 80% and 85% for CTRL vs. M, and 98% and 83.3% for BM vs. GBM, respectively. In the same order of comparisons, AUC values were 0.87, 0.95, 0.82 and 0.9 (Figure 5).

Based on the literature of ROC analysis, our classification models for CTRL vs. GBM and CTRL vs. M comparisons can be considered as "excellent", and "outstanding" for CTRL vs. BM and BM vs. GBM comparisons [66].

Due to its reliable theoretical basis, SVM has become one of the most widely used classification methods in recent years, especially for complex multivariate data sets obtained from spectroscopic analyses, characterized by high variance and probable outliers [65,68–70]. These properties make the SVM classifier particularly suitable to discriminate between clinical samples based on their Raman spectra, even for diseases known to be highly heterogeneous (such as GBM) [31,32]. Furthermore, Neska-Matuszewska highlighted that various malignancies (e.g., BM and GBM) are challenging to be distinguished using conventional neuroimaging techniques [28]. In light of our findings, Raman spectra-based SVM classification may support a reliable differential diagnosis between primary brain tumors and metastatic brain malignancies. However, it should be noted that the future confirmation of our results via the comparison of other primary and metastatic brain tumor types is clearly required.

Using the FreeViz method, PCs that were particularly important in terms of distinguishing between the compared groups could be identified (Figure 6). By examining the contribution of the wavenumbers to the selected PCs, we attempted to find the chemical bonds and functional groups that correlate with the spectral differences revealed to play an important role in our pairwise classifications.

The molecular correlation of the vibrational bands in the Raman spectra is extremely difficult to interpret. The difficulty arises from the complexity of biological samples in which an abundance of organic molecules coexist and share some of the functional groups responsible for the Raman-spectral features [71]. As a result, the overlap of different vibrational bands hinders the precise identification of any specific molecules based on Raman spectral features (Figure 7). Nevertheless, it was possible to identify discriminative spectral differences in the CTRL vs. GBM comparison, defining bands characteristic for carbohydrates and nucleic acids. These differences may be due to the characteristic metabolism of GBM, as it is associated with a significant increase in glycolysis for energy production and abnormal purine and pyrimidine synthesis [72]. Comparing the spectra of the CTRL and BM groups, significant differences were found in the characteristic bands of lipids and amino acids, which can be partly explained by the fact that an NSCLC appears to be reliant on fatty acid and serine catabolism [73]. Comparing the CTRL and M groups, as well as the two malignant groups BM and GBM, the lipid bands had outstanding importance with regard to discriminatory differences. The prominent importance of lipids

in the BM vs. GBM comparison may be explained by the increased lipid catabolism of NSCLC and the elevated level of de novo lipid synthesis in GBM [72,73]. However, more detailed identification based on the difficulties described above is not expedient for complex biological samples.

It should be noted that co-purification of abundant serum proteins and LP particles in EV isolation methods is a common and well-known challenge [74]. Liu and colleagues emphasized that serum is not the perfect choice for representative sampling of circulating EVs, as a high proportion of EVs may be lost during clotting, and blood components enrolled in the coagulation may also (e.g., platelets) release EVs altering the original content of blood samples [58]. Some cancerous diseases, such as GBM, may also have a procoagulant phenotype [75].

Despite these difficulties, we have revealed in a previously published article that EV isolation from the serum samples of the same patient groups significantly improves the signal-to-noise ratio, even in the case of GBM with an elevated procoagulant activity [20]. Although abundant serum proteins and LPs were still present in EV isolates, isolation depleted their concentration and enriched the EV and tumor-specific protein markers. These results are consistent with previous similar researches on serum-derived EVs [19,76]. Nevertheless, examining plasma instead of serum should be considered in further investigations [58,74].

Enciso-Martinez and colleagues have determined Raman spectral signatures which were able to distinguish EVs from LPs and platelets with 95% confidence [77]. These special signature regions were found at 1004 cm^{-1} and between 2811 cm^{-1} and 3023 cm^{-1}. Wavelength 1004 cm^{-1} had a strong peak in EVs but was not present in LPs and platelets. Furthermore, in the spectral range of 2811–3023 cm^{-1}, EVs showed stronger intensity after 2900 cm^{-1} ('protein component of the CH region') compared to the spectra of LPs, where the region before 2900 cm^{-1} ('lipid component of the CH region') proved to be more intense.

The Raman spectra of sEV-enriched isolates in our study show similar properties: a peak with strong intensity is present at 1004 cm^{-1} and the "protein component" of the CH region was found to be much more prominent than the "lipid component".

Considering its feasibility and beneficial properties, the steps of our research work could be incorporated into method developments aiming to establish novel diagnostic tools potentially applicable in clinical practice. Our isolation protocol has several advantages, as it does not require expensive equipment or highly trained professionals, and the entire procedure (along with characterization) is performed in about 4 hours.

Although some isolation methods, such as size exclusion chromatography and precipitation, can be performed more quickly, isolation via differential centrifugation results in fewer particles in the size range potentially LPs, lower intensity of LP markers, higher 61–150 nm EVs to 0–60 nm EVs ratio, and higher intensity of EV markers [78]. Raman spectroscopy provides a comprehensive analysis of the circulating tumor-related molecular content. Besides, Raman spectroscopy has additional advantages, such as operator safety, elimination of disposables and analysis waste, fast analytical response of less than 2 min, reduction of the risk of errors because no intrusion or dilution are needed, and negligible maintenance costs. By employing the appropriate preprocessing steps, classification requires reduced computational time and capacity. Moreover, SVM classification based on Raman spectra is suitable to support the proper assessment of even complex biological samples, despite their high degree of variance. This approach may also support decision-making in challenging clinical cases, such as distinguishing between primary brain tumors and other metastatic brain malignancies.

Besides its advantages, our approach also has limiting factors. LPs and protein aggregates in the same size range of sEVs may co-isolate during the differential centrifugation. Accordingly, it is recommended to refer to the isolates as "particle profile with sEVs", "sEV-sized particles", or "sEV-enriched isolates". Because of this heterogeneity, it is also not evident whether the Raman-based classification differentiates the tumor-specific molecular

information concentrated in the circulating sEVs or different type of particles. Isolation purity could be improved by combining different isolation methods and examining plasma instead of serum [78].

Isolates from serum may be enriched not only with tumor tissue-derived sEVs but also with EVs released by red blood cells, platelets and immune cells. As it is not revealed whether sEVs from other sources are analytical noise or carriers of relevant information, it might be worthwhile to distinguish tumor tissue-derived sEVs based on surface markers and to perform Raman spectroscopic analyses only on them in the future [76].

In conclusion, our results provide a proof of principle for a novel detection technology that might be utilized to develop a relatively easy-to-execute and appropriate method, which could have the potential to support and simplify the diagnosis and monitoring of CNS tumors in the future. However, clinical applicability definitely requires further development.

4. Materials and Methods

4.1. Patients

Blood samples of 138 patients treated at the Department of Neurosurgery at the University of Debrecen were analyzed. Samples were obtained from patients with GBM, BM, M. Patients with spinal disc herniation (a non-cancerous CNS disease) served as control CTRL (Table 1).

Table 1. Patient cohort.

Patient Groups	No. of Patients	Age (years)			Sex	
		Range	Mean	Median	Male (%)	Female (%)
CTRL	36	20–81	53.6	54	16 (44.4)	20 (55.6)
GBM	46	33–82	64.3	66	28 (60.9)	18 (39.1)
BM	28	42–82	63.5	62.6	18 (64.3)	10 (35.7)
M	28	30–79	58.6	60	5 (17.9)	23 (82.1)

Each patient signed an informed consent form. The study was conducted in accordance with the Declaration of Helsinki, and ethical approval was obtained from two independent bodies (51450-2/2015/EKU (0411/15), Medical Research Council, Scientific and Research Ethics Committee, Budapest, October 30, 2015 and 121/2019-SZTE, University of Szeged, Human Investigation Review Board, Albert Szent-Györgyi Clinical Centre, Szeged, 19 July 2019)

4.2. Preparation of Serum Samples, sEV Isolation and Characterization

Preparation of serum samples was described in our previously published article [20].

Briefly, after 1 h of blood clotting at room temperature, sEV isolation from serum samples was performed via differential centrifugation (20 min at 3000× *g*, 10 °C; 30 min at 10,000× *g*, 4 °C; 70 min at 100,000× *g*, 4 °C). After the last centrifugation step, the pellet was resuspended in Dulbecco's phosphate-buffered saline (DPBS) and was stored at −80 °C until further processing.

To characterize sEVs, we followed the main suggestions and requirements included in the guideline 'Minimal Information for Studies of Extracellular Vesicles 2018' (MISEV 2018) [17].

sEVs were diluted in particle-free DPBS and analyzed using a NanoSight NS300 instrument with 532 nm laser (Malvern Panalytical Ltd., Malvern, UK). Six videos of 60 s were recorded for each sample under constant settings (Camera level: 15; Threshold: 4, 25 °C; 60–80 particles/frame) and analyzed to obtain data on size distribution and particle concentration.

Classical EV markers were presented by Western blot analyses using NuPAGE reagents and an XCell SureLock Mini-Cell System (Thermo Fisher Scientific, Waltham, MA, USA) according to the manufacturer's protocols. For detection of the CD81, Alix and Calnexin

markers, we used rabbit anti-human CD81 (1:1000, Sigma-Aldrich, St. Louis, MO, USA), rabbit anti-human Alix (1:1000, Sigma-Aldrich, St. Louis, MO, USA) and rabbit anti-human Calnexin (1:10,000), Sigma-Aldrich, St. Louis, MO, USA) primary antibody and HRP-conjugated anti-rabbit IgG (1:1000, R&D Systems, Minneapolis, MN, USA) secondary antibody. THP-1 cell line (ATCC, Teddington, UK) lysate was used for positive control for Calnexin.

In order to examine sEV morphology, TEM analysis was performed using a Tecnai G2 20 X-Twin type instrument (FEI, Hillsboro, OR, USA), operating at an acceleration voltage of 200 kV. For TEM measurements, the samples were dropped on a grid (carbon film with 200 Mesh copper grids (CF200-Cu, Electron Microscopy Sciences, Hatfield, PA, USA) and dried without staining or other fixation procedure.

4.3. Raman Spectroscopy

Raman characterization of sEVs was carried out with a Senterra II microscope (Bruker) in backscattering configuration. The samples were centrifuged, drop-casted on a calcium fluoride substrate and air-dried at room temperature before the analysis. All the samples were analyzed using the same configuration parameters based on preliminary studies: nominal laser power 12.5 mW, integration time 30 s (2 coadditions), interferometer resolution 1.5 cm^{-1}, excitation wavelength 532 nm. The spectra from all the samples were collected by using a 50× optical objective (Olympus). The described optical setup produces a laser spot of approx. 15 µm, which is the sampling area of the Raman spectra, and it is much smaller than the average size of the air-dried sample of approx. 4 mm, thus the Raman microscope operator can finely tune the position of the sampling spot and avoid duplication. The spectra were baseline-corrected before being averaged (5 spectra per sample) using the OPUS software available with the Bruker equipment. Spectral range between 801 cm^{-1} and 3100.5 cm^{-1} was used for further analyses (Table S2).

4.4. Data Adjustment

Row normalization of baseline-corrected data was performed using the SNV method. SNV transformed the mean to 0 and standard deviation to 1, making all spectra comparable in terms of intensity.

PCA with unit variance scaling was applied on the SNV-normalized spectra [79]. PCA served to reduce the dimensions of multivariate data by transforming the original variables (wavenumbers) into a smaller number of new variables, i.e., the PCs.

Data adjustment was performed using the Orange 3.27.0 software (Ljubljana, Slovenia).

4.5. Classification

To develop and test a classification algorithm, the spectra for the samples from the four patient groups were compared pairwise (each patient group was compared to the control, and BM vs. GBM was compared). Sample classification was carried out using the linear SVM algorithm, yielding classification models for each paired group. First, the data were randomly split into train and test sets in a ratio of 90:10. Using the train set, SVM attempts were executed to find a hyperplane that can separate the compared groups in the PCA-transformed space. The process yielded a trained SVM model. Then, the trained SVM model ordered group-membership scores (from 0 to 1) to the test samples based on their positions and distances from the separating hyperplane. In practice, the decisions were made based on the location of the test samples from the plane, which is expressed by their group-membership scores. To make predictions about the test samples, a minimum threshold for the group-membership score was determined. Test samples with scores above this threshold were classified into the target group of interest. In each case, the train–test split was repeated ten times.

Classification efficacy was assessed by sensitivity (proportion of correctly identified positive samples), specificity (proportion of correctly identified negative samples), and by the AUC value obtained from the ROC analysis [66]. Classification and efficacy evaluations

were performed using the Orange 3.27.0 and GraphPad Prism 8.4.3 (San Diego, CA, USA) software packages.

4.6. Determining the Spectral Differences

The correlation between the obtained PCs and the different groups was determined by the FreeViz method [80]. Briefly, the FreeViz method displays multivariate data in a 2-dimensional scatterplot to separate samples from different patient groups. In the FreeViz plots, the samples and PCs are represented with dots and vectors, respectively (Figure 4). Since FreeViz optimized the display concerning the patient groups, the PCs that played a more important role in classification generally had longer vectors. Directions of the PC vectors were also revealing. When a region in the graph was mainly populated by samples of a certain group, the PC vectors in that direction could be regarded as good indicators of this group membership. The more a PC vector was approaching perpendicularity relative to the line separating the groups, the more useful it was for distinguishing them. Between-group statistical differences in PCs were analyzed using Welch's *t*-test. Regarding that PCs are the linear combination of the original variables (wavenumbers), it is possible to determine the wavenumbers that have the largest contribution to a given PC.

Values of $p < 0.05$ were considered significant. FreeViz was performed using the Orange 3.78.0 software [81].

5. Conclusions

Our study aimed to classify serum-derived sEVs from four patient groups based on their Raman spectral signatures. To the best of our knowledge, we are the first group to investigate the potential role of serum-derived sEVs in the diagnosis of CNS tumors using Raman spectroscopy. Based on various metrics, the classification efficiency proved to be excellent. In conclusion, our results support that Raman spectroscopic analysis of circulating sEV-enriched isolates is a promising liquid-biopsy-based method that could be further developed in order to be applicable in the diagnosis of CNS tumors. Our easy-to-perform analysis offers a novel detection technology that might be utilized in method developments aiming to simplify the diagnosis and monitoring of CNS tumors, and thus it might have the potential to be integrated into clinical practice in the future.

Supplementary Materials: The following are available online at https://www.mdpi.com/2072-6694/13/6/1407/s1. Figure S1: Original images of the Western blot analysis; Figure S2: PCA score plots of the selected PCs; Table S1: Tabular form of the discriminative spectral differences; Table S2: The baseline-corrected Raman spectroscopic data.

Author Contributions: Conceptualization, K.B.; methodology, M.B., G.D., J.G.-P. and K.B.; validation, K.K., A.J. and S.K.; formal analysis, M.B. and G.D.; investigation, M.B., G.D., J.G.-P., M.H. and E.G.-S.; resources, A.K., P.H. and T.B.; writing—original draft preparation, M.B. and G.D.; writing—review and editing, M.B., G.D., K.B., M.H. and E.G.-S.; visualization, M.B.; supervision, K.B., Z.K. and A.K.; project administration, M.B. and K.B.; funding acquisition, K.B. All authors have read and agreed to the published version of the manuscript.

Funding: This study was supported by the following research grants: GINOP-2.3.2-15-2016-00015 (K.B.); GINOP-2.2.1-15-2017-00052 (K.B.), 2017-1.2.1-NKP-2017-00002 "National Brain Research Program NAP 2.0" (A.K.), ÚNKP-19-4-SZTE-63 (K.B.), János Bolyai Research Scholarship of the Hungarian Academic of Sciences (K.B), ÚNKP-20-3-New National Excellence Program of the Ministry for Innovation and Technology from the source of the National Research, Development and Innovation Fund (M.B.), EFOP 3.6.3-VEKOP-16-2017-00009 (M.B.).

Institutional Review Board Statement: The study was conducted in accordance with the Declaration of Helsinki, and ethical approval was obtained from two independent bodies (51450-2/2015/EKU (0411/15), Medical Research Council, Scientific and Research Ethics Committee, Budapest, 30 October 2015 and 121/2019-SZTE, University of Szeged, Human Investigation Review Board, Albert Szent-Györgyi Clinical Centre, Szeged, 19 July 2019).

Informed Consent Statement: Informed consent was obtained from all subjects involved in the study.

Data Availability Statement: All datasets generated during the current study are available from the corresponding author upon reasonable request.

Acknowledgments: The authors thank Lilla Pintér for her technical assistance. The authors thank Dóra Bokor, for proofreading the manuscript. The authors thank László Janovák and Ágota Imre-Deák for the transmission electron microscopic analysis.

Conflicts of Interest: The authors declare no conflict of interest.

References

1. Yáñez-Mó, M.; Siljander, P.R.-M.; Andreu, Z.; Bedina Zavec, A.; Borràs, F.E.; Buzas, E.I.; Buzas, K.; Casal, E.; Cappello, F.; Carvalho, J.; et al. Biological Properties of Extracellular Vesicles and Their Physiological Functions. *J. Extracell. Vesicles* **2015**, *4*, 27066. [CrossRef] [PubMed]
2. Takeuchi, T.; Suzuki, M.; Fujikake, N.; Popiel, H.A.; Kikuchi, H.; Futaki, S.; Wada, K.; Nagai, Y. Intercellular Chaperone Transmission via Exosomes Contributes to Maintenance of Protein Homeostasis at the Organismal Level. *Proc. Natl. Acad. Sci. USA* **2015**, *112*, E2497–E2506. [CrossRef]
3. Harmati, M.; Gyukity-Sebestyen, E.; Dobra, G.; Janovak, L.; Dekany, I.; Saydam, O.; Hunyadi-Gulyas, E.; Nagy, I.; Farkas, A.; Pankotai, T.; et al. Small Extracellular Vesicles Convey the Stress-Induced Adaptive Responses of Melanoma Cells. *Sci. Rep.* **2019**, *9*, 15329. [CrossRef]
4. Desdín-Micó, G.; Mittelbrunn, M. Role of Exosomes in the Protection of Cellular Homeostasis. *Cell Adhes. Migr.* **2017**, *11*, 127–134. [CrossRef] [PubMed]
5. Mathivanan, S.; Simpson, R.J. ExoCarta: A Compendium of Exosomal Proteins and RNA. *Proteomics* **2009**, *9*, 4997–5000. [CrossRef] [PubMed]
6. Schorey, J.S.; Bhatnagar, S. Exosome Function: From Tumor Immunology to Pathogen Biology. *Traffic* **2008**, *9*, 871–881. [CrossRef] [PubMed]
7. Nogués, L.; Benito-Martin, A.; Hergueta-Redondo, M.; Peinado, H. The Influence of Tumour-Derived Extracellular Vesicles on Local and Distal Metastatic Dissemination. *Mol. Asp. Med.* **2018**, *60*, 15–26. [CrossRef]
8. Hoshino, A.; Costa-Silva, B.; Shen, T.-L.; Rodrigues, G.; Hashimoto, A.; Tesic Mark, M.; Molina, H.; Kohsaka, S.; Di Giannatale, A.; Ceder, S.; et al. Tumour Exosome Integrins Determine Organotropic Metastasis. *Nature* **2015**, *527*, 329–335. [CrossRef]
9. Costa-Silva, B.; Aiello, N.M.; Ocean, A.J.; Singh, S.; Zhang, H.; Thakur, B.K.; Becker, A.; Hoshino, A.; Mark, M.T.; Molina, H.; et al. Pancreatic Cancer Exosomes Initiate Pre-Metastatic Niche Formation in the Liver. *Nat. Cell Biol.* **2015**, *17*, 816–826. [CrossRef]
10. Liu, Y.; Gu, Y.; Han, Y.; Zhang, Q.; Jiang, Z.; Zhang, X.; Huang, B.; Xu, X.; Zheng, J.; Cao, X. Tumor Exosomal RNAs Promote Lung Pre-Metastatic Niche Formation by Activating Alveolar Epithelial TLR3 to Recruit Neutrophils. *Cancer Cell* **2016**, *30*, 243–256. [CrossRef]
11. Zeng, Z.; Li, Y.; Pan, Y.; Lan, X.; Song, F.; Sun, J.; Zhou, K.; Liu, X.; Ren, X.; Wang, F.; et al. Cancer-Derived Exosomal MiR-25-3p Promotes Pre-Metastatic Niche Formation by Inducing Vascular Permeability and Angiogenesis. *Nat. Commun.* **2018**, *9*, 5395. [CrossRef] [PubMed]
12. Feng, W.; Dean, D.C.; Hornicek, F.J.; Shi, H.; Duan, Z. Exosomes Promote Pre-Metastatic Niche Formation in Ovarian Cancer. *Mol. Cancer* **2019**, *18*, 124. [CrossRef] [PubMed]
13. Chen, G.; Huang, A.C.; Zhang, W.; Zhang, G.; Wu, M.; Xu, W.; Yu, Z.; Yang, J.; Wang, B.; Sun, H.; et al. Exosomal PD-L1 Contributes to Immunosuppression and Is Associated with Anti-PD-1 Response. *Nature* **2018**, *560*, 382–386. [CrossRef]
14. Lener, T.; Gimona, M.; Aigner, L.; Börger, V.; Buzas, E.; Camussi, G.; Chaput, N.; Chatterjee, D.; Court, F.A.; del Portillo, H.A.; et al. Applying Extracellular Vesicles Based Therapeutics in Clinical Trials—An ISEV Position Paper. *J. Extracell. Vesicles* **2015**, *4*, 30087. [CrossRef]
15. Ma, C.; Jiang, F.; Ma, Y.; Wang, J.; Li, H.; Zhang, J. Isolation and Detection Technologies of Extracellular Vesicles and Application on Cancer Diagnostic. *Dose Response* **2019**, *17*, 1559325819891004. [CrossRef]
16. Sheridan, C. Exosome Cancer Diagnostic Reaches Market. *Nat. Biotechnol.* **2016**, *34*, 359–360. [CrossRef] [PubMed]
17. Théry, C.; Witwer, K.W.; Aikawa, E.; Alcaraz, M.J.; Anderson, J.D.; Andriantsitohaina, R.; Antoniou, A.; Arab, T.; Archer, F.; Atkin-Smith, G.K.; et al. Minimal Information for Studies of Extracellular Vesicles 2018 (MISEV2018): A Position Statement of the International Society for Extracellular Vesicles and Update of the MISEV2014 Guidelines. *J. Extracell. Vesicles* **2018**, *7*, 1535750. [CrossRef]
18. Colombo, M.; Raposo, G.; Théry, C. Biogenesis, Secretion, and Intercellular Interactions of Exosomes and Other Extracellular Vesicles. *Annu. Rev. Cell Dev. Biol.* **2014**, *30*, 255–289. [CrossRef]
19. Ruhen, O.; Meehan, K. Tumor-Derived Extracellular Vesicles as a Novel Source of Protein Biomarkers for Cancer Diagnosis and Monitoring. *Proteomics* **2019**, *19*, 1800155. [CrossRef]
20. Dobra, G.; Bukva, M.; Szabo, Z.; Bruszel, B.; Harmati, M.; Gyukity-Sebestyen, E.; Jenei, A.; Szucs, M.; Horvath, P.; Biro, T.; et al. Small Extracellular Vesicles Isolated from Serum May Serve as Signal-Enhancers for the Monitoring of CNS Tumors. *IJMS* **2020**, *21*, 5359. [CrossRef]
21. Choy, C.; Jandial, R. Breast Cancer Exosomes Breach the Blood-Brain Barrier. *Neurosurgery* **2016**, *78*, N10–N11. [CrossRef]

22. García-Romero, N.; Carrión-Navarro, J.; Esteban-Rubio, S.; Lázaro-Ibáñez, E.; Peris-Celda, M.; Alonso, M.M.; Guzmán-De-Villoria, J.; Fernández-Carballal, C.; de Mendivil, A.O.; García-Duque, S.; et al. DNA Sequences within Glioma-Derived Extracellular Vesicles Can Cross the Intact Blood-Brain Barrier and Be Detected in Peripheral Blood of Patients. *Oncotarget* **2017**, *8*, 1416–1428. [CrossRef]
23. Scavo, M.P.; Depalo, N.; Tutino, V.; De Nunzio, V.; Ingrosso, C.; Rizzi, F.; Notarnicola, M.; Curri, M.L.; Giannelli, G. Exosomes for Diagnosis and Therapy in Gastrointestinal Cancers. *Int. J. Mol. Sci.* **2020**, *21*, 367. [CrossRef] [PubMed]
24. Melo, S.A.; Luecke, L.B.; Kahlert, C.; Fernandez, A.F.; Gammon, S.T.; Kaye, J.; LeBleu, V.S.; Mittendorf, E.A.; Weitz, J.; Rahbari, N.; et al. Glypican-1 Identifies Cancer Exosomes and Detects Early Pancreatic Cancer. *Nature* **2015**, *523*, 177–182. [CrossRef]
25. Aldape, K.; Brindle, K.M.; Chesler, L.; Chopra, R.; Gajjar, A.; Gilbert, M.R.; Gottardo, N.; Gutmann, D.H.; Hargrave, D.; Holland, E.C.; et al. Challenges to Curing Primary Brain Tumours. *Nat. Rev. Clin. Oncol.* **2019**, *16*, 509–520. [CrossRef]
26. Shankar, G.M.; Balaj, L.; Stott, S.L.; Nahed, B.; Carter, B.S. Liquid Biopsy for Brain Tumors. *Expert Rev. Mol. Diagn.* **2017**, *17*, 943–947. [CrossRef]
27. Garden, G.A.; Campbell, B.M. Glial Biomarkers in Human Central Nervous System Disease: Glial Biomarkers in Human CNS Disease. *Glia* **2016**, *64*, 1755–1771. [CrossRef] [PubMed]
28. Neska-Matuszewska, M.; Bladowska, J.; Sąsiadek, M.; Zimny, A. Differentiation of Glioblastoma Multiforme, Metastases and Primary Central Nervous System Lymphomas Using Multiparametric Perfusion and Diffusion MR Imaging of a Tumor Core and a Peritumoral Zone-Searching for a Practical Approach. *PLoS ONE* **2018**, *13*, e0191341. [CrossRef] [PubMed]
29. Pope, W.B.; Brandal, G. Conventional and Advanced Magnetic Resonance Imaging in Patients with High-Grade Glioma. *Q. J. Nucl. Med. Mol. Imaging* **2018**, *62*, 239–253. [CrossRef] [PubMed]
30. Peca, C.; Pacelli, R.; Elefante, A.; Del Basso De Caro, M.L.; Vergara, P.; Mariniello, G.; Giamundo, A.; Maiuri, F. Early Clinical and Neuroradiological Worsening after Radiotherapy and Concomitant Temozolomide in Patients with Glioblastoma: Tumour Progression or Radionecrosis? *Clin. Neurol. Neurosurg.* **2009**, *111*, 331–334. [CrossRef]
31. Saenz-Antoñanzas, A.; Auzmendi-Iriarte, J.; Carrasco-Garcia, E.; Moreno-Cugnon, L.; Ruiz, I.; Villanua, J.; Egaña, L.; Otaegui, D.; Samprón, N.; Matheu, A. Liquid Biopsy in Glioblastoma: Opportunities, Applications and Challenges. *Cancers* **2019**, *11*, 950. [CrossRef]
32. Patel, A.P.; Tirosh, I.; Trombetta, J.J.; Shalek, A.K.; Gillespie, S.M.; Wakimoto, H.; Cahill, D.P.; Nahed, B.V.; Curry, W.T.; Martuza, R.L.; et al. Single-Cell RNA-Seq Highlights Intratumoral Heterogeneity in Primary Glioblastoma. *Science* **2014**, *344*, 1396–1401. [CrossRef] [PubMed]
33. Best, M.G.; Sol, N.; Zijl, S.; Reijneveld, J.C.; Wesseling, P.; Wurdinger, T. Liquid Biopsies in Patients with Diffuse Glioma. *Acta Neuropathol.* **2015**, *129*, 849–865. [CrossRef] [PubMed]
34. Good, D.M.; Thongboonkerd, V.; Novak, J.; Bascands, J.-L.; Schanstra, J.P.; Coon, J.J.; Dominiczak, A.; Mischak, H. Body Fluid Proteomics for Biomarker Discovery: Lessons from the Past Hold the Key to Success in the Future. *J. Proteome Res.* **2007**, *6*, 4549–4555. [CrossRef]
35. Marrugo-Ramírez, J.; Mir, M.; Samitier, J. Blood-Based Cancer Biomarkers in Liquid Biopsy: A Promising Non-Invasive Alternative to Tissue Biopsy. *Int. J. Mol. Sci.* **2018**, *19*, 2877. [CrossRef]
36. Miyauchi, E.; Furuta, T.; Ohtsuki, S.; Tachikawa, M.; Uchida, Y.; Sabit, H.; Obuchi, W.; Baba, T.; Watanabe, M.; Terasaki, T.; et al. Identification of Blood Biomarkers in Glioblastoma by SWATH Mass Spectrometry and Quantitative Targeted Absolute Proteomics. *PLoS ONE* **2018**, *13*, e0193799. [CrossRef] [PubMed]
37. Lin, B.; White, J.T.; Wu, J.; Lele, S.; Old, L.J.; Hood, L.; Odunsi, K. Deep Depletion of Abundant Serum Proteins Reveals Low-Abundant Proteins as Potential Biomarkers for Human Ovarian Cancer. *Prot. Clin. Appl.* **2009**, *3*, 853–861. [CrossRef] [PubMed]
38. Cagney, D.N.; Sul, J.; Huang, R.Y.; Ligon, K.L.; Wen, P.Y.; Alexander, B.M. The FDA NIH Biomarkers, EndpointS, and Other Tools (BEST) Resource in Neuro-Oncology. *Neuro Oncol.* **2018**, *20*, 1162–1172. [CrossRef] [PubMed]
39. Gollapalli, K.; Ray, S.; Srivastava, R.; Renu, D.; Singh, P.; Dhali, S.; Bajpai Dikshit, J.; Srikanth, R.; Moiyadi, A.; Srivastava, S. Investigation of Serum Proteome Alterations in Human Glioblastoma Multiforme. *Proteomics* **2012**, *12*, 2378–2390. [CrossRef] [PubMed]
40. Figueroa, J.M.; Carter, B.S. Detection of Glioblastoma in Biofluids. *J. Neurosurg.* **2018**, *129*, 334–340. [CrossRef] [PubMed]
41. Choi, D.; Montermini, L.; Kim, D.-K.; Meehan, B.; Roth, F.P.; Rak, J. The Impact of Oncogenic EGFRvIII on the Proteome of Extracellular Vesicles Released from Glioblastoma Cells. *Mol. Cell Proteom.* **2018**, *17*, 1948–1964. [CrossRef] [PubMed]
42. Pence, I.; Mahadevan-Jansen, A. Clinical Instrumentation and Applications of Raman Spectroscopy. *Chem. Soc. Rev.* **2016**, *45*, 1958–1979. [CrossRef] [PubMed]
43. Gualerzi, A.; Niada, S.; Giannasi, C.; Picciolini, S.; Morasso, C.; Vanna, R.; Rossella, V.; Masserini, M.; Bedoni, M.; Ciceri, F.; et al. Raman Spectroscopy Uncovers Biochemical Tissue-Related Features of Extracellular Vesicles from Mesenchymal Stromal Cells. *Sci. Rep.* **2017**, *7*, 9820. [CrossRef] [PubMed]
44. Maisano, D.; Mimmi, S.; Russo, R.; Fioravanti, A.; Fiume, G.; Vecchio, E.; Nisticò, N.; Quinto, I.; Iaccino, E. Uncovering the Exosomes Diversity: A Window of Opportunity for Tumor Progression Monitoring. *Pharmaceuticals* **2020**, *13*, 180. [CrossRef]
45. Harris, A.T.; Lungari, A.; Needham, C.J.; Smith, S.L.; Lones, M.A.; Fisher, S.E.; Yang, X.B.; Cooper, N.; Kirkham, J.; Smith, D.A.; et al. Potential for Raman Spectroscopy to Provide Cancer Screening Using a Peripheral Blood Sample. *Head Neck Oncol.* **2009**, *1*, 34. [CrossRef]

46. Pichardo-Molina, J.L.; Frausto-Reyes, C.; Barbosa-García, O.; Huerta-Franco, R.; González-Trujillo, J.L.; Ramírez-Alvarado, C.A.; Gutiérrez-Juárez, G.; Medina-Gutiérrez, C. Raman Spectroscopy and Multivariate Analysis of Serum Samples from Breast Cancer Patients. *Lasers Med. Sci.* **2007**, *22*, 229–236. [CrossRef]
47. Mehta, K.; Atak, A.; Sahu, A.; Srivastava, S.; Krishna C, M. An Early Investigative Serum Raman Spectroscopy Study of Meningioma. *Analyst* **2018**, *143*, 1916–1923. [CrossRef] [PubMed]
48. Park, J.; Hwang, M.; Choi, B.; Jeong, H.; Jung, J.; Kim, H.K.; Hong, S.; Park, J.; Choi, Y. Exosome Classification by Pattern Analysis of Surface-Enhanced Raman Spectroscopy Data for Lung Cancer Diagnosis. *Anal. Chem.* **2017**, *89*, 6695–6701. [CrossRef]
49. Carmicheal, J.; Hayashi, C.; Huang, X.; Liu, L.; Lu, Y.; Krasnoslobodtsev, A.; Lushnikov, A.; Kshirsagar, P.G.; Patel, A.; Jain, M.; et al. Label-Free Characterization of Exosome via Surface Enhanced Raman Spectroscopy for the Early Detection of Pancreatic Cancer. *Nanomed. Nanotechnol. Biol. Med.* **2019**, *16*, 88–96. [CrossRef]
50. Ostrom, Q.T.; Gittleman, H.; Truitt, G.; Boscia, A.; Kruchko, C.; Barnholtz-Sloan, J.S. CBTRUS Statistical Report: Primary Brain and Other Central Nervous System Tumors Diagnosed in the United States in 2011–2015. *Neuro Oncol.* **2018**, *20*, iv1–iv86. [CrossRef]
51. Fox, B.D.; Cheung, V.J.; Patel, A.J.; Suki, D.; Rao, G. Epidemiology of Metastatic Brain Tumors. *Neurosurg. Clin. N. Am.* **2011**, *22*, 1–6. [CrossRef] [PubMed]
52. Zhi, F.; Shao, N.; Li, B.; Xue, L.; Deng, D.; Xu, Y.; Lan, Q.; Peng, Y.; Yang, Y. A Serum 6-MiRNA Panel as a Novel Non-Invasive Biomarker for Meningioma. *Sci. Rep.* **2016**, *6*, 32067. [CrossRef]
53. Taverna, S.; Giallombardo, M.; Gil-Bazo, I.; Carreca, A.P.; Castiglia, M.; Chacártegui, J.; Araujo, A.; Alessandro, R.; Pauwels, P.; Peeters, M.; et al. Exosomes Isolation and Characterization in Serum Is Feasible in Non-Small Cell Lung Cancer Patients: Critical Analysis of Evidence and Potential Role in Clinical Practice. *Oncotarget* **2016**, *7*, 28748–28760. [CrossRef] [PubMed]
54. Osti, D.; Del Bene, M.; Rappa, G.; Santos, M.; Matafora, V.; Richichi, C.; Faletti, S.; Beznoussenko, G.V.; Mironov, A.; Bachi, A.; et al. Clinical Significance of Extracellular Vesicles in Plasma from Glioblastoma Patients. *Clin. Cancer Res.* **2019**, *25*, 266–276. [CrossRef]
55. Lázaro-Ibáñez, E.; Sanz-Garcia, A.; Visakorpi, T.; Escobedo-Lucea, C.; Siljander, P.; Ayuso-Sacido, Á.; Yliperttula, M. Different GDNA Content in the Subpopulations of Prostate Cancer Extracellular Vesicles: Apoptotic Bodies, Microvesicles, and Exosomes. *Prostate* **2014**, *74*, 1379–1390. [CrossRef]
56. König, L.; Kasimir-Bauer, S.; Bittner, A.-K.; Hoffmann, O.; Wagner, B.; Santos Manvailer, L.F.; Kimmig, R.; Horn, P.A.; Rebmann, V. Elevated Levels of Extracellular Vesicles are Associated with Therapy Failure and Disease Progression in Breast Cancer Patients Undergoing Neoadjuvant Chemotherapy. *Oncoimmunology* **2018**, *7*, e1376153. [CrossRef]
57. Gercel-Taylor, C.; Atay, S.; Tullis, R.H.; Kesimer, M.; Taylor, D.D. Nanoparticle Analysis of Circulating Cell-Derived Vesicles in Ovarian Cancer Patients. *Anal. Biochem.* **2012**, *428*, 44–53. [CrossRef]
58. Liu, M.-L.; Werth, V.P.; Williams, K.J. Blood Plasma versus Serum: Which Is Right for Sampling Circulating Membrane Microvesicles in Human Subjects? *Ann. Rheum. Dis.* **2019**, *79*, e73. [CrossRef]
59. Ji, Q.; Ji, Y.; Peng, J.; Zhou, X.; Chen, X.; Zhao, H.; Xu, T.; Chen, L.; Xu, Y. Increased Brain-Specific MiR-9 and MiR-124 in the Serum Exosomes of Acute Ischemic Stroke Patients. *PLoS ONE* **2016**, *11*, e0163645. [CrossRef] [PubMed]
60. Cunha, C.; Silva, A.J.; Pereira, P.; Vaz, R.; Gonçalves, R.M.; Barbosa, M.A. The Inflammatory Response in the Regression of Lumbar Disc Herniation. *Arthritis Res. Ther.* **2018**, *20*, 251. [CrossRef] [PubMed]
61. Gardiner, C.; Harrison, P.; Belting, M.; Böing, A.; Campello, E.; Carter, B.S.; Collier, M.E.; Coumans, F.; Ettelaie, C.; van Es, N.; et al. Extracellular Vesicles, Tissue Factor, Cancer and Thrombosis—Discussion Themes of the ISEV 2014 Educational Day. *J. Extracell. Vesicles* **2015**, *4*, 26901. [CrossRef] [PubMed]
62. Anderson, K.S.; LaBaer, J. The Sentinel Within: Exploiting the Immune System for Cancer Biomarkers †. *J. Proteome Res.* **2005**, *4*, 1123–1133. [CrossRef] [PubMed]
63. Wen, C.; Seeger, R.C.; Fabbri, M.; Wang, L.; Wayne, A.S.; Jong, A.Y. Biological Roles and Potential Applications of Immune Cell-Derived Extracellular Vesicles. *J. Extracell. Vesicles* **2017**, *6*, 1400370. [CrossRef]
64. Salem, N.; Hussein, S. Data Dimensional Reduction and Principal Components Analysis. *Procedia Comput. Sci.* **2019**, *163*, 292–299. [CrossRef]
65. Lyng, F.M.; Traynor, D.; Nguyen, T.N.Q.; Meade, A.D.; Rakib, F.; Al-Saady, R.; Goormaghtigh, E.; Al-Saad, K.; Ali, M.H. Discrimination of Breast Cancer from Benign Tumours Using Raman Spectroscopy. *PLoS ONE* **2019**, *14*, e0212376. [CrossRef]
66. Hajian-Tilaki, K. Receiver Operating Characteristic (ROC) Curve Analysis for Medical Diagnostic Test Evaluation. *Casp. J. Intern. Med.* **2013**, *4*, 627–635.
67. Mandrekar, J.N. Receiver Operating Characteristic Curve in Diagnostic Test Assessment. *J. Thorac. Oncol.* **2010**, *5*, 1315–1316. [CrossRef]
68. Cervantes, J.; Garcia-Lamont, F.; Rodríguez-Mazahua, L.; Lopez, A. A Comprehensive Survey on Support Vector Machine Classification: Applications, Challenges and Trends. *Neurocomputing* **2020**, *408*, 189–215. [CrossRef]
69. Zheng, C.; Qing, S.; Wang, J.; Lü, G.; Li, H.; Lü, X.; Ma, C.; Tang, J.; Yue, X. Diagnosis of Cervical Squamous Cell Carcinoma and Cervical Adenocarcinoma Based on Raman Spectroscopy and Support Vector Machine. *Photodiagn. Photodyn. Ther.* **2019**, *27*, 156–161. [CrossRef]
70. Li, S.; Guo, Z.; Liu, Z. Surface-Enhanced Raman Spectroscopy + Support Vector Machine: A New Noninvasive Method for Prostate Cancer Screening? *Expert Rev. Anticancer Ther.* **2015**, *15*, 5–7. [CrossRef]
71. Socrates, G. *Infrared and Raman Characteristic Group Frequencies: Tables and Charts*, 3rd ed.; John Wiley & Sons Ltd: Chichester, UK, 2010; ISBN 9780470093078.

72. Zhou, W.; Wahl, D.R. Metabolic Abnormalities in Glioblastoma and Metabolic Strategies to Overcome Treatment Resistance. *Cancers* **2019**, *11*, 1231. [CrossRef]
73. Majem, B.; Nadal, E.; Muñoz-Pinedo, C. Exploiting Metabolic Vulnerabilities of Non Small Cell Lung Carcinoma. *Semin. Cell Dev. Biol.* **2020**, *98*, 54–62. [CrossRef]
74. Smolarz, M.; Pietrowska, M.; Matysiak, N.; Mielańczyk, Ł.; Widłak, P. Proteome Profiling of Exosomes Purified from a Small Amount of Human Serum: The Problem of Co-Purified Serum Components. *Proteomes* **2019**, *7*, 18. [CrossRef]
75. Sartori, M.T.; Della Puppa, A.; Ballin, A.; Saggiorato, G.; Bernardi, D.; Padoan, A.; Scienza, R.; d'Avella, D.; Cella, G. Prothrombotic State in Glioblastoma Multiforme: An Evaluation of the Procoagulant Activity of Circulating Microparticles. *J. Neurooncol.* **2011**, *104*, 225–231. [CrossRef]
76. Redzic, J.S.; Ung, T.H.; Graner, M.W. Glioblastoma Extracellular Vesicles: Reservoirs of Potential Biomarkers. *Pharm. Pers. Med.* **2014**, *7*, 65–77. [CrossRef]
77. Enciso-Martinez, A.; Van Der Pol, E.; Hau, C.M.; Nieuwland, R.; Van Leeuwen, T.G.; Terstappen, L.W.M.M.; Otto, C. Label-Free Identification and Chemical Characterisation of Single Extracellular Vesicles and Lipoproteins by Synchronous Rayleigh and Raman Scattering. *J. Extracell. Vesicles* **2020**, *9*, 1730134. [CrossRef]
78. Brennan, K.; Martin, K.; FitzGerald, S.P.; O'Sullivan, J.; Wu, Y.; Blanco, A.; Richardson, C.; Mc Gee, M.M. A Comparison of Methods for the Isolation and Separation of Extracellular Vesicles from Protein and Lipid Particles in Human Serum. *Sci. Rep.* **2020**, *10*, 1039. [CrossRef]
79. Rinnan, Å.; van den Berg, F.; Engelsen, S.B. Review of the Most Common Pre-Processing Techniques for near-Infrared Spectra. *TrAC Trends Anal. Chem.* **2009**, *28*, 1201–1222. [CrossRef]
80. Demšar, J.; Leban, G.; Zupan, B. FreeViz—An Intelligent Multivariate Visualization Approach to Explorative Analysis of Biomedical Data. *J. Biomed. Inform.* **2007**, *40*, 661–671. [CrossRef]
81. Demšar, J.; Tomaz, C.; Erjavec, A.; Gorup, C.; Hocevar, T.; Milutinovic, M.; Mozina, M.; Polajnar, M.; Toplak, M.; StariC, A.; et al. Orange: Data Mining Toolbox in Python. *J. Mach. Learn.* **2013**, *14*, 2349–2353.